# Chapter 7: The Earth's energy budget, climate feedbacks, and climate sensitivity

**Coordinating Lead Authors:**
Piers Forster (UK), Trude Storelvmo (Norway)

**Lead Authors:**
Kyle Armour (USA), William Collins (UK), Jean-Louis Dufresne (France), David Frame (New Zealand), Daniel Lunt (UK), Thorsten Mauritsen (Sweden, Denmark, Germany), Matthew Palmer (UK), Masahiro Watanabe (Japan), Martin Wild (Switzerland), Hua Zhang (China)

**Contributing Authors:**
Kari Alterskjær (Norway), Govindasamy Bala (India, USA), Nicolas Bellouin (UK), Sandrine Bony (France), Natalie Burls (South Africa), Catia M. Domingues (Australia, Brazil), Aaron Donohoe (USA), Mark Flanner (USA), Ryan Padron Flasher (Ecuador), Glen Harris (UK), Seiji Kato (USA), Zhanqing Li (USA), Norman Loeb (USA), Malte Meinshausen (Australia, Germany), Zebedee Nicholls (Australia), Anna Possner (Germany), Cristian Proistosescu (Romania), Johannes Quaas (Germany), Daniel Rosenfeld (Israel), Bjørn Samset (Norway), Abhishek Savita (Australia, India), Chris Smith (UK), Jessica Vial (France), Mark Zelinka (USA), Shuyun Zhao (China)

**Review Editors:**
Robert Colman (Australia), Matthews H. Damon (Canada), Venkatachalam Ramaswamy (USA)

**Chapter Scientists:**
Kari Alterskjær (Norway), Chris Smith (UK)

**Date of Draft:**
02/03/2020

**Notes:**
TSU Compiled Version

**Table of Content**

## Executive Summary


Changes in atmospheric composition, like those caused by anthropogenic greenhouse gas and aerosol emissions, impact climate through perturbations to the Earth's energy budget. Effective Radiative Forcings (ERFs) quantify these perturbations. Climate feedbacks that help understand the response of the climate system to a given forcing are assessed, as are useful aggregate measures of climate response, namely equilibrium climate sensitivity (ECS) and the transient climate response (TCR). This chapter also assesses emission metrics, which are used to quantify how the climate response of an emission of a gas compares to the response from an emission of carbon dioxide. This chapter takes the assessment of aerosol processes from Chapter 6 to quantify the total ERF for aerosols. Chapters 3, 4, 5 and 9 use the assessment of ERF, ECS and TCR from this chapter to help understand historic and future temperature changes, the response to cumulative emissions, the remaining carbon budget and sea-level rise respectively. Unless otherwise noted, the following summary findings confirm or strengthen related findings from the IPCC Fifth Assessment Report (AR5), the Special Report on Global Warming of 1.5ºC (SR1.5) and the Special Report on Ocean and Cryosphere in a Changing Climate (SROCC). Uncertainty is expressed as 5% to 95% *very likely* ranges unless otherwise noted.

### Earth's Energy Budget

**Total earth system warming, i.e., the total change in heat energy of the atmosphere, land, ice and ocean, increased by 406 ± 84 Zeta Joules over 1971-2018 and by 144 ± 24 over 2006-2018**. Ocean heat uptake represents > 90% of the total, with roughly 5% associated with heating of the land surface, about 2% with the melting of ice and less than 1% in heating of the atmosphere. Total earth system warming is a more reliable indicator of the rate of global climate change on decadal timescales than globally averaged near surface temperature (GSAT), because it exhibits less unforced variability. The rate of earth system warming has roughly doubled since the 1970s. (*high confidence*) {Box 7.2, 7.2.2, Table 7.1}

**The rate of total earth system warming corresponds to an Earth's energy imbalance of 0.54 ±0.11 W $m^{-2}$ for the period 1971-2018, increasing to 0.81± 0.14 W $m^{-2}$ for the period 2006-2018 expressed relative to the Earth's surface area (*high confidence*)**. There is increased confidence in the planetary heating rate since IPCC from a consistent closure of the sea-level budget for the period 1971-2018. Heat will continue to accumulate in the Earth system over the 21st Century driving future sea-level rise (*high confidence*) and there is *medium confidence* this will continue beyond 2100 for another century or more, even under strong mitigation of greenhouse gas emissions. {7.2.2, Box 7.2, Table 7.1, Chapter 9 Cross-Chapter Box 9.2}

**Multidecadal dimming and brightening trends in incoming solar radiation at the Earth's surface occurred at widespread locations. These trends are neither a local phenomenon nor a measurement artefact (*high confidence*).** Since AR5, additional evidence for a widespread decline in surface solar radiation is found in the observational records between the 1950s and 1980s ("dimming"), with a partial recovery at many observational sites thereafter ("brightening") (*high confidence*). Decadal variations in aerosol forcing are considered major contributors (*medium confidence*), but multi-decadal variability in cloudiness may also have played a role. There is *medium confidence* that downward thermal radiation has increased in recent decades, as expected from increased greenhouse gas concentrations and atmospheric warming, but *low confidence* in other energy flux changes and their contribution to the Earth's surface energy budget due to limited and uncertain measurements. {7.2.2}

### Effective Radiative Forcing

**The effective radiative forcing framework introduced in the AR5 has become well established and has been shown to provide a useful way of estimating temperature response. The ERF for a doubling of carbon dioxide since preindustrial is 4.0 ± 0.5 W $m^{-2}$.** Climate models' radiative transfer representation has improved since AR5, and they have ERFs that lie within 11% of the assessed best estimate. (*high*

*confidence*) {7.3.1, 7.3.2}

**The total anthropogenic ERF over the industrial era (1750-2018) was 2.53 W $m^{-2}$(1.58 to 3.34 $Wm^{-2}$ range). This is an 11% increase over AR5 estimates for 1750-2011.** Changes in atmospheric concentrations of greenhouse gases since 2011 and upwards revisions of their forcing efficiencies have led to a 15% increase in their ERF. This is partly offset by a new assessment of total aerosol ERF that is 22% more negative compared to AR5. (*high confidence*) {7.3.5}

**Greenhouse gases contribute an ERF of 3.63 $Wm^{-2}$ (3.27 to 3.97 $Wm^{-2}$ range) over the industrial era (1750-2018). 90% of this comes from the well-mixed greenhouse gases, with ozone and stratospheric water vapour changes contributing the remainder.** Carbon dioxide contributes the largest part of this forcing. There has also been an increase in the estimated shortwave forcing from methane. (*high confidence*) {7.3.2, 7.3.5}

**The reactive well-mixed greenhouses gases (methane, nitrous oxide, halocarbons) cause additional chemical adjustments to the atmosphere through changes in ozone and aerosols.** The ERF attributed to the chemical adjustments from methane emissions has a significant contribution (0.45±0.11 W $m^{-2}$).The net ERF attributable to halocarbons is smaller than the direct ERF due to their effect on ozone depletion, such that the range includes zero (0.0 to 0.16 W $m^{-2}$). *(high confidence*) {7.3.5}

**Aerosols contribute an ERF of -1.1 W $m^{-2}$ (-2.0 to -0.4 W $m^{-2}$ range) over the industrial era (1750-2018). The ERF due to aerosol-cloud interactions (ERFaci) contributes most (about 3/4) to the magnitude of the total aerosol ERF, with the remainder due to the forcing associated with aerosol-radiation interactions (ERFari).** There has been an increase in the estimated magnitude but a marked reduction in the uncertainty of the total aerosol ERF relative to AR5, supported by a combination of increased process-understanding, and progress in modelling and observational analyses. Observation-based and modelling-based estimates are now consistent with each other, in contrast to AR5. Compared to AR5, there has been a doubling of the magnitude of ERFaci, and a downward revision of the magnitude of ERFari. *(high confidence)* {7.3.3, 7.3.5}

**Climate Feedbacks and Sensitivity**

**AR5 assessed the net cloud feedback to be positive with *medium confidence*. Major advances in the understanding of cloud processes leads to a *high confidence* assessment that the net cloud feedback is positive and halved its uncertainty range.** Process understanding of tropical-marine low cloud feedbacks within GCMs has been complemented by a better understanding of cloud-climate interactions, satellite-based evidence, and explicit simulations using large-eddy simulations and cloud-system resolving models, altogether leading to strong evidence that the total cloud feedback amplifies global climate warming. The net cloud feedback is assessed to be +0.4 W $m^{-2}$ $°C^{-1}$ (–0.1 to 0.9 W $m^{-2}$ $°C^{-1}$ range). The CMIP5 and CMIP6 ranges of cloud feedback are similar to this assessed range, with CMIP6 having a slightly more positive median cloud feedback. (*high confidence*) {7.4.2, Figure 7.14, Table 7.10}

**Radiative feedbacks will become less negative (more amplifying) in the future as the spatial pattern of surface warming evolves, leading to an ECS that is substantially higher than has been traditionally inferred from warming over the historical record (*high confidence*).** This new understanding, along with updated estimates of historical temperature change, ERF, and energy imbalance, reconciles previously disparate ECS estimates. Historical surface temperature change since 1870 has shown relatively little warming in several key regions of positive feedbacks, including the eastern equatorial Pacific Ocean and the Southern Ocean, while showing greater warming in key regions of negative feedbacks, including the Western Pacific warm pool. Based on process understanding, climate modelling, and paleoclimate reconstructions, it is expected that future warming will become enhanced over the eastern Pacific Ocean (*medium confidence*) and Southern Ocean (*high confidence*) on centennial timescales. While there is robust agreement across climate model simulations that radiative feedbacks will become less negative in the future, there is currently insufficient evidence to quantify a *likely* range of the magnitude of those projected feedback changes. {7.4.4, 7.5.2, 7.5.3, Figure 7.18, Figure 7.19, Figure 7.20}

**Based on multiple lines of evidence the best estimate of ECS is 3 °C, the *likely* range is 2.5 to 4 °C and the *very likely* range is 2 to 5 °C. It is *virtually certain* that ECS is larger than 1.5 °C.** Substantial advances since AR5 have been made in quantifying ECS inferred from feedback process understanding (including dependence on climate state), the instrumental record, paleoclimates (including accounting for long-term Earth system feedbacks) and emergent constraints (a relationship between an observed variable and model field that can be related to the model ECS). There is a high level of agreement among the different lines of evidence. All lines of evidence help rule out ECS values below 1.5 °C. Emergent constraint evidence and paleo evidence help rule out ECS values above 5 °C, but it remains challenging to rule out low-probability but high-impact upper-end ECS, which is indicated by the notable asymmetry of the assessed ranges. (*high confidence*) {7.5.5}

**Based on process understanding, warming over the instrumental record, and emergent constraints, the best estimate of Transient Climate Response (TCR) is 1.8**°C**, the *likely* range is 1.4 to 2.2**°C **and the *very likely* range is 1.2 to 2.4 °C**. There is a high level of agreement among the different lines of evidence. (*high confidence*) {7.5.5}

**The distribution of CMIP6 models have higher average ECS and TCR values than the CMIP5 generation of models and the assessed ranges of ECS and TCR within this Report (*high confidence*).** The higher ECS and TCR values can be traced to changes in extra-tropical cloud feedbacks that have emerged from efforts to reduce biases in these clouds compared to satellite observations (*medium confidence*). The ranges of ECS and TCR from CMIP6 span the assessed *very likely* ranges, in contrast to previous assessment reports. The CMIP6 models with the highest ECS and TCRs values are assigned low probability, but are nevertheless useful as they provide insights into high-risk, low-probability futures. {7.5.6}

**Climate Response**

**It is unequivocal that human activity has had a warming effect on the Earth since 1750. Estimates of ERF, ECS and TCR from this Chapter give an estimate of the human-induced GSAT rise which assumes little knowledge of the observed warming and is more-or-less independent and in strong agreement with attributed warming deduced by Chapter 3. For the period 1750-2018, this human-forced trend is 1.1 °C (0.4 to 1.9 °C range) (*high confidence*).** This warming is comprised of a greenhouse warming that has an increasing trend and an aerosol cooling that has remained relatively constant over the last 20 years (*high confidence*). Changes in solar and volcanic activity are assessed to have contributed a small warming effect since 1750 (< 0.1°C, best estimate 0.04 °C) (*medium confidence*). {7.3.5, Chapter 3 ES, Cross-Chapter Box 7.1}

**Cloud feedbacks are the dominant source of uncertainty in this century's transient global warming under emission scenarios with continued $CO_2$ emissions, whereas uncertainty is dominated by aerosol ERF in scenarios reaching net zero $CO_2$ emissions.** Global ocean heat uptake is a relatively minor source of uncertainty in centennial warming. Carbon cycle feedbacks provide an increasing fraction of uncertainty on longer timescales. (*high confidence*) {7.5.7}

**It is now well understood that the Arctic warms more quickly than the Antarctic due to a combination of asymmetries in radiative feedbacks and ocean heat uptake between the poles, but that surface warming will eventually be amplified in both poles (*very high confidence*).** Since the AR5, progress has been made to understand the mechanisms of polar amplification and its uncertainty. A variety of factors all contribute to Arctic amplification, including positive surface-albedo and lapse-rate feedbacks as well as increases in poleward atmospheric latent heat transport and ocean heat transport, making it a ubiquitous feature of climate model simulations and observations. The Antarctic warms slower than the Arctic owing primarily to upwelling in the Southern Ocean. Compared with the models used for paleoclimate simulations in AR5, the polar amplification simulated in more recent models is now more consistent with paleoclimate observations of past warm climates. There is *high confidence* that the rate of Arctic surface warming will continue to exceed the global average over the 21st century. There is also *high confidence* that Antarctic amplification will emerge as the Southern Ocean surface warms on centennial timescales, although only *low confidence* of the feature emerging this century. {7.2.2, 7.4.4}

**Specifying short and long-lived greenhouse gases separately in emission scenarios generally improves the quantification of surface warming, compared to approaches that aggregate greenhouse gases using $CO_2$ equivalent emission metrics.** New metrics comparing pulse emissions of long-lived greenhouse gases with sustained emission changes in short-lived gases can lead to more equivalence in surface temperature response. Global Warming Potentials and Global Temperature change Potentials are larger compared to AR5, due to the methodological change of accounting for carbon-cycle responses. (*high confidence*) {7.6.1, Box 7.3, 7.6.2, 7.6.3}

## 7.1 Introduction, conceptual framework and innovations since IPCC AR5

This chapter assesses the major physical processes that drive changes in the Earth's energy budget, thereby affecting global warming. It focuses on documenting advances in scientific understanding of radiative forcing, climate feedbacks and climate sensitivity, and covers observations, theoretical developments and climate model evaluation. The chapter integrates elements that were dealt with separately in previous reports. Aggregate measures of climate response such as equilibrium climate sensitivity (ECS) and the transient climate response (TCR) are also assessed here (Box 7.1).

When the Earth's top-of-atmosphere energy budget is perturbed (a radiative forcing) over decadal timescales, the climate system responds by cooling or warming (i.e. the system gains or loses heat). Understanding of the Earth's energy budget helps us to understand the main physical processes driving climate change. It also provides a fundamental test of climate models and their projections. Energy budget related changes can be observed (Chapter 2). These observations are combined with the process understanding developed within this chapter to provide a useful test of model estimates of historic warming (Chapter 3) and temperature projections (Chapter 4). The energy budget also helps us to understand the relationship between anthropogenic emissions (Chapters 5 and 6) and climate system response. The chapter is primarily concerned with global measures of change, but also assesses regional changes in the energy budget and changes to atmospheric heating insofar as they support the assessments of surface warming (Chapters 3 and 4), the hydrological cycle (Chapter 8) and ocean circulation (Chapter 9). Thereby the assessment aids understanding of regional patterns of response (Chapters 10, 11, 12 and the Atlas).

This Chapter principally builds on material presented within the IPCC AR5 WG1 assessment (Boucher, 2012; Church et al., 2013; Collins et al., 2013a; Flato et al., 2013; Hartmann et al., 2013; Myhre et al., 2013b; Rhein et al., 2013). It also makes use of the subsequent IPCC Special Reports on Global Warming of 1.5°C (SR1.5), the Ocean and Cryosphere in a Changing Climate (SROCC) and Climate Change and Land (SRCCL), as well as community-led assessments (e.g. Bellouin et al., 2019; Sherwood et al., submitted) when assessing specific details.

Changes to globally-averaged surface temperature are fundamental to understanding how the Earth's energy budget is affected by climate feedbacks. This chapter adopts globally-averaged near surface air temperature (GSAT) as its measure of surface temperature change (see Cross-Chapter Box 2.3, Chapter 4 Section 4.3.4). The global time integral of Earth's energy budget directly determines the rate of total Earth system warming (i.e. the combined heating rate associated with warming of all climate system components, Box 7.2; Section 7.2.2.2), which represents a metric of global change that is complementary to GSAT. As an integral quantity, total Earth System warming can be considered a more robust measure of global change than GSAT, which has considerably greater unforced variability on interannual-to-decadal timescales (Von Schuckmann et al., 2016). Research and new observations since AR5 have improved scientific understanding of the total Earth system warming and its changes through time (Section 7.2). Improved understanding of rapid adjustments to radiative forcing and of aerosol-cloud interactions have led to revisions of forcing estimates (Section 7.3). New approaches to the quantification and treatment of feedbacks (Section 7.4) have improved the understanding of their nature and time-evolution, leading to a better understanding of how these feedbacks relate to ECS. This has helped to reconcile disparate estimates of ECS from different lines of evidence (Section 7.5). Innovations in the use of emission metrics have clarified the relationships between metric choice and policy goals, linking the chapter to WGIII (Section 7.6).

In Box 7.1 an extended energy budget framework is introduced, which forms the basis for the discussions and scientific assessment in the remainder of this chapter and across the report. The framework reflects advances in the understanding of the Earth system response to climate forcing since the publication of the AR5. A schematic of this framework and the key changes relative to the science reported in AR5 are provided in Figure 7.1.

**[START FIGURE 7.1 HERE]**

**Figure 7.1:** A visual abstract of the chapter, illustrating why the Earth's energy budget matters and how it relates to the underlying chapter assessment. The methods used to assess processes and key new findings relative to IPCC AR5 are highlighted.

**[END FIGURE 7.1 HERE]**

A simple way to characterise the behaviour of different aspects of the climate is to summarise them using single climate metrics. The phrase "climate metrics" can carry a range of implications, depending on the context. This report distinguishes between "climate metrics" (e.g. ECS, TCR) and "emission metrics" (such as the global temperature-change potential; GTP), but this distinction is not definitive. Climate metrics are generally used to summarise aspects of the overall climate system response (Box 7.1). Emission metrics are generally used to summarise the relative effects of emissions of different forcing agents, usually greenhouse gases (see Section 7.6). Figure 7.2 shows how the various climate metrics and emission metrics assessed in this chapter fit within the overall chain of processes from human activities to climate impacts. The climate metrics used in this report typically evaluate how the Earth system response varies with atmospheric gas concentration or change in radiative forcing. Emission metrics evaluate how radiative forcing or a key climate variable (such as GSAT) is affected by the emissions of a certain amount of gas. Emission-related metrics are extensively employed in mitigation policy decisions such as trading greenhouse gas reduction measures to compare their effect on climate. Climate metrics are useful to gauge the range of future climate impacts for adaptation decisions under a given emission pathway. Metrics such as the Transient Climate Response to Emissions (TCRE) are used in both adaptation and mitigation contexts: for gauging future surface temperature change under specific emission scenarios, and to estimate remaining carbon budgets that are used to form mitigation policies (see Chapter 5, Section 5.5).

Given that TCR and ECS are metrics of global mean surface temperature response to an idealized doubling of atmospheric $CO_2$ (Box 7.1), they do not directly correspond to the warming that would occur under realistic forcing scenarios that include time-varying $CO_2$ concentrations and non-$CO_2$ forcing agents (such as aerosols and land-use changes). It has been argued that TCR, as a metric of transient warming, is more policy-relevant than ECS (Frame et al., 2006; Schwartz, 2018). However, as detailed in Chapter 4, both established and recent results (Forster et al., 2013; Gregory et al., 2015; Marotzke and Forster, 2015; Grose et al., 2018; Marotzke, 2019) indicate that TCR, ECS, radiative forcing and variability can all help explain variation across CMIP5 models both over the historical period and across a range of concentration-driven future scenarios. In emission-driven scenarios the carbon cycle response is also important (Smith et al., 2019). The proportion of variation explained by ECS and TCR varies with scenario and the time period considered, but both past and future surface warming are highly correlated with both metrics (Section 7.5.7).

Regional changes in temperature, rainfall, and climate extremes have been found to correlate well with the forced changes in GSAT within coupled General Circulation Models (GCMs) (Giorgetta et al., 2013; Tebaldi and Arblaster, 2014; Seneviratne et al., 2016) (Chapter 4, Section 4.6.1). While this so-called 'pattern scaling' has important limitations arising from, for instance, localized forcings, land-use changes, or internal climate variability (Deser et al., 2012; Luyssaert et al., 2014), changes in GSAT nonetheless explains a substantial fraction of inter-model differences in projections of regional climate changes over the 21st century (Tebaldi and Knutti, 2018). This Chapter's assessments of TCR and ECS thus provide constraints on future global and regional climate change (Chapter 4).

**[START FIGURE 7.2 HERE]**

**Figure 7.2:** A conceptual chain of processes linking human activity to climate impacts, showing where the climate indicators and emission metrics assessed in this chapter fit within the chain and how they associate with other IPCC Working Group Reports.

**[END FIGURE 7.2 HERE]**

**[START BOX 7.1 HERE]**

**BOX 7.1: Forcing, feedbacks and climate sensitivity framework**

The forcing-feedback framework provides a methodology to assess the impact of individual drivers of global mean surface temperature change, and to facilitate the understanding of the key phenomena that set the magnitude of this temperature change. The framework used here is developed from that adopted in previous IPCC reports. *Effective Radiative Forcing* (ERF), introduced in IPCC AR5 (Boucher et al., 2013; Myhre et al., 2013b) is more explicitly defined in this report and is employed as the central definition of radiative forcing (Sherwood et al. 2015, Box 7.1, Figure 1a). The framework has also been extended to allow variations in feedbacks over different timescales and with changing climate state (Section 7.4.4; Section 7.4.3).

The global mean surface temperature response to perturbations to the Earth's energy budget is traditionally approximated by the following linear equation, in which $\Delta N$ (W m$^{-2}$) represents the change in the top-of-atmosphere (TOA) energy budget, $\Delta F$ (W m$^{-2}$) is an ***effective radiative forcing*** perturbation to the energy budget, $\alpha$ (W m$^{-2}$ °C$^{-1}$) is the net ***feedback parameter***, and $\Delta T$ (°C) is the change in ***global mean near-surface air temperature***:

$$\Delta N = \Delta F + \alpha\,\Delta T \qquad \text{Box 7.1, Equation (7.1)}$$

ERF is the TOA energy budget change resulting from the initial perturbation which is not related to a change in global mean surface temperature (i.e. $\Delta T$ =0). Climate feedbacks ($\alpha$) represent those processes that change the TOA energy budget in response to a change in $\Delta T$. AR5 adopted different measures of global surface temperature change in observation and projection chapters (see Cross Chapter Box 2.3). This report employs a consistent measure, associating $\Delta T$ with trends in the globally averaged near surface air temperature (GSAT). Using a single measure helps reconcile divergent estimates of ECS across the different lines of evidence reported in AR5 (see Section 7.5 and Cross Chapter Box 2.3). In previous assessments, $\alpha$ and the related ECS have been associated with a distinct set of physical processes (Planck response, and water vapour, lapse rate, surface albedo and cloud changes) (Charney et al., 1979). In this assessment a more general definition of $\alpha$ and ECS is adopted, whereby many Earth system processes are included.

**[START BOX 7.1, FIGURE 1 HERE]**

**Box 7.1, Figure 1:** Schematics of the forcing-feedback framework adopted within the assessment, following Equation 7.1. Illustrated is how the Earth's energy balance might evolve for a hypothetical doubling of atmospheric $CO_2$ concentration above preindustrial levels, where an initial positive energy imbalance (energy entering the Earth system, shown on the y-axis) is gradually restored towards equilibrium as the surface temperature warms (shown on the x-axis). a) illustrates the definitions of ERF for the special case of a doubling of atmospheric $CO_2$ concentration, the feedback parameter and the ECS. b) illustrates how approximate estimates of these metrics are made within the chapter and how these approximations relate to the exact definitions adopted in panel a).

**[END BOX 7.1, FIGURE 1 HERE]**

The ***effective radiative forcing,*** **ERF** ($\Delta$F; units: W m$^{-2}$) quantifies the change in the net TOA radiative budget of the Earth system due to an imposed perturbation (e.g. change in carbon dioxide concentration, change in incoming solar radiation). ERF is expressed as a change in net downward radiative flux at the TOA following the adjustments in both tropospheric and stratospheric temperatures, water vapour, clouds, and some surface properties, such as surface albedo, prior to any GSAT change. These adjustments affect the energy budget both at the TOA and at the surface. Accounting for such processes gives an estimate of radiative forcing that is more representative of the climate change response associated with forcing agents than stratospheric-temperature-adjusted radiative forcing (SARF) or the instantaneous radiative forcing (IRF) (see Section 7.3.1). Adjustments are processes that are independent of GSAT change, whereas feedbacks refer to processes moderated by GSAT change. Although adjustments generally occur on timescales of hours to several months, and feedbacks on timescales of a year or more, timescale is not used to separate the definitions. ERF has often been approximated as the TOA energy budget change in climate model simulations with sea-surface temperature and sea-ice set to their pre-industrial climatological values (e.g. Myhre et al., 2013). However, to match the adopted forcing-feedback framework, the small effects of any GSAT change from changes in land surface temperatures need to be removed from the equilibrium TOA energy budget in such simulations to give an approximate measure of ERF (see Box 7.1., Figure 1b and Section 7.3.1).

The ***feedback parameter,*** $\alpha$, (units: W $m^{-2}$°$C^{-1}$) quantifies the sensitivity of the change in net energy budget at the TOA for a given change in GSAT. Many climate variables affect the TOA energy budget, and the feedback parameter can be decomposed, to first order, into a sum of terms $\alpha = \sum_x \alpha_x$, where *x* represents a variable of the Earth system that has a direct impact on the energy budget at the TOA. The sum of the feedback terms (i.e. the net $\alpha$ in Equation 7.1) is a measure of how the Earth might respond to an ERF. All Earth system feedbacks that do not affect the atmospheric concentration of $CO_2$ can be included in the sum, such as changes in natural methane emissions and changes to natural aerosol emissions (Section 7.4.1). Note that there is no standardised notation or sign convention for the feedback parameter in the literature. Here the convention is used that the sum of all feedback terms (net $\alpha$) is negative for a stable climate that radiates additional energy to space with a GSAT increase, with a more negative value of $\alpha$ corresponding to a stronger radiative response and thus a smaller GSAT change required to balance a change in ERF (Equation 7.1). A change in variable *x* amplifies the temperature change when the associated feedback parameter $\alpha_x$ is positive (positive feedback) and dampens the temperature change when $\alpha_x$ is negative (negative feedback). New research since AR5 emphasises how feedbacks can vary over different timescales (Section 7.4.4) and with climate state (Section 7.4.3), giving rise to the concept of an *estimated feedback parameter* that may be different from the value of the feedback parameter governing ECS.

The ***equilibrium climate sensitivity***, ***ECS*** (units: °C), is defined as the equilibrium value of $\Delta T$ in response to a sustained doubling of atmospheric $CO_2$ concentration from a pre-industrial reference state (Section 7.5 and Box 7.1, Figure 1a). Equilibrium refers to a steady state where $\Delta N$ averages to zero over a multi-century period. ECS is representative of the multi-century to millennial $\Delta T$ response to an atmospheric $CO_2$ doubling. ECS as employed here excludes the long-term response of the ice-sheets which may take multiple millennia to reach equilibrium. The Earth System Sensitivity (ESS) is a metric related to ECS that addresses changes over these much longer timescales that would allow the ice-sheets to reach a new equilibrium state (assessed in Section 7.4.2.6). Due to a number of factors, studies rarely estimate ECS or $\alpha$ at equilibrium. Rather, they estimate a *feedback parameter* (Section 7.4.1 and Box 7.1, Figure 1b) or an *effective ECS* (Section 7.5.1and Box 7.1, Figure 1b), which represent an approximation to the true value of ECS or $\alpha$. For example, a feedback parameter can be estimated from the linear slope of $\Delta N$ against $\Delta T$ over a set number of years within an abrupt 2×$CO_2$ or 4×$CO_2$ climate model simulation, and the ECS can be estimated from the intersect of this regression line with $\Delta N = 0$ (see Box 7.1, Figure 1b). To estimate ECS from a given estimate of effective ECS necessitates that assumptions are made for how ERF varies with $CO_2$ concentration (Section 7.3.2) and how the slope of $\Delta N$ against $\Delta T$ relates to the slope of the straightline from ERF to ECS (see Section 7.5 and Box 7.1, Figure 1b). Care has to be taken when comparing results across different lines of evidence to translate different estimates of ECS into the ECS definition used here (Section 7.5.1).

The ***transient climate response,*** **TCR** (units: °C), is defined as the change in the global mean near surface air temperature for the hypothetical scenario in which $CO_2$ increases at 1% $yr^{-1}$ from pre-industrial to the time of a doubling of atmospheric $CO_2$ concentration (year 70) (Section 7.5). It is a measure of transient warming accounting for the strength of climate feedbacks, pattern effects and ocean heat uptake. The ***transient climate response to emissions*** (TCRE) is defined as the transient globally averaged near-surface air temperature change per 1000 Gt C of cumulative $CO_2$ emission increase since preindustrial. TCRE combines information on the airborne fraction of cumulative $CO_2$ emissions (the fraction of the total $CO_2$ emitted that remains in the atmosphere at the time of doubling, which is determined by carbon cycle processes) with information on the TCR. TCR is assessed in this chapter, whereas TCRE is assessed in Chapter 5, Section 5.5. TCRE can also be related to the global warming potential (GWP) emission metric covered in Section 7.6.

**[END BOX 7.1 HERE]**

## 7.2 Earth's energy budget and its changes through time

Earth's energy budget encompasses the major energy flows of relevance for the climate system (Figure 7.3). Virtually all the energy that enters or leaves the climate system does so in the form of radiation at the top-of-atmosphere (TOA). The TOA energy budget is determined by the amount of incoming solar (shortwave) radiation and the outgoing radiation that is composed of reflected solar radiation and outgoing thermal (longwave) radiation emitted by the climate system. In a steady state climate, the outgoing and incoming radiative components are essentially in balance in the long-term global mean, although there are still fluctuations around this balanced state that arise through internal climate variability (Brown et al., 2014; Palmer and McNeall, 2014). However, anthropogenic forcing has given rise to a persistent imbalance in the TOA radiation budget, denoted Earth's Energy Imbalance (EEI) (Trenberth et al., 2014; Von Schuckmann et al., 2016), represented by $\Delta N$ in Box 7.1, Equation 7.1. EEI is a fundamental aspect of observed climate change and a critical metric determining the present rate of global climate change (Hansen et al., 2005a). Earth's energy budget constitutes not only the TOA energy fluxes, but also the internal flows of energy within the climate system, which characterize the climate state. The surface energy budget consists of the net solar and thermal radiation exchanges between the surface and atmosphere as well as the non-radiative components of sensible and latent heat, melt and ground heat flux (Figure 7.3 upper panel), and plays a key role as driver of the global water cycle, atmospheric and ocean dynamics, as well as a variety of surface processes.

Assessments of the following aspects of Earth's energy budget are presented in the following sections: the present-day mean energy flows (Section 7.2.1); observed changes in TOA radiative fluxes (Section 7.2.2.1); the accumulation of energy in the climate system (i.e. total Earth system warming) (Section 7.2.2.2); changes in the surface energy budget (Section 7.2.2.3); and the poleward energy transports that shape both present-day climate and its future response (Section 7.2.2.4). A synthesis of the current understanding of observed climate change in the context of radiative forcing, radiative response and total Earth system warming is presented in Box 7.2.

### *7.2.1 Present-day energy budget*

Figure 7.3 (upper panel) shows a schematic representation of Earth's present-day energy budget including quantitative estimates of the global mean magnitudes of its individual components. Clouds are major modulators of the energy flows. Thus, any perturbations in the cloud fields, such as caused by aerosol-cloud interactions (Section 7.3) or through cloud feedbacks (Section 7.4) can have a strong influence on the energy distribution in the climate system. To illustrate the overall effects that clouds exert on the energy flows, the complementary Figure 7.3 (lower panel) additionally depicts the energy budget without clouds, but otherwise identical atmospheric and surface radiative properties. It has been derived by taking into account information contained in clear-sky radiation measurements from both surface and space (Wild et al., 2019). A comparison of Figure 7.3 upper and lower panels shows that without clouds, almost 50 $Wm^{-2}$ less solar radiation is reflected back to space globally (53 ± 2 W $m^{-2}$instead of 100 ± 2 W $m^{-2}$) (Loeb et al., 2018a), thereby increasing absorption of solar radiation at the Earth's surface accordingly. On the other hand, thermal outgoing radiation at the TOA is enhanced without clouds by nearly 30 $Wm^{-2}$ (268 ± 3 W $m^{-2}$ instead of 239± 3 W $m^{-2}$ globally). Since clouds reflect more shortwave radiation than they trap thermal radiation, the overall effect of clouds is to reduce the radiative energy available and thereby cool the climate system.

**[START FIGURE 7.3 HERE]**

**Figure 7.3:** Schematic representation of the global mean energy budget of the Earth (upper panel), and its equivalent without consideration of cloud effects (lower panel). Numbers indicate best estimates for the magnitudes of the globally averaged energy balance components in W $m^{-2}$ together with their uncertainty ranges in parentheses (5% to 95% confidence range), representing present day climate conditions at the beginning of the 21$^{th}$ century. Adapted from Wild et al. (2015, 2019).

**[END FIGURE 7.3 HERE]**

The AR5 (Church et al., 2013; Hartmann et al., 2013; Myhre et al., 2013b) highlighted the progress in quantifying the TOA radiation budget following new satellite observations that became available in the early 21st Century (Clouds and the Earth's Radiant Energy System, CERES; Solar Radiation and Climate Experiment, SORCE). The AR5 used these analyses to understand observed changes and estimate radiative forcing. Progress in the quantification of the magnitude and changes in incoming solar radiation at the TOA since AR5 is discussed in Chapter 2, Section 2.2. Since the AR5, the accuracy of the reflected solar and outgoing thermal fluxes at the TOA has been further enhanced with the release of the CERES Energy Balance EBAF Ed4.0 product, which includes algorithm improvements and consistent input datasets throughout the record (Loeb et al., 2018a). However, the overall accuracy of these fluxes (uncertainty in global mean TOA flux 1.7% (1.7 W $m^{-2}$) for reflected solar and 1.3% (3.0 W $m^{-2}$) for outgoing thermal radiation at the 90% confidence level) is not sufficient to quantify the Earth's energy imbalance in absolute terms. Therefore, one-time adjustments have been made to the reflected solar and emitted thermal TOA fluxes of the CERES EBAF dataset within their uncertainty ranges to ensure that the global mean net TOA flux for July 2005–June 2015 is consistent with an EEI of 0.71 ± 0.10 W $m^{-2}$ (5% to 95% confidence range) inferred from ocean heat content (OHC) measurements using 10 years of Argo measurements and energy uptake by the lithosphere, cryosphere and atmosphere (Johnson et al., 2016; Riser et al., 2016) (Section 7.2.2). Since climate models are typically adjusted to match the magnitudes of their global mean solar and thermal fluxes at the TOA with corresponding satellite references from CERES-EBAF, they often do not greatly deviate from those values on a global mean basis. However they show significant discrepancies on regional scales, often related to their representation of clouds (Trenberth and Fasullo, 2010; Hwang and Frierson, 2013; Li et al., 2013b; Dolinar et al., 2015; Wild et al., 2015).

The surface energy budget is associated with substantially larger uncertainties than the TOA energy budget. The components of the surface energy budget cannot be directly measured by passive satellite sensors from space and require retrieval algorithms and ancillary data for their estimation, which gives rise to additional uncertainties (Raschke et al., 2016; Kato et al., 2018; Huang et al., 2019). On a global mean basis, confidence in the quantification of the surface energy budget has increased, since independent recent estimates converge to within a few W $m^{-2}$ for different surface radiation components (Wild, 2017). Best estimates for downward solar and thermal radiation at Earth's surface are thus near 185 W $m^{-2}$ and slightly above 340 W $m^{-2}$, respectively. These estimates are based on complementary approaches which make use of satellite products from active and passive sensors (L'Ecuyer et al., 2015; Kato et al., 2018) as well as the information contained in surface observations and climate models (Wild et al., 2015). Inconsistencies in the quantification of the global mean energy and water budgets discussed in the AR5 (Hartmann et al., 2013) have been reconciled within the (considerable) uncertainty ranges of their individual components (Wild et al., 2013, 2015; L'Ecuyer et al., 2015). However, on regional scales, the closure of the surface energy budgets remains a challenge with currently available satellite-derived datasets (Loeb et al., 2014; L'Ecuyer et al., 2015; Kato et al., 2016). Nevertheless, attempts have been made to derive reference estimates for the energy budgets separated into land and oceans (Wild et al., 2015) as well as for individual continents and ocean basins (L'Ecuyer et al., 2015).

Since the AR5, quantification of the uncertainties inherent in the different surface energy flux datasets has improved. Uncertainties in global monthly mean downward solar and thermal fluxes in the CERES-EBAF surface dataset are, respectively, 10 W $m^{-2}$ and 8 W $m^{-2}$ (converted to 5% to 95% confidence level) (Kato et al., 2018). The uncertainties in latent and sensible heat fluxes averaged over global oceans are approximately 11 W $m^{-2}$ and 5 W $m^{-2}$ (converted to 5% to 95% confidence level), respectively (L'Ecuyer et al., 2015). A recent review of the latent and sensible heat flux accuracies over the period 2000 to 2007 highlights significant differences between several gridded products over oceans, where root mean squared differences between the multi-product ensemble and data at more than 200 moorings reached up to 25 W $m^{-2}$ for latent heat and 5 W $m^{-2}$ for sensible heat (Bentamy et al., 2017). The uncertainty stems from the retrieval of flux-relevant meteorological variables, as well as from differences in the flux parameterizations (Yu, 2019). Estimating the uncertainty in sensible and latent heat fluxes over land is difficult because of their large temporal and spatial variabilities. The spread of these fluxes over land computed with three global datasets is between 10% to 20% (L'Ecuyer et al., 2015). The uncertainty in the surface energy budget in polar regions is larger than the uncertainty of other regions (e.g. Kato et al., 2018), due to the limited number of surface sites and larger uncertainty in surface observations (Previdi et al., 2015).

Climate models also show larger discrepancies in their energy budgets at the surface than at the TOA due to weaker observational constraints, with a spread of 10-20 W $m^{-2}$ in their surface energy budget components averaged globally, and an even greater spread on more regional scales (Li et al., 2013b; Wild et al., 2013; Boeke and Taylor, 2016; Wild, 2017; Zhang et al., 2018a). The downward thermal and solar radiation in the CMIP5 climate models when averaged over all land surfaces varies by more than 30 and 40 W $m^{-2}$, respectively (Wild et al., 2015).

In summary, since AR5, the magnitudes of the global mean energy budget components have been quantified more accurately, not only at the TOA, but also at the Earth's surface, where independent estimates of the radiative components have converged (*high confidence*). Considerable uncertainties remain in regional surface energy budget estimates, particularly from climate models.

### *7.2.2 Changes in Earth's energy budget*

#### *7.2.2.1 Changes in TOA radiative fluxes*

Since 2000, changes in the TOA energy fluxes can be tracked from space due to the CERES program (Figure 7.4). The variations noted in the TOA energy fluxes reflect the influence of internal variations, particularly that of ENSO, in addition to radiative forcing of the climate system and climate feedbacks (Allan et al., 2014; Loeb et al., 2018a). For example, globally, the reduction in both outgoing thermal and reflected solar radiation during La Nina conditions in 2008/2009 led to an energy gain for the climate system, whereas enhanced outgoing thermal and reflected solar radiation led to an energy loss during the El Niños of 2002/2003 and 2009/2010 (Figure 7.4) (Loeb et al., 2018a). Substantial anomalies in the global mean reflected solar radiation can also be attributed to anomalous sea ice cover in the Arctic and Antarctica (Loeb et al., 2018a). For the estimation of trends, the period for which CERES data is available (since March 2000) is still fairly short and dominated by internal variability of the climate system. Some of the climate models participating in CMIP6 are able to track the variability in the global mean TOA fluxes as observed from space to a considerable degree, when driven with prescribed sea-surface temperatures (SSTs) and all known anthropogenic and natural forcings (Figure 7.4, coloured lines) (Loeb et al., submitted). The correlations between the multimodel means (dotted black lines) and the CERES records (solid black lines) for 12-month running means are 0.85, 0.73 and 0.81 for the global mean reflected solar, outgoing thermal and net TOA radiation, respectively (Loeb et al., submitted). A reconstruction back to 1985 suggests that Earth's energy imbalance increased from 0.27 ± 0.38 W $m^{-2}$ (1985–1999, 5-95% confidence range) to 0.59 ± 0.14 W $m^{-2}$ (2000–2015) based on a satellite record that is homogenized using reanalyses and climate model simulations(Allan et al., 2014; Liu et al., 2017a). The reconstruction is further able to capture the interannual variability in Earth's energy imbalance caused by the volcanic eruption of Pinatubo in 1991 and the ENSO events before 2000. In a similar reconstruction based on a combination of successive satellite missions, Dewitte and Clerbaux (2018) note a rise in thermal outgoing radiation at the TOA since 1985.

In summary, variations in the energy exchange between Earth and space can be accurately tracked since the advent of improved observations in the year 2000 (*high confidence*), while reconstructions indicate that the Earth's energy imbalance was larger in the 2000s than in the 1990s (*high confidence*).

**[START FIGURE 7.4 HERE]**

**Figure 7.4:** Anomalies in global mean all-sky TOA fluxes from EBAF Ed4.0 (solid black lines) and various CMIP6 climate models (coloured lines) in terms of reflected solar (upper panel), emitted thermal (middle panel) and net TOA fluxes (lower panel). The multimodel means are additionally depicted as doted black lines. Model fluxes stem from simulations driven with prescribed SSTs and all known anthropogenic and natural forcings. Shown are anomalies of 12-month running means. Larger reflected shortwave and emitted thermal flux anomalies are defined as positive in upper and middle panels. Net TOA flux is defined as incoming shortwave flux minus reflected and emitted fluxes (i.e. downward positive). Adapted from Loeb et al. (submitted).

**[END FIGURE 7.4 HERE]**

#### 7.2.2.2 Changes in total Earth system warming

Total earth system warming represents the integrated energy gain of the climate system associated with global ocean heat uptake, warming of the atmosphere, warming of the land surface and melting of ice. Due to conservation of energy, and assuming negligible geothermal heat flux, the rate of total Earth system warming (Section 7.1) is equivalent to the Earth's energy imbalance ($\Delta N$ in Box 7.1, Equation 7.1). On annual and longer timescales, changes in total Earth system warming are dominated by changes in global OHC (Palmer et al., 2011; Palmer and McNeall, 2014; Johnson et al., 2016; Wijffels et al., 2016). Thus, observational estimates and climate model simulations of OHC change are critical to the understanding of both past and future climate change.

Recent studies have compared observation-based estimates of multi-decadal global OHC change with those simulated by CMIP5 climate models (Cheng et al., 2016, 2019; Gleckler et al., 2016). In general, there is good agreement in both total ocean heat uptake and its vertical structure between the observations and the CMIP5 multi-model mean (Chapter 3, Section 3.5). However, there is a large spread among CMIP5 models compared to the observations and the spatial patterns of historical climate change may not have evolved in the same way as reality for many climate models. This implies a broad range of net radiative forcings and/or spread in climate feedbacks over the 20$^{th}$ Century among climate models. In addition, the magnitude of internal variability in OHC and Earth's energy imbalance simulated by each model varies substantially across the ensemble (Palmer and McNeall, 2014; Gleckler et al., 2016).

Smith et al. (2015) presented a comparison of the evolution of Earth's energy imbalance between CMIP5 climate models and observation-based estimates of Earth's energy imbalance and global OHC change. Both models and observations exhibited a general tendency towards an increase in Earth's energy imbalance that was punctuated by short-lived cooling episodes associated with major volcanic eruptions. The CMIP5 ensemble mean generally showed good agreement in both the timing and magnitude of the main signals seen in the observations, with a close correspondence between the time-evolution of Earth's energy imbalance and global OHC change.

Since the AR5, novel approaches have been developed that use estimates of time-averaged ocean circulation to propagate observed or reconstructed surface temperature anomalies into the ocean interior in order to estimate the OHC changes (Gebbie and Huybers, 2019; Zanna et al., 2019). These studies are able to offer insights much further back in time than the more conventional in situ-based methods, but with a lower degree of confidence due to the limited number of studies and additional methodological assumptions. Confidence in the ability to track changes in Earth's energy imbalance since 2006 has increased based on comparisons of satellite radiative fluxes and both in situ and satellite-based estimates of global OHC change (Johnson et al., 2016; Meyssignac et al., 2019). These independent methods show strong correlations and form a useful cross-validation of the current observing capabilities. Based on the current observational evidence there is *very high confidence* that global OHC has increased from 1971 to 2018, and there is *medium confidence* that it has increased from the 1870s to 1971.

The total Earth system warming for the periods 1971-2018 and 2006-2018 is assessed following the approach of AR5 (Rhein et al., 2013) using the latest observational estimates (Table 7.1; Box 7.2; Cross-Chapter Box 9.2). Global OHC is assessed by combining a number of estimates for different depth layers based on in situ ocean temperature measurements (Domingues et al., 2008; Purkey and Johnson, 2010; Levitus et al., 2012; Desbruyères et al., 2016) (Chapter 2, Section 2.3.3.1; Chapter 9, Section 9.2.2.1). The estimated heating of the atmosphere is based on satellite measurements of the temperature of the lower troposphere and lower stratosphere (Mears and Wentz, 2009, 2017), accounting for the effect of increasing water vapour content (Held and Soden, 2006) (Chapter 2, Section 2.3.1.3). Heat fluxes into the land surface are estimated through analysis of borehole temperature profiles (Gentine et al., submitted). Estimated mass loss rates for glaciers (Marzeion et al., 2015; Zemp et al., 2019) (Chapter 2, Section 2.3.2.3; Chapter 9, Section 9.5.1), ice sheets (Shepherd et al., 2018; Mouginot et al., 2019) (Chapter 2, Section 2.3.2.4; Chapter 9, Section 9.4.1), and sea-ice (Schweiger et al., 2011) (Chapter 2, Section 2.3.2.1; Chapter 9, Section 9.3) are converted to energy change using reference values for the heat of fusion and ice density. Full details of these calculations are provided in the Chapter 7 Appendix 7.A.

**[START TABLE 7.1 HERE]**

**Table 7.1:** Contributions of the different components of total Earth system warming for the periods 1971 to 2018 and 2006 to 2018 (Box 7.2, Cross-chapter box 9.2). Values are based on analysis of the 1971 to 2015 period with 2006 to 2015 rates extrapolated to 2018.

| Component | 1971 to 2018 | | 2006 to 2018 | | References |
|---|---|---|---|---|---|
| | Heat Gain (Zetta Joules) | Heating Rate (W $m^{-2}$) | Heat Gain (Zetta Joules) | Heating Rate (W $m^{-2}$) | |
| Global Ocean | 373 ± 84 (92%) | 0.49 ± 0.11 | 133 ± 24 (92%) | 0.75 ± 0.14 | (Domingues et al., 2008; Purkey and Johnson, 2010; Levitus et al., 2012; Desbruyères et al., 2016) |
| 0–700 m | 239 ± 76 (59%) | 0.32 ± 0.10 | 72 ± 22 (50%) | 0.41 ± 0.13 | |
| 700–2000 m | 99 ± 7.2 (24%) | 0.13 ± 0.01 | 48 ± 1.7 (33%) | 0.27 ± 0.01 | |
| > 2000 m | 34 ± 15 (8.5%) | 0.05 ± 0.02 | 13 ± 4.6 (8.8%) | 0.07 ± 0.03 | |
| Ice melt | 8.9 ± 3.3 (2.2%) | 0.012 ± 0.004 | 3.8 ± 0.6 (2.6%) | 0.021 ± 0.003 | (Schweiger et al., 2011; Marzeion et al., 2015; Shepherd et al., 2018; Mouginot et al., 2019; Zemp et al., 2019) |
| Atmosphere | 2.4 ± 0.7 (0.6%) | 0.003 ± 0.001 | 0.7 ± 0.2 (0.5%) | 0.004 ± 0.001 | (Held and Soden, 2006; Mears and Wentz, 2009, 2017) |
| Land surface | 21 ± 2.9 (5.2%) | 0.028 ± 0.004 | 6.5 ± 0.4 (4.5%) | 0.037 ± 0.002 | (Cuesta-Valero et al.,submitted; Gentine et al., submitted) |
| TOTAL | 406 ± 84 (100%) | 0.54 ± 0.11 | 144 ± 24 (100%) | 0.81 ± 0.14 | |

**[END TABLE 7.1 HERE]**

The assessment of total Earth system warming (Box 7.2, Figure 1a; Table 7.1) yields an average value for Earth's energy imbalance ($\Delta N$, Box 7.1, Equation 7.1) of 0.54± 0.11 W $m^{-2}$ for the period 1971 to 2018, expressed relative to Earth's surface area(*high confidence*). The estimate for the period 2006 to 2018 is substantially higher (0.81± 0.14 W $m^{-2}$), consistent with the increased radiative forcing from greenhouse gases(*high confidence*). Ocean warming dominates the changes in the total energy inventory, accounting for > 90% of the observed change for the period 1971 to 2018, and the upper ocean (0 to 700m) accounting for about 60% (*high confidence*). Cross-validation of satellite and in situ based observational estimates and consistent closure of the global sea-level budget (Cross-chapter Box 9.2) promote increased confidence relative to AR5.

### *7.2.2.3 Changes in Earth's surface energy budget*

AR5 (Section 2.3.3, Hartmann et al., (2013)) reported pronounced changes in multi-decadal records of in situ observations of surface solar radiation, including a widespread decline between the 1950s and 1980s, known as "global dimming", and a partial recovery thereafter, termed "brightening". Over the past decades, these changes may have impacted key elements of climate change, such as global and regional warming rates (Li et al., 2016b; Wild, 2016; Du et al., 2017), glacier melt (Ohmura et al., 2007; Huss et al., 2009), the intensity of the global water cycle (Wild, 2012) and terrestrial carbon uptake (Mercado et al., 2009). Further, these changes have also been used as emergent constraints to quantify aerosol effective radiative forcing (see Section 7.3.3.3)

Since AR5, additional evidence for dimming and/or subsequent brightening up to several percent per decade based on direct surface observations has been documented in previously less explored areas of the globe, such as in Iran, Bahrain, Tenerife, Hawaii, the Taklaman desert and the Tibetan Plateau (Elagib and Alvi, 2013; You et al., 2013; Garcia et al., 2014; Longman et al., 2014; Rahimzadeh et al., 2015; Wild, 2016). Strong decadal trends in surface solar radiation remain evident after careful data quality assessment and homogenization of long-term records (Sanchez-Lorenzo et al., 2013, 2015; Manara et al., 2015, 2016; Wang et al., 2015a; Li et al., 2016b; Wang and Wild, 2016; He et al., 2018; Yang et al., 2018). Since AR5, further investigations on the potential impacts of urbanization on solar radiation trends were carried out, indicating that these impacts are generally small, with the exception of some specific sites in Russia and China (Wang et al., 2014; Imamovic et al., 2016; Tanaka et al., 2016). Thus, there is *high confidence* that the observed variations outlined in AR5 of dimming between the 1950s and 1980s and brightening thereafter are not measurement artefacts or localised phenomena.

As noted in the AR5 (Hartmann et al., 2013) and substantiated in more recent studies, the tendencies in surface solar radiation are less coherent since the beginning of the 21st century, with evidence for continued brightening in different parts of Europe and in the US, some stabilization in China and India, and dimming in some other areas (Augustine and Dutton, 2013; Sanchez-Lorenzo et al., 2015; Manara et al., 2016; Soni et al., 2016; Wang and Wild, 2016; Wild, 2016; Jahani et al., 2018; Pfeifroth et al., 2018; Yang et al., 2018). The CERES-EBAF satellite-derived dataset of surface solar radiation (Kato et al., 2018) does not indicate a globally significant trend over the short period 2001–2012 (Zhang et al., 2015), whereas a statistically significant increase in surface solar radiation of +3.4 W $m^{-2}$ per decade over the period 1996–2010 has been determined over the area in view of the geostationary satellite Meteosat in the record of the Satellite Application Facility on Climate Monitoring (CM SAF) (Posselt et al., 2014).

Since the AR5 there is additional evidence that strong decadal changes in surface solar radiation occur also under cloud-free conditions, as shown for long term observational records in Europe, USA, China and India (Gan et al., 2014; Manara et al., 2016; Soni et al., 2016; Yang et al., 2019). This suggests that changes in the composition of the cloud-free atmosphere, primarily from aerosols, contribute to these variations, particularly since the second half of the 20$^{th}$ century (Wild, 2016). For Europe and East Asia, modelling studies also point to aerosols as an important factor for the variations in surface solar radiation by comparing simulations including and excluding historical aerosol variations (Golaz et al., 2013; Nabat et al., 2014; Persad et al., 2014; Folini and Wild, 2015; Turnock et al., 2015). On the other hand, further evidence for the influence of changes in cloudiness on dimming and brightening is emphasized in some studies (Augustine and Dutton, 2013; Parding et al., 2014; Stanhill et al., 2014; Pfeifroth et al., 2018). Thus, the relative contribution of aerosol and clouds to dimming and brightening is still debated. The influence of cloud-mediated aerosol effects and direct aerosol radiative effects on dimming and brightening in a specific region may depend on the prevailing pollution levels (Wild, 2016) (see also Section 7.3.3).

Climate models and reanalyses do not reproduce the full extent of observed dimming and brightening (Wild and Schmucki, 2011; Allen et al., 2013; Zhou et al., 2017a; Storelvmo et al., 2018), potentially pointing to inadequacies in the representation of aerosol mediated effects or related emission data. The inclusion of assimilated aerosol optical depth inferred from satellite retrievals in the MERRA2 reanalysis helped to improve the accuracy of the simulated surface solar radiation changes in China (Feng and Wang, 2019). This does not rule out the possibility that also non-aerosol related deficiencies in the representation of model-simulated clouds and circulation, as well as an underestimation of natural variability, could further contribute to the lack of dimming and brightening in the models.

The AR5 reported indications for an increase in surface downward thermal radiation over recent decades, in line with expectation from an increased radiative forcing from greenhouse gases. Updates of the longest observational records from the Baseline Surface Radiation Network continue to show an increase at the majority of the sites, in line with an overall increase predicted by climate models on the order of 2 W $m^{-2}$

decade$^{-1}$ over the coming decades (Wild, 2016).

Uncertainties in measurements of surface turbulent fluxes continue to limit the feasibility of determining their decadal changes. Nevertheless, over the oceans, reanalysis-based estimates of linear trends from 1948 to 2008 indicate high spatial variability and annual seasonality. Increases of 4 to 7 W m$^{-2}$ decade$^{-1}$ for latent heat and 2 to 3 W m$^{-2}$ decade$^{-1}$ for sensible heat in the western boundary current regions are mostly balanced by decreasing trends in other regions (Gulev and Belyaev, 2012). Over land, the terrestrial latent heat flux is estimated to have increased by 0.09 W m$^{-2}$ decade$^{-1}$ from 1989 to 1997, and subsequently decreased by 0.13 W m$^{-2}$ decade$^{-1}$ from 1998 to 2005 due to enhanced soil moisture limitation mainly in the SH (derived from Mueller et al. (2013)). These trends are small in comparison to the uncertainty associated with satellite-derived and in-situ observations, as well as from land surface models forced by observations and atmospheric reanalyses. Temporal and spatial variability in surface solar radiation and precipitation can affect the variability in terrestrial latent heat flux (Oliveira et al., 2011; Douville et al., 2013; Greve et al., 2014). Ongoing advances in remote sensing of evapotranspiration from space (Mallick et al., 2016; Fisher et al., 2017; McCabe et al., 2017b, 2017a), as well as terrestrial water storage (Rodell et al., 2018) may contribute to constrain changes in latent heat flux. Meanwhile, there was also progress in benchmarking the terrestrial sensible heat flux (Siemann et al., 2018).

In summary, since the AR5, multidecadal trends in surface solar radiation up to several percent per decade have been detected at many more locations also in remote areas. There is *high confidence* that these trends are of widespread nature, and not only a local phenomenon or a measurement artefact. The origins of these trends need further investigation, although there are indications that anthropogenic aerosols might have substantially contributed to these changes (*medium confidence*). There is *medium confidence* that downward thermal radiation has increased over recent decades, while there remains *low confidence* in the trends in surface sensible and latent heat.

**[START BOX 7.2 HERE]**

**BOX 7.2: The Global Energy Budget and its Future Changes**

The global energy budget is a fundamental aspect of Earth's climate system and its future evolution under climate change. It represents the balance between radiative forcing, Earth's radiative response and the excess heat taken up by the climate system (i.e. total Earth system warming, Box 7.2, Figure 1d).This box assesses the global energy budget for the period 1971–2018 and the future evolution of total Earth System warming.

The net ERF of the Earth system since 1971 has been positive (Box 7.2, Figure 1b, e; Section 7.3), mainly as a result of increases in atmospheric greenhouse gas concentrations (Chapter 2, Section 2.2.8 and Section 7.3.2). These positive forcing agents have been partly offset by negative radiative ERFs, primarily due to anthropogenic aerosols (Section 7.3.3), which dominate the overall uncertainty. The net energy inflow to the Earth system from ERF since 1971 is estimated to be 825 ZJ (1 ZJ = $10^{21}$ J) with a 5% to 95%range of 44 to 1453 ZJ (Box 7.2, Figure 1b).

The ERF-induced warming of the climate system results in increased thermal radiation to space via the Planck response, but the picture is complicated by the variety of other climate and Earth system feedbacks (Section 7.4.2) that also influence Earth's radiative response (Box 7.2, Figure 1c). The combined effects of these feedbacks can be estimated using atmospheric model simulations with prescribed historical sea-surface temperatures (SSTs) and sea-ice concentrations, resulting in a net feedback parameter, $\alpha$, that varies as the SST pattern evolves over the historical record (Box 7.1, Section 7.4.3). Combining these model-based estimates of time-evolving $\alpha$ with the observed near-surface temperature change provides an estimate of the Earth radiative response (Box 7.2, Figure 1c). The net energy outflow from the Earth system associated with the radiative response since 1971 is estimated to be 838 ZJ with a 5% to 95% range of 605 to 1187 ZJ.

The addition of the estimated ERF-induced changes and those associated with the radiative response lead to an implied energy change of –75 ZJ over the period 1971 to 2018, with a 5% to 95% range of –879 to 605 ZJ

(Box 7.2, Figure 1f). Within these large uncertainties, this estimate is consistent with an independent observation-based assessment of Earth's energy storage change of 406 ZJ (5% to 95% range of 322 to 490 ZJ) for the period 1971 to 2018, which is dominated by the increase in ocean heat storage (Box 7.2, Figure 1d). Confidence in the observed total earth system warming is strengthened by a consistent analysis and closure of the observed global sea level budget (Chapter 9, Box 9.2). Overall, there is *high confidence* that the Earth's energy budget is closed within the estimated uncertainties. However, the large uncertainties associated with historical anthropogenic aerosol forcing limits our ability to constrain future climate sensitivity from the historical record (Section 7.5).

Future projections show that the Earth's energy imbalance remains positive under all RCP scenarios analysed for CMIP5 for several centuries, contributing directly to long-term committed sea-level rise through the associated thermal expansion of the global oceans (Box 7.2, Figure 2, e.g. Nauels et al. (2017); Palmer et al. (2018)).The behaviour of total Earth system warming is in contrast to that of GSAT change in two fundamental ways. The first is the long-term commitment, with the total warming continuing for centuries even under strong mitigation scenarios, in contrast to GSAT that stabilises or even reduces (Chapter 4, Section 4.3.1.1). The second is that GSAT is much more prone to inter-annual-to-multi-decadal variability than total Earth system warming, making the latter a more suitable basis for monitoring the rate of anthropogenic global warming on decadal-to-interannual timescales (Palmer et al., 2011; Palmer and McNeall, 2014; Wijffels et al., 2016).

**[START BOX 7.2, FIGURE 1 HERE]**

**Box 7.2, Figure 1:** Estimates of the net cumulative energy change (ZJ = $10^{21}$ Joules) for the period 1971–2018 associated with: (a) Total Earth System Warming; (b) Effective Radiative Forcing; (c) Earth System Radiative Response. Shaded regions indicate the 5th to 95th percentile uncertainty range. The grey lines indicate equivalent heating rates in W m$^{-2}$, expressed relative to Earth's surface area. Panels (d) and (e) show the breakdown of components, as indicated in the legend, for Total Earth System Warming and Effective Radiative Forcing, respectively. Panel (f) shows the Earth Energy Budget assessed for the period 1971–2018, i.e. the consistency between Total Earth System Warming and the implied heat storage from Effective Radiative Forcing plus Earth System Radiative Response. Shading represents the 5% to 95% uncertainty range. Forcing and Response timeseries are computed using a baseline period of 1850–1900. [placeholder: Total Earth System Warming components to be updated to 2018 for final draft. Reported values for sum of components in main text are based on extrapolation of 2006–2015 rate to 2018. The aerosol ERF estimate is based on AR5 and will be updated for the final draft.]

**[END BOX 7.2, FIGURE 1 HERE]**

**[START BOX 7.2, FIGURE 2 HERE]**

**Box 7.2, Figure 2:** Two-layer model simulations of global mean surface temperature (left) and ocean thermal expansion (right) under the RCP2.6 and RCP4.5 scenarios, following Palmer et al. (2018). Shaded regions indicate the 90% confidence interval based on the ensemble standard deviation. Dotted lines indicate the ensemble mean response. Solid lines show a single CMIP5 model simulation to illustrate the characteristics of variability in each variable. Projections are shown relative to a 1986–2005 baseline period.

**[END BOX 7.2, FIGURE 2 HERE]**

**[END BOX 7.2 HERE]**

### *7.2.2.4 Poleward energy transports and their changes*

Satellite observations show a hemispheric contrast in the present-day TOA radiation budget, namely a net gain of radiative energy of 1.4 W m$^{-2}$ in the Southern Hemisphere (SH) and a net loss in the Northern Hemisphere (NH) of 0.2 W m$^{-2}$. This hemispheric contrast is due to more outgoing thermal radiation in the warmer NH than the colder SH, whereas the absorption of solar radiation is approximately equal in both hemispheres (Voigt et al., 2013; Marshall et al., 2014; Loeb et al., 2016; Stephens et al., 2016; Liu et al., 2017a). This hemispheric contrast gives rise to a net (atmosphere + ocean) cross-equatorial heat-transport of 0.2 ± 0.08 PW (5% to 95% confidence level) from the SH to the NH associated with atmosphere and ocean circulations. From satellite-derived TOA and surface radiation budget observations combined with vertically integrated atmospheric energy divergence estimated from atmospheric reanalyses, Loeb et al. (2016) find that the oceans provide 0.44 ± 0.11 PW of northward cross-equatorial heat transport while the atmosphere transports 0.24 ± 0.07 PW in the opposite (southward) direction (Stephens et al., 2016). Using similar methods, Liu et al. (2015, 2017a) estimate the northward cross-equatorial ocean heat transport to be 0.32 ± 0.13 PW, which is somewhat smaller than estimated by Loeb et al. (2016) due to the consideration of differential rates of heat storage in the NH and SH oceans. Forget and Ferreira (2019) estimate the northward cross-equatorial ocean heat transport to be 0.48 ± 0.3 PW based on eight air-sea heat flux products and 0.08 ± 0.5 PW based on an ocean reanalysis, with northward cross-equatorial heat transport in the Atlantic Ocean partially compensated by southward cross-equatorial heat transport in the Indian Ocean.

To accomplish the southward cross-equatorial atmospheric heat transport, the location of the tropical rainfall peak in the Intertropical Convergence Zone (ITCZ) must be located in the NH in the annual mean (Kang et al., 2008; Frierson and Hwang, 2012; Donohoe et al., 2013; Bischoff and Schneider, 2014). There is *high confidence* that the northward cross-equatorial oceanic heat transport, owing to meridional overturning in the Atlantic Ocean (Chapter 9, Section 9.2.3.1), is a primary reason that the annual mean rainfall peak is located to the north of the equator (Frierson et al., 2013; Marshall et al., 2014), although other factors such as tropical processes and continental features may contribute as well (Xie and Philander, 1994; Takahashi and Battisti, 2007; Zhang and Song, 2010).

The connection to tropical precipitation is one reason that atmospheric cross-equatorial heat transport derived from data products provides a key metric for the evaluation of energy budgets in climate models (Loeb et al., 2016; Lembo et al., 2019). The net cross-equatorial heat transport in the CMIP5 models is on average twice as large as observed, outside the range of observational uncertainties, because they absorb more solar radiation in the SH than the NH, while also emit more outgoing LW radiation in the NH compared to observations (Voigt et al., 2013; Loeb et al., 2016; Lembo et al., 2019). With cross-equatorial ocean heat transport that is near observational estimates (Loeb et al., 2016), this corresponds to too little simulated southward cross-equatorial atmospheric heat transport. This is reflected in a double ITCZ bias with too much rainfall to the south of the equator in the annual mean, which has been a persistent problem in multiple generations of climate models (Hwang and Frierson, 2013; Adam et al., 2016; Loeb et al., 2016; Stephens et al., 2016; Hawcroft et al., 2017).

CMIP5 models capture the overall structure of the observed net heat transport, with peak poleward heat transport of about 6 PW in both hemispheres (Trenberth and Stepaniak, 2003), as well as the structure of atmospheric and oceanic heat transports separately (Figure 7.5). However, as for CMIP3 (Lucarini and Ragone, 2011; Donohoe and Battisti, 2012), many CMIP5 models show large (~1 to 2 PW) errors in the mid-latitudes where the magnitude of net heat transport peaks (Figure 7.5a; Donohoe et al., submitted; Lucarini et al., 2014). Model errors in the net heat transport arise from errors in both atmospheric and oceanic heat transport components, with the majority of models showing too little poleward ocean heat transport in mid-latitudes (Figure 7.5c). The differences in peak net heat transport between models have been linked to differences in their latitudinal structure of absorbed shortwave radiation, suggesting that the heat transport errors arise from cloud biases (Donohoe and Battisti, 2012).

Changes in poleward (meridional) heat transport have important consequences for the large-scale patterns of surface warming in response to greenhouse gas forcing (Section 7.4.4). Figure 7.5 illustrates heat transport changes within CMIP5 models at a century after an idealized abrupt $CO_2$ quadrupling. Models simulate several consistent features including increased poleward atmospheric heat transport and decreased ocean heat transport in both hemispheres (Figure 7.5e, f), except near 70°N where the majority of models show increased poleward oceanic heat transport (Chapter 9, Section 9.2) and decreased poleward atmospheric heat transport (Hwang et al., 2011). Models do not agree on the sign of the net heat transport changes, which are generally small owing to strong compensations between atmospheric and oceanic heat transport changes at all latitudes (Armour et al., 2019; Donohoe et al., submitted; He et al., 2019; Huang and Zhang, 2014), often referred to as Bjerknes compensation (Bjerknes, 1964). Chapter 9 describes improved process understanding of ocean heat transport since AR5, thereby providing *high confidence* in several key aspects of oceanic heat transport changes under global warming.

**[START FIGURE 7.5 HERE]**

**Figure 7.5:** Observation-based and CMIP5 climatological northward energy transports in the atmosphere and ocean (top) and projected heat transport changes at year 100 following $CO_2$ quadrupling (bottom). (a) Climatological net heat transport inferred from CERES TOA (Armour et al., 2019; Donohoe et al., submitted) and simulated by CMIP5 models. (b) Climatological atmospheric heat transport calculated from the NCEP Reanalysis (Trenberth and Stepaniak, 2003) and simulated by CMIP5 models. (c) Climatological oceanic heat transport inferred from surface energy budgets (calculated as a residual between atmospheric heat transport divergence and TOA radiation fluxes). Grey shading shows 5% to 95% range on observational estimates. For net meridional heat transport the range is estimated from inter-annual variability and total CERES calibration error added in quadrature at each latitude. For atmospheric heat transport the range is estimated from inter-annual variability and for oceanic heat transport the range is estimated as a residual from the net and atmospheric heat transports with errors propagated in quadrature. (d-f) Anomalies in net, atmospheric, and implied oceanic heat transports simulated by CMIP5 models under abrupt $CO_2$ quadrupling relative to the pre-industrial control simulations which define their climatologies in (a)-(c) (following Donohoe et al., submitted). Implied ocean heat transport is derived from net sea-surface heat fluxes and thus does not account for the pattern of ocean heat storage.

**[END FIGURE 7.5 HERE]**

Since the AR5 there is also improved understanding of the causes of atmospheric heat transport changes under global warming. Atmospheric heat transport changes are commonly understood in terms of the heat flux divergence required to balance the anomalous energy input into the atmosphere at each latitude by radiative forcing, the radiative response to surface warming (i.e., radiative feedbacks), and local ocean heat uptake (Armour et al., 2019; Donohoe et al., submitted; Feldl and Roe, 2013; Huang et al., 2017; Huang and Zhang, 2014; Trenberth et al., 2014; Zelinka and Hartmann, 2012). ERF from $CO_2$ peaks in the tropics, contributing to increased poleward atmospheric heat transport in both hemispheres. Those radiative feedbacks that preferentially add energy at the TOA to the tropical atmosphere (i.e. water-vapour and cloud feedbacks) contribute to increased mid-latitude poleward atmospheric heat transport, while those that preferentially remove energy at the TOA from the tropical atmosphere (lapse-rate feedback) oppose that increase. CMIP5 models project that net TOA radiation changes are relatively uniform with latitude under a wide range of climate forcings (Donohoe et al., submitted) owing to weak latitudinal structure in both the ERF and the radiative response to warming (Armour et al., 2019). This results in a near-invariance of net meridional heat transport where it peaks in mid-latitudes (Figure 7.5d) and requires strong compensation between atmospheric heat transport changes and patterns of surface ocean heat uptake, which are set by regional oceans circulations (Figure 7.5e,f; Armour et al., 2019). Models show that the TOA radiation changes relatively little with surface warming in the Arctic (owing to the local net radiative feedback being close to zero; Section 7.4.4). Consequently, a reduction in atmospheric heat transport into the Arctic is required to balance the local energy input by greenhouse gas forcing and ocean heat transport changes. The degree of compensation between atmospheric and oceanic heat transport depends on the latitudinal structure of radiative feedbacks (Rose and Ferreira, 2013; Dai et al., 2017; Yang et al., 2017) and thus varies across models.

Atmospheric heat transport changes under global warming also reflect compensations between large changes in the poleward transport of latent energy and dry-static energy (sum of sensible and potential energy) (Alexeev et al., 2005; Donohoe et al., submitted; Held and Soden, 2006; Hwang et al., 2011; Hwang and Frierson, 2010). Models show that within the mid-latitudes, where eddies dominate the heat transport, a large increase in poleward latent energy transport arises from an increase in the equator-to-pole gradient in atmospheric moisture with global warming, as moisture in the tropics increases more than at the poles

(Chapter 8, Section 8.2). However, this change is compensated by a large decrease in dry-static energy transport arising from a weakening of the equator-to-pole temperature gradient with global warming as high latitudes warm more than the tropics. Models show that within the tropics, where the meridional overturning circulation dominates the heat transport, a large increase in equatorward latent energy transport arises from increased moisture in the equatorward branch of the Hadley Cell. However, this is compensated by large increases in poleward dry-static energy in the Hadley Cell. Energy balance models that approximate atmospheric heat transport in terms of a diffusive flux down the near-surface moist static energy (sum of dry-static and latent energy) gradient are able to replicate the atmospheric heat transport changes seen within climate models (Flannery, 1984; Hwang and Frierson, 2010; Hwang et al., 2011; Rose et al., 2014; Roe et al., 2015; Merlis and Henry, 2018), including the partitioning of latent and dry-static energy transports (Siler et al., 2018b; Armour et al., 2019).

There remain open questions regarding how atmospheric heat transport changes can be understood in terms of the changes in atmospheric circulation projected to occur under greenhouse gas forcing – such as a narrowing and shifting of the ITCZ (e.g., Huang et al., 2013; Neelin et al., 2003), a slowdown and poleward expansion of the Hadley Cell (Held and Soden, 2006; Lu et al., 2007), poleward shifts of mid-latitude jets and storm tracks (e.g., Barnes and Polvani, 2013; Yin, 2005), or changing planetary wave activity (e.g., Graversen and Burtu, 2016; Lee, 2014; Liu and Barnes, 2015). Much research since the AR5 has focused on establishing causal links between changes in regional atmospheric energy budgets and the response of atmospheric circulation (e.g., Ceppi and Hartmann, 2015; Ceppi and Shepherd, 2017; Donohoe et al., 2013, 2014; Feldl and Bordoni, 2016; Mbengue and Schneider, 2018; Merlis, 2015; Voigt and Shaw, 2015, 2016), but these changes have yet to be reconciled with energetic and diffusive perspectives on atmospheric heat transport described above (Armour et al., 2019).

These atmospheric heat transport changes strongly reflect the energetic demands set by the spatial patterns of radiative feedbacks and surface ocean heat uptake. They also reflect strong compensations between latent and dry-static energy transport changes. Latent energy transport changes shape the meridional pattern of global warming (Section 7.4.4). They also correspond to changes in the meridional pattern of moisture convergence and thus shape the patterns of rainfall under global warming (Held and Soden, 2006; Siler et al., 2018b) (Chapter 8, Sections 8.2 and 8.4). Based on a high level of agreement across models and mature process understanding, there is *high confidence* in several features of projected poleward atmospheric heat transport changes under transient global warming. These include increased poleward atmospheric heat transport in mid-latitudes and small changes in (or even decreased) poleward heat transport into polar regions.

## 7.3 Effective radiative forcing

The effective radiative forcing (ERF) is the fundamental driver of climate change. It quantifies the energy gained or lost by the Earth system following an imposed perturbation. It is determined by the change in the net downward radiative flux at the top of the atmosphere (see Box 7.1) after allowing the system to adjust to the perturbation, but excluding changes in surface temperature. This section outlines the methodology behind ERF calculations in Section 7.3.1 and then assesses the ERF due to greenhouse gases (long-lived and short-lived) in Section 7.3.2, aerosols in Section 7.3.3 and other natural and anthropogenic forcing agents in Section 7.3.4. These are brought together in an overall assessment of the present-day ERF and its evolution over the historical time period since 1750 until the present day, taken to be 2018 in this chapter.

### *7.3.1 Methodologies and representation in models; overview of adjustments*

As introduced in Box 7.1, the IPCC AR5 report (Boucher et al., 2013; Myhre et al., 2013b) recommended ERF as a more useful measure of the climate effects of a physical driver than the stratospheric-temperature-adjusted radiative forcing (SARF) adopted in earlier assessments. ERF extended the SARF concept to account for not only adjustments to stratospheric temperatures, but also responses in the troposphere arising from the forcing heating profile and effects on clouds, referred to as “adjustments”. These adjustments include changes in the atmospheric temperature profile, as well as the consequences of these temperature changes on clouds and water vapour (Sherwood et al., 2015). For example, absorbing gases and aerosols directly heat the atmosphere, promoting decreased cloud fraction at the altitude of the heating and increased cloud fraction below. Effects of aerosols on clouds spatial or temporal extent are also included in the ERF, as are chemical and biospheric responses, e.g. to changes in $CO_2$ concentration. This chapter defines "adjustments" as those changes caused by the forcing agent that are independent of changes in globally averaged surface temperature (magnitude or pattern), rather than defining a specific timescale. AR5 used the terminology "rapid adjustment", but in this assessment it is the independence from surface temperature that is important rather than the rapidity. This means that changes in land or ocean surface temperature patterns (for instance as identified by Rugenstein et al. (2016)) are not included as adjustments even if they lead to zero global mean change. As in previous assessments (Forster et al., 2007; Myhre et al., 2013b) ERFs can be attributed simply to changes in the concentrations of the forcing agent or attributed to components of emitted gases or activities that are more closely related to human activity and factors we can control (see Figure 7.10). These attributed ERFs can include chemical and biospheric responses to emitted gases, so that ERFs can be attributed to precursor gases even if they do not have a direct radiative effect themselves.

The assessment of ERFs in the AR5 was preliminary as there was no agreed standard for estimating ERF and ERFs were only available for a few forcing agents, so for many forcing agents the report made the assumption that ERF and SARF were equivalent. A body of work since AR5 has computed ERFs across many more forcing agents and models, closely examined the methods of computation, quantified the processes involved in delivering adjustments and examined how well ERFs predict the ultimate temperature response. This work has led to a much-improved understanding and gives increased confidence in the quantification of radiative forcing across the report. These same techniques allow for an evaluation of radiative forcing within climate models as a key test of their ability to represent both historical and future temperature changes (Chapter 3, Section 3.3 and Chapter 4, Section 4.3).

The ERF is the sum of the Instantaneous Radiative Forcing (IRF) plus the adjustments, so theoretically this could be constructed bottom-up by calculating the IRF and adding in the adjustments one-by-one or together. However, there is no simple way to derive the tropospheric adjustment terms without using a comprehensive climate model (e.g. CMIP5/6). There have been two main modelling approaches used to estimate ERF. The first approach is to perform a linear regression (Box 7.1, Equation 7.1) of the net change in the TOA radiation budget ($\Delta N$) against change in global surface temperature ($\Delta T$) following a step change in the concentration of the forcing agent (Gregory et al., 2004). The ERF ($\Delta F$) is then derived from $\Delta N$ when $\Delta T$=0. Regression-based estimates of ERF depend on the temporal resolution of the data used (Modak et al., 2016, 2018). For the first few months of a simulation both surface temperature change and stratospheric temperature adjustment occur at the same time, leading to misattribution of the stratospheric temperature adjustment to the surface temperature feedback. Patterns of sea-surface temperature change also affect the forcing (Andrews et al., 2015). At multidecadal timescales the curvature of the relationship between net TOA radiation and surface temperature can also lead to biases in the ERF estimated from the regression method (Armour et al., 2013; Andrews et al., 2015; Knutti et al., 2017) (Section 7.4). A second modelling approach to estimating ERF is to approximately remove the climate feedback by constraining $\Delta T$ through prescribing the SSTs and sea-ice in a pair of "fixed-SST" simulations with and without the change in forcing agent (Hansen et al., 2005b). $\Delta F_{\mathrm{fsst}}$ is then given by the difference in $\Delta N_{\mathrm{fsst}}$ between the simulations. The fixed-SST method is found to yield less uncertainty than the regression method. Nevertheless a 30-year integration needs to be conducted in order to reduce the 5–95% confidence range to 0.1 W $m^{-2}$ (Forster et al., 2016), thus neither method is useful for quantifying the ERF of agents with forcing magnitudes of order 0.1 W $m^{-2}$ or smaller. The internal variability in the fixed-SST method can be further constrained by nudging winds towards a prescribed climatology (Kooperman et al., 2012). This allows the determination of the ERF of forcing agents with smaller magnitudes (Schmidt et al., 2018).

Since the land surface temperature change $\Delta T_{\mathrm{land}}$ is not constrained in the fixed-SST method, this response needs to be removed for consistency with the Section 7.1 definition. The radiative response to $\Delta T_{\mathrm{land}}$ can be estimated through radiative transfer modelling in which a kernel, $k$, representing the change in radiative flux per change in unit land surface temperature change, is precomputed (Stjern et al., 2017; Smith et al., 2018b; Richardson et al., 2019; Tang et al., 2019). Thus ERF ≈ $\Delta F_{\mathrm{fsst}} - k\,\Delta T_{\mathrm{land}}$. Since $k$ is negative this correction increases the ERF (i.e. $\Delta F_{fsst}$ underestimates the ERF). For 2×$CO_2$ this term is around 0.2 $Wm^{-2}$. Changing the land surface temperature will also induce changes in the tropospheric temperature and water vapour. These were estimated in Tang et al. (2019) to cause radiative responses of comparable magnitude to those directly from $\Delta T_{land}$. However, there is currently insufficient corroborating evidence to recommend including these corrections in this assessment. An alternative to computing the response terms directly is to use the climate feedback parameter α (Hansen et al., 2005b; Sherwood et al., 2015; Tang et al., 2019). Since the response to land surface temperature change is not expected to be the same as α for global mean temperature change (Section 7.4) the kernel approach will be used to correct for $\Delta T_{land}$ in this assessment.

The definition of ERF in Box 7.1 aims to have the cleanest separation between forcing (energy budget changes that are not mediated by surface temperature) and feedbacks (as energy budget changes that are mediated by surface temperature). The definition is also found below (see also Figure 7.6) to have the most constant feedback parameter across forcing agents.

The individual adjustments can be calculated from fixed-SST simulations using radiative kernels (Vial et al., 2013; Zelinka et al., 2014; Zhang and Huang, 2014; Smith et al., 2018b) or a partial radiative perturbation approach (Colman, 2015; Mülmenstädt et al., 2019). The radiative kernel approach is easier to implement through post-processing of output from multiple climate models, whereas it is recognized that the partial radiation perturbation approach gives a more accurate estimate of the adjustments within the setup of a single model and its own radiative transfer code.

Instantaneous Radiative Forcings (IRFs) provide a useful test of climate model radiative transfer codes, but few recent experiments have tested IRFs computed within climate models (Pincus et al., 2016). The IRFs can be estimated from the ERFs by removing the adjustment terms using radiative kernels to quantify the adjustment for each meteorological variable. Kernel analysis by Chung and Soden (2015b) suggested a large spread in $CO_2$ IRF and SARF across climate models, but their analysis was based on regressing variables in a coupled-ocean experiment rather than fixed-SST, and had low vertical resolution in the stratospheric kernels, which is shown to be problematic for IRF calculations (Smith et al., submitted, a). Smith et al. (2018b) find a similar spread in IRF for instantaneous doubling of atmospheric $CO_2$ (2x$CO_2$) and show that kernel methodological errors are typically smaller than 10%. This suggests the kernel method is a useful but not perfect way of estimating IRF. IRFs and adjustments computed from radiative kernels are shown for five forcing experiments across nine models in Figure 7.6 (Smith et al., 2018b). Table 7.2 shows the estimates of IRF, SARF and ERF for 2×$CO_2$ from the nine climate models analysed in Smith et al. (2018b). The larger spread in IRF in climate models (±16% 5–95% confidence) compared to line-by-line models suggests there is still room from improvement in climate model radiative transfer codes (Pincus et al., 2016; Soden et al., 2018). However the SARF shows improved agreement over previous studies (Pincus et al., 2016 and references therein) and are within 10% (except MPI-ESM) of the multi-model mean and the line-by-line assessment of 2×$CO_2$ SARF in Section 7.3.2 (3.80 W $m^{-2}$). The level of agreement in this and earlier intercomparisons gives *high confidence* in climate model representation of radiative forcing from greenhouse gases. The 4×$CO_2$ CMIP6 experiments (Smith et al., submitted, b) in Table 7.2 come from Earth system models with varying levels of complexity in aerosols and reactive gas chemistry. In the CMIP6 experimental setup, impacts of $CO_2$ changes on aerosols and ozone cannot be separated and hence are included within the SARF diagnosis. In these particular models this leads to higher SARF than when only $CO_2$ varies, however there are insufficient studies to make a formal assessment of composition adjustments to $CO_2$.

**[START TABLE 7.2 HERE]**

**Table 7.2:** IRF, SARF, $\Delta F_{fsst}$, and ERF diagnosed from climate models for $CO_2$ experiments. 2×$CO_2$ data taken from fixed composition experiments (Smith et al., 2018b). 4×$CO_2$ data taken from CMIP6 Earth system model experiments with interactive aerosols (and interactive gas phase chemistry in some) (Smith et al., submitted, b).The radiative forcings from the 4x$CO_2$ experiments are scaled by 0.5 for comparison with 2x$CO_2$. The bracketed numbers refer to only the subset of models for which the full kernel analysis was available.

| $2\times CO_2$ ($W\ m^{-2}$) (Smith et al., 2018b) | IRF | SARF | $\Delta F_{fsst}$ | ERF |
|---|---|---|---|---|
| HadGEM2 | 2.13 | 3.45 | 3.37 | 3.58 |
| NorESM | 2.19 | 3.67 | 3.50 | 3.70 |
| GISS | 2.80 | 3.98 | 4.06 | 4.27 |
| CanESM2 | 2.52 | 3.68 | 3.57 | 3.77 |
| MIROC-SPRINTARS | 2.70 | 3.89 | 3.62 | 3.82 |
| CESM1-CAM5 | 2.79 | 3.89 | 4.08 | 4.39 |
| HadGEM3 | 2.39 | 3.48 | 3.64 | 3.90 |
| IPSL-CM5A | 2.39 | 3.50 | 3.39 | 3.61 |
| MPI-ESM | 3.09 | 4.27 | 4.14 | 4.38 |
| CESM1-CAM4 | 2.50 | 3.50 | 3.62 | 3.86 |
| Multi-model Mean and 5-95% confidence range | 2.60 ± 0.43 | 3.73 ± 0.44 | 3.70 ± 0.44 | 3.93 ± 0.48 |
| $0.5\times 4xCO_2$ ($W\ m^{-2}$) (Smith et al., submitted, b) | | | | |
| CanESM5 | 2.42 | 3.85 | 3.80 | 4.02 |
| CESM2 | 2.30 | 3.71 | 4.46 | 4.71 |
| CNRM-CM6-1 | 3.00 | 4.20 | 4.00 | 4.22 |
| CNRM-ESM2-1 | 3.02 | 4.20 | 3.96 | 4.14 |
| GFDL-CM4 | 2.82 | 3.84 | 4.12 | 4.31 |
| GISS-E2-1-G | 2.61 | 3.96 | 3.45 | 3.59 |
| HadGEM3-GC31-LL | 2.40 | 3.82 | 4.04 | 4.28 |
| IPSL-CM6A-LR | 2.64 | 4.02 | 4.00 | 4.24 |
| MIROC6 | 2.40 | 3.80 | 3.66 | 3.88 |
| MPI-ESM1-2-LR | 2.48 | 3.94 | 4.18 | 4.41 |
| MRI-ESM2-0 | 2.66 | 4.00 | 3.82 | 4.00 |
| NorESM2-LM | 2.34 | 3.75 | 4.08 | 4.31 |
| UKESM1-0-LL | 2.48 | 3.67 | 3.97 | 4.21 |
| Multi-model Mean and 5-95% confidence range | 2.58 ± 0.38 | 3.90 ± 0.27 | 3.97 ± 0.39 | 4.18 ± 0.43 |

**[END TABLE 7.2 HERE]**

**[START FIGURE 7.6 HERE]**

**Figure 7.6:** The effective radiative forcing (ERF), instantaneous radiative forcing (IRF) and adjustment (a) and breakdown of the adjustment using radiative kernels (b) for five idealised forcing experiments across nine models. The 90% confidence range is shown. Note that the land-surface response is included in ERF. Data modified from Smith et al. (2018b). Separation of temperature adjustments into tropospheric and stratospheric contributions is approximate based on a fixed tropopause of 100 hPa at the equator, varying linearly in latitude to 300 hPa at the poles. The results are computed from idealized single forcing experiments with the following abrupt perturbations from present day conditions; doubling $CO_2$ concentration ($2\times CO_2$), tripling methane concentration ($3\times CH_4$), two percent increase in insolation (+2%Sol), ten times black carbon concentrations or emissions (10×BC), five times sulphate concentrations or emissions (5×Sul).

**[END FIGURE 7.6 HERE]**

ERFs have been found to yield more consistent values of global temperature change per unit forcing ("efficacy") than SARF, i.e. $\alpha$ shows less variation across different forcing agents (Hansen et al., 2005b; Marvel et al., 2016; Richardson et al., 2019). The definition of ERF used in this assessment, which excludes the land surface temperature response, brings the $\alpha$ values into the closest agreement (Richardson et al., 2019), although for individual models there are still variations particularly for more localised forcings. Figure 7.7 shows a comparison of climate sensitivity for different forcing agents using either SARF or ERF as the forcing. This figure contrasts the relatively constant (within 10%) ERF-based $1/\alpha$ values with the variability in the SARF-based $1/\alpha$(up to 40% lower sensitivity than for $CO_2$). However, even for ERF, studies find that $\alpha$ is not indentical across all forcing agents (Shindell, 2014; Shindell et al., 2015; Modak et al., 2018; Richardson et al., 2019). Analysis of the climate feedbacks (Kang and Xie, 2014; Duan et al., 2018; Persad and Caldeira, 2018; Krishna-Pillai Sukumara-Pillai et al., 2019) suggests a weaker feedback (i.e. less negative $\alpha$) and hence larger sensitivity for forcing of the higher latitudes (particularly the northern hemisphere). Nonetheless, as none of these variations are robust across models, climate sensitivities derived from $2xCO_2$ ERFs can be applied to ERFs from other forcing agents with approximately global distributions within a 10% range (*medium confidence*).

In summary, this report adopts an estimate of ERF based on the change in TOA radiative fluxes in the absence of surface temperature change. This allows for a theoretically cleaner separation between forcing and feedbacks in terms of factors respectively unrelated and related to surface temperature change (Box 7.1). ERF can be computed from prescribed SST and sea-ice experiments after removing the TOA energy budget change associated with the land surface temperature response. To compare these results with line-by-line models the individual tropospheric adjustment terms can be removed to leave the SARF. SARFs for $2\times CO_2$ calculated by Earth System Models (ESMs) from this method agree within 10% with the line-by-line models. The new studies highlighted above suggest that climate feedback parameters computed within this framework have less variation across forcing agents. From high agreement and medium evidence, there is *high confidence* that an $\alpha$ based on ERF as defined here varies by less than 10% across a range of typical forcing agents. For localised forcing patterns there are fewer studies and less agreement between them, resulting in *low confidence* that ERF is a suitable estimator of the resulting surface temperature response.

**[START FIGURE 7.7 HERE]**

**Figure 7.7:** Values of climate sensitivity ($-1/\alpha$) derived from ERF and SARF for twelve forcing experiments. Multi-model means and full model ranges are shown. ERF is derived from prescribed SST and sea-ice experiments. The number of models analysed differs between experiments as indicated on the bars. Data from Richardson et al. (2019).The results are computed from idealized single forcing experiments with the following abrupt perturbations from present day conditions; doubling $CO_2$ concentration ($2xCO_2$), tripling methane concentration ($3xCH_4$), two percent increase in insolation (2%Sol), ten times black carbon concentrations or emissions (10xBC), five times sulphate concentrations or emissions (5xSul), ten times sulphate concentrations or emissions over Asia only (10xSulAsia), ten times sulphate concentrations or emissions over Europe only (10xSulEur), change in CFC-12 mixing ratio to 5ppb (CFC-12), change in CFC-11 mixing to 5ppb (CFC-11), change in $N_2O$ mixing ratio to 1ppm ($N_2O$), five times tropospheric ozone concentration (ozone), change in vegetation to pre-industrial conditions (land use). Black bars represent 90% range of model spread for $2xCO_2$, $3xCH_4$, +2%Sol, 10xBC and 5xSul and the full model range for other experiments.

**[END FIGURE 7.7 HERE]**

### *7.3.2 Well-Mixed Greenhouse Gases, ozone and stratospheric water vapour*

Line-by-line (LBL) models provide the most accurate calculations of the radiative perturbations due to well mixed greenhouse gases (WMGHGs) with errors in the IRF of less than 1% (Mlynczak et al., 2016; Pincus et al., submitted). They can calculate IRFs with no adjustments, or SARFs by accounting for the adjustment of stratospheric temperatures using a fixed dynamical heating. It is not possible with offline radiation models such as LBL models to account for other adjustments, so such models cannot currently calculate ERFs. The LBL model calculations of SARF for carbon dioxide, methane and nitrous oxide have been updated since AR5, which were based on Myhre et al. (1998). The new calculations (Etminan et al., 2016) include the shortwave forcing from methane and updates to the water vapour continuum (increasing the total SARF of methane by 25%) and account for the overlaps between carbon dioxide and nitrous oxide. The associated simplified expressions are given in Supplementary Table SM7.1. The shortwave contribution to the instantaneous radiative forcing of methane has been confirmed independently (Collins et al., 2018). Since they incorporate known missing effects we assess the new calculations as being a more appropriate representation than Myhre et al. (1998).

As described in Section 7.3.1, ERFs can be estimated solely using climate models, however the radiation schemes in climate models are approximations to LBL models with variations and biases in results between the schemes (Soden et al., 2018). Hence climate models alone should not be used to the make best estimates of the ERFs for the WMGHGs. This assessment therefore estimates ERFs from a combined approach that uses the SARF from LBL models and adds the tropospheric adjustments derived from climate models.

In the AR5, the main information used to assess components of ERFs beyond SARF was from Vial et al. (2013) who found a near-zero non-stratospheric adjustment in 4×$CO_2$ CMIP5 model experiments, with an uncertainty of ±10% of the total $CO_2$ ERF. The near-zero adjustment came from an approximate balance between an increase due to water vapour and clouds and a decrease due to increased tropospheric and land surface temperatures. The different adjustment components comprising the ERF for 2×$CO_2$ were broken down by Smith et al. (2018b) where the temperature adjustment was split into land-surface temperature and tropospheric temperature (Table 7.3). Explicit calculation of the land-surface temperature response allows determination of the ERF following the definition in Box 7.1 and section 7.3.1. This gives a tropospheric adjustment of +5% which we add to the Etminan et al. (2016) formula for SARF. Due to the agreement between the studies and the understanding of the physical mechanisms there is *high confidence* in the mechanisms underpinning the tropospheric adjustment. However, due to adjustments of different signs there is only *medium confidence* that the overall tropospheric adjustment is positive.

The impact of WMGHGs in Earth system models can extend beyond their direct radiative effects to include impacts on ozone and aerosol chemistry and natural emissions of ozone and aerosol precursors. In some cases these can have a significant impacts on the overall radiative budget changes from perturbing WMGHGs within Earth system models (O'Connor et al., submitted; Thornhill et al., submitted). These composition adjustments are very model dependent and are not comparable with offline radiation calculations, so are not considered further here.

All uncertainties in this section are given as 5-95% confidence range.

**[START TABLE 7.3 HERE]**

**Table 7.3:** Adjustments to $CO_2$ forcing due to changes in stratospheric temperature, surface and tropospheric temperatures, water vapour, clouds and surface albedo, as a fraction of the SARF. Note that surface temperature changes are excluded from the forcing in our definition.

| Percentage of SARF | Surface temperature response | Tropospheric temperature adjustment | Stratospheric Adjustment | Surface albedo adjustment | Water vapour adjustment | Cloud adjustment |
|---|---|---|---|---|---|---|
| Vial et al. (2013) | -20% | | | 2% | 6% | 11% |
| Zhang and Huang (2014) | -23% | | 26% | | 6% | 16% |
| Smith et al. (2018b) | -6% | -16% | 30% | 3% | 6% | 12% |

**[END TABLE 7.3 HERE]**

#### *7.3.2.1 Carbon Dioxide*

The $2xCO_2$ ERF is assessed to be 4.0 ± 0.5 W $m^{-2}$ (*high confidence*). Its assessed components are given in Table 7.4. The combined spectroscopic and radiative transfer modelling uncertainties give an uncertainty in the $CO_2$ SARF of around 10% or less (Etminan et al., 2016; Mlynczak et al., 2016). The overall uncertainty in $CO_2$ ERF is assessed as ±12%, as the more uncertain adjustments only account for a small fraction of the ERF (Table 7.3). The ERF estimate has increased by 0.3 W $m^{-2}$ since the AR5 partly due to revised LBL model calculations, but mostly due to the combined effects of adjustments. The historical ERF estimate from $CO_2$ is revised upwards from 1.82 ± 0.38 W $m^{-2}$ in AR5 to 2.15 ±0.26 W $m^{-2}$ in this assessment, from a combination of these revisions and the 4% rise in atmospheric concentrations between 2011 and 2018. These ERFs include any impacts on tropospheric adjustments due to changes in evapotranspiration from the $CO_2$-biophysical effects (Doutriaux-Boucher et al., 2009; Cao et al., 2010; Richardson et al., 2018b). The climate model estimates of $2xCO_2$ ERF (Table 7.2) lie within 11% of the assessed value. The definition of ERF can also include further biophysical effects for instance on dust and biogenic emissions from the land and ocean, but these are not typically included in the modelling set up for $2xCO_2$ ERF and would make comparison with LBL calculations difficult.

**[START TABLE 7.4 HERE]**

**Table 7.4:** Assessed ERF, SARF and tropospheric adjustments to 2x$CO_2$ change since preindustrial times compared to the AR5 assessed range (Myhre et al., 2013b). Adjustments are due to changes in tropospheric temperatures, water vapour, clouds and surface albedo and land cover. Uncertainties based on multi-model spread in Smith et al. (2018b). Note some of the uncertainties are anticorrelated.

| 2x$CO_2$ forcing | AR5 SARF/ERF | SARF (W $m^{-2}$) | Tropospheric temperature adjustment (W $m^{-2}$) | Water vapour adjustment (W $m^{-2}$) | Cloud adjustment (W $m^{-2}$) | Surface albedo and land cover adjustment (W $m^{-2}$) | Total tropospheric adjustment (W $m^{-2}$) | ERF (W $m^{-2}$) |
|---|---|---|---|---|---|---|---|---|
| 2x$CO_2$ ERF components | 3.7 | 3.80 | -0.59 | 0.24 | 0.43 | 0.12 | 0.20 | 4.00 |
| 5%-95% uncertainty ranges as percentage of ERF | 10% (SARF) 20% (ERF) | <10% | ±6% | ±4% | ±7% | ±2% | ±7% | ±12% |

**[END TABLE 7.4 HERE]**

#### 7.3.2.2 Methane

$CH_4$ adjustments have been calculated in nine climate models by Smith et al. (2018b). Since $CH_4$ is known to absorb in the shortwave near infrared, only adjustments from those models including this absorption are taken into account. For these models the adjustments are robustly acting as a negative forcing because the shortwave absorption leads to tropospheric heating and changes in clouds. The adjustment is –14% ± 15% which counteracts much of the increase in SARF identified by Etminan et al. (2016). Modak et al. (2018) also found negative forcing adjustments from a methane perturbation including shortwave absorption in the NCAR CAM5 model, in agreement with the above assessment. The uncertainty in the shortwave component leads to a higher spectroscopic uncertainty (14%) than for $CO_2$ (Etminan et al., 2016). When combined with the uncertainty in the adjustment, this gives an overall uncertainty of 20% (5% – 95% range. There is *high confidence* in the spectroscopic revision but only *medium confidence* in the adjustment modification. The historical ERF estimate from $CH_4$ is revised upwards from 0.48 ± 0.10 W $m^{-2}$ in AR5 to 0.54 ± 0.11 W $m^{-2}$ in this assessment

#### 7.3.2.3 Nitrous oxide

There have been no studies of the adjustments to $N_2O$ at the time of this assessment. Nevertheless, the adjustments might be expected to be similar to those from $CO_2$, without the physiological effects. The tropospheric adjustments to $N_2O$ are therefore assessed to be 0 ± 10% with *low confidence*. The spectroscopic uncertainty is ± 10% (Etminan et al., 2016), giving an overall uncertainty of ± 14%. The historical ERF estimate from $N_2O$ is revised upwards from 0.17 ± 0.06 W $m^{-2}$ in AR5 to 0.19 ± 0.03 W $m^{-2}$ in this assessment.

#### 7.3.2.4 Halogenated species

The stratospheric-temperature adjusted radiative efficiencies for halogenated species were reviewed extensively using LBL models in (Hodnebrog et al., 2013) as used in AR5. Many halogenated species have lifetimes short enough that they can be considered short-lived climate forcers (Box 6.1). As such, although they are considered here as WMGHGs, they are not completely "well-mixed" and their vertical distributions are taken into account when determining their radiative efficiencies. The WMO (World Meteorological Organization, 2018) included more recent spectroscopic studies and updated the species lifetimes. They are therefore used for radiative efficiencies in this assessment.

As with $N_2O$ there have been no studies of the adjustments to halogenated species at the time of this assessment. The tropospheric adjustments are therefore assessed to be 0 ± 10% with *low confidence.* The spectroscopic uncertainties are 13% and 23% for species with lifetimes greater than and less than 5 years respectively (Hodnebrog et al., 2013). The overall uncertainty in the ERFs of halogenated species is therefore assessed to be 16% and 25% depending on the lifetime. The ERF from CFCs is slowly decreasing, but this is more than compensated for by the increased forcing from the replacement species (HCFCs and HFCs). The ERF from HFCs (which will be controlled under the Kigali Amendment to the Montreal Protocol) has increased by 0.012 ± 0.03 W $m^{-2}$. Thus, the concentration changes mean that the total ERF from halogenated species has increased since AR5 from 0.360 ± 0.036 W $m^{-2}$ to 0.376 ± 0.058 W $m^{-2}$ (Table 7.5).

#### 7.3.2.5 Ozone

Estimates of the pre-industrial to present-day tropospheric ozone radiative forcing are based entirely on models. The lack of pre-industrial ozone measurements prevents an observational determination. There have been two studies of ozone ERFs, each based on a single model (MacIntosh et al., 2016; Xie et al., 2016). These did not report corresponding IRFs or SARFs, so it is not possible to quantify the effects of tropospheric adjustments. MacIntosh et al. (2016) presented associated changes in cloud cover, suggesting that increases in stratospheric or upper tropospheric ozone would decrease high clouds and increase low clouds (giving a negative forcing from adjustment), whereas an increase in lower tropospheric ozone decreases low cloud (a positive adjustment). Changes in circulation due to decreases in stratospheric ozone are found to affect southern hemisphere clouds and the atmospheric levels of sea salt aerosol which would contribute additional adjustments, possibly of comparable magnitude to the SARF from stratospheric ozone depletion (Grise et al., 2013, 2014).

Without sufficient information yet to assess the ERFs, this assessment relies on offline radiative transfer calculations of SARF for both tropospheric and stratospheric ozone. Since the AR5, the Coupled Chemistry Model Initiative (CCMI) project has used coupled chemistry-climate models to simulate historical trends in tropospheric and stratospheric ozone (Morgenstern et al., 2017). Two of these models were used to generate the ozone forcing data for CMIP6. The SARFs from the CMIP6 ozone forcing were calculated with an offline radiative transfer model (Checa-Garcia et al., 2018). The values for the 1850–1860 to 2009–2014 SARF were 0.33 W $m^{-2}$ for changes in tropospheric ozone, and –0.03 W $m^{-2}$ for changes in stratospheric ozone. These are in agreement with the AR5 values of 0.36 W $m^{-2}$ (0.18 to 0.54 W $m^{-2}$ 5% to 95% range) and –0.05 (–0.15 to 0.05) W $m^{-2}$ for the period 1850 to 2011 (Myhre et al., 2013b). For tropospheric ozone the assessed central estimate follows Checa-Garcia et al. (2018) and maintains the 50% uncertainty (5%–95% range) from AR5 to give 0.33 (0.16 to 0.50) W $m^{-2}$. AR5 used a 1750 to 1850 SARF of 0.04 W $m^{-2}$ following Skeie et al. (2011), however this study assumed larger changes in emissions over this period than in CMIP6 (Van Marle et al., 2017; Hoesly et al., 2018). For reference to 1750 the FaIR model (Smith et al., 2018a) is used to scale the forcing back using the CMIP6 emissions, giving an additional 0.02 W $m^{-2}$. There is insufficient evidence of any tropospheric ozone trend since 2014, so this is assumed to be flat. The overall assessed estimate is 0.35 (0.18 to 0.52, 5%–95% range) W $m^{-2}$ for the change in tropospheric ozone 1750 to 2018.

Stratospheric ozone has been observed by satellite since 1979 (Stolarski and Frith, 2006), covering the period over which much of the stratospheric ozone changes have occurred, see Chapter 2, Section 2.2.5.2. However, these measurements are not able to constrain the forcing (Chapter 6, Section 6.2.2.5.2). In the absence of further evidence, we maintain the AR5 central estimate, but reduce the upper bound to zero as there is no evidence to support a positive SARF. This gives an assessed SARF of –0.05 (–0.15 to 0.0) W $m^{-2}$ for 1850 to 2014 ERF. As the changes in stratospheric ozone since 2014 are small (Chapter 6, Section 6.2.2.5.2), the same estimate is adopted for 1750–2018. There are currently no estimates of the adjustments to stratospheric ozone beyond stratospheric temperature. Hence the assessed value for ERF is the same as SARF.

#### *7.3.2.6 Stratospheric water vapour*

This assessment considers direct anthropogenic impacts on stratospheric water vapour by oxidation of methane. Stratospheric water vapour may also change as an adjustment to species that warm or cool the upper troposphere-lower stratosphere region, in which case it should be included as part of the ERF for that species. Changes in global surface temperature are also associated with changes in stratospheric water vapour as part of the water vapour climate feedback (section 7.4.2.2). There have been no updates to the SARF estimate of 0.07 W $m^{-2}$ of water vapour from methane oxidation by Myhre et al. (2007), and no estimate of associated tropospheric adjustments. The AR5 SARF estimate (Myhre et al., 2013b) is retained as an estimate of the ERF.

#### *7.3.2.7 Synthesis*

The WMGHG ERF over 1750 to 2018 is assessed to be 3.26±0.29 W $m^{-2}$. It has increased by 0.30 W $m^{-2}$ from 2011 (the time period for AR5) to 2018. Most of this has been due to an increase in $CO_2$ concentration (0.25 ± 0.03 W $m^{-2}$), with increases in $CH_4$, $N_2O$ and halogens adding 0.02, 0.02 and 0.01 W $m^{-2}$ respectively (Table 7.5). Changes in the radiative efficiencies (including adjustments) of $CO_2$ and $CH_4$ have increased the ERF by an additional 0.13 W $m^{-2}$ compared to the AR5 values. Note that the ERFs in this section do not include chemical impacts of WMGHGs on production or destruction of ozone or aerosol formation. The ERFs for tropospheric ozone are slightly decreased compared to the AR5 due to a slight reduction in the assumed ozone precursor emissions in CMIP6 compared to CMIP5. The ERFs for stratospheric ozone and water vapour are unchanged.

**[START TABLE 7.5 HERE]**

**Table 7.5:** Present-day mole fractions in ppt (pmol mol$^{-1}$) (except where specified) and ERF (in W m$^{-2}$) for the WMGHGs. Data taken from Chapter 2, Section 2.2. The data for 2011 (the time of the AR5 estimates) are also shown. Some of the concentrations vary slightly from those reported in AR5 owing to averaging different data sources. For some of the halogenated species the ERF is less than 0.5 mW m$^{-2}$. Radiative efficiencies for the minor gases are given in the appendix. Uncertainties in the RF for all gases are dominated by the uncertainties in the radiative efficiencies. Tabulated global mixing ratios of all well mixed GHGs and ERFs from 1750-2018 are provided in Annex V.

| | Concentration | | ERF with respect to 1850 | | ERF with respect to 1750 | |
|---|---|---|---|---|---|---|
| | 2018 | 2011 | 2018 | 2011 | 2018 | 2011 |
| $CO_2$ (ppm) | 407 | 390 | 1.99±0.24 | 1.74 | 2.15±0.26 | 1.90 |
| $CH_4$ (ppb) | 1859 | 1803 | 0.49±0.10 | 0.47 | 0.54±0.11 | 0.52 |
| $N_2O$ (ppb) | 331 | 324 | 0.18±0.03 | 0.16 | 0.19±0.03 | 0.17 |
| CFC-11 | 228 | 237 | 0.059 | 0.062 | 0.059 | 0.062 |
| CFC-12 | 508 | 528 | 0.163 | 0.169 | 0.163 | 0.169 |
| CFC-13 | 3.21 | 3.04 | 0.001 | 0.001 | 0.001 | 0.001 |
| CFC-113 | 70.4 | 74.6 | 0.021 | 0.022 | 0.021 | 0.022 |
| CFC-115 | 8.62 | 8.39 | 0.002 | 0.002 | 0.002 | 0.002 |
| HCFC-22 | 244 | 213 | 0.051 | 0.045 | 0.051 | 0.045 |
| HCFC-141b | 24.4 | 21.4 | 0.004 | 0.003 | 0.004 | 0.003 |
| HCFC-142b | 22.3 | 20.8 | 0.004 | 0.004 | 0.004 | 0.004 |
| HFC-23 | 31.2 | 24.1 | 0.006 | 0.004 | 0.006 | 0.004 |
| HFC-32 | 16.5 | 5.15 | 0.002 | 0.001 | 0.002 | 0.001 |
| HFC-125 | 26.3 | 10.3 | 0.006 | 0.002 | 0.006 | 0.002 |
| HFC-134a | 102 | 62.7 | 0.016 | 0.010 | 0.016 | 0.010 |
| HFC-143a | 22.4 | 12.0 | 0.004 | 0.002 | 0.004 | 0.002 |
| HFC-152a | 7.01 | 6.55 | 0.001 | 0.001 | 0.001 | 0.001 |
| $SF_6$ | 9.59 | 7.30 | 0.005 | 0.004 | 0.005 | 0.004 |
| $SO_2F_2$ | 2.41 | 1.71 | 0.000 | 0.000 | 0.000 | 0.000 |
| $NF_3$ | 1.83 | 0.83 | 0.000 | 0.000 | 0.000 | 0.000 |
| $CF_4$ | 84.6 | 79.0 | 0.005 | 0.004 | 0.005 | 0.004 |
| $C_2F_6$ | 4.76 | 4.17 | 0.001 | 0.001 | 0.001 | 0.001 |
| $CH_3CCl_3$ | 1.90 | 6.29 | 0.000 | 0.000 | 0.000 | 0.000 |
| $CCl_4$ | 78.8 | 86.1 | 0.013 | 0.015 | 0.013 | 0.015 |
| CFCs[1] | | | 0.253 | 0.263 | 0.253 | 0.263 |
| HCFCs | | | 0.059 | 0.052 | 0.059 | 0.052 |
| HFCs | | | 0.036 | 0.021 | 0.036 | 0.021 |
| Halogens | | | 0.376±0.075 | 0.363 | 0.376±0.058 | 0.363 |
| Total | | | 3.04±0.27 | 2.74 | 3.26±0.29 | 2.96 |

[1] Includes CFC-114, Halon-1211, Halon-1301 and Halon-2401

**[END TABLE 7.5 HERE]**

## *7.3.3 Aerosols*

Anthropogenic activity, and particularly burning of biomass and fossil fuel, has led to a substantial increase in aerosol emissions and atmospheric aerosol concentrations since pre-industrial times (Chapter 6, Figure 6.3). This is particularly true for sulphate and carbonaceous aerosols (Chapter 6, Section 6.2.1). This has in turn led to changes in the scattering and absorption of incoming solar radiation, and also affected cloud micro- and macro-physics and thus cloud radiative properties. The aerosol changes have been strongly heterogeneous in both space and time and have impacted not just Earth's radiative energy budget but also air quality (Chapter 6, Section 6.1). Here, the assessment is focused exclusively on the global mean impacts of aerosols on Earth's energy budget, while regional changes are assessed in Chapter 6.

Consistent with the terminology introduced in Box 7.1, the effective radiative forcing due to changes from direct aerosol-radiation interactions (ERFari) is equal to the sum of the instantaneous TOA radiation change (IRFari) and the subsequent rapid adjustments. Likewise, the effective radiative forcing following interactions between anthropogenic aerosols and clouds (ERFaci, previously referred to as "indirect aerosol effects") can be divided into an instantaneous forcing component (IRFaci) due to smaller but more numerous cloud droplets and subsequent adjustments to cloud water content or extent (spatial and/or temporal). The same way these changes are induced by an increase in the abundance of cloud condensation nuclei (CCN), a change in the abundance of ice nucleating particles (INPs), and thus ice crystal number concentration, could also have occurred since pre-industrial times. If so, this would have impacted the properties of mixed-phase and cirrus (ice) clouds, and thus contributed to ERFaci. In the following, an assessment of IRFari and ERFari (Section 7.3.3.1) focusing on satellite-based evidence (Section 7.3.3.1.1) as well as model-based evidence (Section 7.3.3.1.2) is presented. The same lines of evidence are presented for IRFaci and ERFaci in Section 7.3.3.2. The above lines of evidence are thereafter compared with TOA energy budget constraints on the total aerosol ERF (Section 7.3.3.3) before an overall assessment of the total aerosol ERF is given in 7.3.3.4. For the model-based evidence, all estimates are generally valid for the time period 1750 to 2014 (when CMIP6 historical simulations end), while for satellite-based evidence estimates are valid for 1750 to present-day, where present-day is equivalent to the 2010s. For the overall assessment of total aerosol ERF, these estimates are converted to 1750-2018 values.

### *7.3.3.1 Aerosol-radiation interactions*

Since the AR5, deeper understanding of the processes that govern aerosol radiative properties, and thus IRFari, has emerged. Combined with new insights into adjustments to aerosol forcing, this progress has informed new satellite- and model-based estimates of IRFari and ERFari and associated uncertainties.

#### *7.3.3.1.1 Satellite-based lines of evidence*

The total effect of aerosols on present-day radiative fluxes, REari, is easier to estimate from observations than IRFari, because the latter requires knowledge of pre-industrial aerosol distributions. Since the AR5, estimates of REari have progressed by including aerosols above land surfaces and clouds. Using passive and active aerosol remote sensing retrievals, Lacagnina et al. (2017) and Oikawa et al. (2018) both estimate a globally-averaged, all-sky REari of −2.1 W m$^{-2}$ (likely ranges of –3.2 to –1.0 and –1.8 to –2.4 W m$^{-2}$, respectively). That estimate is smaller in magnitude than the average over ocean-only of −4 to −6 W m$^{-2}$ assessed in AR5 (Boucher et al., 2013) because REari is less negative over more reflective surfaces.

Estimating IRFari requires an estimate of industrial-era changes in Aerosol Optical Depth (AOD) and absorption AOD, which are often taken from global aerosol model simulations. Since the AR5, updates to methods of estimating IRFari based on aerosol remote sensing or data-assimilated reanalyses of atmospheric composition have been published. Ma et al. (2014) applied the method of Quaas et al. (2008) to updated broadband radiative flux measurements from CERES, MODIS-retrieved AODs, and modelled anthropogenic aerosol fractions to find a clear-sky IRFari of −0.6 W $m^{-2}$. This would translate into an all-sky estimate of about −0.3 W $m^{-2}$ based on the clear-to-all-sky ratio implied by Kinne (2019). Rémy et al. (2018) applied the methods of Bellouin et al. (2013b) to the reanalysis by the Copernicus Atmosphere Monitoring Service (CAMS), which assimilates MODIS total AOD. Their estimate of IRFari varies between −0.5 W $m^{-2}$and −0.6 W $m^{-2}$ over the period 2003–2018, and they attribute those relatively small variations to variability in biomass-burning activity. The finding that clear-sky IRFari remains constant over 2000–2012 despite the redistribution of aerosols from high latitudes towards the Equator (Chapter 2, Section 2.2.6 and Chapter 6, Section 6.2.1) was also found by Murphy (2013). Kinne (2019) updated his monthly total AOD and absorbing AOD climatologies, obtained by blending multi-model averages with ground-based sun-photometer retrievals, to find a best estimate of IRFari of −0.4 W $m^{-2}$. The updated IRFari estimates are all scattered around the midpoint of the IRFari range of −0.35 ± 0.5 W $m^{-2}$ assessed by AR5 (Boucher et al., 2013).

The more negative estimate of Rémy et al. (2018) is due to neglecting a small positive contribution from absorbing anthropogenic aerosols above clouds and obtaining a larger anthropogenic fraction than Kinne (2019). However, Rémy et al. (2018) did not update their assumptions on black carbon anthropogenic fraction and contribution to anthropogenic absorption to reflect recent downward revisions (Section 7.3.3.1.2). Kinne (2019) made those revisions, so more weight is given to that study to re-assess the best estimate of satellite-based IRFari to be only slightly stronger than reported in the AR5 at –0.4 W $m^{-2}$. The *very likely* 5% to 95% range given by the AR5 was ±0.5 W $m^{-2}$ (Boucher et al., 2013). Continuing uncertainties in the anthropogenic fraction of total AOD and challenges to the basis of satellite-based approaches, combined with improved knowledge of anthropogenic absorption result in a slightly narrower 5% to 95% range here of ±0.4 W $m^{-2}$. The assessed best estimate and likely IRFari range from satellite-based evidence is therefore –0.4 ± 0.4 W $m^{-2}$*(medium confidence).*

### *7.3.3.1.2 Model-based lines of evidence*

While satellite-based evidence can be used to estimate IRFari, global climate models are needed to calculate the associated adjustments and the resulting ERFari, using the methods described in Section 7.3.1. This calculation is complicated by the fact that the adjustments of clouds caused by absorbing aerosols through changes in the thermal structure of the atmosphere (termed the semidirect effect in AR5) are not easily distinguished from cloud adjustments in ERFaci.

#### ***Model-based estimates of IRFari***

A range of developments since AR5 affect model-based estimates of IRFari. Global emissions of most major species are found to be higher in the current inventories, and with increasing trends. Emissions of the sulphate precursor $SO_2$ are a notable exception; they are similar to those used in the AR5 and approximately time-constant over the last couple of decades (Hoesly et al., 2018). Myhre et al. (2017) showed, in a multi-model experiment, that the net result of these revised emissions is an IRFari trend that is flat in recent years (post-2000), a finding confirmed by a single-model study by Paulot et al. (2018). Another recent development is that the positive forcing from the absorbing component of organic aerosols has been found to be somewhat stronger than that assessed in the AR5.

In the AR5 assessment of black carbon IRFari was markedly strengthened in confidence by the review provided by Bond et al. (2013), where a key factor was a perceived underestimate of modelled atmospheric absorption when compared to Aeronet observations (Boucher et al., 2013). This assessment has since been revised considering new knowledge of the impact of the temporal resolution of emission inventories (Wang et al., 2016), the representativeness of Aeronet sites (Wang et al., 2018), issues with comparing their absorption retrieval to models (Andrews et al., 2017a), and the ageing (Peng et al., 2016), lifetime (Lund et al., 2018b) and average optical parameters (Zanatta et al., 2016) of black carbon.

Consistent with the above updates, Lund et al. (2018a) estimated the net IRFari between 1750 and 2014 to be

–0.17 W m$^{-2}$, using CEDS emissions (Hoesly et al., 2018) as input to the chemical transport model OsloCTM3. They attributed the weaker estimate relative to AR5 numbers (–0.35 ± 0.5 W m$^{-2}$; Myhre et al., 2013a) to stronger absorption by organic aerosol, updated parameterization of black carbon absorption, and slightly reduced sulphate cooling. Broadly consistent with Lund et al. (2018a), Petersik et al. (2018) found an IRFari simulated by ECHAM6-HAM2 of –0.19 W m$^{-2}$, while Zhou et al. (2017b) estimated an IRFari between 1850 and 2000 of –0.23 W m$^{-2}$ using the BCC_AGCM2.0_CUACE/Aero model. These model estimates can be compared to the IRFari (5 to 95% confidence) range of -0.45to -0.05 W m$^{-2}$ that emerged from a comprehensive review in which an observation-based estimate of anthropogenic AOD was combined with model-derived ranges for all relevant aerosol radiative properties (Bellouin et al., 2019).

Based on the above studies, the assessed best estimate and *very likely* RFari range from model-based evidence alone is therefore –0.2 ±0.2 W m$^{-2}$ (*medium confidence*). This represents a significant decrease compared to the AR5 due to stronger organic aerosol absorption, further developed black carbon parameterizations and a somewhat reduced sulphate cooling in recent years.

***Model-based estimates of ERFari***

Since AR5 considerable progress has been made in the understanding of rapid adjustments in response to a wide range of climate forcings, as discussed in Section 7.3.1. The adjustments in ERFari are principally caused by cloud changes, but also by lapse rate and atmospheric water vapour changes, all mainly associated with absorbing aerosols (e.g., black carbon). Stjern et al. (2017) found that for black carbon, about 30% of the (positive) IRFari is offset by adjustments of clouds (specifically, an increase in low clouds and decrease in high clouds) and lapse rate, by analysing simulations by five Precipitation Driver Response Model Intercomparison Project (PDRMIP) models. Similar results have been reported from idealized experiments using modified black carbon wet removal and offline radiative transfer (Hodnebrog et al., 2014; Samset and Myhre, 2015). Smith et al. (2018b) considered more models participating in PDRMIP and suggested that half the IRFari was offset by rapid adjustments for black carbon. Using the MIROC-SPRINTARS model, Zhao and Suzuki (2019) and Takemura and Suzuki (2019)also found that the IRFari of black carbon is largely offset by rapid adjustments. However, Allen et al. (2019) found a positive rapid adjustment for black carbon and suggested that most models simulate negative rapid adjustment for black carbon because the corresponding aerosol atmospheric heating profiles are too vertically uniform in the mid- and low troposphere.

Zelinka et al. (2014) used the Approximate Partial Radiation Perturbation technique to quantify the ERFari between 1860 and 2000 in nine CMIP5 models; they estimated the ERFari (accounting for a small contribution from longwave radiation) to be –0.25 ± 0.22 W m$^{-2}$ (Table 7.6). However, it should be noted that in Zelinka et al. (2014) the semidirect effect of aerosols is not included in ERFari but in ERFaci. The corresponding estimate emerging from the CMIP6 RFMIP (Radiative Forcing Model Intercomparison Project) simulations is –0.21 ± 0.18 W m$^{-2}$(Smith et al., submitted, b), which is generally supported by single-model studies published post-AR5 (Zhang et al., 2016; Fiedler et al., 2017; Nazarenko et al., 2017; Zhou et al., 2017c, 2018; Grandey et al., 2018). Combining CMIP5 and CMIP6 results using expert judgement, ERFari based on model-based evidence is assessed to be –0.25 ± 0.25 W m$^{-2}$

*7.3.3.1.3 Overall assessment of IRFari and ERFari*

Combining the observation-based estimate and 5% to 95% range of IRFari of –0.4 ± 0.4 W m$^{-2}$ with the corresponding model-based estimate and range of –0.2 ± 0.2 W m$^{-2}$, emphasizing the extensive work presented in Bellouin et al. (2019), expert judgement is used to assess IRFari to –0.25 ± 0.25 W m$^{-2}$ (*medium confidence*). ERFari from model-based evidence is –0.25 ± 0.2 W m$^{-2}$, which suggests a small negative adjustment of –0.05 W m$^{-2}$, consistent with recent literature on the topic. Adding this small adjustment to our assessed IRFari estimate of –0.25 W m$^{-2}$ we arrive at an assessment of the best estimate and 5% to 95% confidence range for ERFari of –0.3 ± 0.3 (*medium confidence*). This assessment is consistent with the 5% to 95 % confidence range that emerged from Bellouin et al. (2019) of –0.45 to –0.05 W m$^{-2}$. The larger range for ERFari relative to IRFari reflects uncertainty in the magnitude of the adjustments.

**[START TABLE 7.6 HERE]**

**Table 7.6:** ERF due to changes in aerosol-radiation interactions (ERFari) and changes in aerosol-cloud interactions (ERFaci), and total aerosol ERF (ERFari+aci) from GCM CMIP6 (years 1850–2014) (Smith et al., submitted, b) and CMIP5 (years 1850-2000) (Zelinka et al. (2014)). CMIP6 results are simulated as part of RFMIP (Pincus et al., 2016).

| Models | ERFari ($W m^{-2}$) | ERFaci ($W m^{-2}$) | ERFari+aci ($W m^{-2}$) |
|---|---|---|---|
| CanESM5 | –0.02 | –1.04 | –1.06 |
| CESM2 | +0.15 | –1.57 | –1.43 |
| CNRM-CM6-1 | –0.26 | –0.82 | –1.08 |
| CNRM-ESM2-1 | –0.14 | –0.61 | –0.75 |
| GFDL-CM4 | –0.11 | –0.68 | –0.80 |
| GISS-E2-1-G | –0.52 | –0.78 | –1.30 |
| HadGEM3-GC31-LL | –0.28 | –0.83 | –1.11 |
| IPSL-CM6A-LR | –0.37 | –0.28 | –0.65 |
| MIROC6 | –0.22 | –0.75 | –0.96 |
| MRI-ESM2-0 | –0.46 | –0.71 | –1.17 |
| NorESM2-LM | –0.14 | –1.03 | –1.17 |
| UKESM1-0-LL | –0.20 | –0.97 | –1.16 |
| CMIP6 average ± std. dev. (1850-2014) | –0.21 ± 0.18 | –0.84 ± 0.30 | –1.05 ± 0.22 |
| CMIP5 average ± std. dev. (1850-2000) | –0.25 ± 0.22 | –0.92±0.34 | –1.17±0.30 |

**[END TABLE 7.6 HERE]**

#### *7.3.3.2 Aerosol-cloud interactions*

Anthropogenic aerosol particles primarily affect water clouds by serving as additional cloud condensation nuclei (CCN) and thus increasing cloud drop number concentration ($N_d$) (Twomey, 1959). Increasing $N_d$ while holding liquid water path (LWP, i.e., the vertically integrated cloud water) constant reduces cloud drop effective radius ($r_e$), increases the clouds' albedo, and induces an instantaneous negative radiative forcing (IRFari). The clouds are thought to subsequently adjust by slowing the drop coalescence rate, thereby delaying or suppressing rainfall. Rain generally reduces LWP and reduces cloud lifetime and/or cloud fractional coverage (Cf) (Albrecht, 1989), thus any aerosol-induced rain delay or suppression would be expected to increase LWP and/or Cf. Such rapid adjustments could potentially lead to an ERFaci considerably larger in magnitude than the IRFaci alone. However, adding aerosols to non-precipitating clouds has been observed to have the opposite effect on LWP (i.e., a reduction) (Lebsock et al., 2008; Christensen and Stephens, 2011). These findings have been explained by enhanced evaporation of the smaller droplets in the aerosol-enriched environments, and resultant enhanced mixing with ambient air.

A small subset of aerosols can also serve as ice nucleating particles (INPs) that initiate the ice phase in supercooled water clouds and influence ice crystal number in ice (cirrus) clouds. However, the ability of anthropogenic aerosols (specifically black carbon) to serve as INPs in mixed-phase clouds has been found to be negligible in laboratory studies (e.g., Vergara-Temprado et al. (2018)). No assessment of the contribution to ERFaci from cloud phase changes induced by anthropogenic INPs will therefore be presented.

In ice (cirrus) clouds (cloud temperatures <–40° C), INPs can initiate ice crystal formation at relative humidity much lower than that required for droplets to freeze spontaneously. Anthropogenic INPs can thereby influence ice crystal numbers and thus cirrus cloud radiative properties. At cirrus temperatures, certain types of black carbon have in fact been demonstrated to act as INPs in laboratory studies, suggesting a non-negligible anthropogenic contribution to INPs in cirrus clouds. The associated contribution to ERFaci has recently been investigated in global modelling studies and will be assessed in Section 7.3.3.2.2.

*7.3.3.2.1 Satellite-based evidence*

Since the AR5, the analysis of satellite observations to investigate aerosol-cloud interactions has progressed along several axes: (i) The framework of forcing and adjustments introduced rigorously in the AR5 has helped better categorize studies; (ii) the literature assessing statistical relationships between aerosol- and cloud retrievals has grown, and retrieval uncertainties are better characterized, (iii) advances have been made to infer causality in aerosol-cloud relationships.

***Progress in satellite-based investigations of aerosol-cloud interactions.***

In AR5 studies exploiting the statistical relationship between cloud microphysical properties and aerosol index (AI; AOD multiplied by Ångström exponent) to make inferences about IRFaci were assessed alongside other studies which related cloud quantities to AOD. However, it is now well-documented that the latter approach leads to low estimates of IRFaci since AOD is a poor proxy for cloud-base CCN (Penner et al., 2011; Stier, 2016). Gryspeerdt et al. (2017) demonstrated that the statistical relationship between droplet concentration and AOD leads to an inferred IRFaci that is underestimated by at least 30%, while the use of AI leads to estimates of IRFaci to within ±20%, if the anthropogenic perturbation of AI is known.

Further, studies assessed in the AR5 mostly investigated linear relationships between cloud droplet concentration and aerosol (Boucher et al., 2013). Since in most cases the relationships are not linear over the entire spatio-temporal distribution, this leads to a bias (Gryspeerdt et al., 2016). Several studies did not relate cloud droplet concentration, but cloud droplet effective radius to the aerosol (Brenguier et al., 2000). This is problematic since then, in order to infer IRFaci, stratification by cloud LWP is required (McComiskey and Feingold, 2012). Where LWP positively co-varies with aerosol retrievals (which is often the case), IRFaci inferred from such relationships is biased towards low values. Also, it is increasingly evident that different cloud regimes show different sensitivities to aerosols (Stevens and Feingold, 2009). Averaging statistics over regimes thus bias the inferred IRFaci (Gryspeerdt et al., 2014b). The AR5 concluded that IRFaci estimates tied to satellite studies generally show weak IRFaci (Boucher et al., 2013). However, when correcting for the biases identified in these earlier studies, this is no longer the case.

Multiple studies have found a positive relationship between cloud fraction and/or cloud LWP and aerosols (e.g., Nakajima et al., 2001; Kaufman and Koren, 2006; Quaas et al., 2009). Since the AR5, however, it has been documented that factors independent of causal aerosol-cloud interactions heavily influence such statistical relationships. These include the swelling of aerosol in the high relative humidity in the vicinity of clouds (Grandey et al., 2013) and the contamination of aerosol retrievals next to clouds by cloud remnants and cloud-side scattering (Várnai and Marshak, 2015; Christensen et al., 2017). Stratifying relationships by possible influencing factors such as relative humidity (Koren et al., 2010) does not yield satisfying results since observations of the relevant quantities are not available at the resolution and quality required. Another solution to this problem was to assess the relationship of cloud fraction with droplet concentration (Gryspeerdt et al., 2016; Michibata et al., 2016; Sato et al., 2018). The relationship between satellite-retrieved cloud fraction and $N_d$ was found to be positive (Gryspeerdt et al., 2016, Christensen et al., 2016, 2017), implying an overall adjustment that leads to a more negative ERFaci. However, $N_d$ is biased low for broken clouds and this result has therefore been called into question (Grosvenor et al., 2018). Zhu et al. (2018) proposed to circumvent this problem by considering $N_d$ of only the brightest 10% of the clouds, on the basis of which Rosenfeld et al. (2019) obtained a positive cloud fraction – $N_d$ relationship and thus larger indicated Cf susceptibility to $N_d$.

The relationship between LWP and cloud droplet number is debated. Most recent studies (which are primarily based on MODIS data) find negative statistical relationships (Gryspeerdt et al., 2018a; Michibata et al., 2016; Toll et al., 2017; Sato et al., 2018), while Rosenfeld et al. (2019), in contrast, obtain a modest positive relationship between LWP and $N_d$. To increase confidence that observed relationships between aerosol emissions and cloud adjustments are causal, known emissions of aerosols and aerosol precursor gases into otherwise pristine conditions have been exploited. Ship exhaust is one such source. Goren and Rosenfeld (2014) suggested that both LWP and Cf increase in response to the ship emissions, contributing approximately 3/4 to the total $ERF_{aci}$ for a case of mid-latitude stratocumulus. Christensen and Stephens (2011) found that such strong adjustments occur for open-cell regimes, while adjustments are comparatively small in closed-cell regimes. Volcanic emissions have been identified as another important source of information (Gassó, 2008). From satellite observations, Yuan et al. (2011) documented substantially larger Cf, higher cloud tops, reduced precipitation likelihood, and increased albedo in the plume of the Kilauea volcano in cumulus cloud fields. Ebmeier et al. (2014) confirmed the increased LWP and albedo for other volcanoes. In contrast, for the very large eruption of the Holuhraun (Iceland) volcano, Malavelle et al. (2017) did find a strong decrease in cloud droplet effective radius in satellite observations, but no large-scale change in LWP. However, when accounting for meteorological conditions, McCoy et al. (2018) concluded that for cyclonic conditions, the extra Holuhraun aerosol did enhance LWP. Toll et al. (2017) examined a large sample of volcanoes and also found a distinct albedo effect, but small LWP changes on average. Gryspeerdt et al. (2018a) demonstrated that the negative LWP – Nd relationship becomes very small when conditioned on a volcanic eruption, and therefore concluded that LWP adjustments are small in most regions. Similarly, Toll et al. (2019) studied clouds downwind of various anthropogenic aerosol sources using satellite observations and inferred an albedo effect (IRFaci) of –0.52 W $m^{-2}$ that was partly offset by 23% due to aerosol-induced LWP decreases. However, the study did not consider potential aerosol-induced changes to Cf.

Apart from adjustments involving LWP and Cf, several studies have also documented a negative relationship between cloud-top temperature and AOD/AI in satellite observations (e.g. Koren et al., 2005). Wilcox et al. (2016) proposed a mechanism that could be responsible for such a relationship based on measurements from unmanned aerial vehicles; absorption by black carbon reduces boundary layer turbulence, which in turn leads to taller clouds. However, it has been demonstrated that the satellite-derived relationships are affected by spurious co-variation (Gryspeerdt et al., 2014a), and it therefore remains unclear whether a systematic causal effect exists.

Identifying relationships between INP concentrations and cloud properties from satellites is intractable because the INPs generally represent a very small subset of the overall aerosol population at any given time or location. Nevertheless, there has been some advancement since the AR5. Adding anthropogenic aerosols from ship stacks to supercooled cloud decks of Arctic marine stratocumulus was observed to enhance mixed-phase precipitation, which led to a slight decrease in LWP and albedo compared to the effect of ship tracks in warmer clouds (Christensen et al., 2014). No global observational estimates of the ERFaci associated with mixed-phase clouds exist at present. For ice clouds, only few satellite studies have investigated responses to aerosol perturbations so far. Gryspeerdt et al. (2018b) find a positive relationship between aerosol and ice crystal number for cold cirrus under strong dynamical forcing, which could be explained by an overall larger number of solution droplets available for homogeneous freezing in polluted regions. Zhao et al. (2018) conclude that the sign of the ice crystal size – aerosol relationship depends on humidity. While these studies support modelling results finding that ice clouds do respond to anthropogenic aerosols (Section 7.3.3.2.2), no quantitative conclusions about IRFaci or ERFaci for ice clouds can be drawn based on satellite observations at this point.

Summarising the above findings related to statistical relationships and causal aerosol effects on cloud properties, there is *high confidence* that anthropogenic aerosols lead to an increase in cloud droplet concentrations. In terms of the adjustments, multiple studies support the assessment that on average, no large, systematic aerosol-induced changes in LWP occur (*high confidence*). There is *medium confidence* that liquid-cloud fraction increases in response to aerosol increases. There is no observational evidence at present for a significant response of ice clouds to aerosol perturbations.

**[START TABLE 7.7 HERE]**

**Table 7.7:** Studies quantifying aspects of the global ERFaci that are mainly based on satellite retrievals and were published since AR5. All forcings/adjustments as global annual mean values in W m-2. Most studies split the ERFaci into IRFaci and adjustments in LWP and cloud fraction separately. All published studies only considered liquid-water clouds. Some studies assessed the IRFaci and the LWP adjustment together and called this “intrinsic forcing”(Christensen et al., 2017) and the cloud fraction adjustment “extrinsic

forcing". Published uncertainty ranges are converted to 5%–95 % confidence intervals, and "n/a" indicates that the study did not provide an estimate for the relevant IRF/ERF.

| IRFaci | LWP adjustment | Cloud fraction adjustment | Reference |
|---|---|---|---|
| –0.6±0.6 | n/a | n/a | Bellouin et al. (2013a) |
| –0.4 (–0.2 to –1.0) | n/a | n/a | Gryspeerdt et al. (2017) |
| –1.0±0.4 | n/a | n/a | McCoy et al. (2017a) |
| n/a | n/a | –0.5 (–0.1 to –0.6) | Gryspeerdt et al. (2016) |
| n/a | +0.3 to 0 | n/a | Gryspeerdt et al. (2018b) (0 to –60% of IRFaci) |
| –0.8±0.7 | n/a | n/a | Rémy et al. (2018) |
| –0.53 | +0.12 | n/a | Toll et al. (2019) |
| "intrinsic forcing" | | | |
| –0.5±0.5 | | –0.5±0.5 | Chen et al. (2014) |
| –0.4±0.3 | | n/a | Christensen et al. (2016) |
| –0.3±0.4 | | –0.4±0.5 | Christensen et al. (2017) |

**[END TABLE 7.7 HERE]**

***Satellite-based estimates of IRFaci.***

Since the AR5, several studies assessed the global IRFaci from satellite observations using different methods (Table 7.7). All studies relied on statistical relationships between aerosol- and cloud quantities to infer sensitivities. Four studies inferred IRFaci by estimating the anthropogenic perturbation of $N_d$. For this, Bellouin et al. (2013a) and Rémy et al. (2018) made use of regional-seasonal regressions between satellite-derived $N_d$ and AOD following Quaas et al. (2008). Gryspeerdt et al. (2017) demonstrated that aerosol index (AI) is a better proxy to infer IRFaci, corroborating earlier results by Penner et al. (2011) and Stier (2016), and used this in the regression. McCoy et al. (2017) instead used the sulphate specific mass derived in the MERRA aerosol reanalysis that assimilated MODIS AOD (Rienecker et al., 2011). Studies further need to identify the anthropogenic perturbation of the aerosol to assess IRFaci. Gryspeerdt et al. (2017) and Rémy et al. (2018) used the same approach as Bellouin et al. (2013a) that define anthropogenic fraction using a method adapted from Bellouin et al. (2005). In turn, McCoy et al. (2017) used an anthropogenic fraction from the AEROCOM multi-model ensemble (Schulz et al., 2006). Chen et al. (2014), Christensen et al. (2016) and Christensen et al. (2017) derived the combination of IRFaci and the LWP adjustment to IRFaci ("intrinsic forcing" in their terminology). They relate AI and cloud albedo statistically and use the anthropogenic aerosol fraction from Bellouin et al. (2013a). The variant by Christensen et al. (2017) is an update compared to the Chen et al. (2014) and Christensen et al. (2016) studies in that it better accounts for ancillary influences on the aerosol retrievals such as aerosol swelling and 3D radiative effects.

On average across the published studies based on satellite observations and using expert judgement to assess uncertainty (Table 7.7), IRFaci is assessed to be –0.6 W m$^{-2}$, with a 5% to 95% confidence range of ± 0.5 W m$^{-2}$ (*high confidence*). This range is broadly consistent with the IRFaci 5% to 95% confidence range reported from a comprehensive review paper of –1.6 to –0.2 W m$^{-2}$ (Bellouin et al., 2019).

***Satellite-based estimates of ERFaci.***

Only a handful of studies have estimated the LWP and Cf adjustments that are needed for satellite-based estimates of ERFaci. Chen et al. (2014) and Christensen et al. (2017) used the relationship between cloud fraction and AI to infer the cloud fraction adjustment. Gryspeerdt et al. (2017) used a similar approach but tried to account for non-causal aerosol – cloud fraction correlations by using $N_d$ as a mediating factor. The three studies held together suggest a global cloud fraction adjustment that augments ERFaci relative to

IRFaci by –0.5 ± 0.5 W $m^{-2}$.

For global estimates of the LWP adjustment, evidence is even scarcer. Gryspeerdt et al. (2018a) derived an estimate of the LWP adjustment using a method similar to Gryspeerdt et al. (2016). They estimated that the LWP adjustment offsets 0 to 60% of the (negative) IRFaci. Supporting an offsetting LWP adjustment, Toll et al. (2019) estimated a moderate LWP adjustment of 23% (+0.13 W $m^{-2}$). The adjustment due to LWP is assessed to be small, with a best estimate of 0.2 W $m^{-2}$ and a likely range of ± 0.2 W $m^{-2}$ (*medium confidence*). From the above assessments of IRFaci and the associated adjustments, considering only liquid-water clouds and evidence from satellite observations alone, ERFaci is assessed to be –0.9 W $m^{-2}$ with a 5% to 95% confidence range of ± 0.6 W $m^{-2}$ (*medium confidence*).

##### *7.3.3.2.2 Model-based evidence*

As in the AR5, the representation of aerosol-cloud interactions in large-scale model studies remain a challenge, due to the multiple subgrid-scale processes involved, from the emissions of aerosols and/or their precursors to precipitation formation. Large-scale models that simulate ERFaci typically include aerosol-cloud interactions in liquid stratiform clouds only, while very few include aerosol interactions with mixed-phase-, convective-, and ice clouds. Adding to the spread in model-derived estimates of ERFaci is the fact that model set-ups and assumptions vary across studies, for example when it comes to the treatment of oxidants (that influence aerosol formation) and their changes through time (Karset et al., 2018).

In the AR5, ERFaci was assessed as the residual of the total aerosol ERF and ERFari, as the total aerosol ERF was easier to calculate based on available model simulations (Boucher et al., 2013). The best estimates of total aerosol ERF and ERFari in AR5 were –0.9 W $m^{-2}$ and –0.45 W $m^{-2}$, respectively, yielding an ERFaci estimate of –0.45 W $m^{-2}$. This value is much less negative than the bottom-up estimate of ERFaci from GCMs presented in the AR5. Since the AR5, efforts have been made continually to reconcile this difference. Zelinka et al. (2014) estimated ERFaci to be –0.9 W $m^{-2}$with a standard deviation of 0.34 W $m^{-2}$ (including semi-direct effects) based on nine CMIP5 models (Table 7.6). The corresponding ERFaci estimate based on twelve RFMIP models from CMIP6 is slightly less negative at –0.84 W $m^{-2}$ (standard deviation of 0.30 W $m^{-2}$) (see Table 7.6). Other post-AR5 estimates of ERFaci based on single model studies are either in agreement with or slightly larger in magnitude than the CMIP6 estimate (Gordon et al., 2016; Fiedler et al., 2017; Neubauer et al., 2017; Karset et al., 2018; Regayre et al., 2018; Zhou et al., 2018; Diamond et al., 2019).

The adjustment contribution to the CMIP6 ensemble mean ERFaci is –0.20 W $m^{-2}$, though with considerable differences between the models (standard deviation of 0.30 W $m^{-2}$). Generally, this adjustment in GCMs arises mainly from LWP changes (e.g., Ghan et al., (2016)), while satellite observations suggest that cloud cover adjustments should dominate and that aerosol effects on LWP are exaggerated in GCMs (Bender et al., 2019). Large-eddy-simulations also tend to suggest an exaggerated aerosol effect on cloud lifetime in GCMs, but some report an aerosol-induced decrease in cloud cover that is at odds with satellite observations (Seifert et al., 2015). Despite this potential disagreement when it comes to the dominant adjustment mechanism, a non-negligible negative contribution to ERFaci from adjustments is supported both by observational and modeling studies.

Contributions to ERFaci from anthropogenic aerosols acting as INPs are generally not included in CMIP6 models. While laboratory measurements do not support anthropogenic perturbations to INPs active in mixed-phase clouds, they do suggest that certain black carbon particles may contribute for colder temperatures (< –40 °C) (Ullrich et al., 2017; Mahrt et al., 2018). A global modelling study incorporating parameterizations based on recent laboratory studies found a small negative contribution to ERFaci (Penner et al., 2018), with a central estimate of –0.3 W $m^{-2}$. However, previous studies have produced model estimates of opposing signs (see review in Storelvmo (2017)). There is thus limited evidence and medium agreement for a small negative contribution to ERFaci from anthropogenic INP-induced cirrus modifications (*low confidence*).

Based on the above model-based evidence alone, the best estimate and 5% to 95% confidence range for

ERFaci is assessed to –0.9 ± 0.5 W m$^{-2}$ (*medium confidence*)

#### *7.3.3.2.3 Overall assessment of ERFaci*

The assessment of ERFaci based on satellite evidence alone (–0.9 ± 0.6 W m$^{-2}$, 5% to 95% confidence range) is consistent with the one based on model-evidence alone (–0.9 ± 0.5 W m$^{-2}$, 5% to 95% confidence range), in strong contrast to what was reported in the AR5. This reconciliation of satellite-based and model-based estimates is the result of considerable scientific progress and increases confidence in the overall assessment of the best estimate and likely range for ERFaci of –0.9 ± 0.5 W m$^{-2}$ (*high confidence*). The assessed 5% to 95% confidence range is consistent with but narrower than that reported by the review of Bellouin et al. (2019) of –3.1 to –0.1 W m$^{-2}$.

#### *7.3.3.3 Energy budget constraints on the total aerosol ERF*

Energy balance models of reduced complexity have in recent years increasingly been combined with Monte Carlo approaches to provide valuable "top-down" (also called inverse) observational constraints on the total aerosol ERF. These top-down approaches report ranges of aerosol ERF that are found to be consistent with the global mean temperature record. However, the total aerosol ERF is also used together with the historical temperature record in Section 7.5 to constrain ECS and TCR. Using top-down estimates as a separate line of evidence also for the total aerosol ERF would therefore be circular. Nevertheless, it is useful to examine the development of these estimates since AR5 and the degree to which these estimates are consistent with the assessments of ERFari and ERFaci.

When the first top-down estimates emerged (Knutti et al., 2002), it became clear that some of the early ("bottom-up") GCM estimates of total aerosol ERF were inconsistent with the plausible top-down ranges. However, as more inverse estimates have been published, it has increasingly become clear that they too are model-dependent and span a wide range of ERF estimates, with confidence intervals that in some cases do not overlap (Forest, 2018). It has also become evident that these methods are very sensitive to revised estimates of other forcings and/or updates to observational data sets. A recent review of 19 such estimates reported a mean of –0.77 W m$^{-2}$ for the total aerosol ERF, and a 95% confidence interval of –1.15 W m$^{-2}$ to –0.31 W m$^{-2}$ (Forest, 2018). Adding to that review, a more recent study using the same approach reported an estimate of total aerosol ERF of –0.89 W m$^{-2}$ and a 90% confidence interval of –1.82 to –0.01 W m$^{-2}$ (Skeie et al., 2018). However, in the same study, an alternative way of incorporating ocean heat content in the analysis produced a best total aerosol ERF estimate of –1.34 W m$^{-2}$ (90% confidence interval –2.20 to –0.46), illustrating how these methods are very sensitive to the manner in which observations are included. However, a new approach to inverse estimates took advantage of independent climate radiative response estimates from eight prescribed sea surface temperature and sea-ice simulations over the historical period to estimate the total anthropogenic ERF. From this a total aerosol ERF of –0.8 W m$^{-2}$ with a –1.6 to +0.1 5% to 95% range from 1861–1880 until near-present was derived. This range was found to be more invariant to parameter choices than earlier inverse approaches (Andrews and Forster, in press).

Beyond the inverse estimates described above, other efforts have been made since the AR5 to constrain the total aerosol ERF. For example, Stevens (2015) used the global mean temperature record from the early 20$^{th}$ century to argue for a lower bound of –1.0 W m$^{-2}$. This study also used a simplified (1-dimensional) model to simulate the historical total aerosol ERF evolution consistent with the observed temperature record. Given the lack of temporally extensive cooling trends in the temperature record of the 20$^{th}$ century and the fact that the historical evolution of greenhouse gas forcing is relatively well constrained, the study concluded that a more negative total aerosol ERF than –1.0 W m$^{-2}$ was incompatible with the historical temperature record. This was countered by Kretzschmar et al. (2017), who argued that the model employed in Stevens (2015) was too simplistic, and could therefore not account for the impact of geographical redistributions of aerosol emissions over time. Following the logic of Stevens (2015) but basing their estimates on a subset of CMIP5 models as opposed to a simplified modelling framework, they argued that a total aerosol ERF as negative as –1.6 W m$^{-2}$ was consistent with the observed temperature record. Similar arguments were put forward by Booth et al. (2018), who emphasized that the degree of non-linearity of the total aerosol ERF with aerosol emission is a central assumption in Stevens (2015).

The historical temperature record was also the key observational constraint applied in two additional post-AR5 studies (Rotstayn et al., 2015; Shindell et al., 2015) based on a subset of CMIP5 models. Rotstayn et al. (2015) found a strong temporal correlation (> 0.9) between the total aerosol ERF and the global mean surface temperature. They used this relationship to produce a best estimate for the total aerosol ERF of –0.97 W $m^{-2}$, but with considerable unquantified uncertainty, in part due to uncertainties in the TCR. Shindell et al. (2015) came to a similar best estimate for the total aerosol ERF of –1.0 W $m^{-2}$ and a 95% confidence interval of –1.4 to –0.6 W $m^{-2}$ but based this on spatial temperature and ERF patterns in the models in comparison with observed spatial temperature patterns.

A separate observational constraint on the total ERF was proposed by Cherian et al. (2014), who compared trends in downward fluxes of solar radiation observed at surface stations across Europe (described in Section 7.2.2.3) to those simulated by a subset of CMIP5 models. Based on the relationship between solar radiation trends and the total aerosol ERF in the models, they inferred a relatively strong total aerosol ERF of –1.3 W $m^{-2}$ and a standard deviation of ± 0.4 W $m^{-2}$. Related to Cherian et al. (2014), Storelvmo et al. (2018) found that the reduction in downward solar radiation fluxes measured at surface stations worldwide since the middle of the last century (Section 7.2.) was severely underestimated by the CMIP5 model ensemble mean. The dimming has been attributed to, and is anticorrelated with, global aerosol emissions (Storelvmo et al., 2016), and an underestimation of the dimming trend therefore may imply a too weak aerosol radiative effect.

Based solely on energy balance considerations or other observational constraints, it is *virtually certain* that the total aerosol ERF is negative (*high confidence*), but *very unlikely* that the total aerosol ERF is more negative than –1.8 W $m^{-2}$ (*medium confidence*).

#### *7.3.3.4 Overall assessment of total aerosol ERF*

In the AR5 (Boucher et al., 2013), the overall assessment of total aerosol ERF (ERFari+aci) used the median of all GCM estimates published prior to AR5 of –1.5 W $m^{-2}$ (5% to 95% range of –2.4 W $m^{-2}$ to –0.6 W $m^{-2}$) as a starting point, but reduced the magnitude of that estimate based on the following arguments: (i) Models that accounted for aerosol effects on liquid, mixed-phase and ice clouds tended to produce overall smaller ERFari+aci estimates and were deemed more complete in their representation of aerosol-cloud interactions. This subset of models produced a smaller estimate of –1.38 W $m^{-2}$ for the ERFari+aci and consisted of seven semi-independent models. (ii) Studies that constrained models with satellite observations (five in total) were given extra weight. They produced a median estimate of –0.85 W $m^{-2}$. For studies that only reported ERFaci, an ERFari of –0.45 W $m^{-2}$ was added to produce an ERFari+aci estimate. Furthermore, a longwave ERFaci of +0.2 W $m^{-2}$ was added to studies that only reported shortwave ERFaci values. (iii) Based on higher resolution models, doubt was raised regarding the ability of GCMs to represent the cloud adjustment component of ERFaci with fidelity, and particularly the way in which aerosol effects on warm-rain formation were parameterized. The expert judgement was therefore that aerosol effects on cloud lifetime were too strong in the models, reducing the overall ERF estimate. The above lines of argument, combined with the GCM estimate quoted above, resulted in an overall assessment of ERFari+aci of –0.9 W $m^{-2}$ and a 5% to 95% (90%) confidence range of –1.9 W $m^{-2}$ to –0.1 W $m^{-2}$.

Here, the best estimate and range is revised relative to the AR5 (Boucher et al., 2013), partly based on updates to the above lines of argument in post-AR5 publications. Firstly, the studies that included aerosol effects on mixed-phase and ice clouds (argument (i) above) in AR5 relied on the assumption that anthropogenic black carbon could act as INPs in mixed-phase clouds, which has since been challenged by laboratory experiments (Kanji et al., 2017; Vergara-Temprado et al., 2018). There is also no observational evidence of appreciable ERFs associated with these effects (Section 7.3.3.2.2), and modelling studies disagree when it comes to both their magnitude and sign (Storelvmo, 2017). Likewise, very few GCMs incorporate aerosol effects on deep convective clouds, and cloud-resolving modelling studies report different impacts on cloud radiative properties depending on cloud environmental conditions (Tao et al., 2012). Thus, it is not clear whether omitting such effects in GCMs would lead to any appreciable ERF biases, or if so, what the sign of such biases would be. As a result, all models are given equal weight in this assessment whether they include aerosol impacts on convective, ice and mixed-phase cloud processes or not.

In relation to argument (ii), there is now a considerably expanded body of literature which suggests that early modelling studies that incorporated satellite observations may have resulted in overly conservative estimates of the magnitude of ERFaci (Section 7.3.3.2.1). Furthermore, based on an assessment of the longwave ERFaci in the CMIP5 models, the offset of +0.2 W $m^{-2}$ used to account for the longwave contribution to some model's ERF estimate also appears to be too large (Heyn et al., 2017).

Argument (iii) is still valid when it comes to general limitations in the ability of GCMs to simulate adjustments in LWP and cloud cover in response to aerosol perturbation, but as discussed in Section 7.3.3.2.2 it is not clear that this will result in biases that exclusively reduce the magnitude of the total aerosol ERF.

The assessment of total aerosol ERF here uses the following lines of evidence: satellite-based evidence for IRFari, model-based evidence for IRFari and ERFari, satellite-based evidence of IRF/ERFaci, and finally model-based evidence for IRF/ERFaci. Based on this, the central estimate and 90% confidence range for ERFari and ERFaci are assessed to –0.3± 0.3 W $m^{-2}$ and –0.9 ± 0.5 W $m^{-2}$, respectively. There is thus strong evidence for a substantive negative total aerosol ERF, which is supported by broad agreement between satellite-based and model-based lines of evidence for both ERFari and ERFaci. This leads to an overall *high confidence* in the estimate of ERFari+aci and a narrowing of the uncertainty range. Because the estimates informing the different lines of evidence are generally valid for approximately 2014 conditions, a small adjustment of +0.1 W $m^{-2}$ is added to the ERFari+aci central estimate to make it representative of 2018 conditions. This adjustment reflects recent changes in global aerosol emissions supported by satellite observations and global aerosol reanalyses (Paulot et al., 2018; Bellouin et al., 2019). Accounting for this, and combining the lines of evidence using expert judgement, the ERFari+aci is assessed to be –1.1 W $m^{-2}$ (1750–2018), with a *very likely* range of –2.0 W $m^{-2}$ to –0.4 W $m^{-2}$ and a *likely* range of –1.6 W $m^{-2}$ to –0.7 W $m^{-2}$. These ranges are identical to the corresponding confidence ranges in Bellouin et al. (2019) and consistent with the 5% to 95% confidence ranges reported for ERFari and ERFaci above. There is *high confidence* that ERFaci contributes most (about 3/4) to ERFari+aci, with the remainder due to contributions from ERFari. In contrast to AR5 (Boucher et al., 2013), it is now *virtually certain* that the total aerosol ERF is negative. Figure 7.8 depicts the aerosol ERFs from the different lines of evidence along with the overall assessments.

**[START FIGURE 7.8 HERE]**

**Figure 7.8:** Net aerosol ERFari+aci from different lines of evidence. Green bars show the assessment based on satellite observations. Blue bars show the assessment based on climate models, with individual models from CMIP5 (Zelinka et al., 2014) and CMIP6 (Smith et al., submitted, b) depicted. Individual assessed best-estimate contributions from ERFari and ERFaci are shown with darker and paler shading respectively. Overlaid black diamond and black lines shows the best estimate and *very likely* range of satellite- and model-derived ERFari+aci. Grey shading shows the *very likely* range consistent with energy budget constraints. Purple bars show the assessed *very likely* range (thin), *likely* range (thick), and best estimate (black diamond) from all lines of evidence in this assessment.

**[END FIGURE 7.8 HERE]**

### *7.3.4 Other agents*

In addition to the large anthropogenic ERFs associated with WMGHGs and atmospheric aerosols assessed in Sections 7.3.2 and 7.3.3, land use change, contrails and aviation-induced cirrus and light absorbing particles deposited on snow and ice have also contributed to the overall anthropogenic ERF and are assessed in Sections 7.3.4.1, 7.3.4.2 and 7.3.4.3. Changes in solar irradiance, galactic cosmic rays and volcanic eruptions since pre-industrial times combined represent the natural contribution to the total (anthropogenic + natural)

ERF and are discussed in Sections 7.3.4.4, 7.3.4.5 and 7.3.4.6.

#### *7.3.4.1 Land use*

Land use forcing is defined as those changes directly caused by human activity rather than by climate response. Land use change affects the surface albedo. Deforestation replaces darker forested areas with brighter cropland, and thus imposes a negative radiative forcing on climate, while afforestation and reforestation have the opposite effect. Land use change also affects the amount of water transpired by vegetation (Devaraju et al., 2015). Irrigation of land directly affects the evaporation (Sherwood et al., 2018) causing a global increase of 32 500 $m^3 s^{-1}$ due to human activity (Boucher et al., 2004). Changes in evaporation and transpiration affect the latent heat budget, but do not directly affect the top-of-atmosphere radiative fluxes. The lifetime of water vapour is so short that the impact of changes in evaporation on the greenhouse contribution of water vapour are negligible (Sherwood et al., 2018). However, evaporation can affect the ERF through adjustments, particularly through changes in low cloud amounts. Land use change affects the emissions or removal of greenhouse gases from the atmosphere (such as $CO_2$, $CH_4$, $N_2O$). These emission changes have the greatest impact on climate (Ward et al., 2014), however they are already included in greenhouse gas inventories. Land use change also affects the emissions of dust and biogenic volatile organic compounds (BVOCs), which form aerosols and affect the atmospheric concentrations of ozone and methane (Chapter 6, Section 6.2). The impacts of land use on surface temperature and hydrology were recently assessed in the Special Report on Climate Change and Land (Jia et al., 2019).

Using the definition of ERF from Section 7.1, the adjustment in land surface temperature is excluded from the definition of ERF, but changes in vegetation and snow cover are included. Land use change in the mid-latitudes induces a substantial amplifying adjustment in snow cover. Few studies have attempted to quantify the ERF of land use change. Andrews et al. (2017) calculated a very large surface albedo ERF (–0.47 W $m^{-2}$) from 1860 to 2005 in the HadGEM2-ES model although they did not separate out the surface albedo change from snow cover change. HadGEM2-ES is known to overestimate the amount of boreal trees and shrubs in the unperturbed state (Collins et al., 2011) so will tend to overestimate the ERF associated with land use change. The increases in dust in HadGEM2-ES contributed an extra –0.25 W $m^{-2}$, whereas cloud cover changes added a small positive adjustment (0.15 W $m^{-2}$) consistent with a reduction in transpiration. An assessment of radiative adjustments in CMIP6 models (Smith et al., submitted, b) also found a reduction in cloud cover that offset around half of the albedo IRF, with a large model spread that could potentially cancel out the IRF forcing or even change its sign.

One estimate of the indirect SARF from land use change due to reduced BVOCs leads to a negative contribution of –0.11 W $m^{-2}$ over the historical period (Unger, 2014) through decreases in ozone and methane, whereas Scott et al. (2017) find that the decrease in aerosols from BVOCs outweighs the forcing contribution from ozone and methane. This disagreement illustrates that adjustments through changes in aerosols and chemistry are very model dependent, and it is not possible to make an assessment based on such a limited number of studies.

The contribution of land use change to albedo changes has recently been investigated using MODIS and AVHRR to attribute surface albedo to geographically-specific land cover types (Ghimire et al., 2014). When combined with a historical land use map (Hurtt et al., 2011) this gives a 1700 to 2005 SARF of –0.15 ± 0.01 W $m^{-2}$, of which –0.12 W $m^{-2}$ is from 1850. This study accounted for correlations between vegetation type and snow cover, but not the adjustment in snow cover identified in (Andrews et al., 2017b). The cloud adjustment is assessed at half of this (0.075 ± 0.075 W $m^{-2}$). The contribution of irrigation (mainly to low cloud amount) is assessed as -0.05 W $m^{-2}$(–0.1 to 0.05 W $m^{-2}$,5% to 95%range) for the historical period (Sherwood et al., 2018). Thus, the overall assessment of the ERF from land use change is –0.12 W $m^{-2}$ (–0.21 to –0.03 W $m^{-2}$, 5% to 95%range) (*medium confidence*). This does not include the effects of snow-albedo which have not been confirmed by multiple studies.

#### 7.3.4.2 Contrails and aviation-induced cirrus

Aviation-induced cirrus can form in the wake of aircraft exhausts. It can be short-lived or persist for hours and spread, depending on the prevailing atmospheric conditions. It is principally affected by emissions of water vapour, but emissions of aerosols in the aircraft exhaust can also influence contrail formation and properties. These aerosol emissions can also potentially affect low level clouds (Section 7.3.3).

In AR5 the SARF due to contrails and aviation-induced cirrus was assessed to 0.05 (0.02–0.15) W $m^{-2}$, but a *low confidence* was assigned to that estimate (Myhre et al., 2013b). This positive SARF is the net result of a positive longwave ERF and a smaller negative shortwave ERF, as expected for thin cirrus clouds (Section 7.4). There was also climate modelling evidence that this forcing was between 30% and 60% as effective at changing surface temperature as an equivalent forcing from $CO_2$, i.e. the SARF efficacy was 60% or smaller (see Section 7.3.1). Since the AR5, a comprehensive review on the topic (Kaercher, 2018) reported post-AR5 SARF estimates ranging from 0.01–0.06 W $m^{-2}$, based on new studies that all used 2006 as their reference period (Chen and Gettelman, 2013; Schumann and Graf, 2013; Schumann et al., 2015; Bock and Burkhardt, 2016). The first published estimate of contrail and aviation induced cirrus ERF accounts for the efficacy of the contrail forcing and found that ERF was at least 50% smaller than SARF with a best estimate of 35% (Bickel et al. 2019), in good agreement with the efficacy studies presented in the AR5 (Myhre et al., 2013b). The Lee et al. (submitted) assessment carefully compares the above referenced studies, updates them to 2018 based on air traffic growth and uses estimates of contrails to estimate an aviation induced cirrus ERF of 0.04 W $m^{-2}$ with a 5% to 95% confidence interval of 0.01 to 0.07 W $m^{-2}$. This range is adopted as the assessment within this report. Compared to the AR5, there is better process modelling of aviation-induced cirrus within climate models and also a better understanding of how adjustments reduce the contrail induced cirrus, therefore a *medium confidence* is assigned.

#### 7.3.4.3 Light absorbing particles on snow and ice

Light-absorbing particles deposited on snow and ice decrease surface albedo from the cryosphere, contributing a positive radiative forcing (Bond et al., 2013). Most previous research has focused on black carbon, although organic carbon and mineral dust can also contribute to the ERF (Skiles et al., 2018). The majority of present-day carbonaceous aerosol loading, and around half of present-day atmospheric dust loading, is due to anthropogenic activities (McConnell et al., 2007; Mahowald et al., 2010).

The AR5 assessed the forcing due to deposition of anthropogenic black carbon on snow to 0.04 (0.02 to 0.09) W $m^{-2}$ (Myhre et al., 2013b), with the review from Bond et al. (2013) informing this assessment. Since the AR5, one further study of global radiative forcing from black carbon on snow deposition agrees with the AR5 best estimate of 0.04 W $m^{-2}$(Namazi et al., 2015). Organic carbon deposition on snow and ice has been estimated to contribute a small positive radiative forcing of 0.001–0.003 W $m^{-2}$ (Lin et al., 2014). No comprehensive global assessments of mineral dust deposition on snow are available. Most radiative forcing estimates have a regional emphasis, focusing on the Arctic (Jiao et al., 2014), Himalayas (Wang et al., 2015b), and to a lesser extent North America, Europe and northern China (Skiles et al., 2018). Black carbon deposition and associated snow-albedo change over the Antarctic continent is considered to be negligible (Bisiaux et al., 2012; Bauer et al., 2013). The regional focus of most studies makes estimating a global mean radiative forcing from aggregating different studies problematic, but the relative importance of each region is *likely* to change if the global pattern of emission sources changes (Bauer et al., 2013). Changes to surface albedo in the cryosphere are difficult to observe with satellites (Warren, 2013), and so modelling studies are often validated using field measurements (e.g. Jiao et al. (2014)).

Owing to the small effect of organic carbon, and no significant revisions to the radiative forcing from black carbon on snow and ice, the best estimate and uncertainty range of radiative forcing from absorbing aerosol on snow and ice is unchanged since the AR5, remaining at 0.04 (0.02–0.09) W $m^{-2}$. The efficacy of black carbon on snow forcing was estimated to be 2 to 4 times as large as for an equivalent $CO_2$ forcing as the effects are concentrated at high latitudes in the cryosphere (Bond et al., 2013). However, it is unclear how much of this effect would be accounted for if ERF was calculated, and how much comes from the high latitude nature of the forcing. For the overall ERF the radiative forcing is doubled to partly take the efficacy effects into account, giving an overall assessment of 0.08 (0.04–0.18) W $m^{-2}$, with *low confidence*.

### *7.3.4.4 Solar*

Variations in the total solar irradiance (TSI) represent a natural external forcing agent. The dominant cycle is the solar 11-year activity cycle, which is superimposed on longer cycles (Chapter 2, Section 2.2). Over the last three 11-year cycles, the peak-to-trough amplitude in TSI has differed by about 1 W $m^{-2}$ between solar maxima and minima (Chapter 2, Figure 2.1).

Much of the variance in the solar irradiance, over the solar cycle and between solar cycles, occurs at short wavelengths in the 200–400 nm band (Lean et al., 1997, 2005). The IRF can be derived simply by $\Delta$TSI × (1 – albedo)/4 irrespective of wavelength, where the planetary albedo is taken to be 0.29 and $\Delta$TSI represents the change in total solar irradiance (Stephens et al., 2015). The adjustments are expected to be wavelength dependent. Gray et al. (2009) determined a stratospheric temperature adjustment of –22% to spectrally resolved changes in the solar radiance over one solar cycle. This negative adjustment is due to stratospheric heating from increased absorption by ozone at the short wavelengths, increasing the outgoing longwave radiation to space. A multi-model comparison (Smith et al., 2018b) calculated adjustments of –4% due to stratospheric temperatures and –6% due to tropospheric processes (mostly clouds), for a change in TSI across the spectrum. The smaller magnitude of the stratospheric-temperature adjustment is consistent with the broad spectral change rather than the shorter wavelengths characteristic of solar variation. A single model study also found an adjustment that acts to reduce the forcing (Modak et al., 2016). While there has not yet been a calculation based on the appropriate spectral change, the –6% tropospheric adjustment from Smith et al. (2018b) is adopted along with the Gray et al. (2009) stratospheric temperature adjustment. The ERF due to solar variability over the historical period is therefore represented by 0.72 × $\Delta$TSI × (1 – albedo)/4 using the TSI timeseries from Chapter 2, Section 2.2.2.

The AR5 (Myhre et al., 2013b) assessed solar SARF from around 1750 to around 2011 to be 0.05 (0.00–0.10) W $m^{-2}$ which was computed from the 7-year mean around the solar minima in 1745 (being closest to 1750) and 2008 (being the most recent solar minimum). Solar minima are used because they are less variable between cycles and more appropriate to measure changes in activity (Myhre et al., 2013b). The inclusion of tropospheric adjustments that reduce ERF (compared to SARF in AR5) has a negligible impact on the overall forcing. Prior to the satellite era, proxy records are used to reconstruct historical solar activity. In the AR5, historical records were constructed using observations of solar magnetic features. In this assessment historical time series are constructed from radiogenic compounds in the biosphere and in ice cores that are formed from cosmic rays (Steinhilber et al., 2012).

In this assessment the TSI from the Paleoclimate Model Intercomparison Project Phase 4 (PMIP4) reconstruction is used (Jungclaus et al., 2017, Chapter 2, Section 2.2). Proxies constructed from the $^{14}$C and $^{10}$Be radiogenic records for the SATIRE-M model (Vieira et al., 2011) and $^{14}$C record for the PMOD model (Shapiro et al., 2011) for the 1745 solar minimum provide 1745 to 2008 ERFs of –0.01, –0.02 and 0.00 W $m^{-2}$ respectively. Several other proxy reconstructions of TSI have become available since the AR5 (Egorova et al., 2018; Lean, 2018; Wu et al., 2018), resulting in 1745 to 2008 ERFs ranging from –0.05 to +0.10 W $m^{-2}$. One substantially higher ERF estimate of +0.35 W $m^{-2}$ derived from TSI reconstructions in Egorova et al. (2018) is based on a later recovery in solar modulation potential from the Maunder Minimum (Muscheler et al., 2016). However, the estimate from Egorova et al. (2018) hinges on assumptions about long-term changes in the quiet Sun for which there is no observed evidence, so this estimate is not explicitly taken into account in the assessment presented in this section.

The best estimate solar ERF is assessed to be –0.01 W $m^{-2}$, being the mean of the PMIP4 datasets, with a *likely* range of –0.05 to +0.10 W $m^{-2}$ (*low confidence*). The *likely* range is wider than in AR5 and asymmetric due to the increased diversity in TSI reconstructions prior to 1750, notably those that show a negative forcing due to an upward revision of TSI in the 1740s.

### 7.3.4.5 Galactic Cosmic Rays

Variations in the flux of galactic cosmic rays (GCR) reaching the atmosphere is modulated by solar activity and affect new particle formation in the atmosphere through its link to ionization of the troposphere (Lee et al., 2019). It has been suggested that periods of high GCR flux correlate with increased aerosol and CCN concentrations and therefore also with cloud properties (e.g. Dickinson, 1975; Kirkby, 2007), particularly for low altitude clouds (Svensmark and Friis-Christensen, 1997; Marsh and Svensmark, 2000).

Since the AR5, considerable progress has been made connecting GCR to new particle formation, particularly by work performed at the CERN CLOUD chamber (Cosmics Leaving OUtdoor Droplets) (e.g. Dunne et al., 2016; Gordon et al., 2016, 2017; Kirkby et al., 2016), but also by others (e.g. Yu and Luo, 2014). Several studies found that a considerable fraction (up to 50 %) of atmospheric particle nucleation involves ions (Kirkby et al., 2016; Gordon et al., 2017), yet the dependence on ion concentration is relatively weak (Dunne et al., 2016). Combined with small variations in the atmospheric ion concentration over centennial time scales (Usoskin, 2017), it is therefore unlikely that cosmic ray intensity impact present day climate via nucleation (Yu and Luo, 2014; Dunne et al., 2016; Pierce, 2017; Lee et al., 2019). This is supported by Gordon et al. (2017), who linked the GCR-induced new particle formation found from CLOUD experiments to CCN and found the CCN concentration for low clouds to differ by 0.2% to 0.3 % between solar maximum and solar minimum of the solar cycle and concluded that the effect of changes in GCR intensity on CCN is small.

Studies also seek to establish a causal relationship between GCR and properties of the climate system based on correlations and theory. Svensmark et al. (2016) used a Monte Carlo bootstrap-based statistical test to find correlations between Forbush decreases and aerosol and cloud properties in satellite (MODIS and ISCCP) and ground based (Aeronet) data. While this supports the findings of Svensmark et al. (2009), multiple studies investigating this link have challenged such correlations (Kristjánsson et al., 2008; Calogovic et al., 2010; Laken, 2016). No study has corroborated the new findings of Svensmark et al. (2016) to date.

AR5 concluded that while GCR enhance new particle formation, the effect on CCN is too weak to have any detectable impact on climate and no robust association was found between GCR and cloudiness (Boucher et al., 2013). Published literature since then robustly support these conclusions with key laboratory, theoretical and observational evidence. An assessment can now be made with *high confidence* that GCRs contribute a negligible ERF.

### 7.3.4.6 Volcanic

There is large episodic negative radiative forcing associated with aerosols being ejected into the stratosphere from explosive volcanic eruptions, accompanied by smaller eruptions, where only a small amount of aerosol reaches the upper troposphere/stratosphere. The volcanic SARF in the AR5 (Myhre et al., 2013b) was derived by scaling the stratospheric aerosol optical depth (SAOD) by a factor of –25 W m$^{-2}$ per SAOD from Hansen et al. (2005). Quantification of the adjustments to SAOD perturbations from climate model simulations have determined a significant positive rapid adjustment driven by shortwave clouds (Marshall et al., submitted), leading to estimates of –17 and –20 W m$^{-2}$ per SAOD (Gregory et al., 2016; Larson and Portmann, 2016), with some evidence that ERF may be non-linear with SAOD for large eruptions (Marshall et al., submitted). A study where volcanic $SO_2$ emissions were prescribed found a positive forcing through effects on upper tropospheric ice clouds, due to additional ice nucleation on the volcanic sulphate particles (Schmidt et al., 2018). With only one study so far, the contribution to volcanic ERF due to sulphate aerosol impacts on ice clouds is not included in the overall assessment.

Non-explosive volcanic eruptions generally yield negligible global ERFs due to the short atmospheric lifetimes (a few weeks) of volcanic aerosols in the troposphere. However, as discussed in Section 7.3.3.2, the massive fissure eruption in Holuhraun, Iceland persisted for months in 2014 and 2015 and did in fact result in a marked and persistent reduction in cloud droplet radii and a corresponding increase in cloud albedo regionally (Malavelle et al., 2017). This shows that also non-explosive fissure eruptions can lead to strong regional and even global ERFs, but because the Holuhraun eruption occurred in NH winter, solar insolation was weak and the observed albedo changes therefore did not result in an appreciable global ERF.

The adjustment component of ERF for volcanic stratospheric aerosols is assessed to be an average of the three climate model based SAOD efficiency calculations, with a 5% to 95% range estimated from the spread in these results to give a total ERF assessed scaling of $-18 \pm 3$ W $m^{-2}$ per SAOD (*medium confidence*). This is applied to the SAOD timeseries from Chapter 2, Section 2.2 to generate a timeseries of temperature response in Figure 7.12.

### *7.3.5 Synthesis of Global Mean Radiative Forcing, Past and Future*

#### *7.3.5.1 Summary of major changes in forcing since IPCC AR5*

The AR5 introduced the concept of ERF and adjustments and made a preliminary assessment that the tropospheric adjustments were zero for all species other than the effects of aerosol-cloud interaction and black carbon. Since the AR5, new studies have allowed for a tentative assessment of values for tropospheric adjustments to $CO_2$, $CH_4$, and stratospheric aerosols, to place a tighter constraint on adjustments from aerosol-cloud interaction and to assess a likely sign of the tropospheric adjustments for other forcing agents (section 7.3.2, 7.3.4).

The radiative efficiencies for $CO_2$, $CH_4$ and $N_2O$ have been updated since the AR5 (Etminan et al., 2016). The differences for $CO_2$, and $N_2O$ are small at present day concentrations, but the radiative efficiency for $CH_4$ is increased by 25% (see section 7.3.2) (*high confidence*) although the tropospheric adjustment is tentatively assessed to offset that by 14% (*medium confidence*).

#### *7.3.5.2 Summary ERF assessment*

Figure 7.9 shows the industrial-era ERF estimates for 1750 to 2018 for the different forcing agents. The assessed uncertainty distributions for each individual component are combined with a 200,000-member Monte Carlo simulation that samples the different distributions, assuming they are independent, to obtain the overall assessment of total present-day ERF.

**[START FIGURE 7.9 HERE]**

**Figure 7.9:** Effective radiative forcing from 1750 to 2018 by contributing forcing agents.

**[END FIGURE 7.9 HERE]**

**[START TABLE 7.8 HERE]**

**Table 7.8:** Summary table of ERF estimates for AR6 and comparison with the four previous IPCC assessment reports. For AR5 and AR6 these include tropospheric adjustments where known. 5% to 95% ranges are shown. Volcanic ERF is not added to the table due to the episodic nature of volcanic eruptions which makes it difficult to compare to the other forcing mechanisms. Solar ERF is based on TSI and not spectral variation.

| | Global Mean Effective Radiative Forcing (W $m^{-2}$) | | | | | |
|---|---|---|---|---|---|---|
| | *SAR (1750–1993)* | *TAR (1750–1998)* | *AR4 (1750–2005)* | *AR5 (1750–2011)* | *AR6* (1750–2018) | *Comment* |
| $CO_2$ | 1.56 [1.33, | 1.46 [1.31 | 1.66 [1.49, | 1.82 [1.63, | 2.15 [1.89 | Increases in concentrations. |

| | | | | | | |
|---|---|---|---|---|---|---|
| | 1.79] | to 1.61] | 1.83] | 2.01] | to 2.41] | Changes to radiative efficiencies. Inclusion of tropospheric adjustments. |
| $CH_4$ | 0.47 [0.40, 0.54] | 0.48 [0.41, 0.55] | 0.48 [0.43, 0.53] | 0.48 [0.43, 0.53] | 0.54 [0.43, 0.65] | |
| N2O | 0.14 [0.12, 0.16] | 0.15 [0.14, 0.16] | 0.16 [0.14, 0.18] | 0.17 [0.14, 0.20] | 0.19 [0.16, 0.22] | |
| Halogens | 0.26 [0.22, 0.30] | 0.36 [0.31, 0.41] | 0.33 [0.30, 0.36] | 0.36 [0.32, 0.40] | 0.38 [0.32, 0.43] | |
| Tropospheric ozone | +0.40 [0.20, 0.60] | +0.35 [0.20, 0.50] | +0.35 [0.25, 0.65] | +0.40 [0.20, 0.60] | +0.35 [0.18, 0.52] | Most recent model estimates. No tropospheric adjustment assessed. |
| Stratospheric ozone | –0.1 [–0.2, –0.05] | –0.15 [–0.25, –0.05] | –0.05 [–0.15, +0.05] | –0.05 [–0.15, +0.05] | –0.05 [–0.15, 0.0] | No tropospheric adjustment assessed |
| Stratospheric water vapour from $CH_4$ | Not estimated | [0.01, 0.03] | +0.07 [+0.02, +0.12] | +0.07 [+0.02, +0.12] | +0.07 [+0.02, +0.12] | Estimate unchanged. |
| Aerosol–radiation interactions | Not estimated | Not estimated | –0.50 [–0.90, –0.10] | –0.45 [–0.95, +0.05] | –1.1 [–2.0, –0.4] | Ari Reduced by about 55% compared to AR5<br>Aci Increased by 100% compared to AR5 |
| Aerosol–cloud interactions | [0, –1.5] (sulphate only) | [0. –2.0] (all aerosols) | –0.70 [–1.80, –0.30] (all aerosols) | –0.45 [–1.2, 0] | | |
| Land use | Not estimated | –0.20 [–0.40, 0.0] | –0.20 [–0.40, 0.0] | –0.15 [–0.25, –0.05] | –0.12 [–0.21, –0.03] | Includes irrigation, and cloud adjustments. |
| Surface albedo (black+organic carbon aerosol on snow and ice) | Not estimated | Not estimated | +0.10 [0.0 to +0.20] | +0.04 [+0.02 to +0.09] | +0.08 [+0.04 to +0.18] | Increased since AR5 to better account for temperature effects |
| Combined contrails and contrail-induced cirrus | Not estimated | 0 to +0.04 | Not estimated | +0.05 [+0.02 to +0.15] | +0.04 [+0.01 to +0.07] | Narrower range since AR5 |
| Total anthropogenic | Not estimated | Not estimated | 1.6 [0.6 to 2.4] | 2.3 [1.1 to 3.3] | **2.53 [1.56 to 3.32]** | Slight increase due to compensating effects of greenhouse gases and aerosol |
| Solar irradiance | +0.30 [+0.10 to +0.50] | +0.30 [+0.10 to +0.50] | +0.12 [+0.06 to +0.30] | +0.05 [0.0 to +0.10] | –0.01 (–0.05 to +0.10) | Revised historical TSI estimates |

**[END TABLE 7.8 HERE]**

The total anthropogenic ERF over the industrial era (1750–2018) is estimated as 2.53 (1.58 to 3.34, 5% to 95% range) W m$^{-2}$ (Table 7.8) (*high confidence)*. This represents an 11% increase over the assessment made in AR5 (Myhre et al., 2013b) for the period 1750–2011. This increase is a result of compensating effects. Atmospheric concentrations of well-mixed greenhouse gases since 2011 and upwards revisions of their forcing estimates have led to a 15% increase in their ERF. Whereas, the total aerosol ERF is assessed to be 22% more negative compared to AR5, due to revised estimates rather than trends *(high confidence).* This estimate is very similar to an up-to-date inverse estimate of total ERF based on using Box 7.1, Equation 7.1 with estimates of climate response, surface temperature change and energy imbalance over the shorter 1861–1880 to present day of 2.3 W m$^{-2}$ (1.7 to 3.0 W m$^{-2}$, 5% to 95% range) (Andrews and Forster, in press). Anthropogenic ERF from 1750 to the 1850-1900 period, sometimes used as a proxy for pre-industrial temperature observations (Chapter 1, Cross-Chapter Box 1.2), is 0.22 (0.11–0.32) W $m^{-2}$, driven by an increase in greenhouse gas concentrations that were partially offset by aerosols over this time period.

Greenhouse gases, including ozone and stratospheric water vapour from methane oxidation, are estimated to contribute an ERF of 3.63 W $m^{-2}$ (3.27 to 3.97 W $m^{-2}$, 5% to 95% range). 3.26 W $m^{-2}$ (2.97 to 3.55 W $m^{-2}$, 5% to 95% range) of this ERF comes from the well-mixed greenhouse gases, with ozone and stratospheric water vapour changes contributing the remainder. Carbon dioxide continues to contribute the largest part of this ERF (*high confidence*). There has been a significant increase in the estimated shortwave forcing from methane (*high confidence*), somewhat countered by a negative adjustment (*medium confidence*). There is also a 5% upwards revision due to inclusion of tropospheric adjustments for $CO_2$ (*medium confidence*) and 3% increase in the SARF from LBL calculations (*medium confidence*).

Aerosols have in total contributed an ERF of –1.1 W $m^{-2}$ (–2.0 to –0.4 W $m^{-2}$, 5% to 95% range). Aerosol-cloud interactions contribute approximately ¾ to this ERF, with the remainder due to aerosol radiation interaction *(high confidence).*

For the purpose of comparing forcing changes with historical temperature change, longer averaging periods are useful. The change in ERF from the second half of the 19$^{th}$ century (1850–1900) compared with a recent period (2006–2018) is 1.97 W $m^{-2}$ (1.00 to 2.77 W $m^{-2}$, 5% to 95% range), of which 1.70 W $m^{-2}$ (1.50 to 1.90 W $m^{-2}$, 5% to 95% range) is due to $CO_2$.

#### *7.3.5.3 Forcing contribution by emitted species*

Figure 7.10 shows the ERF estimates for 1850 to 2014 for reactive gases and aerosols attributed to emitted species. These estimates are based on CMIP6 models with interactive atmospheric chemistry and aerosols (Thornhill et al. submitted). The diagnosed changes in methane lifetime are used to infer changes in methane concentration and hence ERF, see Chapter 6, Section 6.3.1.1. Diagnosed changes in radiative fluxes for clear-sky and aerosol-free conditions are used to separate the direct aerosol IRFari and cloud effects (Ghan, 2013; Thornhill et al. submitted), where the cloud effects include cloud adjustments (semi-direct effect) and ERFaci. The ERF attributed to methane emissions (0.99±0.18 W $m^{-2}$) is much larger than the ERF from changes in methane concentrations (0.54±0.11 W $m^{-2}$) due mostly to the production of ozone and stratospheric water vapour, but also because methane concentrations would have been higher in the absence of $NO_X$ emissions. This means that the methane ERF from chemical adjustments is 0.45 ± 0.11 W $m^{-2}$ ,which is consistent with AR5 (Myhre et al., 2013b) and there is *high confidence* in this statement.

Halocarbons were assessed as very likely causing a net positive ERF in the AR5, however the more recent studies (O'Connor et al., submitted; Thornhill et al. submitted) find stronger ozone depletion such that the 5% to 95% confidence range in net halocarbon ERF extends to zero (0.0 to 0.16 W $m^{-2}$) (*high confidence*). The WMGHGs ($CH_4$, $N_2O$, halocarbons) are found to induce negative cloud forcings, which in one study are found to be due to increases in oxidation of aerosol precursors and increased natural aerosol emission (O'Connor et al., submitted). There is low confidence in this cloud attribution due to the limited number of models studied. Historical $NO_X$ and volatile organic compound (VOC) emissions have both contributed to the ozone ERF, but $NO_X$ emissions have decreased the methane lifetime giving a net negative ERF whereas VOC emissions have increased the methane lifetime adding to the positive ERF. There is high confidence in the signs of both the $NO_X$ and VOC ERFs, and they agree with the AR5 assessment (Myhre et al., 2013b). $SO_2$ emissions make the dominant contribution to the ERFaci (high confidence). Black carbon emissions offset a significant fraction of the negative IRFari from scattering aerosols (Chapter 6, Section 6.3.1), but there is *low confidence* in this due to the limited number of models.

**[START FIGURE 7.10 HERE]**

**Figure 7.10:** Components of radiative forcing from 1850 to 2014 by emitted species based on CMIP6 models (Thornhill et al. submitted). "VOC" includes CO as well as other non-methane hydrocarbons. WMGHGs are from the analytical formulae in Section 7.3.2, $H_2O$ (strat) is from Table 7.8. Other components are multi-model means from Thornhill et al. (submitted), see Chapter 6, Section 6.3.1.1, and are based on model simulations where one species at a time is increased from 1850 levels to 2014. Error bars are 5-95% and account for uncertainty in radiative efficiencies and multi-model error in the means. IRFari and cloud effects are calculated from separate radiation calls for clear-sky and aerosol free conditions (Ghan, 2013; Thornhill et al. submitted). "Cloud" includes cloud adjustments (semi-direct effect) and ERFaci. The aerosols ($SO_2$, organic carbon, black carbon) components are scaled to sum to -0.25 W $m^{-2}$ for IRFari and -0.95 W $m^{-2}$ for "cloud" (Section 7.3.3).

**[END FIGURE 7.10 HERE]**

### *7.3.5.4 Temperature Contribution of forcing agents*

The estimated contribution of forcing agents to 2018 temperature change relative to 1750 is shown in Figure 7.11. These estimates were produced using the two-layer energy balance model (Cross-Chapter Box 7.1, Appendix 7.A.2) using a 20,000-member Monte Carlo sample of both forcing uncertainty (by sampling ERF ranges) and climate response (by sampling ECS ranges). The distribution of ECS was informed by Section 7.5.5 and chosen to approximately maintain the best estimate and *likely/very likely* ranges assessed in that section. The TCR, which is an emergent property and not prescribed in this model, has an ensemble median value of 1.73°C, in good agreement with Section 7.5.5. Two error bars are shown in Figure 7.11. The dashed error bar shows the contribution of ERF uncertainty employing the best estimate of climate response with an ECS of 3.0 °C. The solid bar is the total response uncertainty using the Section 7.5.5 assessment of ECS. Overall the temperature response in Figure 7.11 is dominated by the uncertainty in ERF, yet for the WMGHG contribution to warming the uncertainty is dominated by the climate response.

These results show that it is clear that anthropogenic activity has had a warming effect on the planet since 1750. Analyses of radiative forcing and climate sensitivity presented in this chapter give an estimated human induced warming of 1.1°C (0.4 to 1.9°C, 5% to 95% range, *high confidence*). Changes in solar and volcanic activity are assessed to have had a small effect (*medium confidence*) with a best estimate of 0.04°C (0.03 to 0.07 °C, 5% to 95% range). The anthropogenic warming is comprised of a greenhouse warming of 1.7°C (1.3–2.3°C) that has an increasing trend and an aerosol cooling of 0.6°C (0.1–1.5°C) that has remained relatively constant over the last 20 years (Figure 7.11) (*high confidence*). This bottom up forced estimate of human induced warming is compared to the attributable warming from comparisons of simulations with the historic warming record in Chapter 3, Section 3.1. Note that the estimates here do not make use of the historic temperature record so can be considered more or less independent of those from Chapter 3.

**[START FIGURE 7.11 HERE]**

**Figure 7.11:** The contribution of forcing agents to 2018 temperature change relative to 1750 produced using the two-layer energy balance model (Cross-Chapter Box 7.1) where ranges for ERF were taken from Section 7.3 and ranges for ECS were taken from Section 7.5. Dashed error bars show the contribution of forcing uncertainty and solid error bars show the combined forcing and climate response uncertainty.

**[END FIGURE 7.11 HERE]**

#### *7.3.5.5 Historical timeseries from models and observations*

Historical timeseries of the assessed ERF and the resulting near surface global temperature changes are shown in Chapter 2, Figure 2.10 and Figure 7.12 respectively. The historical timeseries of ERFs for the WMGHGs can be derived by applying the ERF calculations of Section 7.3.2 to the observed timeseries of WMGHG concentrations in Chapter 2, Section 2.2. Stratospheric ozone ERF is scaled using the present day value in Section 7.3.2 to the observed levels of equivalent effective stratospheric chlorine using values from Daniel et al. (2010) up to 1980 and Engel et al. (2018) after 1980. Changes in solar forcing are derived by scaling observed total solar irradiance (TSI, Chapter 2, Section 2.2.2), changes in volcanic forcing are derived by scaling observed stratospheric aerosol optical depth (SAOD, Chapter 2, Section 2.2.3). Tropospheric ozone ERF follows Checa-Garcia (2018). Aerosol ERF uses historical ERFari and ERFaci determined from five models participating in the Radiative Forcing Model Intercomparison Project (Pincus et al., 2016), scaled to the assessed forcing in 7.3.3. The land use ERF timeseries is based on historical land use reconstructions (Ghimire et al., 2014).

These results show that for most of the historic period the overall multi-decadal trends closely follow the $CO_2$ contribution, as non-$CO_2$ greenhouse gas forcing (from other WMGHGs and ozone) was approximately compensated for by the aerosol cooling. However, the aerosol cooling is no longer increasing at the same rate if at all (Gettelman et al., 2015) so over the last few decades the long-term warming has been occurring at a faster rate than that expected by $CO_2$ alone (*high confidence,* see also Chapter 2, Section 2.2). These estimates of the bottom up forced response are compared with model simulations and attributable warming estimates in Chapter 3, Section 3.1.

**[START FIGURE 7.12 HERE]**

**Figure 7.12:** Timeseries of near surface global temperature changes, using the time series of ERFs assessed in Chapter 2 and calculated using the two-layer energy balance model (Cross-Chapter Box 7.1) with the best estimate of ECS assessed in Section 7.5.

**[END FIGURE 7.12 HERE]**

**[START CROSS-CHAPTER BOX 7.1 HERE]**

### Cross-Chapter Box 7.1: Physical emulation of Earth System Models for scenario classification and knowledge integration in AR6

*Authors: Malte Meinshausen, Zebedee Nicholls, Piers Forster*

**What is the purpose of simple climate models and emulators?**

Since the early days of climate change research, various simple models have been developed, ranging from simple energy balance equations requiring only a few lines of computer code to models with 50 layers and upwelling diffusive entrainment in the ocean (Table 1.3 in Chapter 1, Section 1.5), to Earth System Models of Intermediate Complexity (EMICs), creating a continuum in the model hierarchy in between simple climate models and the existing Earth System Models (ESMs). While in the early days of climate research, simple models were used as stand-alone models in their own right, recent applications have focussed on using simple models as elaborate inter- and extrapolation tools to reflect and combine knowledge from ESMs and many other lines of evidence. Hence, this AR6 report emphasises the term ‘emulators’ to reinforce the focus on this specific usage of simple climate models.

**Past use of emulators in IPCC**

Simple climate models and emulators have a long history of use in previous IPCC reports (see Chapter 1, Section 1.5). The AR5 placed more emphasis on the EMICs than emulation, although the long-term projection chapter (Collins et al., 2013a) featured the MAGICC simple model in an AOGCM-calibrated and probabilistic version (Meinshausen et al., 2011a; Rogelj et al., 2012) as well as a step-approach simple model by Good et al. (2013). The simple models were mainly used for cases where AOGCM results were not available, to provide greenhouse gas projections as input to the AOGCM experiments (Meinshausen et al., 2011b) and to provide evidence in relation to chosen uncertainty range representations. In SR15, two simple models were used to provide temperature projections for the lower new emission pathways, as Earth System Model or AOGCM results were not yet available given the short timeframe. The two models were the FaIR model (Smith et al., 2018a) and MAGICC model (Meinshausen et al., 2011a).

Across this AR6 WGI report, emulators are employed in various Chapters:

- Investigating the temperature response to individual forcings in a bottom up approach, and comparing to top-down detection and attribution results and models (Chapters 3, Section 3.3 and Chapter 7, Section 7.3).
- Deriving emission metrics, based on impulse response functions (Chapter 7, Section 7.6).
- Compiling the state of our understanding of equilibrium climate sensitivity (ECS) and transient climate response (TCR) from multiple lines of evidence, with one important line being derived from constraining simple models with historical observational data (e.g. Skeie et al., 2018) (Chapter 7, Section 7.5).
- Deriving estimates of TCR from ECS values using a two-layer model outlined in Chapter 7 of the Appendix 7.A.2 (Chapter 7, Section 7.5).
- Understanding the spread of CMIP6 models and compare them to independent assessments of key climate system properties like ECS, TCR and effective radiative forcings (ERF), and assess contributions to projected temperature uncertainty (Chapter 4, Box 4.1).
- Assessing the remaining carbon budget, in particular the estimated non-$CO_2$ warming contributions at the time of peak warming (Chapter 5, Section 5.5).
- Combining multiple contributions to global-mean and regional sea level rise (Chapter 9, Section 9.6).

One example of how emulators can be used is to aid understanding of differences between CMIP5 and CMIP6 models (Chapter 4, Box 4.1 and Section 4.3). As CMIP5 and CMIP6 employed different scenario sets (RCPs and SSPs, respectively), it is useful to know how much of the differences in projected temperature are due to the scenario change and how much due to model changes. To test this the emulators have been run with the same model version and configuration for both the RCP and SSP scenarios. Preliminary investigations performed with the FaIR and MAGICC emulators suggest that scenario differences had a minor effect across the scenario sets, and most of the differences between CMIP5 and CMIP6 are caused by ECS and TCR differences in the two generations of models (Forster et al., 2019; Meinshausen et al., 2019).

The main functionality of emulators across the Working Groups is that they play a key role in 'communicating' WGI physical climate science knowledge to the research community associated with Working Group II and III. Some individual studies associated with WGIII, for example, investigate whether current infrastructure, accounting for its technical lifetime, commits the world to 1.5°C global warming or not (Smith et al., 2019). The more overarching application of emulators is, however, related to scenario classifications in WGIII. Analysing various features of the broad scenario database, like the point of peak emissions, or the 2030 emission levels in line with 1.5°C or 2.0ºC global mean temperature goals, requires a large amount of multi-gas scenarios to be analysed regarding their global mean temperature implications. This service has been provided in the past by calibrated physical emulators and this practice continues today.

**Key characteristics and sampling strategies of emulators**

Depending on their complexity, simple climate models can provide good approximations, on the hemispheric-scale and land-/ocean-scale, of surface air temperatures, sea level rise contributions, and global carbon cycle responses from ESMs. Calibrated to a specific ESM, simple climate models are able to reproduce broad scale responses for key variables across a wide range of scenarios, including idealised $CO_2$-

only scenarios with quadrupled or halved $CO_2$ concentrations (Cross-Chapter Box 7.1, Figure 1). A key functional difference between the simple climate model types is how the ocean and its heat uptake are characterised. In its simplest form, a simple 1-dimensional box is used, however this often leads to an overestimated heat uptake in the near-term compared to centennial timescales (Harvey et al., 1997). These days, there are three basic approaches to address this shortcoming of the "too-simple" ocean formulation: an approach that dates back to Schlesinger and Jiang (1990) is to use an upwelling-diffusion modelling approach. Both MAGICC and the CICERO-SCM (Aldrin et al., 2012; Skeie et al., 2018) maintain this basic model structure. The second approach is the 2-layer model formulation by Held et al., (2010) with or without an efficacy term to account for time evolution in the forcing-response relationship (Geoffroy et al., 2013a) (see e.g. one Held two-layer model implementation in Cross-Chapter Box 7.1, Figure 1 below). The third approach makes more direct use of abrupt perturbation simulations in the AOGCMs. Fitting a response curve to the surface temperature change in abrupt-4x$CO_2$ or similar simulations, the response of a given GCM to multiple emission scenarios can be gauged from summing multiple impulse functions (e.g. Boucher and Reddy, 2008; Good et al., 2013). Within the set of currently used models both the MCE (Tsutsui, 2017) and FaIR models employ this third technique.

To perform projections that reflect future uncertainty, emulators can use different strategies. One approach is to calibrate model parameters to individual ESMs and use those ensembles to project climate (e.g. sea-level projections in Palmer et al., 2018). Another approach is to derive parameter likelihood distributions using statistical techniques in comparison with historical observations (e.g. Skeie et al., 2018b; Knutti et al., 2003; Meinshausen et al., 2009; Smith et al., 2018). A third approach is to formally combine multiple lines of evidence, such as radiative forcing ranges, TCR and ECS ranges that have been derived independently (see Chapter 7 Appendix 7.A.2).

**[START CROSS-CHAPTER BOX 7.1, Figure 1 HERE]**

**Cross-Chapter Box 7.1 Figure 1:** A comparison between the global-mean surface air temperature response of various calibrated simple climate model types and one CMIP6 Earth System models, IPSL CM6A-LR. Most of the latest generation emulators incorporate a non-linearity or state-dependency of the climate sensitivity in order to match ESMs results across the wide response space of SSP scenarios (panel a), quadrupled, doubled and halved $CO_2$ concentrations (panel b). This is an advancement over simple climate model as used in the IPCC Second Assessment Report (cf. Figure 17 in Harvey et al., 1997). Figure adapted from Nicholls et al. (submitted).

**[END CROSS-CHAPTER BOX 7.1, Figure 1 HERE]**

**Comparison of emulators with CMIP6 scenario results**

The divergence of two simple climate models found in SR1.5 (specifically their projected non-$CO_2$ forcing (Forster et al., 2018) created interest in a renewed effort to transparently test the skill of various emulators. To address this limitation, it is instructive to compare emulators directly to ESMs. The RCMIP comparison builds on previous efforts to undertake intercomparisons of emulators and simple climate models. Schwarber et al. (2019) compared HECTOR, MAGICC, FaIR and the AR5 impulse response functions. In another carbon-cycle focussed comparison, four simple models (ACC2, BernSAR, MAGICC, TOTEM) were compared with ESMs and EMICs (Joos et al., 2013) with three found to represent the range relatively well, and MAGICC being within the ESM and EMIC range across the full 1000 year time horizon. Earlier comparisons among simple climate modules in DICE, MERGE, FUND, PAGE and IMAGE (which uses MAGICC) are shown in van Vuuren et al. (2011).

RCMIP (Nicholls et al., submitted) found that the simple climate models can reproduce key characteristics of the observed changes in global-mean surface air temperature (GSAT) and other key responses of ESMs over time. In particular, despite their reduced structural complexity they replicate the non-linear aspects of ESMs GSAT response over a range of scenarios. However, they also find that simple climate models tend to underestimate mid-century warming and overestimate recent warming trends, potentially as a result of their lack of natural variability or over-estimation of aerosol-induced cooling (see Cross-Chapter Box 7.1, Figure 1a). This would affect their representation of the remaining carbon budget.

In summary, there is *high confidence* that several simple climate models can emulate the forced GSAT trends simulated by ESMs, across a wide range of scenarios to within the uncertainty of the natural variability in the ESMs, which simple climate models do not reproduce. The two layer model is chosen as the main emulation tool in the report (Chapter 7,Appendix 7.A.2) as 1) it has an established pedigree in the literature; 2) it can be setup to directly take probabilistic ECS ranges as an input; 3) it is of the simplest form that represents both the non-linear behaviour of the ESMs an provides information on both GSAT and the ocean heat contest change necessary to represent sea level rise.

**[END CROSS-CHAPTER BOX 7.1 HERE]**

## 7.4 Climate and Earth system feedbacks

The magnitude of global temperature change primarily depends on the strength of the radiative forcings and feedbacks (Box 7.1, Equation 7.1). Earth system feedbacks are numerous, and it can be helpful to loosely categorise them into three groups: the physical, biophysical/biogeochemical, and long-term feedbacks associated with ice sheets. The physical feedbacks (for example, associated with lapse-rate, water vapour, or clouds; Section 7.4.2.1-7.4.2.4) and biophysical/biogeochemical feedbacks (for example, associated with methane, stratospheric ozone, or vegetation; Section 7.4.2.5) act both on time scales that are used in practice to estimate the ECS in models (typically 150 years) and on longer time scales required to reach equilibrium. Long-term feedbacks associated with ice sheets (Section 7.4.2.6) are relevant primarily after several centuries or more. The feedbacks associated with biophysical/biogeochemical processes and ice sheets are not included in the conventional definition of the climate system (e.g., Hansen et al., 1984), so they are often collectively referred to as Earth system feedbacks. The feedback framework used here, and an overview of model-based estimates of feedbacks, are presented in Section 7.4.1. For each feedback, the basic underlying mechanisms and their assessment are presented in Section 7.4.2.

Up until the AR5, process understanding and quantification of feedback mechanisms were based primarily on global climate models. However, after several decades of model development little progress had been achieved in narrowing down climate feedbacks, and hence ECS, based on global climate models. To address this, the scientific community has undertaken a wealth of different alternative approaches to move the field forward, including observational and fine-scale modelling approaches. This has in some cases led to more constrained feedbacks and, on the other hand, uncovered several shortcomings in global climate models. Consequently, for the AR6 it is possible to achieve a better-founded assessment of feedbacks acting in the climate system which is less reliant on global climate models than in earlier assessment reports.

It has long been recognized that the magnitude of climate feedbacks can change as the climate state evolves (Manabe and Bryan, 1985; Murphy, 1995; Section 7.4.3; Section 7.4.4), but the implications for projected future warming have been clarified only recently. Since the AR5, progress has been made in understanding the key mechanisms behind this time- and state-dependence. Specifically, the state-dependence is assessed by comparing climate feedbacks between warmer and colder climate states inferred from paleoclimate proxies and model simulations (Section 7.4.3). The time-dependence of the feedbacks is evident between the historical period and future projections and is assessed to arise from the evolution of the surface warming pattern related to changes in zonal and meridional temperature gradients (Section 7.4.4).

### *7.4.1 Framework and methodology*

#### *7.4.1.1 Standard framework*

The global temperature changes of the climate system are generally analysed with the classical forcing-feedback theory as described in Box 7.1 (Equation 7.1). In this equation $\alpha$ is the net climate feedback parameter (W m$^{-2}$ °C$^{-1}$). As surface temperature changes in response to the TOA energy imbalance, many other climate variables also change, thus affecting the radiative flux at the TOA. The aggregate feedback parameter can then be decomposed into an approximate sum of terms $\alpha = \sum_x \alpha_x$, where $x$ are vectors representing variables that have a direct impact on the flux at the TOA and $\alpha_x = \frac{\partial N}{\partial x}\frac{dx}{dT}$. Conventionally, the climate feedbacks are decomposed into components associated with a vertically uniform temperature change (Planck response, P), the water vapour specific humidity (WV), the temperature lapse rate (LR), the surface albedo (A), clouds (C), and biogeochemical/biophysical and long-term feedbacks. An alternative and physically meaningful decomposition is to replace the specific humidity with relative humidity (RH) as a feedback variable (Held and Shell, 2012; Ingram, 2013). In this RH-based feedback framework, specific humidity changes required to maintain fixed relative humidity at a perturbed temperature are included in the Planck response (denoted as P*), and the RH feedback isolates the contribution from changes in relative humidity. Since a large cancellation between the WV and LR feedbacks disappears in this decomposition, the inter-model spread of individual feedbacks is reduced (Boucher et al., 2013). While the aggregate feedback parameter is identical between the two frameworks, the assessment in Section 7.4.2 adopts the RH-based decomposition for simplicity. Biogeochemical feedbacks arise due to changes in aerosols and atmospheric chemical composition in response to changes in surface temperature, and Gregory et al. (2009) show that they can be analysed using the same framework (see Chapter 5, Section 5.4 and Chapter 6, Section 6.4). Similarly, longer-term feedbacks associated with vegetation and ice sheet changes can also be incorporated.

#### *7.4.1.2 Updates of climate feedbacks in GCMs and ESMs*

Since the AR5, many modelling groups have newly participated in CMIP experiments with updated climate and Earth system models, leading to an increase in the number of models in CMIP6 (Chapter 1, Section 1.5.4). While some of the CMIP6 models share components and are therefore not independent, they are analysed independently when calculating climate feedbacks. This, and more subtle forms of model inter-dependence, creates challenges when determining appropriate model weighting schemes (Chapter 1, Section 1.5.4). Additionally, it must be kept in mind that the ensemble sizes of the CMIP5 and CMIP6 models are not sufficiently large to sample the full range of model uncertainty.

In GCMs and ESMs, the feedback parameters $\alpha_x$are estimated as the mean differences in the radiative fluxes between atmosphere-only simulations in which the change in SST is prescribed (Cess et al., 1990), or as the regression slope of change in radiation flux against change in global-mean surface air temperature using atmosphere-ocean coupled simulations with abrupt $CO_2$ changes (*abrupt4×CO$_2$*) (Andrews et al., 2012; Gregory et al., 2004; Caldwell et al., 2016). The linear regression for *abrupt4×CO$_2$* simulations also provides an estimate of ERF (see Section 7.3.1). In atmosphere-only simulations, the estimate of $\alpha_x$ depends on the prescribed pattern of SST increase, whereas in coupled simulations the estimate varies with the choice of time period after an abrupt $CO_2$ increase that is included in the regression. Neither method is perfect, but both are useful and the two approaches yield consistent results (Ringer et al., 2014). Consequently, individual feedback terms in the CMIP5 and CMIP6 climate model ensembles are calculated using the linear regression for 150 years in *abrupt4xCO$_2$* experiments (Figure 7.13, see Box 7.1). There is an inconsistency between the regression over years 1-150 and the definition of ERF and feedback in Box 7.1. That is, the radiative effects of land warming are excluded from the ERF due to doubling of $CO_2$, which gives a feedback value too positive by about 10% in the regression framework. However, the feedback calculated using the regression over years 1-150 that lacks multi-centennial scale warming probably gives an underestimate of $\alpha$ by about 10% (Rugenstein et al., 2019a). These effects are both small and may partially cancel, justifying the use of regression over 150 years as an approximation to feedbacks and hence ECS (see Box 7.1).

In order to estimate the feedbacks in a consistent way across models, a 'radiative kernel' method has been used (Soden et al., 2008). In this method, $\partial N/\partial x$ (called the kernel, where $x$ is a climate variable such as water vapour) is evaluated by perturbing $x$ within the radiation code of a GCM; multiplying by d$x$/d$T$ simulated by coupled GCMs then produces a value of $\alpha_x$. Care must be taken for accurate calculation of $\alpha_x$ (Jonko et al., 2013), but the radiative kernel has been shown to successfully decompose the net climate feedback in GCMs (Zelinka et al., 2016). The kernel method can also be applied to atmospheric reanalysis data in order to directly compare the climate feedbacks at interannual time scales between observations and GCMs (Colman and Hanson, 2017). There is a small discrepancy between the aggregate climate feedback calculated directly using the time evolutions of $T$ and $N$ in each model and the accumulation of individual feedbacks (shown at the right of Figure 7.13a) owing to biogeochemical processes included in some models and neglected in this analysis (e.g. methane, ozone or aerosol feedbacks, Section 7.4.2.5) as well as errors in the radiative kernel method (nonlinearities, differences in mean state or in radiative codes, etc.) and correlation among feedbacks.

The multi-model mean values of the Planck feedback, the lapse rate feedback at constant relative humidity (LR*), the relative humidity feedback (RH) and the surface albedo feedback are very consistent between CMIP5 and CMIP6 models (see Table 7.10 for the values). These values, where possible supported by other lines of evidence, are used for assessing feedbacks in Sections 7.4.2.1–7.4.2.3. A difference found between CMIP5 and CMIP6 models is the cloud feedback, especially its shortwave (SW) component; the net cloud feedback is larger in CMIP6 by more than 20% (Table 7.10). This change is the major cause of less negative values of the net climate feedback and hence an increase in modelled ECS (Section 7.5.7). However, the inter-model spread of the cloud feedback remains large, reflecting that uncertainty in cloud feedbacks has not been reduced in CMIP6. When the cloud SW feedback is decomposed into its various components, it is evident that low clouds (below 670 hPa) contribute the most to the enhanced positive feedback in CMIP6 models, through reduction in cloud amount and cloud albedo over the extratropics (Figure 7.13b). In some models, the change in the extratropical cloud feedback has been related to improved representation of mixed-phase clouds (Bodas-Salcedo et al., 2019; Gettelman et al., 2019), which is taken into account when assessing cloud feedbacks in Section 7.4.2.4.

**[START FIGURE 7.13 HERE]**

**Figure 7.13:** (a) Estimates of global-mean climate feedbacks in 28 CMIP5 (blue) and 27 CMIP6 (orange) abrupt4xCO2 simulations. The open circle represents individual models and the black circle with an error bar indicates the multi-model mean and the inter-model standard deviation. Decomposition of temperature and moisture feedbacks follows (Held and Shell, 2012), which divide them into Planck response with fixed relative humidity (P*, denoted as 'Held & Shell' in the figure), Lapse Rate (LR*) and Relative Humidity (RH) feedbacks. The P* term is further separated to the conventional Planck response and a water vapour feedback with fixed RH (represented as 'Conventional' and 'Clausius-Clapeyron'; see Section 7.4.2.2). The net cloud feedback is the sum of cloud shortwave (Cloud SW) and longwave (Cloud LW) feedbacks. The residual between the summed feedback and the net climate feedback (left), the latter directly derived from the models, includes feedbacks neglected in this analysis but considered in some models (e.g. non-biogeochemical feedbacks) and above all errors in the radiative kernel. (b) Decomposition of the global cloud SW feedback into contributions from non-low and low clouds (left), the latter further broken down to the low cloud amount (middle) and albedo (right) feedbacks. Their global means are equal to the average of tropical (30°S–30°N) and extratropical (poleward of 30°S/N) components. All the values are based on six radiative kernels by Zelinka et al. (2019).

**[END FIGURE 7.13 HERE]**

As with past CMIP cycles, CMIP6 models have improved compared to CMIP5 models, even though the improvements are in some respects incremental. For climate feedbacks except for clouds, the mean value is similar between the two ensembles and the inter-model spread was reduced in CMIP6, indicating that improved representation of the relevant physics leads to better model agreement. The inter-model spread for the cloud feedback was increased in CMIP6, indicating that an improved representation of cloud processes does not necessarily reduce uncertainty in the simulated net cloud feedback. This happens because physical processes parameterized in models may have been tuned to compensate errors in order to simulate realistic radiation budgets and mean climate states. An improved parameterization of a particular process may not reduce errors in other processes, which could result in a diverging response of clouds to global warming. However, the large inter-model spread of the cloud feedback in CMIP6 models can be useful for the assessment of feedbacks in individual cloud regimes, which can be verified by the use of observations, process modelling, and emergent constraints (Section 7.4.2.4).

### *7.4.2 Assessing climate feedbacks*

The goal of this section is to provide an overall assessment of individual feedback parameters, $\alpha_x$, by combining different lines of evidence from observations, theory, process models and GCMs. To achieve this, we review the understanding of the key processes governing the feedbacks, why the feedback estimates differ among models, studies or approaches, and the extent to which these approaches yield consistent results. The individual feedback assessed are the Planck (Section 7.4.2.1), water vapour and lapse rate (Section 7.4.2.2), surface albedo (Section 7.4.2.3), cloud (Section 7.4.2.4), biophysical and non-$CO_2$ biogeochemical (Section 7.4.2.5) and long term (Section 7.4.2.6) feedbacks. A synthesis is provided Section 7.4.2.7.

#### *7.4.2.1 Planck response*

The Planck response represents the additional LW emission to space arising from vertically uniform warming of the surface and the atmosphere. The Planck response, often called the Planck feedback, plays a fundamental stabilizing role in Earth's climate and has a feedback value that is strongly negative. This parameter has been estimated using climate simulation output and meteorological reanalysis (Caldwell et al., 2016; Colman and Hanson, 2017; Dessler, 2013b; Soden and Held, 2006; Vial et al., 2013; Zelinka et al., 2019) and the values are generally consistent with theoretical estimates based on Planck radiation. The standard deviation of this feedback parameter across GCMs is approximately 0.04 W $m^{-2}$ $°C^{-1}$. This spread is small and mainly due to differences in climatological cloud and water vapour distributions and the pattern of surface temperature changes. The physical processes that control this response are very well understood and the estimates from observations and climate models are consistent on interannual time scales (Dessler, 2013). However, structural uncertainty arises from the radiative temperature kernel, introducing an additional uncertainty of ±0.1 W $m^{-2}$ $°C^{-1}$ (Soden and Held, 2006; Dessler, 2013; Vial et al., 2013; Caldwell et al., 2016; Colman and Hanson, 2017; Zelinka et al., 2020). Overall, there is *high confidence* in the estimate of the Planck response, which is assessed to be $\alpha_P$ = –3.2 W $m^{-2}$ $°C^{-1}$ with a *very likely* range of –3.4 to –3.0 W $m^{-2}$ $°C^{-1}$ and a *likely range* of –3.3 to –3.1 W $m^{-2}$ $°C^{-1}$.

#### *7.4.2.2 Water vapour and lapse rate feedbacks*

The water vapour (WV) feedback quantifies the change in radiative flux at the TOA due to changes in atmospheric water vapour concentration associated with a change in global mean surface temperature. Since relative humidity (RH) stays nearly constant as the climate warms (Soden and Held, 2006; Held and Shell, 2012), specific humidity increases with temperature approximately following the Clausius-Clapeyron (CC) relationship. Greater atmospheric WV content, particularly in the upper troposphere, results in enhanced absorption of LW and SW radiation and reduced outgoing radiation. These processes represent the water vapor feedback, the largest positive feedback in the climate system. Atmospheric moistening has been detected in satellite records, is simulated by climate models, and the estimates agree within model and observational uncertainty (Soden et al., 2005; Dessler, 2013; Gordon et al., 2013; Chung et al., 2014). The mean and standard deviation of this feedback based on the cited multi-model studies and including structural uncertainty arising from the radiative kernel, are $\alpha_{WV}$ = 1.75 ± 0.20 W $m^{-2}$ $°C^{-1}$, consistent with recent estimates inferred from satellite observations of $\alpha_{WV}$ = 1.85 ± 0.32 W $m^{-2}$ $°C^{-1}$(Liu et al., 2018).

The lapse rate feedback quantifies the change in radiative flux at the TOA due to a non-uniform change in the vertical temperature profile. In the tropics, the vertical temperature profile is mainly driven by moist convection and is close to a moist adiabat. The warming is larger in the upper troposphere than in the lower troposphere (Manabe and Wetherald, 1975; Santer et al., 2005; Bony et al., 2006), leading to a larger radiative emission to space and therefore a negative feedback. In the extra-tropics, the vertical temperature profile is mainly driven by a balance between radiation, meridional heat transport and ocean heat uptake (Rose et al., 2014). This leads to strong wintertime temperature inversions (Payne et al., 2015; Feldl et al., 2017) and a positive lapse rate feedback in polar regions (Manabe and Wetherald, 1975; Pithan and Mauritsen, 2014). However, the tropical contribution strongly dominates, leading to a large negative global mean lapse rate feedback (Soden and Held, 2006; Dessler, 2013; Vial et al., 2013; Caldwell et al., 2016). Estimates of the LR feedback from climate variability are consistent between GCMs and observations (Dessler, 2013; Colman and Hanson, 2017). The mean and standard deviation of this feedback based on the cited multi-model studies including structural uncertainty are $\alpha_{LR} = -0.55 \pm 0.20$ W m$^{-2}$ °C$^{-1}$ (Dessler, 2013; Caldwell et al., 2016; Colman and Hanson, 2017; Zelinka et al., 2020).

Given the coupling between the LR and the WV feedbacks, they are frequently summed into a WV+LR feedback. This combined feedback reduces the inter-model spread compared to the individual LR and WV feedbacks (Colman, 2003; Soden and Held, 2006) for reasons that are better understood since the AR5 (Po-Chedley et al., 2018a). To better quantify sources of uncertainty in the WV+LR feedback, an alternative feedback decomposition has been proposed by Held and Shell (2012) where the feedback is decomposed into three terms: (1) impact of water vapour changes due to an identical temperature increase at the surface and throughout the troposphere assuming constant relative humidity, which will be called the Clausius-Clapeyron (CC) feedback here; (2) the impact of the changes in lapse rate assuming constant relative humidity (LR*); (3) the impact of the change in relative humidity (RH). This feedback decomposition distinguishes model feedback spread due to changes in relative humidity from inter-model spread that results from the pattern of surface warming modulating the lapse rate and associated humidity changes (Po-Chedley et al., 2018a).

These three feedbacks are shown Figure 7.13a. The CC feedback has large positive values due to well understood thermodynamic and radiative processes, and the spread among models is small (Zelinka et al., 2020). The lapse rate feedback LR* has small absolute values, as expected from theoretical arguments (Ingram, 2010, 2013). The relative humidity feedback is also close to zero and the spread among models is confined to the tropics (Sherwood et al., 2010; Vial et al., 2013; Takahashi et al., 2016; Po-Chedley et al., 2018a). At inter-annual time scales, it has been shown that the change in RH in the tropics is related to the change of the spatial organisation of deep convection (Bony et al., submitted). Romps (2014) found that tropical RH is closely tied to the temperature in the free troposphere and recent research shows that the change in upper tropospheric RH is closely related to model representation of current climate (Sherwood et al., 2010; Po-Chedley et al., 2019). Therefore, a reduction in model RH biases is expected to reduce the inter-model spread of the RH feedback.

Models simulate a water vapour increase in the stratosphere with global warming. This increase produces a positive feedback of 0.1–0.3 W m$^{-2}$ °C$^{-1}$ if the stratospheric radiative response is computed assuming temperatures that are adjusted with fixed dynamical heating (Banerjee et al., 2019; Dessler et al., 2013). However, various feedbacks reduce this temperature adjustment and the overall physical (water vapour + temperature + dynamical) stratospheric feedback becomes very small (0.02 ± 0.01 W m$^{-2}$ °C$^{-1}$) (Huang et al., 2016). Because of uncertainties in simulating stratospheric processes in current GCMs, we increase the uncertainty range. The assessed total stratospheric feedback is 0.0 ± 0.1 W m$^{-2}$ °C$^{-1}$.

The combined water vapour plus lapse rate feedback is positive. The main physical processes that drive these feedbacks are well understood and supported by multiple lines of evidence including models, theory and observations. The combined water vapour plus lapse rate feedback is assessed to be $\alpha_{LR+WV} = 1.2$ W m$^{-2}$ °C$^{-1}$, with a *very likely* range of 0.95 to 1.45 W m$^{-2}$ °C$^{-1}$ and a *likely* range of 1.1 to 1.43 W m$^{-2}$ °C$^{-1}$.

#### *7.4.2.3 Surface albedo feedback*

Surface albedo is determined primarily by surface reflectance, but also by the spectral and angular distribution of incident solar radiation. Changes in planetary albedo are roughly one-third the magnitude of surface albedo changes, owing to atmospheric absorption and scattering, with variability and uncertainty arising primarily from clouds (Donohoe and Battisti, 2011). Temperature change induces surface albedo change through several direct and indirect means. In the present climate, the largest contributions by far are changes in the extent of sea ice and seasonal snow cover, as these media are highly reflective and there are large regions that are typically close to the melting temperature. Vegetation changes also make a small contribution, and are considered separately in section 7.4.2.5. Reduced snow cover on sea ice may contribute as much to albedo feedback as reduced extent of sea ice (Zhang et al., 2019). Changes in the snow metamorphic rate, which generally reduces snow albedo with warmer temperature, and warming-induced consolidation of light absorbing impurities near the surface, also contribute secondarily to the albedo feedback (Flanner and Zender, 2006; Qu and Hall, 2007; Doherty et al., 2013; Tuzet et al., 2017). Other contributors to albedo change that are modulated indirectly by global temperature include vegetation state (Section 7.4.2.5), soil wetness, and ocean roughness.

CMIP5 and CMIP6 models show moderate spread in $\alpha_A$ (Qu and Hall, 2014; Schneider et al., 2018; Thackeray and Hall, 2019; Zelinka et al., 2020), owing to variations in modelled sea-ice loss and snow cover response in boreal forest regions, motivating attempts to quantify $\alpha_A$ from global observations. Flanner et al. (2011) applied satellite observations to determine that the northern hemisphere (NH) cryosphere contribution to $\alpha_A$ over 1979–2008 was 0.48 (0.29–0.78) W m$^{-2}$ °C$^{-1}$, with roughly equal contributions from changes in seasonal snow cover and sea ice. Since the AR5, and over similar periods of observation, Crook and Forster (2014) found an estimate of 0.8 ± 0.3 W m$^{-2}$ °C$^{-1}$ for the total NH extratropical surface albedo feedback, when averaged over global temperature change. Pistone et al. (2014) and Cao et al. (2015) estimated the Arctic sea ice contribution alone to be 0.31 ± 0.04 W m$^{-2}$ °C$^{-1}$ and 0.31 ± 0.08 W m$^{-2}$ °C$^{-1}$, respectively, larger than the estimate from Flanner et al. (2011). Much of this NH discrepancy can be traced to different estimates of attenuation by Arctic clouds between model-derived radiative kernels and direct measurements of TOA irradiance, with the latter indicating much less attenuation and therefore suggesting that the two more recent studies showing larger $\alpha_A$ are more realistic. All four studies show larger observational estimates of Arctic albedo change than exhibited by most CMIP3 and CMIP5 models over similar time periods, which can be traced to models generally underestimating the rate of Arctic sea ice loss during recent decades (Flato et al., 2013; Stroeve et al., 2012; Chapter 9, Section 9.3.1). However, this may be an expression of internal variability, since the observed behaviour is captured within large ensemble simulations (Notz, 2015).

Since the AR5, Chen et al. (2016b) estimated that NH land snow changes during 1982–2013 contributed (after converting from NH temperature change to global mean temperature change) 0.1 W m$^{-2}$ °C$^{-1}$ to global $\alpha_A$, smaller than the estimate from Flanner et al. (2011). Qu and Hall (2014) report a CMIP5 multi-model mean NH land snow contribution to $\alpha_A$ of 0.08 W m$^{-2}$°C$^{-1}$, about the same as the average of only the 8 models (ranging from 0.05–0.10 W m$^{-2}$ °C$^{-1}$) whose seasonal cycle of albedo feedback falls within the observational range of uncertainty determined from satellite measurements. Thackeray and Hall (2019) show that the seasonal cycle of Arctic sea-ice $\alpha_A$ also provides an emergent constraint on modelled climate change $\alpha_A$, at least until mid-century when the relationship degrades. They find that the Arctic sea-ice contribution to $\alpha_A$ is 0.13 W m$^{-2}$ °C$^{-1}$ in both the CMIP5 model mean and averaged over only those models that best reproduce the observed seasonal cycle of $\alpha_A$.

These studies all focus on the northern hemisphere, though exclusion of the southern hemisphere (SH) only slightly biases estimates of global $\alpha_A$ because seasonal snow cover extent in the SH is small, and trends in SH sea ice extent are relatively flat over the satellite record (Comiso et al., 2017; see also Chapter 2, Section 2.3). The multi-model mean global-scale $\alpha_A$ (from all contributions) over the 21$^{st}$ century in CMIP5 models under the RCP8.5 scenario is 0.40 W m$^{-2}$ °C$^{-1}$ with a standard deviation of 0.10 W m$^{-2}$ °C$^{-1}$ (Schneider et al., 2018), closely matching the summed observational contributions from NH sea ice and land snow over the satellite era. Moreover, Schneider et al. (2018) found that modelled $\alpha_A$ does not decline over the 21$^{st}$ century, despite large losses of snow and sea ice, though a weakened feedback is apparent after 2100. Using the idealized *abrupt4×CO₂* as for the other feedbacks, the estimate of the global-scale albedo feedback in the CMIP5 models is 0.35 W m$^{-2}$°C$^{-1}$ with a standard deviation of 0.08 W m$^{-2}$ °C$^{-1}$(Vial et al., 2013; Caldwell et al., 2016).

This leads to an overall *high confidence* in the estimate of the surface albedo feedback based on multiple lines of evidence including observations, models and theory. The basic phenomena that drive this feedback are well understood and the different studies cover a large variety of hypotheses or behaviours, including how the evolution of clouds affects this feedback. The global albedo feedback is therefore positive and assessed to be $\alpha_A = 0.35$ W m$^{-2}$ °C$^{-1}$, with a *very likely* range of 0.10–0.60 W m$^{-2}$ °C$^{-1}$ and a *likely* range of 0.25–0.45 W m$^{-2}$ °C$^{-1}$.

#### *7.4.2.4 Cloud feedbacks*

Clouds can be formed almost anywhere when moist air parcels rise and cool, enabling the water vapour to condensate or small water droplets to freeze. The cloud droplets, ice crystals, and their mixture interact with each other to grow into large particles of rain, snow, or drizzle. These microphysical processes interact with aerosols, radiation and atmospheric circulation, resulting in a highly complex set of processes governing cloud formation and lifecycles that operate and interact across a wide range of spatial and temporal scales.

Clouds have various types, from thick convective clouds to thin stratus and cirrus clouds, depending upon thermodynamic conditions and large-scale circulation (Figure 7.14). Over the equatorial warm pool and inter-tropical convergence zone (ITCZ) regions, high SSTs stimulate the development of deep convective systems, which are accompanied by anvil and cirrus clouds near the tropopause where the convective air outflows. The large-scale circulation associated with these convective clouds leads to subsidence over the subtropical cool oceans, where deep convection is suppressed by a lower tropospheric inversion layer maintained by the subsidence and promoting the formation of shallow cumulus and stratocumulus clouds. In the extratropics, mid-latitude storm tracks control cloud formation, which occurs primarily in the frontal bands of the extratropical cyclones. Since liquid droplets cannot freeze spontaneously at temperatures above approximately –40°C and ice nucleating particles that can aid freezing at warmer temperatures are rare, extratropical clouds often consist both of super-cooled liquid and ice crystals, resulting in mixed-phase clouds.

A challenge in understanding cloud feedbacks is to assess separately a thermodynamically driven component of cloud response and a dynamically driven cloud response. The latter is associated with changes in the large-scale atmospheric circulation, for which there is some observational evidence (Chapter 2, Section 2.3.1; Chapter 3, Section 3.3.3), but the associated feedbacks remain highly uncertain. While past cloud change patterns derived from satellite records are largely consistent with the projected changes in GCMs (Norris et al., 2016), this is not sufficient to quantify the net cloud feedback.

##### *7.4.2.4.1 Evaluation of clouds in climate models*

In the global energy budget, clouds affect SW radiation by reflecting solar insolation due to their high albedo (cooling the climate system) and also LW radiation by absorbing the energy emitted from the surface and re-emitting at a lower temperature (i.e., contributing to the greenhouse effect, warming the climate system). These effects of clouds on radiation are measured by the cloud radiative effect (CRE), which is the difference in the TOA radiative energy budget between clear and cloudy skies (see Section 7.2.1). Over the equatorial warm pool, the SW CRE tends to be compensated by the LW CRE, leading to a near-zero net CRE. The net CRE shows large negative values over the eastern part of the subtropical oceans and the extratropical oceans due to the dominant influence of highly reflective marine low clouds. Although current GCMs lack the ability to reproduce some cloud regimes correctly, the overall distribution, as well as the global mean of the net CRE derived from the CMIP5 multi-model mean, is similar to the satellite observations (Wild et al., 2019). However, the large cancellation between the SW and LW CREs in nature has hampered an accurate estimation of cloud-radiative feedbacks.

The ability of GCMs to simulate clouds has been evaluated both for the cloud cover and CRE, and also for cloud properties directly associated with processes of cloud-radiative feedbacks, by means of the satellite observations and the so-called satellite simulators implemented in climate models (Bodas-Salcedo et al., 2011; Tsushima et al., 2017). Recent satellite measurements resolve the vertical distribution of clouds, which can be directly compared with GCMs in which satellite retrieval algorithms are applied to the instantaneous cloud fields. Consequently, a thorough evaluation of the vertical profile of simulated clouds has revealed model errors in the fraction, liquid and ice contents, optical depth, and resultant CRE (Konsta et al., 2015;

Suzuki et al., 2015). A well-known common error in CMIP5 models was the weak negative SW CRE over the Southern Ocean due to insufficient amounts of supercooled liquid droplets and associated cloud optical depths that are biased low (McCoy et al. 2014a; 2014b). This error in representing mixed-phase clouds has been reduced in some CMIP6 models (Bodas-Salcedo et al., 2019), but there still remain other common model errors such as in the subtropical low clouds (Calisto et al., 2014).

**[START FIGURE 7.14 HERE]**

**Figure 7.14:** Schematic cross section of diverse cloud regimes between the tropics and polar regions. Thick solid and dashed curves indicate the tropopause and the subtropical inversion layer in the current climate. Thin grey text and arrows represent robust responses in the thermodynamic structure to greenhouse warming, of relevance to cloud changes. Text and arrows in red show the major cloud responses and the sign of their feedbacks to the surface warming assessed in this chapter.

**[END FIGURE 7.14 HERE]**

*7.4.2.4.2 Assessment of feedbacks for individual cloud regimes*

In a first attempt to systematically evaluate ECS based on fully coupled GCMs in AR4, diverging cloud feedbacks were recognized as a dominant source of uncertainty. A thorough assessment of cloud feedbacks in different cloud regimes was then carried out in the AR5 (Boucher et al., 2013), which assigned *high* or *medium confidence* for some cloud feedbacks but *low* or no *confidence* for others (Table 7.9). Many studies that estimate the net cloud feedback using CMIP5 simulations (Vial et al., 2013; Caldwell et al., 2016; Zelinka et al., 2016; Colman and Hanson, 2017) show slightly different values depending on the methodology and the set of models used, but often report a large inter-model spread of the feedback, with the 90% confidence interval spanning both weak negative and strong positive net feedbacks (Figure 7.13). Part of this diversity arises from the dependence of the model cloud feedbacks on the parameterization of clouds and their coupling to other sub-grid scale processes (Zhao et al., 2015).

Since the AR5, community efforts have been made to understand and quantify the cloud feedbacks in various cloud regimes coupled with large-scale atmospheric circulation (Bony et al., 2015). For some cloud regimes, alternative tools to GCMs, such as observations, theory, high-resolution cloud resolving models (CRMs), and Large Eddy Simulations (LES), help quantify the feedbacks. Consequently, the net cloud feedback derived from GCMs has been revised by assessing the regional cloud feedbacks separately and summing them with weighting by the ratio of fractional coverage of those clouds over the globe to give the global feedback, following an approach adopted in Sherwood et al. (submitted). This bottom-up assessment is explained below with a summary of updated confidence of individual cloud feedback components in Table 7.9. Dependence of cloud feedbacks on evolving patterns of surface warming will be discussed in Section 7.4.3 and is not explicitly taken into account in the assessment presented in this section.

***High-cloud altitude feedback.***

The cloud top altitude increases under global warming, concurrent with the rising of the tropopause at all latitudes (Marvel et al., 2015; Thompson et al., 2017). This increasing altitude of high clouds was identified in early generation GCMs and the tropical high-cloud altitude feedback was assessed to be positive with *high confidence* in the AR5 (Boucher et al., 2013). This is supported by a theoretical argument called the fixed anvil temperature mechanism, which ensures that the temperature of the convective detrainment layer does not change when the altitude of high-cloud tops increases with the rising tropopause (Hartmann and Larson, 2002). Because the cloud top temperature does not change significantly with global warming, cloud longwave emission does not increase even though the surface warms, resulting in an enhancement of the high-cloud greenhouse effect (a positive feedback; Yoshimori et al. (2019)). The upward shift of high clouds with surface warming is detected in observed interannual variability and trends in satellite records for 1983-2009 (Chepfer et al., 2014; Norris et al., 2016), and in CRMs (Khairoutdinov and Emanuel, 2013; Narenpitak et al., 2017; Tsushima et al., 2014). The high-cloud altitude feedback was estimated to be +0.5 W $m^{-2}°C^{-1}$ based on GCMs in the AR5, but is revised, using a recent re-evaluation that excludes aliasing effects by reduced low-cloud amounts, downward to 0.22 ± 0.12 W $m^{-2}°C^{-1}$ (Zelinka et al., 2020). The positive high-cloud altitude feedback simulated in GCMs is supported by theoretical, observational, and process modelling studies, and is assigned *high confidence*.

***Tropical high-cloud amount feedback.***
Updrafts in convective plumes lead to detrainment of moisture at a level where the buoyancy diminishes, and thus deep convective clouds over high SSTs in the tropics are accompanied by anvil clouds in the upper troposphere. The anvil clouds occupy a much larger area than the convective plumes themselves, and thereby contribute substantially to the positive LW CRE in the present climate, so that they would exert a negative feedback if their area was reduced (Figure 7.14). A hypothesis known as the 'iris effect' that suggests a reduction of anvil clouds due to global warming was first proposed by Lindzen et al. (2001), who advocated that an increased precipitation efficiency with warming results in less cloud condensate in the detrained air mass and consequently a strong negative feedback. This hypothetical microphysical process has not been substantiated to date, but a thermodynamic mechanism referred to as the 'stability iris effect' has recently been proposed to explain how the anvil cloud amount decreases with surface warming (Bony et al., 2016). In this mechanism, a temperature-mediated increase of static stability in the upper troposphere, where convective detrainment occurs, acts to balance a weakened mass outflow from convective clouds, and thereby reduce anvil cloud areal coverage. Another mechanism that could support an iris-effect is enhanced convective aggregation with increasing SST (Mauritsen and Stevens, 2015). This phenomenon is found in CRM simulations (Emanuel et al., 2014; Wing and Emanuel, 2014; Cronin and Wing, 2017)) and has been identified in observed interannual variability (Stein et al., 2016; Saint-Lu et al., 2019 submitted; Bony et al. 2019 submitted), which may partly reflect the high-cloud response to large-scale circulation change (Su et al., 2017). Consistently, a combined analysis of TOA radiation and cloud data from multiple satellites shows that the local cloud feedback at interannual time scale is negative up to –5 W $m^{-2}°C^{-1}$ for the net (Williams and Pierrehumbert, 2017) and –3.0 ± 0.39 W $m^{-2}°C^{-1}$ for the cloud LW (Vaillant de Guélis et al., 2018). Since the tropical high-cloud regime occupies about 7% of the globe, the latter estimate leads to a global contribution of –0.21 W $m^{-2}°C^{-1}$. The negative cloud LW feedback, which is partly compensated by the cloud SW feedback (Mauritsen and Stevens, 2015; Li et al., 2019), is considerably underestimated in GCMs (Mauritsen and Stevens, 2015). Current high-resolution convective-permitting simulations cannot reduce uncertainty because the results depend on parametrized cloud microphysics and turbulence (Bretherton et al., 2014; Ohno et al., 2019). Therefore, the tropical high-cloud amount feedback is assessed as negative with *medium confidence*. Taking a partial compensation between LW and SW feedbacks into account, the global contribution of the high-cloud amount feedback is assessed to –0.15 ± 0.2 W $m^{-2}°C^{-1}$.

***Tropical marine low-cloud feedback.***
It has long been argued that the response of low-latitude marine boundary layer clouds to surface warming was the largest contributor to the spread among GCMs in the net cloud feedback (Boucher et al., 2013). However, uncertainty of the marine low-cloud feedback has been considerably narrowed since AR5 by accumulating theoretical, modelling, and observational studies (Klein et al., 2017). Processes that control the low clouds are complex and involve coupling with atmospheric motions on multiple scales, from the boundary layer turbulence to the large-scale subsidence, which may be represented by a combination of shallow and deep convective mixing (Sherwood et al., 2014).

In order to disentangle the large-scale processes that cause the cloud amount either to increase or decrease in response to the surface warming, the cloud feedback has been expressed in terms of several 'cloud controlling factors' (Qu et al., 2014, 2015; Zhai et al., 2015; Brient and Schneider, 2016; Myers and Norris, 2016; McCoy et al., 2017b). The advantage of this approach over conventional calculation of cloud feedbacks is that the temperature-mediated cloud response can be estimated without using information of the simulated cloud responses that are less well-constrained than the changes in the environmental conditions. Two dominant factors are identified for the tropical low clouds: a thermodynamic effect due to rising SST that acts to reduce low cloud by enhancing cloud-top entrainment of dry air, and a stability effect accompanied by an enhanced inversion strength that acts to increase low cloud. These controlling factors compensate with a varying degree in different GCMs, but can be constrained by referring to the observed seasonal or interannual relationship between the low-cloud amount and the controlling factors in the environment as a surrogate. The analysis leads to a positive local feedback of +1.2 W $m^{-2}°C^{-1}$ for the stratocumulus regime and a near-zero feedback for the trade cumulus regime (Cesana et al., 2019; Myers et al., submitted), but the stratocumulus feedback may be underestimated because explicit simulations using LES show a larger local feedback exceeding +2 W $m^{-2}$ °$C^{-1}$ (Bretherton, 2015; Klein et al. 2017). Supported by different lines of evidence, the subtropical marine low-cloud feedback is assessed as positive with *high confidence*. Based on the combined estimate using LESs and the cloud controlling factor analysis, the global contribution of the feedback due to marine stratocumulus clouds equatorward of 30° (about 8% of the globe) is assessed to be 0.16 ± 0.16 W $m^{-2}$°$C^{-1}$, for which the standard deviation considers methodological uncertainties (Sherwood et al., submitted).

***Land cloud feedback.***

Intensification of the global hydrological cycle is a robust feature of global warming, but at the same time, many land areas in the subtropics will experience drying at the surface and in the atmosphere (Chapter 8, Section 8.1). This occurs due to a limited water availability in these regions and consequently the cloudiness is also expected to decrease over subtropical land areas. Reduction in clouds over land are consistently identified in the CMIP5 models and also in a super-parameterized GCM (Bretherton et al., 2014; Kamae et al., 2016). Because low clouds make up the majority of subtropical land clouds, this reduced amount of low clouds reflects less solar insolation and leads to a positive feedback similar to the marine low clouds. The mean estimate of the global land cloud feedback in CMIP5 models is much smaller than the marine low cloud feedback, 0.08±0.08 W $m^{-2}$°$C^{-1}$ (Zelinka et al., 2016). These values are nearly unchanged in CMIP6 (Zelinka et al., 2020). However, GCMs still have considerable biases in the mean temperature and cloud fraction over land and the magnitude of this feedback has not yet been supported by other lines of evidence. Therefore, the feedback due to decreasing land clouds is assessed to be 0.08 ± 0.08 W $m^{-2}$°$C^{-1}$with *medium confidence*.

***Middle latitude cloud amount feedback.***

Poleward shifts in the mid-latitude jets are evident since the 1980s (Chapter 2, Section 2.3.1.3) and are a feature of the large-scale circulation change in future projections (Chapter 4, Section 4.5.1.6). Because mid-latitude clouds over the North Pacific, North Atlantic, and Southern Ocean are induced mainly by extratropical cyclones in the storm tracks along the jets, it has been suggested that the jet shifts should be accompanied by poleward shifts in the extratropical clouds, which would result in a positive feedback through the reduced reflection of insolation (Boucher et al., 2013). However, studies since the AR5 have revealed that this proposed mechanism does not apply in practice (Ceppi and Hartmann, 2015). While a poleward shift of mid-latitude cloud maxima in the free troposphere has been identified in satellite and ground-based observations (Bender et al., 2012; Eastman and Warren, 2013), associated changes in net CRE are found to be small because the warming effect due to high clouds shifted poleward tends to be cancelled by the cooling effect due to low clouds increasing beneath (Grise and Medeiros, 2016; Tselioudis et al., 2016; Zelinka et al., 2018). This compensation is not well captured in GCMs (Lipat et al., 2017), but the above findings show that the middle latitude cloud feedback is not predominantly driven by the poleward jet shifts, which are rather suggested to occur partly in response to high cloud changes (Li et al., 2018). An important process is a thermodynamic control of the extratropical cloud amount equatorward of about 50°.

Recent studies showed using observed cloud controlling factors that the middle latitude low cloud fractions decrease with rising SST, which also acts to weaken stability of the atmosphere unlike the subtropics (McCoy et al., 2017; Myers et al., submitted). GCMs consistently show a decrease of cloud amounts and a resultant positive shortwave feedback in the 30°–40° latitudinal bands, which can be constrained by using seasonal migration of observed cloud amount (Zhai et al., 2015). Based on the qualitative agreement between observations and GCMs, the middle latitude cloud amount feedback is assessed as small positive, but the lack of quantitative observational estimates leads to only *medium confidence* for this assessment, as in the AR5. Following CMIP6 models and emergent constraint studies, the global contribution of net cloud amount feedback over 30°–60° ocean areas, covering 27% of the globe, is assigned +0.09 ± 0.1 W $m^{-2}$°$C^{-1}$, in which the standard deviation is inflated by 50% reflecting potential errors in models' low cloud response to changes in thermodynamic conditions.

***Extratropical cloud optical depth feedback.***

It has been argued that the cloud optical depth (opacity) will increase with surface warming over the

Southern Ocean (50°–80°S) and hence result in a negative feedback (Boucher et al., 2013). The most plausible explanation for this cloud 'brightening' is a phase change from ice-dominated to liquid-dominated clouds with atmospheric temperature rise. Liquid clouds generally consist of many small cloud droplets, while the ice crystals in ice clouds are orders of magnitudes fewer in number and much larger, causing the liquid clouds to be optically thicker. However, the phase change feedback works effectively only below freezing temperature (Lohmann and Neubauer, 2018; Terai et al., 2019) and other processes that increase or decrease liquid water path (LWP) may also affect the optical depth feedback (McCoy et al., 2019). Due to insufficient amounts of super-cooled liquid water in the atmosphere mean state, many CMIP5 models overestimated the negative phase change feedback (Tan et al., 2016), which can be constrained using interannual relationship of LWP against temperature obtained from satellite observations (Gordon and Klein, 2014; Ceppi et al., 2016). The observationally constrained SW feedback is $-0.46$ W $m^{-2}°C^{-1}$ over the Southern Ocean (Terai et al., 2016). In some CMIP6 models, representation of super-cooled liquid water content has been improved, bringing the simulated negative optical depth feedback over the Southern Ocean closer to observational estimates (Bodas-Salcedo et al., 2019). The weakening of the phase change feedback in GCMs at the same time resulted in a positive optical depth feedback over other extratropical oceans where LWP decreased in response to surface warming (Zelinka et al., 2020). Because the Southern Ocean phase-change contribution is small when the low clouds are occupied mostly by liquid (Bjordal et al., submitted), the extratropical optical depth feedback is assessed as neutral with *low confidence* given that the sign is determined as a residual between the local negative and positive feedbacks. Quantitatively, the global contribution of this feedback is assessed to have a value of $0 \pm 0.05$ W $m^{-2}°C^{-1}$ by combining estimates using the cloud controlling factor over 30°–60° (Myers et al., submitted) and an emergent constraint over 60°–80°S (Terai et al., 2016).

***Arctic cloud feedback.***

Clouds in polar regions, especially over the Arctic, form at low altitude above a stable boundary layer and are known to co-vary with sea-ice variability beneath. Because the clouds reflect sunlight during summer but trap longwave radiation throughout the year, seasonality plays an important role for cloud effects on Arctic climate (Kay et al., 2016). The AR5 assessed that Arctic low cloud amount will increase in boreal autumn and winter in response to declining sea ice in a warming climate, due primarily to an enhanced upward moisture flux over open water. The cloudier conditions during these seasons result in more downwelling longwave radiation, acting as a positive feedback on surface warming (Kay and Gettelman, 2009). Over recent years, further evidence of the cloud contribution to the Arctic amplification has been obtained (Goosse et al., 2018; Section 7.4.4.1). Space-borne lidar observations show that the cloud response to summer sea-ice loss is small and cannot overcome the cloud effect in autumn (Taylor et al., 2015; Morrison et al., 2018). Such a seasonality of the cloud response to sea-ice variability is captured by GCMs (Laîné et al., 2016; Yoshimori et al., 2017). The agreement between observations and models supported by theory indicates that the Arctic cloud feedback is positive at the surface. This leads to a cloud feedback at TOA that is also *likely* positive, but small in magnitude (less than +0.1 W $m^{-2}°C^{-1}$) as found in some climate models (Pithan and Mauritsen, 2014; Morrison et al., 2018). Furthermore, CMIP6 models show a large inter-model spread of 0.44 W $m^{-2}°C^{-1}$ over the Arctic covering 3% of the globe which currently cannot be narrowed due to the lack of observational evidence. The Arctic cloud feedback at the TOA is therefore assessed to have the value of $0 \pm 0.05$ W $m^{-2}°C^{-1}$ with *low confidence*.

### *7.4.2.4.3 Synthesis for the net cloud feedback*

The understanding of the response of clouds to greenhouse warming and associated radiative feedback has deepened since the AR5. Particular progress has been made in the assessment of marine low cloud feedback, which has historically been a major contributor to the cloud feedback uncertainty. Multiple lines of evidence (theory, observations, emergent constraints and process modelling) are now available in addition to GCM simulations, and the positive low-cloud feedback is consequently assessed with *high confidence*. However, it is challenging to estimate the net cloud feedback by summing known feedbacks associated with individual cloud regimes because the processes involved in some feedback mechanisms remain poorly understood (Table 7.9).

Using CMIP5 GCMs, broad agreement has been obtained in estimates of net cloud feedback based on interannual variability and longer (decadal to centennial) climate change timescales (Zhou et al., 2015; Colman and Hanson, 2017). This means that the cloud feedback on the interannual time scale, due mostly to natural climate variability, can be a surrogate of the feedback to $CO_2$-induced warming and can be estimated using observations. For the years 2000–2010, the net cloud feedback calculated using two atmospheric reanalyses (ERA-Interim and MERRA) and TOA radiation budgets derived from the CERES satellite observations is $+0.54 \pm 0.35$ W $m^{-2}$ °$C^{-1}$ (Dessler, 2013). However, this estimate would be sensitive to the period used (see Section 7.4.3).

In summary, research since the AR5 leads to an overall *high confidence* in the estimate of the feedback sign. The sum of all cloud feedbacks leads to the assessment of a net cloud feedback of $\alpha_C = 0.4$W $m^{-2}$ °$C^{-1}$. By assuming that uncertainty of individual cloud feedbacks is independent of each other, their standard deviations are added in quadrature. This leads to the *likely* range of 0.1 to 0.7 W $m^{-2}$ °$C^{-1}$ and the *very likely* range of –0.12 to 0.92 W $m^{-2}$ °$C^{-1}$ (Table 7.10). A small probability (10%) of a net negative cloud feedback cannot be ruled out, but this would require an extremely large negative feedback due to decreases in the amount of tropical high clouds or increases in cloud optical depth over the Southern Ocean; neither is supported by current evidence.

**[START TABLE 7.9 HERE]**

**Table 7.9:** Assessed sign and confidence level of cloud feedbacks in difference regimes, compared between AR5 and AR6. For some cloud regimes, the feedback was not assessed in AR5, indicated by N/A.

| Feedback | AR5 | AR6 |
|---|---|---|
| High-cloud altitude feedback | Positive (*high confidence*) | Positive (*high confidence*) |
| Tropical high-cloud amount feedback | N/A | Negative (*medium confidence*) |
| Tropical marine low-cloud feedback | N/A (*low confidence*) | Positive (*high confidence*) |
| Land cloud feedback | N/A | Small positive (*medium confidence*) |
| Middle latitude cloud amount feedback | Positive (*medium confidence*) | Small positive (*medium confidence*) |
| Extratropical cloud optical depth feedback | N/A | Neutral (*low confidence*) |
| Arctic cloud feedback | Small positive (*very low confidence*) | Neutral (*low confidence*) |
| Net cloud feedback | Positive (*medium confidence*) | Positive (*high confidence*) |

**[END TABLE 7.9 HERE]**

### *7.4.2.5 Biophysical and non-$CO_2$ biogeochemical feedbacks*

The feedbacks presented in the previous sections (7.4.2.1–7.4.2.4) were directly linked to physical climate variables (for example temperature, water vapour, clouds, or sea ice). The central role of these phenomena has been recognised since the very first studies on past and future climate change. However, in addition to these physical climate feedbacks, the Earth system includes feedbacks for which the impact of the global mean surface temperature on the radiative budget is mediated by changes in the chemical composition of the atmosphere, or by vegetation. Among those feedbacks, the most important is the $CO_2$ feedback that describes how a change of the global mean surface temperature affects the carbon cycle, the $CO_2$ concentration in the atmosphere, the TOA radiative energy budget, and eventually the global mean surface temperature. This feedback is assessed in Chapter 5, Section 5.4. It is explicitly excluded from our concentration-driven framework (Section 7.1; Box 7.1) and is, therefore, not considered here.

The chemical composition of the atmosphere (beyond $CO_2$ and $H_2O$ changes) is also expected to change in response to a warming climate. These changes in greenhouse gases ($CH_4$, $N_2O$, and ozone) and aerosol amount have the potential to alter the TOA energy budget and are collectively referred to as non-$CO_2$ biogeochemical feedbacks. The non-$CO_2$ biogeochemical feedbacks which are relevant to the aggregated feedback parameter are assessed in Chapter 6, Section 6.3.6, to $-0.2 \pm 0.1$ W m$^{-2}$ °C$^{-1}$. However, there is *low confidence* in the estimates of both the individual non-$CO_2$ biogeochemical feedbacks as well as their total effect, as evident from the large range in the magnitude of $\alpha$ which can be attributed to diversity in how models account for these feedbacks based on limited process-level understanding.

Biophysical feedbacks are associated with changes in the spatial distribution and/or biophysical properties of vegetation induced by climate, altering radiative fluxes via albedo or water vapour changes. These feedbacks act on timescales of decades to centuries (Willeit et al., 2014), longer than non-$CO_2$ biogeochemical feedbacks. Biophysical feedbacks manifest themselves in terms of changes in vegetation distributions and properties in response to temperature change. Vegetation changes induce changes in surface albedo altering the TOA radiation balance. Furthermore, changes in vegetation characteristics alter water fluxes to the atmosphere (evapotranspiration) which can also influence radiation (Bonan, 2008). The timescale of response of vegetation to climate change is relatively uncertain but can be from decades to hundreds of years; equilibrium only occurs when the soil system and associated carbon pools equilibrate, which can take millennia (Brantley, 2008; Sitch et al., 2008). The overall effects of climate-induced vegetation changes may be comparable in magnitude to those from anthropogenic land-use and land cover change (Davies-Barnard et al., 2015).
Climate models that include a dynamical representation of vegetation (e.g. Harper et al., 2018; Reick et al., 2013) are used to explore the importance of biophysical feedbacks (Notaro et al., 2007; Brovkin et al., 2009; O'ishi et al., 2009; Port et al., 2012; Willeit et al., 2014; Alo and Anagnostou, 2017; Zhang et al., 2018b; Armstrong et al., 2019). In the AR5, it was discussed that such model experiments predicted that expansion of vegetation in the high latitudes of the NH would enhance warming due to the associated surface albedo change (Boucher et al., 2013), and that reduction of tropical forests in response to climate change would also lead to warming, due to reduced evapotranspiration.

Since the AR5, several studies have confirmed that biophysical vegetation feedbacks lead to enhanced warming in NH high latitudes (*high confidence*), associated with a shift from tundra to boreal forests and the associated albedo change (Willeit et al., 2014; Zhang et al., 2018b; Armstrong et al., 2019). Although regional modelling indicates that vegetation feedbacks may act to cool climate in the Mediterranean (Alo and Anagnostou, 2017), in the tropics and subtropics the regional response is in general not consistent across models. On a global scale, modelling studies indicate that biophysical vegetation feedbacks are either positive (Armstrong et al., 2019; Notaro et al., 2007; O'ishi et al., 2009) or close to zero (Port et al., 2012; Willeit et al., 2014). Overall, the feedback parameter, $\alpha_x$, for biophysical-vegetation feedbacks is assessed to be *likely* positive, with *medium confidence*, but there is insufficient evidence at this time to give an assessment of its likely range. Higher confidence in the results from coupled climate-vegetation models will be obtained if they are able to better simulate past observed changes in vegetation, such as under orbital forcing in the mid-Holocene. For this period data indicates extensive vegetation in the Sahara that models are currently unable to capture (Braconnot et al., 2012; Brierley et al., submitted), although some progress has recently been made in this regard (Brovkin et al., 2019).

Assessed feedback parameters, $\alpha_x$, for the non-$CO_2$ biogeochemical processes described above, are summarised in Chapter 6, Section 6.3.6 (Table 6.5). In addition, the CMIP6 ensemble provides a number of pairs of instantaneous 4×$CO_2$ simulations carried out with models with and without biophysical and non-$CO_2$ biogeochemical feedbacks. The comparison is not always completely clean because these pairs of models may differ by more than just their inclusion of these processes; furthermore, the models in general do not include all non-$CO_2$ biogeochemical feedbacks. However, a comparison of the pairs of simulations provides a first-order estimate of the magnitude of the combination of these biophysical and non-$CO_2$ biogeochemical feedbacks. Séférian et al. (2019), examining the difference between CNRM-CM6-1 and CNRM-ESM2-1, find a more negative feedback parameter when these additional feedbacks are included (a decrease of 0.02 W m$^{-2}$°C$^{-1}$, using the linear regression method from years 10-150). Sellar et al. (2019) find an ECS for UKESM1 of 5.4°C, for comparison with an ECS for HadGEM3-GC3.1 of 5.5°C. Assuming an identical $CO_2$ forcing in UKESM and HadGEM3, both of these studies suggest a slightly negative feedback parameter, $\alpha_x$, for the combination of biophysical and non-$CO_2$ biogeochemical feedbacks. However, the relatively long timescales associated with vegetation processes compared with the 150 years of the underlying model simulations, combined with the small numbers of studies and the relatively small signals, means that a formal assessment cannot be made at this time. Furthermore, the feedback diagram based on CMIP5/6 models (Figure 7.13) shows that the residual term that should have included the biophysical and non-$CO_2$ biogeochemical feedbacks is nearly zero. Because of insufficient evidence to support a central estimate, the sum of these feedbacks is assessed to have a zero-mean value with *low confidence* and a *likely* range from –0.1 to +0.1 W $m^{-2}$ $°C^{-1}$.

### *7.4.2.6 Long term feedbacks associated with ice sheets.*

Earth's ice sheets (Greenland and Antarctica) are sensitive to climate change (Chapter 9, Section 9.4; Pattyn et al., 2018). Their time-evolution is determined by both their surface mass balance and ice dynamic processes, which are particularly important for the west Antarctic ice sheet. Surface mass balance depends on the net energy and hydrological fluxes at their surface, expressing the net effect of snow accumulation and ice melt. The dynamic ice flows of the Antarctic ice shelves are observed to be accelerating and there are known mechanisms of ice sheet instability that depend on ocean temperatures and basal melt rates (Chapter 9, Section 9.4.1.1). The presence of ice sheets affects Earth's radiative budget, hydrology, and atmospheric circulation due to their characteristic high albedo, low roughness length, and high altitude, and they influence ocean circulation through freshwater input from calving and melt (e.g. Fyke et al., 2018). There is also some evidence that melting ice sheets may affect levels of volcanic activity, through effects of changing surface loading on mantle melt (Swindles et al., 2018). The timescale of response of ice sheets is on the order of thousands of years (Clark et al., 2016). Due to the long timescales involved, it is a major challenge to run fully coupled climate-ice sheet simulations with full complexity models to equilibrium, and as a result, long-term simulations are often carried out with lower complexity models, and/or are asynchronously coupled.

In the AR5, it was described that both the Greenland and Antarctic ice sheets would continue to melt in a warming world (Collins et al., 2013a), with a continuation in sea level rise beyond the year 2500 being assessed as *virtually certain*. However, there was *low confidence* in the associated feedback mechanisms, and as such, there was no assessment of the magnitude of long-term feedbacks associated with ice sheets. This assessment is consistent with SROCC, wherein it was stated that 'with limited published studies to draw from and no simulations run beyond 2100, firm conclusions regarding the net importance of atmospheric versus ocean melt feedbacks on the long-term future of Antarctica cannot be made.'

The magnitude of the feedback associated with changes to ice sheets can be quantified by comparing the global mean long-term equilibrium temperature response to increased $CO_2$ concentrations in simulations that include interactive ice sheets with that of simulations that do not include the associated ice-sheet climate interactions (Swingedouw et al., 2008; Vizcaíno et al., 2010; Goelzer et al., 2011; Bronselaer et al., 2018; Golledge et al., 2019). These simulations indicate that on multi-centennial timescales, fresh water fluxes from melting ice sheets modify ocean circulation (Swingedouw et al., 2008; Goelzer et al., 2011; Bronselaer et al., 2018; Golledge et al., 2019), leading to reduced warming, although other work suggests no net global temperature effect of ice sheet melting (Vizcaíno et al., 2010). However, model simulations in which the Antarctic ice sheet is removed completely in a paleoclimate context indicate a positive global mean feedback on multi-millennial timescales due primarily to the surface albedo change (Goldner et al., 2014; Kennedy-Asser et al., 2019). This net positive feedback due to ice sheets on long timescales is also supported by model simulations of the mid-Pliocene warm period (MPWP, Chapter 2 Box 2.1) in which the volume and area of the Greenland and West Antarctic ice sheets are reduced in model simulations in agreement with geological data (Chandan and Peltier, 2018). As such, overall, on multi-centennial timescales the feedback parameter, $\alpha_x$, associated with ice sheets is *likely* negative (*medium confidence*), but on multi-millennial timescales by the time the ice sheets reach equilibrium (or completely melt) and freshwater fluxes reduce (or stop), the feedback parameter is *likely* positive (*high confidence*). However, there is currently not enough evidence to quantify the magnitude of these feedbacks, or the timescales on which they act.

In the AR5 (Masson-Delmotte et al., 2013), the only overall quantitative assessment of long-term feedbacks was in the context of paleoclimates, wherein it was assessed that evidence from the mid-Pliocene warm period (MPWP) implied that, with *medium confidence*, long-term Earth sensitivity may be up to two times greater than ECS as defined in Box 7.1 ("Charney climate sensitivity"). This implies a positive value of the individual feedback parameter, $\alpha_x$, for the combination of biophysical and ice sheet feedbacks, which has been further supported by more recent work on the MPWP (Haywood et al, submitted, see also Chapter 2 Box 2.4). Results from a combination of models of intermediate complexity and ESMs suggest that including all biophysical, ice sheet and non-$CO_2$ biogeochemical feedbacks may decrease the magnitude of the net feedback parameter, α, by as much as half (Fischer et al., 2018).

#### *7.4.2.7 Synthesis*

Table 7.10 summarises the estimates and the assessment of the individual and the total feedbacks presented in the above sections. The CMIP GCM estimates are computed using a single method whereas the assessed interval also includes uncertainties due to the calculation method. The *medium confidence* in the cloud feedback limits the level of confidence in the total feedback and prevents us from defining a *very likely* range of the total feedback. However, as the net cloud feedback is assessed positive with *high confidence*, the total climate feedback is assessed to be –1.25 ± 0.37 W $m^{-2}$°$C^{-1}$ and *very likely* more positive than –1.9 W $m^{-2}$°$C^{-1}$.

Feedback parameters in climate models are calculated assuming that they are independent of each other, except for a well-known co-dependency between the WV and LR feedbacks. When the inter-model spread of the total climate feedback is computed by adding in quadrature the inter-model spread of individual feedbacks, it is 17% wider than the spread of the net climate feedback directly derived from the ensemble. This indicates that the feedbacks in climate models are partly co-dependent. Two possible co-dependencies have been suggested (Huybers, 2010; Caldwell et al., 2016). One is a negative covariance between the LR and longwave cloud feedbacks, which may be accompanied by a deepening of the troposphere (O'Gorman and Singh, 2013) leading both to greater rising of high clouds and a larger upper-tropospheric warming. The other is a negative covariance between albedo and shortwave cloud feedbacks, which may originate from the Arctic regions: a reduction in sea ice enhances the shortwave cloud radiative effect because the ocean surface is darker than sea ice (Gilgen et al., 2018). This covariance is reinforced as the decrease of sea-ice leads to an increase in low-level clouds (Mauritsen et al., 2013). However, the covariance between these feedbacks is not strong in the CMIP5 ensemble and furthermore not robustly supported by the available observations. Therefore, the synthesis assessment has not considered any co-dependency across individual feedbacks.

**[START TABLE 7.10 HERE]**

**Table 7.10:** Synthesis assessment of climate feedbacks (central estimate shown by boldface). The mean values and their ranges in CMIP5/6 models, derived using multiple radiative kernels (Zelinka et al., 2020), are also presented for comparison.

| Feedback parameter $\alpha_x$ (W $m^{-2}$ °$C^{-1}$) | CMIP5 GCMs | CMIP6 GCMs | AR6 | | | |
|---|---|---|---|---|---|---|
| | Mean and the 5-95% interval | Mean and the 5-95% interval | Central estimate | Very likely interval | Likely interval | Level of confidence |
| Planck | –3.2 (–3.3 to –3.1) | –3.2 (–3.3 to –3.1) | **–3.2** | –3.4 to –3.0 | –3.3 to –3.1 | *high* |
| WV+LR | 1.2 (1.1 to 1.4) | 1.2 (1.1 to 1.4) | **1.2** | 0.95 to 1.5 | 1.1 to 1.3 | *high* |
| Surface albedo | 0.41 (0.25 to 0.57) | 0.41 (0.28 to 0.53) | **0.35** | 0.10 to 0.60 | 0.25 to 0.45 | *high* |
| Clouds | 0.44 (–0.15 to 0.97) | 0.56 (–0.11 to 1.1) | **0.4** | –0.12 to 0.92 | 0.10 to 0.70 | *high* |
| non-$CO_2$ biogeochemistry | Not evaluated | Not evaluated | **0** | –0.17 to 0.17 | –0.10 to 0.10 | *low* |
| Biophysical | Not evaluated | Not evaluated | | | > 0.0 | *medium* |
| **Total** (i.e., relevant for | –1.1 (–1.6 to –0.61) | –1.0 (–1.6 to –0.44) | **–1.25** | –1.9 to –0.6 | –1.6 to –0.9 | *medium* |

| | | | |
|---|---|---|---|
| ECS) | | | |
| Long-term ice sheet feedbacks (millennial scale) | > 0.0 | > 0.0 | *high* |

**[END TABLE 7.10 HERE]**

### *7.4.3 Dependence of feedbacks on climate mean state*

In the standard framework of forcings and feedbacks (Section 7.4.1; Box 7.1), the strength of climate feedbacks is assumed to be independent of the background global mean temperature. More generally, the individual feedback parameters, $\alpha_x$, are assumed to be constant over a range of climate states, including those reconstructed from the past (encompassing a range of states warmer and colder than today, with varying continental geographies) or predicted for the future. If this approximation holds, then the equilibrium global mean temperature response to a unit forcing will be constant, regardless of the climate state to which that forcing is applied.

In reality, this approximation will break down if climate feedbacks behave sufficiently non-linearly, varying as a function of, for example, background temperature (Roe and Baker, 2007; Zaliapin and Ghil, 2010; Roe and Armour, 2011; Bloch-Johnson et al., 2015). If the real climate system exhibits this state-dependence, then future temperature change in response to large forcings may be different from that inferred using the standard framework, and/or different to that inferred from paleoclimates or the observational record. Climate models generally include representations of feedbacks that allow non-linear behaviour, and so model results may also differ from the predictions from the standard framework.

In the AR5 (Boucher et al., 2013), there was a recognition that climate feedbacks could be state-dependent (Colman and McAvaney, 2009), but modelling studies that explored this (e.g. Manabe and Bryan, 1985; Voss and Mikolajewicz, 2001; Stouffer and Manabe, 2003; Hansen, 2005) were not assessed in detail. However, in the AR5 (Masson-Delmotte et al., 2013), paleoclimate evidence was used to assess that climate sensitivity in simulations of the Last Glacial Maximum (LGM, ~19,000 to 21,00 years ago; Table 2.A.1; Cross-Chapter Box 1.4) was less than that in simulations of warm climates ($CO_2$ quadrupling), due to a state dependency in shortwave cloud feedbacks.

Here, recent evidence for state-dependence in feedbacks from modelling studies (Section 7.4.3.1) and from the paleoclimate record (Section 7.4.3.2) are assessed, with an overall assessment in Section 7.4.3.3. Evidence for the dependence of feedbacks on the spatial pattern of warming, independent of global mean temperature change, is assessed separately in Section 7.4.4.

#### *7.4.3.1 Evidence for state-dependence in feedbacks from modelling studies*

There are several modelling studies since the AR5 in which GCMs of varying complexity have been used to explore state-dependency (Caballero and Huber, 2013; Hansen et al., 2013; Jonko et al., 2013; Meraner et al., 2013; Good et al., 2015; Mauritsen et al., 2019; Rugenstein et al., 2019b; Stolpe et al., 2019; Zhu et al., 2019), typically by carrying out multiple simulations across successive $CO_2$ doublings. A non-linear temperature response to these successive doublings may be partly due to forcing that increases more or less than expected from a purely logarithmic dependence (Etminan et al., 2016), and partly due to state-dependence in feedbacks; however, not all modelling studies have partitioned the non-linearities in temperature response between these two effects. Nonetheless, there is general agreement amongst GCMs that the feedback parameter, α, becomes less negative as temperature increases from preindustrial (i.e. climate sensitivity increases as temperature increases; e.g. Meraner et al., 2013; see Figure 7.15). This increase in climate sensitivity is in most models due to the water vapour (Section 7.4.2.2) and cloud (Section 7.4.2.5) feedback parameters increasing with warming (Caballero and Huber, 2013; Meraner et al., 2013; Zhu et al., 2019). These changes are offset partially but not completely by the surface albedo feedback parameter decreasing with warming (Jonko et al., 2013; Meraner et al., 2013), which is a consequence of reduced snow and sea ice cover in a warmer climate. At the same time there is little change in the Planck feedback parameter (Section 7.4.2.1), which is due to competing effects from increasing Planck emission at warmer temperatures and decreasing planetary emissivity due to increased $CO_2$ and water vapour (Mauritsen et al., 2019). Analysis of the spatial patterns of the non-linearities in temperature response (Good et al., 2015) suggests that these patterns are linked to a reduced weakening of the AMOC, and changes to evapotranspiration. The state-dependence of α is also found in model simulations of high-$CO_2$ paleoclimates (Caballero and Huber, 2013; Zhu et al., 2019; Figure 7.15). The state-dependence is not only evident at very high $CO_2$ concentrations in excess of 4×$CO_2$, but also apparent in the difference in temperature response to a 2×$CO_2$ forcing compared with a 4×$CO_2$ forcing (Mauritsen et al., 2019; Figure 7.15), and as such relevant for interpreting century-scale climate predictions.

Despite the general agreement that α becomes less negative (i.e. climate sensitivity increases) as temperature increases (Figure 7.15), one modelling study has found that α becomes more negative as temperature increases from preindustrial times (Stolpe et al., 2019), and there is limited evidence from some models that α may become more negative at extremely high $CO_2$ concentrations (> 4000ppmv) (Caballero and Huber, 2013; Hansen et al., 2013; Popp et al., 2016). Modelling studies exploring state-dependence in climates colder than today, including in cold paleoclimates such as the LGM, support both decreased (Yoshimori et al., 2011) and increased (Kutzbach et al., 2013; Stolpe et al., 2019) temperature response to unit forcing during cold climates compared to the modern era.

In contrast to most ESMs, the majority of EMICs do not exhibit state-dependence, or have a feedback parameter that becomes more negative with increasing temperature (i.e. climate sensitivity decreases as temperature increases) (Pfister and Stocker, 2017). This is perhaps unsurprising since EMICs usually do not represent the water vapour and cloud feedbacks mechanistically. One exception is the FAMOUS model, in which α becomes less negative with increasing $CO_2$ forcing, and which, in contrast to many other EMICs, is more akin to a low-resolution GCM (essentially a low-resolution version of HadCM3). Although Pfister and Stocker (2017) showed that care must be taken when interpreting results from current generation EMICs, they suggested that non-linearities in feedbacks can take a long time to emerge in model simulations, implying that millennial-scale simulations are required to increase confidence in GCM studies examining state-dependence (Rugenstein et al., 2019b).

The possibility of more substantial changes in state has also been suggested from theoretical and modelling studies. Such changes in state, which may occur abruptly (Chapter 4; Section 4.7.3), could lead to substantial changes in climate feedbacks across relatively narrow $CO_2$ increases (Bjordal et al., submitted; Popp et al., 2016; Schneider et al., 2019; Steffen et al., 2018; von der Heydt and Ashwin, 2016). However, even if such behaviour does exist, the threshold at which any such change might occur is highly uncertain.

Overall, the modelling evidence indicates that there is *medium confidence* that the feedback parameter, α, becomes less negative (i.e. climate sensitivity increases) with increasing temperature, at least up to atmospheric $CO_2$ concentrations of about 4000 ppmv, and *medium confidence* that this state-dependence primarily derives from increases in the water vapour and shortwave cloud feedbacks. This state-dependence should be considered when estimating ECS from ESM simulations in which $CO_2$ is quadrupled (Section 7.5.5) or from paleoclimate observations from past time periods colder or warmer than today (Section 7.5.4). However, there is insufficient evidence at this time to provide a quantification of nonlinearities in the feedback parameter, α.

#### *7.4.3.2 Evidence for state-dependence in feedbacks from the paleoclimate proxy record*

Several studies have estimated ECS from observations of the glacial-interglacial cycles of the last ~2 million years, and found a state dependence, with more negative α (i.e. lower climate sensitivity) during colder periods of the cycles and less negative α (i.e. higher climate sensitivity) during warmer periods (von der Heydt et al., 2014; Köhler et al., 2015, 2017; Friedrich et al., 2016; Royer, 2016); see summaries in Skinner (2012) and von der Heydt et al. (2016). However, the nature of the state-dependence derived from these observations is dependent on the assumed ice sheet forcing (Köhler et al., 2015; Stap et al., 2019), which is not well known, due to a relative lack of observations of ice sheet extent and distribution prior to the LGM, 21,000 years ago. Additionally, if the analysis excludes time periods where the temperature and $CO_2$ data are not well correlated, which occurs in general at times when sea level is falling and obliquity is decreasing, the state-dependence reduces (Köhler et al., 2018). Despite these uncertainties, overall, there is *medium confidence* from the paleoclimate proxy record that the feedback parameter, α, is less negative (i.e. climate sensitivity is greater) in the warm periods than in the cold periods of the glacial-interglacial cycles.

There is paleoclimate proxy evidence that during past high-$CO_2$ time periods warmer than present (specifically, the early Eocene and PETM; Chapter 2 Box 2.1), the feedback parameter becomes less negative (i.e. climate sensitivity increases) with increasing temperature (Anagnostou et al., 2016; Shaffer et al., 2016). However, the uncertainties in reconstructing global mean temperature and forcing for these times periods are relatively large; as such, there is only *low confidence* in the existence of state dependence based on the proxy evidence from these past warm periods.

#### *7.4.3.3 Synthesis of state dependence of feedbacks from modelling and paleoclimate records*

Overall, independent lines of evidence from models (Section 7.4.3.1) and from the paleoclimate proxy record (Section 7.4.3.2) indicate that the feedback parameter, α, becomes less negative (i.e. climate sensitivity increases) as temperatures increase (*high confidence*); see Figure 7.15. Although individual lines of evidence have only medium or low confidence, the overall high confidence comes from the multiple models that show this behaviour, the general agreement in evidence from the paleo proxy and modelling lines of evidence, and the agreement between proxy evidence from both cold and warm past climates. Given the time-varying nature of the feedbacks (Section 7.4.4), greater confidence in the modelling lines of evidence would be obtained from simulations carried out for several hundreds of years or millennia (Rugenstein et al., 2019b), substantially longer than in many studies. Greater confidence in the paleoclimate lines of evidence would be obtained from stronger constraints on atmospheric $CO_2$ concentrations during past warm climates.

**[START FIGURE 7.15 HERE]**

**Figure 7.15:** Feedback parameter, α (W $m^{-2}$ °$C^{-1}$), as a function of global mean surface air temperature anomaly relative to preindustrial, for model simulations (coloured circles and lines; Caballero and Huber, 2013; Good et al., 2015; Jonko et al., 2013; Mauritsen et al., 2019; Meraner et al., 2013; Stolpe et al., 2019; Zhu et al., 2019), and from paleoclimate data (grey circles and associated uncertainties; Anagnostou et al., 2016; Shaffer et al., 2016). For the model simulations, the value on the *x*-axis refers to the mean of the temperature before and after the system has equilibrated to a forcing (in most cases a $CO_2$ doubling), and is expressed as an anomaly relative to an associated pre-industrial global mean temperature from that model. The values of α from proxies assume a radiative forcing of 3.7 W $m^{-2}$ for $CO_2$ doubling.

**[END FIGURE 7.15 HERE]**

### *7.4.4 Relationship between feedbacks and temperature patterns*

The large-scale patterns of surface warming in observations since the 19$^{th}$ century (Chapter 2, Section 2.3) and climate model simulations (Chapter 4, Section 4.3; Figure 7.16a) share several common features. In particular, surface warming is greater in the Arctic than in the global average or even southern hemisphere high latitudes; and surface warming is generally greater over land than over nearby oceans. GCMs generally simulate a weakening of the equatorial Pacific Ocean SST gradient on multi-decadal to centennial timescales, with greater warming in the east than the west, although this feature has not yet emerged in observations (Figures7.18, 7.19, Chapter 9, Section 9.2). This section assesses process understanding of these large-scale patterns of surface temperature response from the perspective of a regional energy budget. It then assesses evidence from the paleoclimate proxy record for long-term patterns of surface warming during deep past time periods of high atmospheric $CO_2$ concentration. Finally, it assesses how radiative feedbacks depend on the spatial pattern of surface temperature, and thus that they can change in magnitude as that pattern evolves over time, with important implications for the assessment of ECS based on historical warming (Section 7.4.5.2).

Chapter 4, Section 4.5 discusses patterns of surface warming for 21st century forcing scenarios. Chapter 9, Section 9.2 assesses historical SST trends and the ability of coupled GCMs to replicate the observed changes. Chapter 4, Section 4.5.1 discusses the processes causing the land to warm more than the oceans.

### *7.4.4.1 Polar amplification*

Polar amplification describes the phenomenon that surface temperature changes tend to be amplified at the poles relative to the global mean in response to radiative forcing of the climate system. Arctic amplification, often defined as the ratio of Arctic to global surface warming, is a ubiquitous emergent feature of climate model simulations (Holland and Bitz, 2003; Pithan and Mauritsen, 2014) (Chapter 4, Section 4.5; Figure 7.16a) and is also seen in observations (Chapter 2, Section 2.3). However, both climate models and observations show relatively less warming of the southern hemisphere (SH) high latitudes over the historical record (Chapter 2, Section 2.3) and over the 21st century (Chapter 4, Section 4.5). Since the AR5 there is a much-improved understanding of the processes that drive polar amplification in the northern hemisphere (NH) and delay its emergence in the SH.

**[START FIGURE 7.16 HERE]**

**Figure 7.16:** Contributions of effective radiative forcing, ocean heat uptake and radiative feedbacks to regional surface temperature changes at year 100 of abrupt CO2 quadrupling simulations of CMIP5 models. (a) Pattern of near-surface air temperature change. (b-d) Contributions to net Arctic (>60°N), tropical (30°S-30°N), and Antarctic (<60°S) warming calculated by dividing regional-average energy inputs by the regional-average Planck response, with the contributions from radiative forcing, changes in atmospheric heat transport, ocean heat uptake, and radiative feedbacks summing to the value of net warming; inset shows regional warming contributions associated with individual feedbacks, summing to the total feedback contribution. Uncertainties show 25% and 75% percentiles across models. The warming contributions (units of °C) for each process are diagnosed by calculating the energy flux (units of W $m^{-2}$) that each process contributes to the atmosphere over a given region, either at the TOA or surface, then dividing that energy flux by the regional Planck response (around 3.2 W $m^{-2}$°$C^{-1}$ but varying with latitude). By construction, the individual warming contributions sum to the total warming in each region. Radiative kernel methods (see Section 7.4.1) are used to decompose the net energy input from radiative feedbacks into contributions from changes in atmospheric water vapour, lapse-rate, clouds and surface albedo, leaving a small residual (Shell et al., 2008) and the analysis is based on that of Goosse et al., (2018).

**[END FIGURE 7.16 HERE]**

#### *7.4.4.1.1 Critical processes driving polar amplification*

Feedbacks associated with the loss of sea ice and snow are central to polar amplification (Dai et al., 2019), but other feedbacks and changes in atmospheric and oceanic heat transport contribute as well. Regional energy budget analyses are commonly used to diagnose the relative contributions of the different factors to regional warming as projected by climate models under increased $CO_2$ concentrations (Figure 7.16) (Feldl and Roe, 2013; Pithan and Mauritsen, 2014; Goosse et al., 2018; Stuecker et al., 2018). These suggest that the primary cause of amplified Arctic warming is the latitudinal structure of radiative feedbacks, which warm the Arctic more than the tropics (Figure 7.16b). In turn, this latitudinal structure reflects that of the surface-albedo and lapse-rate feedbacks, which preferentially warm the Arctic (Graversen et al., 2014; Pithan and Mauritsen, 2014; Goosse et al., 2018). Latitudinal structure in the lapse-rate feedback reflects weak radiative damping to space with surface warming in polar regions, where atmospheric warming is constrained to the lower troposphere owing to stably stratified conditions, and strong radiative damping in the tropics, where warming is enhanced in the upper troposphere owing to moist convective processes. This is only partially compensated by latitudinal structure in the water vapour (Taylor et al., 2013) and cloud feedbacks, which favour tropical warming (Pithan and Mauritsen, 2014). A weaker Planck response at high latitudes, owing to less efficient radiative damping where surface and atmospheric temperatures are colder, also contributes to polar amplification (Pithan and Mauritsen, 2014). Since the ERF of $CO_2$ is larger in the tropics than at high latitudes, it contributes more to tropical warming than to polar warming (Figure 7.16b-d).

While asymmetries in radiative feedbacks between the poles contribute to greater warming in the Arctic than the Antarctic (Yoshimori et al., 2017; Goosse et al., 2018), the primary driver of reduced Antarctic warming in transient simulations is the large heat uptake in the Southern Ocean (Marshall et al., 2015; Armour et al., 2016) (Figure 7.16c; Chapter 9). Strong heat uptake also occurs in the subpolar North Atlantic Ocean (Chapter 9). However, this is partially compensated by increased northward heat transport into the Arctic under global warming which leads to increased heat fluxes into the Arctic atmosphere (Rugenstein et al., 2013; Jungclaus et al., 2014; Koenigk and Brodeau, 2014; Marshall et al., 2015; Nummelin et al., 2017; Singh et al., 2017; Oldenburg et al., 2018) (Figures 7.5 and 7.16b). Climate model simulations of the equilibrium response to $CO_2$ forcing project polar amplification in both hemispheres, but generally with less warming in the Antarctic than the Arctic (Li et al., 2013a; Yoshimori et al., 2017).
While energy budget analyses (Figure 7.16) are useful for diagnosing contributions to regional warming, their value for assessing the underlying role of individual factors is limited by interactions inherent to the coupled climate system. For example, the net atmospheric poleward heat transport into the Arctic does not change substantially under $CO_2$ forcing (Figure 7.5), suggesting little to no role for changes in atmospheric heat transport in Arctic amplification (Figure 7.16b). However, this occurs because increases in poleward latent energy transport with warming is compensated by a decrease in poleward dry-static energy (sensible + potential energy) transport (Armour et al., 2019; Donohoe et al., submitted; Huang and Zhang, 2014; Hwang et al., 2011; Kay et al., 2012; Roe et al., 2015) (Section 7.2.3). Episodic increases in latent heat transport into the Arctic enhance the water-vapour feedback and may drive sea-ice loss, at least on sub-seasonal timescales (Woods and Caballero, 2016; Gong et al., 2017; Lee et al., 2017; Luo et al., 2017a), however this may be a smaller driver of sea-ice variability than atmospheric temperature fluctuations (Olonscheck et al., 2019). If Arctic long-term warming also depends on the relative partitioning of atmospheric latent and sensible heat transport, then heat transport changes could play a more prominent role in polar amplification than implied by regional energy budget analyses (Lee, 2014; Graversen and Burtu, 2016; Yoshimori et al., 2017; Armour et al., 2019). Moreover, polar feedback processes are coupled and influenced by warming at lower latitudes through heat transport changes (Screen et al., 2012; Alexeev and Jackson, 2013; Graversen et al., 2014; Graversen and Burtu, 2016; Rose and Rencurrel, 2016; Yoshimori et al., 2017; Feldl et al., 2017; Garuba et al., 2018; Po-Chedley et al., 2018a; Stuecker et al., 2018; Dai et al., 2019) while poleward atmospheric heat transport changes are influenced by the latitudinal structure of regional feedbacks, radiative forcing, and ocean heat uptake (Hwang et al., 2011; Zelinka and Hartmann, 2012; Feldl and Roe, 2013; Huang and Zhang, 2014; Merlis, 2014; Rose et al., 2014; Roe et al., 2015; Stuecker et al., 2018; Armour et al., 2019).

While these various factors are thus not cleanly separable, they work in concert to favour polar amplification. Polar amplification still occurs within GCMs when the surface-albedo feedback (Hall, 2004; Alexeev et al., 2005; Graversen and Wang, 2009) or the lapse-rate feedback (Graversen et al., 2014) are suppressed. It also occurs in models without any sea ice (Feldl and Roe, 2013; Rose et al., 2014; Kim et al., 2018). Moist diffusive energy balance models suggest that polar amplification would occur even in the absence of any latitudinal structure in climate feedbacks owing to increased poleward latent heat transport with warming (Alexeev and Jackson, 2013; Rose et al., 2014; Roe et al., 2015; Merlis and Henry, 2018; Armour et al., 2019). Poleward latent heat transport changes act to favour polar amplification and prevent tropical amplification within climate models (Armour et al., 2019), resulting in strongly polar-amplified warming in response to polar forcing and a more latitudinally-uniform warming in response to tropical forcing (Alexeev et al., 2005; Rose et al., 2014; Stuecker et al., 2018).

Because many factors contribute to polar amplification, projections of polar warming are inherently more uncertain than global mean warming (Holland and Bitz, 2003; Roe et al., 2015; Bonan et al., 2018; Stuecker et al., 2018). The magnitude of Arctic amplification ranges from a factor of two to four in projections of 21$^{st}$ century warming (Chapter 4, Section 4.5). While uncertainty in both global and tropical warming is dominated by cloud feedbacks (Vial et al., 2013), uncertainty in polar warming arises primarily from polar surface-albedo and lapse-rate feedbacks, changes in atmospheric and oceanic poleward heat transport, and ocean heat uptake (Hwang et al., 2011; Mahlstein and Knutti, 2011; Pithan and Mauritsen, 2014; Bonan et al., 2018).

Arctic amplification has a distinct seasonality with a peak in early winter (Nov–Jan) owing to sea-ice loss and associated increases in heat fluxes from the ocean to the atmosphere resulting in strong near-surface warming (Pithan and Mauritsen, 2014; Dai et al., 2019). Surface warming may be further amplified by cloud and lapse-rate feedbacks in autumn and winter (Burt et al., 2016; Morrison et al., 2018). Arctic amplification is weak in summer owing to surface temperatures remaining stable as excess energy goes into thinning the summertime sea-ice cover (which remains at the freezing point) or into the ocean mixed layer. Arctic amplification can also been interpreted through changes in the surface energy budget (Burt et al., 2016; Woods and Caballero, 2016; Boeke and Taylor, 2018; Kim et al., 2019), however such analyses are complicated by the finding that a large portion of the changes in downward longwave radiation can be attributed to surface warming itself (Vargas Zeppetello et al., 2019).

Based on mature process understanding, observational evidence, and a high degree of agreement across a hierarchy of climate models, there is *very high confidence* that polar amplification is a robust feature of the long-term response to greenhouse gas forcing in both hemispheres. There is *high confidence* that the rate of Arctic surface warming will continue to exceed the global average over the 21$^{st}$ century and that polar amplification will eventually emerge in the SH on centennial timescales as the climate equilibrates with radiative forcing and Southern Ocean heat uptake is reduced. However, the timing of the emergence of SH polar amplification remains uncertain due to insufficient knowledge of the timescales associated with Southern Ocean warming and the response to surface wind and freshwater forcing (Bintanja et al., 2013; Kostov et al., 2017, 2018; Pauling et al., 2017; Purich et al., 2018). GCM simulations indicate that large freshwater input to the Southern Ocean from melting ice shelves could substantially delay the emergence of polar amplified warming by stratifying and cooling the surface ocean around Antarctica (Bronselaer et al., 2018; Golledge et al., 2019) (*low confidence* due to medium agreement but limited evidence). However, even a large reduction in the Atlantic meridional overturning circulation (AMOC) due, for instance, to greatly increased freshwater runoff from Greenland would be insufficient to eliminate Arctic amplification (Liu et al., 2017b, 2017c; Wen et al., 2018) (*medium confidence* based on to medium agreement and medium evidence).

##### *7.4.4.1.2 Polar amplification in past high-$CO_2$ climates*

Paleoclimate data from the geological record provides observational evidence of large-scale patterns of surface warming during past time periods of high atmospheric $CO_2$ concentration (Foley and Dowsett, 2019; Hollis et al., 2019; McClymont et al., submitted; Tierney et al., 2019). Furthermore, comparison of these data with paleoclimate model simulations of the same time periods (Haywood et al., submitted; Kageyama et al., submitted; Lunt et al., submitted) allows an evaluation of modelled patterns of surface warming in response to high $CO_2$ and other forcings, and provides insights into the mechanisms that led to these patterns of warming. In particular, these deep past time periods provide paleo evidence for long-term changes in polar amplification, and longitudinal temperature gradients in the tropics. In this context, there has been a community modelling and data focus on the mid-Pliocene warm period (MPWP) (Chapter 2, Table 2.1; Box 2.4; Chapter 5, Section 5.1.3.1, about 3 million years ago, $CO_2$ concentrations of 300 to 450 ppmv, global mean surface temperature 3.0 to 4.5ºC above preindustrial, reduced Greenland and Antarctic ice sheets compared with preindustrial; Haywood et al., 2016b), and the early Eocene climatic optimum (EECO; Chapter 2, Table 2.1, about 50 million years ago, $CO_2$ concentrations >1100 ppmv, global mean surface temperatures about 13ºC above preindustrial, absence of continental ice sheets; Lunt et al., 2017). For both these time periods, in particular the early Eocene, there is a non-$CO_2$ forcing associated with paleogeographic change (Farnsworth et al., 2019), and long-term feedbacks associated with ice sheets play a substantial role (Section 7.4.2.6); as such, the response of the system cannot be interpreted as representative of an ECS as defined in Section 7.1. However, because these non-$CO_2$ forcings can be included in model experimental designs, these time periods allow an assessment of the patterns of modelled response to known forcings (albeit with greater uncertainty in forcing than in more recent time periods).

At the time of the AR5, polar amplification was evident in observations of paleoclimate SST and land temperature from both the MPWP and the early Eocene, but uncertainties associated with proxy calibrations (MPWP and early Eocene; Dowsett et al., 2012; Lunt et al., 2012; Salzmann et al., 2013) and the role of orbital forcing (MPWP; Lisiecki and Raymo, 2005) meant that the degree of polar amplification during these time periods was not accurately known. Furthermore, although some models (CCSM3; Winguth et al., 2010; Huber and Caballero, 2011) at that time were able to reproduce the strong polar amplification implied by temperature proxies of the early Eocene, this was achieved at substantially higher $CO_2$ concentrations than those indicated by $CO_2$ proxies (Beerling and Royer, 2011).

Since the AR5 there has been progress in improving the accuracy of temperature reconstructions of the MPWP and early Eocene time periods (Foley and Dowsett, 2019; Hollis et al., 2019; McClymont et al., submitted; Tierney et al., 2019). In addition, reconstructions of the MPWP have been focused on a short time slice with an orbit similar to modern-day (isotopic stage KM5C; Haywood et al., 2013, 2016). Furthermore, there are more robust constraints on $CO_2$ concentrations from both of these time periods (Martínez-Botí et al., 2015; Anagnostou et al., 2016). Consequently, the degree of polar amplification during these high-$CO_2$ time periods can now be better quantified, and the ability of models to reproduce this pattern can be better assessed (Figure 7.17a,b,d,e,g,h).

**[START FIGURE 7.17 HERE]**

**Figure 7.17:** Temperature anomalies compared with pre-industrial for the high-CO2 EECO and MPWP time periods, and for the Last Glacial Maximum (expressed as LGM minus preindustrial), from paleoclimate proxies and models. (a,b,c) Modelled near-surface air temperature anomalies for ensemble-mean simulations of the (a) EECO (Lunt et al, submitted), (b) Pliocene (Haywood et al, submitted), and (c) Last Glacial Maximum (Kageyama et al, submitted). (d,e,f) Proxy sea surface temperature anomalies (black circles), including published uncertainties (vertical bars), black lines show model ensemble mean SST anomaly (solid back line) and near-surface air temperature anomaly (dashed black line) for the same ensembles as in (a,b,c), coloured lines show the modelled SST anomaly for the individual models that make up each ensemble (LGM, N=1; MPWP, N=15; EECO, N=5). Proxy datasets are (d) (Hollis et al., 2019), (e) (Foley and Dowsett, 2019), and (f) Tierney et al (submitted). (g,h,i) As (a,b,c) but for SST anomalies, and with the proxy SST anomalies from (d,e,f) also shown (coloured circles). For the Eocene maps (c,i), the anomalies are relative to the zonal mean of the preindustrial.

**[END FIGURE 7.17 HERE]**

Since the AR5, there has also been a change in the degree of polar amplification simulated by paleoclimate models of the early Eocene and MPWP. For the early Eocene, initial work indicated that changes to model parameters associated with aerosols and/or clouds could increase simulated polar amplification and improve agreement between models and paleoclimate data (Kiehl and Shields, 2013; Sagoo et al., 2013), but such parameter changes were prescribed and not mechanistically based. In support of these initial findings, a more recent (CMIP5 generation) model, that includes a process-based representation of cloud microphysics, also exhibits increased polar amplification compared to the models assessed in AR5. This model also agrees better with the proxy-based estimates of SST than previous simulations, and obtains this good agreement when forced with $CO_2$ concentrations that are in agreement with the proxy $CO_2$ records (Zhu et al., 2019; Figure 7.17a,d,g). For the MPWP, model simulations are now in better agreement with proxies than at the time of the AR5 (Haywood et al., submitted). In particular, in the tropics new proxy reconstructions of SSTs are warmer and in better agreement with the models, due in part to the narrower time window in the proxy reconstructions. There is also better agreement at higher latitudes, due in part to the absence of some very warm proxy SSTs due to the narrower time window, and in part to a better representation of Arctic gateways in the most recent Pliocene model simulations, which have resulted in warmer SSTs in the North Atlantic (Haywood et al, submitted; Figure 7.17b,e,h). However, few of these simulations are carried out by the latest CMIP6 generation models There is some indication that CMIP6 models with high climate sensitivity may simulate an EECO climate that is too warm compared with proxies (Zhu et al., submitted), but this needs to be confirmed by other models.

The Last Glacial Maximum (LGM) also gives an opportunity to evaluate model simulation of polar amplification under $CO_2$ forcing, albeit under colder conditions than today. As with the EECO, there are substantial regional ice sheet forcings in addition to $CO_2$, but these are also implemented in the model simulations, allowing a like-for-like comparison with the proxies. Both the proxies and models indicate polar amplification when considering a transition from the LGM to preindustrial (Figure 7.17c,f,i), but the more regional SST changes apparent in the proxies are not well simulated by the models (Kageyama et al. (submitted); Chapter 3, Section 3.3.1).

Overall, the proxy reconstructions give *high confidence* that there was polar amplification in both hemispheres in the MPWP and EECO, and this is further supported by model simulations of these time periods (Haywood et al., submitted; Lunt et al., submitted; Zhu et al., 2019), which are more consistent with the proxies than at the time of the AR5. Polar amplification is further supported by models and proxies of the LGM. Overall, the confidence in the ability of models to accurately simulate polar amplification is higher than at the time of the AR5. Further confidence could be obtained if more of the latest generation models (CMIP6) were applied to high-$CO_2$ periods of the past.

*7.4.4.1.3 Overall assessment of polar amplification*

The paleoclimate proxy record of past warm climates, GCM simulations of those past climates, and GCM projections of climate response to $CO_2$ forcing provide robust evidence, a high degree of agreement and thus *very high confidence* that equilibrium warming will be polar amplified in both hemispheres. Arctic amplification has already been observed (Chapter 2, Section 2.3) and its causes are well understood. Polar amplification in the SH has yet to emerge over the historical record (Chapter 2, Section 2.3) owing to delayed warming of the Southern Ocean surface and associated heat uptake.

Southern Ocean SSTs have also been slow to warm over the instrumental period (Figure 7.19a), with cooling since 1980 owing to a combination of upper-ocean freshening from ice-shelf melt, intensification of surface westerly winds from ozone depletion, and variability in ocean convection (Chapter 9, Section 9.2). This stands in contrast to the equilibrium warming pattern either inferred from the proxy record or simulated by GCMs under $CO_2$ forcing. There is *high confidence* that the SH high latitudes will warm by more than the tropics on centennial timescales. However, there is only *low confidence* that this feature will emerge this century.

Since the AR5, there has been an improvement in model simulations of polar amplification in past high-$CO_2$ time periods when compared with proxy reconstructions, in particular the MPWP and the early Eocene (*high confidence*). However, many CMIP6 models are yet to be applied to these time periods and so cannot currently be assessed in this way.

### *7.4.4.2 Tropical sea-surface temperature gradients*

*7.4.4.2.1 Critical processes determining changes in tropical sea-surface temperature gradients*

A weakening of the equatorial Pacific Ocean east-west SST gradient, with greater warming in the east than the west, is a common feature of the equilibrium climate response to $CO_2$ forcing as projected by GCMs (e.g., Figure 7.19b). There are thought to be several factors contributing to this pattern. In the absence of any changes in atmospheric or oceanic circulations, the east-west surface temperature difference is theorized to decrease owing to weaker evaporative damping, and thus greater warming in response to forcing, where climatological temperatures are colder in the eastern Pacific cold tongue (Xie et al., 2010; Luo et al., 2015). Within atmospheric GCMs coupled to mixed-layer oceans, this gradient in damping has been linked to the rate of change with warming of the saturation specific humidity, which is set by the Clausius-Clapeyron relation (Merlis and Schneider, 2011). Gradients in low-cloud feedbacks may also favour eastern equatorial Pacific warming (DiNezio et al., 2009).

In the coupled climate system, changes in atmospheric and oceanic circulations will influence the east-west temperature gradient as well. It is expected that as global temperature increases and as the east-west temperature gradient weakens, east-west sea-level pressure gradients and easterly trade winds (characterizing the Walker circulation) will weaken as well (Vecchi et al., 2006, 2008; Figure 7.18b). This would, in turn, weaken the east-west temperature gradient through a reduction of equatorial upwelling of cold water in the east Pacific and a reduction in the transport of warmer water to the western equatorial Pacific and Indian Ocean (England et al., 2014; Dong and McPhaden, 2017; Li et al., 2017; Maher et al., 2018).

Research since the AR5 (Burls and Fedorov, 2014a; Fedorov et al., 2015; Erfani and Burls, 2019) has built on an earlier theory (Liu and Huang, 1997; Barreiro and Philander, 2008) linking the east-west temperature gradient to the north-south temperature gradient. In particular, model simulations suggest that a reduction in the equator-to-pole temperature gradient (polar amplification) increases the temperature of water subducted in the extra-tropics, which in turn is upwelled in the eastern Pacific. Thus, polar amplified warming, with greater warming in the mid-latitudes and subtropics than in the deep tropics, is expected to contribute to the weakening of the east-west equatorial Pacific SST gradient on decadal to centennial timescales. For all of these reasons, GCMs generally project an El Niño–like pattern of Pacific warming on centennial timescales.

The transient adjustment of the equatorial Pacific SST gradient is influenced by the fact that upwelling waters delay surface warming in the east since they have not been at the surface for years-to-decades to experience the greenhouse gas forcing. This ‘thermostat mechanism’ (Clement et al., 1996; Cane et al., 1997) is not thought to persist to equilibrium since it does not account for the eventual increase in temperatures of upwelled waters (Liu et al., 2005; Xie et al., 2010; Luo et al., 2017b) which will occur as surface warming becomes polar amplified. An individual CMIP5 GCM (GFDL’s ESM2M) has been found to transiently warm with a La Niña–like pattern of Pacific temperature change, more similar to the SST trends seen over the historical record (Chapter 9, Section 9.2; Figure 7.19a), owing to a weakening nonlinear ENSO amplitude (Kohyama et al., 2017), but this pattern does not appear to persist to equilibrium (Paynter et al., 2018).

Since 1870, observed SSTs in the tropical western Pacific Ocean have increased while those in the tropical eastern Pacific Ocean have changed less (Figure 7.19a; Chapter 9, Section 9.2). Much of this strengthening of the equatorial Pacific temperature gradient has occurred since about 1980 due to strong warming in the west and cooling in the east concurrent with an intensification of the surface equatorial easterly trade winds and Walker Circulation (Chapter 9, Section 9.2) (England et al., 2014). This temperature pattern is also reflected in regional ocean heat content trends and sea level changes observed from satellite altimetry since 1993 (Bilbao et al., 2015). With *medium confidence*, the observed Walker circulation strengthening appears to have resulted from a combination of transient factors including sulphate aerosol forcing (Takahashi and Watanabe, 2016; Hua et al., 2018), multi-decadal tropical Atlantic SST trends (Kucharski et al., 2011, 2014, 2015; McGregor et al., 2014; Chafik et al., 2016; Li et al., 2016a; Kajtar et al., 2017; Sun et al., 2017), and coupled ocean–atmosphere dynamics which slow warming in the equatorial eastern Pacific (Clement et al., 1996; Cane et al., 1997; Seager et al., 2019). Coupled GCMs are generally unable to replicate observed trends in the Walker Circulation and Pacific Ocean SSTs over the historical record (Zhou et al., 2016; Coats and Karnauskas, 2017), possibly due to model deficiencies including insufficient multi-decadal Pacific Ocean SST variability (Laepple and Huybers, 2014; Bilbao et al., 2015), mean state biases affecting the forced response or the connection between Atlantic and Pacific basins (Kucharski et al., 2014; Kajtar et al., 2018; Luo et al., 2018; McGregor et al., 2018; Seager et al., 2019), and/or a misrepresentation of radiative forcing (Chapter 9, Section 9.2 and Chapter 3, Section 3.7.6).

Based on medium evidence and a high degree of agreement, GCM simulations and process understanding provides *medium confidence* that the La Niña–like warming pattern seen over the historical record is transient in nature and that SSTs in the eastern tropical Pacific Ocean will increase more than SSTs in the western tropical Pacific Ocean on multi-centennial timescales under greenhouse gas forcing. These trends in tropical Pacific SST gradients reflect changes in the climatology, rather than changes in ENSO amplitude or variability, which is assessed in Chapter 4, Section 4.3.3. There is emerging evidence that the Walker circulation has weakened again since around 2011, suggesting that a transition to an El Niño–like warming pattern may currently be underway (Cha et al., 2018) with *low confidence* due to the possibility that this could be a reflection of natural variability.

*7.4.4.2.2 Tropical longitudinal temperature gradients in past high-$CO_2$ climates*

The AR5 stated that paleoclimate proxies indicate a reduction in the longitudinal SST gradient across the equatorial Pacific during the mid-Pliocene warm period (MPWP) (Masson-Delmotte et al., 2013). This assessment was based on SST reconstructions between two sites situated very close to the equator in the heart of the western Pacific warm pool (ODP 806) and eastern Pacific cold tongue (ODP 847), respectively. SST reconstructions based on the magnesium to calcium ratio (Mg/Ca) in foraminifera and the alkenone unsaturation index ($U_{37}^{K\prime}$) generally agree that during the Pliocene the SST gradient between these two sites was reduced compared with the long-term mean of the modern (Wara et al., 2005; Dekens et al., 2008; Fedorov et al., 2013).

Since the AR5, the generation of a new SST records from the ODP 806 warm pool site based on the $TEX_{86}^{H}$proxy (Zhang et al., 2014), the inclusion of $U_{37}^{K\prime}$ and $TEX_{86}^{H}$ SST reconstructions from sites in the South China Sea as warm pool estimates (O'Brien et al., 2014; Zhang et al., 2014), and the inclusion of several new sites from the eastern Pacific as cold tongue estimates (Zhang et al., 2014; Fedorov et al., 2015), has led to a variety of revised gradient estimates. Published estimates of the reduction in the longitudinal gradient for the Pliocene, relative to either Late Quaternary (0-0.5Ma) or preindustrial values, include 1 to 1.5°C (Zhang et al., 2014), 0.1– 1.9°C (Tierney et al., 2019), and about 3°C (Fedorov et al., 2015). All of these studies report a further weakening of the zonal gradient further back in time based on records extending into the Early Pliocene. While these revised estimates differ in magnitude due to differences in the sites and SST proxies used to evaluate the longitudinal SST gradient, and while there are uncertainties associated with the calibrations of the proxies (Haywood et al., 2016a), there is *medium confidence* that the average longitudinal gradient in the tropical Pacific was weaker during the Pliocene than during the Late Quaternary.

To avoid the influence of local biases, changes in the zonal gradient within Pliocene simulations are typically evaluated using domain-averaged SSTs within chosen east and west Pacific regions and as such there is sensitivity to methodology; gradient changes simulated by PlioMIP1 models are reported as spanning approximately –0.5 to 0.5 °C by Brierley et al. (2015) and approximately –1 to 1 °C by Tierney et al. (2019). Simulations with hypothetical modifications to cloud albedo or ocean mixing can simulate substantially weaker zonal gradients (Fedorov et al., 2013; Burls and Fedorov, 2014b), as is required to simulate reconstructed Early Pliocene gradient reductions.

While more western Pacific warm pool temperature reconstructions are needed to refine estimates of the longitudinal gradient, the availability of several sea surface temperature reconstructions from the east Pacific indicates enhanced equatorial warming in the centre of the eastern equatorial cold tongue upwelling region (Liu et al., 2019). This enhanced warming in the east Pacific cold tongue appears to be dynamically consistent with reconstruction of enhanced subsurface warming (Ford et al., 2015) and enhanced warming in coastal upwelling regions, suggesting that the tropical thermocline was either deeper or less stratified during the Pliocene. The Pliocene data therefore suggests that the observed cooling trend over the last 60 years in the eastern equatorial Pacific (Seager et al., 2019), whether forced or due to internal-variability, involves transient processes likely distinct from the longer-timescale process (Burls and Fedorov, 2014b, 2014a; Heede et al., submitted; Luo et al., 2015) that may have maintained warmer eastern Pacific SST during the Pliocene.

*7.4.4.2.3 Overall assessment of tropical sea-surface temperature gradients under $CO_2$ forcing*

The paleoclimate proxy record of past warm climates, GCM simulations of those past climates, and GCM projections of climate response to $CO_2$ forcing provide medium evidence and a medium degree of agreement and thus *medium confidence* that equilibrium warming will be characterized by a weakening of the east-west tropical Pacific SST gradient.

Overall the observed pattern of warming over the instrumental period, with a warming minimum in the eastern tropical Pacific Ocean (Figure 7.19a), stands in contrast to the equilibrium warming pattern either inferred from the proxy record or simulated by GCMs under $CO_2$ forcing. There is *medium confidence* that the observed strengthening of the east-west SST gradient, which has been associated with increased easterly winds over the tropical Pacific in recent decades, is transient in nature and will eventually transition to a weakening of the SST gradient on centennial timescales.

#### *7.4.4.3 Dependence of feedbacks on temperature patterns*

The expected time-evolution of the spatial pattern of surface warming in the future has important implications for values of ECS inferred from the historical record of observed warming. In particular, changes in the global TOA radiative energy budget can be induced by changes in the spatial pattern of surface temperature, even without a change in the global mean temperature (Zhou et al., 2016; Ceppi and Gregory, 2019). Consequently, the global radiative feedback, characterizing the net TOA radiative response to global surface warming, depends on the *spatial pattern* of that warming. Therefore, if the equilibrium warming pattern is distinct from that observed over the historical record (Sections 7.4.4.1 and 7.4.4.2), then ECS will be distinct from effective ECS inferred from historical warming. This "pattern effect" (Stevens et al., 2016) can result from both internal variability and climate forcing. Importantly, it is distinct from potential radiative feedback dependencies on the global mean surface warming, which are assessed in Section 7.4.3. While changes in global radiative feedbacks under transient warming have been documented in multiple generations of climate models (Andrews et al., 2015; Ceppi and Gregory, 2017; Dong et al., submitted; Williams et al., 2008), research since the AR5 has developed a much-improved understanding of the role of evolving SST patterns in driving feedback changes (Andrews et al., 2015, 2018; Andrews and Webb, 2018; Armour et al., 2013; Ceppi and Gregory, 2017; Dong et al., 2019, submitted; Gregory and Andrews, 2016; Haugstad et al., 2017; Marvel et al., 2018; Proistosescu and Huybers, 2017; Silvers et al., 2018; Zhou et al., 2016, 2017). This section assesses process understanding of the pattern effect, which is dominated by the evolution of SSTs. Section 7.5.3 describes how potential feedback changes affect estimates of ECS based on historical warming.

The radiation changes most sensitive to warming patterns are thought to be those associated with the low-cloud cover (affecting global albedo) and the tropospheric temperature profile (affecting infrared emission to space) (Ceppi and Gregory, 2017; Zhou et al., 2017b; Andrews et al., 2018; Dong et al., 2019). The mechanisms and radiative impacts of these changes are illustrated in Figure 7.18a,b. SSTs in regions of deep convective ascent (e.g., in the western Pacific warm pool) govern the temperature of the tropical free troposphere and, in turn, affect low clouds through the strength of the inversion that caps the boundary layer (i.e., the lower-tropospheric stability) in subsidence regions (Wood and Bretherton, 2006; Klein et al., 2017). Surface warming within ascent regions thus warms the free troposphere and increases low-cloud cover, causing an increase in infrared emission to space and a reduction in absorbed solar radiation. In contrast, sea-surface warming in regions of overall descent preferentially warms the boundary layer and enhances convective mixing with the dry free troposphere, decreasing low-cloud cover (Bretherton et al., 2013; Qu et al., 2014; Zhou et al., 2015) and causing an increase in absorption of solar radiation but little change in infrared emission to space. Consequently, warming in tropical ascent regions results in negative lapse-rate and cloud feedbacks while warming in tropical descent regions results in positive lapse-rate and cloud feedbacks (Figure 7.18; Andrews and Webb, 2018; Dong et al., 2019; Rose and Rayborn, 2016; Zhou et al., 2017b). Surface warming in mid-to-high latitudes causes a weak radiative response owing to compensating changes in infrared emission (Planck and lapse-rate feedbacks) and absorbed solar radiation (shortwave cloud and surface-albedo feedbacks) (Rose and Rayborn, 2016; Dong et al., 2019), however this compensation may weaken due to less-negative shortwave cloud feedbacks at high warming (Bjordal et al., submitted; Dong et al., submitted).

**[START FIGURE 7.18 HERE]**

**Figure 7.18:** Illustration of tropospheric temperature and low-cloud response to observed and projected Pacific Ocean sea-surface temperature trends; adapted from Mauritsen (2016). (a) Atmospheric response to linear sea-surface temperature trend observed over 1870-2018 (HadISST1 dataset; Rayner et al., 2003). (b) Atmospheric response to linear sea-surface temperature trend projected over 150 years following $CO_2$ quadrupling by an average of 22 CMIP6 GCMs (Dong et al., submitted). The historical temperature trend shows relatively large warming in the western tropical Pacific has been communicated aloft (red

atmospheric temperature profile), remotely warming the tropical free troposphere and increasing the strength of the inversion in regions of the tropics where warming has been muted, such as the eastern equatorial Pacific. In turn, an increased inversion strength has increased the low-cloud cover (Zhou et al., 2016) causing an anomalously negative cloud and lapse-rate feedbacks over the historical record (Andrews et al., 2018; Marvel et al., 2018). The projected temperature trend shows relatively large warming in the eastern tropical Pacific which is trapped near the surface (red atmospheric temperature profile), decreasing the strength of the inversion locally. In turn, a decreased inversion strength combined with surface warming is projected to decrease the low-cloud cover, causing the cloud and lapse-rate feedbacks to become less-negative in the future.

**[END FIGURE 7.18 HERE]**

The spatial pattern of SST changes since 1870 shows relatively little warming in key regions of less-negative radiative feedbacks, including the eastern tropical Pacific Ocean and Southern Ocean (Sections 7.4.4.1 and 7.4.4.2; Figure 7.19a). Cooling in these regions since 1980 has occurred along with an increase in the strength of the capping inversion in tropical descent regions, resulting in an observed increase in low-cloud cover over the tropical eastern Pacific (Zhou et al., 2016; Figure 7.18a). Thus, tropical low-cloud cover increased over recent decades even as global-average surface temperature increased, resulting in a negative low-cloud feedback which is at odds with the positive low-cloud feedback expected for the pattern of equilibrium warming under $CO_2$ forcing (Section 7.4.2; Figure 7.18b).

**[START FIGURE 7.19 HERE]**

**Figure 7.19:** Sea-surface temperature linear trends (a) observed over 1870-2018 (HadISST dataset; Rayner et al., 2003), and (b) projected over 150 years following $CO_2$ quadrupling by an average of 22 CMIP6 GCMs (Dong et al., submitted).

**[END FIGURE 7.19 HERE]**

Feedback changes can be estimated within transient warming simulations of coupled GCMs. Armour (2017) and Lewis and Curry (2018) considered changes in radiative feedbacks between the transient response to an idealized 1% $yr^{-1}$ $CO_2$ increase (*1pctCO₂*) and the long-term response under *abrupt4xCO₂* in different CMIP5 models, with the *1pctCO₂* simulations serving as an approximate analogue for transient historical warming since pre-industrial. The majority of models show a less-negative global radiative feedback under *abrupt4xCO₂* than under *1pctCO₂* (Figure 7.20a,b), with an average radiative feedback change of α’[2] = +0.19 W $m^{-2}$ °$C^{-1}$(–0.07 to +0.57 W $m^{-2}$ °$C^{-1}$range across models) from Armour (2017) and α’ = +0.05 W $m^{-2}$ °$C^{-1}$(–0.19 to +0.22 W $m^{-2}$ °$C^{-1}$range across models) from Lewis and Curry (2018). Differences in findings between these two studies can be traced primarily to different methods used to estimate ERF of $CO_2$ doubling and to different assumptions about how that $CO_2$ ERF scales with atmospheric $CO_2$ concentration. Using the early portion of *abrupt4xCO₂* simulations of 22 CMIP6 models as an analogue for historical warming and following the methods of Lewis and Curry (2018), Dong et al. (submitted) find an average radiative feedback change of α’ = +0.04 W $m^{-2}$ °$C^{-1}$(–0.23to +0.32 W $m^{-2}$ °$C^{-1}$range across models) (Figure 7.20c).

The CMIP5 and CMIP6 GCM simulations of strong $CO_2$ forcing described above provide estimates of α’ in the absence of non-$CO_2$ forcing agents and internal variability. The historical ERF has been quantified accurately enough for calculations of the effective radiative feedback from historical simulations within only a few GCMs. Using historical simulations of the latest Hadley Centre Global Environmental Model (HadGEM3-GC3.1-LL), Andrews et al., (2019) find an average radiative feedback change of α’ = +0.23 W

[2] α’ is the change in the radiative feedback parameter between the historical period and the equilibrium response to $CO_2$ forcing.

$m^{-2}$ °C$^{-1}$(–0.17 to +0.63 W $m^{-2}$ °C$^{-1}$range across four ensemble members). This value is on average larger than the α' = +0.06 W $m^{-2}$ °C$^{-1}$ estimated using the early portion of the model's *abrupt4xCO₂* simulation (Dong et al., submitted), suggesting that the value of α' may depend on having a realistic representation of historical forcing and of volcanic forcing in particular (Gregory et al., 2019). However, there is substantial spread in the value of α' across ensemble members. Using the 100-member historical simulation ensemble of the Max Planck Institute Earth System Model (MPI- ESM1.1), Dessler et al. (2018) similarly find that internal climate variability alone results in a 0.5 W $m^{-2}$ °C$^{-1}$ spread in the historical effective radiative feedback, and thus also in the value of α'.

In general, coupled GCMs are not able to reproduce the observed cooling of the eastern tropical Pacific or Southern Ocean over recent decades, even within historical simulations where non-$CO_2$ forcing agents are included and even when allowing for different phasing of internal variability (Zhou et al., 2016; Coats and Karnauskas, 2017; Kostov et al., 2018). This suggests that internal climate variability may have played an important role in these observed SST trends that GCMs are not able to replicate; or that GCMs may have errors in either their applied forcing or forced response (Chapter 3, Section 3.7.6; Chapter 9, Section 9.2). Simulations using prescribed historical warming patterns may thus provide a more realistic representation of the historical pattern effect (Andrews et al., 2018). Andrews et al. (2018) analysed available CMIP5/6 climate model simulations (six in total) comparing effective radiative feedbacks diagnosed within atmosphere-only GCMs using prescribed historical SST and sea-ice concentration patterns with equilibrium radiative feedbacks within coupled GCMs (using identical atmospheres) driven by *abrupt4xCO₂* forcing. The atmosphere-only GCMs show pronounced multi-decadal variations in their effective radiative feedbacks over the last century, with a trend toward strongly negative values in recent decades owing primarily to negative shortwave cloud feedbacks (Zhou et al., 2016; Andrews et al., 2018; Marvel et al., 2018; Dong et al., 2019). Yet, all six models show a less-negative global radiative feedback under *abrupt4xCO₂* than for the historical period (based on regression since 1870 following Andrews et al., 2018), with an average radiative feedback change of α' = 0.6 W $m^{-2}$ °C$^{-1}$(0.3–1.0 W $m^{-2}$ °C$^{-1}$range across models) (Figure 7.20d). These feedback changes imply that the value of ECS may be larger than that inferred from the historical record (Section 7.5.3.1).

These findings can be understood from the fact that, due to a combination of internal variability and transient adjustment to forcing (Section 7.4.4.2), historical sea-surface warming has been relatively large in regions of tropical ascent (Figure 7.18a), leading to enhanced radiation to space per degree of global warming and thus an anomalously large net negative radiative feedback; however, future warming is expected to be largest in tropical descent regions, such as the eastern equatorial Pacific, and at high latitudes (Sections 7.4.4.1 and 7.4.4.2) (Figure 7.18b), leading to a reduction in radiation to space per degree of global warming and thus a less-negative global radiative feedback. The magnitude of the feedback increase found when prescribing observed warming patterns is generally larger than that found within the coupled models (Andrews et al. 2018; Figure 7.20). This arises from the fact that the spatial pattern of warming within transient simulations of most coupled GCMs are distinct from that observed over the historical record and more similar to the pattern simulated under *abrupt4xCO₂*.

The magnitude of α', as quantified by GCMs, depends on the accuracy of both the projected patterns of SST and sea-ice concentration changes in response to $CO_2$ forcing and the radiative response to those patterns (Andrews et al., 2018). It also depends on the accuracy of the historical SST and sea-ice concentration conditions prescribed within atmospheric GCMs to quantify the historical radiative feedback (Figure 7.20d). Historical SSTs are particularly uncertain for the early portion of the historical record (Chapter 2, Section 2.2), and there are few constraints on sea-ice concentration prior to the satellite era. Using alternative SST datasets, Andrews et al. (2018) found little change in the value of α' within two models (HadGEM3 and HadAM3), while Lewis and Mauritsen (submitted) found a smaller value of α' within two other models (ECHAM6.3 and CAM5). The sensitivity of results to the choice of dataset represents a major source of uncertainty in the quantification of the historical pattern effect using atmosphere-only GCMs that has yet to be systematically explored, but the preliminary findings of Lewis and Mauritsen (submitted) suggest that α' could be smaller for some models than the values reported in Andrews et al. (2018).

**[START FIGURE 7.20 HERE]**

**Figure 7.20:** Relationship between effective and equilibrium radiative feedbacks in CMIP5 and CMIP6 models. (a) CMIP5 effective feedback values estimated by using year 100 of 1%/yr $CO_2$ ramping simulations as an analogue for historical warming (Armour, 2017). (b) CMIP5 effective feedback values estimated by using year 100 of 1%/yr $CO_2$ ramping simulations as an analogue for historical warming with updated estimates of $CO_2$ radiative forcing (Lewis & Curry, 2018). (c) CMIP6 effective feedback values estimated by regression over the first 50 years of abrupt $CO_2$ quadrupling (abrupt4xCO2) simulations as an analogue for historical warming with updated estimates of $CO_2$ radiative forcing (Dong et al., submitted). (d) Effective radiative feedbacks estimated from atmospheric GCMs with prescribed observed sea-surface temperature and sea-ice concentration changes (Andrews et al., 2018) based on linear regression of global TOA radiation against global near-surface air temperature over the period 1870-2010 (pattern of warming similar toFigure 7.19a) and compared with equilibrium feedbacks in abrupt4xCO2 simulations of coupled versions of the same GCMs (pattern of warming similar to Figure 7.19b). The inset shows the effective radiative feedback estimated from historical global energy budget constraints (Section 7.5.2.1); vertical bar shows median value, box shows 17 to 83% range, and horizontal line shows 5% to 95% range. In all cases, the equilibrium feedback magnitudes are estimated as $CO_2$ ERF divided by ECS where ECS is derived from linear regression over years 1-150 of abrupt4xCO2 simulations (Box 7.1); similar results are found if the equilibrium feedback is estimated directly from the regression of global TOA radiation against global near-surface air temperature over years 1-150 of abrupt4xCO2 simulations.

**[END FIGURE 7.20 HERE]**

While there are not yet direct observational constraints on the magnitude of the pattern effect, satellite measurements of variations in TOA radiative fluxes show strong co-variation with changing patterns of SSTs, with a strong dependence on SST changes in regions of deep convective ascent (e.g., in the western Pacific warm pool) (Loeb et al., 2018b; Fueglistaler, 2019). Cloud and TOA radiation responses to observed warming patterns in atmospheric models have been found to compare favourably with those observed by satellite (Loeb et al., submitted; Zhou et al., 2016) (Section 7.2.2.1). This observational and modelling evidence indicates the potential for a strong pattern effect in nature that will only be negligible if the observed pattern of warming since pre-industrial persists to equilibrium – an improbable scenario given that Earth is in a relatively early phase of transient warming and that reaching equilibrium would take multiple millennia (Li et al., 2013a). Moreover, there is medium evidence and high agreement across paleoclimate proxies, GCM simulations, and process understanding that strong warming in the eastern equatorial Pacific Ocean and Southern Ocean, largely absent over the historical record, will eventually emerge as the response to $CO_2$ forcing dominates temperature changes in these regions (Sections 7.4.4.1; 7.4.4.2; Chapter 9, Section 9.2). This leads to *medium confidence* that the eastern Pacific SSTs will eventually warm by more than the western Pacific SSTs and *high confidence* that SSTs in the Southern Ocean will eventually warm by more than tropical SSTs. Thus, there is *high confidence* that radiative feedbacks will eventually become less-negative as the pattern of surface warming evolves ($\alpha' > 0$ W m$^{-2}$ °C$^{-1}$). However, there is substantial uncertainty in the magnitude of the net radiative feedback change between the present warming pattern and the projected equilibrium warming pattern in response to $CO_2$ forcing owing to the fact that its quantification currently relies solely on GCM results and is subject to uncertainties in historical SST patterns. Thus, α' is estimated to be in the range 0.0–1.0 W m$^{-2}$ °C$^{-1}$ but with a *low confidence* in the upper end of this range. Section 7.5.2 assesses the implications of changing radiative feedbacks for estimates of ECS based on the historical temperature record.

## 7.5 Estimates of ECS and TCR

Equilibrium Climate Sensitivity (ECS) and Transient Climate Response (TCR) are metrics of the global-mean surface air temperature (GSAT) response to forcing, as defined in Section 7.1; Box 7.1. The ECS is the magnitude of GSAT increase to a doubling of atmospheric $CO_2$ concentration in equilibrium, whereas the TCR is the magnitude of GSAT increase when $CO_2$ concentration is doubled in a 1% yr$^{-1}$ increase scenario. Both are idealised quantities, but can be inferred from observational records or estimated directly using climate simulations, and are strongly correlated with the climate response in realistic future projections (Section 7.5.7).

TCR is always smaller than ECS because ocean heat uptake acts to reduce the rate of surface warming. Yet, TCR is correlated ($r$=0.8) with ECS across CMIP5 models (Armour, 2017; Grose et al., 2018), as expected from the fact that TCR and ECS are inherently related measures of climate response to forcing; both depend on ERF and α. The relationship between TCR and ECS is in reality non-linear and becomes more so if the ECS values are higher than those spanned by climate models (Knutti et al., 2005; Millar et al., 2015) owing to ocean heat uptake processes playing a more important role in setting the rate of warming when α is small (recall that ECS is related to 1/α).

Until the AR5, the assessment of ECS relied on either $CO_2$-doubling experiments using atmospheric GCMs coupled with mixed-layer oceans or standardized $CO_2$-quadrupling (*abrupt4xCO2*) experiments using fully coupled GCMs. The TCR has similarly been diagnosed from GCMs in which the $CO_2$ concentration is increased at 1% $yr^{-1}$ (*1%CO2*, an approximately linear increase in ERF over time) and defined as the average over a 20-year period centred at the time of atmospheric $CO_2$ doubling, i.e., year 70. In the AR6, the assessments of ECS and TCR are made extensively based on multiple lines of evidence, with some information still from GCMs. The constraints on these climate metrics are based on radiative forcing and climate feedbacks assessed from process understanding (Section 7.5.1), climate change and variability seen within the instrumental record (Section 7.5.2), paleoclimate evidence (Section 7.5.3), emergent constraints (Section 7.5.4), and a synthesis of all lines of evidence (Section 7.5.5). In the AR5, these lines of evidence were not explicitly combined in the assessment of climate sensitivity, but as demonstrated by Sherwood et al. (submitted) their combination narrows the uncertainty ranges of ECS (and hence TCR) compared to the AR5. Estimates of ECS from CMIP6 models, some of which exhibit values higher than 4.5 °C (Meehl et al., submitted), are discussed in relation to the AR6 assessment (Section 7.5.6).

### *7.5.1 Process-based estimates*

This section assesses the estimates of ECS and TCR based on process understanding of the ERF to a doubling of $CO_2$ concentration and the net climate feedback (Sections 7.3.2 and 7.4.2). Those estimates are used to assess ECS in Section 7.5.1.1, and then the process-based ECS assessment is transferred to TCR in Section 7.5.1.2.

#### *7.5.1.1 ECS using process-based assessments of the forcing and feedbacks*

The process-based assessment is based on the global energy budget equation (Box 7.1, Equation 7.1), where the ERF ($\Delta F$) is replaced with the effective radiative forcing due to a doubling of $CO_2$ concentration (denoted as $\Delta F_{2\times CO2}$) and the climate state reaches a new equilibrium, i.e., Earth's energy imbalance, $\Delta N = 0$. ECS is calculated as the ratio between the effective radiative forcing and the net climate feedback parameter, $-\Delta F_{2\times CO2}/\alpha$. Estimates of $\Delta F_{2\times CO2}$ and α are obtained separately based on understanding of the key processes that determine each of these quantities. Specifically, $\Delta F_{2\times CO2}$ is estimated based on the SARF that can be accurately obtained using line-by-line calculations, to which uncertainty due to adjustments are added (Section 7.3.2). The range of α is derived by aggregating estimates of individual climate feedbacks based not only on GCMs but also on theory, observations, and high-resolution process modelling (Section 7.4.2).

In Section 7.3.2.1, the $\Delta F_{2\times CO2}$ was assessed to be $\Delta F_{2\times CO2} = 4.0 \pm 0.5$ W $m^{-2}$, while the net feedback parameter was assessed to be $\alpha = -1.25 \pm 0.37$ W $m^{-2}$ $°C^{-1}$ (Section 7.4.2.7, Table 7.9). These values are naturally different from those directly calculated from GCMs because of different approaches to assess them as explained above. Assuming that each of these two parameters follow an independent normal distribution, the uncertainty range of ECS can be obtained by substituting the respective probability density function into the expression of ECS (Figure 7.21). Since α is in the denominator, the normal distribution leads to a long tail in ECS toward high values, indicating the large impact of uncertainty in α in estimating the likelihood of a high ECS (Roe and Baker, 2007; Knutti and Hegerl, 2008). Using the values of $\Delta F_{2\times CO2}$ and α assessed in Sections 7.3.2.1 and 7.4.2.6, the ECS is assessed to have a median value of 3.2 °C with a *likely* range of 2.4–

4.6 °C and *very likely* range of 2.0–6.4 °C. To this assessed range of ECS, the contribution of uncertainty in α is approximately three times as large as the contribution of uncertainty in $\Delta F_{2\times CO2}$. Using the process-based estimates here, the lower bound of the ECS is revised to a higher value than AR5, but the possibility of high ECS remains unchanged.

The wide range of the process-based ECS is not due solely to different estimates of $\Delta F_{2\times CO2}$ and α, but is partly explained by the assumption that $\Delta F_{2\times CO2}$ and α are independent in this approach. In CMIP5 and CMIP6 ensembles, $\Delta F_{2\times CO2}$ and α are negatively correlated when they are calculated using the linear regression to *abrupt4xCO2* simulations ($r^2 = 0.34$) (Andrews et al., 2012; Webb et al., 2013; Zelinka et al., 2020). The negative correlation leads to compensation between the inter-model spreads of these quantities, thereby reducing the ECS range estimated directly from the models. If the process-based ECS distribution is reconstructed from probability distributions of $\Delta F_{2\times CO2}$ and α assuming that they are not correlated, the range of ECS will be narrower by 14%. If, however, the covariance between$\Delta F_{2\times CO2}$ and α is not adopted, there is no change in the mean, but the wide range still applies (pink curve in Figure 7.21).

A significant correlation between $\Delta F_{2\times CO2}$ and α also occurs when the two parameters are estimated separately from AGCM experiments with prescribed SST or $CO_2$ concentration. Hence the relationship is not expected to be an artefact of calculating them using the single linear regression in *abrupt4xCO2* simulations. A possible physical cause may be a compensation between the cloud adjustment and the cloud feedback over the tropical oceans (Ringer et al., 2014; Chung and Soden, 2018). It has been shown that the change in the hydrological cycle is a controlling factor for the low-cloud adjustment (Dinh and Fueglistaler, 2019) and for the low-cloud feedback (Watanabe et al., 2018), and therefore the responses of these clouds to the direct $CO_2$ radiative forcing and to the surface warming may not be independent. However, the robust physical mechanisms are not yet clear, and furthermore, the process-based assessment of the tropical low-cloud feedback does not refer to the GCMs given that physical processes which control the low clouds are not sufficiently well-simulated in models (Section 7.4.2.5). For these reasons, the co-dependency between $\Delta F_{2\times CO2}$ and α is assessed to have *low confidence* and, therefore, the more conservative assumption that they are independent for the process-based assessment of ECS is retained.

**[START FIGURE 7.21 HERE]**

**Figure 7.21:** Probability distributions of ERF to CO2 doubling ($\Delta F_{2\times CO2}$, top) and the total climate feedback (α, right), derived from process-based assessments in Sections 7.3.2 and 7.4.2. Middle panel shows the joint PDF calculated on a two-dimensional plane of $\Delta F_{2\times CO2}$ and α (red), on which the 90% range shown by an ellipse is imposed to the background theoretical values of ECS (colour shading). The white dot, thick and thin curves in the ellipse represent the mean, likely and very likely range of ECS. An alternative estimation of the ECS range (pink) is calculated by assuming that $\Delta F_{2\times CO2}$ and α have a covariance. The assumption about the co-dependence between $\Delta F_{2\times CO2}$ and α does not alter the mean estimate of ECS but affects its uncertainty.

**[END FIGURE 7.21 HERE]**

### *7.5.1.2 Emulating process-based ECS to TCR*

In the previous section, ECS was estimated using the effective radiative forcing due to a doubling of $CO_2$ concentration and the net climate feedback parameter as: ECS = $-\Delta F_{2\times CO2}/\alpha$. This section describes how these estimates of ECS can be translated into the TCR in order to provide consistent information on both metrics of climate sensitivity. Here a two-layer energy balance model (EBM) is used to transfer the process-based assessment of forcing, feedback, pattern-effects and heat uptake to TCR. The EBM (Appendix 7.A.2), a type of physical emulator (Cross-Chapter Box 7.1;Chapter 4, Box 4.1), is an extension of the energy budget equation (Equation 7.1) and allows for heat exchange between the upper- and deep oceans, mimicking the ocean heat uptake that reduces the rate of surface warming under radiative forcing (Armour, 2017; Gregory, 2000; Held et al., 2010; Mauritsen and Pincus, 2017; Rohrschneider et al., 2019). The use of the two-layer EBM is advantageous as it is transparent in terms of processes that connect ECS to TCR. With a suitable choice of parameters, the model can reproduce well the transient surface temperature evolution in GCMs under *1%CO2* simulations and other climate change scenarios, despite the very low degrees of freedom (Held et al., 2010; Geoffroy et al., 2012, 2013a; Palmer et al., 2018).

In the two-layer EBM, additional parameters are introduced: heat capacities of the upper and deep oceans, heat uptake coefficient (κ), and the so-called efficacy parameter (ε) that represents the dependence of radiative feedbacks and heat uptake on the evolving SST pattern under $CO_2$ forcing alone (Section 7.4.3). In the real world, natural internal variability and aerosol radiative forcing also affect the efficacy parameter, but these effects are excluded for the current discussion and returned to later.

The analytical solution of the EBM reveals that the surface temperature change to abrupt increase of the atmospheric $CO_2$ concentration is expressed by a combination of fast and slow responses having time scales of several years and centuries. They represent the fast adjustment of the surface components of the climate system and slow response of the deep ocean, respectively (grey curves in Figure 7.22). The equilibrium response of upper ocean temperature, approximating SST and hence the surface air temperature response, depends, by definition, only on the radiative forcing and the climate feedback parameter. In CMIP5 models, uncertainty in α dominates (80–90%) the corresponding uncertainty range for ECS. For the range of TCR, the contribution from uncertainty in α is reduced to 50–60% while uncertainty in $\Delta F_{2\times \mathrm{CO2}}$ becomes relatively more important (Geoffroy et al., 2013b). TCR reflects the fast response occurring approximately during the first 20 years in the *abrupt4xCO2* simulation (Held et al., 2010), but the fast response is not independent of the slow response because there is a nonlinear co-dependence between them (Andrews et al., 2015). The nonlinearity between ECS and TCR is sometimes approximated as $\mathrm{TCR} \sim \sqrt{\mathrm{ECS}}$ (Meehl et al., submitted), which indicates that the probability of high TCR is not very sensitive to changes in the probability of high ECS.

Considering an idealized time evolution of ERF assessed in Section 7.3.2.1 (1% increase by the time of doubling $CO_2$ and held fixed afterwards, see Figure 7.22a), the TCR defined by the surface temperature response at the year 70 is derived by substituting the process-based ECS into the analytical solution of the EBM (Figure 7.22b, see also Appendix 7.A.2). When additional parameters in the two-layer EBM are prescribed by using CMIP5 multi-model mean values of those estimates, this calculation straightforwardly emulates the range of ECS in Section 7.5.2.1 to the range of TCR, between 1.5 and 2.2 °C. The transient temperature response, in reality, varies with different estimates of the ocean heat uptake efficiency. A fitting of the two-layer EBM to the transient responses in CMIP5 models shows that uncertainty in heat capacities is negligible and differences in κ and ε explain 10–20% of the inter-model spread of TCR among GCMs (Geoffroy et al., 2013b). Specifically, their product, κε, appearing in a simplified form of the solution, i.e., $\mathrm{TCR} \cong -\Delta F_{2\times \mathrm{CO2}}/(\alpha + \kappa\varepsilon)$, gives a single parameter quantifying the damping effects of heat uptake (Jiménez-de-la-Cuesta and Mauritsen 2019). The ocean heat uptake in nature is controlled by multiple processes associated with advection and mixing (Exarchou et al., 2014; Kostov et al., 2014; Kuhlbrodt et al., 2015) but is crudely represented by a single term of heat exchange between the upper- and deep-oceans in the two-layer EBM. Therefore, it is challenging to constrain κ and ε from observations (Section 7.5.2). Because the estimated values are only weakly correlated across models, the mean value and one standard deviation of κε are calculated as $\kappa\varepsilon = 0.86 \pm 0.29$ W m$^{-2}$°C$^{-1}$ by ignoring their covariance (the mean value is very similar to that used for Box 4.1, Figure 1). By incorporating this inter-model spread in κε, the range of TCR is widened by about 10% (blue bar in Figure 7.22b). Yet, the dominant contribution to the uncertainty range of TCR arises from the net climate feedback parameter α, and the previous assessment stating that uncertainty in ocean heat uptake is of secondary importance remains unchanged.

In summary, the process-based estimate of TCR is assessed to have the central value of 1.9°C with the *likely* range of 1.5–2.4°C and the *very likely* range of 1.2–2.7°C (*high confidence*). The upper bound of the assessed range was slightly reduced from the AR5 but can be further constrained using multiple lines of evidence (Section 7.5.5).

**[START FIGURE 7.22 HERE]**

**Figure 7.22:** (a) Time evolution of the effective radiative forcing (ERF) to the CO2 concentration increased by 1% per year until the year 70 (equal to the doubling, grey line) and kept fixed afterword. The range of ERF has been assessed in Section 7.3.2.1. (b) Range of surface temperature response to the CO2 forcing in the two-layer EBM calculated with a given range of ECS, considering uncertainty in $\Delta F_{2\times CO2}$,α and an additional parameter associated with the ocean heat uptake and efficacy (shaded by blue and cyan). For comparison, the step response to abrupt doubling of the CO2 concentration is displayed by a grey curve. The mean and ranges of ECS and TCR are shown at the right (the values of TCR also presented in the panel).

**[END FIGURE 7.22 HERE]**

### *7.5.2 Estimates based on the historical temperature record*

This section assesses the estimates of TCR and ECS based on the instrumental record of climate change and variability with an emphasis on new evidence since AR5. Section 7.5.2.1 considers estimates based on the global energy budget. Section 7.5.2.2 considers estimates based on the use of simple climate models evaluated against the historical temperature record. Section 7.5.2.3 considers estimates based on internal variability in global temperature and TOA radiation. Section 7.5.2.4 provides an overall assessment of TCR and ECS based on the historical temperature record.

#### *7.5.2.1 Estimates based on the global energy budget*

Warming since the pre-industrial period is measured to be around 1°C with small uncertainty (Chapter 2, Section 2.2). Together with estimates of Earth's energy imbalance (Section 7.2) and the global ERF that has driven the observed warming (Section 7.3), the instrumental temperature record enables global energy budget estimates to be used to make estimates of ECS and TCR. While energy budget estimates use instrumental data, they are not based purely on observations. A conceptual model typically based on the global-mean energy budget is needed to relate ECS and TCR to the estimates of global warming, ERF and energy imbalance (Forster, 2016; Knutti et al., 2017). Moreover, GCM simulations partly inform estimates of the historical ERF (Section 7.3) as well as the global energy imbalance in the pre-industrial climate (the period against which changes are measured) (Forster, 2016; Lewis and Curry, 2018). GCMs are also used to estimate uncertainty due the internal climate variability that may have contributed to observed changes in temperature and energy imbalance (e.g. Palmer and McNeall, 2014). Research since the AR5 has shown that the global-mean energy budget that is traditionally used produces values of ECS that are biased low for several reasons, primarily because it does not account for the dependence of radiative feedbacks on the spatial pattern of surface warming (Section 7.4.4.3) and because of improvements in the estimation of global mean surface temperature trends which take better account of data-sparse regions and are more consistent in their treatment of surface temperature data (Chapter 2, Section 2.3.1).

The traditional global-mean energy balance framework employed for global energy budget estimates (Gregory et al., 2002) (Section 7.4.1; Box 7.1) relates the difference between the ERF (ΔF) and the radiative response to observed global warming (αΔT) to the global energy imbalance (ΔN): $\Delta N = \alpha\Delta T + \Delta F$, where α represents the net global radiative feedback parameter (units of W m$^{-2}$ °C$^{-1}$). Given the relationship ECS = $\Delta F_{2\times CO2}/(-\alpha)$, where $\Delta F_{2\times CO2}$ is the ERF from $CO_2$ doubling, ECS can be estimated from historical estimates of ΔT, ΔF, ΔN and $\Delta F_{2\times CO2}$: ECS = $\Delta F_{2\times CO2}\,\Delta T/(\Delta F - \Delta N)$. Since TCR is defined as the temperature change at the time of $CO_2$ doubling under an idealized 1% yr$^{-1}$ $CO_2$ increase, it can be inferred from the historical record as: TCR = $\Delta F_{2\times CO2}\,\Delta T/\Delta F$, under the assumption that radiative forcing increases quickly compared to the adjustment timescales of the deep ocean, but slowly enough and over sufficiently long time that the upper ocean is adjusted, so that ΔT and ΔN increases approximately in proportion to ΔF. Because ΔN is positive, TCR is always smaller than ECS, reflecting weaker transient warming than equilibrium warming. TCR is better constrained than ECS owing to the fact that the denominator of TCR, without the quantity ΔN, is more certain and further from zero than is the denominator of ECS. The upper bounds of both TCR and ECS estimated from historical warming are inherently less certain than their lower bounds because $\Delta F$ is uncertain and in the denominator.

The traditional global-mean energy balance framework lacks a representation of the radiative feedback dependence on the spatial pattern of warming. Studies that employ this model framework to infer ECS (Forster, 2016; Lewis and Curry, 2018) thus implicitly assume that radiative feedbacks will remain constant between the period of historical transient warming and the equilibrium response to $CO_2$ forcing. However, as summarized in Section 7.4.4.3, there are now multiple lines of evidence suggesting that radiative feedbacks will become less negative as the warming pattern evolves in the future (the pattern effect). Extensions to the traditional energy balance framework can be made to capture the pattern effect by allowing for multiple radiative feedbacks operating on different timescales (Armour et al., 2013; Geoffroy et al., 2013a; Armour, 2017; Proistosescu and Huybers, 2017; Goodwin, 2018; Rohrschneider et al., 2019), by allowing feedbacks to vary with the spatial pattern or magnitude of ocean heat uptake (Rose et al., 2014; Rugenstein et al., 2016a), or by allowing feedbacks to vary with the type of radiative forcing agent (Kummer and Dessler, 2014; Shindell, 2014; Marvel et al., 2016). However, a direct way to account for the pattern effect is to use the relationship ECS = $\Delta F_{2\times CO2}/(-\alpha + \alpha')$, where $\alpha = (\Delta N - \Delta F)/\Delta T$ is the effective radiative feedback estimated from historical global energy budget changes and $\alpha'$ represents the change in the radiative feedback parameter between the historical period and the equilibrium response to $CO_2$ forcing, which can be estimated using GCMs (Andrews et al., 2018; Armour, 2017; Dong et al., submitted; Lewis and Curry, 2018) (Section 7.4.4.3). There is *high confidence* that radiative feedbacks will become less-negative in the future ($\alpha' > 0$) owing to the fact that historical warming has shown relatively more warming in key negative feedback regions (e.g., western tropical Pacific Ocean) and less warming in key positive feedback regions (eastern tropical Pacific Ocean and Southern Ocean) than is projected in the near-equilibrium response to *abrupt4xCO2* (Section 7.4.4.3) (Held et al., 2010; Proistosescu and Huybers, 2017), implying that the true ECS will be larger than the effective ECS inferred from historical warming. An alternative approach estimates feedback changes in response to $CO_2$ forcing alone in terms of the ocean heat uptake efficacy (see Section 7.5.1.2).

Energy budget estimates of TCR and ECS have evolved in the literature over recent decades. Prior to the AR5, the global energy budget provided relatively weak constraints, primarily due to large uncertainty in the tropospheric aerosol forcing, giving ranges of ECS that typically included values above 10°C (Forster, 2016; Knutti et al., 2017). Revised estimates of aerosol forcing together with a larger greenhouse-gas forcing by the time of the AR5 led to an estimate of $\Delta F$ that was more positive and better constrained relative to the AR4. Using energy budget estimates and radiative forcing estimates updated to 2009, Otto et al. (2013) found that TCR was 0.9–2.0°C (5–95% range) with a median (best estimate) value of 1.3°C, and that the effective ECS was 2.0°C (1.2–3.9°C). Studies since the AR5 using similar methods have produced similar or slightly narrower ranges for TCR and ECS (Forster, 2016; Knutti et al., 2017).

Energy budget estimates of TCR and ECS assessed here are based on improved observations and understanding of global surface temperature trends (Chapter 2, Section 2.3), revised energy imbalance estimates (Section 7.2), and revised estimates of radiative forcing (Section 7.3). Accurate, in situ-based estimates of global energy imbalance can be made from around 2006 based on near-global ocean temperature observations from autonomous profiling floats (Section 7.2). Over the period 2006 to 2018 the global energy imbalance is estimated to be $0.81 \pm 0.14$ W $m^{-2}$ (90% confidence) (Section 7.2). Anomalies are taken with respect to the baseline period 1850 to 1900, although other baselines could be chosen to avoid major volcanic activity (Otto et al., 2013; Lewis and Curry, 2018). Several lines of evidence, including GCM simulations (Lewis and Curry, 2015), energy balance modelling (Armour, 2017), and inferred ocean warming given observed SSTs using ocean GCMs (Gebbie and Huybers, 2019; Zanna et al., 2019) suggest that global energy imbalance for 1850 to 1900 was $0.2 \pm 0.2$ W $m^{-2}$. Combined with estimates of internal variability in global energy imbalance within periods of equivalent lengths derived from unforced GCM simulations (Palmer and McNeall, 2014; Sherwood et al., submitted), the anomalous energy imbalance is estimated to be $\Delta N = 0.61 \pm 0.3$ W $m^{-2}$. Global near-surface air temperature change between 1850–1900 and 2006–2018 is estimated to be $\Delta T = 0.99 \pm 0.09$°C (based on data from Chapter 2, Section 2.3.1; Box 7.2), accounting for internal variability derived from unforced GCM simulations (Sherwood et al., submitted). The ERF change between 1850–1900 and 2006–2018 is estimated to be $\Delta F = 1.97 \pm 0.61$ W $m^{-2}$ and the ERF from $CO_2$ is estimated to be $\Delta F_{2\times CO2} = 4.0 \pm 0.5$ W m$^{-2}$ (Section 7.3.2), and correlated uncertainties between $\Delta F$ and $\Delta F_{2\times CO2}$ are accounted for. Employing these values within the traditional global-mean energy balance framework described above (following the methods of Otto et al. (2013)) produces values a TCR of 2.0°C (1.5–2.9°C; Figure 7.23a). The effective ECS is 2.9°C (1.9–5.6°C; Figure 7.23b). These TCR and effective ECS ranges are higher than those in the recent literature (Otto et al., 2013; Lewis and Curry, 2015, 2018) but are comparable to those of Sherwood et al. (submitted) who also used updated estimates of observed warming, ocean heat uptake, and ERF.

An important part of the upwards revision of the effective ECS inferred from energy budget studies is the use of global coverage near-surface air temperature indicators to estimate the surface temperature trends. Most studies have relied on HadCRUT4 global warming estimates that had incomplete coverage of some regions, especially the Arctic, and also blended near-surface air temperature observations with temperatures measured below the surface of the oceans. The HadCRUT4 historical trends are around 16% smaller than estimates of global surface air temperature warming and as a result ECS and TCR derived from these have similarly smaller ECS and TCR values (Richardson et al., 2016, 2018a). These surface warming trends are discussed in Chapter 2, Cross Chapter Box 2.3 but it is important to note here that for a like-to-like comparison with ECS and TCR estimates derived from models it is necessary to make sure that the same measure of global surface temperature trends is used. The energy budget studies assessing ECS in the AR5 employed HadCRUT4 or similar measures of surface warming trends. Other lines of evidence assumed global surface air temperature trends, meaning that AR5-based energy budget estimates of ECS were about 16% lower than other lines of evidence adding to the overall disparity (Collins et al., 2013a). In this report, GSAT is chosen as the standard measure of global warming to aid comparison with previous model and process-based estimates of ECS, TCR and climate feedbacks (see Box 7.1, Cross Chapter Box 2.3).

**[START FIGURE 7.23 HERE]**

**Figure 7.23:** (a) Transient climate response (TCR) estimated from global energy budget constraints for the period 2006–2018 relative to 1850–1900; horizontal bar shows median value, box shows 17 to 83% range, and vertical line shows 5% to 95% range. (b) Effective equilibrium climate sensitivity (ECS) estimated from global energy budget constraints for the period 2006–2018 relative to 1850–1900 (blue) and ECS accounting for the pattern effect (orange) (Section 7.4.4.3) based on feedback changes derived from coupled GCM simulations (middle, using $\alpha' = +0.1 \pm 0.3$ W m$^{-2}$ °C–1) or from feedback changes assessed from multiple lines of evidence including GCM simulations with prescribed historical sea-surface temperature and sea-ice concentrations (right, using $\alpha' = +0.5 \pm 0.5$ W m$^{-2}$ °C$^{-1}$). (c) Relationship between effective ECS (blue) and actual ECS (orange) in CMIP5 and CMIP6 GCMs where the effective ECS is derived from coupled GCM simulations ('CMIP5 GCMs' Armour, 2017; 'CMIP6 GCMs' Dong et al., submitted; 'CMIP5 GCMs with updated $CO_2$ ERF' Lewis & Curry, 2018) or from GCM simulations with prescribed historical sea-surface temperature and sea-ice concentrations ('GCMs with observed warming pattern' Andrews et al., 2018). The actual ECS in models is estimated from simulations of abrupt $CO_2$ quadrupling (Box 7.1).

**[END FIGURE 7.23 HERE]**

As summarized in Section 7.4.4.3, net radiative feedback change between the present warming pattern and the projected equilibrium warming pattern in response to $CO_2$ forcing ($\alpha'$) is estimated to be in the range 0.0–1.0 W m$^{-2}$ °C$^{-1}$ (Figure 7.18) based on atmospheric GCMs driven by observed SST patterns (Andrews et al., 2018; Lewis and Mauritsen, submitted), but with a *low confidence* in the upper end of this range. Using the value $\alpha' = 0.5 \pm 0.5$ W m$^{-2}$ °C$^{-1}$ to represent this range illustrates the impact of changing radiative feedbacks on estimates of ECS. While the effective ECS inferred from historical warming lies in the range 1.9–5.6°C with a median value of 2.9°C, ECS = $\Delta F_{2\times CO2}/(-\alpha + \alpha')$ lies in the range 1.9–19.7°C with a median value of 4.3°C (Figure 7.23b). For comparison, values of $\alpha'$ derived from idealized $CO_2$ forcing simulations of coupled climate models (Andrews et al., 2019; Armour, 2017; Dong et al., submitted; Lewis and Curry, 2018) can be approximated as $\alpha' = 0.1 \pm 0.3$ W m$^{-2}$ °C$^{-1}$ (5% to 95% range) (Section 7.4.4.3), corresponding to a value of ECS that lies in the range 1.9–7.2°C with a median value of 3.1°C (Figure 7.23b). In both cases, the low end of the ECS range is similar to that of the effective ECS inferred using the traditional energy balance model framework that assumes α' = 0, reflecting a weak dependence on the value of α' when ECS is small (Armour, 2017; Andrews et al., 2018). However, the high end of the ECS range is substantially larger than that of the effective ECS and strongly dependent on the value of α'.

The values of ECS obtained from the techniques outlined above are all higher than those estimated from both the AR5 and recently published estimates (Collins et al., 2013a; Otto et al., 2013; Lewis and Curry, 2015, 2018; Forster, 2016). Four revisions made in this report are responsible for this increase: (1) An upwards revision of historic surface temperature trends from the adoption of GSAT measure and newly published trend data (Chapter 2, Section 2.3); (2) An 8% increase in the ERF for $\Delta F_{2\times CO2}$ (Section 7.3.2); (3) A 22% more-negative best estimate of aerosol ERF, which acts to reduce estimates of historic ERF trends; and iv) Accounting for the pattern effect on the net feedback parameter α. The combined effect of all these revisions has yet to be tested in the published literature and leads to a cautious assessment at this stage.

Overall, there is *high confidence* ECS is higher than that inferred from the historical global energy budget, but there is substantial uncertainty in how much higher because there is substantial uncertainty in how radiative feedbacks will change in the future. The accuracy of the estimated values of α' hinges on the accuracy of projected changes in the warming pattern under $CO_2$ forcing and on the radiative response to those warming patterns within GCMs. While several lines of evidence indicate that α' > 0, the quantitative accuracy of feedback changes is not known at this time (Section 7.4.4.3): GCMs produce a wide range of results for α' (Figure 7.20) and there are currently no direct observational constraints on its value. Global energy budget constraints thus provide *very high confidence* in the lower bound of ECS which is not sensitive to the value of α': it is *extremely unlikely* to be less than 1.9°C. Estimates of α' that are informed by idealized $CO_2$ forcing simulations of coupled GCMs (Andrews et al., 2019; Armour, 2017; Dong et al., submitted; Lewis and Curry, 2018) indicate a median value of ECS of around 3°C while estimates of α' that are informed by observed historical warming patterns (Andrews et al., 2018) indicate a median value of ECS of around 4°C. Owing to large uncertainties in future feedback changes, the historical energy budget currently provides little information about the upper bound of ECS.

#### *7.5.2.2 Estimates based on simple climate models*

Simple climate models (SCMs) are more complex than global-average energy balance models but far less complex than comprehensive GCMs (see Chapter 1, Section 1.5 Table 1.3 and Cross-Chapter Box 7.1). The numerical efficiency of such SCMs means that they can be empirically constrained by observations: a large number of possible parameter values (e.g., radiative feedback parameter, aerosol radiative forcing and ocean diffusivity) are randomly drawn from prior distributions; forward integrations of the model are performed with these parameters and weighted against observations of surface or ocean warming, producing posterior estimates of quantities of interest such as TCR, ECS and aerosol forcing (see Section 7.3).

Improved estimates of ocean heat uptake over the past two decades (Section 7.2) have diminished the role of ocean diffusivity in driving uncertainty in ECS, leaving the main trade-off between posterior ranges in ECS and aerosol radiative forcing (Forest, 2002; Knutti et al., 2002; Frame et al., 2005). The AR5 (Bindoff et al., 2013) assessed a variety of estimates of ECS based on SCMs and found that they were sensitive to the choice of prior parameter distributions and temperature datasets used, particularly for the upper end of the ECS range, though priors can be chosen to minimize the impact on results (e.g., Lewis, 2013). SCMs generally produced estimates of ECS between 1°C and 5°C and ranges of TCR between 0.9°C and 2.6°C. Padilla et al. (2011) use a simple global-average model with two timescales (see Section 7.5.2) to derive observationally-constrained estimate of TCR to be 1.6°C (1.3–2.6°C). Using the same model, Schwartz (2012) finds TCR in the range 0.9–1.9°C while Schwartz (2018) finds an ECS of 1.7°C provides the best fit to the historical surface temperature record while also finding a median aerosol forcing that is smaller than that assessed in Section 7.3. Using an 8-box representation of the atmosphere–ocean–terrestrial system constrained by historical warming, Goodwin (2016) found ECS to be 2.4°C (1.4–4.4°C) while Goodwin (2018) found ECS to be in the range 2–4.3°C when using a prior for ECS based on paleoclimate constraints.

Using a SCM comprised of northern and southern hemispheres and an upwelling-diffusive ocean (Aldrin et al., 2012), with surface temperature and OHC datasets updated to 2014, Skeie et al. (2018) estimate a TCR of 1.4°C (0.9–2.0°C) and infer ECS of 1.9°C (1.2°C–3.1°C). The median estimate of ECS increases to 2.9°C if the model is not constrained by the depth profile of ocean warming, suggesting that the results depend on the details of vertical heat transport in the ocean. Using a similar SCM comprised of land and ocean regions and an upwelling-diffusive ocean, with surface temperature and OHC datasets through 2011, Johansson et al. (2015) infer an ECS of 2.5°C (2.0–3.2°C). The estimate is found to be sensitive to the choice of dataset endpoint and the representation of internal variability meant to capture the El Niño–Southern Oscillation. Differences between these two studies arise, in part, from their different surface temperature and OHC datasets, different radiative forcing uncertainty ranges, different priors for model parameters, and different representations of internal variability. This leads to different estimates of ECS, with the median estimate of Skeie et al. (2018) lying below the 5% to 95% range of ECS from Johansson et al. (2015). Neither of these studies account for the bias introduced by blending SST and near-surface air temperature data or spatial coverage effects (Richardson et al., 2016, 2018a), suggesting that their derived values of TCR and ECS may be biased low. The Skeie et al. (2018) SCM has a constant value of the radiative feedback parameter, and thus should be compared to values of effective ECS inferred from global energy budget constraints (Section 7.5.3.2) that do not account for feedback changes with warming pattern (Skeie et al., 2018). The Johansson et al. (2015) SCM allows distinct radiative feedbacks for land and ocean, contributing to the different results and making it unclear whether it can be compared directly with ECS values from global energy budget constraints.

The median estimates of effective ECS inferred from SCM studies generally lie within the 5% to 95% range of the effective ECS inferred from historical global energy budget constraints (1.9–5.6°C), which is consistent with higher values of ECS when accounting for changes in radiative feedbacks as the spatial pattern of warming evolves in the future (Section 7.5.2.1).

#### *7.5.2.3 Estimates based on climate variability*

Continuous satellite measurements of TOA radiation fluxes, available since 2000, are now long enough to study inter-annual variations in the global energy budget (Figure 7.4). Although the measurements do not have sufficient accuracy to determine the absolute global energy imbalance (Section 7.2.1), they provide accurate estimates of its variations and trends since the year 2002 that agree well with estimates based on observed changes in global OHC (Loeb et al., 2012; Johnson et al., 2016). When combined with global surface temperature observations and simple models of global energy balance, satellite measurements of TOA radiation afford estimates of the radiative feedback parameter associated with recent climate variability (Tsushima and Manabe, 2013; Donohoe et al., 2014a; Dessler and Forster, 2018). These feedback estimates, derived from the regression of TOA radiation on surface temperature variability, imply values of ECS that are broadly consistent with those from other lines of evidence (Forster, 2016; Knutti et al., 2017) (Figure 7.23). A history of regression-based feedbacks and their uncertainties is summarized in the AR5 in Bindoff et al. (2013).

Since the AR5, it has been noted that regression-based feedback estimates depend on whether annual- or monthly-mean data are used and on the choice of lag employed in the regression, complicating their interpretation (Forster, 2016). The observed lead-lag relationship between global TOA radiation and surface temperature, and its dependence on sampling period, is well replicated within unforced simulations of GCMs (Dessler, 2011; Proistosescu et al., 2018). These features arise because the regression between global TOA radiation and surface temperature reflects a blend of different radiative feedback processes associated with several distinct modes of variability acting on different time scales, such as monthly atmospheric variability and inter-annual El Niño–Southern Oscillation (ENSO) variability (Lutsko and Takahashi, 2018; Proistosescu et al., 2018). It thus appears that regression-based feedbacks provide estimates of the radiative feedbacks that are associated with internal climate variability, and thus do not provide a direct estimate of ECS. Moreover, variations in global surface temperature that do not directly affect TOA radiation may lead to a positive bias in regression-based feedback, although this bias appears to be small, particularly when annual-mean data are used (Murphy and Forster, 2010; Spencer and Braswell, 2010, 2011; Proistosescu et al., 2018). When tested within GCMs, regression-based feedbacks have been found to be weakly correlated with values of ECS (Chung et al., 2010), although cloudy-sky TOA radiation fluxes have been found to be moderately correlated with ECS at ENSO timescales within CMIP5 models (Lutsko and Takahashi, 2018).

Finding such correlations within models requires simulations that span multiple centuries, suggesting that the satellite record may not be of sufficient length to produce robust feedback estimates. However, correlations between regression-based feedbacks and long-term feedbacks have been found to be higher when focused on specific processes or regions, such as for cloud or the water vapour feedback (Dessler, 2013; Zhou et al., 2015; Section 7.4.2). Assessing the global radiative feedback in terms of the more stable relationship between tropospheric temperature and TOA radiation offers another potential avenue for constraining ECS, suggesting that CMIP5 GCMs with ECS values between 2.0°C and 3.9°C are within uncertainties based on satellite measurements (Dessler et al., 2018). The so-called 'emergent constraints' on ECS based on climate variability are summarized in Section 7.5.4.1.

A number of studies consider the observed climate response to volcanic eruptions over the 20$^{th}$ century (Knutti et al., 2017). However, the constraint on ECS is weak, particularly at the high end, because the temperature response to short-term forcing depends only weakly on radiative feedbacks and because it can take decades of a sustained forcing before the magnitude of temperature changes reflects differences in ECS across models (Geoffroy et al., 2013b; Merlis et al., 2014). Based on the results of GCM simulations, radiative feedbacks governing the global temperature response to volcanic eruptions are *likely* different than those governing long-term global warming (Merlis et al., 2014; Marvel et al., 2016). It is also a challenge to separate the response to volcanic eruptions from internal climate variability in the years that follow them (Wigley et al., 2005). Estimates based on the response to volcanic eruptions agree with other lines of evidence (Knutti et al., 2017), but *likely* do not constitute a direct constraint on ECS.

#### *7.5.2.4 Assessment of TCR and ECS based on the historical temperature record*

Evidence from the historical temperature record, including estimates using global energy budget changes, simple climate models, and internal climate variability, produce median ECS estimates that range between 3°C and 4°C, but a best estimate value cannot be given owing to a strong dependence on assumptions about how radiative feedbacks will change in the future. However, there is *robust evidence* and *high agreement* leading to *very high confidence* that ECS is *extremely likely* greater than 1.9°C. There is robust evidence and medium agreement that ECS is *likely* greater than 2.6°C (*high confidence)*. Historical global energy budget changes do not provide constraints on the upper bound of ECS, while estimates based on climate variability are generally consistent with an ECS around 3°C but provide *low confidence* in its value owing to limited evidence.

Global energy budget constraints indicate a best estimate (median) value of TCR of 2.0°C (*high confidence*). There is *high confidence* that TCR is *likely* in the range 1.7°C to 2.4°C and *very likely* in the range 1.5°C to 2.9°C. Studies that constrain TCR based on the instrumental temperature record used in conjunction with GCM simulations are summarized in Section 7.5.4.3.

### ***7.5.3 Estimates based on paleoclimates***

Evidence from paleoclimate data can provide information regarding ECS that is complementary to, and largely independent from, estimates based on process-based studies (Section 7.5.1), and the historical record (Section 7.5.2). The strengths of using the paleoclimate record to estimate climate sensitivity include: (1) the estimates are based on observations of a real-world Earth system response to a forcing, in contrast to using estimates from process-based modelling studies or directly from models; (2) the forcings are often relatively large (similar in magnitude to a $CO_2$ doubling or more), in contrast to data from the historical record; (3) the forcing often changes relatively slowly so the system is close to equilibrium; as such, all individual feedback parameters, $\alpha_x$, are included, and complications associated with accounting for ocean heat uptake are reduced or eliminated, in contrast to the historical record. However, there can be relatively large uncertainties on estimates of both the paleo forcing and paleo temperature response. Furthermore, the state-dependence of feedbacks (Section 7.4.4) means that climate sensitivity during Earth's past may not be the same as it is today, which should be accounted for when interpreting paleoclimate estimates of ECS.

The AR5 stated that data and modelling of the Last Glacial Maximum (LGM, 21,000 to 19,000 years ago) indicated that it was *very unlikely* that ECS lays outside the range 1–6°C (Masson-Delmotte et al., 2013). Furthermore, the AR5 reported that climate records of the last 65 million years indicated a climate sensitivity range of 1.1–7.0°C, a range to which they assigned a 95% confidence interval.

Compared with the AR5, there are now improved constraints on estimates of ECS from paleoclimates. The strengthened understanding and improved lines of evidence come in part from the use of high-resolution paleoclimate data across multiple glacial-interglacial cycles, taking into account state-dependence (von der Heydt et al., 2014; Köhler et al., 2015, 2017, 2018; Friedrich et al., 2016; Stap et al., 2019) and better constrained pre-ice core estimates of atmospheric $CO_2$ concentrations (Martínez-Botí et al., 2015; Anagnostou et al., 2016).

Overall, the paleoclimate lines of evidence regarding climate sensitivity can be broadly categorised into two types: direct estimates of radiative forcing and temperature response resulting in an estimate of the feedback parameter, α (Equation 7.1, Box 7.1), and emergent constraints on paleoclimate model simulations resulting in an estimate of ECS. This section focuses on the first type only; the second type (emergent constraints) are discussed in Section 7.5.4.

#### *7.5.3.1 Direct estimates of radiative forcing and temperature response*

In order to provide direct estimates of ECS, evidence from the paleoclimate record can be used to estimate forcing ($\Delta F$) and global mean temperature response ($\Delta T$) in Equation 7.1, Box 7.1, assuming the system is in equilibrium ($\Delta N$=0). However, there are complicating factors with using the paleoclimate record, and these challenges and uncertainties are somewhat specific to the time period being used.

The Last Glacial Maximum (LGM) can provide direct constraints on climate sensitivity (Sherwood et al., submitted; Tierney et al., submitted) (see Table 7.11 for estimates of ECS since AR5). The major forcings and feedback processes that led to the cold climate at that time (e.g., $CO_2$, non-$CO_2$ greenhouse gases, and ice sheets) are relatively well-known (Chapter 5, Section 5.1), orbital forcing relative to preindustrial was negligible, and there are relatively high spatial resolution and well-dated paleoclimate temperature data available for this time period (Chapter 2, Section 2.3.1). Uncertainties in deriving an ECS from the LGM data arise partly from uncertainties in the calibration from the paleoclimate data to local annual mean temperature, and partly from uncertainties in the conversion of the local temperatures to a global annual mean surface air temperature. As a result of these uncertainties, estimates of global mean LGM cooling relative to pre-industrial vary from 3–8°C (Chapter 2, Section 2.3.1). The LGM climate is often assumed to be in full equilibrium with the forcing, such that $\Delta N$ in Equation 7.1, Box 7.1, is zero. A calculation of sensitivity using solely $CO_2$ forcing, and assuming that the LGM ice sheets were in equilibrium with that forcing, would give an Earth System Sensitivity (ESS) rather than an ECS (see Box 7.1). In order to calculate an ECS, which in our definition includes all feedback processes except ice sheets, the approach of Rohling et al. (2012) can be used. This approach introduces an additional forcing term in Equation 7.1, Box 7.1, that quantifies the resulting forcing associated with the ice sheet feedback (primarily an estimate of the radiative forcing associated with the change in surface albedo). However, differences between studies as to which processes are considered as forcings (for example, some studies also include vegetation and/or aerosol feedbacks as forcings), and uncertainties associated with estimating the ice sheet forcing (Stap et al., 2019) and its interactions with other feedback processes, means that estimates are not always directly comparable. Furthermore, the ECS at the LGM may differ from that of today due to state-dependence (see Section 7.4.4). Here, only studies that report values of climate sensitivity that have accounted for the long-term feedbacks associated with ice sheets, and therefore most closely estimate ECS as defined in this chapter, are assessed (see Table 7.11).

Since the AR5, several studies have extended the Rohling et al. (2012) approach (described above for the LGM) to the glacial-interglacial cycles of the last ~1 to 2 million years (von der Heydt et al., 2014; Köhler et al., 2015, 2017, 2018; Friedrich et al., 2016; Stap et al., 2019). Compared to the LGM, uncertainties in the derived ECS from these periods are in general greater, due to greater uncertainty in: global mean temperature (due to fewer individual sites with proxy temperature records), ice sheet forcing (due to a lack of detailed ice sheet reconstructions), and $CO_2$ forcing (for those studies that include the pre-ice core period, where $CO_2$ proxies are more uncertain). Furthermore, accounting for orbital forcing in the traditional framework of climate sensitivity is challenging (Schmidt et al., 2017), due to seasonal and latitudinal components of the forcing that can directly result in relatively large responses in global annual mean temperature (Liu et al., 2014) and ice volume (Abe-Ouchi et al., 2013), and potentially other feedback processes such as methane (Singarayer et al., 2011), despite a close-to-zero orbital forcing in the global annual mean. In addition, for time periods in which the forcing relative to the modern era is small (interglacials), the inferred climate sensitivity has relatively large uncertainties because the temperature signal ($\Delta T$ in Equation 7.1 in Box 7.1) is close to zero.

In the pre-Quaternary (prior to about 2.5 million years ago), the forcings and response are generally of the same sign and similar magnitude as future projections of climate change (Burke et al., 2018). Similar uncertainties as for the LGM apply, but in this case a major uncertainty relates to the forcing, because prior to the ice core record there are only indirect estimates of $CO_2$ concentration. However, advances in pre-ice-core $CO_2$ reconstruction (e.g. Foster and Rae, 2016; Super et al., 2018; Witkowski et al., 2018) mean that the estimates of pre-Quaternary $CO_2$ are narrower than they were in the AR5, and these time periods can now contribute to an assessment of climate sensitivity (see Table 7.11). The mid-Pliocene warm period (MPWP, 3.3 to 3.0 million years ago; Chapter 2, Box 2.1; Box 2.4) has been targeted for constraints on ECS and Earth system sensitivity (Martínez-Botí et al., 2015; Royer, 2016; Sherwood et al., submitted), due to the fact that $CO_2$ concentrations were relatively high at this time (300–450 ppmv, Chapter 5, Section 5.1.3.1) and because the MPWP is sufficiently recent that topography and continental configuration are similar to modern-day. As such, a comparison of the MPWP with modern provides probably the closest natural geological analogue to the definition of climate sensitivity. Furthermore, the temperatures of the MPWP (between 3.0 and 4.5°C above pre-industrial; Chapter 2, Box 2.4) were such that non-linearities in feedbacks (Section 7.4.3) were relatively modest. Within the MPWP, the KM5c interglacial (3.204–3.207 million years ago) has been identified as a particularly useful time period for assessing ECS (Haywood et al., 2013, 2016b) because Earth's orbit during that time was very similar to that of the modern-day.

Further back in time, in the Eocene (about 50 million years ago), uncertainties in forcing and temperature change become larger, but the signals are generally larger too (Anagnostou et al., 2016; Lunt et al., submitted; Shaffer et al., 2016). Caution must be applied when assessing climate sensitivity estimates from these time periods, due to differing continental position and topography/bathymetry (Farnsworth et al., 2019), and due to state-dependence (Section 7.4.4). Furthermore, on even longer timescales of the last 500 million years (Royer, 2016) the temperature and $CO_2$ measurements are generally asynchronous, presenting challenges in using this information for assessments of ECS.

#### *7.5.3.2 Summary*

This section provides an overall assessment of lines of evidence constraining ECS from paleoclimates (summarised in Table 7.11). Although some of the estimates in Table 7.11 are not independent because they use similar proxy records to each other (e.g. Köhler et al., 2015, 2017; Stap et al., 2019; von der Heydt et al., 2014), there are still multiple independent lines of paleoclimate evidence regarding climate sensitivity, from differing past time periods (LGM (Sherwood et al., submitted; Tierney et al., submitted); glacial-interglacial (Friedrich et al., 2016; Köhler et al., 2017), Pliocene (Martínez-Botí et al., 2015; Sherwood et al., submitted) and Eocene (Anagnostou et al., 2016; Shaffer et al., 2016)), with differing proxies for estimating forcing (e.g. $CO_2$ from ice cores or boron isotopes) and response (e.g. temperature from $\delta^{18}O$, Mg/Ca or Antarctic $\delta D$). Furthermore, although different studies have uncertainty estimates that account for differing sources of uncertainty, some studies (Friedrich et al., 2016; Martínez-Botí et al., 2015; Sherwood et al., submitted) do consider many of the uncertainties discussed in Section 7.5.3.1. All the studies based on glacial-interglacial cycles explicitly account for state-dependence of climate sensitivity (Section 7.4.4) by considering only the warm phases of the Pleistocene, although what constitutes a warm phase is defined differently across the studies.

**[START TABLE 7.11 HERE]**

**Table 7.11:** Estimates of ECS derived from paleoclimates; from AR5 (above double lines) and from post-AR5 studies (below double lines). Many studies provide an estimate of ECS that includes only $CO_2$ and the ice sheet feedback as forcings, providing an estimate of $S_{[CO2,\ LI]}$ using the nomenclature of Rohling et al. (2012), which is equivalent to our definition of ECS (Box 7.1). However, some studies provide estimates of other types of sensitivity (column 4). Different studies (column 1) focus on different time periods (column 2) and use a variety of different paleoclimate proxies and models (column 3) to give a best estimate (column 5) and/or a range (column 5). The ranges given account for varying sources of uncertainty (column 6).

| (1) Study (* = contributes to assessed range) | (2) Time period | (3) Proxies/models used for $CO_2$, temperature (T), and global scaling (S). | (4) Climate sensitivity classification according to Rohling et al. (2012). | (5) Published best estimate of ECS [and/or range] | (6) Range accounts for uncertainty in: |
|---|---|---|---|---|---|
| AR5 (Masson-Delmotte et al., 2013) | Last Glacial Maximum (21,000 years ago) | Assessment of multiple lines of evidence | S[a] | [very likely > 1.0 ; very unlikely > 6.0 °C] | Multiple sources of uncertainty |
| AR5 (Masson-Delmotte et al., 2013) | Cenozoic (last 65 million years) | Assessment of multiple lines of evidence | $S_{[CO2,LI]}$ | [95% range: 1.1 – 7.0 °C] | Multiple sources of uncertainty |
| Tierney et al. (submitted) | LGM | $CO_2$: ice core<br>T: multiproxy | $S_{[CO2,LI]}$ | [95% range: 2.6 – 4.5 °C] | Multiple sources of uncertainty |
| Sherwood et al (submitted) | LGM | $CO_2$: ice core<br>T: multiple lines of evidence | $S_{[CO2,\ LI,\ CH4,\ N2O,\ dust]}$ | 3.4°C [17% - 83% likelihood: 2.0 – 6.3 °C] | Multiple sources of uncertainty |
| von der Heydt et al. (2014) | Warm states of glacial-interglacial cycles of last 800 kyrs. | $CO_2$: ice core<br>T: ice core δD, benthic $\delta^{18}O$.<br>S: Annan and Hargreaves, Schneider von Deimling | $S_{[CO2,LI]}$ | 3.5°C [range: 3.1 – 5.4 °C][a] | Range of LGM global mean temperatures used for scaling. |
| Köhler et al. (2015) | Warm states of glacial-interglacial cycles of last 2 Myrs. | $CO_2$: ice core and boron isotopes<br>T: benthic $\delta^{18}O$<br>S: PMIP LGM and PlioMIP MPWP | $S_{[CO2,LI]}$ | 5.7 °C [68% range: 3.7 – 8.1 °C][a] | Temporal variability in records. |
| Köhler et al. (2017) | Warm states of glacial-interglacial cycles of last 2 Myrs. | $CO_2$: boron isotopes<br>T: benthic $\delta^{18}O$<br>S: PMIP LGM and PlioMIP MPWP | $S_{[CO2,LI]}$ | 5.6 °C [$16^{th}$ to $84^{th}$ percentile: 3.6 – 8.1 °C][a] | Temporal variability in records. |
| Köhler et al. (2018) | Warm states of glacial-interglacial cycles of last 800 kyrs, excluding those for which $CO_2$ and T | $CO_2$: ice cores<br>T: alkenone, Mg/Ca, MAT, and faunal SST<br>S: PMIP3 LGM | $S_{[CO2,\ LI]}$ | [range: 3.0 – 5.9 °C][a] | Range of 2 different temperature reconstruction s. |

| | | | | | |
|---|---|---|---|---|---|
| | diverge. | | | | |
| (Stap et al., 2019) | States of glacial-interglacial cycles of last 800 kyrs for which forcing is zero compared with modern, excluding those for which $CO_2$ and T diverge. | $CO_2$: ice cores<br>T: benthic $\delta^{18}O$<br>S: PMIP LGM and PlioMIP MPWP | $S_{[CO2, LI]}$ | [range: 6.1 - 11.0 °C][a] | Range of efficacy of ice sheet forcing |
| Friedrich et al. (2016) | Warm states of glacial-interglacial cycles of last 780 kyrs. | $CO_2$: ice cores<br>T: alkenone, Mg/Ca, MAT, and faunal SST<br>S: PMIP3 LGM. | $S_{[GHG,LI,AE]}$ | 4.9 °C<br>[*Likely* range: 4.3 - 5.4 °C] | Range of LGM global mean temperatures, aerosol forcing. |
| Martínez-Botí et al. (2015) | Pliocene | $CO_2$: boron isotopes<br>T: benthic $\delta^{18}O$ | $S_{[CO2,LI]}$ | 3.7 °C<br>[68% range: 3.0 – 4.4 °C][a] | Pliocene sea level, temporal variability in records. |
| Anagnostou et al. (2016) | Early Eocene | $CO_2$: boron isotopes<br>T: various terrestrial MAT, Mg/Ca, TEX, $\delta^{18}O$ SST. | $S_{[CO2,LI]}$ | [66% range: 2.1 – 4.6 °C] | Calibrations for temperature and $CO_2$. |
| Shaffer et al. (2016) | Pre-PETM | $CO_2$: mineralogical, carbon cycling, and isotope constraints<br>T: various terrestrial MAT, Mg/Ca, TEX, $\delta^{18}O$ SST. | $S_{[GHG,AE,VEG,LI]}$ | [range: 3.3 – 5.6 °C] | Calibration of temperature and $CO_2$. |
| Royer (2016) | Pliocene | $CO_2$: boron isotopes<br>T: benthic $\delta^{18}O$ | $S_{[CO2,LI]}$ | 7.7 °C<br>[range: 3.7 – 12.2 °C] | Temporal variability in records. |
| Sherwood et al. (submitted) | Pliocene | $CO_2$: boron isotopes<br>T: multiple lines of evidence | $S_{[CO2, LI,N2O,CH4,VEG]}$ | 3.7 °C<br>[17% - 83% likelihood: 2.2 – 5.9 °C] | Multiple sources of uncertainty |

**Notes:** Note that S[a] in this table denotes a classification of climate sensitivity following (Rohling et al., 2012).
[(a)] = Best estimate and range calculated from published estimate assuming ERF due to $CO_2$ doubling of 3.7 W $m^{-2}$.

**[END TABLE 7.11 HERE]**

None of the post-AR5 studies in Table 7.13 have an estimated lower range for ECS below 2.0°C per $CO_2$ doubling. Although some of the estimates are based on similar time periods to each other and use the same proxies, there are still multiple independent estimates from multiple time periods over the last 55 million years, using multiple proxies, all of which confirm this lower bound. As such, based solely on the paleoclimate record, it is *very likely* that ECS is greater than 2°C (*high confidence*). At the upper end there is more variation amongst the different studies. In general, it is the studies based on the warm periods of the glacial-interglacial cycles of the last 800,000 years that give the largest values, in particular those based on temperatures derived from estimates of bottom-water temperature from $\delta^{18}O$ (Köhler et al., 2015, 2017; Stap et al., 2019). Given the large uncertainties associated with estimating the efficacy of the ice sheet forcing during these intervals (Stap et al., 2019), and uncertainties associated with extrapolating ECS estimates from cold states to warm states (Köhler et al., 2015, 2017), and with the conversion of a $\delta^{18}O$ temperature to a global mean surface air temperature, there is only *low confidence* in these upper estimates. Estimates of ECS from the warmer Pliocene and Eocene that include a quantitative estimate of the underlying uncertainty distribution (Martínez-Botí et al., 2015; Anagnostou et al., 2016) both indicate likely upper ranges of less than 5°C. As such, and accounting for uncertainties discussed in Section 7.5.4, the state-dependence of feedbacks discussed in Section 7.4.4, and the evidence assessed previously in the AR5, the paleoclimate record on its own indicates that ECS is *likely* less than 5°C. Given that there are fewer studies associated with these past warm time periods, and given the uncertainties associated with quantifying the $CO_2$ forcing, this upper value has only *medium* confidence.

The overall qualitative assessment using paleo constraints alone, of *very likely* greater than 2°C (*high confidence*) and *likely* less than 5°C (*medium confidence*), is for comparison with the assessment of Sherwood et al. (submitted) who, using Bayesian approaches, combined evidence from past cold and warm climates together to give a best estimate of 3.1°C, and likelihoods characterised by 17% and 83% percentiles of 2.1 and 4.7°C respectively. At the upper end, their quantitative approach results in a lower probability of ECS > 5°C than the range assessed here. This may partly be related to the fact that their definition of ECS explicitly excludes positive feedbacks associated with non-$CO_2$ greenhouse gases ($N_2O$ and $CH_4$) and vegetation (Table 7.13, column 4). It is also consistent with the possibility that ice sheet forcing may have relatively low efficacy (Stap et al., 2019), a possibility that was not accounted for in the LGM estimates of Sherwood et al. (submitted).

### *7.5.4 Emergent constraints on ECS*

Global climate models continue to exhibit substantial spread in ECS and TCR (Section 7.5.7) and to leverage this spread in order to narrow estimates of Earth's climate sensitivity, numerous studies have employed methods based on "emergent constraints" (Chapter 1, Section 1.5.4). These methods establish a relationship between an observable and either ECS or TCR based on an ensemble of models, and combine this information with observations to derive probability distributions. Most studies of this kind are relatively recent and have clearly benefitted from the international efforts to coordinate the CMIP multi-model ensembles.

A number of considerations must be taken into account when assessing the diverse literature on ECS and TCR emergent constraints. For instance, it is important to have physical and theoretical basis for the connection between the observable and the target quantity since in model ensembles thousands of statistically significant relationships can be found simply by chance (Caldwell et al., 2014). Also, correctly accounting for uncertainties in both observable, which can be of both instrumental origin and due to natural variability, and statistical relationship, can be challenging, in particular in cases where the latter is not expected to be linear (Annan et al., submitted). Likewise, there is some methodological ambiguity in estimating a GCM's true ECS value. A number of proposed emergent constraints leverage variations in modelled ECS arising from tropical low clouds, which was the dominant source of inter-model spread in the CMIP5 ensemble used in most emergent constraint studies. Since ECS is dependent on the sum of individual feedbacks (Section 7.5.1) these studies implicitly assume that all other feedback processes in models are unbiased and should therefore rather be thought of as constraints on tropical low-cloud feedback (Klein and Hall, 2015; Qu et al., 2018). However, also studies that rely on transient warming may make implicit assumptions that ocean heat uptake, pattern effects and long-term sea ice feedbacks are unbiased. Section 7.5.4.1 goes through the spectrum of emergent constraints, discussing their strengths and limitations in detail.

#### *7.5.4.1 Emergent constraints using global or near-global temperature change*

Perhaps the simplest class of emergent constraints regress past equilibrium paleoclimate temperature change against modelled ECS to obtain a relationship that can be used to translate a past climate change to ECS. The advantage is that these are constraints on the sum of all feedbacks, and furthermore unlike constraints on the instrumental record they are based on climate states that are equilibrated. Thus far these emergent constraints have been limited to the last glacial maximum (LGM) cooling (Hargreaves et al., 2012; Schmidt et al., 2014) and warming in the Pliocene epoch (Hargreaves and Annan, 2016) due to the availability of sufficiently large multi-model ensembles. The paleo-climate emergent constraints are particularly useful in estimating ECS as they utilize past climates in equilibrium but are limited by structural uncertainties in the proxy-based temperature and forcing reconstructions (Section 7.5.4), possible differences in equilibrium patterns between models and the real world, and a small number of model simulations participating which has led to divergent results. For example, Hopcroft and Valdes (2015) repeated the study based on the LGM by Hargreaves et al. (2012) using another model ensemble finding no emergent constraint, whereas studies using multiple available ensembles retain useful constraints (Renoult et al., submitted; Schmidt et al., 2014). Also, the results are somewhat dependent on the applied statistical methods (Hargreaves and Annan, 2016). However, Renoult et al. (submitted) explored this and found 95$^{th}$ percentiles of ECS consistently below 5°C for LGM and Pliocene individually, regardless of statistical approach, and by combining the two estimates the 95$^{th}$ percentile dropped to 3.9°C. The consistence between the cold LGM and warm Pliocene emergent constraint estimates increases confidence.

Various approaches to using warming over the instrumental record have been proposed. These benefit from more accurate data compared with paleoclimates, but suffer from the fact that the climate is not in equilibrium, thereby assuming that GCMs on average accurately depicts the ratio of short term to long term warming. Centennial historical global warming in models exhibit no correlation with ECS (Forster et al., 2013), which is partly due to models being able to compensate e.g. a high sensitivity with strong aerosol cooling (Kiehl, 2007). However, the aerosol cooling increased up until the 1970s when air quality regulations reduced the emissions from Europe and North America whereas other regions saw increases resulting in a subsequently reduced pace of aerosol ERF increase. Energy balance considerations over the 1970-2010 period gave a best estimate ECS of 2.0°C (Bengtsson and Schwartz, 2013), however this estimate did not account for pattern effects. To alleviate this problem an emergent constraint on 1970-2005 global warming was demonstrated to yield a best estimate ECS of 2.83°C (1.72–4.12°C), but if pattern effects are stronger than in GCMs the upper bound could be higher (Jiménez-de-la-Cuesta and Mauritsen, 2019).

A study that developed an emergent constraint based on the response to the Mount Pinatubo 1991 eruption yielded a best estimate of 2.4°C (*likely* range 1.7–4.1°C) (Bender et al., 2010). When accounting for ENSO variations they found a somewhat higher best estimate of 2.7°C, which is in line with results of later studies that suggest ECS inferred from periods with volcanic activity are low-biased due to strong pattern effects (Gregory et al., 2019).

Lagged-correlations present in short term variations in the global mean surface temperature can be linked to climate sensitivity through the fluctuation-dissipation theorem which is derived from a mixed-layer model (Einstein, 1905; Hasselmann, 1976; Schwartz, 2007; Cox et al., 2018a). From this it follows that the memory carried by the heat capacity of the oceans results in low-frequency global temperature variability (red noise) arising from high frequency (white noise) fluctuations in the radiation balance, e.g. caused by weather. Initial attempts to apply the theorem to observations yielded a fairly low median ECS estimate of 1.1°C (Schwartz, 2007), but recently it was proposed by Cox et al. (2018a) to use variations in the historical experiments of the CMIP5 climate models as an emergent constraint giving a median ECS estimate of 2.8 (2.2–3.4°C, 17$^{th}$ to 83$^{rd}$ percentiles). A particular challenge associated with these approaches is to separate short-term from long-term variability, and slightly arbitrary choices regarding the methodology of separating these in the global mean temperature from long-term signals in the historical record, omission of the later strongly forced period, as well as input data choices, can lead to median ECS estimates ranging from 2.5–3.5°C (Brown et al., 2018; Po-Chedley et al., 2018b; Rypdal et al., 2018). Calibrating the emergent constraint using CMIP5 modelled internal variability as measured in pre-industrial control simulations (Po-Chedley et al., 2018b) will inevitably lead to an overestimated ECS due to externally forced short term variability present in the historical record (Cox et al., 2018b). A more problematic issue is raised by Annan et al. (submitted), showing that the upper bound on ECS estimated this way is less certain when considering deep ocean heat uptake and pattern effects.

Short term variations in the Earth's energy budget, observable from satellites, arising from variations in the tropical tropospheric temperature has been linked to ECS through models, either as a range of models consistent with observations (Dessler et al., 2018) or as a formal emergent constraint by deriving further model-based relationships to yield a median of 3.3°C and a *likely* range of 2.4-4.5°C (Dessler and Forster, 2018). There are major challenges associated with short term variability in the energy budget, in particular how it relates to the long-term forced response of clouds (Colman and Hanson, 2017; Lutsko and Takahashi, 2018), and variations in the surface temperature that are not directly affecting the radiation balance lead to an overestimated ECS when using linear regression techniques where it appears as noise in the independent variable (Proistosescu et al., 2018; Gregory et al., 2019). The latter issue is largely overcome when using the tropospheric mean or mid-tropospheric temperature (Trenberth et al., 2015; Dessler et al., 2018).

#### *7.5.4.2 Emergent constraints focussed on cloud feedbacks and present-day climate*

A substantial number of emergent constraint studies focus on observables that are related to tropical low-cloud feedback processes (Volodin, 2008; Sherwood et al., 2014; Zhai et al., 2015; Brient and Schneider, 2016; Brient et al., 2016). These studies yield median ECS estimates of 3.5–4°C and in many cases indicate low likelihoods of values below 3°C. The approach is attractive since most of the spread in the CMIP5 and earlier model ensemble climate sensitivity arises from low cloud feedbacks (Bony and Dufresne, 2005; Wyant et al., 2006; Randall et al., 2007), but nevertheless the approach assumes that all other feedback processes are unbiased (Klein and Hall, 2015; Qu et al., 2018). For example, accounting for a missing representation of the anvil cloud area feedback (section 7.4.2.4) with an assessed mean of –0.2 W $m^{-2}$ °$C^{-1}$, shifts the median estimates range of this class of emergent constraints down to 2.9–3.3°C and accordingly grants substantial probability to values below 3°C. Thus, the subset of emergent constraints that focus on low-level tropical clouds are not inconsistent with other emergent constraints of ECS, but at the same time an inter-dependence with the process-based estimates (Section 7.5.2) is introduced. Related emergent constraints that focus on aspects of the tropical circulation and ECS have led to conflicting results (Su et al., 2014; Tian, 2015; Lipat et al., 2017), probably because these processes are not the dominant factors in causing the inter-model spread (Caldwell et al., 2018).

The fidelity of models in reproducing aspects of temperature variability or the radiation budget has also been proposed as emergent constraints on ECS (Covey et al., 2000; Knutti et al., 2006; Huber et al., 2010; Bender et al., 2012; Brown and Caldeira, 2017; Siler et al., 2018a). Here indices based on spatial or seasonal variability are linked to modelled ECS, and overall the group of emergent constraints yields best estimates of 3.3°C to 3.7°C. Some of these emergent constraints are subject to the same issue as identified for the low-level cloud feedbacks-based constraints of implicitly assuming that processes not probed for are unbiased in the underlying model ensemble and are thus assessed to be less reliable than other emergent constraints. Further, the physical relevance of present-day biases to the sum of climate change feedbacks is in many cases unclear.

#### *7.5.4.3 Assessed ECS and TCR based on emergent constraints*

The available emergent constraint studies have been divided into two classes: those that deal with global or near-global temperature change, and those that focus on other aspects, such as the fidelity of processes related to low-level cloud feedbacks or present-day climate biases. The former class is arguably superior in representing ECS, being a global temperature change, whereas the latter class is perhaps best thought of as constraints showing that low-level cloud feedbacks are positive. The latter is consistent with and confirms process-based estimates of low cloud feedbacks (Section 7.5.1) and is accordingly not taken into account here. A limiting case here is (Dessler and Forster, 2018) which is focused on monthly co-variability in the global radiation budget with mid-tropospheric temperature, at which time scale the surface albedo feedback is unlikely to operate.

In the first group of emergent constraints there is broad agreement on the best estimate of ECS ranging from 2.4–3.3°C. At the lower end nearly all studies find lower bounds ($5^{th}$ percentiles) around 1.5°C, whereas several studies indicate $95^{th}$ percentiles as low as 4°C, with the exception of Cox et al. (2018a), which is deemed to not produce a reliable upper bound estimate (Annan et al., submitted). Considering both classes of studies, none of them yield upper bounds above 5°C. Since several of the emergent constraints can be considered nearly independent one could assume that emergent constraints provide very strong evidence on ECS by combining them. Nevertheless, this is not done here because there are sufficient cross-dependencies, as for instance models are re-used in many of the derived emergent constraints, and furthermore the methodology has not yet reached a sufficient level of maturity since often systematic biases have not been accounted for. Uncertainty is therefore conservatively added to reflect these potential issues. This leads to the assessment that ECS inferred from emergent constraints is *very likely* 1.5 to 5°C with *high confidence*.

Emergent constraints on TCR with a focus on the instrumental temperature record, though less abundant, have also been proposed. In the simplest form Gillett et al. (2012) regressed the response of one model to individual historical forcing components to obtain a tight range, but later when an ensemble of models was used the range was widened (Gillett et al., 2013), and updated by (Schurer et al., 2018). A related data-assimilation based approach that accounted also for uncertainty in response patterns gave similar results (Ribes et al., submitted), but is dependent on the choice of prior ensemble distribution (CMIP5 or CMIP6). Another study used the response to the Pinatubo volcanic eruption to obtain a similar range (Bender et al., 2010). A tighter range, notably at the lower end, was found in an emergent constraint focusing on the post-1970s warming exploiting the lower spread in aerosol forcing change over this period (Jiménez-de-la-Cuesta and Mauritsen, 2019). Their estimate was 1.67 °C (1.17–2.16 °C). Two studies tested this idea: Tokarska et al. (submitted) found similar best estimates and showed that the results were independent of whether CMIP5, CMIP6 or both model ensembles were used, whereas Nijsse et al. (submitted) found slightly larger best estimates but broader uncertainty and a small sensitivity to choice of ensemble. Combining the eight studies gives a best estimate of 1.7°C and a *very likely* range of TCR of 1.2–2.2°C with *high confidence*.

**[START TABLE 7.12 HERE]**

**Table 7.12:** Collection of emergent constraint studies estimating ECS. Studies marked with a star (*) are of the type that rely on global or near-global temperature change.

| Study | Emergent constraint description | Published best estimate and uncertainty (°C) | Uncertainty estimate: |
|---|---|---|---|
| (Bender et al., 2010)* | Pinatubo integrated forcing normalized by CMIP3 models own forcing versus temperature change regressed against ECS. | 2.4 [1.7-4.1] | 5% to 95% |
| (Brient et al., 2016) | Shallowness of low-level tropical clouds | [2.4-4.6] | Model range consistent with observations |
| (Brient and Schneider, 2016) | Cloud fraction variability versus SST anomalies | 4 [2.3-5.0] | 5% to 95% |
| (Brown and Caldeira, 2017) | Aspects of the representation of the present-day top-of-atmosphere radiation balance | 3.7 [3.0-4.2] | 25% to 75% |
| (Cox et al., 2018a)* | Persistence of variability in global mean temperature in instrumental record. Upper bound not deemed reliable | 2.8 [2.2-3.4] | 17% to 83% |
| (Dessler and Forster, 2018)* | Emergent constraint on TOA radiation variations linked to mid-tropospheric temperature | 3.3 [2.4-4.5] | 17% to 83% |
| (Hargreaves et al., 2012)* | Last Glacial Maximum tropical SSTs | 2.5 [1.3-4.2] | 5% to 95% |
| (Hargreaves and Annan, 2016)* | Pliocene tropical SSTs | [1.9-3.7] | 5% to 95% |
| (Huber et al., 2014) | Aspects of the representation of the present-day top-of-atmosphere radiation balance | 3.4 [2.9-4.0] | 17% to 83% |
| (Jiménez-de-la-Cuesta and Mauritsen, 2019)* | Post-1970s global warming | 2.83 [1.72-4.12] | 5% to 95% |
| (Knutti et al., 2006) | Regional seasonal cycle in land surface temperature | 3.3 [2.2-4.4] | 5% to 95% |
| (Renoult et al., submitted)* | Combined Last Glacial Maximum and Pliocene tropical SSTs | 2.6 [1.1-3.9] | 5% to 95% |

| | | | |
|---|---|---|---|
| (Sherwood et al., 2014) | Indicators of tropical convective mixing | Around 4 [ >3] | Model range consistent with observations |
| (Siler et al., 2018a) | Spatial distribution of planetary albedo (shortwave reflectivity) | 3.68 [2.38-4.98] | 5% to 95% |
| (Volodin, 2008) | Variations in tropical cloud fraction and humidity | 3.6 [3.3-3.9] | 5% to 95% |
| (Zhai et al., 2015) | Subsidence regime tropical low-level cloud variations | 3.9 [3.45-4.35] | 17% to 83% |

**[END TABLE 7.12 HERE]**

### *7.5.5 Combined assessment of ECS and TCR*

Substantial quantitative progress has been made in interpreting evidence of Earth's climate sensitivity since the previous report, through innovation, scrutiny, theoretical advances and a rapidly evolving data base from current, recent and past climates. Noteworthy is that ECS as derived directly from climate models is not taken into account, and that focus is on the process-understanding, instrumental record warming, paleo-climate records and emergent constraints in the assessment. GCMs remain essential tools throughout establishing these lines of evidence.

A key advance over the AR5 assessment is that across the lines of evidence there is broad agreement that the central estimates of ECS are close to, or not inconsistent with, 3°C. This advance is foremost following an improved quantification of Earth's imbalance, instrumental record global temperature change, and the strength of anthropogenic forcing. Further advances include increased understanding of how pattern-effects influence ECS inferred from historical warming (Sections 7.4.3 and 7.5.3), improved quantification of paleo climate change from proxy evidence and a deepened understanding of how feedback mechanisms depend on the climate mean state such that they increase ECS in warmer climates (Sections 7.4.4 and 7.5.4), and also an improved quantification of cloud feedback mechanisms (Sections 7.4.2 and 7.5.2). The assessed statements are summarized in Table 7.13 for ECS and Table 7.14 for TCR.

Whereas the AR5 chose to embrace the bulk of the evidence available at the time in the then assessed ECS *likely* range of 1.5–4.5°C (Collins et al., 2013a), the broader evidence-base presented here and the general agreement among the lines of evidence encourages the combination of the evidence to yield a tighter range. This can be done formally using Bayesian statistics (Annan and Hargreaves, 2006; Stevens et al., 2016), though such a process is fairly complex and involves formulating subjective priors (Sherwood et al., submitted). However, it is straightforward to understand that if two lines of independent evidence each give a low probability of an outcome being true, e.g. that ECS is less than 1.5°C, then the combined probability that ECS is less than 1.5°C is true is lower than that of either line of evidence. On the contrary, if one line of evidence is unable to rule out an outcome, but another is able to assign a low probability, then there is a low probability that the outcome is true. This logic applies also when there are slight dependencies between the lines of evidence, for instance between historical evidence and those emergent constraints that use historical warming. Even in this case the combined constraint will be closer to the tighter of the individual lines of evidence.

In the process of providing a combined and self-consistent ECS assessment of all the evidence, these notions were kept in mind. Furthermore, a 0.5°C precision was chosen, as in earlier reports. Starting with the *very likely* lower bound, there is broad support for a value of 2.0°C, including the instrumental record warming (Table 7.12). At the upper bound emergent constraints give 5.0°C, bearing in mind that those emergent constraints that are assessed more reliable all were below this value. Support for an upper bound of this magnitude is furthermore provided by both process-understanding and paleoclimates. The *likely* range must necessarily reside inside the very likely range and is therefore supported by evidence pertaining to both the *likely* and *very likely* ranges. In summary, based on multiple lines of evidence the best estimate of ECS is close to 3°C, it is *likely* 2.5 to 4°C and *very likely* 2 to 5°C. It is *virtually certain* that ECS is larger than 1.5°C. The assessed ranges are all assigned *high confidence* due to the agreement among the different lines of evidence. It remains challenging to rule out low-probability but high impact upper end ECS, which is indicated by the notable asymmetry of the assessed ranges.

It is worthwhile contemplating whether the consensus of the median ECS estimates is an expression of groupthink, i.e. whether evidence supporting a certain ECS that has long been the consensus (Charney et al., 1979) is being sub-consciously favoured over other values. In this regard it is worth remembering the many failed attempts to challenge an ECS of this magnitude, starting as early as (Ångström, 1900) criticizing the results of (Arrhenius, 1896) arguing that the atmosphere was already saturated in infrared absorption such that adding more $CO_2$ would not lead to warming. The assertion of Ångström was understood half a century later to be incorrect. History has seen a multitude of challenges, e.g. Lindzen et al., (2001); Schwartz, (2007); Svensmark (1998), mostly implying lower ECS than the range assessed as *very likely* here. However, there are also examples of the opposite such as very large ECS based on the Pleistocene records (Snyder, 2016), as disproven by Schmidt et al. (2017), or suggestions that global climate instabilities may occur in the near future (Steffen et al., 2018; Schneider et al., 2019). There is, however, no evidence for such instabilities in the paleo record temperatures of more than 10°C above present (Zachos et al., 2008). Looking back, the resulting debates have led to a deeper understanding, strengthened the consensus, and have been scientifically valuable.

.

In the climate sciences, there are often good reasons to consider representing deep uncertainty, or what is sometimes referred to as unknown unknowns. This is natural in a field that considers a system that is both complex and at the same time challenging to observe. For instance, since emergent constraints represent a relatively new line of evidence, important feedback mechanisms may be biased in the process-level understanding, pattern effects and aerosol cooling may be large and paleo evidence inherently works with indirect and incomplete evidence of past climate states, there certainly can be valid reasons to add uncertainty to the ranges assessed on individual lines of evidence. This has indeed been done throughout Sections 7.5.1–7.5.4. However, in light of the century-long history of research testing, scrutinizing and criticizing the understanding broadly represented in this chapter, and since it is improbable that all lines of evidence represented here are collectively biased, it is not considered necessary to add deep uncertainty to the combined assessment of ECS.

**[START TABLE 7.13 HERE]**

**Table 7.13:** Summary of ECS assessment

| ECS | Central value | *Likely* range | *Very likely* range | *Extremely likely* |
|---|---|---|---|---|
| Process understanding (7.5.1) | 3.2°C | 2.4–4.6°C | 2.0–6.4°C | |
| Warming over instrumental record (7.5.2) | 3–4°C | > 2.6°C | | > 1.9°C |
| Paleoclimates (7.5.3) | | < 5.0°C | > 2.0°C | |
| Emergent constraints (7.5.4) | 2.4–3.3°C | | 1.5–5.0°C | |
| Combined assessment | 3°C | 2.5–4.0°C | 2.0–5.0°C | |

**[END TABLE 7.13 HERE]**

The evidence for TCR is less abundant than for ECS, and for natural reasons it focuses on the instrumental temperature record (Sections 7.5.3 and 7.5.6) and process understanding (Section 7.5.2), though substantially strengthened over the situation in AR5 which assessed a *likely* range of 1.0–2.5°C. TCR and ECS are not unrelated, though, and in any case TCR is less than ECS (see section introduction). Furthermore, unlike ECS, estimates of TCR from the historical record are not strongly influenced by externally forced surface temperature pattern effects since both historical transient warming and TCR are affected in the same way by this phenomenon (Section 7.4.3). As a result, uncertainty is substantially lower than in the AR5 and 0.1°C precision is therefore used here. Also, given the interdependencies of the lines of evidence, a conservative approach is adopted, in particular at the 95th percentile, to combining them as reflected in the assessment.

Based on process understanding, warming over the instrumental record and emergent constraints the best estimate TCR is 1.8°C, it is *likely* 1.4–2.2°C and *very likely* 1.2–2.4°C. The assessed ranges are all assigned *high confidence* due to the high level of agreement among the lines of evidence.

**[START TABLE 7.14 HERE]**

**Table 7.14:** Summary of TCR assessment

| TCR | Central value | *Likely* range | *Very likely* range |
|---|---|---|---|
| Process understanding (7.5.1) | 1.9°C | 1.5–2.4 °C | 1.2–2.7 °C |
| Warming over instrumental record (7.5.2) | 2.0 °C | 1.7–2.4 °C | 1.5–2.9 °C |
| Emergent constraints (7.5.4) | 1.7 °C | | 1.2–2.2 °C |
| Combined assessment | 1.8 °C | 1.4–2.2 °C | 1.2–2.4 °C |

**[END TABLE 7.14 HERE]**

### *7.5.6 Considerations on the ECS and TCR in global climate models and their role in the assessment*

Coupled climate models, such as those participating in CMIP, have long played a central role in assessments of ECS and TCR. In reports up until and including the AR4, raw climate sensitivities from GCMs were the primary line of evidence but in the AR5, historical warming and paleoclimates provided useful additional lines of evidence. As new lines of evidence have evolved, in the AR6 various numerical models are used where they are considered accurate evidence, or in some cases the only available source of information, and thereby support all four lines of evidence (Sections 7.5.1-7.5.4). However, the AR6 differs from previous reports in not directly using climate model values of ECS and TCR in the assessed ranges of climate sensitivity (Section 7.5.5). The purpose of this section is to explain why this approach has been taken and to provide a perspective on the interpretation of the climate sensitivities exhibited in CMIP6 models.

The ECS of a model is the net result of the model's effective radiative forcing from a doubling of $CO_2$ and the sum of the individual feedback parameters. It is well known that among models most of the spread arises from cloud feedbacks, and is dominated by spread in the response of low-level clouds (Bony and Dufresne, 2005; Zelinka et al., 2020). Since these clouds are small-scale and shallow, the representation of such clouds is foremost controlled by the parameterizations in the models. It is sometimes assumed that improving such parameterizations will eventually lead to convergence in model response and therefore a decrease in the model spread of ECS.

Nevertheless, over decades of model development there have not been signs of convergence of ECS in models. In fact, the overall spread in CMIP6 (total range of 1.8–5.5 °C) is larger than that in CMIP5 (total range of 2.0–4.7 °C) (Flynn and Mauritsen, submitted). ECS and TCR values are given for CMIP5 and CMIP6 models respectively in Appendix Table 7.A.2. Flynn and Mauritsen (submitted) show that the ECS in CMIP6 (3.7°C mean) is significantly higher than that in CMIP5 (3.2°C mean). The TCR in CMIP6 is also higher (2.0°C mean) than in CMIP5 (1.8°C mean). The upward shift does not apply to all models, but a substantial subset of models have seen an increase in ECS between the two model generations. The increased ECS values are likely due to shortwave cloud feedbacks (Flynn and Mauritsen, submitted) and it appears that extra-tropical clouds with mixed ice- and liquid phases are central to the behaviour (Zelinka et al., 2020), probably borne out of a recent focus on biases in these types of clouds (McCoy et al., 2016; Tan et al., 2016). These biases have recently been reduced in many models, guided by laboratory experiments, field measurements and satellite observations (Lohmann and Neubauer, 2018; Bodas-Salcedo et al., 2019;

Gettelman et al., 2019). However, this and other known model biases are already factored into the process-level assessment of cloud feedback (Section 7.4.2.4), and furthermore the emergent constraints used here focus on net feedback and so are presumably insensitive to common model biases (Section 7.5.4). The higher ECS and TCR values in CMIP6 lead to stronger projected GSAT warming in many CMIP6 models compared to CMIP5 and also compared to what might be expected from the assessed ranges of ECS, TCR and ERF (Chapter 4 Box 4.1, Forster et al., 2019).

Models frequently share code components and in some cases entire sub-model systems are shared and slightly modified. Therefore, models cannot be considered independent developments, but rather families of models with interdependencies (Knutti et al., 2013). It is therefore difficult to interpret the collection of models (Knutti, 2010), and it cannot be ruled out that there are common limitations and therefore systematic biases to model ensembles that are reflected in the distribution of ECS as derived from them.

It is generally challenging to determine which information enters the formulation and development of parameterizations used in GCMs. Although GCMs are typically well-documented, in ways that increasingly also include information on decisions regarding tuning, the full history of development decisions could involve both process-understanding and sometimes also other information such as historical warming. As outlier or poorly performing models emerge from the development process, they can become re-tuned, reconfigured or discarded and so might not see publication (Hourdin et al., 2017). Modelling groups might for example have perceived a model's ECS as unrealistic, have specific difficulties to reproduce the instrumental record warming (Mauritsen and Roeckner, submitted), or a model might be prone to entering run-away warming or cooling for routinely applied forcings. In the process of correcting for such issues, modelling groups may, whether intentional or not, modify the emerging ECS. Efforts to explain inter-model differences in ECS would greatly benefit from increased transparency about the tuning choices made by individual modelling groups.

It is well-understood that the multi-model ensemble mean provides an inaccurate estimate of an underlying best estimate ECS coming out of climate modelling in general. The primary source of inter-model spread is variations in the net feedback parameter, which is inversely proportional to ECS. Thus, a positive error in the feedback parameter has a larger positive impact on ECS than an equally large negative error, leading to a distribution with a mean that is skewed towards higher values which results in the mean usually being higher than the median (Roe and Baker, 2007). Even under ideal conditions, though, one would expect distributions of ECS from GCMs to be wider than that of the assessment building on multiple lines of evidence presented in Section 7.5.5. Climate models are built principally on process-understanding, but far from all information on relevant processes can adequately be represented in sub-grid-scale parameterizations. Examples are information on low-cloud feedback estimates from large-eddy simulations or variations in cloudiness observed from satellites that are not easily translated into parameterizations that are used in GCMs. Likewise, the assessment (Section 7.5.5) includes information from historical warming, paleoclimates and emergent constraints which is not routinely used to inform GCM evaluation and development. Therefore, the distributions of ECS and TCR from a model ensemble alone would be expected to have more spread than the assessed ECS range, which is based on several lines of somewhat independent evidence.

A final and important consideration is that information from climate models is indirectly incorporated in several lines of evidence used in the assessment: GCMs are partly used to estimate historical- and paleoclimate ERFs (Sections 7.5.2 and 7.5.3); how feedbacks change with SST patterns (Section 7.4.4.3); and to establish emergent constraints on ECS (Section 7.5.4). They are also used as primary evidence in the process understanding of the temperature and water vapour feedbacks, whereas other lines of evidence are used exclusively for cloud feedbacks, where the climate model evidence is weak (Section 7.4.2.5).

Because climate models both inform and are informed by the four lines of evidence for ECS considered in this chapter, the approach taken here is to not use the raw model ECS range as an independent line of evidence for ECS. Furthermore, it is problematic and not obviously constructive to provide weights for, or rule out, individual CMIP6 model ensemble members based solely on their ECS and TCR values. Rather these models must be tested in a like-with-like way against multiple lines of observational evidence. Therefore, in this report projections are produced using climate model emulators that are constrained by the assessments of ECS, TCR and ERF, and CMIP6 model simulations are provided for context. In reports up to and including the AR5, GCM values of ECS did not fully span the assessed *very likely* range of ECS, raising the possibility that past multi-model ensembles underestimated the uncertainty in climate change projections that existed at the times of those reports (e.g., Knutti, 2010). However, due to an increase in the modelled ECS spread and a decrease in the assessed ECS spread based on improved knowledge in multiple lines of evidence, the CMIP6 ensemble spans the *very likely* range of ECS (2–5°C) assessed in Section 7.5.5. Models outside of this range are useful for establishing emergent constraints on ECS and TCR and provide useful examples of "tail risk" (Sutton, 2018), producing dynamically consistent realisations of future climate change to inform impacts studies and risk assessments.

In summary, the distribution of CMIP6 models have higher average ECS and TCR values than the CMIP5 generation of models and the assessed ranges of ECS and TCR within the Chapter (*high confidence*). Their high ECS and TCR values can be traced to extra-tropical cloud feedbacks (*medium confidence*). The ranges of ECS and TCR from these models are not considered as robust samples of possible values and the models are not considered as a separate line of evidence for ECS and TCR. Solely based on their ECS or TCR values an individual CMIP6 model cannot be ruled out as implausible. The high climate sensitivity leads to generally higher projected warming in CMIP6 compared to CMIP5 (Chapter 4, Box 4.1).

### *7.5.7 Critical processes determining global temperature response to forcing*

The magnitude of long-term global temperature change in response to a given radiative forcing can be understood in terms of the factors contributing to the global atmospheric energy budget: the effective radiative forcing (ERF), which drives the global energy imbalance and associated surface temperature change; the TOA radiative response to this surface warming, as set by radiative feedbacks which govern the rate and magnitude of warming through radiative energy loss to space; and global ocean heat uptake, which offsets some of the transient surface warming.

A variety of studies evaluate the contribution that each of these factors makes to surface warming within coupled GCM simulations by diagnosing so-called 'warming contributions' for each process (Dufresne and Bony, 2008; Crook et al., 2011; Feldl and Roe, 2013; Vial et al., 2013; Pithan and Mauritsen, 2014; Goosse et al., 2018). By construction, the individual warming contributions sum to the total global surface warming (Figure 7.24b). For long-term warming in response to $CO_2$ forcing in CMIP5 models, the energy added to the climate system by radiative feedbacks is larger than the ERF of $CO_2$ (Figure 7.24a), implying that feedbacks more than double the magnitude of global warming (Figure 7.24b). Radiative kernel methods (see Section 7.4.1) can be used to decompose the net energy input from radiative feedbacks into its components. The water-vapour, cloud and surface-albedo feedbacks enhance global warming, while the lapse-rate feedback reduces global warming. Ocean heat uptake reduces the rate of global surface warming by sequestering heat at depth away from the ocean surface. Section 7.4.4.1 shows the warming contributions from these factors at the regional scale.

**[START FIGURE 7.24 HERE]**

**Figure 7.24:** Contributions of effective radiative forcing, ocean heat uptake and radiative feedbacks to global atmospheric energy input and near-surface air temperature change at year 100 of abrupt $CO_2$ quadrupling simulations of CMIP5 models. (a) The energy flux to the global atmosphere associated with the effective $CO_2$ forcing, global ocean heat uptake, Planck response, and radiative feedbacks, which together sum to zero; inset shows energy input from individual feedbacks, summing to the total feedback energy input. (b) Contributions to net global warming calculated by dividing the energy inputs by the global Planck response (3.2 W $m^{-2}$°$C^{-1}$), with the contributions from radiative forcing, ocean heat uptake, and radiative feedbacks summing to the value of net warming; inset shows warming contributions associated with individual feedbacks, summing to the total feedback contribution. Uncertainties show 25% and 75% percentiles across models. Feedbacks are calculated using radiative kernels (Shell et al., 2008) and the analysis is based on that of Goosse et al. (2018).

**[END FIGURE 7.24 HERE]**

Differences in projected transient global surface warming across GCMs are dominated by differences in their radiative feedbacks, while differences in ocean heat uptake and radiative forcing play secondary roles (Figure 7.24b) (Vial et al., 2013). The uncertainty in projected global surface temperature change associated with inter-model differences in cloud feedbacks is the largest source of uncertainty in CMIP5 and CMIP6 models (Figure 7.24b), just as they were for CMIP3 models (Dufresne and Bony, 2008). Extending this energy budget analysis to equilibrium surface warming suggests that about 70% of the inter-model differences in ECS arises from uncertainty in cloud feedbacks, with the largest contribution to that spread coming from shortwave low-cloud feedbacks (Vial et al., 2013; Zelinka et al., 2020).

An important limitation of understanding global warming and its uncertainty based on energy budget diagnostics within the coupled climate system is that different feedbacks interact (Section 7.4.2). For example, water-vapour and lapse-rate feedbacks are correlated (Held and Soden, 2006) owing to their joint dependence on the spatial pattern of warming (Po-Chedley et al., 2018a). Moreover, feedbacks are not independent of ocean heat uptake because the spatial pattern of heat uptake influences the SST pattern on which global feedbacks depend (Section 7.4.4.3). However, alternative decompositions of warming contributions that better account for correlations between feedbacks produce similar results (Caldwell et al., 2016). The key role of radiative feedbacks in governing the magnitude of global warming is also supported by the high correlation between radiative feedbacks (or ECS) and transient warming within GCMs (Grose et al., 2018).

Another approach to evaluating the roles of forcing, feedbacks and ocean heat uptake in projected warming employs idealized energy balance models that emulate the response of GCMs, and which preserve the interactions between system components. One such emulator, used in Section 7.5.1.2, resolves the heat capacity of both the surface components of the climate system and the deep ocean (Held et al., 2010; Geoffroy et al., 2013a, 2013b; Kostov et al., 2014; Armour, 2017). Using this emulator, Geoffroy et al. (2012) find that: under an idealized 1% per year increase in atmospheric $CO_2$, radiative feedbacks constitute the greatest source of uncertainty (about 60% of variance) in transient warming beyond several decades; ERF uncertainty plays a secondary but important role in warming uncertainty (about 20% of variance) that diminishes beyond several decades; and ocean heat uptake processes play a minor role in warming uncertainty (less than 10% of variance) at all timescales.

More computationally intensive approaches evaluate how the climate response depends on perturbations to key parameter or structural choices within GCMs. Large ‘perturbed physics ensembles’ wherein a range of parameters associated with cloud physics are explored within atmospheric GCMs reliably produces a wide range of ECS due to changes in cloud feedbacks, but often produce unrealistic climate states (Joshi et al., 2010). Rowlands et al. (2012) performed a multi-thousand member perturbed-physics ensemble of coupled GCMs by perturbing model parameters associated with radiative forcing, cloud feedbacks, and ocean vertical diffusivity (an important parameter for ocean heat uptake). After constraining the ensemble to have a reasonable climatology and to match the observed historical warming, they found a wide range of projected warming by the year 2050 under the SRES A1B scenario (1.4–3°C relative to the 1961–1990 average) that is dominated by differences in radiative feedbacks. By swapping out different versions of the atmospheric or oceanic components in a coupled GCM, Winton et al. (2013) found that TCR and ECS depend on which atmospheric component was used (using two versions with different atmospheric physics), but that only TCR is sensitive to which oceanic component of the model was used (using two versions with different vertical coordinate systems, among other differences); TCR and ECS changed by 0.4°C and 1.4°C, respectively, when the atmospheric model component was changed, while TCR and ECS changed by 0.3°C and < 0.05°C, respectively, when the oceanic model component was changed. However, Krasting et al. (2018) found that perturbing ocean vertical diffusivity over a wide range within the GFDL climate model changed ECS by about 0.6°C, with this difference linked to different radiative feedbacks associated with different spatial patterns of sea-surface warming (see Section 7.4.4.3).

There is *robust evidence* and *high agreement* across a diverse range of modelling approaches and thus *high confidence* that radiative feedbacks are the largest source of uncertainty in projected global warming out to 2100 under increasing or stable emissions scenarios, and that cloud feedbacks in particular are the dominant source of that uncertainty. Uncertainty in radiative forcing plays an important but generally secondary role. Uncertainty in global ocean heat uptake plays a relatively minor role in global warming uncertainty, but ocean dynamics could play an important role on long timescales through the impact on sea-surface warming patterns which in turn project onto radiative feedbacks (Section 7.4.4.3).

The spread in historical surface warming across CMIP5 GCMs shows a weak correlation with inter-model differences in radiative feedback or ocean heat uptake processes but a high correlation with inter-model differences in radiative forcing owing to large variations in aerosol forcing across models (Forster et al., 2013). Likewise, the spread in projected 21st century warming across GCMs depends strongly on emissions scenario (Hawkins and Sutton, 2012; Chapter 4, Section 4.1). Strong emissions reductions would remove aerosol forcing and this could dominate the uncertainty in near-term warming projections (Armour and Roe, 2011; Mauritsen and Pincus, 2017; Schwartz, 2018; Smith et al., 2019). On post 2100 timescales carbon cycle uncertainty such as the uncertainty permafrost thawing becomes increasingly important, especially under high emission scenarios (Chapter 5, Section 5.3)

In summary, cloud feedbacks are the dominant source of uncertainty in this century's transient global warming under increasing or stable emissions scenarios (*high confidence*), whereas uncertainty is dominated by aerosol ERF in strong mitigation scenarios. Global ocean heat uptake is a relatively minor source of uncertainty in long-term surface warming. Carbon cycle feedbacks provide an increasing fraction of uncertainty on longer timescales (*high confidence*).

## 7.6 Metrics to evaluate emissions

### *7.6.1 Introduction to metrics and innovations since IPCC AR5*

Emission metrics attempt to summarise the contribution emissions of different gases and forcing agents make to some aspect of climate change (see Section 7.1). They do this by comparing the relative effects of emissions of different gases on a key climate variable (such as global-mean surface temperature), according to some formula. These formulae are assessed and updated in Section 7.6.2. Chapter 8 of the AR5 (Myhre et al., 2013b) comprehensively discussed different physical metrics so this section focuses on key updates since that report.

The cause-effect chain from linking emissions to climate forcing, climate response, and climate impacts is displayed in Figure 7.2 (Fuglestvedt et al., 2003). Each step in the causal chain requires an inference or modelling framework that maps causes to effects. Emission metrics map from emissions of some species to somewhere further down the chain, radiative forcing (e.g., Global Warming Potential or GWP) or temperature (e.g., Global Temperature-change Potential or GTP) or impacts (such as sea-level rise or socioeconomic impacts). While variables lower in the chain have greater policy relevance, they are also subject to greater uncertainty because each step in the chain includes more modelling systems, each of which brings its own uncertainty. Work since the AR5 on multi-metric approaches has continued to consider how to address fundamental differences between the climate response of short- and long-lived gases. These aspects and related developments are assessed in Section 7.6.3. Box 7.3 assesses physical aspects of emission metric use within climate policy.

### *7.6.2 Physical description of metrics*

This section discusses metrics that relate emissions to physical changes in the climate system. One such metric, the 100-year GWP, has extensively been employed in climate policy to put emissions of different greenhouse gases on the same scale. Yet other physical metrics exist, which are discussed in this section.

Emission metrics are a simple way of representing the magnitude of the effect a unit mass emission of a species has on a key measure of climate change. Examples of these key measures are the radiative forcing, global average surface temperature, global precipitation and global sea level (Myhre et al., 2013b; Sterner et al., 2014; Shine et al., 2015). When used to represent a climate impact, the metrics are referred to as absolute metrics and expressed in units of impact per kg (e.g. Absolute Global Warming Potential, AGWP or Absolute Global Temperature-change Potential, AGTP). More commonly, these are compared with a standard species (almost always $CO_2$ in kg($CO_2$), although $CH_4$ has been used (Cherubini and Tanaka, 2016; Tanaka et al., 2019)) to give a dimensionless factor (written as e.g. GWP or GTP). The unit mass is usually taken as a 1 kg instantaneous "pulse" (Myhre et al., 2013b), but can refer to a "step" in emission rate of 1 kg $yr^{-1}$.

Since the AR5, understanding of the radiative effects of emitted species has continued to evolve and these changes are assessed in Section 7.6.2.1. Since the AR5, metrics relating to precipitation and sea level have been quantified (Section 7.6.2.2). Understanding how the carbon-cycle response to temperature affects emission metrics has improved sufficiently that the carbon cycle response to temperature is more fully included in the emission metrics presented here (Section 7.6.2.3). There have also been developments in understanding how to compare short-lived forcers (SLCFs) to $CO_2$ (Section 7.6.2.4).

#### *7.6.2.1 Radiative properties*

Since the AR5, there have been advances in the understanding of the radiative properties of various species (see Sections 7.3.1, 7.3.2, 7.3.3), and hence their effective radiative efficiencies (ERFs per unit change in concentration). For $CO_2$, $CH_4$ and $N_2O$, better accounting of the spectral properties of these gases has led to re-evaluation of their SARF radiative efficiencies and their dependence on the background gas concentrations (Etminan et al., 2016). For $CO_2$ and $CH_4$ the tropospheric rapid adjustments are assessed to be non-zero. The re-evaluated effective radiative efficiency for $CO_2$ will affect all emission metrics relative to $CO_2$.

The effective radiative efficiencies (including rapid adjustments from 7.3.2) for 2018 background concentrations for $CO_2$, $CH_4$ and $N_2O$ are assessed to be $1.35\times10^{-5}$, $3.78\times10^{-4}$ and $2.91\times10^{-3}$ W m$^{-2}$ ppb$^{-1}$ respectively (see Table 7.15 for uncertainties), compared to the AR5 assessment of $1.37\times10^{-5}$, $3.63\times10^{-4}$ and $3.00\times10^{-3}$ W m$^{-2}$ ppb$^{-1}$. For $CO_2$, increases due to the re-evaluated radiative properties and rapid adjustments balance the decreases due to the increasing background concentrations. For $CH_4$ increases due to the re-evaluated radiative properties and rapid adjustments more than offset the decreases due to the increasing background concentration. For $N_2O$ both the re-evaluated radiative properties and the increasing background concentration act to decrease the effective radiative efficiency.

#### *7.6.2.2 Physical quantities*

Emission metrics can be derived from simple climate models (Myhre et al., 2013b; Tanaka et al., 2013; Gasser et al., 2017), but more fundamentally can be built up from analytical expressions. All the emission metrics are related to the ERF $\Delta F_X$ following a change in emission, which can be considered an Absolute Global Forcing Potential AGFP (similar to the Instantaneous Climate Impact of Edwards and Trancik (2014)). A GTP can be derived by convolving the radiative forcing with a temperature response function $R_{\mathrm{T}}(t)$ (which is the temperature at time $t$ following a unit pulse forcing at $t$=0) derived from a two-layer energy balance model (Myhre et al., 2013b). A metric for precipitation, absolute global precipitation potential AGPP (Shine et al., 2015) combines both the AGTP and the AGFP. Sterner et al. (2014) used an upwelling-diffusion energy balance model to derive the thermosteric component of sea level rise (SLR) as a SLR response function to radiative forcing or as a response function to global surface temperature $R_{\mathrm{SLR}}(t)$. The equations relating these metrics are given in the Appendix 7.A.1.

Each step from radiative forcing to temperature to SLR includes longer timescales and therefore prolongs further the contribution of short-lived species. Thus, SLCFs become relatively more important for SLR than for temperature or radiative forcing. SLR depends on the integrals of radiative imbalance and temperature rise (Section 7.2), whereas the impacts of pulse emissions of SLCF on temperature decay over time so become less important.

For species perturbations that lead to a strong regional variation in forcing pattern, the regional response can be different to the global mean. Regional equivalents to the global metrics can be derived by replacing the global temperature response function with a regional response matrix relating forcing changes in one region to temperature changes in another (Collins et al., 2013b; Myhre et al., 2013b; Aamaas et al., 2017; Lund et al., 2017).

It has been shown that for the physical variables discussed, metrics can be constructed that are linear functions of radiative forcing. Similar metrics could be devised for other climate variables provided they can be related by response functions to radiative forcing or temperature change. Global damage potentials that are more closely aligned with the economic and social costs of pollutant emissions have been designed (e.g. Sarofim and Giordano, 2018). These are related to powers of the surface temperature change so, being non-linear, they depend on the size of the emission and rely on the assumption of an ideal climate state from which the perturbations are measured.

The physical metrics described above are instantaneous or endpoint values defined at a time $H$ after the emission. These are appropriate when the goal is to not exceed a fixed target such as a temperature limit or sea-level rise limit at a specific time. The above metrics can also be integrated from the time of emission, so the impact is in degree-years for temperature or metre-years for sea-level rise. These reflect that the impact depends on how long the change occurs for, not just how large the change is. The integrated version of a metric iAGxx is given by $\mathrm{iAGxx}(H) = \int_0^H \mathrm{AGxx}(\mathrm{t})\, dt$. The metrics relative to $CO_2$ iGxx are given by the ratio of the iAGxx for the species to that for $CO_2$, e.g. the commonly used GWP metric is the integrated form of the radiative forcing metric, (GWP=iGFP). Integrated metrics include the effects of a pulse emission from the shortest timescales up to the time horizon, whereas endpoint metrics only include the effects that persist out to the time horizon. Because the largest impacts of SLCFs occur shortly after their emission and decline towards the end of the time period, SLCFs have relatively higher integrated metrics than endpoint metrics (Levasseur et al., 2016).

#### *7.6.2.3 Carbon cycle responses and other indirect contributions*

The AR5 included a contribution to emission metrics from carbon-cycle responses, representing an adjustment to conventional approaches, which consider more of the causal chain displayed in Figure 7.2. Any agent that warms the surface perturbs the terrestrial and oceanic carbon fluxes, typically causing a net flux of $CO_2$ into the atmosphere and hence further warming. This aspect is already included in the carbon cycle models that are used to generate the radiative effects of a pulse of $CO_2$, but was neglected for non-$CO_2$ species in the conventional metrics so this introduces an inconsistency and bias in the metric values (Gillett and Matthews, 2010), and also affects calculations of allowable carbon budget (MacDougall et al., 2015; Tokarska et al., 2018). A simplistic account of the carbon cycle response was tentatively included in the AR5 based on a single study (Collins et al., 2013b). Since the AR5 this understanding has been revised (Gasser et al., 2017; Sterner and Johansson, 2017) using simple parameterised carbon cycle models to derive the time evolution of $CO_2$ following a unit pulse emission $CO_2$ flux perturbation following a unit temperature pulse. In Collins et al. (2013a) the response to a temperature pulse was assumed to be simply a $CO_2$ emission pulse, whereas the newer studies include a more complete functional form accounting for subsequent re-uptake after the removal of the temperature increase. This has the effect of reducing the carbon-cycle responses compared to the AR5, particularly at large time horizons. The increase in any metric due to the carbon cycle response can be derived from the convolution of the temperature response with the $CO_2$ flux response to temperature and the equivalent metric for $CO_2$ (equation 7.SM.5 in the Appendix 7.A7.SM.3).

Including the carbon cycle response for non-$CO_2$ treats $CO_2$ and non-$CO_2$ species consistently. There is *high confidence* in the methodology for calculating the carbon cycle response, therefore we assess that its inclusion more accurately represents the climate effects of non-$CO_2$ species. The OSCAR 2.2 model used in Gasser et al. (2017) is based on parameters derived from CMIP5 models. The climate-carbon feedback magnitude is therefore similar to the CMIP5 multi-model mean (Lade et al., 2018). The magnitude of the carbon cycle response contributions to the emission metrics in Sterner and Johansson (2017) is about twice that of Gasser et al (2017). There is *medium confidence* in the magnitude of the carbon cycle response, but as values have only been calculated in two simple parameterised carbon cycle models the error is assessed to be ±100%. Carbon cycle responses are included in all the metrics presented in Table 7.15 and Table 7.A.1 using the response function of Gasser et al. (2017) (their Appendix C3).

Emissions of non-$CO_2$ species can affect the carbon cycle in other ways: emissions of ozone precursors can reduce the carbon uptake by plants (Collins et al., 2013b); emissions of reactive nitrogen species can fertilize plants and hence increase the carbon uptake (Zaehle et al., 2015); and emissions of aerosols or their precursors can affect the utilisation of light by plants (Cohan et al., 2002; Mercado et al., 2009). There is *robust evidence* that these processes occur and are important, but *insufficient evidence* to determine the magnitude of their contributions to emission metrics. Ideally emission metrics should include all indirect effects to be consistent, but limits to our knowledge restrict how much can be included in practice.

Emissions of chemically reactive species can lead to indirect contributions from chemical production or destruction of other greenhouse gases (Chapter 6). For methane, the AR5 assessed that the contributions from effects on ozone and stratospheric water vapour add 50% and 15% respectively. Hence methane emission metrics are scaled by 1.65. Methane can also affect the oxidation pathways of aerosol formation (O'Connor et al., submitted; Shindell et al., 2009) but the available literature is insufficient to make a robust assessment of this. Hydrocarbon and molecular hydrogen oxidation also leads to tropospheric ozone production and change in methane lifetime (Collins et al., 2002; Hodnebrog et al., 2018). For reactive species the emission metrics can depend on from where the emissions occur, and the season of emission (Aamaas et al., 2016; Lund et al., 2017; Persad and Caldeira, 2018). The AR5 included a contribution to the emission metrics for ozone-depleting substances (ODSs) from the loss of stratospheric ozone. These contributions are unchanged for the AR6.

Oxidation of methane and other hydrocarbons leads ultimately to the production of $CO_2$ (Boucher et al., 2009). For hydrocarbons from fossil sources this will lead to new $CO_2$ in the atmosphere in which case a value 2.75 can be added to all the methane metrics (1 kg of methane generates 2.75 kg $CO_2$). The $CO_2$ can already be included in carbon emission totals (Muñoz and Schmidt, 2016) so care needs to be taken when applying the fossil correction.

Note that although there has been greater understanding since the AR5 of the carbon cycle responses to $CO_2$ emissions (Chapter 5, Section 5.5), there has been no new quantification of the response of the carbon-cycle to an instantaneous pulse of $CO_2$ emission since Joos et al. (2013).

#### *7.6.2.4 Comparing short-lived climate forcers (SLCFs) with CO2*

For climate forcers with lifetimes of over a century, the standard emission metrics such as GTP vary only slowly with time horizon, so an approximate $CO_2$ equivalence can readily be determined. In contrast, emission metrics for SLCFs with lifetimes less than twenty years are very sensitive to the choice of time horizon. GTPs compare the response to a pulse emission of a species with a pulse emission for $CO_2$. GTPs for 50-year and 100-year time horizons for methane are estimated as 14.6 to 6.7, respectively (Table 7.15 and Table 7.A.1). The time dependence occurs because the temperature changes following a pulse of $CO_2$ (in kg) emissions are roughly constant in time (the principle behind TCRE, Section 7.1, Figure 7.25b) whereas the temperature change following a pulse of SLCF emission declines due to the decrease in SLCF concentration. In contrast a step change in SLCF emissions (in kg $yr^{-1}$) that is maintained indefinitely causes a change in temperature (Figure 7.25a) that after a few decades increases only slowly and hence has a more similar behaviour to a pulse of $CO_2$ (Smith et al., 2012; Allen et al., 2016, 2018b). This is because a step change in SLCF emissions will lead to a constant change in SLCF abundance (for timescales a few times longer than the lifetime of the SLCF).

Metrics for step emission changes (e.g. $\mathrm{AGTP}_X^S$ ) can be derived by integrating the more standard pulse emission changes up to the time horizon. The response to a step emission change is therefore equivalent to the integrated response to a pulse emission ($\mathrm{AGTP}_X^S = \mathrm{iAGTP}_X$).

The ratio of the step metric for SLCFs with the pulse metric for $CO_2$ leads to a combined-GTP CGTP = $\mathrm{AGTP}_X^S/\mathrm{AGTP}_{\mathrm{CO2}}$(Collins et al., 2019). This has the units of years (the standard GTP is dimensionless). This combined-GTP shows less variation with time than the standard GTP (comparing Figure 7.25c with d) and provides a scaling for comparing a change in emission rate (in kg $yr^{-1}$) of SLCF with a pulse emission or change in cumulative $CO_2$ emissions (in kg). Allen et al. (2016) show that an approximation (which they designate GWP* in Allen et al. (2018b)) to the combined-GTP metric can be derived by simply scaling the GWP by the time horizon $H$. While the combined-GTP can be calculated for any species, it is most stable (i.e., least dependent on time horizon) for short-lived species, i.e. those with lifetimes less than the around half the time horizon of the metric (Collins et al., 2019). The time variance of metrics can be accounted for exactly using the $CO_2$ forcing equivalent metric (Wigley, 1998; Allen et al., 2018b). Such metrics provide a way of effectively comparing emissions of short- and long-lived greenhouse gases on globally averaged surface temperature. However, they could be challenging to implement into single-basket policy approaches as discussed in Section 7.6.3.

**[START FIGURE 7.25 HERE]**

**Figure 7.25:** Emission metrics for two SLCFs: HFC-32 and $CH_4$, (lifetimes of 5.2 and 12.4) years. The temperature response function comes from (Geoffroy et al., 2013a) which has a climate sensitivity of 0.885 °C (W $m^{-2})^{-1}$. Values for non-$CO_2$ species include the carbon cycle response (Section 7.6.2.3). Results for HFC-32 have been divided by 100 to show on the same scale. (a) temperature response to a step change in SLCF emission. (b) temperature response to a pulse $CO_2$ emission. (c) conventional GTP metrics (pulse vs pulse). (d) combined-GTP metric (step vs pulse).

**[END FIGURE 7.25 HERE]**

*7.6.2.5 Emission metrics by species*

Emission metrics for selected species are presented in Table 7.15, with further species presented in the Appendix Table 7.A.2. The evolution of the $CO_2$ concentrations is as in the AR5 (Myhre et al., 2013b), the perturbation lifetimes for $CH_4$ and $N_2O$ are from Chapter 6, Section 6.2.2. The lifetimes and radiative efficiencies for halogenated species are taken from WMO (2018), except that the lifetime of SF6 is updated to 1258 years following recent evaluation (Kovács et al., 2017; Ray et al., 2017). GWP(100) values are included for consistency with previous reports, but this does not imply a recommendation of their use. GWP(500) values are included as a measure of the long-term energy budget changes. Combined metrics (CGTPs) comparing step changes in SLCFs with pulse emissions of $CO_2$ are presented for shorter-lived species. The decrease in radiative efficiency of $CO_2$ at higher concentrations is compensated by the increase due to rapid adjustments (Section 7.6.2.1) leading to no change in the denominator for the emission metrics. The emission metrics for methane have increased due to the increase in the methane radiative efficiency (Etminan et al., 2016) although much of this is offset by the rapid adjustment (Section 7.3.2) leading to an increase of 4% in the methane radiative efficiency. The radiative efficiency of $N_2O$ is decreased following Etminan et al. (2016) leading to lower emission metrics compared to the AR5. The responses of the carbon cycle to temperature changes caused by non-$CO_2$ species are assessed to contribute less with the process-based analysis than in the AR5 so that for all halogenated species the emission metrics are slightly smaller than in AR5.

**[START TABLE 7.15 HERE]**

**Table 7.15:** Emission metrics for selected species: Global Warming Potential (GWP), Global Temperature-change Potential (GTP). All values include carbon cycle responses as described in Section 7.6.2.3. Combined-GTPs (CGTPs) are shown for species with a lifetime less than 20 years (see Section 7.6.2.4). The radiative efficiencies are as described in Section 7.3.2 and include rapid adjustments where assessed to be non-zero in Section 7.6.2.1. The climate response function is from Geoffroy et al. (2013). Chemical

effects of $CH_4$ and $N_2O$ are included as in AR5. Contributions from stratospheric ozone depletion are not included.

| Species | Lifetime (years) | Radiative efficiency ($Wm^{-2}$ $ppb^{-1}$) | GWP (100) | GWP (500) | GTP (50) | GTP (100) | CGTP(50) (years) | CGTP(100) (years) |
|---|---|---|---|---|---|---|---|---|
| $CO_2$ | Multiple | $1.36\times10^{-5}$ (1.12 to 1.57) $\times10^{-5}$ | 1 | 1 | 1 | 1 | | |
| $CH_4$ | 12.4 | $3.78\times10^{-4}$ (3.14 to 4.42) $\times10^{-4}$ | 32 | 9.1 | 14.6 | 6.7 | 3100 | 3800 |
| $N_2O$ | 109 | $2.91\times10^{-3}$ (2.62 to 3.2) $\times10^{-3}$ | 260 | 124 | 280 | 220 | | |
| HFC-32 | 5.4 | 0.11 (0.9 to 1.2) | 750 | 210 | 200 | 150 | 76000 | 90000 |
| HFC-134a | 14 | 0.16 (0.14 to 0.18) | 1450 | 410 | 750 | 310 | 140000 | 170000 |
| CFC-11 | 52 | 0.26 (0.23 to 0.29) | 5500 | 1900 | 5700 | 3200 | | |
| $CF_4$ | 50000 | 0.09 (0.08 to 0.10) | 670 | 9600 | 6900 | 8100 | | |

**[END TABLE 7.15 HERE]**

**[START BOX 7.3 HERE]**

**BOX 7.3: Which metric should I use?**

IPCC does not recommend an emission metric because the appropriateness of the choice depends on the purposes for which gases or forcing agents are being compared. Emission metrics can facilitate the comparison of effects of emissions of forcing agents in support of policy goals. They cannot define policy goals or targets but can support the evaluation and implementation of choices within multi-component policies (e.g., they can help prioritise which emissions to abate). Consideration of what is an appropriate emission metric involves both scientific aspects and value related choices. It will depend on which aspects of climate change are most important to a particular application or stakeholder, and different climate policy goals may lead to different conclusions about what is the most suitable emission metric.

When emissions are rising, the most commonly used emission metrics can reflect the warming contributions made by forcing agents. However, some emission metrics can fail to give the correct sign of contributions to warming under scenarios in which emissions decline, due to limitations in their ability to represent the combined effects of pollutants with different lifetimes. Emission metrics which preserve the distinction between long-lived and short-lived climate forcings can better capture the net contribution to warming, at the expense of more complexity (see Section 7.6.3).

Environmental science and related disciplines often draw the distinction between stock pollution, in which pollutants and damages are essentially cumulative, and flow pollution, in which pollutants are short-lived and damages follow the transients of the pollutant flow. This distinction is highly relevant to climate change: some forcing agents ($CO_2$, $N_2O$ and other GHGs with centennial or longer residence times) behave as stock pollutants, while methane, HCFC-22, and other short-lived climate forcers (see Chapter 6) behave much more as flow pollutants. Therefore, the impacts of $CO_2$, $N_2O$ and other long-lived gases are usually functions of cumulative emissions. This is why there is a near-linear relationship between GSAT change and cumulative $CO_2$ emissions for instance (see Chapter 5, Section 5.5). The climate effects of short-lived climate forcers and methane are generally not cumulative: warming from these species more closely follows the time evolution of emissions themselves (Wigley, 1998; Bowerman et al., 2013).

The distinction is particularly important when emissions of different species are declining, as in mitigation scenarios: as emissions decline to zero, the climate effects of $CO_2$ asymptote to a value implied by the total amount of anthropogenic $CO_2$ emissions emitted since the pre-industrial period, while the climate effects of methane decline to zero if methane emissions decline to zero. Many of the most commonly discussed metrics like GWP and fixed time-horizon GTP, fail to capture this difference. GTP(100) is designed to accurately simulate the warming associated with a single pulse emission of methane in 100 years' time. Pulse emission metrics like GWP and GTP compare the effects of pulse emissions of different gases from a single year, and cannot easily replicate the warming influence of emissions time-series.

Whether or not the distinction between stock pollution and flow pollution is relevant within a pollution management regime depends upon the goals of the regime and the considerations (including value judgements) underpinning it. Pulse emission metrics are well-aligned with some uses of metrics. For instance, if a policy-maker is concerned primarily with operating in a cost-benefit framework, then GWP might be an appropriate choice, given its alignment with global damage potential (Tol et al., 2012; Myhre et al., 2013b). If, on the other hand, a policy-maker is working in a cost-effectiveness framework and is concerned with the effects of a single year's emissions, then GTP might be an appropriate choice because of its alignment with global cost potential. Furthermore, metrics that relate emissions to more general “damage” or “cost” changes may be useful when analysing the economics of mitigation pathways (Johansson, 2012; Sarofim and Giordano, 2018). These are also discussed in AR5 WG III Chapter 2 (Kunreuther et al., 2014).

However, the distinction is important in the calculation of the warming implied by a given emissions portfolio (Allen et al., 2018a; Box 2, 2018b). It is not possible to unambiguously calculate the future warming trajectory, or compliance with a temperature target, implied by an emissions portfolio containing substantial short-lived climate pollutants and long-lived gases when emission trajectories of different gases are not reported individually, unless the emission metric itself preserves the distinction between stock and flow pollution (Fuglestvedt et al., 2018; Tanaka and O'Neill, 2018; Cain et al., 2019). The scale of this effect varies with the emissions scenario. For scenarios aiming at limiting warming to 1.5°C above pre-industrial levels, the ambiguity regarding global warming arising from reporting emissions using GWP(100) is 0.17°C, or around a third of the remaining warming budget (Denison et al., 2019).

No single emission metric captures the relative roles of different emissions across all potential climate change variables of interest. No matter how it is done, the way emissions of different gases are compared is value-laden. Value judgements are implied or embedded in several choices which underpin emission metrics, such as the variable against which the comparison between forcing agents is made, as well as the associated functional form, and timescales across which comparisons are made. If the purposes of the comparison are to compare the effects of a species emitted in a single year, then pulse emissions may be advisable. If the purposes of the comparison are to consider the effects of a scenario of emissions over time, then a metric which captures the fundamental differences between LLCFs and SLCFs may be a better choice.

While emission metrics can provide a useful way of comparing the effects of different gases, they are not always required if gases or forcing agents are treated separately (Harvey, 2000, p. 294-295). Although there is a history of using single-basket approaches, supported by emission metrics, in climate policy via the Kyoto Protocol, multi-basket approaches also have many precedents in environmental management, including the Montreal Protocol.

**[END BOX 7.3 HERE]**

### *7.6.3 Applications of emission metrics*

#### *7.6.3.1 Interpretations of emission metrics*

The timescale associated with the comparison is an important choice. Partly to show the effects of timescale on emission metrics, previous IPCC reports reported 20-year, 100-year, and 500-year values for GWP (Forster et al., 2007), and 20-year and 100-year values for GWP and GTP, with and without the inclusion of carbon cycle feedbacks (Myhre et al., 2013b). Time-varying emission metrics also involve the choice of a time-horizon, though in these cases the time horizon is usually derived from a climate target (most commonly a temperature target). Time horizon is a choice that, ideally, ought to reflect decision-makers' needs, depending on the specific application and the appropriate weighting of different aspects of climate change for a given situation. The most common approach uses a 100-year timescale, but this is not universally appropriate (Myhre et al., 2013b; Chapter 8, Section 8.7). In fact, Houghton et al. (1990), specifically noted that 20, 100, and 500-year timescales they discussed were merely 'candidates for discussion [that] should not be considered as having any special significance'.

One important interpretation of the role of emission metrics lies in seeking cost-effective reductions of GHG emissions: by comparing the discounted marginal abatement costs and damages associated with one unit emission of a greenhouse gas against a unit emission of another greenhouse gas (Manne and Richels, 2001).

Another key role for emission metrics which has received attention since the AR5 is their use in life cycle analysis (LCA). Life cycle analysis approaches seek 'to quantitatively assess the environmental impacts of goods and processes from "cradle to grave."' (Hellweg and Milà i Canals, 2014). Several papers have reviewed the issue of metric choice for LCA, noting that analysts should be aware of the challenges and value judgements inherent in attempting to aggregate the effects of forcing agents with different timescales onto a common scale (e.g. Mallapragada and Mignone (2017)) and recommend aligning metric choice with policy goals as well as testing sensitivities of results to metric choice (Cherubini et al., 2016). Furthermore, LCA analyses which are sensitive to choice of emission metric should be accompanied by careful communication of the reasons for the sensitivity (Levasseur et al., 2016).

One prominent use of emission metrics is for comparison of efforts against climate change targets. The most commonly discussed climate change targets are the global mean temperature targets established by Article 2 of the Paris Agreement. The Paris Agreement has no other numerical targets, but it does have two other implicit science targets in Article 4 which articulated in support of the temperature goals in Article 2: these are an early peaking target, and the aim to "achieve a balance between anthropogenic emissions by sources and removals by sinks of greenhouse gases in the second half of this century". The Article 4 goals also contain important constraints regarding international equity, sustainable development, and poverty reduction. The relationship between metric choice, interpretation of the Paris Agreement, and the meaning of "net zero" emissions is an active area of research. New research shows that there are several possible interpretations of the Article 4 goals, and these, along with metric choice, have implications for the timing and meaning of "net zero" emissions (Fuglestvedt et al., 2018). Significantly, net zero greenhouse gas emissions are not necessarily required to remain below 1.5°C or 2°C, and that a target of net zero $CO_2$ emissions, rather than net zero $CO_2$-equivalent, is more likely to be consistent with the Paris temperature targets without overshoot (Tanaka and O'Neill, 2018). Limiting on-going temperature increase at any level requires net zero $CO_2$ emissions, and while stabilising, reducing or eliminating short-lived forcing agents can play a secondary role, the main requirement for stabilisation of temperature is to limit cumulative emissions of $CO_2$. This is true whether or not the aims of the Paris Agreement are met (Allen et al., 2009; Pierrehumbert, 2014; Tanaka and O'Neill, 2018).

Awareness of the consequences of metric choice has continued to develop, as have critiques of the default use of GWP(100). Many of these critiques apply to any emission metrics which do not draw the distinction between short- and long-lived forcing agents. It is clear that the traditional emission metric, GWP(100), gives the wrong sign of the contribution of SLCFs, including methane, to warming when emissions are declining, and this is a general property of pulse metrics. Multi-metric techniques or newer emission metrics which compare a step-change in short-lived forcing with a pulse of long-lived gases more accurately correlate with the temperature effects of emissions scenarios. In response to the fact that the GWP does not, under most scenarios, do a good job of representing the temperature effects of emissions, Myhre et al. (2013) observed that 'the name "Global Warming Potential" may be somewhat misleading, and "relative cumulative forcing index" would be more appropriate.'

Since the AR5, alternative methods for comparing the warming effects of greenhouse gases have been developed. Some of these give a more faithful simulation of the temperature effects of a portfolio of gases, especially under mitigation scenarios, such as those implied by successful attainment of the temperature goals set out in Article 2 of the Paris Agreement. As was pointed out in the AR5, ultimately, it is a matter for policy-makers to decide which emission metric to use, because they have the social licence to make the normative judgements regarding timescale, variable choice and functional form that underpin emission metric choice. Physical science can only form a subset of the inputs to those choices.

In summary, specifying short and long-lived greenhouse gases separately in emission scenarios generally improves the quantification of surface warming, compared to approaches that aggregate greenhouse gases using $CO_2$ equivalent emission metrics (*high confidence*)**.** New metrics comparing pulse emissions of long-lived greenhouse gases with sustained emission changes in short-lived gases can lead to more equivalence in surface temperature response (*high confidence*). Global Warming Potentials and Global Temperature change Potentials are larger compared to the AR5, due to the methodological change of accounting for carbon-cycle responses (*high confidence*).

## Frequently Asked Questions

### FAQ 7.1: Clouds – What have we learned since IPCC AR5?

*One of the biggest challenges for climate science has been predicting how clouds will change in a warming world and whether those changes will amplify or partially offset the warming caused by increasing concentrations of greenhouse gases and other human activities. Scientists have made significant progress over the past few years and can now conclude that it is very likely that clouds will change in ways that will amplify, rather than offset, global warming in the future.*

On average, clouds cover two thirds of the Earth's surface. They generally form when water vapour present in updrafts condenses around small particles known as aerosols (such as salt, dust, or smoke) to form water droplets. We see the reflections from these little droplets of water as clouds. When the droplets grow large enough or freeze to make ice crystals, they can fall to the surface as rain, snow, or other forms of precipitation. Clouds therefore play a key role in Earth's water cycle.

Clouds also play a critical role in Earth's energy budget—the balance between the amount of incoming solar radiation and the energy radiated back to space. Clouds reflect some of the incoming radiation, which has a cooling effect. But water vapour is a greenhouse gas, so clouds also trap (i.e., absorb and re-emit) some outgoing radiation, resulting in a warming effect. Over the last four decades, measurements from satellites and aircraft-based instruments have shown that high clouds tend to trap more radiation than they reflect, while low clouds reflect more than they trap. On average, the reflection of incoming radiation currently wins out, so that, overall, clouds have a cooling influence on the climate.

Scientists have known for decades that the radiative properties of clouds (that is, how much energy they reflect and trap) depend on the abundance of the aerosol particles upon which cloud droplets and ice crystals form. The atmosphere now contains more aerosols than in the pre-industrial period, and this increase has had two important effects on clouds. First, they are now more reflective because cloud droplets have become more numerous and smaller. There is broad agreement that the resulting cooling effect has counteracted a considerable portion of the warming caused by increases in greenhouse gas concentrations over the last century, though exact quantification has been a challenge. Second, it has also been proposed that the shift towards more numerous but smaller droplets acts to extend cloud lifetimes by delaying rain formation, although this effect remains controversial. While quantification is still a challenge, recent evidence suggests that increases in the lifetime and/or number of cloud droplets have amplified the cooling influence of clouds.

Clouds are also expected to change as the planet continues to warm as a result of increasing concentrations of greenhouse gases, and these changes could act to amplify or offset some of the warming by altering the radiative fluxes, the effect called the cloud feedback. Exactly how various cloud properties, including the amount, altitude, and reflectivity of clouds will change in a warmer world, and how these changes will affect the energy budget of the Earth (FAQ7.1, Figure 1) constitutes the largest component of uncertainty in projections of global warming for a given emission pathway. The key question is whether cloud changes will have a net warming effect, amplifying the greenhouse warming (a positive cloud feedback) or a net cooling effect, offsetting some of the warming (a negative cloud feedback). In particular, the response of subtropical marine boundary layer clouds to surface warming has been the largest source of uncertainty in assessing the net cloud feedback.

The problem stems from the fact that clouds can change in many ways and their processes occur on much smaller scales than can be represented by global climate models. The latest generation of climate models do a better job of modelling cloud behaviour thanks to increases in spatial resolution and more sophisticated representations of processes that occur at even finer scales (Section 1.4.3). Yet, this improvement is incremental, and the representation of cloud processes even in the latest climate models remains a challenge.

Since the AR5, observational and modelling efforts have been further developed and integrated to build a more complete understanding of cloud processes. For example, the interaction between aerosols and clouds are now routinely included in model simulations. Furthermore, extensive analyses of the latest climate model simulations have enabled scientists to propose a number of emergent constraints on the magnitude of the overall cloud feedback. Combined with a coordinated set of fine-scale process modelling for stratocumulus and trade cumulus clouds, these studies have revealed how low clouds over the subtropical oceans are reduced and thinned in response to surface warming, providing evidence that this cloud feedback is positive (Section 7.4.2.4). Namely, the low-cloud feedback is no longer the biggest issue of climate feedback assessments. While uncertainties in feedbacks associated with other cloud regimes, such as tropical anvil clouds and extratropical mixed-phase clouds, have emerged instead, this reflects the fact that new problems arise when old problems are resolved as our understanding of clouds and their feedbacks improves.

In summary, cloud processes are now better understood and can be simulated more accurately, enabling us to narrow the range of possible cloud feedback and responses to aerosol changes. Also, the magnitude of the cooling effect of clouds enhanced by emissions of polluting gases such as sulphur dioxide and particles can now be better understood (Section 7.3).

**[START FIGURE FAQ7.1, Figure 1 HERE]**

**FAQ7.1, Figure 1:** Schematic illustration of different types of clouds in the present climate (grey) and their response to surface warming (red). From the left to right: high-level thick clouds, low-level thin clouds, and mixed-phase clouds over the high latitudes. Arrows represent radiative fluxes. Physical processes associated with the changes in cloud property and the resultant sign of the feedback are described at the bottom.

**[END FIGURE FAQ7.1, Figure 1 HERE]**

**FAQ 7.2: How does climate sensitivity relate to climate projections and the latest climate models?**

*For a given future emission scenario, climate models give a range of future global surface temperature projections. This range is strongly related to the models' equilibrium climate sensitivity, where high climate sensitivity models give stronger future warming. The new models have higher average climate sensitivity than the best estimate of climate sensitivity from other lines of evidence. This leads to end of century temperature changes up to 2°C stronger in some simulations of the latest generation of models, compared to the earlier model generation. The high warming levels in these high sensitivity models are useful as representations of high risk, low-probability futures.*

The equilibrium climate sensitivity is an idealised measure of climate response, defined as the equilibrium globally averaged surface temperature change caused by a doubling of carbon dioxide from its preindustrial concentration (Box 7.1). Even though an idealised quantity, it is found to strongly relate to future projections of surface temperature within climate models. Around 90% of the globally averaged projected surface temperature range in 2100 can be explained by the model range of equilibrium climate sensitivity (Section 7.5.7).

Equilibrium climate sensitivity estimates have been persistently uncertain across previous IPCC reports. A primary cause of this uncertainty is the way clouds respond to warming, which is difficult to estimate (see FAQ 7.1). This report makes considerable progress in quantifying equilibrium climate sensitivity by examining four different lines of evidence. 1) Process based evidence quantifies how the underlying physical processes such as how changes in clouds, water vapour, and surface reflectance contribute to climate sensitivity. 2) Historical evidence infers climate sensitivity from observed changes in the global energy budget and surface temperature over recent centuries. 3) Paleoclimate evidence infers climate sensitivity from what we know about ancient climates, particularly from the height of the last ice age (20,000 years ago). 4) Emergent constraint evidence looks at how a factor in climate models that can be observed (such as the warming rate in recent decades) varies with equilibrium climate sensitivity, and then uses observations of this factor to bound plausible sensitivity estimates (Section 7.5.1).

Simulations from previous and current generations of climate models are employed to some extent in each of these four lines of evidence but the climate models are not considered as a line of evidence in their own right. This is because they are already used as part of the other lines of evidence, and treating them again as a separate line would be circular. Additionally, it is possible to construct a physically plausible model with a wide variety of climate sensitivity values and the available model range is derived from a limited sample that is not expected to be statistically representative of the real-world value (Section 7.5.6).

Chapter 7 uses the four lines of evidence to make a probabilistic estimate of equilibrium climate sensitivity, giving a best estimate of 3°C. Although this sensitivity is *likely* between 2.5 °C and 4 °C, there remains a 5% chance it could be larger than 5°C and a 5% chance it could be smaller than 2°C. Nevertheless, this reduction of uncertainty represents considerable progress over the broader range of possible values given in the AR5.

The equilibrium climate sensitivity across the latest climate models is, on average, both higher than that in the previous generation of models and higher than the best estimate of climate sensitivity estimated within Chapter 7 (see Figure FAQ7.2, Figure 1 left panel). Around 20% of the models have an equilibrium climate sensitivity larger than 5°C. Their high climate sensitivity values can be traced to cloud feedbacks. Yet, some of the cloud feedback changes are directly traceable to improved representations of clouds as compared to satellite observations. Furthermore, increased understanding of how climate feedbacks may change over time implies that models could display medium sensitivity in historical simulations, but transition to a higher sensitivity state under sustained warming. Therefore, an individual model cannot be ruled out as implausible solely based on their high equilibrium climate sensitivity. The overall shift towards higher sensitivity leads to generally higher projected warming compared to earlier generations of models, by up to 2°C in some simulations (see Figure FAQ7.2, Figure 1 right panel). Individual high sensitivity models provide important insights into low-probability, high-risk futures, but the best estimate of future warming does not rely on the latest models alone but factors in other lines of evidence that are included in the assessed climate sensitivity range. (Chapter 4, Box 4.1).

**[START FIGURE FAQ 7.2, Figure 1 HERE]**

**FAQ7.2, Figure 1:** The left panel shows equilibrium climate sensitivity estimated from the latest generation of climate models (CMIP6), the previous generation used in the AR5 assessment report (CMIP5) and the assessed *very likely* range from Chapter 7. The right panel shows the projected temperature change for a future high emission scenario over 2090-2100 for CMIP6, CMIP5, and from the assessed range in Chapter 4.

**[END FIGURE FAQ 7.2, Figure 1 HERE]**

## References


Aamaas, B., Berntsen, T. K., Fuglestvedt, J. S., Shine, K. P., and Bellouin, N. (2016). Regional emission metrics for short-lived climate forcers from multiple models. *Atmos. Chem. Phys.* doi:10.5194/acp-16-7451-2016.

Aamaas, B., Berntsen, T. K., Fuglestvedt, J. S., Shine, K. P., and Collins, W. J. (2017). Regional temperature change potentials for short-lived climate forcers based on radiative forcing from multiple models. *Atmos. Chem. Phys.* doi:10.5194/acp-17-10795-2017.

Abe-Ouchi, A., Saito, F., Kawamura, K., Raymo, M. E., Okuno, J., Takahashi, K., et al. (2013). Insolation-driven 100,000-year glacial cycles and hysteresis of ice-sheet volume. *Nature* 500, 190–193. doi:10.1038/nature12374.

Adam, O., Schneider, T., Brient, F., and Bischoff, T. (2016). Relation of the double-ITCZ bias to the atmospheric energy budget in climate models. *Geophys. Res. Lett.* doi:10.1002/2016GL069465.

Albrecht, B. A. (1989). Aerosols, cloud microphysics, and fractional cloudiness. *Science* 245, 1227–30. doi:10.1126/science.245.4923.1227.

Aldrin, M., Holden, M., Guttorp, P., Skeie, R. B., Myhre, G., and Berntsen, T. K. (2012). Bayesian estimation of climate sensitivity based on a simple climate model fitted to observations of hemispheric temperatures and global ocean heat content. *Environmetrics* 23, 253–271. doi:10.1002/env.2140.

Alexeev, V. A., and Jackson, C. H. (2013). Polar amplification: is atmospheric heat transport important? *Clim. Dyn.* 41, 533–547. doi:10.1007/s00382-012-1601-z.

Alexeev, V. A., Langen, P. L., and Bates, J. R. (2005). Polar amplification of surface warming on an aquaplanet in ``ghost forcing'' experiments without sea ice feedbacks. *Clim. Dyn.* 24, 655–666. doi:10.1007/s00382-005-0018-3.

Allan, R. P., Liu, C., Loeb, N. G., Palmer, M., Roberts, M., Smith, D., et al. (2014). Changes in global net radiative imbalance 1985–2012. *Geophys. Res. Lett.* 41, 5588–5597. doi:10.1002/2014GL060962.

Allen, M. R., Dube, O. P., Solecki, W., Aragón-Durand, F., Cramer, W., Humphreys, S., et al. (2018a). “Framing and Context,” in *Global Warming of 1.5°C. An IPCC Special Report on the impacts of global warming of 1.5°C above pre-industrial levels and related global greenhouse gas emission pathways, in the context of strengthening the global response to the threat of climate change,* eds. V. Masson-Delmotte, P. Zhai, H.-O. Pörtner, D. Roberts, J. Skea, P. R. Shukla, et al. (In Press).

Allen, M. R., Frame, D. J., Huntingford, C., Jones, C. D., Lowe, J. A., Meinshausen, M., et al. (2009). Warming caused by cumulative carbon emissions towards the trillionth tonne. *Nature* 458, 1163.

Allen, M. R., Fuglestvedt, J. S., Shine, K. P., Reisinger, A., Pierrehumbert, R. T., and Forster, P. M. (2016). New use of global warming potentials to compare cumulative and short-lived climate pollutants. *Nat. Clim. Chang.* 6, 773–776. doi:10.1038/nclimate2998.

Allen, M. R., Shine, K. P., Fuglestvedt, J. S., Millar, R. J., Cain, M., Frame, D. J., et al. (2018b). A solution to the misrepresentations of CO2-equivalent emissions of short-lived climate pollutants under ambitious mitigation. *npj Clim. Atmos. Sci.* 1. doi:10.1038/s41612-018-0026-8.

Allen, R. J., Amiri-Farahani, A., Lamarque, J.-F., Smith, C., Shindell, D., Hassan, T., et al. (2019). Observationally constrained aerosol–cloud semi-direct effects. *npj Clim. Atmos. Sci.* 2, 1–12. doi:10.1038/s41612-019-0073-9.

Allen, R. J., Norris, J. R., and Wild, M. (2013). Evaluation of multidecadal variability in CMIP5 surface solar radiation and inferred underestimation of aerosol direct effects over Europe, China, Japan, and India. *J. Geophys. Res.* 118, 6311–6336. doi:Doi 10.1002/Jgrd.50426.

Alo, C. A., and Anagnostou, E. N. (2017). A sensitivity study of the impact of dynamic vegetation on simulated future climate change over Southern Europe and the Mediterranean. *Int. J. Climatol.* 37, 2037–2050. doi:10.1002/joc.4833.

Anagnostou, E., John, E. H., Edgar, K. M., Foster, G. L., Ridgwell, A., Inglis, G. N., et al. (2016). Changing atmospheric CO2 concentration was the primary driver of early Cenozoic climate. *Nature* 533, 380–384. doi:10.1038/nature17423.

Andrews, E., Ogren, J. A., Kinne, S., and Samset, B. (2017a). Comparison of AOD, AAOD and column single scattering albedo from AERONET retrievals and in situ profiling measurements. *Atmos. Chem. Phys.* 17, 6041–6072. doi:10.5194/acp-17-6041-2017.

Andrews, T., Andrews, M. B., Bodas-Salcedo, A., Jones, G. S., Kulhbrodt, T., Manners, J., et al. (2019). Forcings, feedbacks and climate sensitivity in HadGEM3-GC3.1 and UKESM1. *J. Adv. Model. Earth Syst.*, 2019MS001866. doi:10.1029/2019MS001866.

Andrews, T., Betts, R. A., Booth, B. B. B., Jones, C. D., and Jones, G. S. (2017b). Effective radiative forcing from historical land use change. *Clim. Dyn.* 48, 3489–3505. doi:10.1007/s00382-016-3280-7.

Andrews, T., and Forster, P. M. (9998). Energy budget constraints on historical radiative forcing. *Nat. Clim. Chang.* (in press).

Andrews, T., Gregory, J. M., Paynter, D., Silvers, L. G., Zhou, C., Mauritsen, T., et al. (2018). Accounting for Changing Temperature Patterns Increases Historical Estimates of Climate Sensitivity. *Geophys. Res. Lett.* 45, 8490–8499. doi:10.1029/2018GL078887.

Andrews, T., Gregory, J. M., and Webb, M. J. (2015). The Dependence of Radiative Forcing and Feedback on Evolving Patterns of Surface Temperature Change in Climate Models. *J. Clim.* 28, 1630–1648. doi:10.1175/JCLI-D-14-00545.1.
Andrews, T., Gregory, J. M., Webb, M. J., and Taylor, K. E. (2012). Forcing, feedbacks and climate sensitivity in CMIP5 coupled atmosphere-ocean climate models. *Geophys. Res. Lett.* 39, L09712. doi:10.1029/2012GL051607.
Andrews, T., and Webb, M. J. (2018). The dependence of global cloud and lapse rate feedbacks on the spatial structure of tropical pacific warming. *J. Clim.* doi:10.1175/JCLI-D-17-0087.1.
Ångström, K. (1900). Ueber die Bedeutung des Wasserdampfes und der Kohlensäure bei der Absorption der Erdatmosphäre. *Ann. Phys.* 308, 720–732. doi:10.1002/andp.19003081208.
Annan, J. D., and Hargreaves, J. C. (2006). Using multiple observationally-based constraints to estimate climate sensitivity. *Geophys. Res. Lett.* 33. doi:10.1029/2005GL025259.
Annan, J. D., Hargreaves, J. C., Mauritsen, T., and Stevens, B. (9999). What could we learn about climate sensitivity from variability in the surface temperature record? *Earth Syst. Dyn. Discuss.* (submitted, 1–21.
Armour, K. C. (2017). Energy budget constraints on climate sensitivity in light of inconstant climate feedbacks. *Nat. Clim. Chang.* doi:10.1038/nclimate3278.
Armour, K. C., Bitz, C. M., and Roe, G. H. (2013). Time-Varying Climate Sensitivity from Regional Feedbacks. *J. Clim.* doi:10.1175/JCLI-D-12-00544.1.
Armour, K. C., Marshall, J., Scott, J. R., Donohoe, A., and Newsom, E. R. (2016). Southern Ocean warming delayed by circumpolar upwelling and equatorward transport. *Nat. Geosci.* doi:10.1038/ngeo2731.
Armour, K. C., and Roe, G. H. (2011). Climate commitment in an uncertain world. *Geophys. Res. Lett.* doi:10.1029/2010GL045850.
Armour, K. C., Siler, N., Donohoe, A., and Roe, G. H. (2019). Meridional Atmospheric Heat Transport Constrained by Energetics and Mediated by Large-Scale Diffusion. *J. Clim.* 32, 3655–3680. doi:10.1175/JCLI-D-18-0563.1.
Armstrong, E., Valdes, P., House, J., and Singarayer, J. (2019). Investigating the feedbacks between CO2, vegetation and the AMOC in a coupled climate model. *Clim. Dyn.* 53, 2485–2500. doi:10.1007/s00382-019-04634-2.
Arora, V. K., Boer, G. J., Friedlingstein, P., Eby, M., Jones, C. D., Christian, J. R., et al. (2013). Carbon-concentration and carbon-climate feedbacks in CMIP5 earth system models. *J. Clim.* 26, 5289–5314. doi:10.1175/JCLI-D-12-00494.1.
Arrhenius, S. (1896). On the Influence of Carbonic Acid in the Air upon the Temperature of the Ground. *Philos. Mag. J. Sci.* 41, 237–279.
Augustine, J. A., and Dutton, E. G. (2013). Variability of the surface radiation budget over the United States from 1996 through 2011 from high-quality measurements. *J. Geophys. Res.* 118, 43–53. doi:Doi 10.1029/2012jd018551.
Banerjee, A., Chiodo, G., Previdi, M., Ponater, M., Conley, A. J., and Polvani, L. M. (2019). Stratospheric water vapor: an important climate feedback. *Clim. Dyn.* 53, 1697–1710. doi:10.1007/s00382-019-04721-4.
Barnes, E. A., and Polvani, L. (2013). Response of the midlatitude jets, and of their variability, to increased greenhouse gases in the CMIP5 models. *J. Clim.* 26, 7117–7135. doi:10.1175/JCLI-D-12-00536.1.
Barreiro, M., and Philander, S. G. (2008). Response of the tropical Pacific to changes in extratropical clouds. *Clim. Dyn.* doi:10.1007/s00382-007-0363-5.
Bauer, S. E., Bausch, A., Nazarenko, L., Tsigaridis, K., Xu, B., Edwards, R., et al. (2013). Historical and future black carbon deposition on the three ice caps: Ice core measurements and model simulations from 1850 to 2100. *J. Geophys. Res. Atmos.* 118, 7948–7961. doi:10.1002/jgrd.50612.
Beerling, D. J., and Royer, D. L. (2011). Convergent Cenozoic CO2 history. *Nat. Geosci.* 4, 418–420. doi:10.1038/ngeo1186.
Bellouin, N., Boucher, O., Haywood, J., and Reddy, M. S. (2005). Global estimate of aerosol direct radiative forcing from satellite measurements. *Nature* 438, 1138–1141. doi:10.1038/nature04348.
Bellouin, N., Mann, G. W., Woodhouse, M. T., Johnson, C., Carslaw, K. S., and Dalvi, M. (2013a). Impact of the modal aerosol scheme GLOMAP-mode on aerosol forcing in the Hadley Centre Global Environmental Model. *Atmos. Chem. Phys.* 13, 3027–3044. doi:10.5194/acp-13-3027-2013.
Bellouin, N., Quaas, J., Gryspeerdt, E., Kinne, S., Stier, P., Watson-Parris, D., et al. (2019). Bounding global aerosol radiative forcing of climate change. *Rev. Geophys.*, 2019RG000660. doi:10.1029/2019RG000660.
Bellouin, N., Quaas, J., Morcrette, J.-J., and Boucher, O. (2013b). Estimates of aerosol radiative forcing from the MACC re-analysis. *Atmos. Chem. Phys.* 13, 2045–2062. doi:10.5194/acp-13-2045-2013.
Bender, F. A. M., Ekman, A. M. L., and Rodhe, H. (2010). Response to the eruption of Mount Pinatubo in relation to climate sensitivity in the CMIP3 models. *Clim. Dyn.* 35, 875–886. doi:10.1007/s00382-010-0777-3.
Bender, F. A. M., Frey, L., McCoy, D. T., Grosvenor, D. P., and Mohrmann, J. K. (2019). Assessment of aerosol–cloud–radiation correlations in satellite observations, climate models and reanalysis. *Clim. Dyn.* 52, 4371–4392. doi:10.1007/s00382-018-4384-z.
Bender, F. A. M., Ramanathan, V., and Tselioudis, G. (2012). Changes in extratropical storm track cloudiness 1983-2008: Observational support for a poleward shift. *Clim. Dyn.* 38, 2037–2053.
Bengtsson, L., and Schwartz, S. (2013). Determination of a lower bound on Earth's climate sensitivity. *Tellus B* 1, 1–16. Available at: http://www.tellusb.net/index.php/tellusb/article/view/21533.

Bentamy, A., Piolle, J. F., Grouazel, A., Danielson, R., Gulev, S., Paul, F., et al. (2017). Review and assessment of latent and sensible heat flux accuracy over the global oceans. *Remote Sens. Environ.* 201, 196–218. doi:10.1016/j.rse.2017.08.016.
Bickel, M., Ponater, M., Bock, L., Burkhardt, U., and Reineke, S. (2019). Estimating the Effective Radiative Forcing of Contrail Cirrus. *J. Clim.*, JCLI-D-19-0467.1. doi:10.1175/JCLI-D-19-0467.1.
Bilbao, R. A. F., Gregory, J. M., and Bouttes, N. (2015). Analysis of the regional pattern of sea level change due to ocean dynamics and density change for 1993–2099 in observations and CMIP5 AOGCMs. *Clim. Dyn.* 45, 2647–2666. doi:10.1007/s00382-015-2499-z.
Bindoff, N. L., Stott, P. A., AchutaRao, K. ., Allen, M. R., Gillett, N., Gutzler, D., et al. (2013). "Detection and Attribution of Climate Change, from Global to Regional," in *Climate Change 2013: The Physical Science Basis. Contribution of Working Group I to the Fifth Assessment Report of the Intergovernmental Panel on Climate Change*, eds. T. F. Stocker, D. Qin, G.-K. Plattner, M. Tignor, S. K. Allen, J. Boschung, et al. (Cambridge, United Kingdom and New York, NY, USA: Cambridge University Press).
Bintanja, R., Van Oldenborgh, G. J., Drijfhout, S. S., Wouters, B., and Katsman, C. A. (2013). Important role for ocean warming and increased ice-shelf melt in Antarctic sea-ice expansion. *Nat. Geosci.* doi:10.1038/ngeo1767.
Bischoff, T., and Schneider, T. (2014). Energetic constraints on the position of the intertropical convergence zone. *J. Clim.* doi:10.1175/JCLI-D-13-00650.1.
Bisiaux, M. M., Edwards, R., McConnell, J. R., Curran, M. A. J., Van Ommen, T. D., Smith, A. M., et al. (2012). Changes in black carbon deposition to Antarctica from two high-resolution ice core records, 1850–2000 AD. *Atmos. Chem. Phys.* 12, 4107–4115. doi:10.5194/acp-12-4107-2012.
Bjerknes, J. (1964). Atlantic Air-Sea Interaction. *Adv. Geophys.* 10, 1–82. doi:10.1016/S0065-2687(08)60005-9.
Bjordal, J., Storelvmo, T., Alterskjaer, K., and Carlsen, T. (9999). State-dependent cloud phase feedback makes equilibrium climate sensitivity > 5°C plausible. (submitted.
Bloch-Johnson, J., Pierrehumbert, R. T., and Abbot, D. S. (2015). Feedback temperature dependence determines the risk of high warming. *Geophys. Res. Lett.* 42, 4973–4980. doi:10.1002/2015GL064240.
Bock, L., and Burkhardt, U. (2016). Reassessing properties and radiative forcing of contrail cirrus using a climate model. *J. Geophys. Res.* doi:10.1002/2016JD025112.
Bodas-Salcedo, A., Mulcahy, J. P., Andrews, T., Williams, K. D., Ringer, M. A., Field, P. R., et al. (2019). Strong Dependence of Atmospheric Feedbacks on Mixed-Phase Microphysics and Aerosol-Cloud Interactions in HadGEM3. *J. Adv. Model. Earth Syst.* 11, 1735–1758. doi:10.1029/2019MS001688.
Bodas-Salcedo, A., Webb, M. J., Bony, S., Chepfer, H., Dufresne, J.-L., Klein, S. A., et al. (2011). COSP: Satellite simulation software for model assessment. *Bull. Am. Meteorol. Soc.* 92, 1023–1043. doi:10.1175/2011BAMS2856.1.
Bodas-Salcedo, A., Williams, K. D., Field, P. R., and Lock, A. P. (2012). The Surface Downwelling Solar Radiation Surplus over the Southern Ocean in the Met Office Model: The Role of Midlatitude Cyclone Clouds. *J. Clim.* 25, 7467–7486. doi:10.1175/JCLI-D-11-00702.1.
Boeke, R. C., and Taylor, P. C. (2016). Evaluation of the Arctic surface radiation budget in CMIP5 models. *J. Geophys. Res.* 121, 8525–8548. doi:10.1002/2016JD025099.
Boeke, R. C., and Taylor, P. C. (2018). Seasonal energy exchange in sea ice retreat regions contributes to differences in projected Arctic warming. *Nat. Commun.* 9. doi:10.1038/s41467-018-07061-9.
Bonan, D. B., Armour, K. C., Roe, G. H., Siler, N., and Feldl, N. (2018). Geophysical Research Letters Sources of Uncertainty in the Meridional Pattern of Climate Change. *Geophys. Res. Lett.* doi:10.1029/2018GL079429.
Bonan, G. B. (2008). Forests and climate change: Forcings, feedbacks, and the climate benefits of forests. *Science (80-. ).* 320, 1444–1449. doi:10.1126/science.1155121.
Bond, T. C., Doherty, S. J., Fahey, D. W., Forster, P. M., Berntsen, T., DeAngelo, B. J., et al. (2013). Bounding the role of black carbon in the climate system: A scientific assessment. *J. Geophys. Res. Atmos.* 118, 5380–5552. doi:10.1002/jgrd.50171.
Bony, S., Colman, R., Kattsov, V. M., Allan, R. P., Bretherton, C. S., Dufresne, J.-L., et al. (2006). How Well do we Understand and Evaluate Climate Change Feedback Processes? *J. Clim.* 19, 3445–3482, doi: 10.1175/JCLI3819.1.
Bony, S., and Dufresne, J. L. (2005). Marine boundary layer clouds at the heart of tropical cloud feedback uncertainties in climate models. *Geophys. Res. Lett.* 32, L20806. doi:10.1029/2005GL023851.
Bony, S., Semie, A., Kramer, R. J., Soden, B., and Tompkins, A. M. (9999). Observed modulation of the tropical radiation budget by deep convective organization and lower-tropospheric stability. *AGU Adv.* (submitted.
Bony, S., Stevens, B., Coppin, D., Becker, T., Reed, K. A., Voigt, A., et al. (2016). Thermodynamic control of anvil cloud amount. *Proc. Natl. Acad. Sci. U. S. A.* 113, 8927–8932. doi:10.1073/pnas.1601472113.
Bony, S., Stevens, B., Frierson, D. M. W., Jakob, C., Kageyama, M., Pincus, R., et al. (2015). Clouds, circulation and climate sensitivity. *Nat. Geosci.* 8, 261–268. doi:10.1038/ngeo2398.
Booth, B. B. B., Harris, G. R., Jones, A., Wilcox, L., Hawcroft, M., Carslaw, K. S., et al. (2018). Comments on "Rethinking the Lower Bound on Aerosol Radiative Forcing." *J. Clim.* 31, 9407–9412. doi:10.1175/JCLI-D-17-0369.1.

Boucher, O. (2012). Comparison of physically- and economically-based CO 2- equivalences for methane. *Earth Syst. Dyn.* doi:10.5194/esd-3-49-2012.
Boucher, O., Friedlingstein, P., Collins, B., and Shine, K. P. (2009). The indirect global warming potential and global temperature change potential due to methane oxidation. *Environ. Res. Lett.* 4. doi:10.1088/1748-9326/4/4/044007.
Boucher, O., Myhre, G., and Myhre, A. (2004). Direct human influence of irrigation on atmospheric water vapour and climate. *Clim. Dyn.* doi:10.1007/s00382-004-0402-4.
Boucher, O., Randall, D., Artaxo, P., Bretherton, C., Feingold, G., Forster, P., et al. (2013). "Clouds and Aerosols," in *Climate Change 2013: The Physical Science Basis. Contribution of Working Group I to the Fifth Assessment Report of the Intergovernmental Panel on Climate Change*, eds. T. F. Stocker, D. Qin, G.-K. Plattner, M. Tignor, S. K. Allen, J. Boschung, et al. (Cambridge, United Kingdom and New York, NY, USA: Cambridge Univeristy Press), 571–657. doi:10.1017/CBO9781107415324.016.
Boucher, O., and Reddy, M. S. (2008). Climate trade-off between black carbon and carbon dioxide emissions. *Energy Policy* 36, 193–200. doi:10.1016/j.enpol.2007.08.039.
Bowerman, N. H. A., Frame, D. J., Huntingford, C., Lowe, J. A., Smith, S. M., and Allen, M. R. (2013). The role of short-lived climate pollutants in meeting temperature goals. *Nat. Clim. Chang.* 3, 1021.
Braconnot, P., Harrison, S. P., Kageyama, M., Bartlein, P. J., Masson-Delmotte, V., Abe-Ouchi, A., et al. (2012). Evaluation of climate models using palaeoclimatic data. *Nat. Clim. Chang.* 2, 417.
Brantley, S. L. (2008). Understanding Soil Time. *Science (80-. ).* 321, 1454–1455. doi:10.1126/science.1161132.
Brenguier, J.-L., Pawlowska, H., Schüller, L., Preusker, R., Fischer, J., Fouquart, Y., et al. (2000). Radiative Properties of Boundary Layer Clouds: Droplet Effective Radius versus Number Concentration. *J. Atmos. Sci.* 57, 803–821. doi:10.1175/1520-0469(2000)057<0803:RPOBLC>2.0.CO;2.
Bretherton, C. S. (2015). Insights into low-latitude cloud feedbacks from high-resolution models. *Philos. Trans. R. Soc. A Math. Phys. Eng. Sci.* 373. doi:10.1098/rsta.2014.0415.
Bretherton, C. S., Blossey, P. N., and Jones, C. R. (2013). Mechanisms of marine low cloud sensitivity to idealized climate perturbations: A single-LES exploration extending the CGILS cases. *J. Adv. Model. Earth Syst.* doi:10.1002/jame.20019.
Bretherton, C. S., Blossey, P. N., and Stan, C. (2014). Cloud feedbacks on greenhouse warming in the superparameterized climate model SP-CCSM4. *J. Adv. Model. Earth Syst.* 6, 1185–1204. doi:10.1002/2014MS000355.
Brient, F., and Schneider, T. (2016). Constraints on climate sensitivity from space-based measurements of low-cloud reflection. *J. Clim.* 29, 5821–5835. doi:10.1175/JCLI-D-15-0897.1.
Brient, F., Schneider, T., Tan, Z., Bony, S., Qu, X., and Hall, A. (2016). Shallowness of tropical low clouds as a predictor of climate models' response to warming. *Clim. Dyn.* 47, 433–449. doi:10.1007/s00382-015-2846-0.
Brierley, C., Burls, N., Ravelo, C., and Fedorov, A. (2015). Pliocene warmth and gradients. *Nat. Geosci.* 8, 419–420. doi:10.1038/ngeo2444.
Brierley, C. M., Zhao, A., Harrison, S. P., Braconnot, P., Williams, C. J. R., Thornalley, D. J. R., et al. (9999). Large-scale features and evaluation of the PMIP4-CMIP6 midHolocene simulations. (submitted, 1–42.
Bronselaer, B., Stouffer, R. J., Winton, M., Griffies, S. M., Hurlin, W. J., Russell, J. L., et al. (2018). Change in future climate due to Antarctic meltwater. *Nature* 564, 53–58. doi:10.1038/s41586-018-0712-z.
Brovkin, V., Lorenz, S., Raddatz, T., Ilyina, T., Stemmler, I., Toohey, M., et al. (2019). What was the source of the atmospheric CO2 increase during the Holocene? *Biogeosciences* 16, 2543–2555. doi:10.5194/bg-16-2543-2019.
Brovkin, V., Raddatz, T., Reick, C. H., Claussen, M., and Gayler, V. (2009). Global biogeophysical interactions between forest and climate. *Geophys. Res. Lett.* 36. doi:10.1029/2009GL037543.
Brown, P. T., and Caldeira, K. (2017). Greater future global warming inferred from Earth's recent energy budget. *Nature* 552, 45–50. doi:10.1038/nature24672.
Brown, P. T., Li, W., Li, L., and Ming, Y. (2014). Top-of-atmosphere radiative contribution to unforced decadal global temperature variability in climate models. *Geophys. Res. Lett.* 41, 5175–5183. doi:10.1002/2014GL060625.
Brown, P. T., Stolpe, M. B., and Caldeira, K. (2018). Assumptions for emergent constraints. *Nature* 563, E1–E3. doi:10.1038/s41586-018-0638-5.
Burke, K. D., Williams, J. W., Chandler, M. A., Haywood, A. M., Lunt, D. J., and Otto-Bliesner, B. L. (2018). Pliocene and Eocene provide best analogs for near-future climates. *Proc. Natl. Acad. Sci.* 115, 13288–13293. doi:10.1073/pnas.1809600115.
Burls, N. J., and Fedorov, A. V. (2014a). What controls the mean east-west sea surface temperature gradient in the equatorial pacific: The role of cloud albedo. *J. Clim.* 27, 2757–2778. doi:10.1175/JCLI-D-13-00255.1.
Burls, N. J., and Fedorov, A. V (2014b). Simulating Pliocene warmth and a permanent El Niño-like state: The role of cloud albedo. *Paleoceanography* 29, 893–910. doi:10.1002/2014PA002644.
Burt, M. A., Randall, D. A., and Branson, M. D. (2016). Dark warming. *J. Clim.* doi:10.1175/JCLI-D-15-0147.1.
Caballero, R., and Huber, M. (2013). State-dependent climate sensitivity in past warm climates and its implications for future climate projections. *Proc. Natl. Acad. Sci.* 110, 14162–14167. doi:10.1073/pnas.1303365110.
Cain, M., Lynch, J., Allen, M. R., Fuglestvedt, J. S., Frame, D. J., and Macey, A. H. (2019). Improved calculation of warming-equivalent emissions for short-lived climate pollutants. *NPJ Clim. Atmos. Sci.* 2, 1–7.

doi:10.1038/s41612-019-0086-4.
Caldwell, P. M., Bretherton, C. S., Zelinka, M. D., Klein, S. A., Santer, B. D., and Sanderson, B. M. (2014). Statistical significance of climate sensitivity predictors obtained by data mining. *Geophys. Res. Lett.* 41, 1803–1808. doi:10.1002/2014GL059205.
Caldwell, P. M., Zelinka, M. D., and Klein, S. A. (2018). Evaluating Emergent Constraints on Equilibrium Climate Sensitivity. *J. Clim.* 31, 3921–3942. doi:10.1175/JCLI-D-17-0631.1.
Caldwell, P. M., Zelinka, M. D., Taylor, K. E., and Marvel, K. (2016). Quantifying the sources of intermodel spread in equilibrium climate sensitivity. *J. Clim.* 29, 513–524. doi:10.1175/JCLI-D-15-0352.1.
Calisto, M., Folini, D., Wild, M., and Bengtsson, L. (2014). Cloud radiative forcing intercomparison between fully coupled CMIP5 models and CERES satellite data. *Ann. Geophys.* 32, 793–807. doi:10.5194/angeo-32-793-2014.
Calogovic, J., Albert, C., Arnold, F., Beer, J., Desorgher, L., and Flueckiger, E. O. (2010). Sudden cosmic ray decreases: No change of global cloud cover. *Geophys. Res. Lett.* 37, n/a-n/a. doi:10.1029/2009GL041327.
Cane, M. A., Clement, A. C., Kaplan, A., Kushnir, Y., Pozdnyakov, D., Seager, R., et al. (1997). Twentieth-Century Sea Surface Temperature Trends. *Science (80-. ).* 275, 957–960. doi:10.1126/science.275.5302.957.
Cao, L., Bala, G., Caldeira, K., Nemani, R., and Ban-Weiss, G. (2010). Importance of carbon dioxide physiological forcing to future climate change. *Proc. Natl. Acad. Sci. U. S. A.* 107. doi:10.1073/pnas.0913000107.
Cao, Y., Liang, S., Chen, X., and He, T. (2015). Assessment of Sea Ice Albedo Radiative Forcing and Feedback over the Northern Hemisphere from 1982 to 2009 Using Satellite and Reanalysis Data. *J. Clim.* 28, 1248–1259. doi:10.1175/JCLI-D-14-00389.1.
Ceppi, P., and Gregory, J. M. (2017). Relationship of tropospheric stability to climate sensitivity and Earth's observed radiation budget. *Proc. Natl. Acad. Sci.* 114, 13126–13131. doi:10.1073/pnas.1714308114.
Ceppi, P., and Gregory, J. M. (2019). A refined model for the Earth's global energy balance. *Clim. Dyn.* 53, 4781–4797. doi:10.1007/s00382-019-04825-x.
Ceppi, P., and Hartmann, D. L. (2015). Connections between clouds, radiation, and midlatitude dynamics: A review. *Curr. Clim. Chang. Rep.* 1, 94–102.
Ceppi, P., McCoy, D. T., and Hartmann, D. L. (2016). Observational evidence for a negative shortwave cloud feedback in middle to high latitudes. *Geophys. Res. Lett.* 43, 1331–1339. doi:10.1002/2015GL067499.
Ceppi, P., and Shepherd, T. G. (2017). Contributions of climate feedbacks to changes in atmospheric circulation. *J. Clim.* 30, 9097–9118. doi:10.1175/JCLI-D-17-0189.1.
Cesana, G., Del Genio, A. D., Ackerman, A. S., Kelley, M., Elsaesser, G., Fridlind, A. M., et al. (2019). Evaluating models' response of tropical low clouds to SST forcings using CALIPSO observations. *Atmos. Chem. Phys.* 19, 2813–2832. doi:10.5194/acp-19-2813-2019.
Cess, R. D., Potter, G. L., Blanchet, J. P., Boer, G. J., Del Genio, A. D., Deque, M., et al. (1990). Intercomparison and interpretation of climate feedback processes in 19 atmospheric general circulation models. *J. Geophys. Res.* 95, 16601–16615. doi:10.1029/JD095iD10p16601.
Cha, S. C., Moon, J. H., and Song, Y. T. (2018). A Recent Shift Toward an El Niño-Like Ocean State in the Tropical Pacific and the Resumption of Ocean Warming. *Geophys. Res. Lett.* 45, 11,885-11,894. doi:10.1029/2018GL080651.
Chafik, L., Häkkinen, S., England, M. H., Carton, J. A., Nigam, S., Ruiz-Barradas, A., et al. (2016). Global linkages originating from decadal oceanic variability in the subpolar North Atlantic. *Geophys. Res. Lett.* 43, 10,909-10,919. doi:10.1002/2016GL071134.
Chandan, D., and Richard Peltier, W. (2018). On the mechanisms of warming the mid-Pliocene and the inference of a hierarchy of climate sensitivities with relevance to the understanding of climate futures. *Clim. Past* 14, 825–856. doi:10.5194/cp-14-825-2018.
Charney, J. G., Arakawa, A., Baker, D. J., Bolin, B., Dickinson, R. E., Goody, R. M., et al. (1979). *Carbon Dioxide and Climate: A Scientific Assessment*. Washington, DC: The National Academies Press doi:10.17226/12181.
Checa-Garcia, R., Hegglin, M. I., Kinnison, D., Plummer, D. A., and Shine, K. P. (2018). Historical Tropospheric and Stratospheric Ozone Radiative Forcing Using the CMIP6 Database. *Geophys. Res. Lett.* 45, 3264–3273. doi:10.1002/2017GL076770.
Chen, C. C., and Gettelman, A. (2013). Simulated radiative forcing from contrails and contrail cirrus. *Atmos. Chem. Phys.* doi:10.5194/acp-13-12525-2013.
Chen, X., Liang, S., and Cao, Y. (2016). Satellite observed changes in the Northern Hemisphere snow cover phenology and the associated radiative forcing and feedback between 1982 and 2013. *Environ. Res. Lett.* 11, 84002. doi:10.1088/1748-9326/11/8/084002.
Chen, Y.-C., Christensen, M. W., Stephens, G. L., and Seinfeld, J. H. (2014). Satellite-based estimate of global aerosol–cloud radiative forcing by marine warm clouds. *Nat. Geosci.* 7, 643–646. doi:10.1038/ngeo2214.
Cheng, L., Abraham, J., Hausfather, Z., and Trenberth, K. E. (2019). How fast are the oceans warming? *Science (80-. ).* 363, 128–129. doi:10.1126/science.aav7619.
Cheng, L., Trenberth, K. E., Palmer, M. D., Zhu, J., and Abraham, J. P. (2016). Observed and simulated full-depth ocean heat-content changes for 1970--2005. *Ocean Sci.* 12, 925–935. doi:10.5194/os-12-925-2016.
Chepfer, H., Noel, V., Winker, D., and Chiriaco, M. (2014). Where and when will we observe cloud changes due to

climate warming'. *Geophys. Res. Lett.* 41, 8387–8395. doi:10.1002/2014GL061792.
Cherian, R., Quaas, J., Salzmann, M., and Wild, M. (2014). Pollution trends over Europe constrain global aerosol forcing as simulated by climate models. *Geophys. Res. Lett.* doi:10.1002/2013GL058715.
Cherubini, F., Fuglestvedt, J., Gasser, T., Reisinger, A., Cavalett, O., Huijbregts, M. A. J., et al. (2016). Bridging the gap between impact assessment methods and climate science. *Environ. Sci. Policy* 64, 129–140. doi:10.1016/j.envsci.2016.06.
Cherubini, F., and Tanaka, K. (2016). Amending the inadequacy of a single indicator for climate impact analyses. *Environ. Sci. Technol.* doi:10.1021/acs.est.6b05343.
Christensen, M. W., Chen, Y. C., and Stephens, G. L. (2016). Aerosol indirect effect dictated by liquid clouds. *J. Geophys. Res.* 121. doi:10.1002/2016JD025245.
Christensen, M. W., Neubauer, D., Poulsen, C. A., Thomas, G. E., McGarragh, G. R., Povey, A. C., et al. (2017). Unveiling aerosol–cloud interactions – Part 1: Cloud contamination in satellite products enhances the aerosol indirect forcing estimate. *Atmos. Chem. Phys.* 17, 13151–13164. doi:10.5194/acp-17-13151-2017.
Christensen, M. W., and Stephens, G. L. (2011). Microphysical and macrophysical responses of marine stratocumulus polluted by underlying ships: Evidence of cloud deepening. *J. Geophys. Res.* 116, D03201. doi:10.1029/2010JD014638.
Christensen, M. W., Suzuki, K., Zambri, B., and Stephens, G. L. (2014). Ship track observations of a reduced shortwave aerosol indirect effect in mixed-phase clouds. *Geophys. Res. Lett.* 41, 6970–6977. doi:10.1002/2014GL061320.
Chung, E.-S., and Soden, B. J. (2015). An assessment of methods for computing radiative forcing in climate models. *Environ. Res. Lett.* 10, 074004. doi:10.1088/1748-9326/10/7/074004.
Chung, E.-S., and Soden, B. J. (2018). On the compensation between cloud feedback and cloud adjustment in climate models. *Clim. Dyn.* 50, 1267–1276. doi:10.1007/s00382-017-3682-1.
Chung, E.-S., Soden, B., Sohn, B. J., and Shi, L. (2014). Upper-tropospheric moistening in response to anthropogenic warming. *Proc. Natl. Acad. Sci.* 111, 11636–11641. doi:10.1073/pnas.1409659111.
Chung, E. S., Soden, B. J., and Sohn, B. J. (2010). Revisiting the determination of climate sensitivity from relationships between surface temperature and radiative fluxes. *Geophys. Res. Lett.* doi:10.1029/2010GL043051.
Church, J. a., Clark, P. U., Cazenave, A., Gregory, J. M., Jevrejeva, S., Levermann, A., et al. (2013). "Sea level change," in *Climate Change 2013: The Physical Science Basis. Contribution of Working Group I to the Fifth Assessment Report of the Intergovernmental Panel on Climate Change*, eds. T. F. Stocker, D. Qin, G.-K. Plattner, M. Tignor, S. K. Allen, J. Boschung, et al. (Cambridge, United Kingdom and New York, NY, USA, United Kingdom and New York, NY, USA: Cambridge University Press), 1137–1216. doi:10.1017/CB09781107415315.026.
Clark, P. U., Shakun, J. D., Marcott, S. A., Mix, A. C., Eby, M., Kulp, S., et al. (2016). Consequences of twenty-first-century policy for multi-millennial climate and sea-level change. *Nat. Clim. Chang.* 6, 360–369. doi:10.1038/nclimate2923.
Clement, A. C., Seager, R., Cane, M. A., and Zebiak, S. E. (1996). An ocean dynamical thermostat. *J. Clim.* doi:10.1175/1520-0442(1996)009<2190:AODT>2.0.CO;2.
Coats, S., and Karnauskas, K. B. (2017). Are Simulated and Observed Twentieth Century Tropical Pacific Sea Surface Temperature Trends Significant Relative to Internal Variability? *Geophys. Res. Lett.* 44, 9928–9937. doi:10.1002/2017GL074622.
Cohan, D. S., Xu, J., Greenwald, R., Bergin, M. H., and Chameides, W. L. (2002). Impact of atmospheric aerosol light scattering and absorption on terrestrial net primary productivity. *Global Biogeochem. Cycles*. doi:10.1029/2001gb001441.
Collins, M., Knutti, R., Arblaster, J., Dufresne, J.-L. J.-L., Fichefet, T., Friedlingstein, P., et al. (2013a). "Long-term Climate Change: Projections, Commitments and Irreversibility," in *Climate Change 2013: The Physical Science Basis. Contribution of Working Group I to the Fifth Assessment Report of the Intergovernmental Panel on Climate Change*, eds. T. F. Stocker, D. Qin, G.-K. Plattner, M. Tignor, S. K. Allen, J. Boschung, et al. (Cambridge, United Kingdom and New York, NY, USA: Cambridge University Press), 1029–1136. doi:10.1017/CBO9781107415324.024.
Collins, W. D., Feldman, D. R., Kuo, C., and Nguyen, N. H. (2018). Large regional shortwave forcing by anthropogenic methane informed by Jovian observations. *Sci. Adv.* doi:10.1126/sciadv.aas9593.
Collins, W. J. (Bill), Frame, D. J., Fuglestvedt, J., and Shine, K. P. (2019). Stable climate metrics for emissions of short and long-lived species – combining steps and pulses. *Environ. Res. Lett.* (in press). doi:10.1088/1748-9326/ab6039.
Collins, W. J., Bellouin, N., Doutriaux-Boucher, M., Gedney, N., Halloran, P., Hinton, T., et al. (2011). Development and evaluation of an Earth-System model – HadGEM2. *Geosci. Model Dev.* doi:10.5194/gmd-4-1051-2011.
Collins, W. J., Derwent, R. G., Johnson, C. E., and Stevenson, D. S. (2002). The oxidation of organic compounds in the troposphere and their global warming potentials. *Clim. Change*. doi:10.1023/A:1014221225434.
Collins, W. J., Fry, M. M., Yu, H., Fuglestvedt, J. S., Shindell, D. T., and West, J. J. (2013b). Global and regional temperature-change potentials for near-term climate forcers. *Atmos. Chem. Phys.* doi:10.5194/acp-13-2471-2013.

Colman, R. (2003). A comparison of climate feedbacks in general circulation models. *Clim. Dyn.* 20, 865–873. doi:10.1007/s00382-003-0310-z.
Colman, R. A. (2015). Climate radiative feedbacks and adjustments at the Earth's surface. *J. Geophys. Res.* 120, 3173–3182. doi:10.1002/2014JD022896.
Colman, R., and Hanson, L. (2017). On the relative strength of radiative feedbacks under climate variability and change. *Clim. Dyn.* 49, 2115–2129. doi:10.1007/s00382-016-3441-8.
Colman, R., and McAvaney, B. (2009). Climate feedbacks under a very broad range of forcing. *Geophys. Res. Lett.* 36, 1–5. doi:10.1029/2008GL036268.
Comiso, J. C., Gersten, R. A., Stock, L. V, Turner, J., Perez, G. J., and Cho, K. (2017). Positive Trend in the Antarctic Sea Ice Cover and Associated Changes in Surface Temperature. *J. Clim.* 30, 2251–2267. doi:10.1175/JCLI-D-16-0408.1.
Covey, C., Abe-Ouchi, A., Boer, G. J., Boville, B. A., Cubasch, U., Fairhead, L., et al. (2000). The seasonal cycle in coupled ocean-atmosphere general circulation models. *Clim. Dyn.* 16, 775–787. doi:10.1007/s003820000081.
Cox, P. M., Huntingford, C., and Williamson, M. S. (2018a). Emergent constraint on equilibrium climate sensitivity from global temperature variability. *Nature* 553, 319–322. doi:10.1038/nature25450.
Cox, P. M., Williamson, M. S., Nijsse, F. J. M. M., and Huntingford, C. (2018b). Cox et al. reply. *Nature* 563, E10–E15. doi:10.1038/s41586-018-0641-x.
Cronin, T. W., and Wing, A. A. (2017). Clouds, Circulation, and Climate Sensitivity in a Radiative-Convective Equilibrium Channel Model. *J. Adv. Model. Earth Syst.* 9, 2883–2905. doi:10.1002/2017MS001111.
Crook, J. A., and Forster, P. M. (2014). Comparison of surface albedo feedback in climate models and observations. *Geophys. Res. Lett.* 41, 1717–1723. doi:10.1002/2014GL059280.Received.
Crook, J. A., Forster, P. M., and Stuber, N. (2011). Spatial patterns of modeled climate feedback and contributions to temperature response and polar amplification. *J. Clim.* doi:10.1175/2011JCLI3863.1.
Cuesta-Valero, F. J., García-García, A., Beltrami, H., González-Rouco, J. F., and García-Bustamante, E. (9999). Long-term Global Ground Heat Flux and Continental Heat Content from Geothermal Data. *J. Geophys. Res. Earth Surf.* (submitted.
Dai, A., Luo, D., Song, M., and Liu, J. (2019). Arctic amplification is caused by sea-ice loss under increasing CO2. *Nat. Commun.* 10, 121. doi:10.1038/s41467-018-07954-9.
Dai, H., Yang, H., and Yin, J. (2017). Roles of energy conservation and climate feedback in Bjerknes compensation: a coupled modeling study. *Clim. Dyn.* doi:10.1007/s00382-016-3386-y.
Daniel, J. S., Fleming, E. L., Portmann, R. W., Velders, G. J. M., Jackman, C. H., and Ravishankara, A. R. (2010). Options to accelerate ozone recovery: Ozone and climate benefits. *Atmos. Chem. Phys.* doi:10.5194/acp-10-7697-2010.
Davies-Barnard, T., Valdes, P. J., Singarayer, J. S., Wiltshire, A. J., and Jones, C. D. (2015). Quantifying the relative importance of land cover change from climate and land use in the representative concentration pathways. *Global Biogeochem. Cycles* 29, 842–853. doi:10.1002/2014GB004949.
Dekens, P. S., Ravelo, A. C., McCarthy, M. D., and Edwards, C. A. (2008). A 5 million year comparison of Mg/Ca and alkenone paleothermometers. *Geochemistry, Geophys. Geosystems* 9. doi:10.1029/2007GC001931.
Denison, S., Forster, P. M., and Smith, C. J. (2019). Guidance on emissions metrics for nationally determined contributions under the Paris Agreement. *Environ. Res. Lett.* 14, 124002. doi:10.1088/1748-9326/ab4df4.
Desbruyères, D. G., Purkey, S. G., McDonagh, E. L., Johnson, G. C., and King, B. A. (2016). Deep and abyssal ocean warming from 35 years of repeat hydrography. *Geophys. Res. Lett.* 43, 10,356-10,365. doi:10.1002/2016GL070413.
Deser, C., Knutti, R., Solomon, S., and Phillips, A. S. (2012). Communication of the role of natural variability in future North American climate. doi:10.1038/NCLIMATE1562.
Dessler, A. E. (2011). Cloud variations and the Earth's energy budget. *Geophys. Res. Lett.* doi:10.1029/2011GL049236.
Dessler, A. E. E. (2013). Observations of climate feedbacks over 2000-10 and comparisons to climate models. *J. Clim.* 26, 333–342. doi:10.1175/JCLI-D-11-00640.1.
Dessler, A. E., and Forster, P. M. (2018). An estimate of equilibrium climate sensitivity from interannual variability. *J. Geophys. Res. Atmos.* doi:10.1029/2018JD028481.
Dessler, A. E., Mauritsen, T., and Stevens, B. (2018). The influence of internal variability on Earth's energy balance framework and implications for estimating climate sensitivity. *Atmos. Chem. Phys.* 18, 5147–5155. doi:10.5194/acp-18-5147-2018.
Dessler, A. E., Schoeberl, M. R., Wang, T., Davis, S. M., and Rosenlof, K. H. (2013). Stratospheric water vapor feedback. *Proc. Natl. Acad. Sci.* 110, 18087–18091. doi:10.1073/pnas.1310344110.
Devaraju, N., Bala, G., and Nemani, R. (2015). Modelling the influence of land-use changes on biophysical and biochemical interactions at regional and global scales. *Plant, Cell Environ.* 38, 1931–1946. doi:10.1111/pce.12488.
Dewitte, S., and Clerbaux, N. (2018). Decadal Changes of Earth's Outgoing Longwave Radiation. *Remote Sens.* 10. doi:10.3390/rs10101539.
Diamond, M., Director, H., Eastman, R., Possner, A., and Wood, R. (2019). Substantial Cloud Brightening from

Shipping in Subtropical Low Clouds. doi:10.1002/ESSOAR.10501145.1.

Dickinson, R. E. (1975). Solar Variability and the Lower Atmosphere. *Bull. Am. Meteorol. Soc.* 56, 1240–1248. doi:10.1175/1520-0477(1975)056<1240:svatla>2.0.co;2.

DiNezio, P. N., Clement, A. C., Vecchi, G. A., Soden, B. J., Kirtman, B. P., and Lee, S.-K. (2009). Climate Response of the Equatorial Pacific to Global Warming. *J. Clim.* 22, 4873–4892. doi:10.1175/2009jcli2982.1.

Dinh, T., and Fueglistaler, S. (2019). On the Causal Relationship between the Moist Diabatic Circulation and Cloud Rapid Adjustment to Increasing CO2. *J. Adv. Model. Earth Syst.* n/a. doi:10.1029/2019MS001853.

Doherty, S. J., Grenfell, T. C., Forsstrom, S., Hegg, D. L., Brandt, R. E., and Warren, S. G. (2013). Observed vertical redistribution of black carbon and other insoluble light-absorbing particles in melting snow. *J. Geophys. Res. Atmos* 118, 5553–5569. doi:10.1002/jgrd.50235.

Dolinar, E. K., Dong, X., Xi, B., Jiang, J. H., and Su, H. (2015). Evaluation of CMIP5 simulated clouds and TOA radiation budgets using NASA satellite observations. *Clim. Dyn.* 44, 2229–2247. doi:10.1007/s00382-014-2158-9.

Domingues, C. M., Church, J. A., White, N. J., Gleckler, P. J., Wijffels, S. E., Barker, P. M., et al. (2008). Improved estimates of upper-ocean warming and multi-decadal sea-level rise. *Nature*. doi:10.1038/nature07080.

Dong, L., and McPhaden, M. J. (2017). The effects of external forcing and internal variability on the formation of interhemispheric sea surface temperature gradient trends in the Indian Ocean. *J. Clim.* 30, 9077–9095. doi:10.1175/JCLI-D-17-0138.1.

Dong, Y., Armour, K. C., Proistosescu, C., and Battisti, D. S. (2019). Attributing Historical and Future Evolution of Radiative Feedbacks to Regional Warming. *J. Clim.* 32, 9. doi:10.1175/JCLI-D-18-0843.1.

Dong, Y., Armour, K. C., Zelinka, M. D., Proistosescu, C., Battisti, D. S., Zhou, C., et al. (9999). Inter-model spread in the sea-surface temperature pattern effect and its contribution to climate sensitivity in CMIP5 and CMIP6 models. *J. Clim.* (submitted.

Donohoe, A., Armour, K. C., Pendergrass, A. G., and Battisti, D. S. (2014a). Shortwave and longwave radiative contributions to global warming under increasing $CO_2$. *Proc. Natl. Acad. Sci.* doi:10.1073/pnas.1412190111.

Donohoe, A., Armour, K. C., Roe, G. H., Battisti, D. S., and Hahn, L. (9999). The partitioning of meridional heat transport from the Last Glacial Maximum to CO2 quadrupling in coupled climate models. *J. Clim.* (submitted.

Donohoe, A., and Battisti, D. S. (2011). Atmospheric and Surface Contributions to Planetary Albedo. *J. Clim.* 24, 4402–4418. doi:10.1175/2011JCLI3946.1.

Donohoe, A., and Battisti, D. S. (2012). What determines meridional heat transport in climate models? *J. Clim.* doi:10.1175/JCLI-D-11-00257.1.

Donohoe, A., Marshall, J., Ferreira, D., Armour, K., and Mcgee, D. (2014b). The interannual variability of tropical precipitation and interhemispheric energy transport. *J. Clim.* 27, 3377–3392. doi:10.1175/JCLI-D-13-00499.1.

Donohoe, A., Marshall, J., Ferreira, D., and Mcgee, D. (2013). The relationship between ITCZ location and cross-equatorial atmospheric heat transport: From the seasonal cycle to the last glacial maximum. *J. Clim.* doi:10.1175/JCLI-D-12-00467.1.

Doutriaux-Boucher, M., Webb, M. J., Gregory, J. M., and Boucher, O. (2009). Carbon dioxide induced stomatal closure increases radiative forcing via a rapid reduction in low cloud. *Geophys. Res. Lett.* 36, 1–5. doi:10.1029/2008GL036273.

Douville, H., Ribes, A., Decharme, B., Alkama, R., and Sheffield, J. (2013). Anthropogenic influence on multidecadal changes in reconstructed global evapotranspiration. *Nat. Clim. Chang.* 3, 59–62. doi:10.1038/NCLIMATE1632.

Dowsett, H. J., Robinson, M. M., Haywood, A. M., Hill, D. J., Dolan, A. M., Stoll, D. K., et al. (2012). Assessing confidence in Pliocene sea surface temperatures to evaluate predictive models. *Nat. Clim. Chang.* 2, 365–371. doi:10.1038/nclimate1455.

Du, J., Wang, K., Wang, J., and Ma, Q. (2017). Contributions of surface solar radiation and precipitation to the spatiotemporal patterns of surface and air warming in China from 1960 to 2003. *Atmos. Chem. Phys.* 17, 4931–4944. doi:10.5194/acp-17-4931-2017.

Duan, L., Cao, L., Bala, G., and Caldeira, K. (2018). Comparison of the Fast and Slow Climate Response to Three Radiation Management Geoengineering Schemes. *J. Geophys. Res. Atmos.* 123, 11,980-12,001. doi:10.1029/2018JD029034.

Dufresne, J. L., and Bony, S. (2008). An assessment of the primary sources of spread of global warming estimates from coupled atmosphere-ocean models. *J. Clim.* doi:10.1175/2008JCLI2239.1.

Dunne, E. M., Gordon, H., Kürten, A., Almeida, J., Duplissy, J., Williamson, C., et al. (2016). Global atmospheric particle formation from CERN CLOUD measurements. *Science (80-. ).* 354, 1119–1124. doi:10.1126/science.aaf2649.

Eastman, R., and Warren, S. G. (2013). A 39-yr survey of cloud changes from land stations worldwide 1971-2009: Long-term trends, relation to aerosols, and expansion of the tropical belt. *J. Clim.* 26, 1286–1303. doi:10.1175/JCLI-D-12-00280.1.

Ebmeier, S. K., Sayer, A. M., Grainger, R. G., Mather, T. A., and Carboni, E. (2014). Systematic satellite observations of the impact of aerosols from passive volcanic degassing on local cloud properties. *Atmos. Chem. Phys.* 14, 10601–10618. doi:10.5194/acp-14-10601-2014.

Edwards, M. R., and Trancik, J. E. (2014). Climate impacts of energy technologies depend on emissions timing. *Nat. Clim. Chang.* doi:10.1038/nclimate2204.

Egorova, T., Schmutz, W., Rozanov, E., Shapiro, A. ~I., Usoskin, I., Beer, J., et al. (2018). Revised historical solar irradiance forcing. *\aap* 615, A85. doi:10.1051/0004-6361/201731199.

Einstein, A. (1905). Über die von der molekularkinetischen Theorie der Wärme geforderte Bewegung von in ruhenden Flüssigkeiten suspendierten Teilchen. *Ann. Phys.* 322, 549–560. doi:10.1002/andp.19053220806.

Elagib, N. A., and Alvi, S. H. (2013). Moderate solar dimming in an accelerating warming climate of Bahrain. *Int. J. Glob. Warm.* 5, 96–107.

Emanuel, K., Wing, A. A., and Vincent, E. M. (2014). Radiative-convective instability. *J. Adv. Model. Earth Syst.* 6, 75–90. doi:10.1002/2013MS000270.

Engel, A., Bönisch, H., Ostermöller, J., Chipperfield, M. P., Dhomse, S., and Jöckel, P. (2018). A refined method for calculating equivalent effective stratospheric chlorine. *Atmos. Chem. Phys.* doi:10.5194/acp-18-601-2018.

England, M. H., Mcgregor, S., Spence, P., Meehl, G. A., Timmermann, A., Cai, W., et al. (2014). Recent intensification of wind-driven circulation in the Pacific and the ongoing warming hiatus. *Nat. Clim. Chang.* 4, 222–227. doi:10.1038/nclimate2106.

Erfani, E., and Burls, N. J. (2019). The Strength of Low-Cloud Feedbacks and Tropical Climate: A CESM Sensitivity Study. *J. Clim.*, JCLI-D-18-0551.1. doi:10.1175/JCLI-D-18-0551.1.

Etminan, M., Myhre, G., Highwood, E. J., and Shine, K. P. (2016). Radiative forcing of carbon dioxide, methane, and nitrous oxide: A significant revision of the methane radiative forcing. *Geophys. Res. Lett.* 43, 12,614-12,623. doi:10.1002/2016GL071930.

Exarchou, E., Kuhlbrodt, T., Gregory, J. M., and Smith, R. S. (2014). Ocean Heat Uptake Processes: A Model Intercomparison. *J. Clim.* 28, 887–908. doi:10.1175/JCLI-D-14-00235.1.

Farnsworth, A., Lunt, D. J., O'Brien, C. L., Foster, G. L., Inglis, G. N., Markwick, P., et al. (2019). Climate Sensitivity on Geological Timescales Controlled by Nonlinear Feedbacks and Ocean Circulation. *Geophys. Res. Lett.* 46, 9880–9889. doi:10.1029/2019GL083574.

Fedorov, A. V., Brierley, C. M., Lawrence, K. T., Liu, Z., Dekens, P. S., and Ravelo, A. C. (2013). Patterns and mechanisms of early Pliocene warmth. *Nature* 496, 43–49. doi:10.1038/nature12003.

Fedorov, A. V., Burls, N. J., Lawrence, K. T., and Peterson, L. C. (2015). Tightly linked zonal and meridional sea surface temperature gradients over the past five million years. *Nat. Geosci.* doi:10.1038/ngeo2577.

Feldl, N., Anderson, B. T., and Bordoni, S. (2017). Atmospheric eddies mediate lapse rate feedback and arctic amplification. *J. Clim.* doi:10.1175/JCLI-D-16-0706.1.

Feldl, N., and Bordoni, S. (2016). Characterizing the Hadley circulation response through regional climate feedbacks. *J. Clim.* 29, 613–622. doi:10.1175/JCLI-D-15-0424.1.

Feldl, N., and Roe, G. H. (2013). The nonlinear and nonlocal nature of climate feedbacks. *J. Clim.* doi:10.1175/JCLI-D-12-00631.1.

Feng, F., and Wang, K. (2019). Does the modern-era retrospective analysis for research and applications-2 aerosol reanalysis introduce an improvement in the simulation of surface solar radiation over China? *Int. J. Climatol.* 39, 1305–1318. doi:10.1002/joc.5881.

Fiedler, S., Stevens, B., and Mauritsen, T. (2017). On the sensitivity of anthropogenic aerosol forcing to model-internal variability and parameterizing a Twomey effect. *J. Adv. Model. Earth Syst.* 9, 1325–1341. doi:10.1002/2017MS000932.

Fischer, H., Meissner, K. J., Mix, A. C., Abram, N. J., Austermann, J., Brovkin, V., et al. (2018). Palaeoclimate constraints on the impact of 2 °C anthropogenic warming and beyond. *Nat. Geosci.* 11, 474–485. doi:10.1038/s41561-018-0146-0.

Fisher, J. B., Melton, F., Middleton, E., Hain, C., Anderson, M., Allen, R., et al. (2017). The future of evapotranspiration: Global requirements for ecosystem functioning, carbon and climate feedbacks, agricultural management, and water resources. *WATER Resour. Res.* 53, 2618–2626. doi:10.1002/2016WR020175.

Flanner, M. G., Shell, K. M., Barlage, M., Perovich, D. K., and Tschudi, M. A. (2011). Radiative forcing and albedo feedback from the {Northern Hemisphere} cryosphere between 1979 and 2008. *Nat. Geosci.* 4, 151–155. doi:10.1038/ngeo1062.

Flanner, M. G., and Zender, C. S. (2006). Linking snowpack microphysics and albedo evolution. *J. Geophys. Res.* 111. doi:10.1029/2005JD006834.

Flannery, B. P. (1984). Energy Balance Models Incorporating Transport of Thermal and Latent Energy. *J. Atmos. Sci.* 41. doi:10.1175/1520-0469(1984)041<0414:EBMITO>2.0.CO;2.

Flato, G., Marotzke, J., Abiodun, B., Braconnot, P., Chou, S. C. C., Collins, W., et al. (2013). "Evaluation of Climate Models," in *Climate Change 2013: The Physical Science Basis. Contribution of Working Group I to the Fifth Assessment Report of the Intergovernmental Panel on Climate Change*, eds. T. F. Stocker, D. Qin, G.-K. Plattner, M. Tignor, S. K. Allen, J. Boschung, et al. (Cambridge University Press, Cambridge, United Kingdom and New York, NY, USA), 741–866. doi:10.1017/CBO9781107415324.020.

Flynn, C. M., and Mauritsen, T. (9999). On the Climate Sensitivity and Historical Warming Evolution in Recent Coupled Model Ensembles. *Atmos. Chem. Phys. Discuss.* (submitted, n/a.

Foley, K. M., and Dowsett, H. J. (2019). Community sourced mid-Piacenzian sea surface temperature (SST) data. *U.S. Geol. Surv. data release*. doi:10.5066/P9YP3DTV.
Folini, D., and Wild, M. (2015). The effect of aerosols and sea surface temperature on China's climate in the late twentieth century from ensembles of global climate simulations. *J. Geophys. Res.* 120, 2261–2279. doi:10.1002/2014JD022851.
Ford, H. L., Ravelo, A. C., Dekens, P. S., LaRiviere, J. P., and Wara, M. W. (2015). The evolution of the equatorial thermocline and the early Pliocene El Padre mean state. *Geophys. Res. Lett.* 42, 4878–4887. doi:10.1002/2015GL064215.
Forest, C. E. (2002). Quantifying Uncertainties in Climate System Properties with the Use of Recent Climate Observations. *Science (80-. ).* 295, 113–117. doi:10.1126/science.1064419.
Forest, C. E. (2018). Inferred Net Aerosol Forcing Based on Historical Climate Changes: a Review. *Curr. Clim. Chang. Reports* 4, 11–22. doi:10.1007/s40641-018-0085-2.
Forget, G., and Ferreira, D. (2019). Global ocean heat transport dominated by heat export from the tropical Pacific. *Nat. Geosci.* 12, 351–354. doi:10.1038/s41561-019-0333-7.
Forster, P., Huppmann, D., Kriegler, E., Mundaca, L., Smith, C., Rogelj, J., et al. (2018). "Mitigation Pathways Compatible with 1.5°C in the Context of Sustainable Development Supplementary Material," in *Global Warming of 1.5°C. An IPCC Special Report on the impacts of global warming of 1.5°C above pre-industrial levels and related global greenhouse gas emission pathways, in the context of strengthening the global response to the threat of climate change,* eds. V. Masson-Delmotte, P. Zhai, H.-O. Pörtner, D. Roberts, J. Skea, P. R. Shukla, et al. (In Press). Available at: https://www.ipcc.ch/sr15.
Forster, P. M. (2016). Inference of Climate Sensitivity from Analysis of Earth's Energy Budget. *Annu. Rev. Earth Planet. Sci.* 44, 85–106. doi:10.1146/annurev-earth-060614-105156.
Forster, P. M., Andrews, T., Good, P., Gregory, J. M., Jackson, L. S., and Zelinka, M. (2013). Evaluating adjusted forcing and model spread for historical and future scenarios in the CMIP5 generation of climate models. *J. Geophys. Res. Atmos.* 118, 1139–1150. doi:10.1002/jgrd.50174.
Forster, P. M., Maycock, A. C., McKenna, C. M., and Smith, C. J. (2019). Latest climate models confirm need for urgent mitigation. *Nat. Clim. Chang.* doi:10.1038/s41558-019-0660-0.
Forster, P. M., Richardson, T., Maycock, A. C., Smith, C. J., Samset, B. H., Myhre, G., et al. (2016). Recommendations for diagnosing effective radiative forcing from climate models for CMIP6. *J. Geophys. Res.* doi:10.1002/2016JD025320.
Forster, P., Ramaswamy, V., Artaxo, P., Berntsen, T., Betts, R., Fahey, D. W., et al. (2007). "Changes in Atmospheric Constituents and in Radiative Forcing," in *Climate Change 2007. The Physical Science Basis*, eds. S. Solomon, D. Qin, M. Manning, Z. Chen, M. Marquis, K. B. Averyt, et al. (United Kingdom: Cambridge University Press). Available at: http://www.ipcc.ch/pdf/assessment-report/ar4/wg1/ar4-wg1-chapter2.pdf.
Foster, G. L., and Rae, J. W. B. (2016). Reconstructing Ocean pH with Boron Isotopes in Foraminifera. *Annu. Rev. Earth Planet. Sci.* 44, 207–237. doi:10.1146/annurev-earth-060115-012226.
Frame, D. J., Booth, B. B. B., Kettleborough, J. A., Stainforth, D. A., Gregory, J. M., Collins, M., et al. (2005). Constraining climate forecasts: The role of prior assumptions. *Geophys. Res. Lett.* 32. doi:10.1029/2004GL022241.
Frame, D. J., Stone, D. A., Stott, P. A., and Allen, M. R. (2006). Alternatives to stabilization scenarios. *Geophys. Res. Lett.* doi:10.1029/2006GL025801.
Friedrich, T., Timmermann, A., Tigchelaar, M., Timm, O. E., and Ganopolski, A. (2016). Nonlinear climate sensitivity and its implications for future greenhouse warming. *Sci. Adv.* 2. doi:10.1126/sciadv.1501923.
Frierson, D. M. W., and Hwang, Y. T. (2012). Extratropical influence on ITCZ shifts in slab ocean simulations of global warming. *J. Clim.* doi:10.1175/JCLI-D-11-00116.1.
Frierson, D. M. W., Hwang, Y. T., Fučkar, N. S., Seager, R., Kang, S. M., Donohoe, A., et al. (2013). Contribution of ocean overturning circulation to tropical rainfall peak in the Northern Hemisphere. *Nat. Geosci.* 6, 940–944. doi:10.1038/ngeo1987.
Fueglistaler, S. (2019). Observational Evidence for Two Modes of Coupling Between Sea Surface Temperatures, Tropospheric Temperature Profile, and Shortwave Cloud Radiative Effect in the Tropics. *Geophys. Res. Lett.* 46, 9890–9898. doi:10.1029/2019GL083990.
Fuglestvedt, J., Rogelj, J., Millar, R. J., Allen, M., Boucher, O., Cain, M., et al. (2018). Implications of possible interpretations of'greenhouse gas balance' in the Paris Agreement. *Philos. Trans. R. Soc. A Math. Phys. Eng. Sci.* 376. doi:10.1098/rsta.2016.0445.
Fuglestvedt, J. S., Berntsen, T. K., Godal, O., Sausen, R., Shine, K. P., and Skodvin, T. (2003). Metrics of climate change: Assessing radiative forcing and emission indices. *Clim. Change* 58, 267–331. doi:10.1023/A:1023905326842.
Fyke, J., Sergienko, O., Löfverström, M., Price, S., and Lenaerts, J. T. M. (2018). An Overview of Interactions and Feedbacks Between Ice Sheets and the Earth System. *Rev. Geophys.* 56, 361–408. doi:10.1029/2018RG000600.
Gan, C. M., Pleim, J., Mathur, R., Hogrefe, C., Long, C. N., Xing, J., et al. (2014). Assessment of the effect of air pollution controls on trends in shortwave radiation over the United States from 1995 through 2010 from multiple

observation networks. *Atmos. Chem. Phys.* 14, 1701–1715. doi:Doi 10.5194/Acp-14-1701-2014.
Garcia, R. D., Cuevas, E., Garcia, O. E., Cachorro, V. E., Palle, P., Bustos, J. J., et al. (2014). Reconstruction of global solar radiation time series from 1933 to 2013 at the Izana Atmospheric Observatory. *Atmos. Meas. Tech.* 7, 3139–3150. doi:Doi 10.5194/Amt-7-3139-2014.
Garuba, O. A., Lu, J., Liu, F., and Singh, H. A. (2018). The Active Role of the Ocean in the Temporal Evolution of Climate Sensitivity. *Geophys. Res. Lett.* doi:10.1002/2017GL075633.
Gasser, T., Peters, G. P., Fuglestvedt, J. S., Collins, W. J., Shindell, D. T., and Ciais, P. (2017). Accounting for the climate–carbon feedback in emission metric. *Earth Syst. Dyn.* 8, 235–253. doi:10.5194/esd-8-235-2017.
Gassó, S. (2008). Satellite observations of the impact of weak volcanic activity on marine clouds. *J. Geophys. Res.* 113, D14S19. doi:10.1029/2007JD009106.
Gebbie, G., and Huybers, P. (2019). The Little Ice Age and 20th Century Deep Pacific Cooling. *Science (80-. ).* 363, 70–74. doi:10.1126/science.aar8413.
Gentine, P., García García, A., Meier, R., Cuesta-Valero, F. J., Beltrami, H., Davin, E. L., et al. (9999). Large recent continental heat storage. *Nature* (submitted.
Geoffroy, O., Saint-Martin, D., Bellon, G., Voldoire, A., Olivié, D. J. L. L., and Tytéca, S. (2013a). Transient Climate Response in a Two-Layer Energy-Balance Model. Part II: Representation of the Efficacy of Deep-Ocean Heat Uptake and Validation for CMIP5 AOGCMs. *J. Clim.* 26, 1859–1876. doi:10.1175/JCLI-D-12-00196.1.
Geoffroy, O., Saint-martin, D., Olivié, D. J. L., Voldoire, A., Bellon, G., and Tytéca, S. (2013b). Transient climate response in a two-layer energy-balance model. Part I: Analytical solution and parameter calibration using CMIP5 AOGCM experiments. *J. Clim.* 26, 1841–1857. doi:10.1175/JCLI-D-12-00195.1.
Geoffroy, O., Saint-Martin, D., and Ribes, A. (2012). Quantifying the sources of spread in climate change experiments. *Geophys. Res. Lett.* 39. doi:10.1029/2012GL054172.
Gettelman, A., Hannay, C., Bacmeister, J. T., Neale, R. B., Pendergrass, A. G., Danabasoglu, G., et al. (2019). High Climate Sensitivity in the Community Earth System Model Version 2 (CESM2). *Geophys. Res. Lett.* 46, 8329–8337. doi:10.1029/2019GL083978.
Gettelman, A., Kay, J. E., and Shell, K. M. (2012). The evolution of climate sensitivity and climate feedbacks in the Community Atmosphere Model. *J. Clim.* 25, 1453–1469. doi:10.1175/JCLI-D-11-00197.1.
Gettelman, A., Shindell, D. T., and Lamarque, J. F. (2015). Impact of aerosol radiative effects on 2000–2010 surface temperatures. *Clim. Dyn.* doi:10.1007/s00382-014-2464-2.
Ghan, S. J. (2013). Technical note: Estimating aerosol effects on cloud radiative forcing. *Atmos. Chem. Phys.* doi:10.5194/acp-13-9971-2013.
Ghan, S., Wang, M., Zhang, S., Ferrachat, S., Gettelman, A., Griesfeller, J., et al. (2016). Challenges in constraining anthropogenic aerosol effects on cloud radiative forcing using present-day spatiotemporal variability. *Proc. Natl. Acad. Sci. U. S. A.* 113, 5804–11. doi:10.1073/pnas.1514036113.
Ghimire, B., Williams, C. A., Masek, J., Gao, F., Wang, Z., Schaaf, C., et al. (2014). Global albedo change and radiative cooling from anthropogenic land cover change, 1700 to 2005 based on MODIS, land use harmonization, radiative kernels, and reanalysis. *Geophys. Res. Lett.* doi:10.1002/2014GL061671.
Gilgen, A., Huang, W. T. K., Ickes, L., Neubauer, D., and Lohmann, U. (2018). How important are future marine and shipping aerosol emissions in a warming Arctic summer and autumn? *Atmos. Chem. Phys.* 18, 10521–10555. doi:10.5194/acp-18-10521-2018.
Gillett, N. P., Arora, V. K., Flato, G. M., Scinocca, J. F., and Von Salzen, K. (2012). Improved constraints on 21st-century warming derived using 160 years of temperature observations. *Geophys. Res. Lett.* 39, 1–5. doi:10.1029/2011GL050226.
Gillett, N. P., Arora, V. K., Matthews, D., and Allen, M. R. (2013). Constraining the ratio of global warming to cumulative CO2 emissions using CMIP5 simulations. *J. Clim.* 26, 6844–6858. doi:10.1175/JCLI-D-12-00476.1.
Gillett, N. P., and Matthews, H. D. (2010). Accounting for carbon cycle feedbacks in a comparison of the global warming effects of greenhouse gases. *Environ. Res. Lett.* 5. doi:10.1088/1748-9326/5/3/034011.
Giorgetta, M. A., Jungclaus, J., Reick, C. H., Legutke, S., Bader, J., Böttinger, M., et al. (2013). Climate and carbon cycle changes from 1850 to 2100 in MPI-ESM simulations for the Coupled Model Intercomparison Project phase 5. *J. Adv. Model. Earth Syst.* 5, 572–597. doi:10.1002/jame.20038.
Gleckler, P. J., Durack, P. J., Stouffer, R. J., Johnson, G. C., and Forest, C. E. (2016). Industrial-era global ocean heat uptake doubles in recent decades. *Nat. Clim. Chang.* 6, 394. Available at: http://dx.doi.org/10.1038/nclimate2915.
Goelzer, H., Huybrechts, P., Loutre, M. F., Goosse, H., Fichefet, T., and Mouchet, A. (2011). Impact of Greenland and Antarctic ice sheet interactions on climate sensitivity. *Clim. Dyn.* 37, 1005–1018. doi:10.1007/s00382-010-0885-0.
Golaz, J. C., Golaz, J. C., and Levy, H. (2013). Cloud tuning in a coupled climate model: Impact on 20th century warming. *Geophys. Res. Lett.* 40, 2246–2251. doi:10.1002/grl.50232.
Goldner, A., Herold, N., and Huber, M. (2014). Antarctic glaciation caused ocean circulation changes at the Eocene-Oligocene transition. *Nature* 511, 574–577. doi:10.1038/nature13597.
Golledge, N. R., Keller, E. D., Gomez, N., Naughten, K. A., Bernales, J., Trusel, L. D., et al. (2019). Global environmental consequences of twenty-first-century ice-sheet melt. *Nature* 566, 65–72. doi:10.1038/s41586-019-

0889-9.
Gong, T., Feldstein, S., and Lee, S. (2017). The role of downward infrared radiation in the recent arctic winter warming trend. *J. Clim.* doi:10.1175/JCLI-D-16-0180.1.
Good, P., Gregory, J. M., Lowe, J. A., and Andrews, T. (2013). Abrupt CO2 experiments as tools for predicting and understanding CMIP5 representative concentration pathway projections. *Clim. Dyn.* 40, 1041–1053. doi:10.1007/s00382-012-1410-4.
Good, P., Lowe, J. A., Andrews, T., Wiltshire, A., Chadwick, R., Ridley, J. K., et al. (2015). Nonlinear regional warming with increasing CO2 concentrations. *Nat. Clim. Chang.* 5, 138–142. doi:10.1038/nclimate2498.
Goodwin, P. (2016). How historic simulation–observation discrepancy affects future warming projections in a very large model ensemble. *Clim. Dyn.* 47, 2219–2233. doi:10.1007/s00382-015-2960-z.
Goodwin, P. (2018). On the Time Evolution of Climate Sensitivity and Future Warming. *Earth's Futur.* 6, 1336–1348. doi:10.1029/2018EF000889.
Goosse, H., Kay, J. E., Armour, K. C., Bodas-Salcedo, A., Chepfer, H., Docquier, D., et al. (2018). Quantifying climate feedbacks in polar regions. *Nat. Commun.* doi:10.1038/s41467-018-04173-0.
Gordon, H., Kirkby, J., Baltensperger, U., Bianchi, F., Breitenlechner, M., Curtius, J., et al. (2017). Causes and importance of new particle formation in the present-day and preindustrial atmospheres. *J. Geophys. Res. Atmos.* 122, 8739–8760. doi:10.1002/2017JD026844.
Gordon, H., Sengupta, K., Rap, A., Duplissy, J., Frege, C., Williamson, C., et al. (2016). Reduced anthropogenic aerosol radiative forcing caused by biogenic new particle formation. *Proc. Natl. Acad. Sci. U. S. A.* 113, 12053–12058. doi:10.1073/pnas.1602360113.
Gordon, N. D., Jonko, A. K., Forster, P. M., and Shell, K. M. (2013). An observationally based constraint on the water-vapor feedback. *J. Geophys. Res. Atmos.* 118, 12435–12443. doi:10.1002/2013JD020184.
Gordon, N. D., and Klein, S. A. (2014). Low-cloud optical depth feedback in climate models. *J. Geophys. Res. Atmos.* 119, 6052–6065. doi:10.1002/2013JD021052.
Goren, T., and Rosenfeld, D. (2014). Decomposing aerosol cloud radiative effects into cloud cover, liquid water path and Twomey components in marine stratocumulus. *Atmos. Res.* 138, 378–393. doi:10.1016/J.ATMOSRES.2013.12.008.
Grandey, B. S., Rothenberg, D., Avramov, A., Jin, Q., Lee, H. H., Liu, X., et al. (2018). Effective radiative forcing in the aerosol-climate model CAM5.3-MARC-ARG. *Atmos. Chem. Phys.* 18, 15783–15810. doi:10.5194/acp-18-15783-2018.
Grandey, B. S., Stier, P., and Wagner, T. M. (2013). Investigating relationships between aerosol optical depth and cloud fraction using satellite, aerosol reanalysis and general circulation model data. *Atmos. Chem. Phys.* 13, 3177–3184. doi:10.5194/acp-13-3177-2013.
Graversen, R. G., and Burtu, M. (2016). Arctic amplification enhanced by latent energy transport of atmospheric planetary waves. *Q. J. R. Meteorol. Soc.* 142, 2046–2054. doi:10.1002/qj.2802.
Graversen, R. G., Langen, P. L., and Mauritsen, T. (2014). Polar Amplification in CCSM4: Contributions from the Lapse Rate and Surface Albedo Feedbacks. *J. Clim.* 27, 4433–4450. doi:10.1175/JCLI-D-13-00551.1.
Graversen, R. G., and Wang, M. (2009). Polar amplification in a coupled climate model with locked albedo. *Clim. Dyn.* doi:10.1007/s00382-009-0535-6.
Gray, L. J., Rumbold, S. T., and Shine, K. P. (2009). Stratospheric Temperature and Radiative Forcing Response to 11-Year Solar Cycle Changes in Irradiance and Ozone. *J. Atmos. Sci.* 66, 2402–2417. doi:10.1175/2009jas2866.1.
Gregory, J. M. (2000). Vertical heat transports in the ocean and their effect on time-dependent climate change. *Clim. Dyn.* doi:10.1007/s003820000059.
Gregory, J. M., and Andrews, T. (2016). Variation in climate sensitivity and feedback parameters during the historical period. *Geophys. Res. Lett.* doi:10.1002/2016GL068406.
Gregory, J. M., Andrews, T., Ceppi, P., Mauritsen, T., and Webb, M. J. (2019). How accurately can the climate sensitivity to CO2 be estimated from historical climate change? *Clim. Dyn.* doi:10.1007/s00382-019-04991-y.
Gregory, J. M., Andrews, T., and Good, P. (2015). The inconstancy of the transient climate response parameter under increasing CO2. *Philos. Trans. R. Soc. A Math. Phys. Eng. Sci.* 373. doi:10.1098/rsta.2014.0417.
Gregory, J. M., Andrews, T., Good, P., Mauritsen, T., and Forster, P. M. (2016). Small global-mean cooling due to volcanic radiative forcing. *Clim. Dyn.* 47, 3979–3991. doi:10.1007/s00382-016-3055-1.
Gregory, J. M., Ingram, W. J., Palmer, M. A., Jones, G. S., Stott, P. A., Thorpe, R. B., et al. (2004). A new method for diagnosing radiative forcing and climate sensitivity. *Geophys. Res. Lett.* 31, L03205. doi:10.1029/2003GL018747.
Gregory, J. M., Jones, C. D., Cadule, P., and Friedlingstein, P. (2009). Quantifying carbon cycle feedbacks. *J. Clim.* 22, 5232–5250. doi:10.1175/2009JCLI2949.1.
Gregory, J. M., Stouffer, R. J., Raper, S. C. B., Stott, P. A., and Rayner, N. A. (2002). An observationally based estimate of the climate sensitivity. *J. Clim.* 15, 3117–3121. doi:10.1175/1520-0442(2002)015<3117:AOBEOT>2.0.CO;2.
Greve, P., Orlowsky, B., Mueller, B., Sheffield, J., Reichstein, M., and Seneviratne, S. I. (2014). Global assessment of trends in wetting and drying over land (vol 7, pg 716, 2014). *Nat. Geosci.* 7. doi:10.1038/NGEO2274.

Grise, K. M., and Medeiros, B. (2016). Understanding the Varied Influence of Midlatitude Jet Position on Clouds and Cloud Radiative Effects in Observations and Global Climate Models. *J. Clim.* 29, 9005–9025. doi:10.1175/JCLI-D-16-0295.1.

Grise, K. M., Polvani, L. M., Tselioudis, G., Wu, Y., and Zelinka, M. D. (2013). The ozone hole indirect effect: Cloud-radiative anomalies accompanying the poleward shift of the eddy-driven jet in the Southern Hemisphere. *Geophys. Res. Lett.* doi:10.1002/grl.50675.

Grise, K. M., Son, S. W., Correa, G. J. P., and Polvani, L. M. (2014). The response of extratropical cyclones in the Southern Hemisphere to stratospheric ozone depletion in the 20th century. *Atmos. Sci. Lett.* doi:10.1002/asl2.458.

Grose, M. R., Gregory, J., Colman, R., and Andrews, T. (2018). What Climate Sensitivity Index Is Most Useful for Projections? *Geophys. Res. Lett.* 45, 1559–1566. doi:10.1002/2017GL075742.

Grosvenor, D. P., Sourdeval, O., Zuidema, P., Ackerman, A., Alexandrov, M. D., Bennartz, R., et al. (2018). Remote Sensing of Droplet Number Concentration in Warm Clouds: A Review of the Current State of Knowledge and Perspectives. *Rev. Geophys.* 56, 409–453. doi:10.1029/2017RG000593.

Gryspeerdt, E., Goren, T., Sourdeval, O., Quaas, J., Mülmenstädt, J., Dipu, S., et al. (2018a). Constraining the aerosol influence on cloud liquid water path. *Atmos. Chem. Phys. Discuss.*, 1–25. doi:10.5194/acp-2018-885.

Gryspeerdt, E., Quaas, J., and Bellouin, N. (2016). Constraining the aerosol influence on cloud fraction. *J. Geophys. Res. Atmos.* 121, 3566–3583. doi:10.1002/2015JD023744.

Gryspeerdt, E., Quaas, J., Ferrachat, S., Gettelman, A., Ghan, S., Lohmann, U., et al. (2017). Constraining the instantaneous aerosol influence on cloud albedo. *Proc. Natl. Acad. Sci. U. S. A.* 114, 4899–4904. doi:10.1073/pnas.1617765114.

Gryspeerdt, E., Sourdeval, O., Quaas, J., Delanoë, J., Krämer, M., and Kühne, P. (2018b). Ice crystal number concentration estimates from lidar–radar satellite remote sensing – Part 2: Controls on the ice crystal number concentration. *Atmos. Chem. Phys.* 18, 14351–14370. doi:10.5194/acp-18-14351-2018.

Gryspeerdt, E., Stier, P., and Grandey, B. S. (2014a). Cloud fraction mediates the aerosol optical depth-cloud top height relationship. *Geophys. Res. Lett.* 41, 3622–3627. doi:10.1002/2014GL059524.

Gryspeerdt, E., Stier, P., and Partridge, D. G. (2014b). Satellite observations of cloud regime development: the role of aerosol processes. *Atmos. Chem. Phys.* 14, 1141–1158. doi:10.5194/acp-14-1141-2014.

Gulev, S. K., and Belyaev, K. (2012). Probability Distribution Characteristics for Surface Air-Sea Turbulent Heat Fluxes over the Global Ocean. *J. Clim.* 25, 184–206. doi:10.1175/2011JCLI4211.1.

Hall, A. (2004). The role of surface albedo feedback in climate. *J. Clim.* 17, 1550–1568. doi:10.1175/1520-0442(2004)017<1550:TROSAF>2.0.CO;2.

Hansen, J., Lacis, A., Rind, D., Russell, G., Stone, P., Fung, I., et al. (1984). "Climate sensitivity: Analysis of feedback mechanisms," in *AGU Geophysical Monograph*, eds. J. E. Hansen and T. Takahashi (Washington, D. C., D. C.: AGU), 130–163.

Hansen, J., Nazarenko, L., Ruedy, R., Sato, M., Willis, J., Del Genio, A., et al. (2005a). Earth's energy imbalance: Confirmation and implications. *Science (80-. ).* 308, 1431–1435. doi:10.1126/science.1110252.

Hansen, J., Russell, G., Lacis, A., Fung, I., Rind, D., and Stone, P. (1985). Climate Response Times: Dependence on Climate Sensitivity and Ocean Mixing. *Science (80-. ).* 229, 857–859. doi:10.1126/science.229.4716.857.

Hansen, J., Sato, M., Ruedy, R., Nazarenko, L., Lacis, A., Schmidt, G. a., et al. (2005b). Efficacy of climate forcings. *J. Geophys. Res.* 110, 1–45. doi:10.1029/2005JD005776.

Hansen, J., Sato, M., Russell, G., and Kharecha, P. (2013). Climate sensitivity, sea level and atmospheric carbon dioxide. *Philos. Trans. R. Soc. A Math. Phys. Eng. Sci.* 371. doi:10.1098/rsta.2012.0294.

Hargreaves, J. C., and Annan, J. D. (2016). Could the Pliocene constrain the equilibrium climate sensitivity? *Clim. Past* 12, 1591–1599. doi:10.5194/cp-12-1591-2016.

Hargreaves, J. C., Annan, J. D., Yoshimori, M., and Abe-Ouchi, A. (2012). Can the Last Glacial Maximum constrain climate sensitivity? *Geophys. Res. Lett.* 39, 1–5. doi:10.1029/2012GL053872.

Harper, A. B., Wiltshire, A. J., Cox, P. M., Friedlingstein, P., Jones, C. D., Mercado, L. M., et al. (2018). Vegetation distribution and terrestrial carbon cycle in a carbon cycle configuration of JULES4.6 with new plant functional types. *Geosci. Model Dev.* 11, 2857–2873. doi:10.5194/gmd-11-2857-2018.

Hartmann, D. J., Klein Tank, A. M. G., Rusticucci, M., Alexander, L. V, Brönnimann, S., Charabi, Y. A.-R., et al. (2013). "Observations: Atmosphere and Surface," in *Climate Change 2013: The Physical Science Basis. Contribution of Working Group I to the Fifth Assessment Report of the Intergovernmental Panel on Climate Change*, eds. T. F. Stocker, D. Qin, G.-K. Plattner, M. Tignor, S. K. Allen, J. Boschung, et al. (Cambridge, United Kingdom and New York, NY, USA: Cambridge University Press), 159–254. doi:10.1017/CBO9781107415324.008.

Hartmann, D. L., and Larson, K. (2002). An important constraint on tropical cloud - climate feedback. *Geophys. Res. Lett.* 29, 1951. doi:10.1029/2002GL015835.

Harvey, L. D. D. (2000). *Global warming : the hard science*. Prentice Hall.

Harvey, L. D. D., Gregrory, J., Hoffert, M., Jain, A., Lal, M., Leemans, R., et al. (1997). "An Introduction to Simple Climate Models used in the IPCC Second Assessment Report," in, eds. J. Houghton, L. G. Meira Filho, D. Griggs, and K. Maskell.

Hasselmann, K. (1976). Stochastic climate models Part I. Theory. *Tellus* 28, 473–485. doi:10.1111/j.2153-3490.1976.tb00696.x.
Haugstad, A. D., Armour, K. C., Battisti, D. S., and Rose, B. E. J. (2017). Relative roles of surface temperature and climate forcing patterns in the inconstancy of radiative feedbacks. *Geophys. Res. Lett.* 44, 7455–7463. doi:10.1002/2017GL074372.
Hawcroft, M., Haywood, J. M., Collins, M., Jones, A., Jones, A. C., and Stephens, G. (2017). Southern Ocean albedo, inter-hemispheric energy transports and the double ITCZ: global impacts of biases in a coupled model. *Clim. Dyn.* 48, 2279–2295. doi:10.1007/s00382-016-3205-5.
Hawkins, E., and Sutton, R. (2012). Time of emergence of climate signals. *Geophys. Res. Lett.* 39. doi:10.1029/2011GL050087.
Haywood, A. M., Dolan, A. M., Pickering, S. J., Dowsett, H. J., McClymont, E. L., Prescott, C. L., et al. (2013). On the identification of a Pliocene time slice for data model comparison. *Philos. Trans. R. Soc. London A Math. Phys. Eng. Sci.* 371. doi:10.1098/rsta.2012.0515.
Haywood, A. M., Dowsett, H. J., and Dolan, A. M. (2016a). Integrating geological archives and climate models for the mid-Pliocene warm period. *Nat. Commun.* 7, 10646. doi:10.1038/ncomms10646.
Haywood, A. M., Dowsett, H. J., Dolan, A. M., Rowley, D., Abe-Ouchi, A., Otto-Bliesner, B., et al. (2016b). The Pliocene Model Intercomparison Project (PlioMIP) Phase 2: scientific objectives and experimental design. *Clim. Past* 12, 663–675. doi:10.5194/cp-12-663-2016.
Haywood, A. M., Tindall, J. C., Dowsett, H. J., Dolan, A. M., Foley, K. M., Hunter, J., et al. (9999). A return to large-scale features of Pliocene climate: the Pliocene Model Intercomparison Project Phase 2. *Clim. Past Discuss.* (submitted. doi:10.5194/cp-2019-145.
He, C., Liu, Z., and Hu, A. (2019). The transient response of atmospheric and oceanic heat transports to anthropogenic warming. *Nat. Clim. Chang.* doi:10.1038/s41558-018-0387-3.
He, Y., Wang, K., Zhou, C., and Wild, M. (2018). A Revisit of Global Dimming and Brightening Based on the Sunshine Duration. *Geophys. Res. Lett.* 45, 4281–4289. doi:10.1029/2018GL077424.
Heede, U. K., Fedorov, A. V., and Burls, N. (9999). Timescales and Mechanisms for the Tropical Pacific Response to Global Warming. (submitted.
Held, I. M., and Shell, K. M. (2012). Using Relative Humidity as a State Variable in Climate Feedback Analysis. 25, 2578–2582. doi:10.1175/JCLI-D-11-00721.1.
Held, I. M., and Soden, B. J. (2006). Robust Responses of the Hydrological Cycle to Global Warming. *J. Clim.* 19, 5686–5699. doi:10.1175/JCLI3990.1.
Held, I. M., Winton, M., Takahashi, K., Delworth, T., Zeng, F., and Vallis, G. K. (2010). Probing the Fast and Slow Components of Global Warming by Returning Abruptly to Preindustrial Forcing. *J. Clim.* 23, 2418–2427. doi:10.1175/2009JCLI3466.1.
Hellweg, S., and Milà i Canals, L. (2014). Emerging approaches, challenges and opportunities in life cycle assessment. *Science (80-. ).* 344, 1109–1113. doi:10.1126/science.1248361.
Heyn, I., Block, K., Mülmenstädt, J., Gryspeerdt, E., Kühne, P., Salzmann, M., et al. (2017). Assessment of simulated aerosol effective radiative forcings in the terrestrial spectrum. *Geophys. Res. Lett.* doi:10.1002/2016GL071975.
Hodnebrog, Ø., Dalsøren, S. B., and Myhre, G. (2018). Lifetimes, direct and indirect radiative forcing, and global warming potentials of ethane (C2H6), propane (C3H8), and butane (C4H10). *Atmos. Sci. Lett.* doi:10.1002/asl.804.
Hodnebrog, Ø., Etminan, M., Fuglestvedt, J. S., Marston, G., Myhre, G., Nielsen, C. J., et al. (2013). Global warming potentials and radiative efficiencies of halocarbons and related compounds: A comprehensive review. *Rev. Geophys.* 51, 300–378. doi:10.1002/rog.20013.
Hodnebrog, Ø., Myhre, G., and Samset, B. H. (2014). How shorter black carbon lifetime alters its climate effect. *Nat. Commun.* 5, 5065. doi:10.1038/ncomms6065.
Hoesly, R. M., Smith, S. J., Feng, L., Klimont, Z., Janssens-Maenhout, G., Pitkanen, T., et al. (2018). Historical (1750–2014) anthropogenic emissions of reactive gases and aerosols from the Community Emissions Data System (CEDS). *Geosci. Model Dev.* 11, 369–408. doi:10.5194/gmd-11-369-2018.
Holland, M. M., and Bitz, C. M. (2003). Polar amplification of climate change in coupled models. *Clim. Dyn.* doi:10.1007/s00382-003-0332-6.
Hollis, C. J., Dunkley Jones, T., Anagnostou, E., Bijl, P. K., Cramwinckel, M. J., Cui, Y., et al. (2019). The DeepMIP contribution to PMIP4: methodologies for selection, compilation and analysis of latest Paleocene and early Eocene climate proxy data, incorporating version 0.1 of the DeepMIP database. *Geosci. Model Dev.* 12, 3149–3206. doi:10.5194/gmd-12-3149-2019.
Hopcroft, P. O., and Valdes, P. J. (2015). How well do simulated last glacial maximum tropical temperatures constrain equilibrium climate sensitivity? *Geophys. Res. Lett.* 42, 5533–5539. doi:10.1002/2015GL064903.
Houghton, J. T., Jenkins, G. J., and Ephraums, J. J. (1990). *Climate Change The IPCC Scientific Assessment*. doi:10.1097/MOP.0b013e3283444c89.
Hourdin, F., Mauritsen, T., Gettelman, A., Golaz, J.-C., Balaji, V., Duan, Q., et al. (2017). The Art and Science of Climate Model Tuning. *Bull. Am. Meteorol. Soc.* 98, 589–602. doi:10.1175/BAMS-D-15-00135.1.

Hua, W., Dai, A., and Qin, M. (2018). Contributions of Internal Variability and External Forcing to the Recent Pacific Decadal Variations. *Geophys. Res. Lett.* 45, 7084–7092. doi:10.1029/2018GL079033.
Huang, G., Li, Z., Li, X., Liang, S., Yang, K., Wang, D., et al. (2019). Estimating surface solar irradiance from satellites: Past, present, and future perspectives. *Remote Sens. Environ.* 233, 111371. doi:10.1016/J.RSE.2019.111371.
Huang, P., Xie, S. P., Hu, K., Huang, G., and Huang, R. (2013). Patterns of the seasonal response of tropical rainfall to global warming. *Nat. Geosci.* 6, 357–361. doi:10.1038/ngeo1792.
Huang, Y., Xia, Y., and Tan, X. (2017). On the pattern of $CO_2$ radiative forcing and poleward energy transport. *J. Geophys. Res. Atmos.* doi:10.1002/2017JD027221.
Huang, Y., and Zhang, M. (2014). The implication of radiative forcing and feedback for meridional energy transport. *Geophys. Res. Lett.* doi:10.1002/2013GL059079.
Huang, Y., Zhang, M., Xia, Y., Hu, Y., and Son, S.-W. (2016). Is there a stratospheric radiative feedback in global warming simulations? *Clim. Dyn.* 46, 177–186. doi:10.1007/s00382-015-2577-2.
Huber, M., Beyerle, U., and Knutti, R. (2014). Estimating climate sensitivity and future temperature in the presence of natural climate variability. *Geophys. Res. Lett.* 41, 2086–2092. doi:10.1002/2013GL058532.
Huber, M., and Caballero, R. (2011). The early Eocene equable climate problem revisited. *Clim. Past* 7, 603–633. doi:10.5194/cp-7-603-2011.
Huber, M., Mahlstein, I., Wild, M., Fasullo, J., and Knutti, R. (2010). Constraints on Climate Sensitivity from Radiation Patterns in Climate Models. *J. Clim.* 24, 1034–1052. doi:10.1175/2010JCLI3403.1.
Hurtt, G. C., Chini, L. P., Frolking, S., Betts, R. A., Feddema, J., Fischer, G., et al. (2011). Harmonization of land-use scenarios for the period 1500-2100: 600 years of global gridded annual land-use transitions, wood harvest, and resulting secondary lands. *Clim. Change*. doi:10.1007/s10584-011-0153-2.
Huss, M., Funk, M., and Ohmura, A. (2009). Strong Alpine glacier melt in the 1940s due to enhanced solar radiation. *Geophys. Res. Lett.* 36. doi:10.1029/2009GL040789.
Huybers, P. (2010). Compensation between Model Feedbacks and Curtailment of Climate Sensitivity. *J. Clim.* 23, 3009–3018. doi:10.1175/2010JCLI3380.1.
Hwang, Y.-T., and Frierson, D. M. W. (2013). Link between the double-Intertropical Convergence Zone problem and cloud biases over the Southern Ocean. *Proc. Natl. Acad. Sci.* doi:10.1073/pnas.1213302110.
Hwang, Y. T., and Frierson, D. M. W. (2010). Increasing atmospheric poleward energy transport with global warming. *Geophys. Res. Lett.* doi:10.1029/2010GL045440.
Hwang, Y. T., Frierson, D. M. W., and Kay, J. E. (2011). Coupling between Arctic feedbacks and changes in poleward energy transport. *Geophys. Res. Lett.* doi:10.1029/2011GL048546.
Imamovic, A., Tanaka, K., Folini, D., and Wild, M. (2016). Global dimming and urbanization: did stronger negative SSR trends collocate with regions of population growth? *Atmos. Chem. Phys.* 16, 2719–2725. doi:10.5194/acp-16-2719-2016.
Ingram, W. (2010). A very simple model for the water vapour feedback on climate change. *Q. J. R. Meteorol. Soc.* 136, 30–40. doi:10.1002/qj.546.
Ingram, W. (2013). A new way of quantifying GCM water vapour feedback. *Clim. Dyn.* 40, 913–924. doi:10.1007/s00382-012-1294-3.
Jahani, B., Dinpashoh, Y., and Wild, M. (2018). Dimming in Iran since the 2000s and the potential underlying causes. *Int. J. Climatol.* 38, 1543–1559. doi:10.1002/joc.5265.
Jia, G., Shevliakova, E., Artaxo, P., De Noblt-Ducoudre, N., and Houghton, R. (2019). "Land-Climate Interactions," in *SRCCL Special Report on Climate Change and Land*.
Jiao, C., Flanner, M. G., Balkanski, Y., Bauer, S. E., Bellouin, N., Berntsen, T. K., et al. (2014). An AeroCom assessment of black carbon in Arctic snow and sea ice. *Atmos. Chem. Phys.* 14, 2399–2417. doi:10.5194/acp-14-2399-2014.
Jiménez-de-la-Cuesta, D., and Mauritsen, T. (2019). Emergent constraints on Earth's transient and equilibrium response to doubled CO2 from post-1970s global warming. *Nat. Geosci.* 2015. doi:10.1038/s41561-019-0463-y.
Johansson, D. J. A. (2012). Economics- and physical-based metrics for comparing greenhouse gases. *Clim. Change*. doi:10.1007/s10584-011-0072-2.
Johansson, D. J. A., O'Neill, B. C., Tebaldi, C., and Häggström, O. (2015). Equilibrium climate sensitivity in light of observations over the warming hiatus. *Nat. Clim. Chang.* 5, 449. Available at: https://doi.org/10.1038/nclimate2573.
Johnson, G. C., Lyman, J. M., and Loeb, N. G. (2016). Improving estimates of Earth's energy imbalance. *Nat. Clim. Chang.* 6, 639–640. doi:10.1038/nclimate3043.
Jonko, A. K., Shell, K. M., Sanderson, B. M., and Danabasoglu, G. (2013). Climate Feedbacks in CCSM3 under Changing CO2 Forcing. Part II: Variation of Climate Feedbacks and Sensitivity with Forcing. *J. Clim.* 26, 2784–2795. doi:10.1175/JCLI-D-12-00479.1.
Joos, F., Roth, R., Fuglestvedt, J. S., Peters, G. P., Enting, I. G., Von Bloh, W., et al. (2013). Carbon dioxide and climate impulse response functions for the computation of greenhouse gas metrics: A multi-model analysis. *Atmos. Chem. Phys.* 13, 2793–2825. doi:10.5194/acp-13-2793-2013.

Joshi, M. M., Webb, M. J., Maycock, A. C., and Collins, M. (2010). Stratospheric water vapour and high climate sensitivity in a version of the HadSM3 climate model. *Atmos. Chem. Phys.* 10, 7161–7167. doi:10.5194/acp-10-7161-2010.
Jungclaus, J. H., Bard, E., Baroni, M., Braconnot, P., Cao, J., Chini, L. P., et al. (2017). The PMIP4 contribution to CMIP6 -- Part 3: The last millennium, scientific objective, and experimental design for \hack{\newline} the PMIP4 \textit{past1000} simulations. *Geosci. Model Dev.* 10, 4005–4033. doi:10.5194/gmd-10-4005-2017.
Jungclaus, J. H., Lohmann, K., and Zanchettin, D. (2014). Enhanced 20th century heat transfer to the Arctic simulated in the context of climate variations over the last millennium. *Clim. Past Discuss.* doi:10.5194/cpd-10-2895-2014.
Kaercher, B. (2018). Formation and radiative forcing of contrail cirrus. *Nat. Commun.* doi:10.1038/s41467-018-04068-0.
Kageyama, M., Harrison, S. P., Kapsch, M., Löfverström, M., Lora, J. M., Sherriff-tadano, S., et al. (9999). The PMIP4-CMIP6 Last Glacial Maximum experiments: preliminary results and comparison with the PMIP3-CMIP5 simulations. (submitted.
Kajtar, J. B., Santoso, A., England, M. H., and Cai, W. (2017). Tropical climate variability: interactions across the Pacific, Indian, and Atlantic Oceans. *Clim. Dyn.* 48, 2173–2190. doi:10.1007/s00382-016-3199-z.
Kajtar, J. B., Santoso, A., McGregor, S., England, M. H., and Baillie, Z. (2018). Model under-representation of decadal Pacific trade wind trends and its link to tropical Atlantic bias. *Clim. Dyn.* 50, 1471–1484. doi:10.1007/s00382-017-3699-5.
Kamae, Y., Ogura, T., Watanabe, M., Xie, S. P., and Ueda, H. (2016). Robust cloud feedback over tropical land in a warming climate. *J. Geophys. Res.* 121, 2593–2609. doi:https://doi.org/10.1002/2015JD024525.
Kang, S. M., Held, I. M., Frierson, D. M. W., and Zhao, M. (2008). The response of the ITCZ to extratropical thermal forcing: Idealized slab-ocean experiments with a GCM. *J. Clim.* doi:10.1175/2007JCLI2146.1.
Kang, S. M., and Xie, S. P. (2014). Dependence of climate response on meridional structure of external thermal forcing. *J. Clim.* 27, 5593–5600. doi:10.1175/JCLI-D-13-00622.1.
Kanji, Z. A., Ladino, L. A., Wex, H., Boose, Y., Burkert-Kohn, M., Cziczo, D. J., et al. (2017). Overview of Ice Nucleating Particles. *Meteorol. Monogr.* 58, 1.1-1.33. doi:10.1175/AMSMONOGRAPHS-D-16-0006.1.
Karset, I. H. H., Berntsen, T. K., Storelvmo, T., Alterskjær, K., Grini, A., Olivié, D., et al. (2018). Strong impacts on aerosol indirect effects from historical oxidant changes. *Atmos. Chem. Phys.* 18, 7669–7690. doi:10.5194/acp-18-7669-2018.
Kato, S., Rose, F. G., Rutan, D. A., Thorsen, T. J., Loeb, N. G., Doelling, D. R., et al. (2018). Surface Irradiances of Edition 4.0 Clouds and the Earth’s Radiant Energy System (CERES) Energy Balanced and Filled (EBAF) Data Product. *J. Clim.* 31, 4501–4527. doi:10.1175/JCLI-D-17-0523.1.
Kato, S., Xu, K.-M., Wong, T., Loeb, N. G., Rose, F. G., Trenberth, K. E., et al. (2016). Investigation of the Residual in Column-Integrated Atmospheric Energy Balance Using Cloud Objects. *J. Clim.* 29, 7435–7452. doi:10.1175/JCLI-D-15-0782.1.
Kaufman, Y. J., and Koren, I. (2006). Smoke and pollution aerosol effect on cloud cover. *Science* 313, 655–8. doi:10.1126/science.1126232.
Kay, J. E., and Gettelman, A. (2009). Cloud influence on and response to seasonal Arctic sea ice loss. *J. Geophys. Res. Atmos.* 114. doi:10.1029/2009JD011773.
Kay, J. E., Holland, M. M., Bitz, C. M., Blanchard-Wrigglesworth, E., Gettelman, A., Conley, A., et al. (2012). The Influence of Local Feedbacks and Northward Heat Transport on the Equilibrium Arctic Climate Response to Increased Greenhouse Gas Forcing. *J. Clim.* 25, 5433–5450. doi:10.1175/JCLI-D-11-00622.1.
Kay, J. E., L’Ecuyer, T., Chepfer, H., Loeb, N., Morrison, A., and Cesana, G. (2016). Recent Advances in Arctic Cloud and Climate Research. *Curr. Clim. Chang. Reports* 2, 159–169. doi:10.1007/s40641-016-0051-9.
Kennedy-Asser, A. T., Lunt, D. J., Farnsworth, A., and Valdes, P. J. (2019). Assessing Mechanisms and Uncertainty in Modeled Climatic Change at the Eocene-Oligocene Transition. *Paleoceanogr. Paleoclimatology*. doi:10.1029/2018PA003380.
Khairoutdinov, M., and Emanuel, K. (2013). Rotating radiative-convective equilibrium simulated by a cloud-resolving model. *J. Adv. Model. Earth Syst.* 5, 816–825. doi:10.1002/2013ms000253.
Kiehl, J. T. (2007). Twentieth century climate model response and climate sensitivity. *Geophys. Res. Lett.* 34, 1–4. doi:10.1029/2007GL031383.
Kiehl, J. T., and Shields, C. A. (2013). Sensitivity of the Palaeocene-Eocene Thermal Maximum climate to cloud properties. *Philos. Trans. R. Soc. London A Math. Phys. Eng. Sci.* 371. doi:10.1098/rsta.2013.0093.
Kim, D., Kang, S. M., Shin, Y., and Feldl, N. (2018). Sensitivity of Polar Amplification to Varying Insolation Conditions. *J. Clim.* 31, 4933–4947. doi:10.1175/JCLI-D-17.
Kim, K. Y., Kim, J. Y., Kim, J., Yeo, S., Na, H., Hamlington, B. D., et al. (2019). Vertical Feedback Mechanism of Winter Arctic Amplification and Sea Ice Loss. *Sci. Rep.* 9. doi:10.1038/s41598-018-38109-x.
Kinne, S. (2019). Aerosol radiative effects with MACv2. *Atmos. Chem. Phys. Discuss.*, 1–50. doi:10.5194/acp-2018-949.
Kirkby, J. (2007). Cosmic rays and climate. *Surv. Geophys.* 28, 333–375. doi:10.1007/s10712-008-9030-6.
Kirkby, J., Duplissy, J., Sengupta, K., Frege, C., Gordon, H., Williamson, C., et al. (2016). Ion-induced nucleation of

pure biogenic particles. *Nature* 533, 521–526. doi:10.1038/nature17953.
Klein, S. A., and Hall, A. (2015). Emergent Constraints for Cloud Feedbacks. *Curr. Clim. Chang. Reports* 1, 276–287. doi:10.1007/s40641-015-0027-1.
Klein, S. A., Hall, A., Norris, J. R., and Pincus, R. (2017). Low-cloud feedbacks from cloud-controlling factors: A review. *Surv. Geophys.* 38, 1307–1329. doi:https://doi.org/10.1007/s10712-017-9433-3.
Knutti, R. (2010). The end of model democracy? *Clim. Change* 102, 395–404. doi:10.1007/s10584-010-9800-2.
Knutti, R., and Hegerl, G. C. (2008). The equilibrium sensitivity of the Earth's temperature to radiation changes. *Nat. Geosci.* 1, 735. doi:10.1038/ngeo337.
Knutti, R., Joos, F., Müller, S. A., Plattner, G. K., and Stocker, T. F. (2005). Probabilistic climate change projections for CO2 stabilization profiles. *Geophys. Res. Lett.* 32, 1–4. doi:10.1029/2005GL023294.
Knutti, R., Masson, D., and Gettelman, A. (2013). Climate model genealogy: Generation CMIP5 and how we got there. *Geophys. Res. Lett.* 40, 1194–1199. doi:10.1002/grl.50256.
Knutti, R., Meehl, G. A., Allen, M. R., and Stainforth, D. A. (2006). Constraining Climate Sensitivity from the Seasonal Cycle in Surface Temperature. *J. Clim.* 19, 4224–4233. doi:10.1175/JCLI3865.1.
Knutti, R., Rugenstein, M. A. A., and Hegerl, G. C. (2017). Beyond equilibrium climate sensitivity. *Nat. Geosci.* 10, 727–736. doi:10.1038/NGEO3017.
Knutti, R., Stocker, T. F., Joos, F., and Plattner, G.-K. (2002). Constraints on radiative forcing and future climate change from observations and climate model ensembles. *Nature* 416, 719–723. doi:10.1038/416719a.
Knutti, R., Stocker, T. F., Joos, F., and Plattner, G. K. (2003). Probabilistic climate change projections using neural networks. *Clim. Dyn.* 21, 257–272. doi:10.1007/s00382-003-0345-1.
Koenigk, T., and Brodeau, L. (2014). Ocean heat transport into the Arctic in the twentieth and twenty-first century in EC-Earth. *Clim. Dyn.* doi:10.1007/s00382-013-1821-x.
Köhler, P., De Boer, B., Von Der Heydt, A. S., Stap, L. B., and Van De Wal, R. S. W. (2015). On the state dependency of the equilibrium climate sensitivity during the last 5 million years. *Clim. Past* 11, 1801–1823. doi:10.5194/cp-11-1801-2015.
Köhler, P., Knorr, G., Stap, L. B., Ganopolski, A., De Boer, B., Van De Wal, R. S. W., et al. (2018). The Effect of Obliquity-Driven Changes on Paleoclimate Sensitivity During the Late Pleistocene. *Geophys. Res. Lett.* 45. doi:10.1029/2018GL077717.
Köhler, P., Stap, L. B., von der Heydt, A. S., de Boer, B., Van De Wal, R. S. W., and Bloch-Johnson, J. (2017). A state-dependent quantification of climate sensitivity based on paleo data of the last 2.1 million years. *Paleoceanography*, 1–13. doi:10.1002/2017PA003190.
Kohyama, T., Hartmann, D. L., and Battisti, D. S. (2017). La Niña-like mean-state response to global warming and potential oceanic roles. *J. Clim.* 30, 4207–4225. doi:10.1175/JCLI-D-16-0441.1.
Konsta, D., Dufresne, J.-L., Chepfer, H., Idelkadi, A., and Cesana, G. (2015). Use of A-train satellite observations (CALIPSO–PARASOL) to evaluate tropical cloud properties in the LMDZ5 GCM. *Clim. Dyn.* 47, 1263–1284. doi:10.1007/s00382-016-3050-6.
Kooperman, G. J., Pritchard, M. S., Ghan, S. J., Wang, M., Somerville, R. C. J., and Russell, L. M. (2012). Constraining the influence of natural variability to improve estimates of global aerosol indirect effects in a nudged version of the Community Atmosphere Model 5. *J. Geophys. Res. Atmos.* doi:10.1029/2012JD018588.
Koren, I., Feingold, G., and Remer, L. A. (2010). The invigoration of deep convective clouds over the Atlantic: aerosol effect, meteorology or retrieval artifact? *Atmos. Chem. Phys.* 10, 8855–8872. doi:10.5194/acp-10-8855-2010.
Koren, I., Kaufman, Y. J., Rosenfeld, D., Remer, L. A., and Rudich, Y. (2005). Aerosol invigoration and restructuring of Atlantic convective clouds. *Geophys. Res. Lett.* 32, n/a-n/a. doi:10.1029/2005GL023187.
Kostov, Y., Armour, K. C., and Marshall, J. (2014). Impact of the Atlantic meridional overturning circulation on ocean heat storage and transient climate change. *Geophys. Res. Lett.* doi:10.1002/2013GL058998.
Kostov, Y., Ferreira, D., Armour, K. C., and Marshall, J. (2018). Contributions of Greenhouse Gas Forcing and the Southern Annular Mode to Historical Southern Ocean Surface Temperature Trends. *Geophys. Res. Lett.* doi:10.1002/2017GL074964.
Kostov, Y., Marshall, J., Hausmann, U., Armour, K. C., Ferreira, D., and Holland, M. M. (2017). Fast and slow responses of Southern Ocean sea surface temperature to SAM in coupled climate models. *Clim. Dyn.* doi:10.1007/s00382-016-3162-z.
Kovács, T., Feng, W., Totterdill, A., Plane, J. M. C., Dhomse, S., Gómez-Martín, J. C., et al. (2017). Determination of the atmospheric lifetime and global warming potential of sulfur hexafluoride using a three-dimensional model. *Atmos. Chem. Phys.* 17, 883–898. doi:10.5194/acp-17-883-2017.
Krasting, J. P., Stouffer, R. J., Griffies, S. M., Hallberg, R. W., Malyshev, S. L., Samuels, B. L., et al. (2018). Role of Ocean Model Formulation in Climate Response Uncertainty. *J. Clim.* doi:10.1175/JCLI-D-18-0035.1.
Kretzschmar, J., Salzmann, M., Mülmenstädt, J., Boucher, O., and Quaas, J. (2017). Comment on "Rethinking the Lower Bound on Aerosol Radiative Forcing." *J. Clim.* 30, 6579–6584. doi:10.1175/JCLI-D-16-0668.1.
Krishna-Pillai Sukumara-Pillai, K., Bala, G., Cao, L., Duan, L., and Caldeira, K. (2019). Climate System Response to Stratospheric Sulfate Aerosols: Sensitivity to Altitude of Aerosol Layer. *Earth Syst. Dyn. Discuss.* doi:10.5194/esd-2019-21.

Kristjánsson, J. E., Stjern, C. W., Stordal, F., Fjæraa, A. M., Myhre, G., and Jónasson, K. (2008). Cosmic rays, cloud condensation nuclei and clouds – a reassessment using MODIS data. *Atmos. Chem. Phys.* 8, 7373–7387. doi:10.5194/acp-8-7373-2008.
Kucharski, F., Kang, I.-S. S., Farneti, R., and Feudale, L. (2011). Tropical Pacific response to 20th century Atlantic warming. *Geophys. Res. Lett.* 38, n/a-n/a. doi:10.1029/2010GL046248.
Kucharski, F., No, H.-H., King, M. P., Ikram, F., Mogensen, K., Molteni, F., et al. (2015). Atlantic forcing of Pacific decadal variability. *Clim. Dyn.* 46, 2337–2351. doi:10.1007/s00382-015-2705-z.
Kucharski, F., Syed, F. S., Burhan, A., Farah, I., and Gohar, A. (2014). Tropical Atlantic influence on Pacific variability and mean state in the twentieth century in observations and CMIP5. *Clim. Dyn.* 44, 881–896. doi:10.1007/s00382-014-2228-z.
Kuhlbrodt, T., Gregory, J. M., and Shaffrey, L. C. (2015). A process-based analysis of ocean heat uptake in an AOGCM with an eddy-permitting ocean component. *Clim. Dyn.* 45, 3205–3226. doi:10.1007/s00382-015-2534-0.
Kummer, J. R., and Dessler, A. E. (2014). The impact of forcing efficacy on the equilibrium climate sensitivity. *Geophys. Res. Lett.* 41, 3565–3568. doi:10.1002/2014GL060046.
Kunreuther, H., Gupta, S., Bosetti, V., Cooke, R., Dutt, V., Ha-Duong, M., et al. (2014). "Integrated Risk and Uncertainty Assessment of Climate Change Response Policies," in *Climate Change 2014: Mitigation of Climate Change. Contribution of Working Group III to the Fifth Assessment Report of the Intergovernmental Panel on Climate Change*, eds. O. Edenhofer, R. Pichs-Madruga, Y. Sokona, E. Farahani, S. Kadner, K. Seyboth, et al. (Cambridge, United Kingdom and New York, USA: Cambridge Univeristy Press).
Kutzbach, J. E., He, F., Vavrus, S. J., and Ruddiman, W. F. (2013). The dependence of equilibrium climate sensitivity on climate state: Applications to studies of climates colder than present. *Geophys. Res. Lett.* 40, 3721–3726. doi:10.1002/grl.50724.
L'Ecuyer, T. S., Beaudoing, H. K., Rodell, M., Olson, W., Lin, B., Kato, S., et al. (2015). The Observed State of the Energy Budget in the Early Twenty-First Century. *J. Clim.* 28, 8319–8346. doi:10.1175/Jcli-D-14-00556.1.
Lacagnina, C., Hasekamp, O. P., and Torres, O. (2017). Direct radiative effect of aerosols based on PARASOL and OMI satellite observations. *J. Geophys. Res. Atmos.* 122, 2366–2388. doi:10.1002/2016JD025706.
Lade, S. J., Donges, J. F., Fetzer, I., Anderies, J. M., Beer, C., Cornell, S. E., et al. (2018). Analytically tractable climate–carbon cycle feedbacks under 21st century anthropogenic forcing. *Earth Syst. Dyn.* doi:10.5194/esd-9-507-2018.
Laepple, T., and Huybers, P. (2014). Ocean surface temperature variability: Large model-data differences at decadal and longer periods. *Proc. Natl. Acad. Sci. U. S. A.* 111, 16682–16687. doi:10.1073/pnas.1412077111.
Laîné, A., Yoshimori, M., and Abe-Ouchi, A. (2016). Surface Arctic Amplification Factors in CMIP5 Models: Land and Oceanic Surfaces and Seasonality. *J. Clim.* 29, 3297–3316. doi:10.1175/JCLI-D-15-0497.1.
Laken, B. A. (2016). Can Open Science save us from a solar-driven monsoon? *J. Sp. Weather Sp. Clim.* 6, A11. doi:10.1051/swsc/2016005.
Larson, E. J. L., and Portmann, R. W. (2016). A temporal kernel method to compute effective radiative forcing in CMIP5 transient simulations. *J. Clim.* doi:10.1175/JCLI-D-15-0577.1.
Lean, J. L. (2018). Estimating Solar Irradiance Since 850 CE. *Earth Sp. Sci.* 5, 133–149. doi:10.1002/2017EA000357.
Lean, J. L., Rottman, G. J., Kyle, H. L., Woods, T. N., Hickey, J. R., and Puga, L. C. (1997). Detection and parameterization of variations in solar mid- and near-ultraviolet radiation (200-400 nm). *J. Geophys. Res. Atmos.* doi:10.1029/97JD02092.
Lean, J., Rottman, G., Harder, J., and Kopp, G. (2005). "SORCE contributions to new understanding of global change and solar variability," in *The Solar Radiation and Climate Experiment (SORCE): Mission Description and Early Results* doi:10.1007/0-387-37625-9_3.
Lebsock, M. D., Stephens, G. L., and Kummerow, C. (2008). Multisensor satellite observations of aerosol effects on warm clouds. *J. Geophys. Res.* 113, D15205. doi:10.1029/2008JD009876.
Lee, D. S., Fahey, D. W., Skowron, A., Allen, M. R., Burkhardt, U., Chen, Q., et al. (9999). A comprehensive analysis of the contribution of global aviation to anthropogenic climate forcing in 2018. *PNAS* (submitted.
Lee, S. (2014). A theory for polar amplification from a general circulation perspective. *Asia-Pacific J. Atmos. Sci.* doi:10.1007/s13143-014-0024-7.
Lee, S., Gong, T., Feldstein, S. B., Screen, J. A., and Simmonds, I. (2017). Revisiting the Cause of the 1989–2009 Arctic Surface Warming Using the Surface Energy Budget: Downward Infrared Radiation Dominates the Surface Fluxes. *Geophys. Res. Lett.* doi:10.1002/2017GL075375.
Lee, S. H., Gordon, H., Yu, H., Lehtipalo, K., Haley, R., Li, Y., et al. (2019). New Particle Formation in the Atmosphere: From Molecular Clusters to Global Climate. *J. Geophys. Res. Atmos.* 124, 7098–7146. doi:10.1029/2018JD029356.
Lembo, V., Folini, D., Wild, M., and Lionello, P. (2019). Inter-hemispheric differences in energy budgets and cross-equatorial transport anomalies during the 20th century. *Clim. Dyn.* doi:10.1007/s00382-018-4572-x.
Levasseur, A., Cavalett, O., Fuglestvedt, J. S., Gasser, T., Johansson, D. J. A., Jørgensen, S. V., et al. (2016). Enhancing life cycle impact assessment from climate science: Review of recent findings and recommendations for application to LCA. *Ecol. Indic.* doi:10.1016/j.ecolind.2016.06.049.

Levitus, S., Antonov, J. I., Boyer, T. P., Baranova, O. K., Garcia, H. E., Locarnini, R. A., et al. (2012). World ocean heat content and thermosteric sea level change (0–2000 m), 1955–2010. *Geophys. Res. Lett.* 39. doi:10.1029/2012GL051106.
Lewis, N. (2013). An objective bayesian improved approach for applying optimal fingerprint techniques to estimate climate sensitivity. *J. Clim.* 26, 7414–7429. doi:10.1175/JCLI-D-12-00473.1.
Lewis, N., and Curry, J. (2018). The impact of recent forcing and ocean heat uptake data on estimates of climate sensitivity. *J. Clim.*, JCLI-D-17-0667.1. doi:10.1175/JCLI-D-17-0667.1.
Lewis, N., and Curry, J. A. (2015). The implications for climate sensitivity of AR5 forcing and heat uptake estimates. *Clim. Dyn.* 45, 1009–1023. doi:10.1007/s00382-014-2342-y.
Lewis, N., and Mauritsen, T. (9999). No unforced pattern effect on climate feedback over the historical period when using HadISST data. *J. Clim.* (submitted.
Li, C., von Storch, J. S., and Marotzke, J. (2013a). Deep-ocean heat uptake and equilibrium climate response. *Clim. Dyn.* 40, 1071–1086. doi:10.1007/s00382-012-1350-z.
Li, J.-L. F., Waliser, D. E., Stephens, G., Lee, S., L'Ecuyer, T., Kato, S., et al. (2013b). Characterizing and understanding radiation budget biases in CMIP3/CMIP5 GCMs, contemporary GCM, and reanalysis. *J. Geophys. Res.* 118, 8166–8184. doi:10.1002/jgrd.50378.
Li, R. L., Storelvmo, T., Fedorov, A. V, and Choi, Y.-S. (2019). A Positive Iris Feedback: Insights from Climate Simulations with Temperature-Sensitive Cloud–Rain Conversion. *J. Clim.* 32, 5305–5324. doi:10.1175/JCLI-D-18-0845.1.
Li, X., Xie, S.-P. P., Gille, S. T., and Yoo, C. (2016a). Atlantic-induced pan-tropical climate change over the past three decades. *Nat. Clim. Chang.* 6, 275–279. doi:10.1038/nclimate2840.
Li, Y., Han, W., and Zhang, L. (2017). Enhanced Decadal Warming of the Southeast Indian Ocean During the Recent Global Surface Warming Slowdown. *Geophys. Res. Lett.* 44, 9876–9884. doi:10.1002/2017GL075050.
Li, Y., Thompson, D. W. J., Bony, S., and Merlis, T. M. (2018). Thermodynamic Control on the Poleward Shift of the Extratropical Jet in Climate Change Simulations: The Role of Rising High Clouds and Their Radiative Effects. *J. Clim.* 32, 917–934. doi:10.1175/JCLI-D-18-0417.1.
Li, Z., Lau, W. K.-M., Ramanathan, V., Wu, G., Ding, Y., Manoj, M. G., et al. (2016b). Aerosol and monsoon climate interactions over Asia. *Rev. Geophys.* 54, 866–929. doi:10.1002/2015RG000500.
Lin, G., Penner, J. E., Flanner, M. G., Sillman, S., Xu, L., and Zhou, C. (2014). Radiative forcing of organic aerosol in the atmosphere and on snow: Effects of SOA and brown carbon. *J. Geophys. Res. Atmos.* 119, 7453–7476. doi:10.1002/2013JD021186.
Lindzen, R. S., Chou, M. D., and Hou, A. Y. (2001). Does the Earth Have an Adaptive Infrared Iris? *Bull. Am. Meteorol. Soc.* 82, 417–432. doi:10.1175/1520-0477(2001)082<0417:DTEHAA>2.3.CO;2.
Lipat, B. R., Tselioudis, G., Grise, K. M., and Polvani, L. M. (2017). CMIP5 models' shortwave cloud radiative response and climate sensitivity linked to the climatological Hadley cell extent. *Geophys. Res. Lett.* 44, 5739–5748. doi:10.1002/2017GL073151.
Lisiecki, L. E., and Raymo, M. E. (2005). A Pliocene-Pleistocene stack of 57 globally distributed benthic δ18O records. *Paleoceanography* 20. doi:10.1029/2004PA001071.
Liu, C., Allan, R. P., Berrisford, P., Mayer, M., Hyder, P., Loeb, N., et al. (2015). Combining satellite observations and reanalysis energy transports to estimate global net surface energy fluxes 1985-2012. *J. Geophys. Res.* 120, 9374–9389. doi:10.1002/2015JD023264.
Liu, C., Allan, R. P., Mayer, M., Hyder, P., Loeb, N. G., Roberts, C. D., et al. (2017a). Evaluation of satellite and reanalysis-based global net surface energy flux and uncertainty estimates. *J. Geophys. Res.* 122, 6250–6272. doi:10.1002/2017JD026616.
Liu, C., and Barnes, E. A. (2015). Extrememoisture transport into the Arctic linked to Rossby wave breaking. *J. Geophys. Res.* 120, 3774–3788. doi:10.1002/2014JD022796.
Liu, J., Tian, J., Liu, Z., Herbert, T. D., Fedorov, A. V, and Lyle, M. (2019). Eastern equatorial Pacific cold tongue evolution since the late Miocene linked to extratropical climate. *Sci. Adv.* 5. doi:10.1126/sciadv.aau6060.
Liu, R., Su, H., Liou, K.-N., Jiang, J. H., Gu, Y., Liu, S. C., et al. (2018). An Assessment of Tropospheric Water Vapor Feedback Using Radiative Kernels. *J. Geophys. Res. Atmos.* 123, 1499–1509. doi:10.1002/2017JD027512.
Liu, W., Xie, S. P., Liu, Z., and Zhu, J. (2017b). Overlooked possibility of a collapsed atlantic meridional overturning circulation in warming climate. *Sci. Adv.* doi:10.1126/sciadv.1601666.
Liu, Y., Hallberg, R., Sergienko, O., Samuels, B. L., Harrison, M., and Oppenheimer, M. (2017c). Climate response to the meltwater runoff from Greenland ice sheet: evolving sensitivity to discharging locations. *Clim. Dyn.* doi:10.1007/s00382-017-3980-7.
Liu, Z., and Huang, B. (1997). A coupled theory of tropical climatology: Warm pool, cold tongue, and walker circulation. *J. Clim.* 10, 1662–1679. doi:10.1175/1520-0442(1997)010<1662:ACTOTC>2.0.CO;2.
Liu, Z., Vavrus, S., He, F., Wen, N., and Zhong, Y. (2005). Rethinking Tropical Ocean Response to Global Warming: The Enhanced Equatorial Warming*. *J. Clim.* 18, 4684–4700. doi:10.1175/jcli3579.1.
Liu, Z., Zhu, J., Rosenthal, Y., Zhang, X., Otto-Bliesner, B. L., Timmermann, A., et al. (2014). The Holocene temperature conundrum. *Proc. Natl. Acad. Sci.* 111, E3501--E3505. doi:10.1073/pnas.1407229111.

Loeb, N. G., Doelling, D. R., Wang, H. L., Su, W. Y., Nguyen, C., Corbett, J. G., et al. (2018a). Clouds and the Earth's Radiant Energy System (CERES) Energy Balanced and Filled (EBAF) Top-of-Atmosphere (TOA) Edition-4.0 Data Product. *J. Clim.* 31, 895–918. doi:10.1175/Jcli-D-17-0208.1.
Loeb, N. G., Lyman, J. M., Johnson, G. C., Allan, R. P., Doelling, D. R., Wong, T., et al. (2012). Observed changes in top-of-the-atmosphere radiation and upper-ocean heating consistent within uncertainty. *Nat. Geosci.* doi:10.1038/ngeo1375.
Loeb, N. G., Rutan, D. A., Kato, S., and Wang, W. (2014). Observing Interannual Variations in Hadley Circulation Atmospheric Diabatic Heating and Circulation Strength. *J. Clim.* 27, 4139–4158. doi:10.1175/JCLI-D-13-00656.1.
Loeb, N. G., Thorsen, T. J., Norris, J. R., Wang, H., and Su, W. (2018b). Changes in Earth's Energy Budget during and after the "Pause" in Global Warming: An Observational Perspective. doi:10.3390/cli6030062.
Loeb, N. G., Wang, H., Allan, R., Andrews, T., Armour, K., Cole, J. N. N. S., et al. (9999). New Generation of Climate Models Track Recent Unprecedented Changes in Earth's Radiation Budget Observed by CERES. *Geophys. Res. Lett.* (submitted.
Loeb, N. G., Wang, H., Cheng, A., Kato, S., Fasullo, J. T., Xu, K.-M., et al. (2016). Observational constraints on atmospheric and oceanic cross-equatorial heat transports: revisiting the precipitation asymmetry problem in climate models. *Clim. Dyn.* 46, 3239–3257. doi:10.1007/s00382-015-2766-z.
Lohmann, U., and Neubauer, D. (2018). The importance of mixed-phase and ice clouds for climate sensitivity in the global aerosol–climate model ECHAM6-HAM2. *Atmos. Chem. Phys.* 18, 8807–8828. doi:10.5194/acp-18-8807-2018.
Longman, R. J., Giambelluca, T. W., Alliss, R. J., and Barnes, M. L. (2014). Temporal solar radiation change at high elevations in Hawai'i. *J. Geophys. Res.* 119, 6022–6033. doi:Doi 10.1002/2013jd021322.
Lu, J., Vecchi, G. A., and Reichler, T. (2007). Expansion of the Hadley cell under global warming. *Geophys. Res. Lett.* 34. doi:10.1029/2006GL028443.
Lucarini, V., Blender, R., Herbert, C., Ragone, F., Pascale, S., and Wouters, J. (2014). Mathematical and physical ideas for climate science. *Rev. Geophys.* 52, 809–859. doi:10.1002/2013RG000446.
Lucarini, V., and Ragone, F. (2011). Energetics of climate models: Net energy balance and meridional enthalpy transport. *Rev. Geophys.* 49. doi:10.1029/2009RG000323.
Lund, M. T., Aamaas, B., Berntsen, T., Bock, L., Burkhardt, U., Fuglestvedt, J. S., et al. (2017). Emission metrics for quantifying regional climate impacts of aviation. *Earth Syst. Dyn.* doi:10.5194/esd-8-547-2017.
Lund, M. T., Myhre, G., Haslerud, A. S., Skeie, R. B., Griesfeller, J., Platt, S. M., et al. (2018a). Concentrations and radiative forcing of anthropogenic aerosols from 1750 to 2014 simulated with the Oslo CTM3 and CEDS emission inventory. *Geosci. Model Dev.* 11, 4909–4931. doi:10.5194/gmd-11-4909-2018.
Lund, M. T., Samset, B. H., Skeie, R. B., Watson-Parris, D., Katich, J. M., Schwarz, J. P., et al. (2018b). Short Black Carbon lifetime inferred from a global set of aircraft observations. *npj Clim. Atmos. Sci.* 1, 31. doi:10.1038/s41612-018-0040-x.
Lunt, D. J., Bragg, F., Chan, W., Hutchinson, D. K., Ladant, J., Niezgodzki, I., et al. (9999). DeepMIP: Model intercomparison of early Eocene climatic optimum ( EECO ) large-scale climate features and comparison with proxy data. (submitted. doi:10.5194/cp-2019-149.
Lunt, D. J., Dunkley Jones, T., Heinemann, M., Huber, M., LeGrande, A., Winguth, A., et al. (2012). A model–data comparison for a multi-model ensemble of early Eocene atmosphere–ocean simulations: EoMIP. *Clim. Past* 8, 1717–1736. doi:10.5194/cp-8-1717-2012.
Lunt, D. J., Huber, M., Anagnostou, E., Baatsen, M. L. J., Caballero, R., DeConto, R., et al. (2017). The DeepMIP contribution to PMIP4: experimental design for model simulations of the EECO, PETM, and pre-PETM (version 1.0). *Geosci. Model Dev.* 10, 889–901. doi:10.5194/gmd-10-889-2017.
Luo, B., Luo, D., Wu, L., Zhong, L., and Simmonds, I. (2017a). Atmospheric circulation patterns which promote winter Arctic sea ice decline. *Environ. Res. Lett.* 12. doi:10.1088/1748-9326/aa69d0.
Luo, J. J., Wang, G., and Dommenget, D. (2018). May common model biases reduce CMIP5's ability to simulate the recent Pacific La Niña-like cooling? *Clim. Dyn.* 50, 1335–1351. doi:10.1007/s00382-017-3688-8.
Luo, Y., Lu, J., Liu, F., and Garuba, O. (2017b). The role of ocean dynamical thermostat in delaying the El Niño-Like response over the equatorial Pacific to climate warming. *J. Clim.* 30, 2811–2827. doi:10.1175/JCLI-D-16-0454.1.
Luo, Y., Lu, J., Liu, F., and Liu, W. (2015). Understanding the El Niño-like oceanic response in the tropical Pacific to global warming. *Clim. Dyn.* doi:10.1007/s00382-014-2448-2.
Lutsko, N. J., and Takahashi, K. (2018). What Can the Internal Variability of CMIP5 Models Tell Us about Their Climate Sensitivity? *J. Clim.* 31, 5051–5069. doi:10.1175/JCLI-D-17-0736.1.
Luyssaert, S., Jammet, M., Stoy, P. C., Estel, S., Pongratz, J., Ceschia, E., et al. (2014). Land management and land-cover change have impacts of similar magnitude on surface temperature. *Nat. Clim. Chang.* doi:10.1038/nclimate2196.
Ma, X., Yu, F., and Quaas, J. (2014). Reassessment of satellite-based estimate of aerosol climate forcing. *J. Geophys. Res. Atmos.* 119, 10,310-394,409. doi:10.1002/2014JD021670.
MacDougall, A. H., Zickfeld, K., Knutti, R., and Matthews, H. D. (2015). Sensitivity of carbon budgets to permafrost

carbon feedbacks and non-CO2 forcings. *Environ. Res. Lett.* doi:10.1088/1748-9326/10/12/125003.

MacIntosh, C. R. R., Allan, R. P. P., Baker, L. H. H., Bellouin, N., Collins, W., Mousavi, Z., et al. (2016). Contrasting fast precipitation responses to tropospheric and stratospheric ozone forcing. *Geophys. Res. Lett.* 43, 1263–1271. doi:10.1002/2015GL067231.

Maher, N., England, M. H., Gupta, A. Sen, and Spence, P. (2018). Role of Pacific trade winds in driving ocean temperatures during the recent slowdown and projections under a wind trend reversal. *Clim. Dyn.* 51, 321–336. doi:10.1007/s00382-017-3923-3.

Mahlstein, I., and Knutti, R. (2011). Ocean heat transport as a cause for model uncertainty in projected arctic warming. *J. Clim.* doi:10.1175/2010JCLI3713.1.

Mahowald, N. M., Kloster, S., Engelstaedter, S., Moore, J. K., Mukhopadhyay, S., McConnell, J. R., et al. (2010). Observed 20th century desert dust variability: impact on climate and biogeochemistry. *Atmos. Chem. Phys.* 10, 10875–10893. doi:10.5194/acp-10-10875-2010.

Mahrt, F., Marcolli, C., David, R. O., Grönquist, P., Barthazy Meier, E. J., Lohmann, U., et al. (2018). Ice nucleation abilities of soot particles determined with the Horizontal Ice Nucleation Chamber. *Atmos. Chem. Phys.* 18, 13363–13392. doi:10.5194/acp-18-13363-2018.

Malavelle, F. F., Haywood, J. M., Jones, A., Gettelman, A., Clarisse, L., Bauduin, S., et al. (2017). Strong constraints on aerosol-cloud interactions from volcanic eruptions. *Nature* 546, 485–491. doi:10.1038/nature22974.

Mallapragada, D., and Mignone, B. K. (2017). A consistent conceptual framework for applying climate metrics in technology life cycle assessment. *Environ. Res. Lett.* doi:10.1088/1748-9326/aa7397.

Mallick, K., Trebs, I., Boegh, E., Giustarini, L., Schlerf, M., Drewry, D. T., et al. (2016). Canopy-scale biophysical controls of transpiration and evaporation in the Amazon Basin. *Hydrol. EARTH Syst. Sci.* 20, 4237–4264. doi:10.5194/hess-20-4237-2016.

Manabe, S., and Bryan, K. (1985). CO2-induced change in a coupled ocean-atmosphere model and its paleoclimatic implications. *J. Geophys. Res.* 90, 11,611-689,707. doi:10.1029/JC090iC06p11689.

Manabe, S., and Wetherald, R. T. (1975). The Effects of Doubling the CO2 Concentration on the climate of a General Circulation Model. *J. Atmos. Sci.* 32, 3–15. doi:10.1175/1520-0469(1975)032<0003:TEODTC>2.0.CO;2.

Manara, V., Beltrano, M. C., Brunetti, M., Maugeri, M., Sanchez-Lorenzo, A., Simolo, C., et al. (2015). Sunshine duration variability and trends in Italy from homogenized instrumental time series (1936-2013). *J. Geophys. Res.* 120, 3622–3641. doi:Doi 10.1002/2014jd022560.

Manara, V., Brunetti, M., Celozzi, A., Maugeri, M., Sanchez-Lorenzo, A., and Wild, M. (2016). Detection of dimming/brightening in Italy from homogenized all-sky and clear-sky surface solar radiation records and underlying causes (1959-2013). *Atmos. Chem. Phys.* 16, 11145–11161. doi:10.5194/acp-16-11145-2016.

Manne, A. S., and Richels, R. G. (2001). An alternative approach to establishing trade-offs among greenhouse gases. *Nature* 410, 675. Available at: http://dx.doi.org/10.1038/35070541.

Marotzke, J. (2019). Quantifying the irreducible uncertainty in near-term climate projections. *Wiley Interdiscip. Rev. Clim. Chang.* 10, e563. doi:10.1002/wcc.563.

Marotzke, J., and Forster, P. M. (2015). Forcing, feedback and internal variability in global temperature trends. *Nature* 517, 565–570. doi:10.1038/nature14117.

Marsh, N. D., and Svensmark, H. (2000). Low cloud properties influenced by cosmic rays. *Phys. Rev. Lett.* 85, 5004–5007. doi:10.1103/PhysRevLett.85.5004.

Marshall, J., Donohoe, A., Ferreira, D., and McGee, D. (2014). The ocean's role in setting the mean position of the Inter-Tropical Convergence Zone. *Clim. Dyn.* 42, 1967–1979. doi:10.1007/s00382-013-1767-z.

Marshall, J., Scott, J. R., Armour, K. C., Campin, J. M., Kelley, M., and Romanou, A. (2015). The ocean's role in the transient response of climate to abrupt greenhouse gas forcing. *Clim. Dyn.* doi:10.1007/s00382-014-2308-0.

Marshall, L., Smith, C. J., Forster, P. M., Schmidt, A., and Aubry, T. J. (9999). Large variations in volcanic aerosol forcing efficiency due to eruption source parameters and rapid adjustments. *Geophys. Res. Lett.* (submitted.

Martínez-Botí, M. A., Foster, G. L., Chalk, T. B., Rohling, E. J., Sexton, P. F., Lunt, D. J., et al. (2015). Plio-Pleistocene climate sensitivity evaluated using high-resolution CO2 records. *Nature* 518, 49–54. doi:10.1038/nature14145.

Marvel, K., Pincus, R., Schmidt, G. A., and Miller, R. L. (2018). Internal Variability and Disequilibrium Confound Estimates of Climate Sensitivity From Observations. *Geophys. Res. Lett.* 45, 1595–1601. doi:10.1002/2017GL076468.

Marvel, K., Schmidt, G. A., Miller, R. L., and Nazarenko, L. S. (2016). Implications for climate sensitivity from the response to individual forcings. *Nat. Clim. Chang.* 6, 386–389. doi:10.1038/nclimate2888.

Marvel, K., Zelinka, M., Klein, S. A., Bonfils, C., Caldwell, P., Doutriaux, C., et al. (2015). External influences on modeled and observed cloud trends. *J. Clim.* 28, 4820–4840. doi:10.1175/JCLI-D-14-00734.1.

Marzeion, B., Leclercq, P. W., Cogley, J. G., and Jarosch, A. H. (2015). Brief Communication: Global reconstructions of glacier mass change during the 20th century are consistent. *Cryosph.* 9, 2399–2404. doi:10.5194/tc-9-2399-2015.

Masson-Delmotte, V., Schulz, M., Abe-Ouchi, A., Beer, J., Ganopolski, A., González Rouco, J. F., et al. (2013). "Information from Paleoclimate Archives," in *Climate Change 2013: The Physical Science Basis. Contribution of*

*Working Group I to the Fifth Assessment Report of the Intergovernmental Panel on Climate Change*, eds. T. F. Stocker, D. Qin, G.-K. Plattner, M. Tignor, S. K. Allen, J. Boschung, et al. (Cambridge, United Kingdom and New York, NY, USA, United Kingdom and New York, NY, USA: Cambridge University Press), 383–464. doi:10.1017/CBO9781107415324.013.

Mauritsen, T. (2016). Global warming: Clouds cooled the Earth. *Nat. Geosci.* 9, 865–867. doi:10.1038/ngeo2838.

Mauritsen, T., Bader, J., Becker, T., Behrens, J., Bittner, M., Brokopf, R., et al. (2019). Developments in the MPI-M Earth System Model version 1.2 (MPI-ESM 1.2) and its response to increasing CO2. *J. Adv. Model. Earth Syst.* 0. doi:10.1029/2018MS001400.

Mauritsen, T., Graversen, R. G., Klocke, D., Langen, P. L., Stevens, B., and Tomassini, L. (2013). Climate feedback efficiency and synergy. *Clim. Dyn.* 41, 2539–2554. doi:10.1007/s00382-013-1808-7.

Mauritsen, T., and Pincus, R. (2017). Committed warming inferred from observations. *Nat. Clim. Chang.* 7, 652–655. doi:10.1038/nclimate3357.

Mauritsen, T., and Roeckner, E. (9999). Tuning the climate sensitivity of the MPI-ESM1.2 global model to improve the match with instrumental record warming. *J. Adv. Model. Earth Syst.* (submitted.

Mauritsen, T., and Stevens, B. (2015). Missing iris effect as a possible cause of muted hydrological change and high climate sensitivity in models. *Nat. Geosci.* 8, 346–351. doi:10.1038/ngeo2414.

Mbengue, C., and Schneider, T. (2018). Linking Hadley Circulation and Storm Tracks in a Conceptual Model of the Atmospheric Energy Balance. *J. Atmos. Sci.* 75, 841–856. doi:10.1175/jas-d-17-0098.1.

McCabe, M. F., Aragon, B., Houborg, R., and Mascaro, J. (2017a). CubeSats in Hydrology: Ultrahigh-Resolution Insights Into Vegetation Dynamics and Terrestrial Evaporation. *WATER Resour. Res.* 53, 10017–10024. doi:10.1002/2017WR022240.

McCabe, M. F., Rodell, M., Alsdorf, D. E., Miralles, D. G., Uijlenhoet, R., Wagner, W., et al. (2017b). The future of Earth observation in hydrology. *Hydrol. EARTH Syst. Sci.* 21, 3879–3914. doi:10.5194/hess-21-3879-2017.

McClymont, E. L., Ford, H. L., Ho, S. L., Tindall, J. C., Haywood, A. M., Bailey, I., et al. (9999). Lessons from a high CO2 world: an ocean view from ~ 3 million years ago. *Clim. Past Discuss.* (submitted. doi:10.5194/cp-2019-161.

McComiskey, A., and Feingold, G. (2012). The scale problem in quantifying aerosol indirect effects. *Atmos. Chem. Phys.* 12, 1031–1049. doi:10.5194/acp-12-1031-2012.

McConnell, J. R., Edwards, R., Kok, G. L., Flanner, M. G., Zender, C. S., Saltzman, E. S., et al. (2007). 20th-Century Industrial Black Carbon Emissions Altered Arctic Climate Forcing. *Science (80-. ).* 317, 1381–1384. doi:10.1126/science.1144856.

McCoy, D. T., Bender, F. A.-M., Mohrmann, J. K. C., Hartmann, D. L., Wood, R., and Grosvenor, D. P. (2017a). The global aerosol-cloud first indirect effect estimated using MODIS, MERRA, and AeroCom. *J. Geophys. Res. Atmos.* 122, 1779–1796. doi:10.1002/2016JD026141.

McCoy, D. T., Eastman, R., Hartmann, D. L., and Wood, R. (2017b). The Change in Low Cloud Cover in a Warmed Climate Inferred from AIRS, MODIS, and ERA-Interim. *J. Clim.* 30, 3609–3620. doi:10.1175/JCLI-D-15-0734.1.

McCoy, D. T., Field, P. R., Elsaesser, G. S., Bodas-Salcedo, A., Kahn, B. H., Zelinka, M. D., et al. (2019). Cloud feedbacks in extratropical cyclones: Insight from long-term satellite data and high-resolution global simulations. *Atmos. Chem. Phys.* doi:10.5194/acp-19-1147-2019.

McCoy, D. T., Field, P. R., Schmidt, A., Grosvenor, D. P., Bender, F. A.-M., Shipway, B. J., et al. (2018). Aerosol midlatitude cyclone indirect effects in observations and high-resolution simulations. *Atmos. Chem. Phys.* 18, 5821–5846. doi:10.5194/acp-18-5821-2018.

McCoy, D. T., Hartmann, D. L., and Grosvenor, D. P. (2014a). Observed Southern Ocean Cloud Properties and Shortwave Reflection. Part I: Calculation of SW Flux from Observed Cloud Properties. *J. Clim.* 27, 8836–8857. doi:10.1175/JCLI-D-14-00287.1.

McCoy, D. T., Hartmann, D. L., and Grosvenor, D. P. (2014b). Observed Southern Ocean Cloud Properties and Shortwave Reflection. Part II: Phase Changes and Low Cloud Feedback. *J. Clim.* 27, 8858–8868. doi:10.1175/JCLI-D-14-00288.1.

McCoy, D. T., Tan, I., Hartmann, D. L., Zelinka, M. D., and Storelvmo, T. (2016). On the relationships among cloud cover, mixed-phase partitioning, and planetary albedo in GCMs. *J. Adv. Model. Earth Syst.* 8, 650–668.

McGregor, S., Stuecker, M. F., Kajtar, J. B., England, M. H., and Collins, M. (2018). Model tropical Atlantic biases underpin diminished Pacific decadal variability. *Nat. Clim. Chang.* 8, 493–498. doi:10.1038/s41558-018-0163-4.

McGregor, S., Timmermann, A., Stuecker, M. F., England, M. H., Merrifield, M., Jin, F.-F. F., et al. (2014). Recent Walker circulation strengthening and Pacific cooling amplified by Atlantic warming. *Nat. Clim. Chang.* 4, 888–892. doi:10.1038/nclimate2330.

Mears, C. A., and Wentz, F. J. (2009). Construction of the Remote Sensing Systems V3.2 Atmospheric Temperature Records from the MSU and AMSU Microwave Sounders. *J. Atmos. Ocean. Technol.* 26, 1040–1056. doi:10.1175/2008JTECHA1176.1.

Mears, C. A., and Wentz, F. J. (2017). A Satellite-Derived Lower-Tropospheric Atmospheric Temperature Dataset Using an Optimized Adjustment for Diurnal Effects. *J. Clim.* 30, 7695–7718. doi:10.1175/JCLI-D-16-0768.1.

Meehl, G. A., Senior, C. A., Eyring, V., Flato, G., Stouffer, R. J., Taylor, K. E., et al. (9999). Context for interpreting equilibrium climate sensitivity and transient climate response from the CMIP6 earth system models. *Sci. Adv.*

(submitted.

Meinshausen, M., Meinshausen, N., Hare, W., Raper, S. C. B., Frieler, K., Knutti, R., et al. (2009). Greenhouse-gas emission targets for limiting global warming to 2 °C. *Nature* 458, 1158–1162. doi:10.1038/nature08017.

Meinshausen, M., Nicholls, Z., Lewis, J., Gidden, M., Vogel, E., Freund, M., et al. (2019). The SSP greenhouse gas concentrations and their extensions to 2500. *Geosci. Model Dev. Discuss.*, 1–77. doi:10.5194/gmd-2019-222.

Meinshausen, M., Raper, S. C. B., and Wigley, T. M. L. (2011a). Emulating coupled atmosphere-ocean and carbon cycle models with a simpler model, MAGICC6 – Part 1: Model description and calibration. *Atmos. Chem. Phys.* 11, 1417–1456. doi:10.5194/acp-11-1417-2011.

Meinshausen, M., Smith, S. J., Calvin, K., Daniel, J. S., Kainuma, M. L. T., Lamarque, J., et al. (2011b). The RCP greenhouse gas concentrations and their extensions from 1765 to 2300. *Clim. Change* 109, 213–241. doi:10.1007/s10584-011-0156-z.

Meraner, K., Mauritsen, T., and Voigt, A. (2013). Robust increase in equilibrium climate sensitivity under global warming. *Geophys. Res. Lett.* 40, 5944–5948. doi:10.1002/2013GL058118.

Mercado, L. M., Bellouin, N., Sitch, S., Boucher, O., Huntingford, C., Wild, M., et al. (2009). Impact of changes in diffuse radiation on the global land carbon sink. *Nature*. doi:10.1038/nature07949.

Merlis, T. M. (2014). Interacting components of the top-of-atmosphere energy balance affect changes in regional surface temperature. *Geophys. Res. Lett.* 41, 7291–7297. doi:10.1002/2014GL061700.

Merlis, T. M. (2015). Direct weakening of tropical circulations from masked CO 2 radiative forcing . *Proc. Natl. Acad. Sci.* 112, 13167–13171. doi:10.1073/pnas.1508268112.

Merlis, T. M., Held, I. M., Stenchikov, G. L., Zeng, F., and Horowitz, L. W. (2014). Constraining transient climate sensitivity using coupled climate model simulations of volcanic eruptions. *J. Clim.* doi:10.1175/JCLI-D-14-00214.1.

Merlis, T. M., and Henry, M. (2018). Simple estimates of polar amplification in moist diffusive energy balance models. *J. Clim.* doi:10.1175/JCLI-D-17-0578.1.

Merlis, T. M., and Schneider, T. (2011). Changes in zonal surface temperature gradients and Walker circulations in a wide range of climates. *J. Clim.* 24, 4757–4768. doi:10.1175/2011JCLI4042.1.

Meyssignac, B., Boyer, T., Zhao, Z., Hakuba, M. Z., Landerer, F. W., Stammer, D., et al. (2019). Measuring Global Ocean Heat Content to Estimate the Earth Energy Imbalance. *Front. Mar. Sci.* 6, 432. doi:10.3389/fmars.2019.00432.

Michibata, T., Suzuki, K., Sato, Y., and Takemura, T. (2016). The source of discrepancies in aerosol–cloud–precipitation interactions between GCM and A-Train retrievals. *Atmos. Chem. Phys.* 16, 15413–15424. doi:10.5194/acp-16-15413-2016.

Millar, R. J., Otto, A., Forster, P. M., Lowe, J. A., Ingram, W. J., and Allen, M. R. (2015). Model structure in observational constraints on transient climate response. *Clim. Change* 131, 199–211. doi:10.1007/s10584-015-1384-4.

Mlynczak, M. G., Daniels, T. S., Kratz, D. P., Feldman, D. R., Collins, W. D., Mlawer, E. J., et al. (2016). The spectroscopic foundation of radiative forcing of climate by carbon dioxide. *Geophys. Res. Lett.* doi:10.1002/2016GL068837.

Modak, A., Bala, G., Caldeira, K., and Cao, L. (2018). Does shortwave absorption by methane influence its effectiveness? *Clim. Dyn.*, 1–20. doi:10.1007/s00382-018-4102-x.

Modak, A., Bala, G., Cao, L., and Caldeira, K. (2016). Why must a solar forcing be larger than a CO<inf>2</inf>forcing to cause the same global mean surface temperature change? *Environ. Res. Lett.* 11. doi:10.1088/1748-9326/11/4/044013.

Morgenstern, O., Hegglin, M., Rozanov, E., O'Connor, F., Luke Abraham, N., Akiyoshi, H., et al. (2017). Review of the global models used within phase 1 of the Chemistry-Climate Model Initiative (CCMI). *Geosci. Model Dev.* doi:10.5194/gmd-10-639-2017.

Morrison, A. L., Kay, J. E., Frey, W. R., Chepfer, H., and Guzman, R. (2018). Cloud Response to Arctic Sea Ice Loss and Implications for Future Feedbacks in the CESM1 Climate Model. *J. Geophys. Res. Atmos.* doi:10.1029/2018jd029142.

Mouginot, J., Rignot, E., Bjørk, A. A., van den Broeke, M., Millan, R., Morlighem, M., et al. (2019). Forty-six years of Greenland Ice Sheet mass balance from 1972 to 2018. *Proc. Natl. Acad. Sci.* 116, 9239 LP – 9244. doi:10.1073/pnas.1904242116.

Mueller, B., Hirschi, M., Jimenez, C., Ciais, P., Dirmeyer, P. A., Dolman, A. J., et al. (2013). Benchmark products for land evapotranspiration: LandFlux-EVAL multi-data set synthesis. *Hydrol. EARTH Syst. Sci.* 17, 3707–3720. doi:10.5194/hess-17-3707-2013.

Muller, C. J., and Held, I. M. (2012). Detailed Investigation of the Self-Aggregation of Convection in Cloud-Resolving Simulations. *J. Atmos. Sci.* 69, 2551–2565. doi:10.1175/JAS-D-11-0257.1.

Mülmenstädt, J., Gryspeerdt, E., Salzmann, M., Ma, P.-L., Dipu, S., and Quaas, J. (2019). Separating radiative forcing by aerosol–cloud interactions and fast cloud adjustments in the ECHAM-HAMMOZ aerosol–climate model using the method of partial radiative perturbations. *Atmos. Chem. Phys. Discuss.* doi:10.5194/acp-2018-1304.

Muñoz, I., and Schmidt, J. H. (2016). Methane oxidation, biogenic carbon, and the IPCC's emission metrics. Proposal for a consistent greenhouse-gas accounting. *Int. J. Life Cycle Assess.* doi:10.1007/s11367-016-1091-z.

Murphy, D. M. (2013). Little net clear-sky radiative forcing from recent regional redistribution of aerosols. *Nat. Geosci.* 6, 258–262. doi:10.1038/ngeo1740.

Murphy, D. M., and Forster, P. M. (2010). On the accuracy of deriving climate feedback parameters from correlations between surface temperature and outgoing radiation. *J. Clim.* doi:10.1175/2010JCLI3657.1.

Murphy, J. M. (1995). Transient Response of the Hadley Centre Coupled Ocean-Atmosphere Model to Increasing Carbon Dioxide. Part III: Analysis of Global-Mean Response Using Simple Models. *J. Clim.* doi:10.1175/1520-0442(1995)008<0496:TROTHC>2.0.CO;2.

Muscheler, R., Adolphi, F., Herbst, K., and Nilsson, A. (2016). The Revised Sunspot Record in Comparison to Cosmogenic Radionuclide-Based Solar Activity Reconstructions. *Sol. Phys.* 291, 3025–3043. doi:10.1007/s11207-016-0969-z.

Myers, T. A., and Norris, J. R. (2016). Reducing the uncertainty in subtropical cloud feedback. *Geophys. Res. Lett.* 43, 2144–2148. doi:10.1002/2015GL067416.

Myers, T. A., Scott, R. C., Zelinka, M. D., Klein, S. A., and Norris, J. R. (9999). Robust observational evidence that marine low clouds amplify climate warming. (submitted, 1–29.

Myhre, G., Aas, W., Cherian, R., Collins, W., Faluvegi, G., Flanner, M., et al. (2017). Multi-model simulations of aerosol and ozone radiative forcing due to anthropogenic emission changes during the period 1990–2015. *Atmos. Chem. Phys.* doi:10.5194/acp-17-2709-2017.

Myhre, G., Highwood, E. J., Shine, K. P., and Stordal, F. (1998). New estimates of radiative forcing due to well mixed greenhouse gases. *Geophys. Res. Lett.* 25, 2715–2718. doi:10.1029/98GL01908.

Myhre, G., Nilsen, J. S., Gulstad, L., Shine, K. P., Rognerud, B., and Isaksen, I. S. A. (2007). Radiative forcing due to stratospheric water vapour from $CH_4$ oxidation. *Geophys. Res. Lett.* doi:10.1029/2006GL027472.

Myhre, G., Samset, B. H., Schulz, M., Balkanski, Y., Bauer, S., Berntsen, T. K., et al. (2013a). Radiative forcing of the direct aerosol effect from AeroCom Phase II simulations. *Atmos. Chem. Phys.* 13, 1853–1877. doi:10.5194/acp-13-1853-2013.

Myhre, G., Shindell, D., Bréon, F.-M., Collins, W., Fuglestvedt, J., Huang, J., et al. (2013b). "Anthropogenic and Natural Radiative Forcing," in *Climate Change 2013: The Physical Science Basis. Contribution of Working Group I to the Fifth Assessment Report of the Intergovernmental Panel on Climate Change*, eds. T. F. Stocker, D. Qin, G.-K. Plattner, M. Tignor, S. K. Allen, J. Boschung, et al. (Cambridge, United Kingdom and New York, NY, USA, United Kingdom and New York, NY, USA: Cambridge University Press), 659–740. doi:10.1017/CBO9781107415324.018.

Nabat, P., Somot, S., Mallet, M., Sanchez-Lorenzo, A., and Wild, M. (2014). Contribution of anthropogenic sulfate aerosols to the changing Euro-Mediterranean climate since 1980. *Geophys. Res. Lett.* 41, 5605–5611. doi:Doi 10.1002/2014gl060798.

Nakajima, T., Higurashi, A., Kawamoto, K., and Penner, J. E. (2001). A possible correlation between satellite-derived cloud and aerosol microphysical parameters. *Geophys. Res. Lett.* 28, 1171–1174. doi:10.1029/2000GL012186.

Nam, C. C. W., and Quaas, J. (2012). Evaluation of Clouds and Precipitation in the ECHAM5 General Circulation Model Using CALIPSO and CloudSat Satellite Data. *J. Clim.* 25, 4975–4992. doi:10.1175/JCLI-D-11-00347.1.

Namazi, M., von Salzen, K., and Cole, J. N. S. (2015). Simulation of black carbon in snow and its climate impact in the Canadian Global Climate Model. *Atmos. Chem. Phys.* 15, 10887–10904. doi:10.5194/acp-15-10887-2015.

Narenpitak, P., Bretherton, C. S., and Khairoutdinov, M. F. (2017). Cloud and circulation feedbacks in a nearglobal aquaplanet cloudresolving model. *J. Adv. Model. Earth Syst.* 9, 1069–1090.

Nauels, A., Meinshausen, M., Mengel, M., Lorbacher, K., and Wigley, T. M. L. (2017). Synthesizing long-term sea level rise projections -- the MAGICC sea level model v2.0. *Geosci. Model Dev.* 10, 2495–2524. doi:10.5194/gmd-10-2495-2017.

Nazarenko, L., Rind, D., Tsigaridis, K., Del Genio, A. D., Kelley, M., and Tausnev, N. (2017). Interactive nature of climate change and aerosol forcing. *J. Geophys. Res. Atmos.* 122, 3457–3480. doi:10.1002/2016JD025809.

Neelin, J. D., Chou, C., and Su, H. (2003). Tropical drought regions in global warming and El Niño teleconnections. *Geophys. Res. Lett.* 30. doi:10.1029/2003GL018625.

Neubauer, D., Christensen, M. W., Poulsen, C. A., and Lohmann, U. (2017). Unveiling aerosol–cloud interactions – Part 2: Minimising the effects of aerosol swelling and wet scavenging in ECHAM6-HAM2 for comparison to satellite data. *Atmos. Chem. Phys.* 17, 13165–13185. doi:10.5194/acp-17-13165-2017.

Nicholls, Z. R., Meinshausen, M., Lewis, J., and Smith, C. J. (9999). Reduced complexity model intercomparison project phase 1: Protocol, results and initial observations. *Geosci. Model Dev. Discuss.* (submitted.

Nijsse, F. J. M. M., Cox, P. M., and Williamson, M. S. (9999). An emergent constraint on Transient Climate Response from simulated historical warming in CMIP6 models. *Earth Syst. Dyn. Discuss.* (submitted. doi:10.5194/esd-2019-86.

Norris, J. R., Allen, R. J., Evan, A. T., Zelinka, M. D., O'Dell, C. W., and Klein, S. A. (2016). Evidence for climate change in the satellite cloud record. *Nature* 536, 72. doi:10.1038/nature18273.

Notaro, M., Vavrus, S., and Liu, Z. (2007). Global vegetation and climate change due to future increases in $CO_2$ as

projected by a fully coupled model with dynamic vegetation. *J. Clim.* 20, 70–90. doi:10.1175/JCLI3989.1.
Notz, D. (2015). How well must climate models agree with observations? *Philos. Trans. R. Soc. A Math. Phys. Eng. Sci.* 373, 20140164. doi:10.1098/rsta.2014.0164.
Nummelin, A., Li, C., and Hezel, P. J. (2017). Connecting ocean heat transport changes from the midlatitudes to the Arctic Ocean. *Geophys. Res. Lett.* doi:10.1002/2016GL071333.
O'Brien, C. L., Foster, G. L., Martínez-Botí, M. A., Abell, R., Rae, J. W. B., and Pancost, R. D. (2014). High sea surface temperatures in tropical warm pools during the Pliocene. *Nat. Geosci.* 7, 606–611. doi:10.1038/ngeo2194.
O'Connor, F. M., Abraham, N. L., Dalvi, M., Folberth, G. A., Griffiths, P. T., Hardacre, C., et al. (9999). Pre-industrial to present-day anthropogenic effective radiative forcings (ERFs) from UKESM1. *Atmos. Chem. Phys. Discuss.* (submitted.
O'Gorman, P. A., and Singh, M. S. (2013). Vertical structure of warming consistent with an upward shift in the middle and upper troposphere. *Geophys. Res. Lett.* 40, 1838–1842. doi:10.1002/grl.50328.
O'ishi, R., Abe-Ouchi, A., Prentice, I. C., and Sitch, S. (2009). Vegetation dynamics and plant CO2responses as positive feedbacks in a greenhouse world. *Geophys. Res. Lett.* 36, 1–5. doi:10.1029/2009GL038217.
Ohmura, A., Bauder, A., Mueller, H., and Kappenberger, G. (2007). Long-term change of mass balance and the role of radiation. in *ANNALS OF GLACIOLOGY, VOL 46, 2007* Annals of Glaciology-Series., ed. Sharp, M, 367+. doi:10.3189/172756407782871297.
Ohno, T., Satoh, M., and Noda, A. (2019). Fine Vertical Resolution Radiative-Convective Equilibrium Experiments: Roles of Turbulent Mixing on the High-Cloud Response to Sea Surface Temperatures. *J. Adv. Model. Earth Syst.* 11, 1637–1654. doi:10.1029/2019MS001704.
Oikawa, E., Nakajima, T., and Winker, D. (2018). An Evaluation of the Shortwave Direct Aerosol Radiative Forcing Using CALIOP and MODIS Observations. *J. Geophys. Res. Atmos.* 123, 1211–1233. doi:10.1002/2017JD027247.
Oldenburg, D., Armour, K. C., Thompson, L., and Bitz, C. M. (2018). Distinct mechanisms of ocean heat transport into the Arctic under internal variability and climate change. *Geophys. Res. Lett.* doi:10.1029/2018GL078719.
Oliveira, P. J. C., Davin, E. L., Levis, S., and Seneviratne, S. I. (2011). Vegetation-mediated impacts of trends in global radiation on land hydrology: a global sensitivity study. *Glob. Chang. Biol.* 17, 3453–3467. doi:10.1111/j.1365-2486.2011.02506.x.
Olonscheck, D., Mauritsen, T., and Notz, D. (2019). Arctic sea-ice variability is primarily driven by atmospheric temperature fluctuations. *Nat. Geosci.* 12, 430–434. doi:10.1038/s41561-019-0363-1.
Otto, A., Otto, F. E. L., Boucher, O., Church, J., Hegerl, G., Forster, P. M., et al. (2013). Energy budget constraints on climate response. *Nat. Geosci.* 6, 415–416. doi:10.1038/ngeo1836.
Padilla, L. E., Vallis, G. K., and Rowley, C. W. (2011). Probabilistic estimates of transient climate sensitivity subject to uncertainty in forcing and natural variability. *J. Clim.* doi:10.1175/2011JCLI3989.1.
Palm, S. P., Strey, S. T., Spinhirne, J., and Markus, T. (2010). Influence of Arctic sea ice extent on polar cloud fraction and vertical structure and implications for regional climate. *J. Geophys. Res. Atmos.* 115. doi:10.1029/2010JD013900.
Palmer, M. D., Harris, G. R., and Gregory, J. M. (2018). Extending CMIP5 projections of global mean temperature change and sea level rise due to thermal expansion using a physically-based emulator. *Environ. Res. Lett.* 13, 84003. Available at: http://stacks.iop.org/1748-9326/13/i=8/a=084003.
Palmer, M. D., and McNeall, D. J. (2014). Internal variability of Earth's energy budget simulated by CMIP5 climate models. *Environ. Res. Lett.* 9, 34016. Available at: http://stacks.iop.org/1748-9326/9/i=3/a=034016.
Palmer, M. D., McNeall, D. J., and Dunstone, N. J. (2011). Importance of the deep ocean for estimating decadal changes in Earth's radiation balance. *Geophys. Res. Lett.* 38. doi:10.1029/2011GL047835.
Parding, K., Olseth, J. A., Dagestad, K. F., and Liepert, B. G. (2014). Decadal variability of clouds, solar radiation and temperature at a high-latitude coastal site in Norway. *Tellus Ser. B-Chemical Phys. Meteorol.* 66. doi:Artn 25897 Doi 10.3402/Tellusb.V66.25897.
Pattyn, F., Ritz, C., Hanna, E., Asay-Davis, X., DeConto, R., Durand, G., et al. (2018). The Greenland and Antarctic ice sheets under 1.5 °C global warming. *Nat. Clim. Chang.* 8, 1053–1061. doi:10.1038/s41558-018-0305-8.
Pauling, A. G., Smith, I. J., Langhorne, P. J., and Bitz, C. M. (2017). Time-Dependent Freshwater Input From Ice Shelves: Impacts on Antarctic Sea Ice and the Southern Ocean in an Earth System Model. *Geophys. Res. Lett.* doi:10.1002/2017GL075017.
Paulot, F., Paynter, D., Ginoux, P., Naik, V., and Horowitz, L. W. (2018). Changes in the aerosol direct radiative forcing from 2001 to 2015: Observational constraints and regional mechanisms. *Atmos. Chem. Phys.* 18, 13265–13281. doi:10.5194/acp-18-13265-2018.
Payne, A. E., Jansen, M. F., and Cronin, T. W. (2015). Conceptual model analysis of the influence of temperature feedbacks on polar amplification. *Geophys. Res. Lett.* 42, 9561–9570. doi:10.1002/2015GL065889.
Paynter, D., Frölicher, T. L., Horowitz, L. W., and Silvers, L. G. (2018). Equilibrium Climate Sensitivity Obtained From Multimillennial Runs of Two GFDL Climate Models. *J. Geophys. Res. Atmos.* 123, 1921–1941. doi:10.1002/2017JD027885.
Peng, J., Hu, M., Guo, S., Du, Z., Zheng, J. J., Shang, D., et al. (2016). Markedly enhanced absorption and direct

radiative forcing of black carbon under polluted urban environments. *Proc. Natl. Acad. Sci. U. S. A.* 113, 4266–71. doi:10.1073/pnas.1602310113.
Penner, J. E., Xu, L., and Wang, M. (2011). Satellite methods underestimate indirect climate forcing by aerosols. *Proc. Natl. Acad. Sci. U. S. A.* 108, 13404–8. doi:10.1073/pnas.1018526108.
Penner, J. E., Zhou, C., Garnier, A., and Mitchell, D. L. (2018). Anthropogenic Aerosol Indirect Effects in Cirrus Clouds. *J. Geophys. Res. Atmos.* 123, 11,652-11,677. doi:10.1029/2018JD029204.
Persad, G. G., and Caldeira, K. (2018). Divergent global-scale temperature effects from identical aerosols emitted in different regions. *Nat. Commun.* doi:10.1038/s41467-018-05838-6.
Persad, G. G., Ming, Y., and Ramaswamy, V. (2014). The role of aerosol absorption in driving clear-sky solar dimming over East Asia. *J. Geophys. Res.* 119, 10,410–10,424. doi:Doi 10.1002/2014jd021577.
Petersik, P., Salzmann, M., Kretzschmar, J., Cherian, R., Mewes, D., and Quaas, J. (2018). Subgrid-scale variability in clear-sky relative humidity and forcing by aerosol–radiation interactions in an atmosphere model. *Atmos. Chem. Phys.* 18, 8589–8599. doi:10.5194/acp-18-8589-2018.
Pfeifroth, U., Sanchez-Lorenzo, A., Manara, V., Trentmann, J., and Hollmann, R. (2018). Trends and Variability of Surface Solar Radiation in Europe Based On Surface- and Satellite-Based Data Records. *J. Geophys. Res.* 123, 1735–1754. doi:10.1002/2017JD027418.
Pfister, P. L., and Stocker, T. F. (2017). State-Dependence of the Climate Sensitivity in Earth System Models of Intermediate Complexity. *Geophys. Res. Lett.* 44, 10,643-10,653. doi:10.1002/2017GL075457.
Pierce, J. R. (2017). Cosmic rays, aerosols, clouds, and climate: Recent findings from the CLOUD experiment. *J. Geophys. Res. Atmos.* 122, 8051–8055. doi:10.1002/2017JD027475.
Pierrehumbert, R. T. (2014). *Short-Lived Climate Pollution*. doi:10.1146/annurev-earth-060313-054843.
Pincus, R., Evans, K. F., Buehler, S. A., Brath, M., Jamil, O., Manners, J., et al. (9999). Benchmark calculations of radiative forcing by greenhouse gases. *Geophys. Res. Lett.* (submitted, 1–15.
Pincus, R., Forster, P. M., and Stevens, B. (2016). The Radiative Forcing Model Intercomparison Project (RFMIP): Experimental protocol for CMIP6. *Geosci. Model Dev.* 9, 3447–3460. doi:10.5194/gmd-9-3447-2016.
Pistone, K., Eisenman, I., and Ramanathan, V. (2014). Observational determination of albedo decrease caused by vanishing Arctic sea ice. *Proc. Natl. Acad. Sci.* 111, 3322–3326. doi:10.1073/pnas.1318201111.
Pithan, F., and Mauritsen, T. (2014). Arctic amplification dominated by temperature feedbacks in contemporary climate models. *Nat. Geosci.* 7, 181–184. doi:10.1038/ngeo2071.
Po-Chedley, S., Armour, K. C., Bitz, C. M., Zelinka, M. D., and Santer, B. D. (2018a). Sources of intermodel spread in the lapse rate and water vapor feedbacks. *J. Clim.* doi:10.1175/JCLI-D-17-0674.1.
Po-Chedley, S., Proistosescu, C., Armour, K. C., and Santer, B. D. (2018b). Climate constraint reflects forced signal. *Nature* 563, E6–E9. doi:10.1038/s41586-018-0640-y.
Po-Chedley, S., Zelinka, M. D., Jeevanjee, N., Thorsen, T. J., and Santer, B. D. (2019). Climatology explains intermodel spread in tropical upper tropospheric cloud and relative humidity response to greenhouse warming. *Geophys. Res. Lett.* 0. doi:10.1029/2019gl084786.
Popp, M., Schmidt, H., and Marotzke, J. (2016). Transition to a Moist Greenhouse with CO2 and solar forcing. *Nat. Commun.* 7, 10627. Available at: https://doi.org/10.1038/ncomms10627.
Port, U., Brovkin, V., and Claussen, M. (2012). The influence of vegetation dynamics on anthropogenic climate change. *Earth Syst. Dyn.* 3, 233–243. doi:10.5194/esd-3-233-2012.
Posselt, R., Mueller, R., Trentrnann, J., Stockli, R., and Liniger, M. A. (2014). A surface radiation climatology across two Meteosat satellite generations. *Remote Sens. Environ.* 142, 103–110. doi:Doi 10.1016/J.Rse.2013.11.007.
Previdi, M., Smith, K. L., and Polvani, L. M. (2015). How Well Do the CMIP5 Models Simulate the Antarctic Atmospheric Energy Budget? *J. Clim.* 28, 7933–7942. doi:10.1175/JCLI-D-15-0027.1.
Proistosescu, C., Donohoe, A., Armour, K. C., Roe, G. H., Stuecker, M. F., and Bitz, C. M. (2018). Radiative Feedbacks From Stochastic Variability in Surface Temperature and Radiative Imbalance. *Geophys. Res. Lett.* doi:10.1029/2018GL077678.
Proistosescu, C., and Huybers, P. J. (2017). Slow climate mode reconciles historical and model-based estimates of climate sensitivity. *Sci. Adv.* 3, 1–7. doi:10.1126/sciadv.1602821.
Purich, A., England, M. H., Cai, W., Sullivan, A., and Durack, P. J. (2018). Impacts of broad-scale surface freshening of the Southern Ocean in a coupled climate model. *J. Clim.* doi:10.1175/JCLI-D-17-0092.1.
Purkey, S. G., and Johnson, G. C. (2010). Warming of Global Abyssal and Deep Southern Ocean Waters between the 1990s and 2000s: Contributions to Global Heat and Sea Level Rise Budgets. *J. Clim.* 23, 6336–6351. doi:10.1175/2010JCLI3682.1.
Qu, X., and Hall, A. (2007). What controls the strength of snow-albedo feedback? *J. Clim.* 20, 3971–3981.
Qu, X., and Hall, A. (2014). On the persistent spread in snow-albedo feedback. *Clim. Dyn.* 42, 69–81. doi:10.1007/s00382-013-1774-0.
Qu, X., Hall, A., DeAngelis, A. M., Zelinka, M. D., Klein, S. A., Su, H., et al. (2018). On the emergent constraints of climate sensitivity. *J. Clim.* 31, 863–875. doi:10.1175/JCLI-D-17-0482.1.
Qu, X., Hall, A., Klein, S. A., and Caldwell, P. M. (2014). On the spread of changes in marine low cloud cover in climate model simulations of the 21st century. *Clim. Dyn.* doi:10.1007/s00382-013-1945-z.

Qu, X., Hall, A., Klein, S. A., and DeAngelis, A. M. (2015). Positive tropical marine lowcloud cover feedback inferred from cloudcontrolling factors. *Geophys. Res. Lett.* 42, 7767–7775. doi:10.1002/2015GL065627.

Quaas, J., Boucher, O., Bellouin, N., and Kinne, S. (2008). Satellite-based estimate of the direct and indirect aerosol climate forcing. *J. Geophys. Res. Atmos.* 113, n/a-n/a. doi:10.1029/2007JD008962.

Quaas, J., Ming, Y., Menon, S., Takemura, T., Wang, M., Penner, J. E., et al. (2009). Aerosol indirect effects – general circulation model intercomparison and evaluation with satellite data. *Atmos. Chem. Phys.* 9, 8697–8717. doi:10.5194/acp-9-8697-2009.

Rahimzadeh, F., Sanchez-Lorenzo, A., Hamedi, M., Kruk, M. C., and Wild, M. (2015). New evidence on the dimming/brightening phenomenon and decreasing diurnal temperature range in Iran (1961-2009). *Int. J. Clim.* 35, 2065–2079. doi:DOI: 10.1002/joc.4107.

Randall, D. A., Wood, R. A., Bony, S., Colman, R., Fichefet, T., Fyfe, J., et al. (2007). "Climate Models and Their Evaluation," in *Climate Change 2007: The Scientific Basis. Contribution of Working Group I to the Fourth Assessment Report of the Intergovernmental Panel on Climate Change*, eds. S. Solomon, D. Qin, M. Manning, Z. Chen, M. Marquis, K. B. Averyt, et al. (Cambridge, United Kingdom and New York, USA: Cambirdge University Press), 589–662.

Raschke, E., Kinne, S., Rossow, W. B., Stackhouse, P. W., and Wild, M. (2016). Comparison of Radiative Energy Flows in Observational Datasets and Climate Modeling. *J. Appl. Meteorol. Climatol.* 55, 93–117. doi:10.1175/Jamc-D-14-0281.1.

Ray, E. A., Moore, F. L., Elkins, J. W., Rosenlof, K. H., Laube, J. C., Röckmann, T., et al. (2017). Quantification of the SF 6 lifetime based on mesospheric loss measured in the stratospheric polar vortex. *J. Geophys. Res.* doi:10.1002/2016JD026198.

Rayner, N. A., Parker, D. E., Horton, E. B., Folland, C. K., Alexander, L. V., Rowell, D. P., et al. (2003). Global analyses of sea surface temperature, sea ice, and night marine air temperature since the late nineteenth century. *J. Geophys. Res.* 108, 4407. doi:10.1029/2002JD002670.

Regayre, L. A., Johnson, J. S., Yoshioka, M., Pringle, K. J., Sexton, D. M. H., Booth, B. B. B., et al. (2018). Aerosol and physical atmosphere model parameters are both important sources of uncertainty in aerosol ERF. *Atmos. Chem. Phys.* 18, 9975–10006. doi:10.5194/acp-18-9975-2018.

Reick, C. H., Raddatz, T., Brovkin, V., and Gayler, V. (2013). Representation of natural and anthropogenic land cover change in MPI-ESM. *J. Adv. Model. Earth Syst.* 5, 459–482. doi:10.1002/jame.20022.

Rémy, S., Bellouin, N., Benedetti, A., and Boucher, O. (2018). Aerosols [in "State of the Climate in 2017"]. *Bull. Amer. Meteor. Soc.,* 99, S49–S51. doi:doi:10.1175/2018BAMSStateoftheClimate.1.

Renoult, M., Annan, J. D., Hargreaves, J. C., Sagoo, N., Flynn, C., Mikolajewicz, U., et al. (9999). A Bayesian framework for emergent constraints: case studies of climate sensitivity with PMIP. *Clim. Past Discuss.* (submitted.

Rhein, M., Rintoul, S. R., Aoki, S., Campos, E., Chambers, D., Feely, R. A., et al. (2013). "Observations: Ocean," in *Climate Change 2013: The Physical Science Basis. Contribution of Working Group I to the Fifth Assessment Report of the Intergovernmental Panel on Climate Change*, eds. T. F. Stocker, D. Qin, G.-K. Plattner, M. Tignor, S. K. Allen, J. Boschung, et al. (Cambridge, United Kingdom and New York, NY, USA, United Kingdom and New York, NY, USA: Cambridge University Press), 255�316. doi:10.1017/CBO9781107415324.010.

Ribes, A., Qasmi, S., and Gillett, N. (9999). Kriging climate change to narrow uncertainty on past and future human-induced warming. *Nat. Clim. Chang.* (submitted.

Richardson, M., Cowtan, K., Hawkins, E., and Stolpe, M. B. (2016). Reconciled climate response estimates from climate models and the energy budget of Earth. *Nat. Clim. Chang.* 6, 931–935. doi:10.1038/nclimate3066.

Richardson, M., Cowtan, K., and Millar, R. J. (2018a). Global temperature definition affects achievement of long-term climate goals. *Environ. Res. Lett.* 13, 054004. doi:10.1088/1748-9326/aab305.

Richardson, T. B., Forster, P. M., Andrews, T., Boucher, O., Faluvegi, G., Fläschner, D., et al. (2018b). Carbon Dioxide Physiological Forcing Dominates Projected Eastern Amazonian Drying. *Geophys. Res. Lett.* doi:10.1002/2017GL076520.

Richardson, T. B., Forster, P. M., Smith, C. J., Maycock, A. C., Wood, T., Andrews, T., et al. (2019). Efficacy of climate forcings in PDRMIP models. *J. Geophys. Res. Atmos.* 124, 12,824-12,844. doi:10.1029/2019JD030581.

Rienecker, M. M., Suarez, M. J., Gelaro, R., Todling, R., Bacmeister, J., Liu, E., et al. (2011). MERRA: NASA's Modern-Era Retrospective Analysis for Research and Applications. *J. Clim.* 24, 3624–3648. doi:10.1175/JCLI-D-11-00015.1.

Ringer, M. A., Andrews, T., and Webb, M. J. (2014). Global-mean radiative feedbacks and forcing in atmosphere-only and coupled atmosphereocean climate change experiments. *Geophys. Res. Lett.* 41, 4035–4042. doi:10.1002/ 2014GL060347.

Riser, S. C., Freeland, H. J., Roemmich, D., Wijffels, S., Troisi, A., Belbéoch, M., et al. (2016). Fifteen years of ocean observations with the global Argo array. *Nat. Clim. Chang.* 6, 145–153. doi:10.1038/nclimate2872.

Rodell, M., Famiglietti, J. S., Wiese, D. N., Reager, J. T., Beaudoing, H. K., Landerer, F. W., et al. (2018). Emerging trends in global freshwater availability. *Nature* 557, 650+. doi:10.1038/s41586-018-0123-1.

Roe, G. H., and Armour, K. C. (2011). How sensitive is climate sensitivity? *Geophys. Res. Lett.*

doi:10.1029/2011GL047913.
Roe, G. H., and Baker, M. B. (2007). Why Is Climate Sensitivity So Unpredictable? *Science (80-. ).* 318, 629–632. doi:10.1126/science.1144735.
Roe, G. H., Feldl, N., Armour, K. C., Hwang, Y. T., and Frierson, D. M. W. (2015). The remote impacts of climate feedbacks on regional climate predictability. *Nat. Geosci.* doi:10.1038/ngeo2346.
Rogelj, J., Meinshausen, M., and Knutti, R. (2012). Global warming under old and new scenarios using IPCC climate sensitivity range estimates. *Nat. Clim. Chang.* 2, 248–253. doi:10.1038/nclimate1385.
Rohling, E. J., Sluijs, A., Dijkstra, H. A., Köhler, P., Van De Wal, R. S. W., Von Der Heydt, A. S., et al. (2012). Making sense of palaeoclimate sensitivity. *Nature* 491, 683–691. doi:10.1038/nature11574.
Rohrschneider, T., Stevens, B., and Mauritsen, T. (2019). On simple representations of the climate response to external radiative forcing. *Clim. Dyn.* doi:10.1007/s00382-019-04686-4.
Romps, D. M. (2014). An Analytical Model for Tropical Relative Humidity. *J. Clim.* 27, 7432–7449. doi:10.1175/JCLI-D-14-00255.1.
Rose, B. E. J., Armour, K. C., Battisti, D. S., Feldl, N., and Koll, D. D. B. (2014). The dependence of transient climate sensitivity and radiative feedbacks on the spatial pattern of ocean heat uptake. *Geophys. Res. Lett.* doi:10.1002/2013GL058955.
Rose, B. E. J., and Ferreira, D. (2013). Ocean heat transport and water vapor greenhouse in a warm equable climate: A new look at the low gradient paradox. *J. Clim.* doi:10.1175/JCLI-D-11-00547.1.
Rose, B. E. J., and Rayborn, L. (2016). The Effects of Ocean Heat Uptake on Transient Climate Sensitivity. *Curr. Clim. Chang. Reports*. doi:10.1007/s40641-016-0048-4.
Rose, B. E. J., and Rencurrel, M. C. (2016). The Vertical Structure of Tropospheric Water Vapor: Comparing Radiative and Ocean-Driven Climate Changes. *J. Clim.* 29, 4251–4268. doi:10.1175/JCLI-D-15-0482.1.
Rosenfeld, D., Zhu, Y., Wang, M., Zheng, Y., Goren, T., and Yu, S. (2019). Aerosol-driven droplet concentrations dominate coverage and water of oceanic low level clouds. *Science*. doi:10.1126/science.aav0566.
Rotstayn, L. D., Collier, M. A., Shindell, D. T., and Boucher, O. (2015). Why does aerosol forcing control historical global-mean surface temperature change in CMIP5 models? *J. Clim.* 28, 6608–6625. doi:10.1175/JCLI-D-14-00712.1.
Rowlands, D. J., Frame, D. J., Ackerley, D., Aina, T., Booth, B. B. B., Christensen, C., et al. (2012). Broad range of 2050 warming from an observationally constrained large climate model ensemble. *Nat. Geosci.* doi:10.1038/ngeo1430.
Royer, D. L. (2016). Climate Sensitivity in the Geologic Past. *Annu. Rev. Earth Planet. Sci.* 44, 277–293. doi:10.1146/annurev-earth-100815-024150.
Rugenstein, M. A. A., Caldeira, K., and Knutti, R. (2016a). Dependence of global radiative feedbacks on evolving patterns of surface heat fluxes. *Geophys. Res. Lett.* doi:10.1002/2016GL070907.
Rugenstein, M. A. A., Gregory, J. M., Schaller, N., Sedlácek, J., and Knutti, R. (2016b). Multiannual ocean-atmosphere adjustments to radiative forcing. *J. Clim.* 29, 5643–5659. doi:10.1175/JCLI-D-16-0312.1.
Rugenstein, M. A. A., Winton, M., Stouffer, R. J., Griffies, S. M., and Hallberg, R. (2013). Northern High-Latitude Heat Budget Decomposition and Transient Warming. *J. Clim.* 26, 609–621. doi:10.1175/JCLI-D-11-00695.1.
Rugenstein, M., Bloch-Johnson, J., Abe-Ouchi, A., Andrews, T., Beyerle, U., Cao, L., et al. (2019a). LongRunMIP – motivation and design for a large collection of millennial-length AO-GCM simulations. *Bull. Am. Meteorol. Soc.* doi:10.1175/bams-d-19-0068.1.
Rugenstein, M., Bloch-Johnson, J., Gregory, J., Andrews, T., Mauritsen, T., Li, C., et al. (2019b). Equilibrium climate sensitivity estimated by equilibrating climate models. *Geophys. Res. Lett.*, 2019GL083898. doi:10.1029/2019GL083898.
Rypdal, M., Fredriksen, H.-B., Rypdal, K., and Steene, R. J. (2018). Emergent constraints on climate sensitivity. *Nature* 563, E4–E5. doi:10.1038/s41586-018-0639-4.
Sagoo, N., Valdes, P., Flecker, R., Gregoire, L. J., and A, P. T. R. S. (2013). The Early Eocene equable climate problem: can perturbations of climate model parameters identify possible solutions? *Philos. Trans. R. Soc. London A Math. Phys. Eng. Sci.* 371. doi:10.1098/rsta.2013.0123.
Salzmann, U., Dolan, A. M., Haywood, A. M., Chan, W. Le, Voss, J., Hill, D. J., et al. (2013). Challenges in quantifying Pliocene terrestrial warming revealed by data-model discord. *Nat. Clim. Chang.* 3, 969–974. doi:10.1038/nclimate2008.
Samset, B. H., and Myhre, G. (2015). Climate response to externally mixed black carbon as a function of altitude. *J. Geophys. Res. Atmos.* 120, 2913–2927. doi:10.1002/2014JD022849.
Sanchez-Lorenzo, A., Calbo, J., and Wild, M. (2013). Global and diffuse solar radiation in Spain: Building a homogeneous dataset and assessing their trends. *Glob. Planet. Change* 100, 343–352. doi:Doi 10.1016/J.Gloplacha.2012.11.010.
Sanchez-Lorenzo, A., Wild, M., Brunetti, M., Guijarro, J. A., Hakuba, M. Z., Calbo, J., et al. (2015). Reassessment and update of long-term trends in downward surface shortwave radiation over Europe (1939-2012). *J. Geophys. Res.* 120, 9555–9569. doi:10.1002/2015jd023321.
Santer, B. D., Wigley, T. M. L., Mears, C., Wentz, F. J., Klein, S. A., Seidel, D. J., et al. (2005). Amplification of

Surface Temperature Trends and Variability in the Tropical Atmosphere. *Science (80-. ).* 309, 1551–1556. doi:10.1126/science.1114867.

Sarofim, M. C., and Giordano, M. R. (2018). A quantitative approach to evaluating the GWP timescale through implicit discount rates. *Earth Syst. Dyn.* 9, 1013–1024. doi:10.5194/esd-9-1013-2018.

Sato, Y., Goto, D., Michibata, T., Suzuki, K., Takemura, T., Tomita, H., et al. (2018). Aerosol effects on cloud water amounts were successfully simulated by a global cloud-system resolving model. *Nat. Commun.* 9, 985. doi:10.1038/s41467-018-03379-6.

Schlesinger, M. E., and Jiang, X. (1990). Simple Model Representation of Atmosphere-Ocean GCMs and Estimation of the Time Scale of C0 2 -Induced Climate Change . *J. Clim.* 3, 1297–1315. doi:10.1175/1520-0442(1990)003<1297:smroao>2.0.co;2.

Schmidt, A., Mills, M. J., Ghan, S., Gregory, J. M., Allan, R. P., Andrews, T., et al. (2018). Volcanic Radiative Forcing From 1979 to 2015. *J. Geophys. Res. Atmos.* doi:10.1029/2018JD028776.

Schmidt, G. A., Annan, J. D., Bartlein, P. J., Cook, B. I., Guilyardi, E., Hargreaves, J. C., et al. (2014). Using palaeo-climate comparisons to constrain future projections in CMIP5. *Clim. Past* 10, 221–250. doi:10.5194/cp-10-221-2014.

Schmidt, G. A., Severinghaus, J., Abe-Ouchi, A., Alley, R. B., Broecker, W., Brook, E., et al. (2017). Overestimate of committed warming. *Nature* 547, E16–E17. doi:10.1038/nature22803.

Schneider, A., Flanner, M., and Perket, J. (2018). Multidecadal Variability in Surface Albedo Feedback Across CMIP5 Models. *Geophys. Res. Lett.* 45, 1972–1980. doi:10.1002/2017GL076293.

Schneider, T., Kaul, C. M., and Pressel, K. G. (2019). Possible climate transitions from breakup of stratocumulus decks under greenhouse warming. *Nat. Geosci.* 12, 163–167. doi:10.1038/s41561-019-0310-1.

Schulz, M., Textor, C., Kinne, S., Balkanski, Y., Bauer, S., Berntsen, T., et al. (2006). Radiative forcing by aerosols as derived from the AeroCom present-day and pre-industrial simulations. *Atmos. Chem. Phys.* 6, 5225–5246. doi:10.5194/acp-6-5225-2006.

Schumann, U., and Graf, K. (2013). Aviation-induced cirrus and radiation changes at diurnal timescales. *J. Geophys. Res. Atmos.* doi:10.1002/jgrd.50184.

Schumann, U., Penner, J. E., Chen, Y., Zhou, C., and Graf, K. (2015). Dehydration effects from contrails in a coupled contrail-climate model. *Atmos. Chem. Phys. Discuss.* doi:10.5194/acpd-15-19553-2015.

Schurer, A., Hegerl, G., Ribes, A., Polson, D., Morice, C., and Tett, S. (2018). Estimating the Transient Climate Response from Observed Warming. *J. Clim.* 31, 8645–8663. doi:10.1175/JCLI-D-17-0717.1.

Schwarber, A. K., Smith, S. J., Hartin, C. A., Vega-Westhoff, B. A., and Sriver, R. (2019). Evaluating climate emulation: fundamental impulse testing of simple climate models. *Earth Syst. Dyn.* 10, 729–739. doi:10.5194/esd-10-729-2019.

Schwartz, S. E. (2007). Heat capacity, time constant, and sensitivity of Earth's climate system. *J. Geophys. Res. Atmos.* 112, 1–12. doi:10.1029/2007JD008746.

Schwartz, S. E. (2012). Determination of Earth's Transient and Equilibrium Climate Sensitivities from Observations Over the Twentieth Century: Strong Dependence on Assumed Forcing. *Surv. Geophys.* 33, 745–777. doi:10.1007/s10712-012-9180-4.

Schwartz, S. E. (2018). Unrealized Global Temperature Increase: Implications of Current Uncertainties. *J. Geophys. Res. Atmos.* 123, 3462–3482. doi:10.1002/2017JD028121.

Schweiger, A., Lindsay, R., Zhang, J., Steele, M., Stern, H., and Kwok, R. (2011). Uncertainty in modeled Arctic sea ice volume. *J. Geophys. Res. Ocean.* 116. doi:10.1029/2011JC007084.

Scott, C. E., Monks, S. A., Spracklen, D. V., Arnold, S. R., Forster, P. M., Rap, A., et al. (2017). Impact on short-lived climate forcers (SLCFs) from a realistic land-use change scenario: Via changes in biogenic emissions. *Faraday Discuss.* doi:10.1039/c7fd00028f.

Screen, J. A., Deser, C., and Simmonds, I. (2012). Local and remote controls on observed Arctic warming. *Geophys. Res. Lett.* 39. doi:10.1029/2012GL051598.

Seager, R., Cane, M., Henderson, N., Lee, D.-E., Abernathey, R., and Zhang, H. (2019). Strengthening tropical Pacific zonal sea surface temperature gradient consistent with rising greenhouse gases. *Nat. Clim. Chang.* 9, 517–522. doi:10.1038/s41558-019-0505-x.

Séférian, R., Nabat, P., Michou, M., Saint-Martin, D., Voldoire, A., Colin, J., et al. (2019). Evaluation of CNRM Earth-System model, CNRM-ESM 2-1: role of Earth system processes in present-day and future climate. *J. Adv. Model. Earth Syst.* 11, 2019MS001791. doi:10.1029/2019MS001791.

Seifert, A., Heus, T., Pincus, R., and Stevens, B. (2015). Large-eddy simulation of the transient and near-equilibrium behavior of precipitating shallow convection. *J. Adv. Model. Earth Syst.* 7, 1918–1937. doi:10.1002/2015MS000489.

Sellar, A. A., Jones, C. G., Mulcahy, J., Tang, Y., Yool, A., Wiltshire, A., et al. (2019). UKESM1: Description and evaluation of the UK Earth System Model. *J. Adv. Model. Earth Syst.* 11. doi:10.1029/2019ms001739.

Seneviratne, S. I., Donat, M. G., Pitman, A. J., Knutti, R., and Wilby, R. L. (2016). Allowable $CO_2$emissions based on regional and impact-related climate targets. *Nature*. doi:10.1038/nature16542.

Shaffer, G., Huber, M., Rondanelli, R., and Pepke Pedersen, J. O. (2016). Deep time evidence for climate sensitivity

increase with warming. *Geophys. Res. Lett.* 43, 6538–6545. doi:10.1002/2016GL069243.
Shapiro, A. V. A. I., Schmutz, W., Rozanov, E., Schoell, M., Haberreiter, M., Shapiro, A. V. A. I., et al. (2011). A new approach to the long-term reconstruction of the solar irradiance leads to large historical solar forcing. *Astron. Astrophys.* 529, A67. doi:10.1051/0004-6361/201016173.
Shell, K. M., Kiehl, J. T., and Shields, C. A. (2008). Using the Radiative Kernel Technique to Calculate Climate Feedbacks in NCAR's Community Atmospheric Model. *J. Clim.* 21, 2269–2282. doi:10.1175/2007JCLI2044.1.
Shepherd, A., Ivins, E., Rignot, E., Smith, B., Van Den Broeke, M., Velicogna, I., et al. (2018). Mass balance of the Antarctic Ice Sheet from 1992 to 2017. *Nature* 558, 219–222. doi:10.1038/s41586-018-0179-y.
Sherwood, S. C., Bony, S., Boucher, O., Bretherton, C., Forster, P. M., Gregory, J. M., et al. (2015). Adjustments in the forcing-feedback framework for understanding climate change. *Bull. Am. Meteorol. Soc.* 96, 217–228. doi:10.1175/BAMS-D-13-00167.1.
Sherwood, S. C., Bony, S., and Dufresne, J.-L. (2014). Spread in model climate sensitivity traced to atmospheric convective mixing. *Nature* 505, 37–42. doi:10.1038/nature12829.
Sherwood, S. C., Dixit, V., and Salomez, C. (2018). The global warming potential of near-surface emitted water vapour. *Environ. Res. Lett.* doi:10.1088/1748-9326/aae018.
Sherwood, S. C., Ingram, W., Tsushima, Y., Satoh, M., Roberts, M., Vidale, P. L., et al. (2010). Relative humidity changes in a warmer climate. *J. Geophys. Res. Atmos.* 115. doi:10.1029/2009JD012585.
Sherwood, S. C., Webb, M., Forster, P. M., and Armour, K. C. (9999). WCRP estimate of ECS. *Rev. Geophys.* (submitted.
Shindell, D. T. (2014). Inhomogeneous forcing and transient climate sensitivity. *Nat. Clim. Chang.* doi:10.1038/nclimate2136.
Shindell, D. T. D. T., Faluvegi, G., Rotstayn, L., and Milly, G. (2015). Spatial patterns of radiative forcing and surface temperature response. *J. Geophys. Res. Atmos.* 120, 1–19. doi:10.1002/2014JD022752.
Shindell, D. T., Faluvegi, G., Koch, D. M., Schmidt, G. A., Linger, N., and Bauer, S. E. (2009). Improved attribution of climate forcing to emissions. *Science (80-. ).* doi:10.1126/science.1174760.
Shine, K. P. P., Allan, R. P. P., Collins, W. J. J., and Fuglestvedt, J. S. S. (2015). Metrics for linking emissions of gases and aerosols to global precipitation changes. *Earth Syst. Dyn.* 6, 525–540. doi:10.5194/esd-6-525-2015.
Siemann, A. L., Chaney, N., and Wood, E. F. (2018). Development and Validation of a Long-Term, Global, Terrestrial Sensible Heat Flux Dataset. *J. Clim.* 31, 6073–6095. doi:10.1175/JCLI-D-17-0732.1.
Siler, N., Po-Chedley, S., and Bretherton, C. S. (2018a). Variability in modeled cloud feedback tied to differences in the climatological spatial pattern of clouds. *Clim. Dyn.* 50, 1209–1220. doi:10.1007/s00382-017-3673-2.
Siler, N., Roe, G. H., and Armour, K. C. (2018b). Insights into the zonal-mean response of the hydrologic cycle to global warming from a diffusive energy balance model. *J. Clim.* doi:10.1175/JCLI-D-18-0081.1.
Silvers, L. G., Paynter, D., and Zhao, M. (2018). The Diversity of Cloud Responses to Twentieth Century Sea Surface Temperatures. *Geophys. Res. Lett.* 45, 391–400. doi:10.1002/2017GL075583.
Singarayer, J. S., Valdes, P. J., Friedlingstein, P., Nelson, S., and Beerling, D. J. (2011). Late Holocene methane rise caused by orbitally controlled increase in tropical sources. *Nature* 470, 82–85. doi:10.1038/nature09739.
Singh, H. A., Rasch, P. J., and Rose, B. E. J. (2017). Increased Ocean Heat Convergence Into the High Latitudes With CO2 Doubling Enhances Polar-Amplified Warming. *Geophys. Res. Lett.* doi:10.1002/2017GL074561.
Sitch, S., Huntingford, C., Gedney, N., Levy, P. E., Lomas, M., Piao, S. L., et al. (2008). Evaluation of the terrestrial carbon cycle, future plant geography and climate-carbon cycle feedbacks using five Dynamic Global Vegetation Models (DGVMs). *Glob. Chang. Biol.* 14, 2015–2039. doi:10.1111/j.1365-2486.2008.01626.x.
Skeie, R. B., Berntsen, T., Aldrin, M., Holden, M., and Myhre, G. (2018). Climate sensitivity estimates - Sensitivity to radiative forcing time series and observational data. *Earth Syst. Dyn.* 9, 879–894. doi:10.5194/esd-9-879-2018.
Skeie, R. B., Berntsen, T. K., Myhre, G., Tanaka, K., Kvalevåg, M. M., and Hoyle, C. R. (2011). Anthropogenic radiative forcing time series from pre-industrial times until 2010. *Atmos. Chem. Phys.* doi:10.5194/acp-11-11827-2011.
Skiles, S. M., Flanner, M., Cook, J. M., Dumont, M., and Painter, T. H. (2018). Radiative forcing by light-absorbing particles in snow. *Nat. Clim. Chang.* 8, 964–971. doi:10.1038/s41558-018-0296-5.
Skinner, L. (2012). A Long View on Climate Sensitivity. *Science (80-. ).* 337, 917–919. doi:10.1126/science.1224011.
Smith, C. J., Forster, P. M., Allen, M., Fuglestvedt, J., Millar, R. J., Rogelj, J., et al. (2019). Current fossil fuel infrastructure does not yet commit us to 1.5 °C warming. *Nat. Commun.* doi:10.1038/s41467-018-07999-w.
Smith, C. J., Forster, P. M., Allen, M., Leach, N., Millar, R. J., Passerello, G. A., et al. (2018a). FAIR v1.3: A simple emissions-based impulse response and carbon cycle model. *Geosci. Model Dev.* doi:10.5194/gmd-11-2273-2018.
Smith, C. J., Kramer, R. J., Myhre, G., Forster, P. M., Soden, B. J., Andrews, T., et al. (2018b). Understanding Rapid Adjustments to Diverse Forcing Agents. *Geophys. Res. Lett.* 45. doi:10.1029/2018GL079826.
Smith, C. J., Kramer, R. J., and Sima, A. (9999a). The HadGEM3-GA7.1 radiative kernel: the importance of a well-resolved stratosphere. *Earth Syst. Sci. Data* (submitted.
Smith, C. J., Kramer, R., Myhre, G., Alterskjær, K., Pincus, R., Collins, W., et al. (9999b). Effective radiative forcing and adjustments in CMIP6 models. *Atmos. Chem. Phys. Discuss.* (submitted.
Smith, D. M., Allan, R. P., Coward, A. C., Eade, R., Hyder, P., Liu, C., et al. (2015). Earth's energy imbalance since

1960 in observations and CMIP5 models. *Geophys. Res. Lett.* 42, 1205–1213. doi:10.1002/2014GL062669.
Smith, S. M., Lowe, J. A., Bowerman, N. H. A., Gohar, L. K., Huntingford, C., and Allen, M. R. (2012). Equivalence of greenhouse-gas emissions for peak temperature limits. *Nat. Clim. Chang.* 2, 535–538. doi:10.1038/nclimate1496.
Snyder, C. W. (2016). Evolution of global temperature over the past two million years. *Nature* 538, 226–228. doi:10.1038/nature19798.
Soden, B. J., and Held, I. M. (2006). An Assessment of Climate Feedbacks in Coupled Ocean–Atmosphere Models. *J. Clim.* 19, 3354–3360. doi:10.1175/JCLI3799.1.
Soden, B. J., Held, I. M., Colman, R. C., Shell, K. M., Kiehl, J. T., and Shields, C. A. (2008). Quantifying climate feedbacks using radiative kernels. *J. Clim.* 21, 3504–3520. doi:10.1175/2007JCLI2110.1.
Soden, B. J. J., Collins, W. D. D., and Feldman, D. R. R. (2018). Reducing uncertainties in climate models. *Science (80-. ).* 361, 326–327. doi:10.1126/science.aau1864.
Soden, B. J., Jackson, D. L., Ramaswamy, V., Schwarzkopf, M. D., and Huang, X. (2005). The Radiative Signature of Upper Tropospheric Moistening. *Science (80-. ).* 310, 841–844. doi:10.1126/science.1115602.
Soni, V. K., Pandithurai, G., and Pai, D. S. (2016). Is there a transition of solar radiation from dimming to brightening over India? *Atmos. Res.* 169, 209–224. doi:10.1016/j.atmosres.2015.10.010.
Spencer, R. W., and Braswell, W. D. (2010). On the diagnosis of radiative feedback in the presence of unknown radiative forcing. *J. Geophys. Res. Atmos.* doi:10.1029/2009JD013371.
Spencer, R. W., and Braswell, W. D. (2011). On the misdiagnosis of surface temperature feedbacks from variations in Earth's radiant energy balance. *Remote Sens.* doi:10.3390/rs3081603.
Stanhill, G., Achiman, O., Rosa, R., and Cohen, S. (2014). The cause of solar dimming and brightening at the Earth's surface during the last half century: Evidence from measurements of sunshine duration. *J. Geophys. Res.* 119, 10902–10911. doi:10.1002/2013JD021308.
Stap, L. B., Köhler, P., and Lohmann, G. (2019). Including the efficacy of land ice changes in deriving climate sensitivity from paleodata. *Earth Syst. Dyn.* 10, 333–345. doi:10.5194/esd-10-333-2019.
Steffen, W., Rockström, J., Richardson, K., Lenton, T. M., Folke, C., Liverman, D., et al. (2018). Trajectories of the Earth System in the Anthropocene. *Proc. Natl. Acad. Sci.* 115, 8252–8259. doi:10.1073/pnas.1810141115.
Stein, T. H. M., Holloway, C. E., Tobin, I., and Bony, S. (2016). Observed Relationships between Cloud Vertical Structure and Convective Aggregation over Tropical Ocean. *J. Clim.* 30, 2187–2207. doi:10.1175/JCLI-D-16-0125.1.
Steinhilber, F., Abreu, J. A., Beer, J., Brunner, I., Christl, M., Fischer, H., et al. (2012). 9,400 years of cosmic radiation and solar activity from ice cores and tree rings. *Proc. Natl. Acad. Sci.* 109, 5967–5971. doi:10.1073/pnas.1118965109.
Stephens, G. L., Hakuba, M. Z., Hawcroft, M., Haywood, J. M., Behrangi, A., Kay, J. E., et al. (2016). The Curious Nature of the Hemispheric Symmetry of the Earth's Water and Energy Balances. *Curr. Clim. Chang. Reports* 2, 135–147. doi:10.1007/s40641-016-0043-9.
Stephens, G. L., O'Brien, D., Webster, P. J., Pilewski, P., Kato, S., and Li, J. (2015). The albedo of Earth. *Rev. Geophys.* 53, 141–163. doi:10.1002/2014RG000449.
Sterner, E., Johansson, D. J. A., and Azar, C. (2014). Emission metrics and sea level rise. *Clim. Change* 127, 335–351. doi:10.1007/s10584-014-1258-1.
Sterner, E. O., and Johansson, D. J. A. (2017). The effect of climate-carbon cycle feedbacks on emission metrics. *Environ. Res. Lett.* doi:10.1088/1748-9326/aa61dc.
Stevens, B. (2015). Rethinking the lower bound on aerosol radiative forcing. *J. Clim.* 28, 4794–4819. doi:10.1175/JCLI-D-14-00656.1.
Stevens, B., and Feingold, G. (2009). Untangling aerosol effects on clouds and precipitation in a buffered system. *Nature* 461, 607.
Stevens, B., Sherwood, S. C., Bony, S., and Webb, M. J. (2016). Prospects for narrowing bounds on Earth's equilibrium climate sensitivity. *Earth's Futur.* 4, 512–522. doi:10.1002/2016EF000376.
Stier, P. (2016). Limitations of passive remote sensing to constrain global cloud condensation nuclei. *Atmos. Chem. Phys.* 16, 6595–6607. doi:10.5194/acp-16-6595-2016.
Stjern, C. W., Samset, B. H., Myhre, G., Forster, P. M., Hodnebrog, Ø., Andrews, T., et al. (2017). Rapid Adjustments Cause Weak Surface Temperature Response to Increased Black Carbon Concentrations. *J. Geophys. Res. Atmos.* doi:10.1002/2017JD027326.
Stolarski, R. S., and Frith, S. M. (2006). Search for evidence of trend slow-down in the long-term TOMS/SBUV total ozone data record: The importance of instrument drift uncertainty. *Atmos. Chem. Phys.* doi:10.5194/acp-6-4057-2006.
Stolpe, M. B., Medhaug, I., Beyerle, U., and Knutti, R. (2019). Weak dependence of future global mean warming on the background climate state. *Clim. Dyn.* 53, 5079–5099. doi:10.1007/s00382-019-04849-3.
Storelvmo, T. (2017). Aerosol Effects on Climate via Mixed-Phase and Ice Clouds. *Annu. Rev. Earth Planet. Sci.* doi:10.1146/annurev-earth-060115-012240.
Storelvmo, T., Heede, U. K., Leirvik, T., Phillips, P. C. B., Arndt, P., and Wild, M. (2018). Lethargic response to aerosol emissions in current climate models. *Geophys. Res. Lett.* 45, 9. doi:10.1029/2018GL078298.

Storelvmo, T., Leirvik, T., Lohmann, U., Phillips, P. C. B., and Wild, M. (2016). Disentangling greenhouse warming and aerosol cooling to reveal Earth's climate sensitivity. *Nat. Geosci.* 9, 286–289. doi:10.1038/ngeo2670.
Stouffer, R. J., and Manabe, S. (2003). Equilibrium response of thermohaline circulation to large changes in atmospheric CO2 concentration. *Clim. Dyn.* 20, 759–773. doi:10.1007/s00382-002-0302-4.
Stroeve, J. C., Kattsov, V., Barrett, A., Serreze, M., Pavlova, T., Holland, M., et al. (2012). Trends in Arctic sea ice extent from CMIP5, CMIP3 and observations. *Geophys. Res. Lett.* 39. doi:10.1029/2012GL052676.
Stuecker, M. F., Bitz, C. M., Armour, K. C., Proistosescu, C., Kang, S. M., Xie, S. P., et al. (2018). Polar amplification dominated by local forcing and feedbacks. *Nat. Clim. Chang.* 8, 1076–1081. doi:10.1038/s41558-018-0339-y.
Su, H., Jiang, J. H., Neelin, J. D., Shen, T. J., Zhai, C., Yue, Q., et al. (2017). Tightening of tropical ascent and high clouds key to precipitation change in a warmer climate. *Nat. Commun.* 8, 15771. doi:10.1038/ncomms15771.
Su, H., Jiang, J. H., Zhai, C., Shen, T. J., Neelin, J. D., Stephens, G. L., et al. (2014). Weakening and strengthening structures in the Hadley Circulation change under global warming and implications for cloud response and climate sensitivity. *J. Geophys. Res. Atmos.* 119, 5787–5805. doi:10.1002/2014JD021642.
Sun, C., Kucharski, F., Li, J., Jin, F. F., Kang, I. S., and Ding, R. (2017). Western tropical Pacific multidecadal variability forced by the Atlantic multidecadal oscillation. *Nat. Commun.* 8. doi:10.1038/ncomms15998.
Super, J. R., Thomas, E., Pagani, M., Huber, M., O'Brien, C., and Hull, P. M. (2018). North Atlantic temperature and pCO2 coupling in the early-middle Miocene. *Geology* 46, 519–522. doi:10.1130/G40228.1.
Sutton, R. T. (2018). ESD Ideas: A simple proposal to improve the contribution of IPCC WGI to the assessment and communication of climate change risks. *Earth Syst. Dyn.* 9, 1155–1158. doi:10.5194/esd-9-1155-2018.
Suzuki, K., Stephens, G., Bodas-Salcedo, A., Wang, M., Golaz, J.-C., Yokohata, T., et al. (2015). Evaluation of the Warm Rain Formation Process in Global Models with Satellite Observations. *J. Atmos. Sci.* 72, 3996–4014. doi:10.1175/JAS-D-14-0265.1.
Svensmark, H. (1998). Influence of Cosmic Rays on Earth's Climate. *Phys. Rev. Lett.* 81, 5027–5030. doi:10.1103/PhysRevLett.81.5027.
Svensmark, H., Bondo, T., and Svensmark, J. (2009). Cosmic ray decreases affect atmospheric aerosols and clouds. *Geophys. Res. Lett.* 36, n/a-n/a. doi:10.1029/2009GL038429.
Svensmark, H., and Friis-Christensen, E. (1997). Variation of cosmic ray flux and global cloud coverage - A missing link in solar-climate relationships. *J. Atmos. Solar-Terrestrial Phys.* 59, 1225–1232. doi:10.1016/S1364-6826(97)00001-1.
Svensmark, J., Enghoff, M. B., Shaviv, N. J., and Svensmark, H. (2016). The response of clouds and aerosols to cosmic ray decreases. *J. Geophys. Res. Sp. Phys.* 121, 8152–8181. doi:10.1002/2016JA022689.
Swindles, G. T., Savov, I. P., Schmidt, A., Hooper, A., Connor, C. B., and Carrivick, J. L. (2018). Climatic control on Icelandic volcanic activity during the mid-Holocene. *Geology* 46, e444–e444. doi:10.1130/G40290Y.1.
Swingedouw, D., Fichefet, T., Huybrechts, P., Goosse, H., Driesschaert, E., and Loutre, M.-F. (2008). Antarctic ice-sheet melting provides negative feedbacks on future climate warming. *Geophys. Res. Lett.* 35. doi:10.1029/2008GL034410.
Takahashi, C., and Watanabe, M. (2016). Pacific trade winds accelerated by aerosol forcing over the past two decades. *Nat. Clim. Chang.* 6, 768–772. doi:10.1038/nclimate2996.
Takahashi, H., Su, H., and Jiang, J. H. (2016). Water vapor changes under global warming and the linkage to present-day interannual variabilities in CMIP5 models. *Clim. Dyn.* 47, 3673–3691. doi:10.1007/s00382-016-3035-5.
Takahashi, K., and Battisti, D. S. (2007). Processes Controlling the Mean Tropical Pacific Precipitation Pattern. Part I: The Andes and the Eastern Pacific ITCZ. *J. Clim.* 20, 3434–3451. doi:10.1175/JCLI4198.1.
Takemura, T., and Suzuki, K. (2019). Weak global warming mitigation by reducing black carbon emissions. *Sci. Rep.* 9. doi:10.1038/s41598-019-41181-6.
Tan, I., Storelvmo, T., and Zelinka, M. D. (2016). Observational constraints on mixed-phase clouds imply higher climate sensitivity. *Science (80-. ).* 352, 224–227. doi:10.1126/science.aad5300.
Tanaka, K., Cavalett, O., Collins, W. J., and Cherubini, F. (2019). Asserting the climate benefits of the coal-to-gas shift across temporal and spatial scales. *Nat. Clim. Chang.* doi:10.1038/s41558-019-0457-1.
Tanaka, K., Johansson, D. J. A., O'Neill, B. C., and Fuglestvedt, J. S. (2013). Emission metrics under the 2 °C climate stabilization target. *Clim. Change*. doi:10.1007/s10584-013-0693-8.
Tanaka, K., and O'Neill, B. C. (2018). The Paris Agreement zero-emissions goal is not always consistent with the 1.5 °c and 2 °c temperature targets. *Nat. Clim. Chang.* doi:10.1038/s41558-018-0097-x.
Tanaka, K., Ohmura, A., Folini, D., Wild, M., and Ohkawara, N. (2016). Is global dimming and brightening in Japan limited to urban areas? *Atmos. Chem. Phys.* 16, 13969–14001. doi:10.5194/acp-16-13969-2016.
Tang, T., Shindell, D., Faluvegi, G., Myhre, G., Olivié, D., Voulgarakis, A., et al. (2019). Comparison of Effective Radiative Forcing Calculations Using Multiple Methods, Drivers, and Models. *J. Geophys. Res. Atmos.* 124, 4382–4394. doi:10.1029/2018JD030188.
Tao, W. K., Chen, J. P., Li, Z., Wang, C., and Zhang, C. (2012). Impact of aerosols on convective clouds and precipitation. *Rev. Geophys.* doi:10.1029/2011RG000369.
Taylor, P. C., Cai, M., Hu, A., Meehl, J., Washington, W., and Zhang, G. J. (2013). A Decomposition of Feedback Contributions to Polar Warming Amplification. *J. Clim.* 26, 7023–7043. doi:10.1175/JCLI-D-12-00696.1.

Taylor, P. C., Kato, S., Xu, K.-M., and Cai, M. (2015). Covariance between Arctic sea ice and clouds within atmospheric state regimes at the satellite footprint level. *J. Geophys. Res. Atmos.* 120, 12656–12678. doi:10.1002/2015JD023520.

Tebaldi, C., and Arblaster, J. M. (2014). Pattern scaling: Its strengths and limitations, and an update on the latest model simulations. *Clim. Change*. doi:10.1007/s10584-013-1032-9.

Tebaldi, C., and Knutti, R. (2018). Evaluating the accuracy of climate change pattern emulation for low warming targets. *Environ. Res. Lett.* 13, 55006. doi:10.1088/1748-9326/aabef2.

Terai, C. R., Klein, S. A., and Zelinka, M. D. (2016). Constraining the lowcloud optical depth feedback at middle and high latitudes using satellite observations. *J. Geophys. Res.* 121, 9696–9716. doi:10.1002/2016JD025233.

Terai, C. R., Zhang, Y., Klein, S. A., Zelinka, M. D., Chiu, J. C., and Min, Q. (2019). Mechanisms Behind the Extratropical Stratiform Low-Cloud Optical Depth Response to Temperature in ARM Site Observations. *J. Geophys. Res. Atmos.* 124, 2127–2147. doi:10.1029/2018JD029359.

Thackeray, C. W., and Hall, A. (2019). An emergent constraint on future Arctic sea-ice albedo feedback. *Nat. Clim. Chang.* doi:10.1038/s41558-019-0619-1.

Thompson, D. W. J., Bony, S., and Li, Y. (2017). Thermodynamic constraint on the depth of the global tropospheric circulation. *Proc. Natl. Acad. Sci.* 114, 8181 LP – 8186. doi:10.1073/pnas.1620493114.

Thornhill, G., Collins, W., Connor, F. O., Smith, C., Kramer, R., Forster, P., et al. (9999). Effective Radiative forcing from emissions of reactive gases and aerosols. *Atmos. Chem. Phys* (submitted.

Tian, B. (2015). Spread of model climate sensitivity linked to double-Intertropical Convergence Zone bias. *Geophys. Res. Lett.* 42, 4133–4141. doi:10.1002/2015GL064119.

Tierney, J. E., Haywood, A. M., Feng, R., Bhattacharya, T., and Otto-Bliesner, B. L. (2019). Pliocene Warmth Consistent With Greenhouse Gas Forcing. *Geophys. Res. Lett.* 46, 9136–9144. doi:10.1029/2019GL083802.

Tierney, J. E., Zhu, J., King, J., Malevich, S. B., Hakim, G. J., Poulsen, C. J., et al. (9999). Glacial cooling and climate sensitivity revisited. *Nature* (submitted.

Tobin, I., Bony, S., Holloway, C. E., Grandpeix, J.-Y., Sèze, G., Coppin, D., et al. (2013). Does convective aggregation need to be represented in cumulus parameterizations? *J. Adv. Model. Earth Syst.* 5, 692–703. doi:10.1002/jame.20047.

Tokarska, K. B., Gillett, N. P., Arora, V. K., Lee, W. G., and Zickfeld, K. (2018). The influence of non-CO 2 forcings on cumulative carbon emissions budgets. *Environ. Res. Lett.* doi:10.1088/1748-9326/aaafdd.

Tokarska, K. B., Stolpe, M. B., Sippel, S., Fischer, E. M., Smith, C. J., Lehner, F., et al. (9999). Past warming trend constrains future warming in CMIP6 models. *Sci. Adv.* (submitted.

Tol, R. S. J., Berntsen, T. K., O'Neill, B. C., Fuglestvedt, J. S., and Shine, K. P. (2012). A unifying framework for metrics for aggregating the climate effect of different emissions. *Environ. Res. Lett.* 7, 044006. doi:10.1088/1748-9326/7/4/044006.

Toll, V., Christensen, M., Gassó, S., and Bellouin, N. (2017). Volcano and Ship Tracks Indicate Excessive Aerosol-Induced Cloud Water Increases in a Climate Model. *Geophys. Res. Lett.* 44, 12,492-12,500. doi:10.1002/2017GL075280.

Toll, V., Christensen, M., Quaas, J., and Bellouin, N. (2019). Weak average liquid-cloud-water response to anthropogenic aerosols. *Nature* 572, 51–55. doi:10.1038/s41586-019-1423-9.

Trenberth, K. E., and Fasullo, J. T. (2010). Simulation of Present-Day and Twenty-First-Century Energy Budgets of the Southern Oceans. *J. Clim.* 23, 440–454. doi:10.1175/2009JCLI3152.1.

Trenberth, K. E., Fasullo, J. T., and Balmaseda, M. A. (2014). Earth's Energy Imbalance. *J. Clim.* 27, 3129–3144. doi:10.1175/JCLI-D-13-00294.1.

Trenberth, K. E., and Stepaniak, D. P. (2003). Seamless poleward atmospheric energy transports and implications for the Hadley circulation. *J. Clim.* doi:10.1175/1520-0442(2003)016<3706:SPAETA>2.0.CO;2.

Trenberth, K. E., Zhang, Y., Fasullo, J. T., and Taguchi, S. (2015). Climate variability and relationships between top-of-atmosphere radiation and temperatures on Earth. *J. Geophys. Res. Atmos.* 120, 3642–3659. doi:10.1002/2014JD022887.

Tselioudis, G., Lipat, B. R., Konsta, D., Grise, K. M., and Polvani, L. M. (2016). Midlatitude cloud shifts, their primary link to the Hadley cell, and their diverse radiative effects. *Geophys. Res. Lett.* 43, 4594–4601. doi:10.1002/2016GL068242.

Tsushima, Y., Brient, F., Klein, S. A., Konsta, D., Nam, C. C., Qu, X., et al. (2017). The Cloud Feedback Model Intercomparison Project (CFMIP) Diagnostic Codes Catalogue – metrics, diagnostics and methodologies to evaluate, understand and improve the representation of clouds and cloud feedbacks in climate models. *Geosci. Model Dev.* 10, 4285–4305. doi:10.5194/gmd-10-4285-2017.

Tsushima, Y., Iga, S. I., Tomita, H., Satoh, M., Noda, A. T., and Webb, M. J. (2014). High cloud increase in a perturbed SST experiment with a global nonhydrostatic model including explicit convective processes. *J. Adv. Model. Earth Syst.* 6, 571–585. doi:https://doi.org/10.1002/2013MS000301.

Tsushima, Y., and Manabe, S. (2013). Assessment of radiative feedback in climate models using satellite observations of annual flux variation. *Proc. Natl. Acad. Sci.* doi:10.1073/pnas.1216174110.

Tsushima, Y., Ringer, M. A., Webb, M. J., and Williams, K. D. (2013). Quantitative evaluation of the seasonal

variations in climate model cloud regimes. *Clim. Dyn.* 41, 2679–2696. doi:10.1007/s00382-012-1609-4.
Tsutsui, J. (2017). Quantification of temperature response to CO2 forcing in atmosphere–ocean general circulation models. *Clim. Change* 140, 287–305. doi:10.1007/s10584-016-1832-9.
Turnock, S. T., Spracklen, D. V, Carslaw, K. S., Mann, G. W., Woodhouse, M. T., Forster, P. M., et al. (2015). Modelled and observed changes in aerosols and surface solar radiation over Europe between 1960 and 2009. *Atmos. Chem. Phys.* 15, 9477–9500. doi:10.5194/acp-15-9477-2015.
Tuzet, F., Dumont, M., Lafaysse, M., Picard, G., Arnaud, L., Voisin, D., et al. (2017). A multilayer physically based snowpack model simulating direct and indirect radiative impacts of light-absorbing impurities in snow. *Cryosph.* 11, 2633–2653. doi:10.5194/tc-11-2633-2017.
Twomey, S. (1959). The nuclei of natural cloud formation part II: The supersaturation in natural clouds and the variation of cloud droplet concentration. *Geofis. Pura e Appl.* 43, 243–249. doi:10.1007/BF01993560.
Ullrich, R., Hoose, C., Möhler, O., Niemand, M., Wagner, R., Höhler, K., et al. (2017). A New Ice Nucleation Active Site Parameterization for Desert Dust and Soot. *J. Atmos. Sci.* 74, 699–717. doi:10.1175/JAS-D-16-0074.1.
Unger, N. (2014). Human land-use-driven reduction of forest volatiles cools global climate. *Nat. Clim. Chang.* doi:10.1038/nclimate2347.
Usoskin, I. G. (2017). A history of solar activity over millennia. *Living Rev. Sol. Phys.* 14, 3. doi:10.1007/s41116-017-0006-9.
Vaillant de Guélis, T., Chepfer, H., Guzman, R., Bonazzola, M., Winker, D. M., and Noel, V. (2018). Space lidar observations constrain longwave cloud feedback. *Sci. Rep.* 8, 16570. doi:10.1038/s41598-018-34943-1.
Van Marle, M. J. E., Kloster, S., Magi, B. I., Marlon, J. R., Daniau, A. L., Field, R. D., et al. (2017). Historic global biomass burning emissions for CMIP6 (BB4CMIP) based on merging satellite observations with proxies and fire models (1750-2015). *Geosci. Model Dev.* 10, 3329–3357. doi:10.5194/gmd-10-3329-2017.
van Vuuren, D. P., Lowe, J., Stehfest, E., Gohar, L., Hof, A. F., Hope, C., et al. (2011). How well do integrated assessment models simulate climate change? *Clim. Change* 104, 255–285. doi:10.1007/s10584-009-9764-2.
Vargas Zeppetello, L. R., Donohoe, A., and Battisti, D. S. (2019). Does Surface Temperature Respond to or Determine Downwelling Longwave Radiation? *Geophys. Res. Lett.* 46, 2781–2789. doi:10.1029/2019GL082220.
Várnai, T., and Marshak, A. (2015). Effect of Cloud Fraction on Near-Cloud Aerosol Behavior in the MODIS Atmospheric Correction Ocean Color Product. *Remote Sens.* 7, 5283–5299. doi:10.3390/rs70505283.
Vecchi, G. A., Soden, B. J., Wittenberg, A. T., Held, I. M., Leetmaa, A., and Harrison, M. J. (2006). Weakening of tropical Pacific atmospheric circulation due to anthropogenic forcing. *Nature* 441, 73–76. doi:10.1038/nature04744.
Vecchi, G., Clement, A., and Soden, B. J. (2008). Examining the Tropical Pacific's Response to Global Warming. *Eos (Washington. DC).*
Vergara-Temprado, J., Holden, M. A., Orton, T. R., O'Sullivan, D., Umo, N. S., Browse, J., et al. (2018). Is Black Carbon an Unimportant Ice-Nucleating Particle in Mixed-Phase Clouds? *J. Geophys. Res. Atmos.* doi:10.1002/2017JD027831.
Vial, J., Dufresne, J.-L. L., and Bony, S. (2013). On the interpretation of inter-model spread in CMIP5 climate sensitivity estimates. *Clim. Dyn.* 41, 3339–3362. doi:10.1007/s00382-013-1725-9.
Vieira, L. E. A., Solanki, S. K., Krivova, N. A., and Usoskin, I. (2011). Evolution of the solar irradiance during the Holocene. *Astron. Astrophys.* 531, A6. doi:10.1051/0004-6361/201015843.
Vizcaíno, M., Mikolajewicz, U., Jungclaus, J., and Schurgers, G. (2010). Climate modification by future ice sheet changes and consequences for ice sheet mass balance. *Clim. Dyn.* 34, 301–324. doi:10.1007/s00382-009-0591-y.
Voigt, A., and Shaw, T. A. (2015). Circulation response to warming shaped by radiative changes of clouds and water vapour. *Nat. Geosci.* 8, 102. doi:10.1038/ngeo2345.
Voigt, A., and Shaw, T. A. (2016). Impact of regional atmospheric cloud radiative changes on shifts of the extratropical jet stream in response to global warming. *J. Clim.* 29, 8399–8421. doi:10.1175/JCLI-D-16-0140.1.
Voigt, A., Stevens, B., Bader, J., and Mauritsen, T. (2013). The observed hemispheric symmetry in reflected shortwave irradiance. *J. Clim.* 26, 468–477. doi:10.1175/JCLI-D-12-00132.1.
Volodin, E. M. (2008). Relation between temperature sensitivity to doubled carbon dioxide and the distribution of clouds in current climate models. *Izv. Atmos. Ocean. Phys.* 44, 288–299. doi:10.1134/S0001433808030043.
von der Heydt, A. S., and Ashwin, P. (2016). State dependence of climate sensitivity: attractor constraints and palaeoclimate regimes. *Dyn. Stat. Clim. Syst.* 1, 1–21. doi:10.1093/climsys/dzx001.
von der Heydt, A. S., Dijkstra, H. A., Köhler, P., and Wal, R. Van De (2014). On the background state dependency of ( palaeo ) climate sensitivity. *Geophys. Res. Lett.* 41, 6484–6492. doi:doi:10.1002/2014GL061121.
von der Heydt, A. S., Dijkstra, H. A., van de Wal, R. S. W., Caballero, R., Crucifix, M., Foster, G. L., et al. (2016). Lessons on Climate Sensitivity From Past Climate Changes. *Curr. Clim. Chang. Reports* 2, 148–158. doi:10.1007/s40641-016-0049-3.
Von Schuckmann, K., Palmer, M. D., Trenberth, K. E., Cazenave, A., Chambers, D., Champollion, N., et al. (2016). An imperative to monitor Earth's energy imbalance. *Nat. Clim. Chang.* 6, 138–144. doi:10.1038/nclimate2876.
Voss, R., and Mikolajewicz, U. (2001). Long-term climate changes due to increased CO2 concentration in the coupled atmosphere-ocean general circulation model ECHAM3/LSG. *Clim. Dyn.* 17, 45–60. doi:10.1007/pl00007925.

Wang, K. C., Ma, Q., Wang, X. Y., and Wild, M. (2014). Urban impacts on mean and trend of surface incident solar radiation. *Geophys. Res. Lett.* 41, 4664–4668. doi:Doi 10.1002/2014gl060201.
Wang, K., Ma, Q., Li, Z., and Wang, J. (2015a). Decadal variability of surface incident solar radiation over China: Observations, satellite retrievals, and reanalyses. *J. Geophys. Res.* 120, 6500–6514. doi:10.1002/2015JD023420.
Wang, M., Xu, B., Cao, J., Tie, X., Wang, H., Zhang, R., et al. (2015b). Carbonaceous aerosols recorded in a southeastern Tibetan glacier: analysis of temporal variations and model estimates of sources and radiative forcing. *Atmos. Chem. Phys.* 15, 1191–1204. doi:10.5194/acp-15-1191-2015.
Wang, R., Andrews, E., Balkanski, Y., Boucher, O., Myhre, G., Samset, B. H., et al. (2018). Spatial Representativeness Error in the Ground-Level Observation Networks for Black Carbon Radiation Absorption. *Geophys. Res. Lett.* 45, 2106–2114. doi:10.1002/2017GL076817.
Wang, R., Balkanski, Y., Boucher, O., Ciais, P., Schuster, G. L., Chevallier, F., et al. (2016). Estimation of global black carbon direct radiative forcing and its uncertainty constrained by observations. *J. Geophys. Res. Atmos.* 121, 5948–5971. doi:10.1002/2015JD024326.
Wang, Y., and Wild, M. (2016). A new look at solar dimming and brightening in China. *Geophys. Res. Lett.* 43, 11777–11785. doi:10.1002/2016GL071009.
Wara, M. W., Ravelo, A. C., and Delaney, M. L. (2005). Climate change: Permanent El Niño-like conditions during the Pliocene warm period. *Science (80-. ).* 309, 758–761. doi:10.1126/science.1112596.
Ward, D. S., Mahowald, N. M., and Kloster, S. (2014). Potential climate forcing of land use and land cover change. *Atmos. Chem. Phys.* doi:10.5194/acp-14-12701-2014.
Warren, S. G. (2013). Can black carbon in snow be detected by remote sensing? *J. Geophys. Res. Atmos.* 118, 779–786. doi:10.1029/2012JD018476.
Watanabe, M., Kamae, Y., Shiogama, H., DeAngelis, A. M., and Suzuki, K. (2018). Low clouds link equilibrium climate sensitivity to hydrological sensitivity. *Nat. Clim. Chang.* 8, 901–906. doi:10.1038/s41558-018-0272-0.
Watanabe, M., Shiogama, H., Yokohata, T., Kamae, Y., Yoshimori, M., Ogura, T., et al. (2012). Using a multiphysics ensemble for exploring diversity in cloud-shortwave feedback in GCMs. *J. Clim.* 25, 5416–5431.
Webb, M. J., Lambert, F. H., and Gregory, J. M. (2013). Origins of differences in climate sensitivity, forcing and feedback in climate models. *Clim. Dyn.* 40, 677–707. doi:10.1007/s00382-012-1336-x.
Wen, Q., Yao, J., Döös, K., and Yang, H. (2018). Decoding hosing and heating effects on global temperature and meridional circulations in a warming climate. *J. Clim.* doi:10.1175/JCLI-D-18-0297.1.
Wigley, T. M. L. (1998). The Kyoto Protocol: CO 2 CH 4 and climate implications . *Geophys. Res. Lett.* doi:10.1029/98gl01855.
Wigley, T. M. L., Ammann, C. M., Santer, B. D., and Raper, S. C. B. (2005). Effect of climate sensitivity on the response to volcanic forcing. *J. Geophys. Res. D Atmos.* doi:10.1029/2004JD005557.
Wijffels, S., Roemmich, D., Monselesan, D., Church, J., and Gilson, J. (2016). Ocean temperatures chronicle the ongoing warming of Earth. *Nat. Clim. Chang.* 6, 116–118. doi:10.1038/nclimate2924.
Wilcox, E. M., Thomas, R. M., Praveen, P. S., Pistone, K., Bender, F. A. M., and Ramanathan, V. (2016). Black carbon solar absorption suppresses turbulence in the atmospheric boundary layer. *Proc. Natl. Acad. Sci. U. S. A.* 113, 11794–11799. doi:10.1073/pnas.1525746113.
Wild, M. (2012). Enlightening global dimming and brightening. *Bull. Am. Meteorol. Soc.* 93, 27–37. doi:10.1175/BAMS-D-11-00074.1.
Wild, M. (2016). Decadal changes in radiative fluxes at land and ocean surfaces and their relevance for global warming. *Wiley Interdiscip. Rev. Chang.* 7, 91–107. doi:10.1002/wcc.372.
Wild, M. (2017). Towards Global Estimates of the Surface Energy Budget. *Curr. Clim. Chang. Reports* 3, 87–97. doi:10.1007/s40641-017-0058-x.
Wild, M., Folini, D., Hakuba, M. Z., Schär, C., Seneviratne, S. I., Kato, S., et al. (2015). The energy balance over land and oceans: an assessment based on direct observations and CMIP5 climate models. *Clim. Dyn.* 44, 3393–3429. doi:10.1007/s00382-014-2430-z.
Wild, M., Folini, D., Schar, C., Loeb, N., Dutton, E. G., and König-Langlo, G. (2013). The global energy balance from a surface perspective. *Clim. Dyn.* 40, 3107–3134. doi:10.1007/S00382-012-1569-8.
Wild, M., Hakuba, M. Z., Folini, D., Dörig-Ott, P., Schär, C., Kato, S., et al. (2019). The cloud-free global energy balance and inferred cloud radiative effects: an assessment based on direct observations and climate models. *Clim. Dyn.* doi:https://doi.org/10.1007/s00382-018-4413-y.
Wild, M., and Schmucki, E. (2011). Assessment of global dimming and brightening in IPCC-AR4/CMIP3 models and ERA40. *Clim. Dyn.* 37, 1671–1688. doi:Doi 10.1007/S00382-010-0939-3.
Willeit, M., Ganopolski, A., and Feulner, G. (2014). Asymmetry and uncertainties in biogeophysical climate-vegetation feedback over a range of CO2 forcings. *Biogeosciences* 11, 17–32. doi:10.5194/bg-11-17-2014.
Williams, I. N., and Pierrehumbert, R. T. (2017). Observational evidence against strongly stabilizing tropical cloud feedbacks. *Geophys. Res. Lett.* 44, 1503–1510. doi:10.1002/2016GL072202.
Williams, K. D., Ingram, W. J., and Gregory, J. M. (2008). Time variation of effective climate sensitivity in GCMs. *J. Clim.* doi:10.1175/2008JCLI2371.1.
Wing, A. A., and Emanuel, K. A. (2014). Physical mechanisms controlling self-aggregation of convection in idealized

numerical modeling simulations. *J. Adv. Model. Earth Syst.* 6, 59–74. doi:10.1002/2013MS000269.
Winguth, A., Shellito, C., Shields, C., and Winguth, C. (2010). Climate Response at the Paleocene–Eocene Thermal Maximum to Greenhouse Gas Forcing—A Model Study with CCSM3. *J. Clim.* 23, 2562–2584. doi:10.1175/2009JCLI3113.1.
Winton, M., Adcroft, A., Griffies, S. M., Hallberg, R. W., Horowitz, L. W., and Stouffer, R. J. (2013). Influence of ocean and atmosphere components on simulated climate sensitivities. *J. Clim.* doi:10.1175/JCLI-D-12-00121.1.
Witkowski, C. R., Weijers, J. W. H., Blais, B., Schouten, S., and Sinninghe Damsté, J. S. (2018). Molecular fossils from phytoplankton reveal secular Pco2 trend over the Phanerozoic. *Sci. Adv.* 4. doi:10.1126/sciadv.aat4556.
WMO (World Meteorological Organization) (2018). *SCIENTIFIC ASSESSMENT OF OZONE DEPLETION: 2018 World Meteorological Organization Global Ozone Research and Monitoring Project-Report No. 58 World Meteorological Organization United Nations Environment Programme National Oceanic and Atmospheric Administrat*. Geneva Available at: http://ozone.unep.org/science/assessment/sap [Accessed July 12, 2019].
Wood, R., and Bretherton, C. S. (2006). On the relationship between stratiform low cloud cover and lower-tropospheric stability. *J. Clim.* doi:10.1175/JCLI3988.1.
Woods, C., and Caballero, R. (2016). The role of moist intrusions in winter arctic warming and sea ice decline. *J. Clim.* doi:10.1175/JCLI-D-15-0773.1.
Wu, C.-J., Krivova, N. A., Solanki, S. K., and Usoskin, I. G. (2018). Solar total and spectral irradiance reconstruction over the last 9000 years. *Astron. Astrophys.* 620, A120. doi:10.1051/0004-6361/201832956.
Wyant, M. C., Bretherton, C. S., Bacmeister, J. T., Kiehl, J. T., Held, I. M., Zhao, M., et al. (2006). A comparison of low-latitude cloud properties and their response to climate change in three AGCMs sorted into regimes using mid-tropospheric vertical velocity. 27, 261–279, doi: 10.1007/s00382-006-0138–4.
Xie, B., Zhang, H., Wang, Z., Zhao, S., and Fu, Q. (2016). A Modeling Study of E ff ective Radiative Forcing and Climate Response Due to Tropospheric Ozone. 33, 819–828.
Xie, S.-P., and Philander, S. G. H. (1994). A coupled ocean-atmosphere model of relevance to the ITCZ in the eastern Pacific. *Tellus A* 46, 340–350. doi:10.1034/j.1600-0870.1994.t01-1-00001.x.
Xie, S. P., Deser, C., Vecchi, G. A., Ma, J., Teng, H., and Wittenberg, A. T. (2010). Global warming pattern formation: Sea surface temperature and rainfall. *J. Clim.* doi:10.1175/2009JCLI3329.1.
Yang, H., Wen, Q., Yao, J., and Wang, Y. (2017). Bjerknes compensation in meridional heat transport under freshwater forcing and the role of climate feedback. *J. Clim.* doi:10.1175/JCLI-D-16-0824.1.
Yang, S., Wang, X. L., and Wild, M. (2018). Homogenization and Trend Analysis of the 1958-2016 In Situ Surface Solar Radiation Records in China. *J. Clim.* 31, 4529–4541. doi:10.1175/JCLI-D-17-0891.1.
Yang, S., Wang, X. L., and Wild, M. (2019). Causes of Dimming and Brightening in China Inferred from Homogenized Daily Clear-Sky and All-Sky in situ Surface Solar Radiation Records (1958-2016). *J. Clim.* 32, 5901–5913. doi:10.1175/JCLI-D-18-0666.1.
Yin, J. H. (2005). A consistent poleward shift of the storm tracks in simulations of 21st century climate. *Geophys. Res. Lett.* 32, 1–4. doi:10.1029/2005GL023684.
Yoshimori, M., Abe-Ouchi, A., and Laîné, A. (2017). The role of atmospheric heat transport and regional feedbacks in the Arctic warming at equilibrium. *Clim. Dyn.* doi:10.1007/s00382-017-3523-2.
Yoshimori, M., Hargreaves, J. C., Annan, J. D., Yokohata, T., and Abe-Ouchi, A. (2011). Dependency of feedbacks on forcing and climate state in physics parameter ensembles. *J. Clim.* 24, 6440–6455. doi:10.1175/2011JCLI3954.1.
Yoshimori, M., Lambert, F. H., Webb, M. J., and Andrews, T. (2019). Fixed anvil temperature feedback - positive, zero or negative? *J. Clim.*, JCLI-D-19-0108.1. doi:10.1175/JCLI-D-19-0108.1.
You, Q. L., Sanchez-Lorenzo, A., Wild, M., Folini, D., Fraedrich, K., Ren, G. Y., et al. (2013). Decadal variation of surface solar radiation in the Tibetan Plateau from observations, reanalysis and model simulations. *Clim. Dyn.* 40, 2073–2086. doi:Doi 10.1007/S00382-012-1383-3.
Yu, F., and Luo, G. (2014). Effect of solar variations on particle formation and cloud condensation nuclei. *Environ. Res. Lett.* 9. doi:10.1088/1748-9326/9/4/045004.
Yu, L. (2019). "Global Air-Sea Fluxes of Heat, Fresh Water, and Momentum: Energy Budget Closure and Unanswered Questions," in *ANNUAL REVIEW OF MARINE SCIENCE, VOL 11* Annual Review of Marine Science., ed. S. Carlson, CA and Giovannoni (ANNUAL REVIEWS), 227–248. doi:10.1146/annurev-marine-010816-060704.
Yuan, T., Remer, L. A., and Yu, H. (2011). Microphysical, macrophysical and radiative signatures of volcanic aerosols in trade wind cumulus observed by the A-Train. *Atmos. Chem. Phys.* 11, 7119–7132. doi:10.5194/acp-11-7119-2011.
Zachos, J. C., Dickens, G. R., and Zeebe, R. E. (2008). An early Cenozoic perspective on greenhouse warming and carbon-cycle dynamics. *Nature* 451, 279–283. doi:10.1038/nature06588.
Zaehle, S., Jones, C. D., Houlton, B., Lamarque, J. F., and Robertson, E. (2015). Nitrogen availability reduces CMIP5 projections of twenty-first-century land carbon uptake. *J. Clim.* doi:10.1175/JCLI-D-13-00776.1.
Zaliapin, I., and Ghil, M. (2010). Nonlinear Processes in Geophysics Another look at climate sensitivity. *Nonlin. Process. Geophys* 17, 113–122. doi:10.5194/npg-17-113-2010.
Zanatta, M., Gysel, M., Bukowiecki, N., Müller, T., Weingartner, E., Areskoug, H., et al. (2016). A European aerosol phenomenology-5: Climatology of black carbon optical properties at 9 regional background sites across Europe.

*Atmos. Environ.* 145, 346–364. doi:10.1016/J.ATMOSENV.2016.09.035.

Zanna, L., Khatiwala, S., Gregory, J. M., Ison, J., and Heimbach, P. (2019). Global reconstruction of historical ocean heat storage and transport. *Proc. Natl. Acad. Sci.* 116, 1126–1131. doi:10.1073/pnas.1808838115.

Zelinka, M. D., Andrews, T., Forster, P. M., and Taylor, K. E. (2014). Quantifying components of aerosol-cloud-radiation interactions in climate models. *J. Geophys. Res. Atmos.* 119, 7599–7615. doi:10.1002/2014JD021710.

Zelinka, M. D., Grise, K. M., Klein, S. A., Zhou, C., DeAngelis, A. M., and Christensen, M. W. (2018). Drivers of the Low-Cloud Response to Poleward Jet Shifts in the North Pacific in Observations and Models. *J. Clim.* 31, 7925–7947. doi:10.1175/JCLI-D-18-0114.1.

Zelinka, M. D., and Hartmann, D. L. (2010). Why is longwave cloud feedback positive? *J. Geophys. Res.* 115, D16117. doi:10.1029/2010JD013817.

Zelinka, M. D., and Hartmann, D. L. (2012). Climate feedbacks and their implications for poleward energy flux changes in a warming climate. *J. Clim.* doi:10.1175/JCLI-D-11-00096.1.

Zelinka, M. D., Myers, T. A., McCoy, D. T., Po-Chedley, S., Caldwell, P. M., Ceppi, P., et al. (2020). Causes of higher climate sensitivity in CMIP6 models. *Geophys. Res. Lett.* 46, 2019GL085782. doi:10.1029/2019GL085782.

Zelinka, M. D., Zhou, C., and Klein, S. A. (2016). Insights from a refined decomposition of cloud feedbacks. *Geophys. Res. Lett.* 43, 9259–9269. doi:10.1002/2016GL069917.

Zemp, M., Huss, M., Thibert, E., Eckert, N., McNabb, R., Huber, J., et al. (2019). Global glacier mass changes and their contributions to sea-level rise from 1961 to 2016. *Nature* 568, 382–386. doi:10.1038/s41586-019-1071-0.

Zhai, C., Jiang, J. H., and Su, H. (2015). Long-term cloud change imprinted in seasonal cloud variation: More evidence of high climate sensitivity. *Geophys. Res. Lett.* 42, 8729–8737. doi:10.1002/2015GL065911.

Zhang, C., Xie, S., Klein, S. A., Ma, H., Tang, S., Van Weverberg, K., et al. (2018a). CAUSES: Diagnosis of the Summertime Warm Bias in CMIP5 Climate Models at the ARM Southern Great Plains Site. *J. Geophys. Res.* 123, 2968–2992. doi:10.1002/2017JD027200.

Zhang, G. J., and Song, X. (2010). Convection Parameterization, Tropical Pacific Double ITCZ, and Upper-Ocean Biases in the NCAR CCSM3. Part II: Coupled Feedback and the Role of Ocean Heat Transport. *J. Clim.* 23, 800–812. doi:10.1175/2009JCLI3109.1.

Zhang, H., Zhao, S., Wang, Z., Zhang, X., and Song, L. (2016). The updated effective radiative forcing of major anthropogenic aerosols and their effects on global climate at present and in the future. *Int. J. Climatol.* 36, 4029–4044. doi:10.1002/joc.4613.

Zhang, M., and Huang, Y. (2014). Radiative Forcing of Quadrupling CO2. *J. Clim.* 27, 2496–2508. doi:10.1175/JCLI-D-13-00535.1.

Zhang, R., Wang, H., Fu, Q., Rasch, P. J., and Wang, X. (2019). Unraveling driving forces explaining significant reduction in satellite-inferred Arctic surface albedo since the 1980s. *Proc. Natl. Acad. Sci.* doi:10.1073/pnas.1915258116.

Zhang, W., Miller, P. A., Jansson, C., Samuelsson, P., Mao, J., and Smith, B. (2018b). Self-Amplifying Feedbacks Accelerate Greening and Warming of the Arctic. *Geophys. Res. Lett.* 45, 7102–7111. doi:10.1029/2018GL077830.

Zhang, X. T., Liang, S. L., Wild, M., and Jiang, B. (2015). Analysis of surface incident shortwave radiation from four satellite products. *Remote Sens. Environ.* 165, 186–202. doi:10.1016/j.rse2015.05.015.

Zhang, Y. G., Pagani, M., and Liu, Z. (2014). A 12-Million-Year Temperature History of the Tropical Pacific Ocean. *Science (80-. ).* 344, 84 LP – 87. doi:10.1126/science.1246172.

Zhao, B., Liou, K.-N., Gu, Y., Jiang, J. H., Li, Q., Fu, R., et al. (2018). Impact of aerosols on ice crystal size. *Atmos. Chem. Phys.* 18, 1065–1078. doi:10.5194/acp-18-1065-2018.

Zhao, M., Golaz, J.-C., Held, I. M., Ramaswamy, V., Lin, S.-J., Ming, Y., et al. (2015). Uncertainty in Model Climate Sensitivity Traced to Representations of Cumulus Precipitation Microphysics. *J. Clim.* 29, 543–560. doi:10.1175/JCLI-D-15-0191.1.

Zhao, S., and Suzuki, K. (2019). Differing Impacts of Black Carbon and Sulfate Aerosols on Global Precipitation and the ITCZ Location via Atmosphere and Ocean Energy Perturbations. *J. Clim.* 32, 5567–5582. doi:10.1175/JCLI-D-18-0616.1.

Zhou, C., Wang, K., and Ma, Q. (2017a). Evaluation of Eight Current Reanalyses in Simulating Land Surface Temperature from 1979 to 2003 in China. *J. Clim.* 30, 7379–7398. doi:10.1175/JCLI-D-16-0903.1.

Zhou, C., Zelinka, M. D., Dessler, A. E., and Klein, S. A. (2015). The relationship between interannual and long-term cloud feedbacks. *Geophys. Res. Lett.* doi:10.1002/2015GL066698.

Zhou, C., Zelinka, M. D., and Klein, S. A. (2016). Impact of decadal cloud variations on the Earth's energy budget. *Nat. Geosci.* 9, 871–874. doi:10.1038/ngeo2828.

Zhou, C., Zelinka, M. D., and Klein, S. A. (2017b). Analyzing the dependence of global cloud feedback on the spatial pattern of sea surface temperature change with a Green's function approach. *J. Adv. Model. Earth Syst.* 9, 2174–2189. doi:10.1002/2017MS001096.

Zhou, C., Zhang, H., Zhao, S., and Li, J. (2017c). Simulated effects of internal mixing of anthropogenic aerosols on the aerosol–radiation interaction and global temperature. *Int. J. Climatol.* 37, 972–986. doi:10.1002/joc.5050.

Zhou, C., Zhang, H., Zhao, S., and Li, J. (2018). On Effective Radiative Forcing of Partial Internally and Externally

Mixed Aerosols and Their Effects on Global Climate. *J. Geophys. Res. Atmos.* 123, 401–423. doi:10.1002/2017JD027603.
Zhu, J., Poulsen, C. J., and Otto-Bliesner, B. (9999). High climate sensitivity in CMIP6 models not supported by past warm climates. *Nat. Clim. Chang.* (submitted.
Zhu, J., Poulsen, C. J., and Tierney, J. E. (2019). Simulation of Eocene extreme warmth and high climate sensitivity through cloud feedbacks. *Sci. Adv.* 5. doi:10.1126/sciadv.aax1874.
Zhu, Y., Rosenfeld, D., and Li, Z. (2018). Under What Conditions Can We Trust Retrieved Cloud Drop Concentrations in Broken Marine Stratocumulus? *J. Geophys. Res. Atmos.* 123, 8754–8767. doi:10.1029/2017JD028083.

# Appendix 7.A Technical formulae and tables

## 7.A.1 Well-Mixed Greenhouse Gas Radiative Forcing Formulae

The formulae used to calculate the radiative forcings (RFs) from carbon dioxide (CO2), CH4 and nitrous oxide (N2O) are taken from Etminan et al. (2016), their table 1.

**Table 7.A.1:** Simplified Expressions for Radiative Forcing of $CO_2$, $CH_4$, and $N_2O$, Where *C* Is the $CO_2$ Concentration (in ppm), *M* Is the $CH_4$ Concentration (in ppb), and N is the $N_2O$ Concentration (in ppb).

| Gas | Simplified Expression | Coefficients |
|---|---|---|
| $CO_2$ | $[a_1(C-C_0)^2 + b_1\lvert C-C_0\rvert + c_1\bar{N} + 5.36] \times \ln\left(C/C_0\right)$ | $a_1 = -2.4 \times 10^{-7}$ Wm$^{-2}$ ppm$^{-1}$ |
| | | $b_1 = 7.2 \times 10^{-4}$ Wm$^{-2}$ ppm$^{-1}$ |
| | | $c_1 = -2.1 \times 10^{-4}$ Wm$^{-2}$ ppb$^{-1}$ |
| $N_2O$ | $[a_2\bar{C} + b_2\bar{N} + c_2\bar{M} + 0.117](\sqrt{N} - \sqrt{N_0})$ | $a_2 = -8.0 \times 10^{-6}$ Wm$^{-2}$ ppb$^{-1}$ |
| | | $b_2 = 4.2 \times 10^{-6}$ Wm$^{-2}$ ppb$^{-1}$ |
| | | $c_2 = -4.9 \times 10^{-6}$ Wm$^{-2}$ ppb$^{-1}$ |
| $CH_4$ | $[a_3\bar{M} + b_3\bar{N} + 0.043](\sqrt{M} - \sqrt{M_0})$ | $a_3 = -1.3 \times 10^{-6}$ Wm$^{-2}$ ppb$^{-1}$ |
| | | $b_3 = -8.2 \times 10^{-6}$ Wm$^{-2}$ ppb$^{-1}$ |

*C*, *M*, and *N* are concentration at the time at which the forcing is required, and *Co*, *Mo*, and *No* are the initial concentrations. For terms within the square brackets, the gas concentrations are the mean of the initial and final concentrations (e.g., $\bar{M} = 0.5(M + M_0)$ for methane) when the concentrations of those overlapping gases are also changing. The expressions are valid in the ranges 180–2000 ppm for $CO_2$, 200–525 ppb for $N_2O$, and 340–3500 ppb for $CH_4$.

## 7.A.2 Two-layer simple climate energy balance model (EBM) used in Section 7.5.1.2.

$$C\frac{d}{d}\Delta T = \Delta F(t) + \alpha\Delta T - \varepsilon\kappa(\Delta T - \Delta T_d)$$
$$C_d\frac{d}{d}\Delta T_d = \kappa(\Delta T - \Delta T_d),$$

*Equation 7.A.2.1*

where $\Delta T_d$ is the temperature change in the deep ocean layer, *C* and $C_d$ are the heat capacities for the surface and deep layers, the values adopted from the CMIP5 multi-model mean (*C*=8.2 and $C_d$=109 W year m$^{-2}$ K$^{-1}$; Geoffroy et al., 2013). The analytical solution of Eq. (7.A.2.1) is expressed by a combination of fast and slow modes with the decay time scales of $\tau_f$ and $\tau_s$, which are approximately 4 and 280 years, respectively. For a given value of ECS is obtained as

$$TCR = ECS\left\{1 - \tau_f a_f\left(1 - e^{-\frac{t_0}{\tau_f}}\right) - \tau_s a_s\left(1 - e^{-\frac{t_0}{\tau_s}}\right)\right\}.$$

*Equation 7.A.2.2*

The TCR is equal to $\Delta T$ at year $t = t_0$=70 in response to the forcing $\Delta F$ increasing at a rate of 1% per year, and all parameters ($\tau_f$, $\tau_s$, $a_f$, and $a_s$) can be calculated using *C*,$C_d$, $\varepsilon\kappa$and the net feedback parameter $\alpha$ (the value of $\varepsilon\kappa$ is given in Section 7.5.1.2 and the formulae are presented in Geoffroy et al. (2013).

### 7.A.3 Definitions of climate metrics in Section 7.6.2.

Absolute Global Forcing Potential:

$$AGFP_X(H) = \Delta F_X(H) \qquad \textit{Equation 7.A.3.1}$$

Absolute Global Warming Potential

$$AGWP_X(H) = \int_0^H \Delta F_X(t)dt \qquad \textit{Equation 7.A.3.2}$$

Absolute Global Temperature-change Potential:

$$AGTP^X(H) = \Delta T^X(H) = \int_0^H AGFP^X(t)R_T(H-t)dt \qquad \textit{Equation 7.A.3.3}$$

Absolute Global Sea-level Rise:

$$\begin{aligned} AGSR^X(H) = \Delta SLR^X(H) &= \int_0^H AGTP^X(t)R_{SLR}(H-t)dt \\ &= \int_0^H \int_0^t AGFP^X(t')R_T(t-t')R_{SLR}(H-t)dt'dt \end{aligned} \qquad \textit{Equation 7.A.3.4}$$

Increase in absolute metric ($\Delta AGxx^X$) due to the carbon cycle response:

$$\Delta AGxx^X = \int_0^H \int_0^t AGTP^X(t')R_F(t-t')AGxx^{CO2}(H-t)dt'dt \qquad \textit{Equation 7.A.3.5}$$

where $R_F(t)$ is the $CO_2$ flux perturbation following a unit temperature pulse in kg($CO_2$) $yr^{-1}$ $K^{-1}$

Metrics for step emission changes can be derived by integrating the more standard pulse emission changes up to the time horizon:

$$AGTP_X^S = \int_0^H AGTP_X(H-t)dt \qquad \textit{Equation 7.A.3.6}$$

**[START Table7.A.2 HERE]**

**Table 7.A.2:** Equilibrium Climate Sensitivity (ECS) and Transient Climate Response (TCR) values in CMIP6 and CMIP5 models, data from Flynn and Mauritsen (submitted).

| CMIP6 | | | CMIP5 | | |
|---|---|---|---|---|---|
| Model | ECS (°C) | TCR(°C) | Model | ECS(°C) | TCR(°C) |
| MIROC6 | 2.6 | 1.58 | MPI-ESM-LR | 3.48 | 1.94 |
| IPSL-CM6A-LR | 4.5 | 2.39 | MPI-ESM-MR | 3.31 | 1.93 |
| CNRM-CM6-1 | 4.81 | 2.23 | MPI-ESM-P | 3.31 | 1.96 |
| BCC-CSM2-MR | 3.07 | 1.6 | MIROC5 | 2.7 | 1.49 |
| MRI-ESM2 | 3.11 | 1.67 | MIROC-ESM | 4.68 | 2.15 |
| CanESM5 | 5.58 | 2.75 | IPSL-CM5B-LR | 2.58 | 1.44 |
| CESM2 | 5.15 | 1.99 | IPSL-CM5A-MR | 4.03 | 1.96 |
| GISS-E2-1-H | 2.99 | 1.81 | IPSL-CM5A-LR | 3.97 | 1.94 |
| GISS-E2-1-G | 2.6 | 1.66 | INM-CM4 | 2.01 | 1.22 |
| SAM0-UNICON | 3.3 | 2.08 | CSIRO-Mk3.6.0 | 4.05 | 1.76 |
| E3SM-1-0 | 5.09 | 2.91 | CNRM-CM5 | 3.21 | 2.04 |
| UKESM1-0-LL | 5.31 | 2.79 | CNRM-CM5-2 | 3.4 | 1.63 |
| CNRM-ESM2-1 | 4.75 | 1.82 | BNU | 3.98 | 2.58 |
| BCC-ESM1 | 3.29 | 1.77 | BCC-CSM1.1 | 2.81 | 1.74 |
| CESM2-WACCM | 4.65 | 1.92 | BCC-CSM1.1(m) | 2.77 | 2 |
| MIROC-ES2L | 2.66 | 1.51 | MRI-CGCM3 | 2.65 | 1.58 |
| EC-EARTH3-VEG | 3.93 | 2.76 | NORESM1-M | 2.75 | 1.34 |
| HADGEM3-GC31-LL | 5.46 | 2.47 | ACCESS1.0 | 3.76 | 1.72 |
| NORCPM-1 | 2.78 | 1.55 | CanESM2 | 3.71 | 2.37 |
| GFDL-CM4 | 3.79 | - | GFDL-ESM2M | 2.33 | 1.23 |
| GFDL-ESM4 | 2.56 | - | GFDL-ESM2G | 2.3 | 0.96 |
| NESM3 | 4.5 | - | GFDL-CM3 | 3.85 | 1.85 |
| NORESM2-LM | 2.49 | 1.48 | CCSM4 | 2.9 | 1.64 |
| MPI-ESM1-2-HR | 2.84 | 1.57 | FGOALS-g2 | 3.39 | 1.42 |
| INM-CM4-8 | 1.81 | 1.3 | GISS-E2-H | 2.33 | 1.69 |
| | | | GISS-E2-R | 2.06 | 1.41 |
| | | | HADGEM2-ES | 3.96 | 2.38 |
| | | | | | |
| **Mean** | **3.74** | **1.98** | **Mean** | **3.20** | **1.75** |
| **95% percentile** | **5.43** | **2.79** | **95% percentile** | **4.04** | **2.38** |
| **5% percentile** | **2.50** | **1.48** | **5% percentile** | **2.13** | **1.22** |

**[END Table 7.A.2 HERE]**

**[START Table 7.A.3 HERE]**

**Table 7.A.3:** Radiative efficiencies, lifetimes, AGWP and GWP values for 100 years. AGTP, GTP, iAGTP and CGTP values for 50 and 100 years (see Section 7.7.2 for definitions). Carbon cycle responses are included for all species. Radiative efficiencies and lifetimes of halogenated species are from WMO (2018).

| Species | Lifetime yr | Radiative Efficiency W $m^{-2}ppb^{-1}$ | AGWP 100 W $m^{-2}yr\ kg^{-1}$ | GWP 100 | AGWP 100 W $m^{-2}yr\ kg^{-1}$ | GWP 100 | AGTP 50 K $kg^{-1}$ | GTP 50 | AGTP 100 K $kg^{-1}$ | GTP 100 | iAGTP 50 K yr $kg^{-1}$ | CGTP 50 yr | iAGTP 100 K yr $kg^{-1}$ | CGTP 100 yr |
|---|---|---|---|---|---|---|---|---|---|---|---|---|---|---|
| CO2 | | 1.37E-05 | 9.20E-14 | 1 | 3.21E-13 | 1 | 5.24E-16 | 1 | 4.86E-16 | 1 | 2.78E-14 | 53 | 5.28E-14 | 109 |
| CH4 | 12.4 | 3.79E-04 | 2.91E-12 | 32 | 2.91E-12 | 9 | 7.62E-15 | 15 | 3.23E-15 | 7 | 1.60E-12 | 3048 | 1.82E-12 | 3750 |
| N2O | 121 | 2.92E-03 | 2.49E-11 | 271 | 3.98E-11 | 124 | 1.51E-13 | 288 | 1.17E-13 | 242 | 7.67E-12 | 14637 | 1.44E-11 | 29524 |
| CFC-11 | 45 | 2.60E-01 | 4.56E-07 | 4954268 | 5.95E-10 | 1855 | 2.63E-09 | 5019926 | 1.26E-09 | 2590162 | 1.80E-07 | 3.43E+08 | 2.72E-07 | 5.59E+08 |
| CFC-12 | 100 | 3.18E-01 | 9.94E-07 | 10805581 | 1.62E-09 | 5053 | 6.03E-09 | 11511359 | 4.38E-09 | 9014812 | 3.18E-07 | 6.07E+08 | 5.76E-07 | 1.19E+09 |
| CFC-13 | 640 | 2.55E-01 | 1.35E-06 | 14641035 | 5.01E-09 | 15636 | 8.00E-09 | 15260722 | 8.23E-09 | 16923247 | 3.54E-07 | 6.75E+08 | 7.61E-07 | 1.56E+09 |
| CFC-113 | 85 | 3.02E-01 | 5.67E-07 | 6162404 | 8.96E-10 | 2795 | 3.44E-09 | 6554303 | 2.33E-09 | 4797607 | 1.88E-07 | 3.59E+08 | 3.30E-07 | 6.79E+08 |
| CFC-114 | 190 | 3.07E-01 | 8.33E-07 | 9061019 | 1.93E-09 | 6004 | 5.03E-09 | 9594424 | 4.42E-09 | 9092699 | 2.40E-07 | 4.58E+08 | 4.76E-07 | 9.8E+08 |
| CFC-115 | 1020 | 2.02E-01 | 7.42E-07 | 8067808 | 2.55E-09 | 7950 | 4.39E-09 | 8380913 | 4.63E-09 | 9531719 | 1.92E-07 | 3.66E+08 | 4.18E-07 | 8.6E+08 |
| HCFC-21 | 1.7 | 1.45E-01 | 1.45E-08 | 157233 | 1.50E-11 | 47 | 2.05E-11 | 39078 | 1.48E-11 | 30451 | 8.36E-09 | 15940980 | 9.21E-09 | 18950765 |
| HCFC-22 | 11.9 | 2.08E-01 | 1.73E-07 | 1877204 | 1.74E-10 | 544 | 4.33E-10 | 825769 | 1.90E-10 | 390377 | 9.51E-08 | 1.81E+08 | 1.08E-07 | 2.22E+08 |
| HCFC-122 | 0.97 | 1.68E-01 | 5.81E-09 | 63162 | 5.45E-12 | 17 | 8.17E-12 | 15582 | 5.93E-12 | 12190 | 3.36E-09 | 6415062 | 3.71E-09 | 7621491 |
| HCFC-122a | 3.4 | 2.09E-01 | 2.53E-08 | 275391 | 2.32E-11 | 72 | 3.66E-11 | 69808 | 2.61E-11 | 53780 | 1.46E-08 | 27801948 | 1.61E-08 | 33102825 |

| | | | | | | | | | | | | | | |
|---|---|---|---|---|---|---|---|---|---|---|---|---|---|---|
| HCFC-123 | 1.3 | 1.52E-01 | 7.80E-09 | 84826 | 7.69E-12 | 24 | 1.10E-11 | 20996 | 7.97E-12 | 16397 | 4.51E-09 | 8608420 | 4.97E-09 | 10230211 |
| HCFC-123a | 4 | 2.30E-01 | 3.63E-08 | 394882 | 3.63E-11 | 113 | 5.29E-11 | 101013 | 3.76E-11 | 77348 | 2.09E-08 | 39802717 | 2.31E-08 | 47420389 |
| HCFC-124 | 5.9 | 1.98E-01 | 5.17E-08 | 561781 | 5.22E-11 | 163 | 7.96E-11 | 151859 | 5.40E-11 | 111145 | 2.95E-08 | 56311433 | 3.27E-08 | 67255616 |
| HCFC-132c | 4.3 | 1.73E-01 | 3.33E-08 | 361858 | nan | nan | 4.88E-11 | 93078 | 3.45E-11 | 70989 | 1.91E-08 | 36444707 | 2.11E-08 | 43433680 |
| HCFC-141b | 9.2 | 1.62E-01 | 7.69E-08 | 836169 | 7.76E-11 | 242 | 1.51E-10 | 287341 | 8.21E-11 | 168922 | 4.33E-08 | 82530384 | 4.84E-08 | 99556576 |
| HCFC-142b | 17.2 | 1.89E-01 | 1.94E-07 | 2113593 | 2.06E-10 | 641 | 7.03E-10 | 1341810 | 2.41E-10 | 495725 | 1.01E-07 | 1.93E+08 | 1.21E-07 | 2.48E+08 |
| HCFC-225ca | 1.9 | 2.21E-01 | 1.25E-08 | 135831 | 1.24E-11 | 39 | 1.77E-11 | 33831 | 1.28E-11 | 26331 | 7.21E-09 | 13764450 | 7.96E-09 | 16366166 |
| HCFC-225cb | 5.9 | 2.93E-01 | 5.14E-08 | 559076 | 5.09E-11 | 159 | 7.92E-11 | 151127 | 5.38E-11 | 110610 | 2.94E-08 | 56040289 | 3.25E-08 | 66931775 |
| trans-CF3C | 0.071 | 4.40E-02 | 1.45E-10 | 1576 | 3.61E-13 | 1 | 2.02E-13 | 385 | 1.47E-13 | 303 | 8.41E-11 | 160418 | 9.26E-11 | 190444 |
| HFC-23 | 222 | 1.75E-01 | 1.20E-06 | 13051373 | 3.11E-09 | 9706 | 7.23E-09 | 13786181 | 6.56E-09 | 13485873 | 3.40E-07 | 6.48E+08 | 6.85E-07 | 1.41E+09 |
| HFC-32 | 5.2 | 1.10E-01 | 6.64E-08 | 721576 | 6.89E-11 | 215 | 9.95E-11 | 189900 | 6.91E-11 | 142223 | 3.80E-08 | 72488638 | 4.20E-08 | 86484542 |
| HFC-41 | 2.8 | 2.30E-02 | 1.14E-08 | 124193 | 9.93E-12 | 31 | 1.64E-11 | 31244 | 1.18E-11 | 24181 | 6.58E-09 | 12556977 | 7.26E-09 | 14942637 |
| HFC-125 | 28.2 | 2.26E-01 | 3.10E-07 | 3372397 | 3.47E-10 | 1083 | 1.56E-09 | 2980016 | 5.64E-10 | 1159782 | 1.42E-07 | 2.71E+08 | 1.89E-07 | 3.89E+08 |
| HFC-134 | 9.7 | 1.91E-01 | 1.10E-07 | 1191235 | 1.12E-10 | 351 | 2.25E-10 | 428687 | 1.18E-10 | 241655 | 6.14E-08 | 1.17E+08 | 6.89E-08 | 1.42E+08 |
| HFC-134a | 13.4 | 1.61E-01 | 1.27E-07 | 1385744 | 1.33E-10 | 413 | 3.61E-10 | 689601 | 1.44E-10 | 295446 | 6.92E-08 | 1.32E+08 | 7.96E-08 | 1.64E+08 |
| HFC-143 | 3.5 | 1.28E-01 | 3.22E-08 | 349885 | 3.36E-11 | 105 | 4.66E-11 | 88814 | 3.32E-11 | 68362 | 1.85E-08 | 35313286 | 2.04E-08 | 42050435 |
| HFC-143a | 47.1 | 1.58E-01 | 4.67E-07 | 5083399 | 5.87E-10 | 1830 | 2.72E-09 | 5188006 | 1.34E-09 | 2755301 | 1.82E-07 | 3.47E+08 | 2.78E-07 | 5.73E+08 |

| | | | | | | | | | | | | | | |
|---|---|---|---|---|---|---|---|---|---|---|---|---|---|---|
| HFC-152 | 0.4 | 4.40E-02 | 1.61E-09 | 17491 | 1.83E-12 | 6 | 2.25E-12 | 4291 | 1.64E-12 | 3367 | 9.32E-10 | 1778932 | 1.03E-09 | 2112475 |
| HFC-152a | 1.5 | 9.80E-02 | 1.34E-08 | 146086 | 1.46E-11 | 46 | 1.90E-11 | 36232 | 1.37E-11 | 28265 | 7.77E-09 | 14818110 | 8.56E-09 | 17612820 |
| HFC-161 | 0.181 | 1.60E-02 | 3.63E-10 | 3951 | 5.52E-13 | 2 | 5.07E-13 | 967 | 3.69E-13 | 760 | 2.11E-10 | 402031 | 2.32E-10 | 477324 |
| HFC-227ca | 28.2 | 2.67E-01 | 2.59E-07 | 2812421 | 2.88E-10 | 897 | 1.30E-09 | 2485193 | 4.70E-10 | 967203 | 1.18E-07 | 2.26E+08 | 1.58E-07 | 3.24E+08 |
| HFC-227ea | 38.9 | 2.58E-01 | 3.27E-07 | 3558610 | 3.33E-10 | 1037 | 1.84E-09 | 3502301 | 8.00E-10 | 1645927 | 1.35E-07 | 2.58E+08 | 1.97E-07 | 4.04E+08 |
| HFC-236cb | 13.1 | 2.28E-01 | 1.18E-07 | 1287660 | 1.22E-10 | 382 | 3.28E-10 | 625929 | 1.33E-10 | 273008 | 6.45E-08 | 1.23E+08 | 7.40E-08 | 1.52E+08 |
| HFC-236ea | 11 | 3.00E-01 | 1.31E-07 | 1423613 | 1.36E-10 | 423 | 3.03E-10 | 577896 | 1.42E-10 | 292626 | 7.27E-08 | 1.39E+08 | 8.21E-08 | 1.69E+08 |
| HFC-236fa | 242 | 2.43E-01 | 7.81E-07 | 8489842 | 1.84E-09 | 5732 | 4.69E-09 | 8955812 | 4.33E-09 | 8898926 | 2.19E-07 | 4.18E+08 | 4.45E-07 | 9.15E+08 |
| HFC-245ca | 6.5 | 2.40E-01 | 7.02E-08 | 763705 | 7.13E-11 | 222 | 1.12E-10 | 212820 | 7.37E-11 | 151597 | 4.00E-08 | 76389767 | 4.44E-08 | 91339699 |
| HFC-245cb | 47.1 | 2.43E-01 | 4.51E-07 | 4901646 | 4.32E-10 | 1346 | 2.62E-09 | 5002513 | 1.29E-09 | 2656787 | 1.76E-07 | 3.35E+08 | 2.68E-07 | 5.52E+08 |
| HFC-245ea | 3.2 | 1.60E-01 | 2.31E-08 | 250705 | 2.31E-11 | 72 | 3.32E-11 | 63383 | 2.38E-11 | 48910 | 1.33E-08 | 25322705 | 1.47E-08 | 30145053 |
| HFC-245eb | 3.1 | 2.04E-01 | 2.85E-08 | 309661 | 2.88E-11 | 90 | 4.10E-11 | 78189 | 2.94E-11 | 60382 | 1.64E-08 | 31285632 | 1.81E-08 | 37239983 |
| HFC-245fa | 7.7 | 2.43E-01 | 8.42E-08 | 915917 | 8.54E-11 | 266 | 1.45E-10 | 276790 | 8.90E-11 | 183105 | 4.78E-08 | 91151564 | 5.31E-08 | 1.09E+08 |
| HFC-263fb | 1.2 | 1.00E-01 | 7.39E-09 | 80322 | 6.77E-12 | 21 | 1.04E-11 | 19861 | 7.54E-12 | 15519 | 4.27E-09 | 8153371 | 4.71E-09 | 9688602 |
| HFC-272ca | 2.6 | 7.20E-02 | 1.41E-08 | 153438 | 4.75E-11 | 148 | 2.02E-11 | 38512 | 1.45E-11 | 29846 | 8.14E-09 | 15521687 | 8.98E-09 | 18467189 |
| HFC-329p | 28.4 | 3.06E-01 | 2.31E-07 | 2506382 | 2.72E-10 | 849 | 1.16E-09 | 2221763 | 4.22E-10 | 867659 | 1.05E-07 | 2.01E+08 | 1.40E-07 | 2.89E+08 |
| HFC-365mfc | 8.7 | 2.23E-01 | 7.91E-08 | 859636 | 7.80E-11 | 243 | 1.48E-10 | 282400 | 8.41E-11 | 173008 | 4.46E-08 | 85102447 | 4.98E-08 | 1.02E+08 |

| | | | | | | | | | | | | | | |
|---|---|---|---|---|---|---|---|---|---|---|---|---|---|---|
| HFC-43-10m | 16.1 | 4.20E-01 | 1.61E-07 | 1754942 | 1.46E-10 | 456 | 5.50E-10 | 1048529 | 1.94E-10 | 398644 | 8.51E-08 | 1.62E+08 | 1.00E-07 | 2.06E+08 |
| HFC-1132a | 0.011 | 4.00E-03 | 4.15E-12 | 45 | 4.75E-15 | 0 | 5.77E-15 | 11 | 4.21E-15 | 9 | 2.41E-12 | 4592 | 2.65E-12 | 5451 |
| HFC-1141 | 0.006 | 2.00E-03 | 1.52E-12 | 17 | 1.79E-15 | 0 | 2.12E-15 | 4 | 1.54E-15 | 3 | 8.82E-13 | 1684 | 9.72E-13 | 1999 |
| (Z)-HFC-12 | 0.023 | 2.10E-02 | 2.24E-11 | 243 | 2.50E-14 | 0 | 3.11E-14 | 59 | 2.27E-14 | 47 | 1.30E-11 | 24766 | 1.43E-11 | 29400 |
| (E)-HFC-12 | 0.013 | 1.30E-02 | 7.96E-12 | 87 | 7.13E-15 | 0 | 1.11E-14 | 21 | 8.09E-15 | 17 | 4.62E-12 | 8817 | 5.09E-12 | 10467 |
| (Z)-HFC-12 | 0.027 | 1.90E-02 | 2.76E-11 | 300 | 2.75E-14 | 0 | 3.84E-14 | 73 | 2.80E-14 | 58 | 1.60E-11 | 30506 | 1.76E-11 | 36215 |
| HFC-1234yf | 0.029 | 2.30E-02 | 3.51E-11 | 381 | 3.48E-14 | 0 | 4.88E-14 | 93 | 3.56E-14 | 73 | 2.03E-11 | 38815 | 2.24E-11 | 46079 |
| (E)-HFC-12 | 0.045 | 3.90E-02 | 9.27E-11 | 1008 | 1.10E-13 | 0 | 1.29E-13 | 246 | 9.42E-14 | 194 | 5.38E-11 | 102606 | 5.92E-11 | 121809 |
| (Z)-HFC-13 | 0.06 | 7.40E-02 | 1.64E-10 | 1785 | 1.90E-13 | 1 | 2.29E-13 | 436 | 1.67E-13 | 343 | 9.53E-11 | 181755 | 1.05E-10 | 215774 |
| HFC-1243zf | 0.019 | 1.20E-02 | 1.45E-11 | 157 | 1.55E-14 | 0 | 2.02E-14 | 38 | 1.47E-14 | 30 | 8.40E-12 | 16030 | 9.25E-12 | 19029 |
| HFC-1345zf | 0.021 | 1.40E-02 | 1.20E-11 | 131 | 1.43E-14 | 0 | 1.68E-14 | 32 | 1.22E-14 | 25 | 6.98E-12 | 13323 | 7.69E-12 | 15816 |
| C4F9CH=CH2 | 0.021 | 2.60E-02 | 1.33E-11 | 144 | 1.81E-14 | 0 | 1.85E-14 | 35 | 1.35E-14 | 28 | 7.70E-12 | 14687 | 8.48E-12 | 17435 |
| C6F13CH=CH | 0.021 | 2.90E-02 | 1.05E-11 | 114 | 1.29E-14 | 0 | 1.47E-14 | 28 | 1.07E-14 | 22 | 6.11E-12 | 11647 | 6.72E-12 | 13827 |
| C8F17CH=CH | 0.021 | 3.20E-02 | 9.00E-12 | 98 | 1.00E-14 | 0 | 1.25E-14 | 24 | 9.15E-15 | 19 | 5.23E-12 | 9971 | 5.75E-12 | 11837 |
| Methyl_chl | 5 | 6.90E-02 | 1.56E-08 | 169750 | 1.58E-11 | 49 | 2.33E-11 | 44403 | 1.63E-11 | 33423 | 8.94E-09 | 17062901 | 9.89E-09 | 20351953 |
| Carbon_tet | 26 | 1.70E-01 | 1.69E-07 | 1840001 | 2.19E-10 | 682 | 8.19E-10 | 1563388 | 2.85E-10 | 587122 | 7.94E-08 | 1.51E+08 | 1.03E-07 | 2.13E+08 |
| Methyl_chl | 1 | 1.00E-02 | 1.20E-09 | 13003 | 4.30E-13 | 1 | 1.68E-12 | 3209 | 1.22E-12 | 2510 | 6.92E-10 | 1320519 | 7.63E-10 | 1568898 |

| | | | | | | | | | | | | | | |
|---|---|---|---|---|---|---|---|---|---|---|---|---|---|---|
| Methylene_ | 0.395 | 3.10E-02 | 8.69E-10 | 9453 | 9.81E-13 | 3 | 1.22E-12 | 2319 | 8.85E-13 | 1820 | 5.04E-10 | 961476 | 5.55E-10 | 1141744 |
| Chloroform | 0.408 | 7.80E-02 | 1.61E-09 | 17511 | 1.77E-12 | 6 | 2.25E-12 | 4296 | 1.64E-12 | 3371 | 9.33E-10 | 1780939 | 1.03E-09 | 2114873 |
| CH2ClCH2Cl | 0.178 | 8.00E-03 | 8.69E-11 | 945 | 1.37E-13 | 0 | 1.21E-13 | 231 | 8.84E-14 | 182 | 5.04E-11 | 96186 | 5.55E-11 | 114200 |
| Methyl bromide | 0.8 | 5.00E-03 | 2.54E-10 | 2766 | 2.03E-13 | 1 | 3.57E-13 | 681 | 2.59E-13 | 533 | 1.47E-10 | 281043 | 1.62E-10 | 333849 |
| Methylene_ | 0.337 | 9.00E-03 | 1.05E-10 | 1145 | 1.43E-13 | 0 | 1.47E-13 | 281 | 1.07E-13 | 220 | 6.11E-11 | 116520 | 6.73E-11 | 138359 |
| Halon-1201 | 5.2 | 1.54E-01 | 3.69E-08 | 401474 | 3.39E-11 | 106 | 5.54E-11 | 105658 | 3.85E-11 | 79131 | 2.11E-08 | 40331633 | 2.34E-08 | 48118752 |
| Halon-1202 | 2.9 | 2.72E-01 | 2.27E-08 | 246797 | 1.94E-11 | 61 | 3.26E-11 | 62163 | 2.34E-11 | 48076 | 1.31E-08 | 24946965 | 1.44E-08 | 29689328 |
| Halon-1211 | 16 | 2.94E-01 | 1.71E-07 | 1861172 | 1.69E-10 | 528 | 5.79E-10 | 1105469 | 2.05E-10 | 421614 | 9.04E-08 | 1.72E+08 | 1.06E-07 | 2.19E+08 |
| Halon-1301 | 65 | 2.98E-01 | 6.12E-07 | 6651008 | 8.76E-10 | 2732 | 3.67E-09 | 7006772 | 2.19E-09 | 4496652 | 2.17E-07 | 4.14E+08 | 3.60E-07 | 7.4E+08 |
| Halon-2301 | 3.4 | 1.35E-01 | 1.70E-08 | 184915 | 1.76E-11 | 55 | 2.46E-11 | 46873 | 1.76E-11 | 36111 | 9.78E-09 | 18667971 | 1.08E-08 | 22227313 |
| Halon-2311 | 1 | 1.32E-01 | 4.04E-09 | 43905 | 3.97E-12 | 12 | 5.68E-12 | 10834 | 4.12E-12 | 8475 | 2.34E-09 | 4458829 | 2.58E-09 | 5297499 |
| Halon-2401 | 2.9 | 1.86E-01 | 1.80E-08 | 195704 | 1.84E-11 | 57 | 2.58E-11 | 49293 | 1.85E-11 | 38123 | 1.04E-08 | 19782326 | 1.14E-08 | 23542902 |
| Halon-2402 | 20 | 3.13E-01 | 1.44E-07 | 1567586 | 2.02E-10 | 629 | 5.91E-10 | 1127285 | 1.96E-10 | 403349 | 7.26E-08 | 1.38E+08 | 8.90E-08 | 1.83E+08 |
| NF3 | 500 | 2.05E-01 | 1.56E-06 | 16954171 | 5.38E-09 | 16765 | 9.28E-09 | 17713820 | 9.37E-09 | 19275919 | 4.14E-07 | 7.9E+08 | 8.82E-07 | 1.81E+09 |
| SF6 | 3200 | 5.67E-01 | 2.28E-06 | 24745411 | 1.09E-08 | 33984 | 1.34E-08 | 25598479 | 1.46E-08 | 29974695 | 5.78E-07 | 1.1E+09 | 1.28E-06 | 2.63E+09 |
| SF5CF3 | 800 | 5.92E-01 | 1.69E-06 | 18384008 | 6.75E-09 | 21060 | 1.00E-08 | 19127977 | 1.05E-08 | 21501068 | 4.41E-07 | 8.41E+08 | 9.54E-07 | 1.96E+09 |
| SO2F2 | 36 | 2.01E-01 | 3.99E-07 | 4343208 | 4.26E-10 | 1329 | 2.20E-09 | 4190325 | 9.11E-10 | 1874658 | 1.69E-07 | 3.23E+08 | 2.41E-07 | 4.95E+08 |

| | | | | | | | | | | | | | | |
|---|---|---|---|---|---|---|---|---|---|---|---|---|---|---|
| PFC-14 | 50000 | 9.50E-02 | 6.42E-07 | 6981426 | 3.07E-09 | 9570 | 3.78E-09 | 7208145 | 4.16E-09 | 8549339 | 1.62E-07 | 3.09E+08 | 3.61E-07 | 7.42E+08 |
| PFC-116 | 10000 | 2.51E-01 | 1.08E-06 | 11715575 | 5.33E-09 | 16618 | 6.34E-09 | 12102511 | 6.95E-09 | 14304086 | 2.72E-07 | 5.2E+08 | 6.06E-07 | 1.25E+09 |
| PFC-c216 | 3000 | 2.28E-01 | 8.90E-07 | 9677948 | 4.26E-09 | 13284 | 5.25E-09 | 10012939 | 5.69E-09 | 11714024 | 2.26E-07 | 4.32E+08 | 5.01E-07 | 1.03E+09 |
| PFC-218 | 2600 | 2.77E-01 | 8.61E-07 | 9357971 | 4.09E-09 | 12744 | 5.08E-09 | 9685100 | 5.50E-09 | 11305090 | 2.19E-07 | 4.18E+08 | 4.84E-07 | 9.96E+08 |
| PFC-318 | 3200 | 3.15E-01 | 9.23E-07 | 10038443 | 4.47E-09 | 13931 | 5.44E-09 | 10384506 | 5.91E-09 | 12159801 | 2.35E-07 | 4.48E+08 | 5.19E-07 | 1.07E+09 |
| PFC-31-10 | 2600 | 3.63E-01 | 8.91E-07 | 9686921 | 4.15E-09 | 12943 | 5.26E-09 | 10025549 | 5.69E-09 | 11702485 | 2.27E-07 | 4.33E+08 | 5.01E-07 | 1.03E+09 |
| c-C5F8 | 0.085 | 7.60E-02 | 1.84E-10 | 1998 | 8.76E-12 | 27 | 2.56E-13 | 488 | 1.87E-13 | 384 | 1.07E-10 | 203329 | 1.17E-10 | 241390 |
| PFC-41-12 | 4100 | 4.05E-01 | 8.27E-07 | 8993522 | 4.04E-09 | 12605 | 4.87E-09 | 9299395 | 5.31E-09 | 10921944 | 2.10E-07 | 4E+08 | 4.65E-07 | 9.57E+08 |
| PFC-51-14 | 3100 | 4.42E-01 | 7.66E-07 | 8330772 | 3.63E-09 | 11307 | 4.52E-09 | 8618530 | 4.90E-09 | 10087468 | 1.95E-07 | 3.72E+08 | 4.31E-07 | 8.87E+08 |
| PFC-61-16 | 3000 | 5.02E-01 | 7.58E-07 | 8237969 | 3.58E-09 | 11164 | 4.47E-09 | 8523117 | 4.85E-09 | 9971099 | 1.93E-07 | 3.68E+08 | 4.26E-07 | 8.77E+08 |
| PFC-71-18 | 3000 | 5.52E-01 | 7.38E-07 | 8024393 | 3.49E-09 | 10879 | 4.35E-09 | 8302148 | 4.72E-09 | 9712589 | 1.88E-07 | 3.58E+08 | 4.15E-07 | 8.54E+08 |
| PFC-91-18 | 2000 | 5.53E-01 | 6.95E-07 | 7558792 | 3.18E-09 | 9908 | 4.10E-09 | 7828816 | 4.42E-09 | 9092320 | 1.78E-07 | 3.39E+08 | 3.91E-07 | 8.05E+08 |
| Z-C10F18 | 2000 | 5.57E-01 | 7.00E-07 | 7613467 | 3.24E-09 | 10088 | 4.13E-09 | 7885444 | 4.45E-09 | 9158088 | 1.79E-07 | 3.41E+08 | 3.94E-07 | 8.11E+08 |
| E-C10F18 | 2000 | 4.84E-01 | 6.08E-07 | 6615651 | 2.77E-09 | 8647 | 3.59E-09 | 6851984 | 3.87E-09 | 7957836 | 1.55E-07 | 2.97E+08 | 3.42E-07 | 7.04E+08 |
| PFC-1114 | 0.003 | 2.00E-03 | 3.62E-13 | 4 | 3.97E-16 | 0 | 5.04E-16 | 1 | 3.68E-16 | 1 | 2.10E-13 | 401 | 2.31E-13 | 476 |
| PFC-1216 | 0.013 | 1.30E-02 | 7.01E-12 | 76 | 6.06E-15 | 0 | 9.76E-15 | 19 | 7.12E-15 | 15 | 4.07E-12 | 7760 | 4.48E-12 | 9212 |
| CF2=CFCF=C | 0.003 | 3.00E-03 | 3.35E-13 | 4 | 3.37E-16 | 0 | 4.67E-16 | 1 | 3.41E-16 | 1 | 1.95E-13 | 371 | 2.14E-13 | 441 |

| | | | | | | | | | | | | | | |
|---|---|---|---|---|---|---|---|---|---|---|---|---|---|---|
| CF3CF2CF=C | 0.016 | 1.80E-02 | 8.91E-12 | 97 | 9.91E-15 | 0 | 1.24E-14 | 24 | 9.05E-15 | 19 | 5.17E-12 | 9862 | 5.69E-12 | 11708 |
| CF3CF=CFCF | 0.085 | 6.80E-02 | 1.74E-10 | 1895 | 1.79E-13 | 1 | 2.43E-13 | 463 | 1.77E-13 | 364 | 1.01E-10 | 192848 | 1.11E-10 | 228947 |
| HFE-125 | 119 | 4.05E-01 | 1.20E-06 | 13083203 | 2.40E-09 | 7484 | 7.30E-09 | 13933229 | 5.65E-09 | 11619111 | 3.72E-07 | 7.1E+08 | 6.94E-07 | 1.43E+09 |
| HFE-134 (H | 24.4 | 4.45E-01 | 5.44E-07 | 5920792 | 6.06E-10 | 1889 | 2.55E-09 | 4859604 | 8.68E-10 | 1785076 | 2.60E-07 | 4.96E+08 | 3.34E-07 | 6.86E+08 |
| HFE-143a | 4.8 | 1.77E-01 | 5.13E-08 | 557432 | 5.32E-11 | 166 | 7.60E-11 | 145019 | 5.33E-11 | 109640 | 2.94E-08 | 56064230 | 3.25E-08 | 66854371 |
| HFE-227ea | 51.6 | 4.42E-01 | 6.29E-07 | 6840954 | 7.83E-10 | 2443 | 3.70E-09 | 7066705 | 1.93E-09 | 3971403 | 2.38E-07 | 4.55E+08 | 3.73E-07 | 7.68E+08 |
| HCFE-235ca | 4.3 | 4.07E-01 | 5.73E-08 | 622665 | 5.93E-11 | 185 | 8.39E-11 | 160163 | 5.94E-11 | 122153 | 3.29E-08 | 62711999 | 3.63E-08 | 74738230 |
| HCFE-235da | 3.5 | 4.21E-01 | 4.82E-08 | 524278 | 4.81E-11 | 150 | 6.98E-11 | 133081 | 4.98E-11 | 102435 | 2.77E-08 | 52914554 | 3.06E-08 | 63009714 |
| HFE-236ca | 20.8 | 5.62E-01 | 4.16E-07 | 4518807 | 4.43E-10 | 1381 | 1.75E-09 | 3345212 | 5.81E-10 | 1196149 | 2.07E-07 | 3.95E+08 | 2.56E-07 | 5.27E+08 |
| HFE-236ea2 | 10.8 | 4.53E-01 | 1.76E-07 | 1909817 | 2.28E-10 | 711 | 3.99E-10 | 761190 | 1.90E-10 | 391670 | 9.77E-08 | 1.86E+08 | 1.10E-07 | 2.27E+08 |
| HFE-236fa | 7.5 | 3.57E-01 | 9.62E-08 | 1045641 | 9.43E-11 | 294 | 1.63E-10 | 311228 | 1.02E-10 | 208780 | 5.46E-08 | 1.04E+08 | 6.07E-08 | 1.25E+08 |
| HFE-245cb2 | 4.9 | 3.26E-01 | 6.43E-08 | 698756 | 6.64E-11 | 207 | 9.55E-11 | 182269 | 6.68E-11 | 137508 | 3.68E-08 | 70257995 | 4.07E-08 | 83790278 |
| HFE-245fa1 | 6.6 | 3.06E-01 | 8.12E-08 | 883337 | 8.35E-11 | 261 | 1.30E-10 | 247579 | 8.53E-11 | 175444 | 4.63E-08 | 88322648 | 5.13E-08 | 1.06E+08 |
| HFE-245fa2 | 5.5 | 3.60E-01 | 7.96E-08 | 866084 | 7.96E-11 | 248 | 1.21E-10 | 230309 | 8.31E-11 | 170979 | 4.56E-08 | 86926114 | 5.04E-08 | 1.04E+08 |
| CF3CF2CH2O | 0.33 | 1.39E-01 | 1.85E-09 | 20069 | 1.69E-12 | 5 | 2.58E-12 | 4920 | 1.88E-12 | 3862 | 1.07E-09 | 2041510 | 1.18E-09 | 2424146 |
| HFE-254cb1 | 2.5 | 2.58E-01 | 2.95E-08 | 320624 | 2.97E-11 | 93 | 4.21E-11 | 80383 | 3.03E-11 | 62335 | 1.70E-08 | 32442221 | 1.88E-08 | 38595146 |
| HFE-263fb1 | 0.063 | 3.90E-02 | 1.30E-10 | 1414 | 1.62E-13 | 1 | 1.81E-13 | 346 | 1.32E-13 | 272 | 7.54E-11 | 143937 | 8.31E-11 | 170877 |

| | | | | | | | | | | | | | | |
|---|---|---|---|---|---|---|---|---|---|---|---|---|---|---|
| HFE-263m1 | 0.43 | 1.27E-01 | 2.89E-09 | 31430 | 2.73E-12 | 9 | 4.04E-12 | 7712 | 2.94E-12 | 6051 | 1.68E-09 | 3196350 | 1.85E-09 | 3795749 |
| CF3CH2CH2O | 0.033 | 2.20E-02 | 3.84E-11 | 418 | 4.35E-14 | 0 | 5.35E-14 | 102 | 3.90E-14 | 80 | 2.23E-11 | 42534 | 2.45E-11 | 50494 |
| HFE-329mcc | 22.5 | 5.29E-01 | 3.00E-07 | 3262689 | 3.39E-10 | 1057 | 1.34E-09 | 2548712 | 4.46E-10 | 918331 | 1.47E-07 | 2.8E+08 | 1.84E-07 | 3.79E+08 |
| HFE-338mmz | 21.2 | 4.42E-01 | 2.57E-07 | 2789107 | 2.72E-10 | 847 | 1.10E-09 | 2092939 | 3.64E-10 | 748956 | 1.27E-07 | 2.43E+08 | 1.58E-07 | 3.25E+08 |
| HFE-338mcf | 7.5 | 4.39E-01 | 9.11E-08 | 990913 | 9.13E-11 | 285 | 1.55E-10 | 294939 | 9.62E-11 | 197853 | 5.17E-08 | 98707137 | 5.75E-08 | 1.18E+08 |
| Sevofluran | 2.2 | 3.20E-01 | 2.12E-08 | 231008 | 1.83E-11 | 57 | 3.03E-11 | 57722 | 2.18E-11 | 44847 | 1.23E-08 | 23391878 | 1.35E-08 | 27820777 |
| HFE-347mcc | 5 | 3.45E-01 | 5.20E-08 | 565945 | 5.38E-11 | 168 | 7.76E-11 | 148040 | 5.42E-11 | 111431 | 2.98E-08 | 56887708 | 3.30E-08 | 67853407 |
| HFE-347mcf | 6.6 | 4.21E-01 | 8.38E-08 | 911513 | 8.49E-11 | 265 | 1.34E-10 | 255476 | 8.80E-11 | 181040 | 4.78E-08 | 91139887 | 5.30E-08 | 1.09E+08 |
| HFE-347pcf | 6 | 4.82E-01 | 8.72E-08 | 948755 | 8.83E-11 | 275 | 1.35E-10 | 257641 | 9.13E-11 | 187808 | 4.98E-08 | 95068594 | 5.52E-08 | 1.14E+08 |
| HFE-347mmy | 3.7 | 3.19E-01 | 3.56E-08 | 387268 | 3.57E-11 | 111 | 5.17E-11 | 98589 | 3.68E-11 | 75742 | 2.05E-08 | 39066072 | 2.26E-08 | 46528442 |
| HFE-356mec | 3.8 | 3.01E-01 | 3.79E-08 | 412372 | 2.49E-11 | 78 | 5.51E-11 | 105141 | 3.92E-11 | 80692 | 2.18E-08 | 41587547 | 2.41E-08 | 49536580 |
| HFE-356mff | 0.288 | 1.72E-01 | 1.64E-09 | 17843 | 1.98E-12 | 6 | 2.29E-12 | 4372 | 1.67E-12 | 3433 | 9.51E-10 | 1815236 | 1.05E-09 | 2155387 |
| HFE-356pcf | 5.7 | 3.73E-01 | 7.05E-08 | 766426 | 7.36E-11 | 229 | 1.08E-10 | 205408 | 7.36E-11 | 151468 | 4.03E-08 | 76874933 | 4.46E-08 | 91785391 |
| HFE-356pcf | 3.5 | 3.77E-01 | 4.37E-08 | 475724 | 4.41E-11 | 137 | 6.33E-11 | 120756 | 4.52E-11 | 92949 | 2.52E-08 | 48014105 | 2.78E-08 | 57174346 |
| HFE-356pcc | 3.8 | 3.22E-01 | 4.06E-08 | 441142 | 2.65E-11 | 83 | 5.90E-11 | 112477 | 4.20E-11 | 86322 | 2.33E-08 | 44489003 | 2.58E-08 | 52992621 |
| HFE-356mmz | 0.266 | 1.51E-01 | 1.33E-09 | 14483 | 8.85E-13 | 3 | 1.86E-12 | 3548 | 1.35E-12 | 2786 | 7.72E-10 | 1473486 | 8.50E-10 | 1749567 |
| HFE-365mcf | 0.053 | 4.70E-02 | 9.16E-11 | 997 | 1.26E-13 | 0 | 1.28E-13 | 244 | 9.31E-14 | 192 | 5.32E-11 | 101453 | 5.85E-11 | 120441 |

| | | | | | | | | | | | | | | |
|---|---|---|---|---|---|---|---|---|---|---|---|---|---|---|
| HFE-365mcf | 0.59 | 2.64E-01 | 5.73E-09 | 62322 | 5.74E-12 | 18 | 8.03E-12 | 15317 | 5.84E-12 | 12007 | 3.32E-09 | 6335564 | 3.66E-09 | 7524644 |
| HFE-374pc2 | 5 | 2.98E-01 | 6.16E-08 | 669439 | 2.58E-12 | 8 | 9.18E-11 | 175112 | 6.41E-11 | 131808 | 3.53E-08 | 67290751 | 3.90E-08 | 80261746 |
| CF3(CH2)2C | 0.011 | 5.00E-03 | 1.79E-12 | 19 | 4.82E-15 | 0 | 2.50E-15 | 5 | 1.82E-15 | 4 | 1.04E-12 | 1986 | 1.15E-12 | 2357 |
| -(CF2)4CH | 0.3 | 1.60E-01 | 1.26E-09 | 13698 | 1.27E-12 | 4 | 1.76E-12 | 3357 | 1.28E-12 | 2635 | 7.30E-10 | 1393447 | 8.04E-10 | 1654577 |
| HFE-43-10p | 13.5 | 1.02E+00 | 2.76E-07 | 3001958 | 2.89E-10 | 902 | 7.89E-10 | 1505413 | 3.12E-10 | 641261 | 1.50E-07 | 2.86E+08 | 1.72E-07 | 3.55E+08 |
| HFE-449s1 | 4.7 | 3.64E-01 | 4.13E-08 | 449046 | 4.17E-11 | 130 | 6.11E-11 | 116528 | 4.29E-11 | 88276 | 2.37E-08 | 45176049 | 2.62E-08 | 53864121 |
| n-HFE-7100 | 4.7 | 4.20E-01 | 4.76E-08 | 518130 | 4.87E-11 | 152 | 7.05E-11 | 134455 | 4.95E-11 | 101856 | 2.73E-08 | 52126211 | 3.02E-08 | 62150908 |
| i-HFE-7100 | 4.7 | 3.52E-01 | 3.99E-08 | 434243 | 4.05E-11 | 126 | 5.91E-11 | 112686 | 4.15E-11 | 85365 | 2.29E-08 | 43686729 | 2.53E-08 | 52088380 |
| HFE-569sf2 | 0.8 | 3.05E-01 | 5.58E-09 | 60654 | 5.48E-12 | 17 | 7.83E-12 | 14938 | 5.69E-12 | 11697 | 3.23E-09 | 6162886 | 3.56E-09 | 7320841 |
| n-HFE-7200 | 0.8 | 3.47E-01 | 6.35E-09 | 69007 | 6.40E-12 | 20 | 8.91E-12 | 16995 | 6.47E-12 | 13308 | 3.68E-09 | 7011546 | 4.05E-09 | 8328957 |
| i-HFE-7200 | 0.8 | 2.38E-01 | 4.35E-09 | 47330 | 3.45E-12 | 11 | 6.11E-12 | 11656 | 4.44E-12 | 9127 | 2.52E-09 | 4809072 | 2.78E-09 | 5712656 |
| HFE-236ca1 | 25 | 6.53E-01 | 5.24E-07 | 5698730 | 5.65E-10 | 1763 | 2.49E-09 | 4741652 | 8.53E-10 | 1755372 | 2.49E-07 | 4.74E+08 | 3.21E-07 | 6.6E+08 |
| HFE-338pcc | 12.9 | 8.58E-01 | 2.85E-07 | 3100304 | 2.97E-10 | 927 | 7.77E-10 | 1483146 | 3.18E-10 | 654996 | 1.56E-07 | 2.97E+08 | 1.78E-07 | 3.67E+08 |
| (CF3)2CHOH | 1.9 | 2.61E-01 | 1.78E-08 | 193733 | 1.77E-11 | 55 | 2.53E-11 | 48252 | 1.83E-11 | 37556 | 1.03E-08 | 19631888 | 1.14E-08 | 23342651 |
| HG-02 | 26 | 1.15E+00 | 4.86E-07 | 5287752 | 5.16E-10 | 1609 | 2.36E-09 | 4492829 | 8.20E-10 | 1687257 | 2.28E-07 | 4.35E+08 | 2.97E-07 | 6.11E+08 |
| HG-03 | 26 | 1.43E+00 | 4.46E-07 | 4854215 | 4.74E-10 | 1478 | 2.16E-09 | 4124467 | 7.53E-10 | 1548921 | 2.09E-07 | 3.99E+08 | 2.73E-07 | 5.61E+08 |
| HG-20 | 25 | 9.20E-01 | 5.19E-07 | 5638632 | 5.62E-10 | 1752 | 2.46E-09 | 4691647 | 8.44E-10 | 1736860 | 2.46E-07 | 4.69E+08 | 3.17E-07 | 6.53E+08 |

| | | | | | | | | | | | | | | |
|---|---|---|---|---|---|---|---|---|---|---|---|---|---|---|
| HG-21 | 13.5 | 1.72E+00 | 3.81E-07 | 4145449 | 3.78E-10 | 1179 | 1.09E-09 | 2078848 | 4.30E-10 | 885527 | 2.07E-07 | 3.95E+08 | 2.38E-07 | 4.9E+08 |
| HG-30 | 25 | 1.65E+00 | 7.18E-07 | 7802266 | 7.77E-10 | 2422 | 3.40E-09 | 6491908 | 1.17E-09 | 2403321 | 3.40E-07 | 6.49E+08 | 4.39E-07 | 9.04E+08 |
| CF3CF2CF2O | 0.75 | 2.81E-01 | 5.94E-09 | 64627 | 5.92E-12 | 18 | 8.34E-12 | 15908 | 6.06E-12 | 12460 | 3.44E-09 | 6567301 | 3.79E-09 | 7800915 |
| Fluoroxene | 0.01 | 1.10E-02 | 5.26E-12 | 57 | 4.72E-15 | 0 | 7.33E-15 | 14 | 5.35E-15 | 11 | 3.06E-12 | 5831 | 3.37E-12 | 6922 |
| CH2FOCF2CF | 6.2 | 3.43E-01 | 8.55E-08 | 930164 | 8.48E-11 | 264 | 1.34E-10 | 255067 | 8.96E-11 | 184331 | 4.88E-08 | 93141232 | 5.41E-08 | 1.11E+08 |
| C12H5F19O2 | 1 | 4.89E-01 | 5.45E-09 | 59214 | 4.42E-12 | 14 | 7.66E-12 | 14612 | 5.56E-12 | 11430 | 3.15E-09 | 6013668 | 3.47E-09 | 7144791 |
| CH3OCH2F | 0.2 | 6.50E-02 | 1.23E-09 | 13323 | 1.32E-12 | 4 | 1.71E-12 | 3262 | 1.25E-12 | 2562 | 7.11E-10 | 1355662 | 7.82E-10 | 1609580 |
| CH3OCHF2 | 1.1 | 1.74E-01 | 1.41E-08 | 153144 | 1.38E-11 | 43 | 1.98E-11 | 37829 | 1.44E-11 | 29575 | 8.15E-09 | 15549151 | 8.98E-09 | 18475390 |
| CH2FOCH2F | 0.9 | 1.93E-01 | 1.28E-08 | 138983 | 1.26E-11 | 39 | 1.80E-11 | 34262 | 1.30E-11 | 26815 | 7.40E-09 | 14118148 | 8.15E-09 | 16772241 |
| CH2FOCHF2 | 3.3 | 3.04E-01 | 6.05E-08 | 658269 | 5.97E-11 | 186 | 8.73E-11 | 166639 | 6.25E-11 | 128486 | 3.48E-08 | 66472163 | 3.85E-08 | 79138448 |
| CH2FOCF3 | 4.4 | 3.28E-01 | 7.38E-08 | 802594 | 7.09E-11 | 221 | 1.08E-10 | 206865 | 7.66E-11 | 157532 | 4.24E-08 | 81081633 | 4.68E-08 | 96319521 |
| HG'-01 | 2 | 2.92E-01 | 2.18E-08 | 236539 | 1.84E-11 | 57 | 3.09E-11 | 58976 | 2.23E-11 | 45876 | 1.26E-08 | 23963763 | 1.39E-08 | 28495850 |
| HG'-02 | 2 | 5.64E-01 | 2.32E-08 | 251804 | 1.95E-11 | 61 | 3.29E-11 | 62782 | 2.37E-11 | 48837 | 1.34E-08 | 25510279 | 1.47E-08 | 30334847 |
| HG'-03 | 2 | 7.65E-01 | 2.17E-08 | 235732 | 1.83E-11 | 57 | 3.08E-11 | 58775 | 2.22E-11 | 45720 | 1.25E-08 | 23882065 | 1.38E-08 | 28398701 |
| HFE-329me3 | 40 | 4.76E-01 | 4.44E-07 | 4833187 | 4.13E-10 | 1287 | 2.51E-09 | 4787070 | 1.11E-09 | 2290343 | 1.82E-07 | 3.48E+08 | 2.67E-07 | 5.48E+08 |
| HFE-338mec | 0.055 | 6.10E-02 | 9.25E-11 | 1006 | 5.37E-14 | 0 | 1.29E-13 | 246 | 9.40E-14 | 193 | 5.37E-11 | 102447 | 5.91E-11 | 121622 |
| CF3(CF2)6C | 0.055 | 6.80E-02 | 3.22E-11 | 350 | 2.81E-14 | 0 | 4.48E-14 | 86 | 3.27E-14 | 67 | 1.87E-11 | 35619 | 2.06E-11 | 42285 |

| | | | | | | | | | | | | | | |
|---|---|---|---|---|---|---|---|---|---|---|---|---|---|---|
| CF3(CF2)8C | 0.055 | 5.10E-02 | 1.85E-11 | 201 | 1.54E-14 | 0 | 2.57E-14 | 49 | 1.88E-14 | 39 | 1.07E-11 | 20453 | 1.18E-11 | 24281 |
| CH3OCF2CHF | 1.4 | 2.11E-01 | 1.20E-08 | 130583 | 1.22E-11 | 38 | 1.70E-11 | 32354 | 1.23E-11 | 25254 | 6.94E-09 | 13248800 | 7.65E-09 | 15746175 |
| PFPMIE(pe | 800 | 6.48E-01 | 9.40E-07 | 10221291 | 3.78E-09 | 11785 | 5.57E-09 | 10634929 | 5.81E-09 | 11954339 | 2.45E-07 | 4.67E+08 | 5.30E-07 | 1.09E+09 |
| HFE-216 | 0.023 | 2.50E-02 | 2.09E-11 | 227 | 3.19E-15 | 0 | 2.91E-14 | 56 | 2.12E-14 | 44 | 1.21E-11 | 23147 | 1.34E-11 | 27478 |
| HCOOCF3 | 3.5 | 3.11E-01 | 5.76E-08 | 626715 | 5.74E-11 | 179 | 8.34E-11 | 159083 | 5.95E-11 | 122450 | 3.32E-08 | 63253319 | 3.66E-08 | 75320932 |
| HCOOCF2CF3 | 3.5 | 4.42E-01 | 5.69E-08 | 619124 | 5.83E-11 | 182 | 8.24E-11 | 157157 | 5.88E-11 | 120966 | 3.28E-08 | 62487240 | 3.62E-08 | 74408698 |
| HCOOCF2CF2 | 2.6 | 5.03E-01 | 3.69E-08 | 401118 | 3.67E-11 | 114 | 5.28E-11 | 100678 | 3.79E-11 | 78023 | 2.13E-08 | 40576824 | 2.35E-08 | 48276960 |
| HCOOCF2CF2 | 3 | 5.61E-01 | 3.85E-08 | 418419 | 3.33E-11 | 104 | 5.53E-11 | 105519 | 3.96E-11 | 81549 | 2.22E-08 | 42284308 | 2.45E-08 | 50327189 |
| HCOOCH2CF3 | 0.44 | 1.58E-01 | 3.28E-09 | 35646 | 4.13E-12 | 13 | 4.59E-12 | 8748 | 3.34E-12 | 6863 | 1.90E-09 | 3624993 | 2.09E-09 | 4304809 |
| HCOOCH2CH2 | 0.3 | 1.34E-01 | 1.71E-09 | 18577 | 1.50E-12 | 5 | 2.39E-12 | 4553 | 1.74E-12 | 3574 | 9.91E-10 | 1889792 | 1.09E-09 | 2243936 |
| HCOOCHFCF3 | 3.2 | 3.49E-01 | 4.62E-08 | 502025 | 4.48E-11 | 140 | 6.65E-11 | 126921 | 4.76E-11 | 97940 | 2.66E-08 | 50707555 | 2.93E-08 | 60364085 |
| HCOOCH(CF3 | 3.2 | 3.33E-01 | 3.26E-08 | 354985 | 3.13E-11 | 98 | 4.70E-11 | 89747 | 3.37E-11 | 69254 | 1.88E-08 | 35855610 | 2.08E-08 | 42683800 |
| CH3COOCF2C | 0.06 | 1.25E-01 | 1.63E-10 | 1770 | 1.57E-13 | 0 | 2.27E-13 | 433 | 1.65E-13 | 340 | 9.45E-11 | 180239 | 1.04E-10 | 213974 |
| CH3COOCF2C | 0.06 | 1.07E-01 | 1.70E-10 | 1848 | 1.75E-13 | 1 | 2.37E-13 | 452 | 1.73E-13 | 355 | 9.86E-11 | 188117 | 1.09E-10 | 223326 |
| CH3COOCF2C | 0.06 | 9.90E-02 | 2.01E-10 | 2190 | 2.04E-13 | 1 | 2.81E-13 | 535 | 2.05E-13 | 421 | 1.17E-10 | 222939 | 1.29E-10 | 264666 |
| CH3COOCF3 | 0.06 | 7.20E-02 | 2.04E-10 | 2215 | 1.99E-13 | 1 | 2.84E-13 | 541 | 2.07E-13 | 426 | 1.18E-10 | 225465 | 1.30E-10 | 267665 |
| FCOOCH3 | 1.8 | 6.70E-02 | 9.33E-09 | 101463 | 9.74E-12 | 30 | 1.32E-11 | 25244 | 9.56E-12 | 19660 | 5.39E-09 | 10284308 | 5.94E-09 | 12227141 |

| | | | | | | | | | | | | | | |
|---|---|---|---|---|---|---|---|---|---|---|---|---|---|---|
| FCOOCF2CH3 | 0.33 | 1.69E-01 | 2.63E-09 | 28596 | 2.41E-12 | 8 | 3.67E-12 | 7010 | 2.68E-12 | 5502 | 1.53E-09 | 2908799 | 1.68E-09 | 3453990 |
| CF3COOCF2C | 0.33 | 2.70E-01 | 3.02E-09 | 32853 | 2.76E-12 | 9 | 4.22E-12 | 8054 | 3.07E-12 | 6322 | 1.75E-09 | 3341908 | 1.93E-09 | 3968275 |
| CF3COOCH2C | 0.06 | 5.30E-02 | 1.35E-10 | 1469 | 1.28E-13 | 0 | 1.88E-13 | 359 | 1.37E-13 | 282 | 7.84E-11 | 149577 | 8.63E-11 | 177573 |
| CF3COOCH2C | 0.15 | 1.45E-01 | 6.70E-10 | 7284 | 2.28E-12 | 7 | 9.34E-13 | 1782 | 6.81E-13 | 1400 | 3.89E-10 | 741245 | 4.28E-10 | 880046 |
| CF3COOCH3 | 0.61 | 1.79E-01 | 5.15E-09 | 55986 | 8.48E-12 | 26 | 7.21E-12 | 13762 | 5.24E-12 | 10787 | 2.98E-09 | 5691163 | 3.29E-09 | 6759412 |
| HCF2COOCH3 | 0.11 | 5.30E-02 | 3.20E-10 | 3478 | 9.31E-13 | 3 | 4.46E-13 | 851 | 3.25E-13 | 669 | 1.86E-10 | 353971 | 2.04E-10 | 420239 |
| CF3COOCHF2 | 0.3 | 2.41E-01 | 2.66E-09 | 28939 | 2.66E-12 | 8 | 3.72E-12 | 7092 | 2.71E-12 | 5568 | 1.54E-09 | 2943959 | 1.70E-09 | 3495653 |
| CHF2CHFOCF | 9.834 | 3.45E-01 | 1.22E-07 | 1324619 | 1.13E-10 | 353 | 2.53E-10 | 482666 | 1.31E-10 | 269034 | 6.82E-08 | 1.3E+08 | 7.66E-08 | 1.58E+08 |
| CF3CHFCF2O | 0.389 | 1.91E-01 | 2.29E-09 | 24874 | 2.35E-12 | 7 | 3.20E-12 | 6101 | 2.33E-12 | 4788 | 1.33E-09 | 2529893 | 1.46E-09 | 3004212 |
| CF3CF2CF2O | 67 | 5.81E-01 | 6.32E-07 | 6867726 | 7.28E-10 | 2270 | 3.80E-09 | 7247104 | 2.30E-09 | 4726507 | 2.22E-07 | 4.24E+08 | 3.71E-07 | 7.63E+08 |
| CHF2CF2CH2 | 0.25 | 1.12E-01 | 1.28E-09 | 13920 | 1.28E-12 | 4 | 1.79E-12 | 3410 | 1.30E-12 | 2677 | 7.42E-10 | 1416216 | 8.17E-10 | 1681544 |
| CF3CHFCF2C | 0.26 | 1.94E-01 | 1.67E-09 | 18188 | 2.31E-12 | 7 | 2.34E-12 | 4456 | 1.70E-12 | 3499 | 9.70E-10 | 1850414 | 1.07E-09 | 2197107 |
| CF3CF2CF2C | 0.55 | 1.98E-01 | 3.29E-09 | 35736 | 3.32E-12 | 10 | 4.60E-12 | 8779 | 3.35E-12 | 6884 | 1.90E-09 | 3633246 | 2.10E-09 | 4315002 |
| CHF2CF2CH2 | 0.039 | 3.20E-02 | 5.16E-11 | 561 | 8.83E-14 | 0 | 7.18E-14 | 137 | 5.24E-14 | 108 | 2.99E-11 | 57090 | 3.29E-11 | 67774 |
| perfluoro- | 0.019 | 2.80E-02 | 9.68E-12 | 105 | 9.68E-15 | 0 | 1.35E-14 | 26 | 9.84E-15 | 20 | 5.62E-12 | 10723 | 6.19E-12 | 12730 |
| CF3CH2CHO | 0.005 | 4.00E-03 | 1.19E-12 | 13 | 2.95E-15 | 0 | 1.65E-15 | 3 | 1.20E-15 | 2 | 6.88E-13 | 1312 | 7.57E-13 | 1558 |
| CH2FCH2OH | 0.056 | 1.60E-02 | 8.41E-11 | 915 | 8.26E-14 | 0 | 1.17E-13 | 224 | 8.55E-14 | 176 | 4.88E-11 | 93135 | 5.37E-11 | 110566 |

| | | | | | | | | | | | | | | |
|---|---|---|---|---|---|---|---|---|---|---|---|---|---|---|
| CHF2CH2OH | 0.11 | 3.70E-02 | 2.98E-10 | 3245 | 4.92E-13 | 2 | 4.16E-13 | 794 | 3.03E-13 | 624 | 1.73E-10 | 330235 | 1.91E-10 | 392060 |
| CF3CH2OH | 0.321 | 1.01E-01 | 1.95E-09 | 21243 | 2.76E-12 | 9 | 2.73E-12 | 5207 | 1.99E-12 | 4088 | 1.13E-09 | 2160949 | 1.25E-09 | 2565951 |
| HCF2O(CF2C | 26 | 1.46E+00 | 3.55E-07 | 3860431 | 3.77E-10 | 1174 | 1.72E-09 | 3280082 | 5.99E-10 | 1231817 | 1.67E-07 | 3.18E+08 | 2.17E-07 | 4.46E+08 |

**[END Table 7.A.3 HERE]**

# Figures

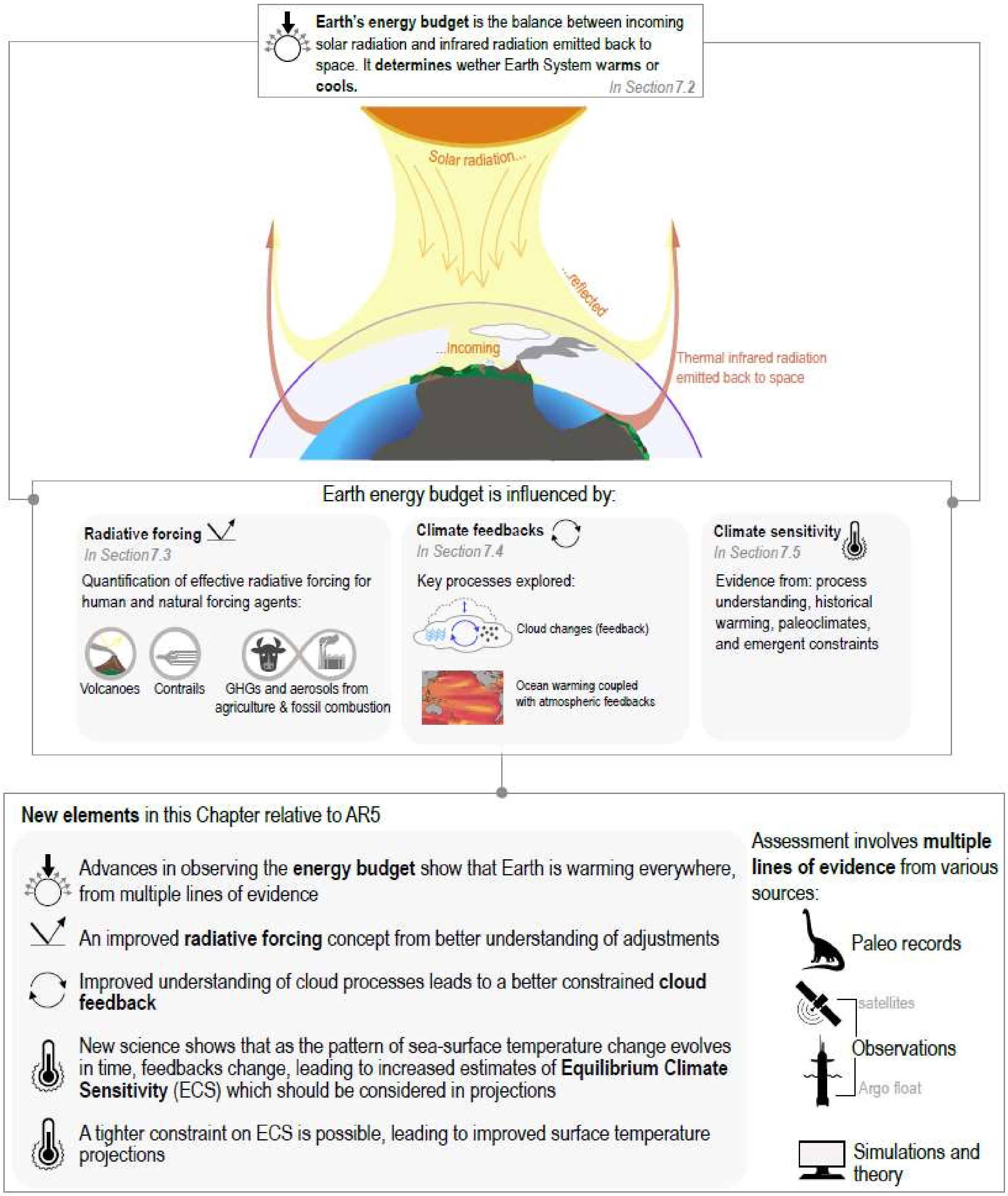


**Figure 7.1:** A visual abstract of the Chapter, illustrating why the Earth's Energy budget matters and how it relates to the underlying Chapter assessment. The methods used to assess processes and key new findings relative to IPCC AR5 are highlighted.

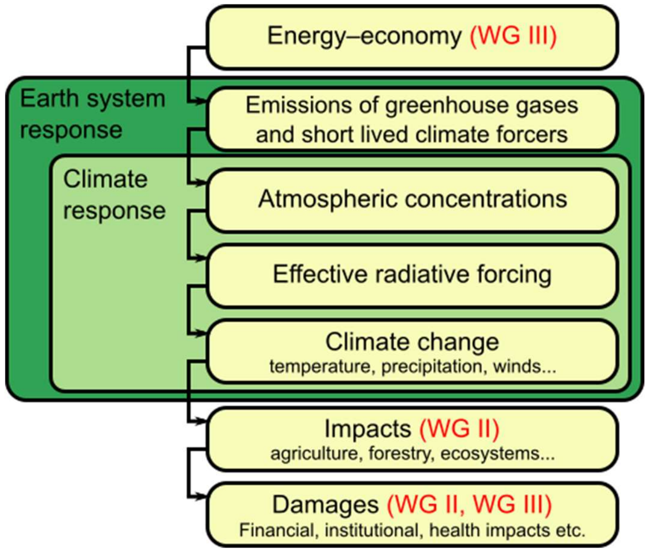


**Figure 7.2:** A conceptual chain of processes linking human activity to climate impacts, showing where the climate indicators and emission metrics assessed in this chapter fit within the chain and how they associate with other IPCC Working Groups.

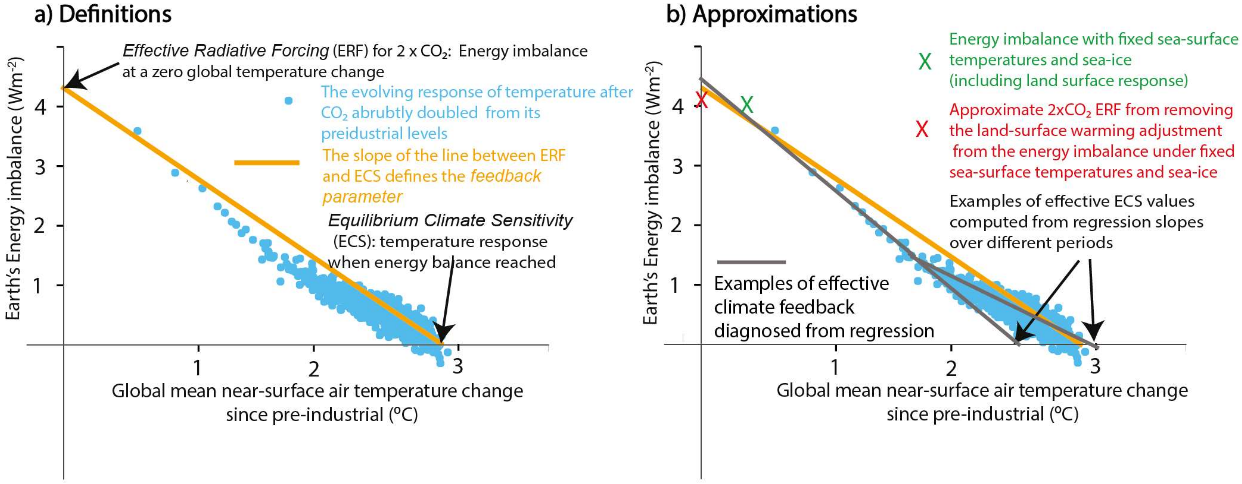


**Box 7.1, Figure 1:** Schematics of the forcing-feedback framework adopted within the assessment, following Equation 7.1. Illustrated is how the Earth's energy balance might evolve for a hypothetical doubling of atmospheric $CO_2$ concentration above preindustrial levels, where an initial positive energy imbalance (energy entering the Earth system, shown on the y-axis) is gradually restored towards equilibrium as the surface temperature warms (shown on the x-axis). a) illustrates the definitions of ERF for the special case of a doubling atmospheric $CO_2$ concentration, the feedback parameter and the ECS. b) illustrates how approximate estimates of these metrics are made within the Chapter and how these approximations relate to the exact definition adopted in panel a).

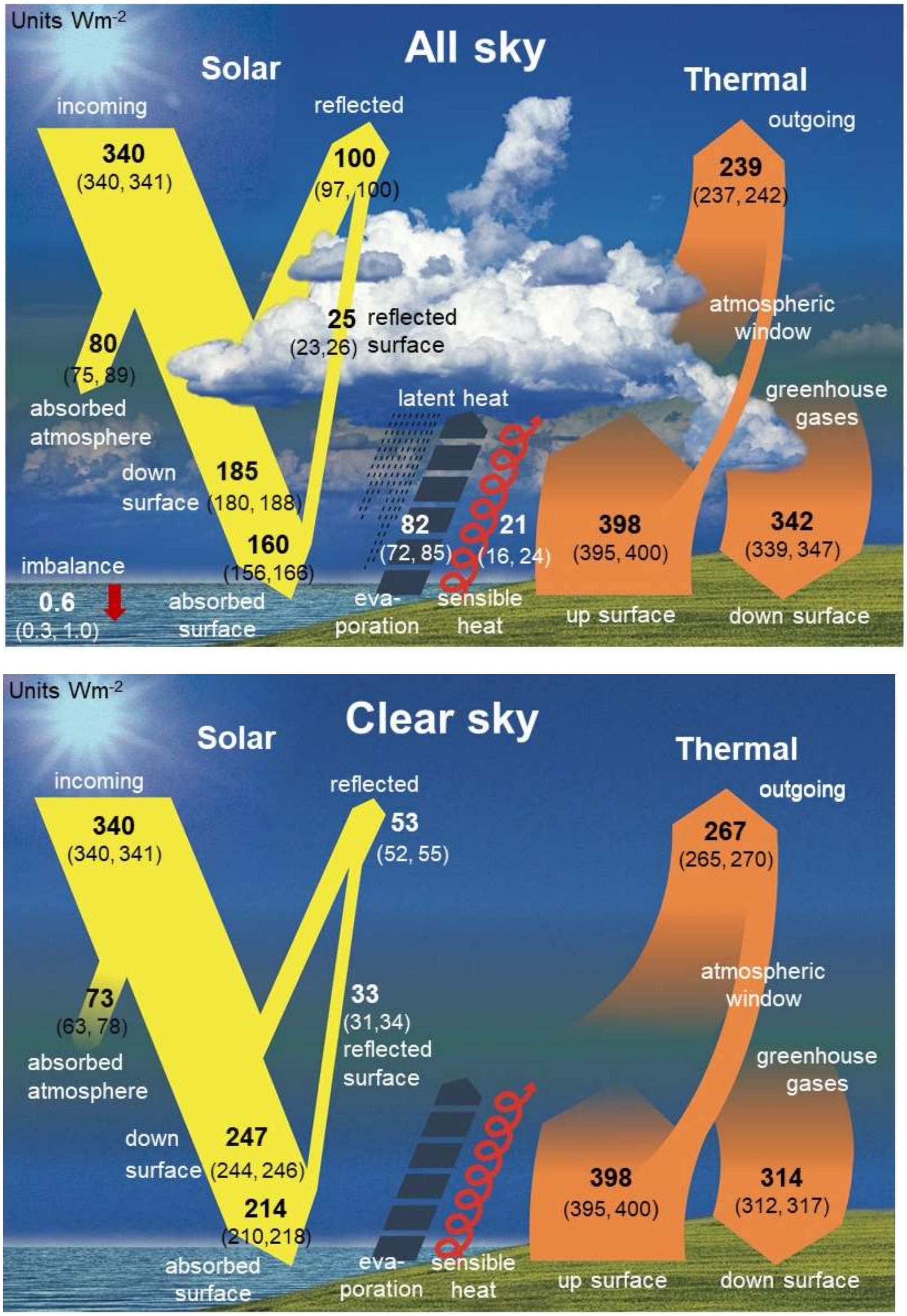


**Figure 7.3:** Schematic representation of the global mean energy budget of the Earth (upper panel), and its equivalent without considerations of cloud effects (lower panel). Numbers indicate best estimates for the magnitudes of the globally averaged energy balance components in W $m^{-2}$ together with their uncertainty ranges in parentheses (5 % to 95 % confidence range), representing present day climate conditions at the beginning of the 21[th] century. Adapted from Wild et al. (2015, 2019).

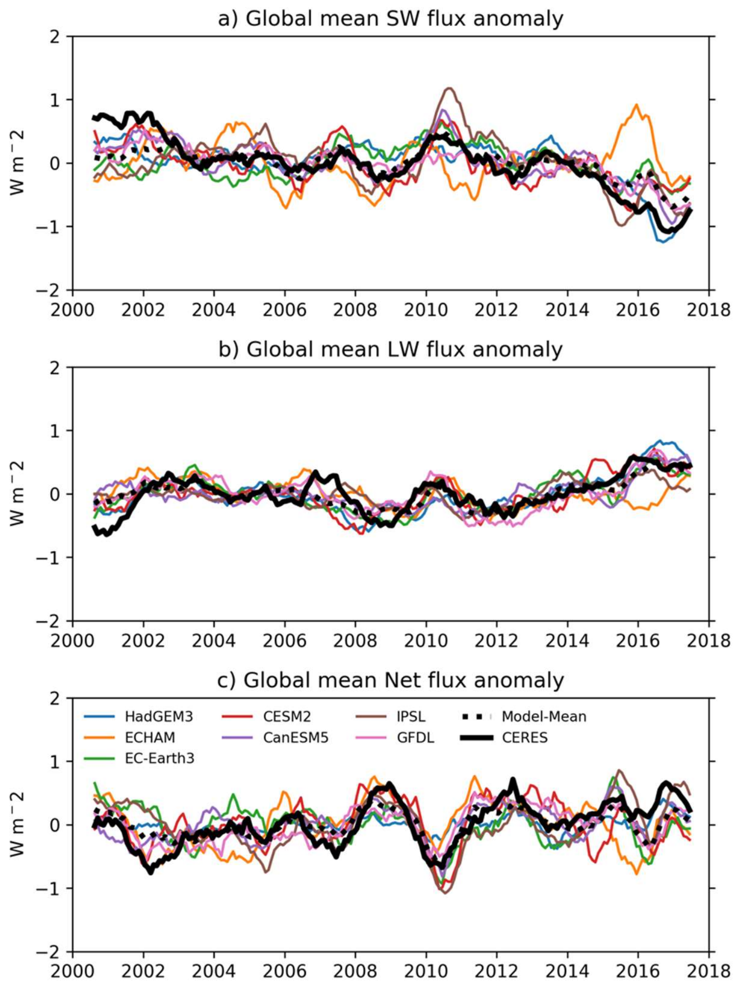


**Figure 7.4:** Anomalies in global mean all-sky TOA fluxes from EBAF Ed4.0 (solid black lines) and various CMIP6 climate models (coloured lines) in terms of reflected solar (upper panel), emitted thermal (middle panel) and net TOA fluxes (lower panel). The multimodel means are additionally depicted as doted black lines. Model fluxes stem from simulations driven with prescribed SSTs and all known anthropogenic and natural forcings. Shown are anomalies of 12-month running means. Larger reflected shortwave and emitted thermal flux anomalies are defined as positive in upper and middle panels. Net TOA flux is defined as incoming shortwave flux minus reflected and emitted fluxes (i.e. downward positive). Adapted from Loeb et al. (submitted).

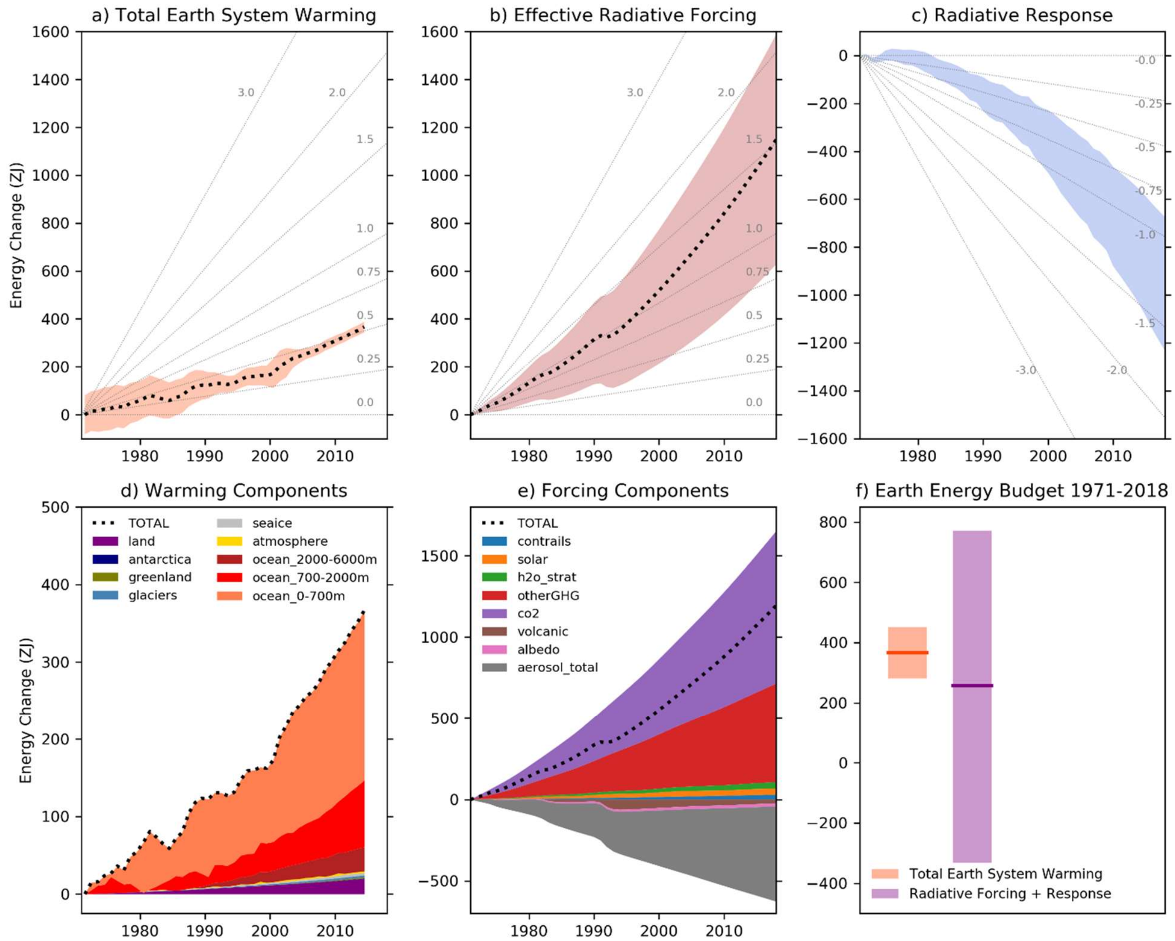


**Box 7.2, Figure 1:** Estimates of the net cumulative energy change (ZJ = $10^{21}$ Joules) for the period 1971–2018 associated with: (a) Total Earth System Warming; (b) Effective Radiative Forcing; (c) Earth System Radiative Response. Shaded regions indicate the 5th to 95th percentile uncertainty range. The grey lines indicate equivalent heating rates in W $m^{-2}$, expressed relative to Earth's surface area. Panels (d) and (e) show the breakdown of components, as indicated in the legend, for Total Earth System Warming and Effective Radiative Forcing, respectively. Panel (f) shows the Earth Energy Budget assessed for the period 1971–2018, i.e. the consistency between Total Earth System Warming and the implied heat storage from Effective Radiative Forcing plus Earth System Radiative Response. Shading represents the 5% to 95% uncertainty range. Forcing and Response timeseries are computed using a baseline period of 1850–1900. [placeholder: Total Earth System Warming components to be updated to 2018 for final draft. Reported values for sum of components in main text are based on extrapolation of 2006–2015 rate to 2018. The aerosol ERF estimate is based on AR5 and will be updated for the final draft.]

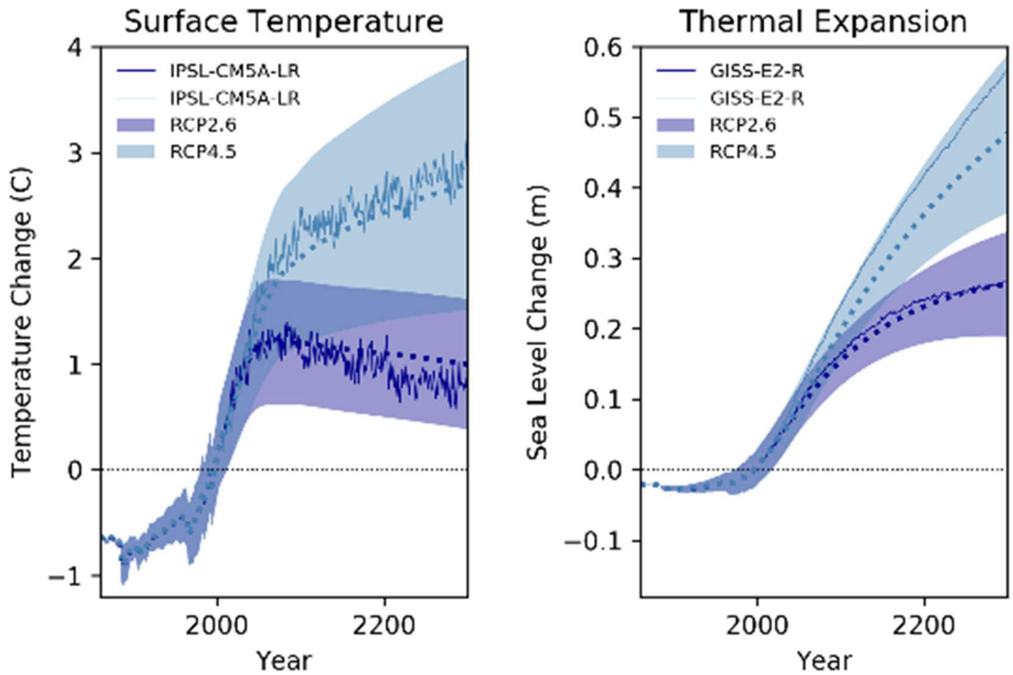


**Box 7.2, Figure 2:** Two-layer model simulations of global mean surface temperature (left) and ocean thermal expansion (right) under the RCP2.6 and RCP4.5 scenarios, following Palmer et al. (2018). Shaded regions indicate the 90% confidence interval based on the ensemble standard deviation. Dotted lines indicate the ensemble mean response. Solid lines show a single CMIP5 model simulation to illustrate the characteristics of variability in each variable. Projections are shown relative to a 1986-2005 baseline period.

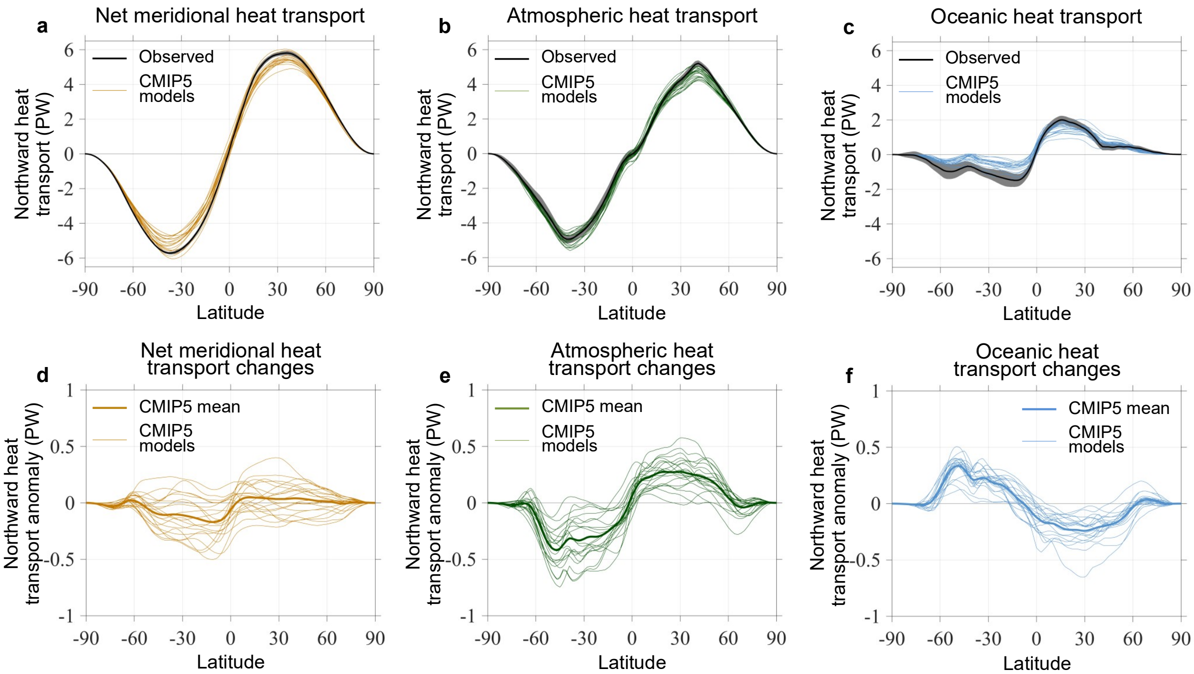


**Figure 7.5:** Observation-based and CMIP5 climatological northward energy transports in the atmosphere and ocean (top) and projected heat transport changes at year 100 following $CO_2$ quadrupling (bottom). (a) Climatological net heat transport inferred from CERES TOA (Armour et al., 2019; Donohoe et al., submitted) and simulated by CMIP5 models. (b) Climatological atmospheric heat transport calculated from the NCEP Reanalysis (Trenberth and Stepaniak, 2003) and simulated by CMIP5 models. (c) Climatological oceanic heat transport inferred from surface energy budgets (calculated as a residual between atmospheric heat transport divergence and TOA radiation fluxes). Grey shading shows 5% to 95% range on observational estimates. For total meridional heat transport the range is estimated from inter-annual variability and total CERES calibration error added in quadrature at each latitude. For atmospheric heat transport the range is estimated from inter-annual variability and for oceanic heat transport the range is estimated as a residual from the total and atmospheric heat transports with errors propagated in quadrature. (d-f) Anomalies in net, atmospheric, and implied oceanic heat transports simulated by CMIP5 models under abrupt $CO_2$ quadrupling relative to the pre-industrial control simulations which define their climatologies in (a)-(c) (following Donohoe et al., submitted). Implied ocean heat transport changes are derived from net sea-surface heat fluxes and thus do not account for the pattern of ocean heat storage.

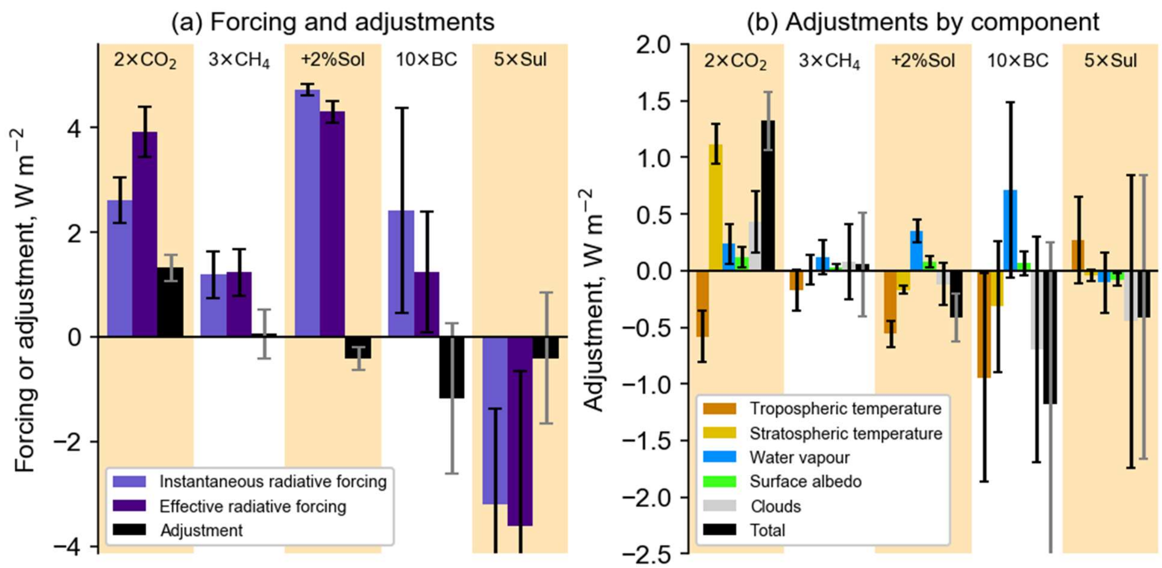


**Figure 7.6:** The effective radiative forcing (ERF), instantaneous radiative forcing (IRF) and adjustment (a) and breakdown of the adjustment using radiative kernels (b) for five idealised forcing experiments across nine models. The 90% confidence range is shown. Note that the land-surface response is included in ERF. Data modified from Smith et al. (2018b). Separation of temperature adjustments into tropospheric and stratospheric contributions is approximate based on a fixed tropopause of 100 hPa at the equator, varying linearly in latitude to 300 hPa at the poles. The results are computed from idealized single forcing experiments with the following abrupt perturbations from present day conditions; doubling $CO_2$ concentration (2×$CO_2$), tripling methane concentration (3×$CH_4$), two percent increase in insolation (+2%Sol), ten times black carbon concentrations or emissions (10×BC), five times sulphate concentrations or emissions (5×Sul).

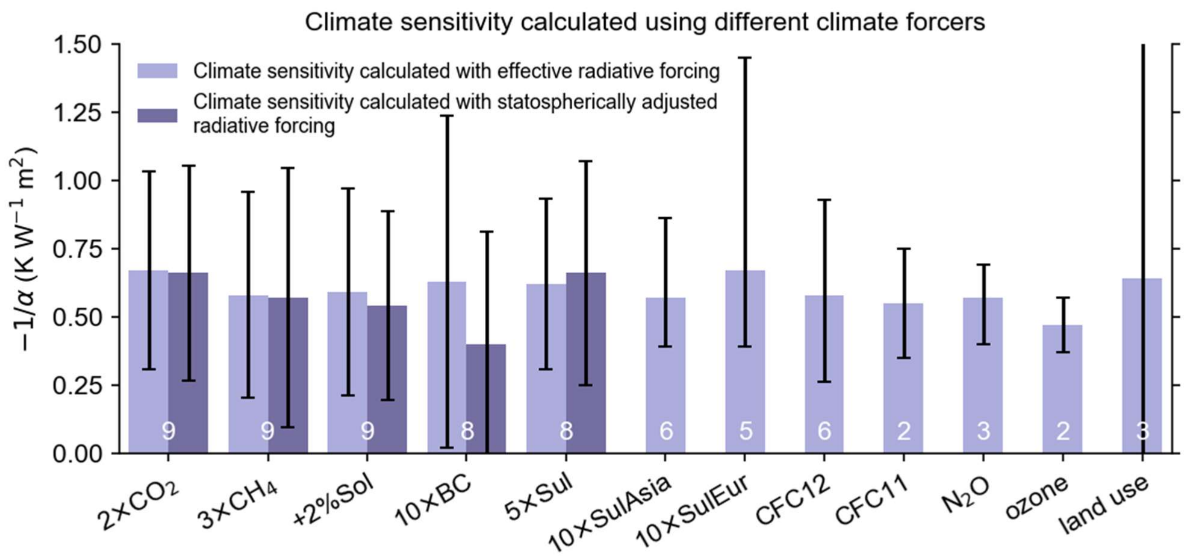


**Figure 7.7:** Values of climate sensitivity ($-1/\alpha$) derived from ERF and SARF for twelve forcing experiments. Multi-model means and full model ranges are shown. ERF is derived from prescribed SST and sea-ice experiments. The number of models analysed differs between experiments as indicated on the bars. Data from Richardson et al. (2019). The results are computed from idealized single forcing experiments with the following abrupt perturbations from present day conditions; doubling $CO_2$ concentration (2x$CO_2$), tripling methane concentration (3x$CH_4$), two percent increase in insolation (2%Sol), ten times black carbon concentrations or emissions (10xBC), five times sulphate concentrations or emissions (5xSul), ten times sulphate concentrations or emissions over Asia only (10xSulAsia), ten times sulphate concentrations or emissions over Europe only (10xSulEur), change in CFC-12 mixing ratio to 5ppb (CFC-12), change in CFC-11 mixing to 5ppb (CFC-11), change in $N_2O$ mixing ratio to 1ppm ($N_2O$), five times tropospheric ozone concentration (ozone), change in vegetation to pre-industrial conditions (land use). Black bars represent 90% range of model spread for 2x$CO_2$, 3x$CH_4$, +2%Sol, 10xBC and 5xSul and the full model range for other experiments.

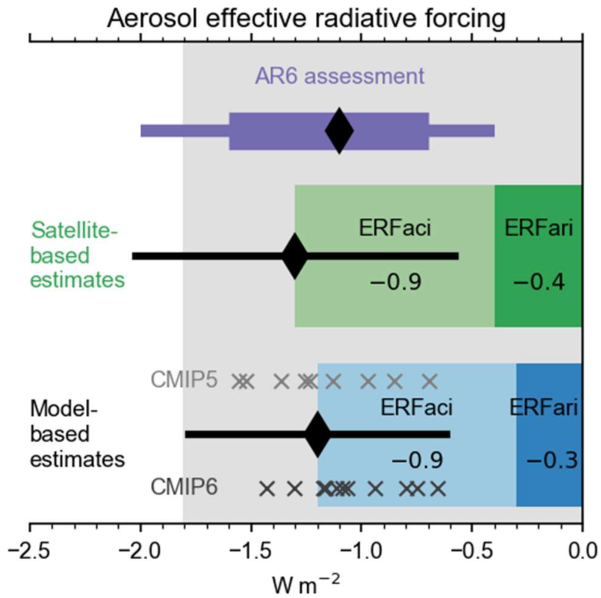


**Figure 7.8:** Net aerosol ERFari+aci from different lines of evidence. Green bars show the assessment based on satellite observations. Blue bars show the assessment based on climate models, with individual models from CMIP5 (Zelinka et al., 2014) and CMIP6 (Smith et al., submitted, b) depicted. Individual assessed best-estimate contributions from ERFari and ERFaci are shown with darker and paler shading respectively. Overlaid black diamond and black lines shows the best estimate and *very likely* range of satellite- and model-derived ERFari+aci. Grey shading shows the *very likely* range consistent with energy budget constraints. Purple bars show the assessed *very likely* range (thin), *likely* range (thick), and best estimate (black diamond) from all lines of evidence in this assessment.

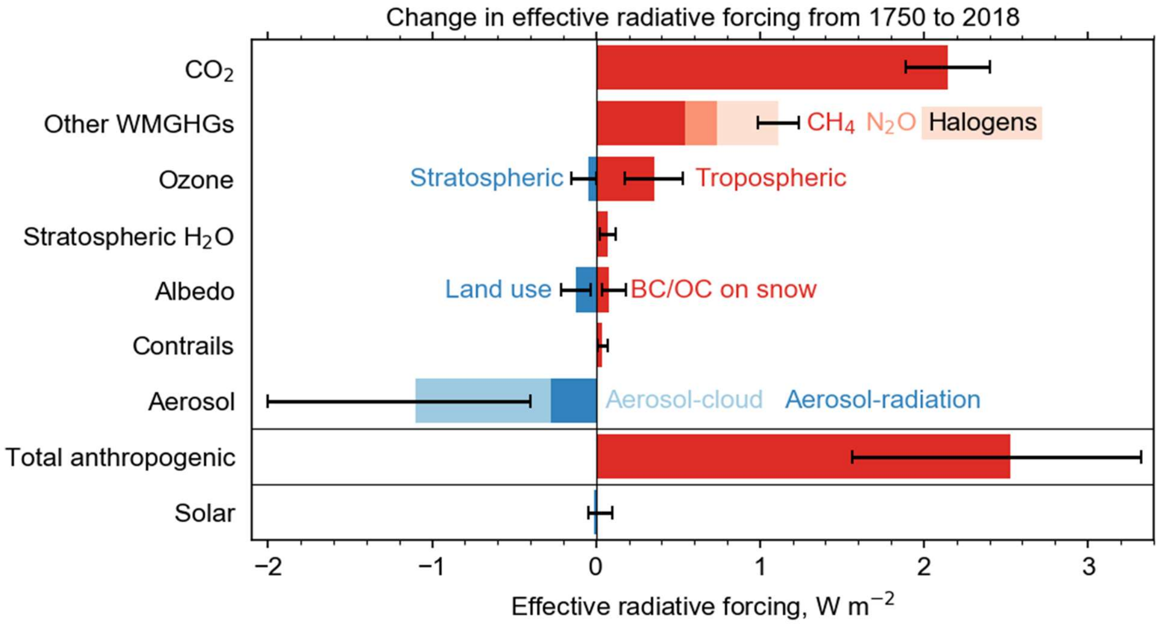


**Figure 7.9:** Effective radiative forcing from 1750 to 2018 by contributing forcing agents.

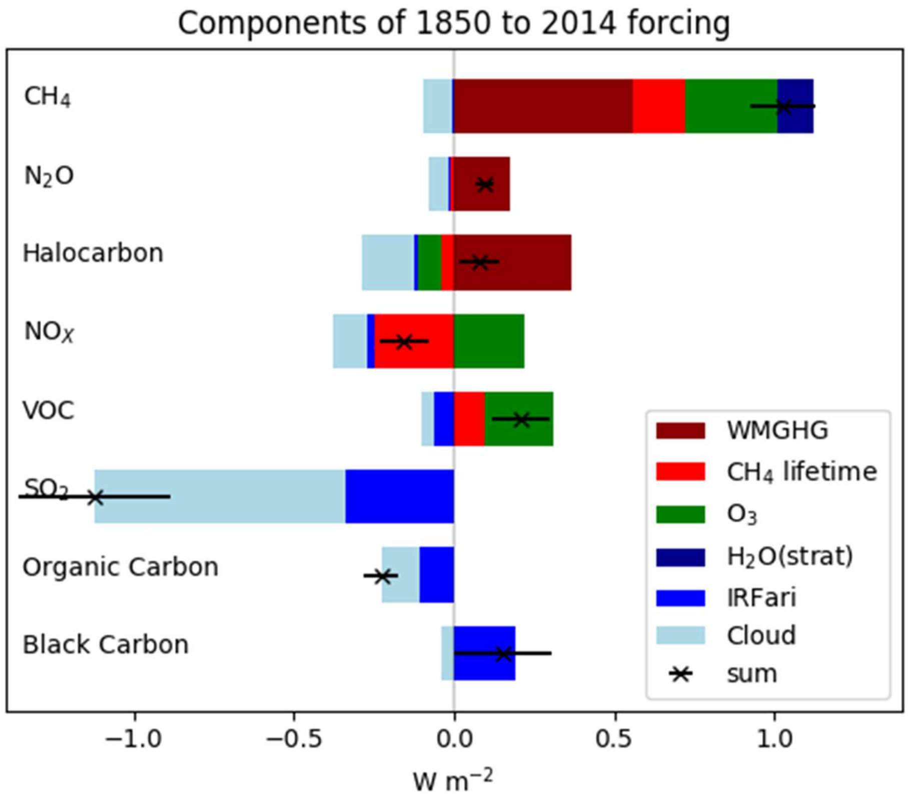


**Figure 7.10:** Components of radiative forcing from 1850 to 2014 by emitted species based on CMIP6 models (Thornhill et al. submitted). "VOC" includes CO as well as other non-methane hydrocarbons. WMGHGs are from the analytical formulae in section 7.3.2, $H_2O$ (strat) is from table 7.8. Other components are multi-model means from Thornhill et al. (submitted), see Chapter 6, Section 6.3.1.1, and are based on model simulations where one species at a time is increased from 1850 levels to 2014. Error bars are 5-95% and account for uncertainty in radiative efficiencies and multi-model error in the means. IRFari and cloud effects are calculated from separate radiation calls for clear-sky and aerosol free conditions (Ghan, 2013; Thornhill et al. submitted). "Cloud" includes cloud adjustments (semi-direct effect) and ERFaci. The aerosols ($SO_2$, organic carbon, black carbon) components are scaled to sum to -0.25 W $m^{-2}$ for IRFari and -0.95 W $m^{-2}$ for "cloud" (section 7.3.3).

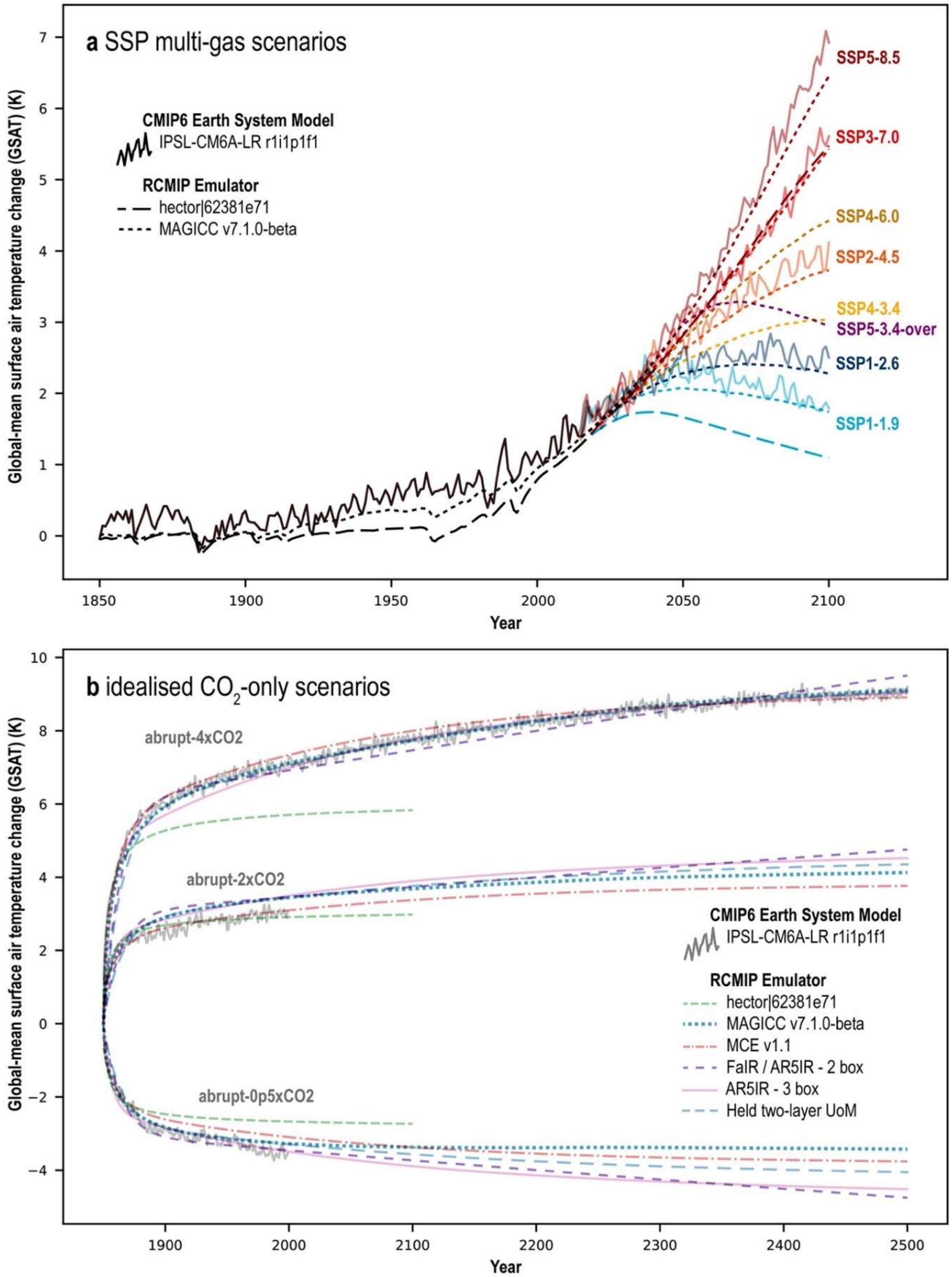


**Cross-Chapter Box 7.1, Figure 1:** A comparison between the global-mean surface air temperature response of various calibrated simple climate model types and one CMIP6 Earth System models, IPSL CM6A-LR. Most of the latest generation emulators incorporate a non-linearity or state-dependency of the climate sensitivity in order to match ESMs results across the wide response space of SSP scenarios (panel a), quadrupled, doubled and halved $CO_2$ concentrations (panel b). This is an advancement over simple climate model as used in the IPCC Second Assessment Report (cf. Figure 17 in Harvey et al., 1997). Figure adapted from Nicholls et al.

(submitted).

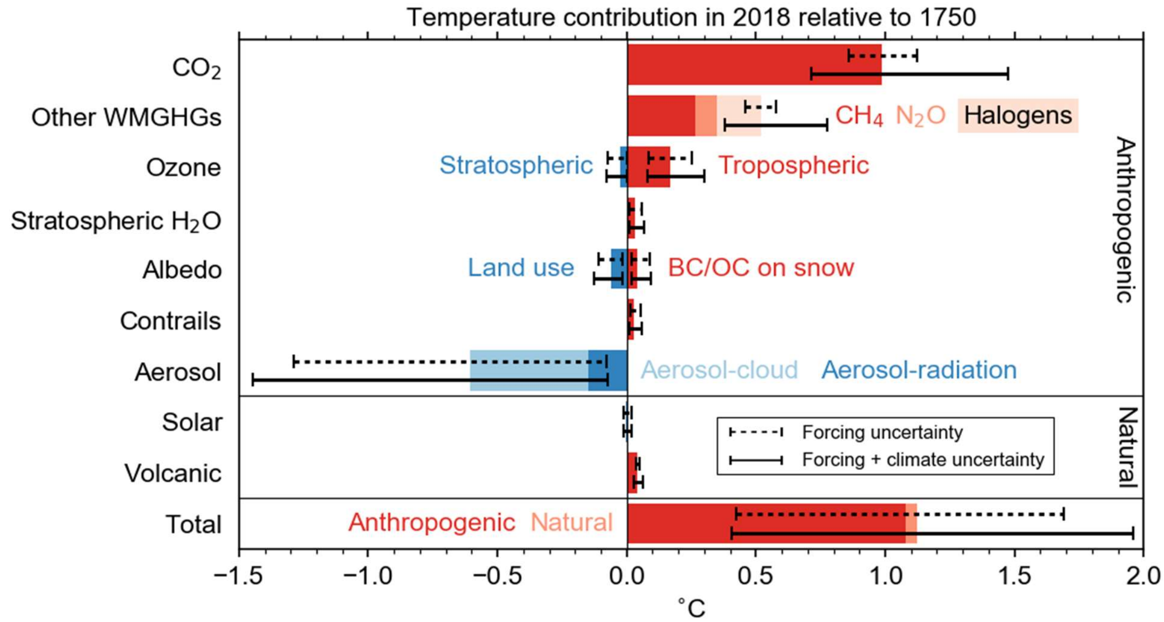


**Figure 7.11:** The contribution of forcing agents to 2018 temperature change relative to 1750 produced using the two-layer energy balance model (Cross-Chapter Box 7.1) where ranges for ERF were taken from Section 7.3 and ranges for ECS were taken from Section 7.5. Dashed error bars show the contribution of forcing uncertainty and solid error bars show the combined forcing and climate response uncertainty.

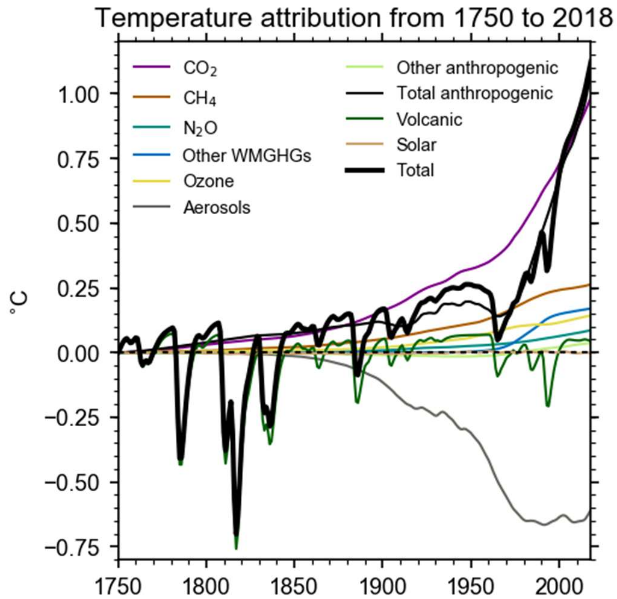


**Figure 7.12:** Timeseries of near surface global temperature changes, using the time series of ERFs assessed in Chapter 2 and calculated using the two-layer energy balance model (Cross-Chapter Box 7.4) with the best estimate of ECS assessed in Section 7.5.

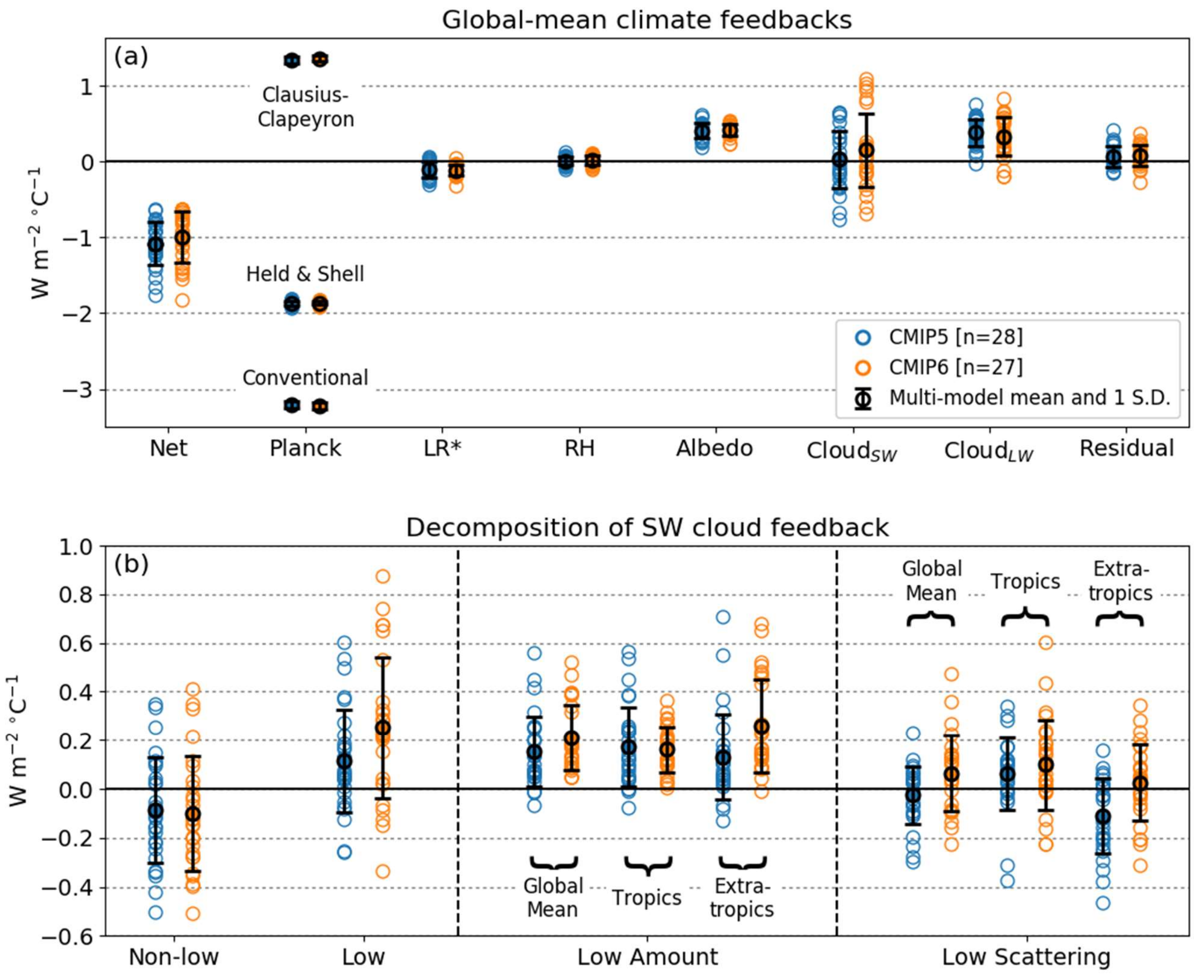


**Figure 7.13:** (a) Estimates of global−mean climate feedbacks in 28 CMIP5 (blue) and 27 CMIP6 (orange) *abrupt4xCO₂* simulations. The open circle represents individual models and the black circle with an error bar indicates the multi-model mean and the inter-model standard deviation. Decomposition of temperature and moisture feedbacks follows (Held and Shell, 2012), which divide them into Planck response with fixed relative humidity (P*, denoted as 'Held & Shell' in the figure), Lapse Rate (LR*) and Relative Humidity (RH) feedbacks. The P* term is further separated to the conventional Planck response and a water vapour feedback with fixed RH (represented as 'Conventional' and 'Clausius-Clapeyron'; see Section 7.4.2.2). The net cloud feedback is the sum of cloud shortwave (Cloud SW) and longwave (Cloud LW) feedbacks. The residual between the summed feedback and the net climate feedback (left), the latter directly derived from the models, includes feedbacks neglected in this analysis but considered in some models (e.g. non-biogeochemical feedbacks) and above all errors in the radiative kernel. (b) Decomposition of the global cloud SW feedback into contributions from non-low and low clouds (left), the latter further broken down to the low cloud amount (middle) and albedo (right) feedbacks. Their global means are equal to the average of tropical (30°S–30°N) and extratropical (poleward of 30°S/N) components. All the values are based on six radiative kernels by Zelinka et al. (2019).

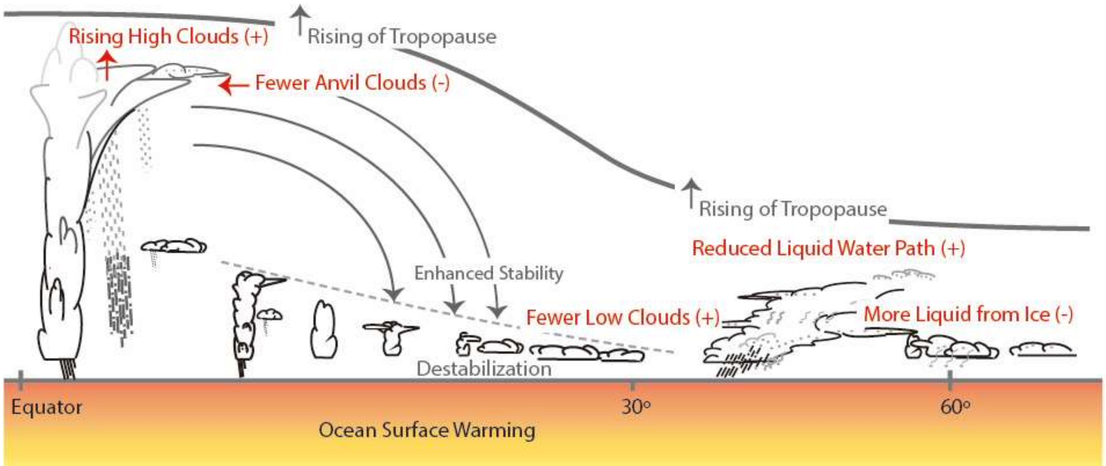


**Figure 7.14:** Schematic cross section of diverse cloud regimes between the tropics and polar regions. Thick solid and dashed curves indicate the tropopause and the subtropical inversion layer in the current climate. Thin grey text and arrows represent robust responses in the thermodynamic structure to greenhouse warming, of relevance to cloud changes. Text and arrows in red show the major cloud responses and the sign of their feedbacks to the surface warming assessed in this chapter.

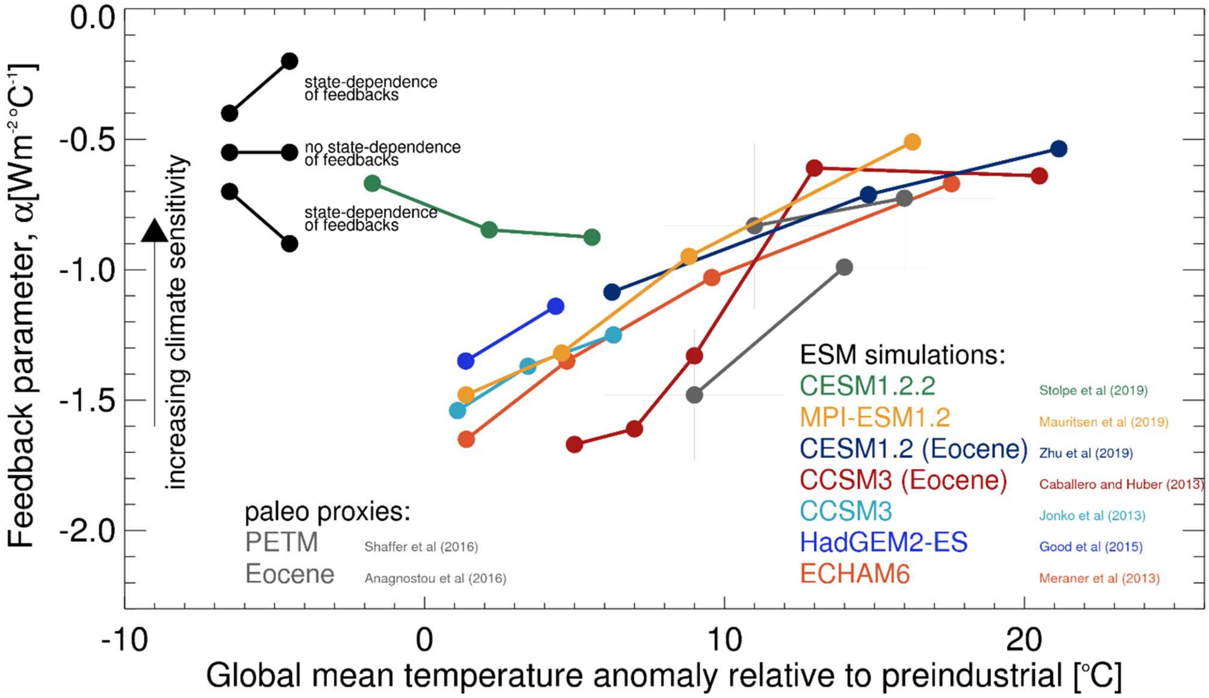


**Figure 7.15:** Feedback parameter, α (W $m^{-2}$ $°C^{-1}$), as a function of global mean surface air temperature anomaly relative to preindustrial, for model simulations (coloured circles and lines; Caballero and Huber, 2013; Good et al., 2015; Jonko et al., 2013; Mauritsen et al., 2019; Meraner et al., 2013; Stolpe et al., 2019; Zhu et al., 2019), and from paleoclimate data (grey circles and associated uncertainties; Anagnostou et al., 2016; Shaffer et al., 2016). For the model simulations, the value on the x-axis refers to the mean of the temperature before and after the system has equilibrated to a forcing (in most cases a $CO_2$ doubling), and is expressed as an anomaly relative to an associated pre-industrial global mean temperature from that model. The values of α from proxies assume a radiative forcing of 3.7 W $m^{-2}$ for $CO_2$ doubling.

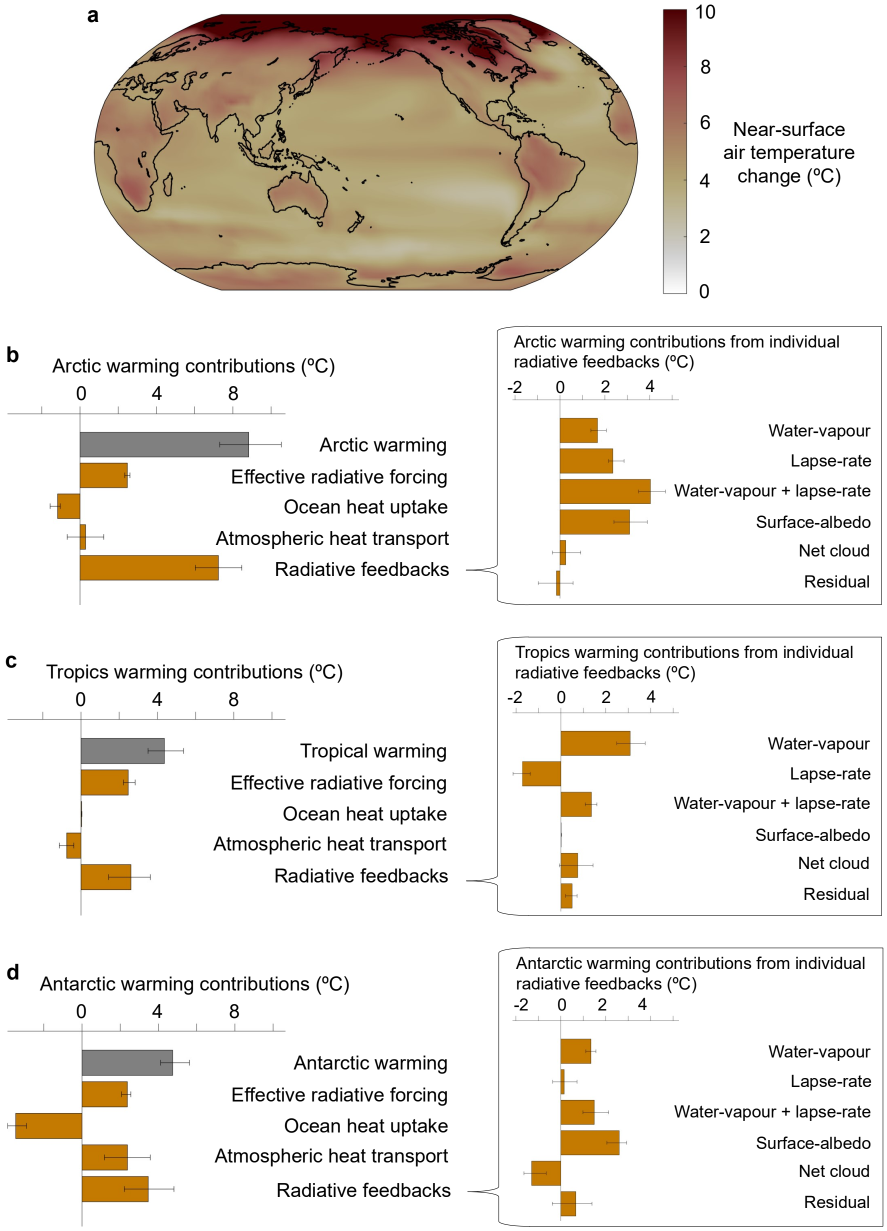


**Figure 7.16:** Contributions of effective radiative forcing, ocean heat uptake and radiative feedbacks to regional surface temperature changes at year 100 of abrupt $CO_2$ quadrupling simulations of CMIP5 models. (a) Pattern of near-surface air temperature change. (b-d) Contributions to net Arctic (>60°N), tropical (30°S-30°N), and Antarctic (<60°S) warming calculated by dividing regional-average energy inputs by the regional-average Planck response, with the contributions from radiative forcing, changes in atmospheric heat transport, ocean heat uptake, and radiative feedbacks summing to the value of net warming; inset shows regional warming contributions associated with individual feedbacks, summing to the total feedback contribution. Uncertainties show 25% and 75% percentiles across models. The warming contributions (units of °C) for each process are diagnosed by calculating the energy flux (units of W m$^{-2}$) that each process contributes to the atmosphere over a given region, either at the TOA or surface, then dividing that energy flux by the regional Planck response (around 3.2 W m$^{-2}$ °C$^{-1}$ but varying with latitude). By construction, the individual warming contributions sum to the total warming in each region. Radiative kernel methods (see Section 7.4.1) are used to decompose the net energy input from radiative feedbacks into contributions from changes in atmospheric water vapour, lapse-rate, clouds and surface albedo, leaving a small residual (Shell et al., 2008) and the analysis is based on that of Goosse et al., (2018).

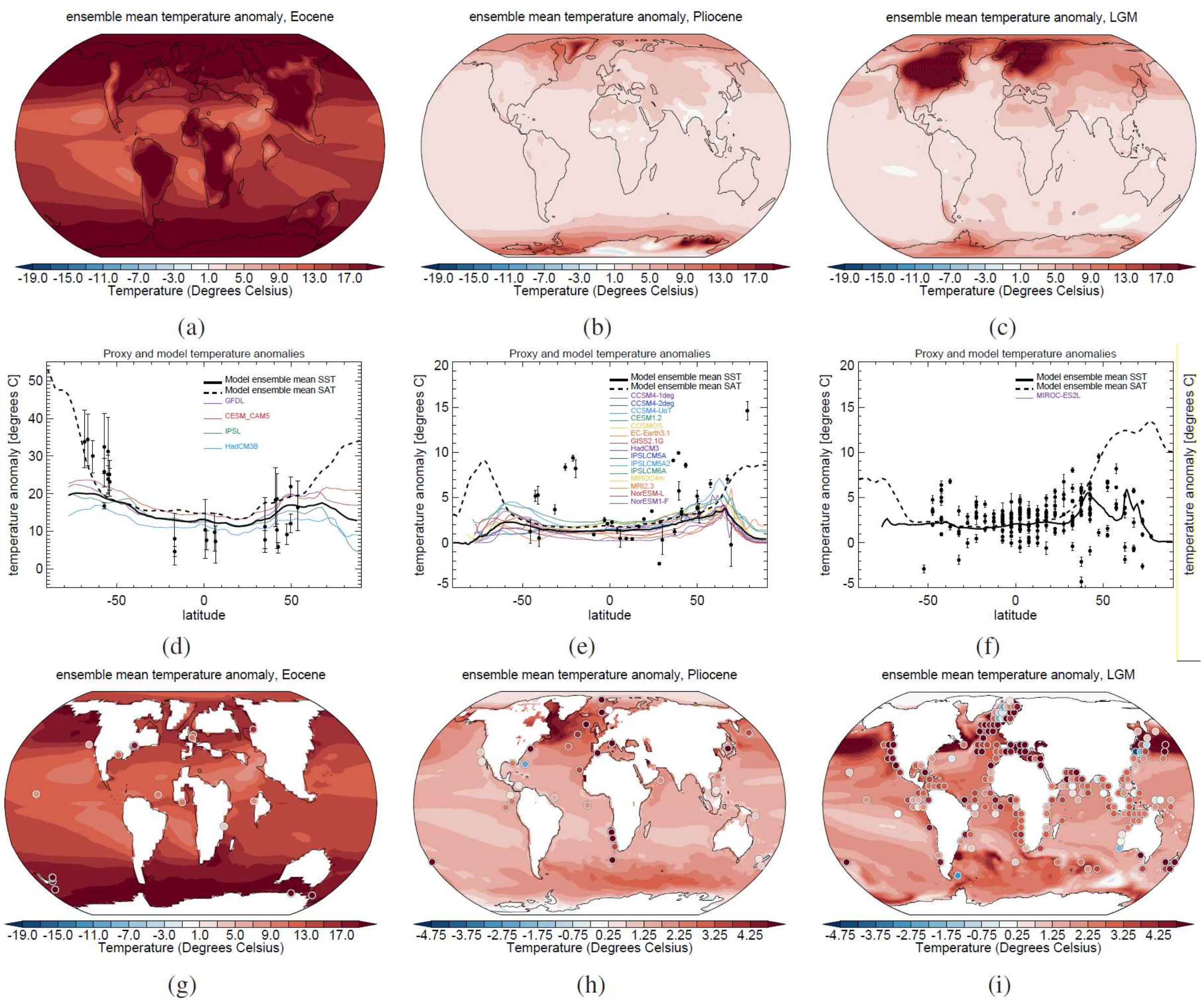


**Figure 7.17:** Temperature anomalies compared with pre-industrial for the high-$CO_2$ EECO and MPWP time periods, and for the Last Glacial Maximum (expressed as LGM minus preindustrial), from paleoclimate proxies and models. (a,b,c) Modelled near-surface air temperature anomalies for ensemble-mean simulations of the (a) EECO (Lunt et al, submitted), (b) Pliocene (Haywood et al, submitted), and (c) Last Glacial Maximum (Kageyama et al, submitted). (d,e,f) Proxy sea surface temperature anomalies (black circles), including published uncertainties (vertical bars), black lines show model ensemble mean SST anomaly (solid back line) and near-surface air temperature anomaly (dashed black line) for the same ensembles as in (a,b,c), coloured lines show the modelled SST anomaly for the individual models that make up each ensemble (LGM, N=1; MPWP, N=15; EECO, N=5). Proxy datasets are (d) (Hollis et al., 2019), (e) (Foley and Dowsett, 2019), and (f) Tierney et al (submitted). (g,h,i) As (a,b,c) but for SST anomalies, and with the proxy SST anomalies from (d,e,f) also shown (coloured circles). For the Eocene maps (c,i), the anomalies are relative to the zonal mean of the preindustrial.

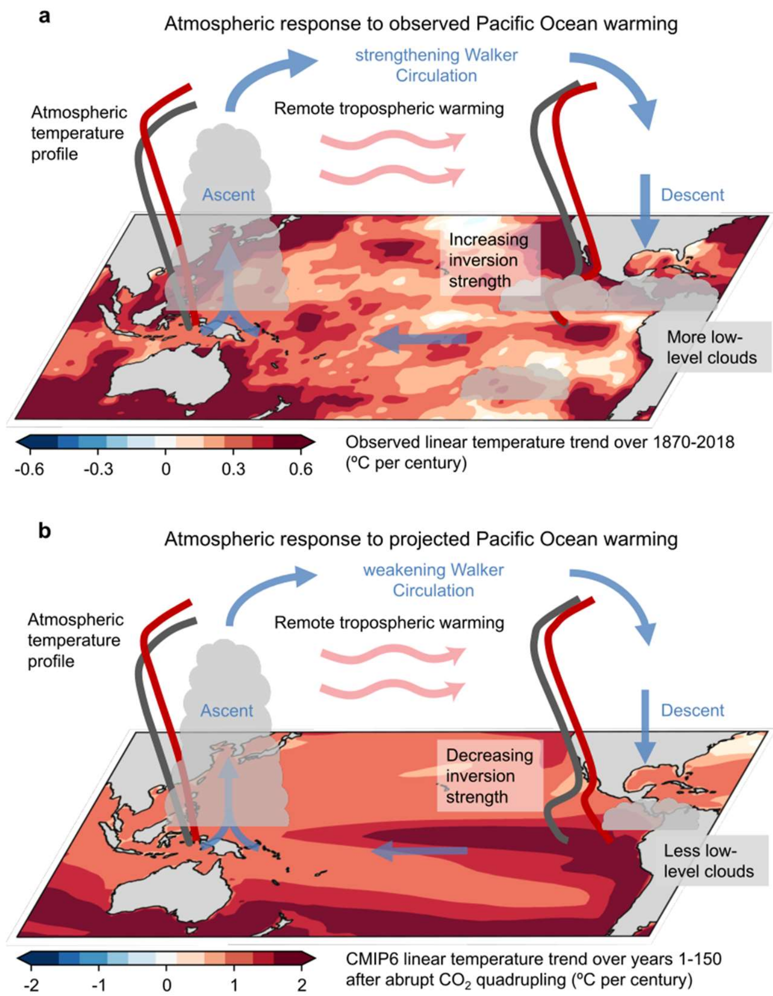


**Figure 7.18:** Illustration of tropospheric temperature and low-cloud response to observed and projected Pacific Ocean sea-surface temperature trends; adapted from Mauritsen (2016). (a) Atmospheric response to linear sea-surface temperature trend observed over 1870-2018 (HadISST1 dataset; Rayner et al., 2003). (b) Atmospheric response to linear sea-surface temperature trend projected over 150 years following $CO_2$ quadrupling by an average of 22 CMIP6 GCMs (Dong et al.,submitted). The historical temperature trend shows relatively large warming in the western tropical Pacific has been communicated aloft (red atmospheric temperature profile), remotely warming the tropical free troposphere and increasing the strength of the inversion in regions of the tropics where warming has been muted, such as the eastern equatorial Pacific. In turn, an increased inversion strength has increased the low-cloud cover (Zhou et al., 2016) causing an anomalously negative cloud and lapse-rate feedbacks over the historical record (Andrews et al., 2018; Marvel et al., 2018). The projected temperature trend shows relatively large warming in the eastern tropical Pacific which is trapped near the surface (red atmospheric temperature profile), decreasing the strength of the inversion locally. In turn, a decreased inversion strength combined with surface warming is projected to decrease the low-cloud cover, causing the cloud and lapse-rate feedbacks to become less-negative in the future.

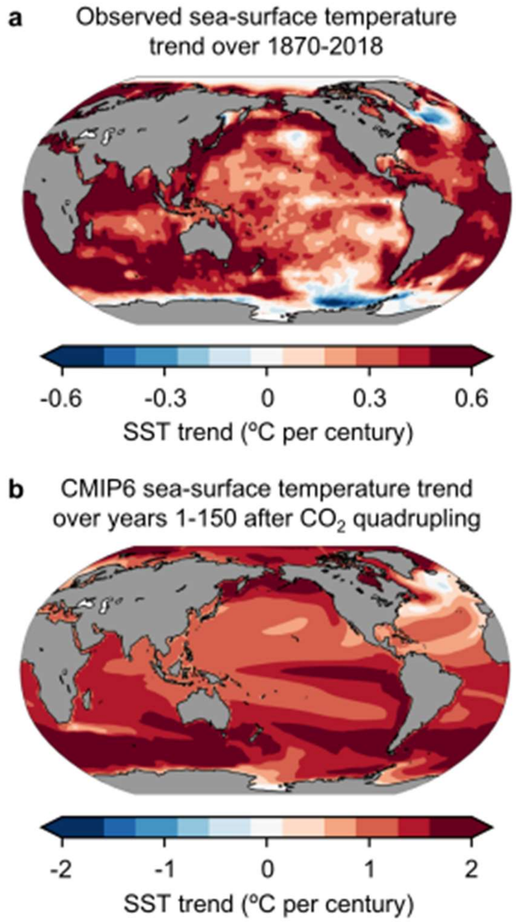


**Figure 7.19:** Sea-surface temperature linear trends (a) observed over 1870-2018 (HadISST dataset; Rayner et al., 2003), and (b) projected over 150 years following $CO_2$ quadrupling by an average of 22 CMIP6 GCMs (Dong et al., submitted)

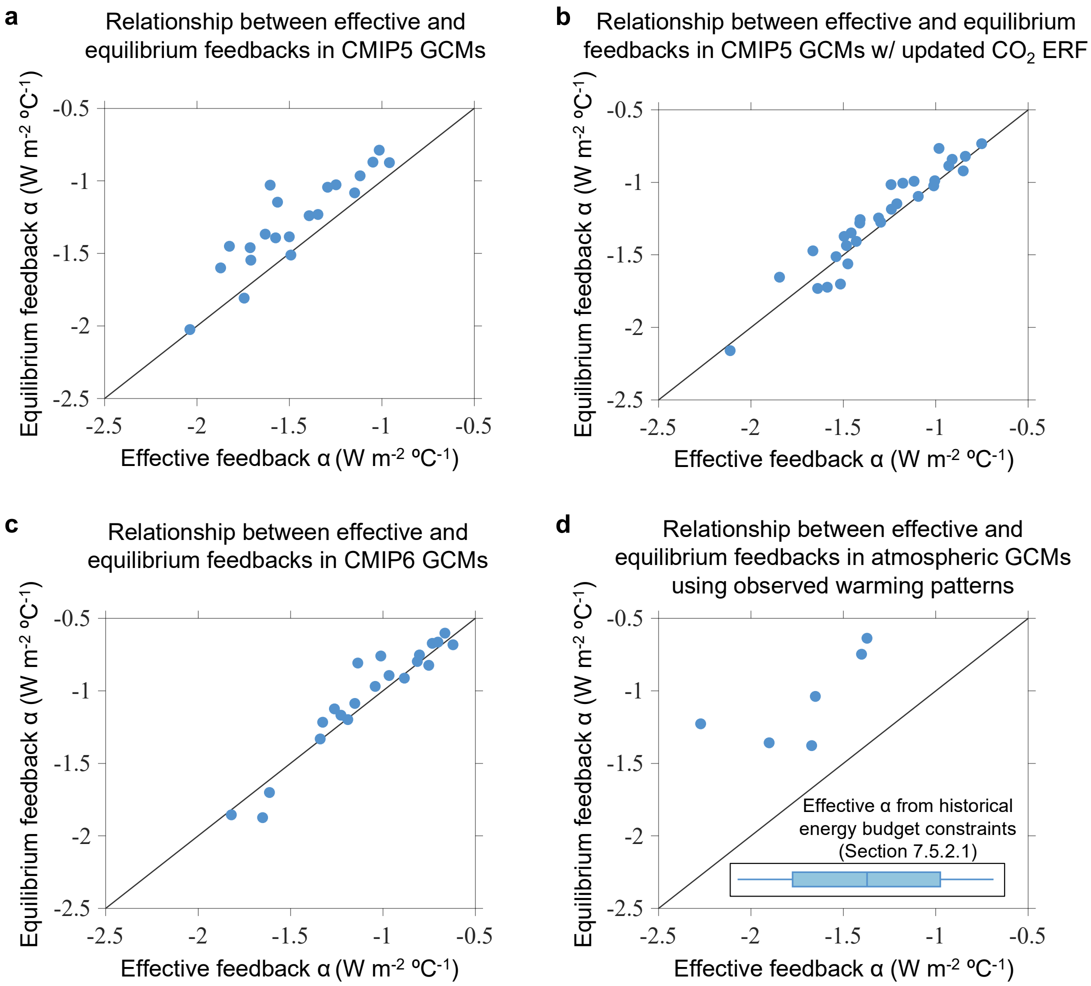


**Figure 7.20:** Relationship between effective and equilibrium radiative feedbacks in CMIP5 and CMIP6 models. (a) CMIP5 effective feedback values estimated by using year 100 of 1%/yr $CO_2$ ramping simulations as an analog for historical warming (Armour, 2017). (b) CMIP5 effective feedback values estimated by using year 100 of 1%/yr $CO_2$ ramping simulations as an analog for historical warming with updated estimates of $CO_2$ radiative forcing (Lewis & Curry, 2018). (c) CMIP6 effective feedback values estimated by regression over the first 50 years of abrupt $CO_2$ quadrupling (abrupt4xCO2) simulations as an analog for historical warming with updated estimates of $CO_2$ radiative forcing (Dong et al., submitted). (d) Effective radiative feedbacks estimated from atmospheric GCMs with prescribed observed sea-surface temperature and sea-ice concentration changes (Andrews et al., 2018) based on linear regression of global TOA radiation against global near-surface air temperature over the period 1870-2010 (pattern of warming similar to Figure 7.19a) and compared with equilibrium feedbacks in abrupt4xCO2 simulations of coupled versions of the same GCMs (pattern of warming similar to Figure 7.19b). The inset shows the effective radiative feedback estimated from historical global energy budget constraints (Section 7.5.2.1); vertical bar shows median value, box shows 17 to 83% range, and horizontal line shows 5% to 95% range. In all cases, the equilibrium feedback magnitudes are estimated as $CO_2$ ERF divided by ECS where ECS is derived from linear regression over years 1-150 of abrupt4xCO2 simulations (Box 7.1); similar results are found if the equilibrium feedback is estimated directly from the regression of global TOA radiation against global near-surface air temperature over years 1-150 of abrupt4xCO2 simulations.

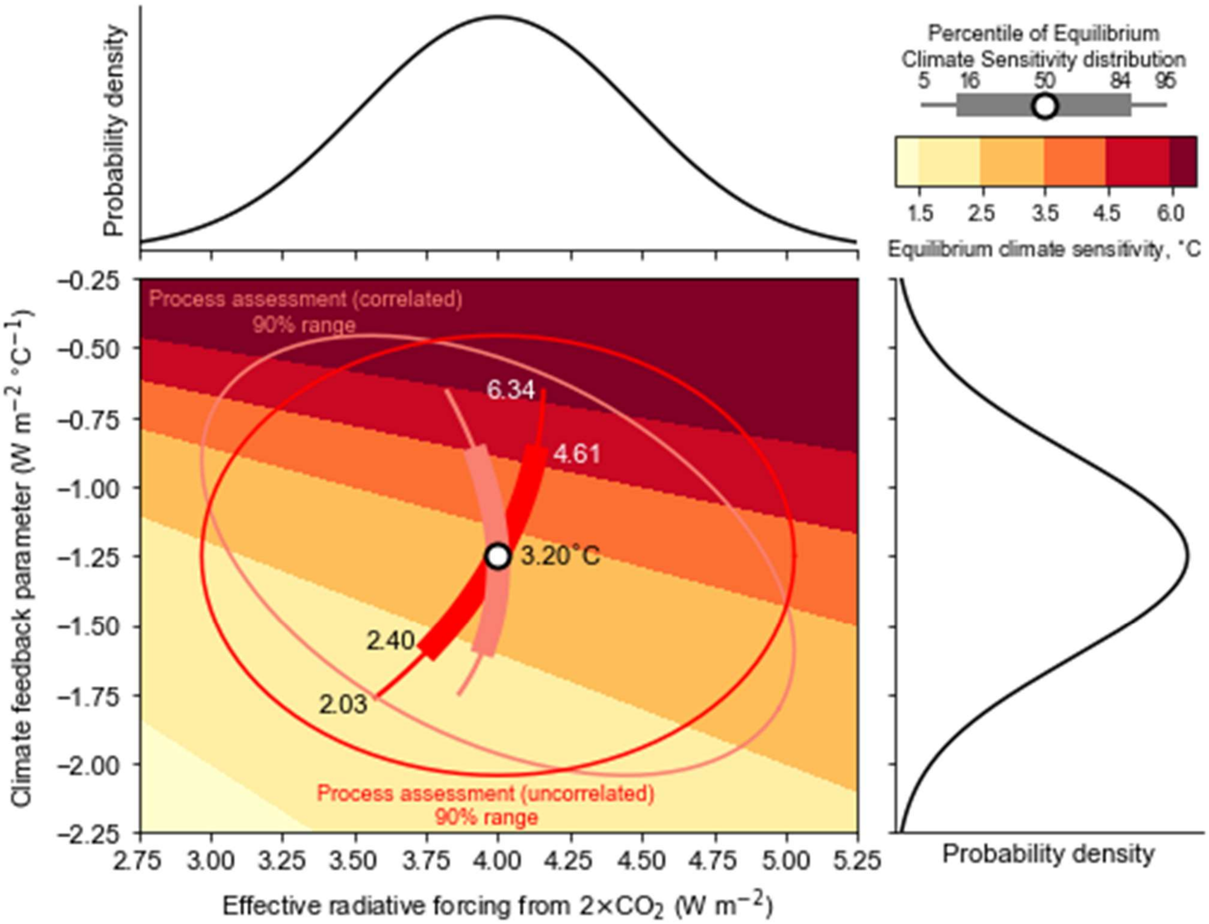


**Figure 7.21:** Probability distributions of ERF to CO2 doubling ($\Delta F_{2\times CO2}$, top) and the total climate feedback (α, right), derived from process-based assessments in Sections 7.3.2 and 7.4.2. Middle panel shows the joint PDF calculated on a two-dimensional plane of $\Delta F_{2\times CO2}$ and α (red), on which the 90% range shown by an ellipse is imposed to the background theoretical values of ECS (colour shading). The white dot, thick and thin curves in the ellipse represent the mean, likely and very likely range of ECS. An alternative estimation of the ECS range (pink) is calculated by assuming that $\Delta F_{2\times CO2}$ and α have a covariance. The assumption about the co-dependence between $\Delta F_{2\times CO2}$ and α does not alter the mean estimate of ECS but affects its uncertainty.

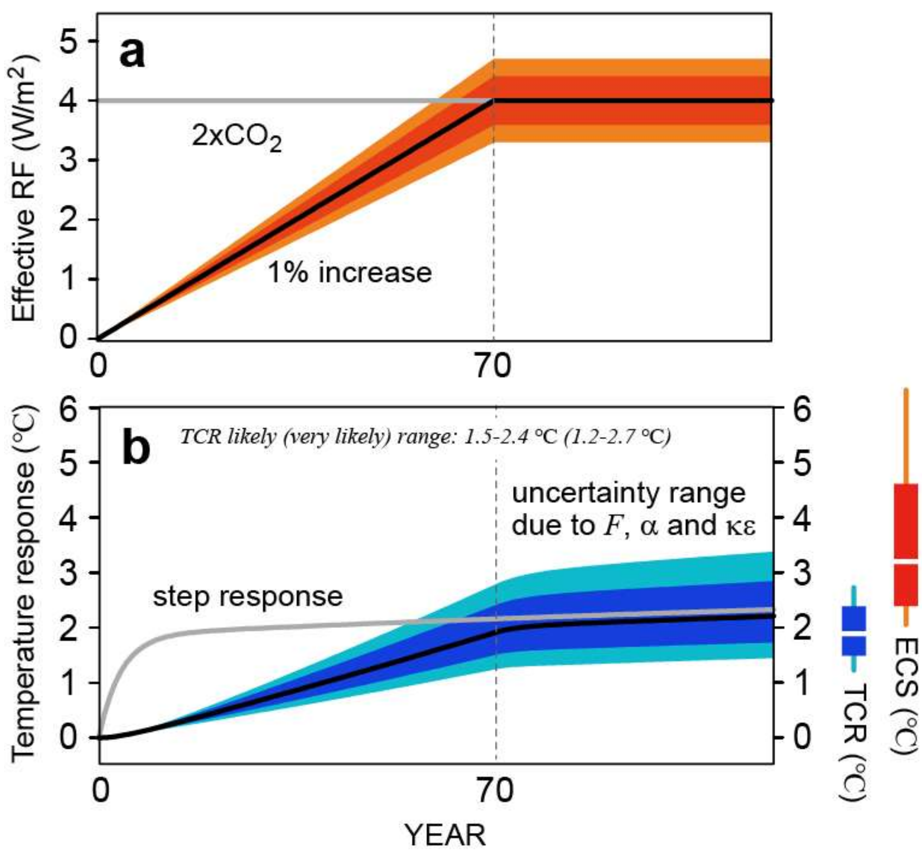


**Figure 7.22:** (a) Time evolution of the effective radiative forcing (ERF) to the $CO_2$ concentration increased by 1% per year until the year 70 (equal to the doubling, grey line) and kept fixed afterword. The range of ERF has been assessed in Section 7.3.2.1. (b) Range of surface temperature response to the $CO_2$ forcing in the two-layer EBM calculated with a given range of ECS, considering uncertainty in $\Delta F_{2\times CO2}$,$\alpha$ and an additional parameter associated with the ocean heat uptake and efficacy (shaded by blue and cyan). For comparison, the step response to abrupt doubling of the $CO_2$ concentration is displayed by a grey curve. The mean and ranges of ECS and TCR are shown at the right (the values of TCR also presented in the panel).

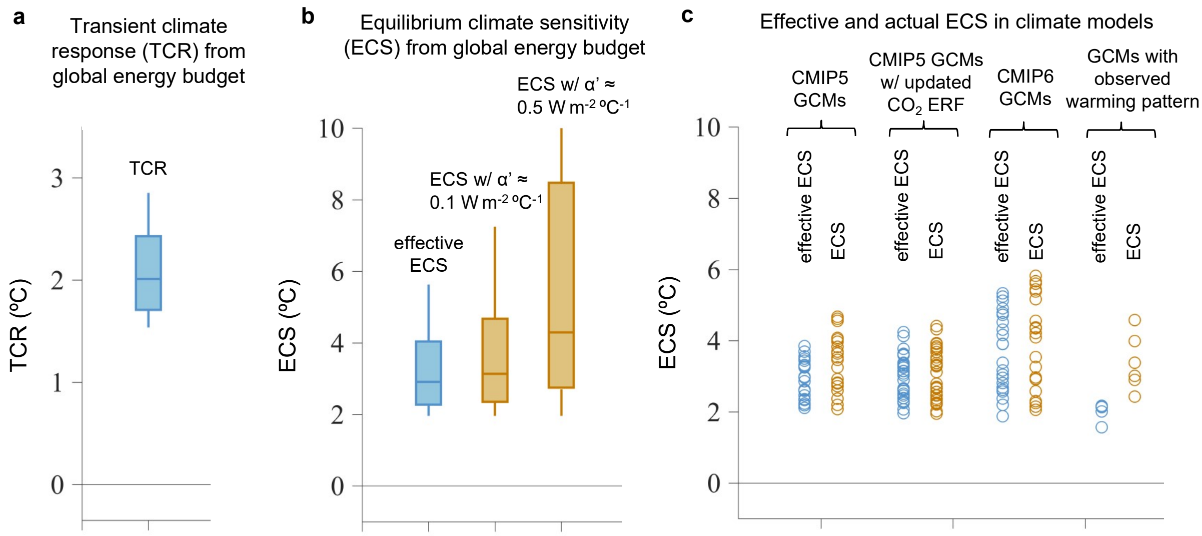


**Figure 7.23:** (a) Transient climate response (TCR) estimated from global energy budget constraints for the period 2006–2018 relative to 1850–1900; horizontal bar shows median value, box shows 17 to 83% range, and vertical line shows 5% to 95% range. (b) Effective equilibrium climate sensitivity (ECS) estimated from global energy budget constraints for the period 2006–2018 relative to 1850–1900 (blue) and ECS accounting for the pattern effect (orange) (Section 7.4.4.3) based on feedback changes derived from coupled GCM simulations (middle, using $\alpha' = +0.1 \pm 0.3$ W m$^{-2}$ °C–1) or from feedback changes assessed from multiple lines of evidence including GCM simulations with prescribed historical sea-surface temperature and sea-ice concentrations (right, using $\alpha' = +0.5 \pm 0.5$ W m$^{-2}$ °C$^{-1}$). (c) Relationship between effective ECS (blue) and actual ECS (orange) in CMIP5 and CMIP6 GCMs where the effective ECS is derived from coupled GCM simulations ('CMIP5 GCMs' Armour, 2017; 'CMIP6 GCMs' Dong et al., submitted; 'CMIP5 GCMs with updated $CO_2$ ERF' Lewis & Curry, 2018) or from GCM simulations with prescribed historical sea-surface temperature and sea-ice concentrations ('GCMs with observed warming pattern' Andrews et al., 2018). The actual ECS in models is estimated from simulations of abrupt $CO_2$ quadrupling (Box 7.1).

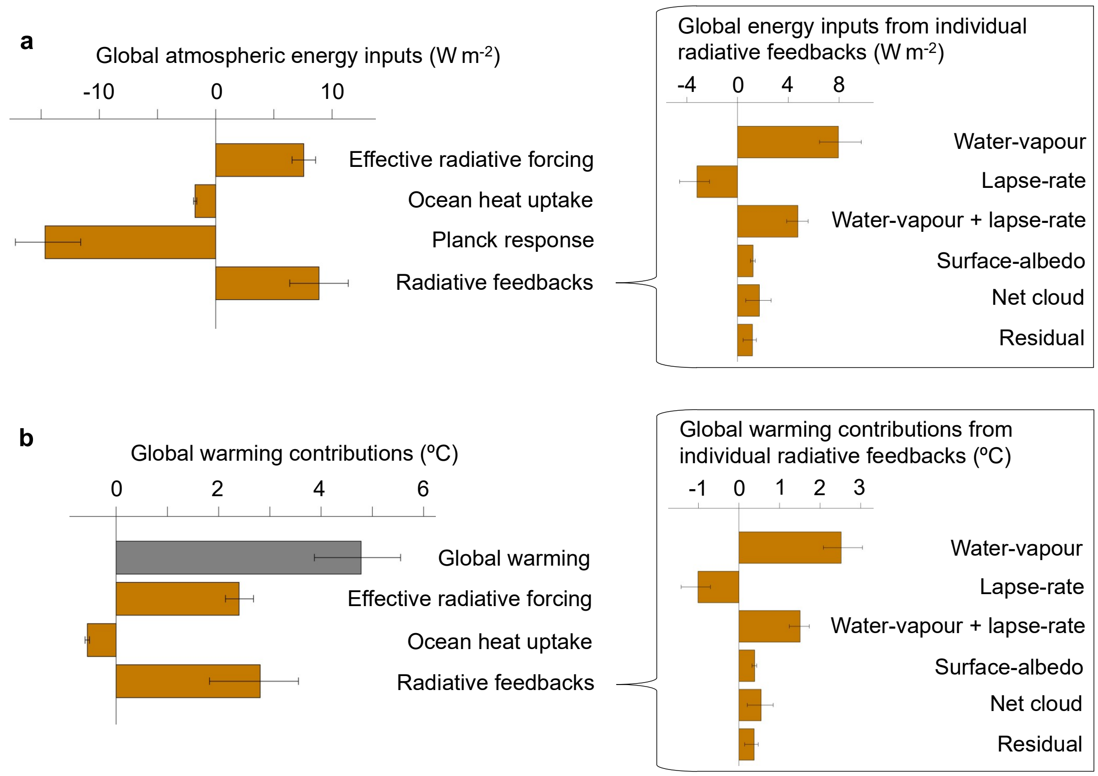


**Figure 7.24:** Contributions of effective radiative forcing, ocean heat uptake and radiative feedbacks to global atmospheric energy input and near-surface air temperature change at year 100 of abrupt $CO_2$ quadrupling simulations of CMIP5 models. (a) The energy flux to the global atmosphere associated with the effective $CO_2$ forcing, global ocean heat uptake, Planck response, and radiative feedbacks, which together sum to zero; inset shows energy input from individual feedbacks, summing to the total feedback energy input. (b) Contributions to net global warming calculated by dividing the energy inputs by the global Planck response (3.2 W $m^{-2}$ $°C^{-1}$), with the contributions from radiative forcing, ocean heat uptake, and radiative feedbacks summing to the value of net warming; inset shows warming contributions associated with individual feedbacks, summing to the total feedback contribution. Uncertainties show 25% and 75% percentiles across models. Feedbacks are calculated using radiative kernels (Shell et al., 2008) and the analysis is based on that of Goosse et al. (2018).

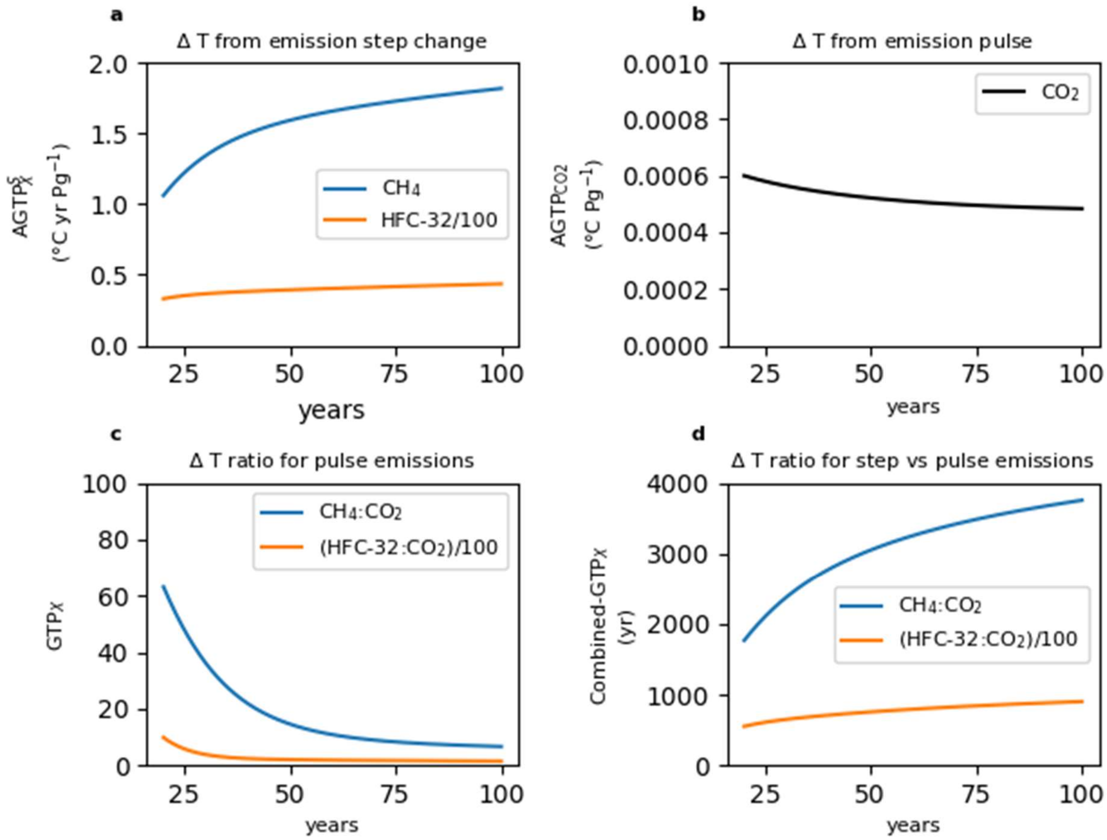


**Figure 7.25:** Emission metrics for two SLCFs: HFC-32 and $CH_4$, (lifetimes of 5.2 and 12.4) years. The temperature response function comes from (Geoffroy et al., 2013a) which has a climate sensitivity of 0.885 °C (W $m^{-2})^{-1}$. Values for non-$CO_2$ species include the carbon cycle response (Section 7.6.2.3). Results for HFC-32 have been divided by 100 to show on the same scale. (a) temperature response to a step change in SLCF emission. (b) temperature response to a pulse $CO_2$ emission. (c) conventional GTP metrics (pulse vs pulse). (d) combined-GTP metric (step vs pulse).

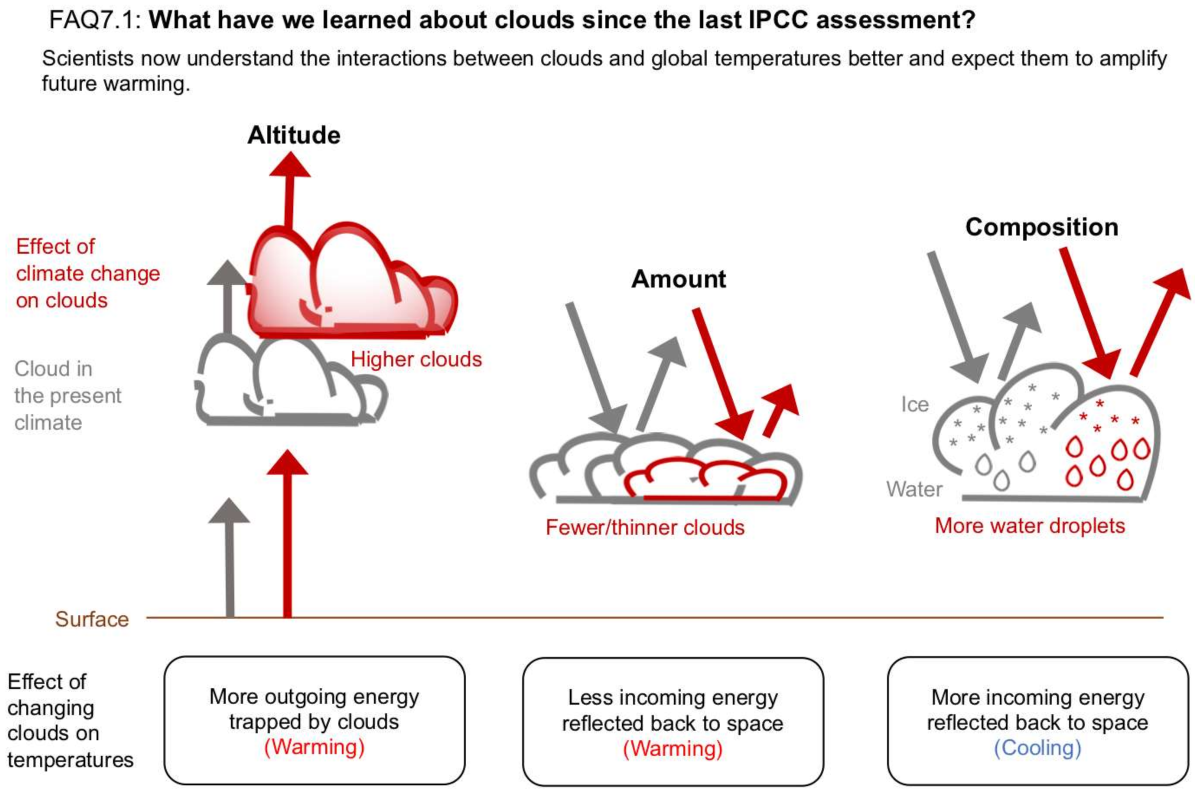


**FAQ 7.1, Figure 1**: Schematic illustration of different types of clouds in the present climate (grey) and their response to surface warming (red). From the left to right: high-level thick clouds, low-level thin clouds, and mixed-phase clouds over the high latitudes. Arrows represent radiative fluxes. Physical processes associated with the changes in cloud property and the resultant sign of the feedback are described at the bottom.

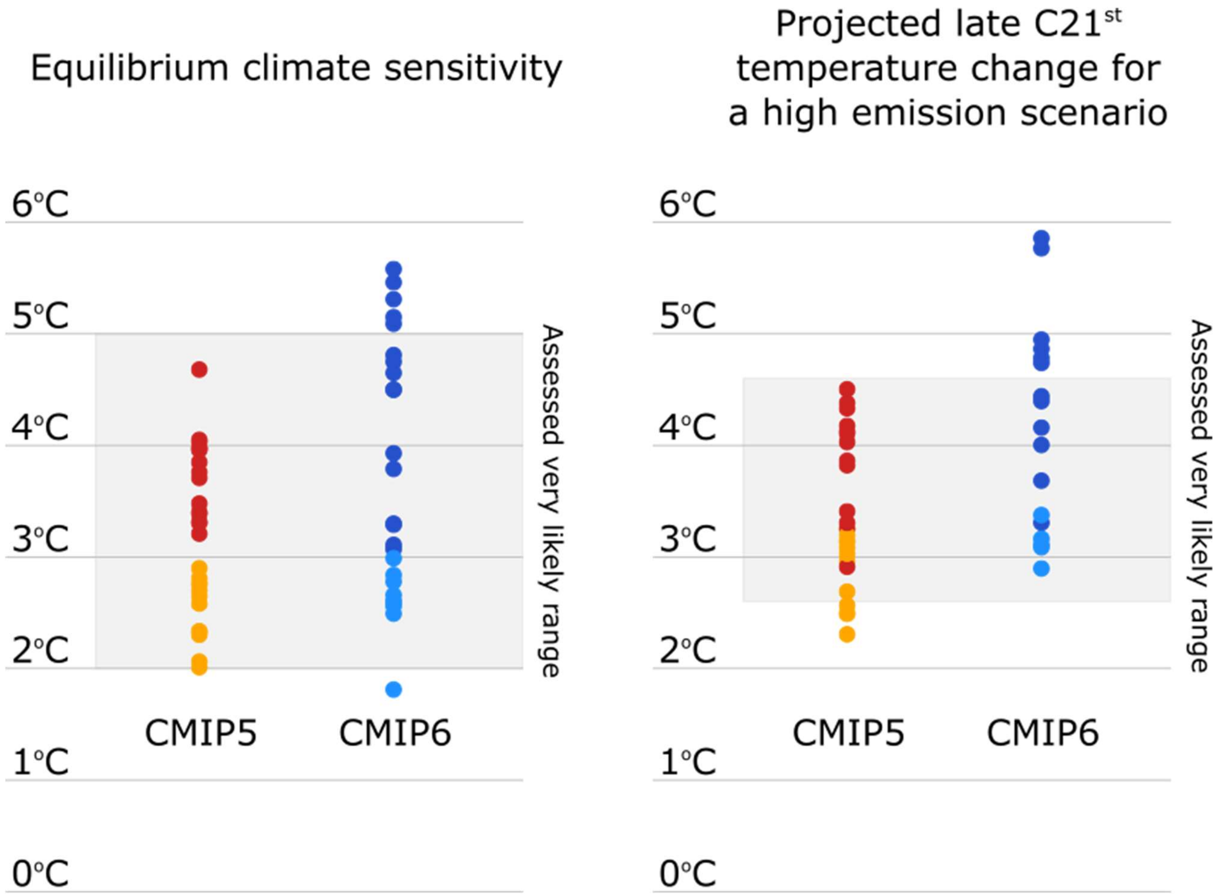


**FAQ7.2, Figure 1:** The left panel shows equilibrium climate sensitivity estimated from the latest generation of climate models (CMIP6), the previous generation used in the AR5 assessment report (CMIP5) and the assessed *very likely* range from Chapter 7. The right panel shows the projected temperature change for a future high emission scenario over 2090-2100 for CMIP6, CMIP5, and from the assessed range in Chapter 4.